

Round Robin Posttest Analysis of a Steel Containment Vessel Model

Sandia National Laboratories

**U.S. Nuclear Regulatory Commission
Washington, DC 20555-0001**

**Nuclear Power Engineering Corporation
Tokyo, Japan**



AVAILABILITY NOTICE

Availability of Reference Materials Cited in NRC Publications

NRC publications in the NUREG series, NRC regulations, and *Title 10, Energy, of the Code of Federal Regulations*, may be purchased from one of the following sources:

1. The Superintendent of Documents
U.S. Government Printing Office
P.O. Box 37082
Washington, DC 20402-9328
<http://www.access.gpo.gov/su_docs>
202-512-1800
2. The National Technical Information Service
Springfield, VA 22161-0002
<<http://www.ntis.gov>>
1-800-553-6847 or locally 703-605-6000

The NUREG series comprises (1) brochures (NUREG/BR-XXXX), (2) proceedings of conferences (NUREG/CP-XXXX), (3) reports resulting from international agreements (NUREG/IA-XXXX), (4) technical and administrative reports and books [(NUREG-XXXX) or (NUREG/CR-XXXX)], and (5) compilations of legal decisions and orders of the Commission and Atomic and Safety Licensing Boards and of Office Directors' decisions under Section 2.206 of NRC's regulations (NUREG-XXXX).

A single copy of each NRC draft report for comment is available free, to the extent of supply, upon written request as follows:

Address: Office of the Chief Information Officer
Reproduction and Distribution
Services Section
U.S. Nuclear Regulatory Commission
Washington, DC 20555-0001
E-mail: <DISTRIBUTION@nrc.gov>
Facsimile: 301-415-2289

A portion of NRC regulatory and technical information is available at NRC's World Wide Web site:

<<http://www.nrc.gov>>

After January 1, 2000, the public may electronically access NUREG-series publications and other NRC records in NRC's Agencywide Document Access and Management System (ADAMS), through the Public Electronic Reading Room (PERR), link <<http://www.nrc.gov/NRC/ADAMS/index.html>>.

Publicly released documents include, to name a few, NUREG-series reports; *Federal Register* notices; applicant, licensee, and vendor documents and correspondence; NRC correspondence and internal memoranda; bulletins and information notices; inspection and investigation reports; licensee event reports; and Commission papers and their attachments.

Documents available from public and special technical libraries include all open literature items, such as books, journal articles, and transactions, *Federal Register* notices, Federal and State legislation, and congressional reports. Such documents as theses, dissertations, foreign reports and translations, and non-NRC conference proceedings may be purchased from their sponsoring organization.

Copies of industry codes and standards used in a substantive manner in the NRC regulatory process are maintained at the NRC Library, Two White Flint North, 11545 Rockville Pike, Rockville, MD 20852-2738. These standards are available in the library for reference use by the public. Codes and standards are usually copyrighted and may be purchased from the originating organization or, if they are American National Standards, from—

American National Standards Institute
11 West 42nd Street
New York, NY 10036-8002
<<http://www.ansi.org>>
212-642-4900

DISCLAIMER

This report was prepared as an account of work sponsored by an agency of the United States Government. Neither the United States Government nor any agency thereof, nor any of their employees, makes any warranty, expressed or implied, or assumes

any legal liability or responsibility for any third party's use, or the results of such use, of any information, apparatus, product, or process disclosed in this report, or represents that its use by such third party would not infringe privately owned rights.

NUREG/CR-5678
SAND98-2700

Round Robin Posttest Analysis of a Steel Containment Vessel Model

Manuscript Completed: November 1999
Date Published: January 2000

Prepared by
V.K. Luk, E.W. Klamerus

Sandia National Laboratories
Albuquerque, NM 87185-0744

Prepared for

Systems Safety Department
Nuclear Power Engineering Corporation
Tokyo 105, Japan
Under Funds-in-Agreement
No. DE-F104-91AL73734

Office of Nuclear Regulatory Research
U.S. Nuclear Regulatory Commission
Washington, DC 20555-0001 USA
Under Containment Integrity Under
Extreme Loads NRC Job Code A1401

NUPEC Project Manager: T. Hashimoto

NRC Project Manager: J.F. Costello



**NUREG/CR-5678 has been
reproduced from the best available copy.**

Abstract

The Nuclear Power Engineering Corporation (NUPEC)^{*} of Japan and the U.S. Nuclear Regulatory Commission (NRC), Office of Nuclear Regulatory Research, are co-sponsoring and jointly funding a Cooperative Containment Research Program at Sandia National Laboratories (SNL). As a part of this program, a steel containment vessel (SCV) model and contact structure assembly was tested to failure at SNL on December 11–12, 1996. The SCV model is representative of a steel containment for an improved Mark-II Boiling Water Reactor plant in Japan. The geometric scale is 1:10, and the thickness scale is 1:4. The contact structure, a thick, bell-shaped steel shell separated at a nominally uniform distance from the SCV model, provides a simplified representation of some features of the concrete reactor shield building in the actual plant. The objective of the internal pressurization test is to provide measurement data of the structural response of the SCV model up to its failure in order to validate analytical modeling, to find its pressure capacity, and to observe the failure mode and mechanisms.

Eight international groups participated in a Round Robin pretest analysis effort to predict the structural response of the SCV model under pressurization. Before the SCV high pressure test, the Round Robin pretest analysis report was released, and a pretest analysis meeting was arranged for participants to discuss their modeling approaches and analysis results.

Seven of the eight participants also performed the posttest analyses. They are:

Agenzia Nazionale per la Protezione dell'Ambienti (ANPA) [Italy]
Argonne National Laboratory (ANL) [U.S.]
Bhabha Atomic Research Centre (BARC) [India]
General Dynamics Electric Boat Division (GD-EB) [U.S.]
Japan Atomic Energy Research Institute (JAERI) [Japan]
Nuclear Power Engineering Corporation (NUPEC) [Japan]
Sandia National Laboratories (SNL) [U.S.]

Each organization was supplied with the same basic information to use in its analyses. The information package included the design drawings of the SCV model and contact structure, material properties, and certain as-built geometrical measurements of the model for the pretest analysis, and the SCV high pressure test data and the posttest metallurgical evaluation results for the posttest analysis.

This report contains the posttest analysis reports and results submitted by the seven participants. Their analysis results at the 52 specified locations on the SCV model were compiled in comparison plots to facilitate discussions at the posttest analysis meeting held May 20–21, 1998, in Albuquerque, New Mexico.

^{*} The work of the Nuclear Power Engineering Corporation is performed under the contract by the Ministry of International Trade and Industry, Japan.

Contents

Abstract.....	iii
Executive Summary.....	vii
Acknowledgments	ix
Acronyms.....	xi
1. INTRODUCTION	1-1
1.1 Background.....	1-1
1.2 Program Description.....	1-1
1.3 Organization of Report	1-2
2. DESIGN AND INSTRUMENTATION OF STEEL CONTAINMENT VESSEL MODEL AND CONTACT STRUCTURE	2-1
2.1 Design of SCV Model and Contact Structure.....	2-1
2.2 Material Properties.....	2-1
2.3 Model Instrumentation.....	2-2
2.4 Standard Output Locations	2-2
3. SUMMARY OF INTERNAL PRESSURIZATION TEST	3-1
3.1 Low Pressure Testing	3-1
3.2 High Pressure Testing.....	3-1
4. PRETEST ANALYSIS PREDICTIONS VS. EXPERIMENTAL DATA.....	4-1
4.1 Milestones.....	4-1
4.2 Global Structural Response	4-1
4.3 Failure Predictions	4-2
5. POSTTEST EVALUATIONS.....	5-1
5.1 Compilation of Posttest Analysis Results from Participants.....	5-1
5.1.1 Equipment Hatch Area.....	5-1
5.1.2 Free-Field Response	5-2
5.1.3 Top Head Area	5-2
5.1.4 Transition Regions	5-2
5.1.5 General Displacements.....	5-3

5.2	Posttest Metallurgical Evaluation	5-3
5.3	Lessons Learned	5-4
6.	SUMMARY.....	6-1
7.	REFERENCES	7-1
APPENDIX A	COMPILATION OF ANALYSIS RESULTS FROM PARTICIPANTS	A-1
APPENDIX B	ROUND ROBIN PARTICIPANTS' ANALYSIS REPORTS AND RESULTS	B-1
B-1	Agenzia per la Protezione dell' Ambienti (ANPA) Italy	B-3
B-2	Argonne National Laboratory (ANL) U.S.	B-29
B-3	Bhabha Atomic Research Centre (BARC) India	B-49
B-4	General Dynamics Electric Boat Division (GD-EB) U.S.	B-113
B-5	Japan Atomic Energy Research Institute (JAERI) Japan.....	B-169
B-6	Nuclear Power Engineering Corporation (NUPEC) Japan	B-221
B-7	Sandia National Laboratories (SNL) U.S.	B-275

Figures

2.1.	Sketch of the steel containment vessel (SCV) model and the contact structure (CS).....	2-3
3.1.	Posttest interior view of the equipment hatch.....	3-2
3.2.	Interior view of the equipment hatch.....	3-3
3.3.	Posttest interior view of the small tear at the middle stiffening ring.	3-4
4.1.	Standard Output Location #24 (zero friction case).....	4-3
4.2.	Standard Output Location #24 (nonzero friction case).....	4-3
5.1.	Free-field SCV model response recorded by interior gages in upper conical shell section.....	5-5
5.2.	Free-field SCV model response recorded by exterior gages in upper conical shell section.	5-5

Tables

2.1.	List of SCV Standard Output Locations for the Pretest Analysis.....	2-4
4.1.	Locations and Pressures of First Yield and First Contact between the SCV Model and the CS	4-4
4.2.	Predicted Failure Pressure and Mechanisms.....	4-5

Executive Summary

For the past twenty years, Sandia National Laboratories (SNL) tested and analyzed numerous scale models of containment vessels that had been pressurized to failure as a part of the Containment Integrity Programs sponsored by the U.S. Nuclear Regulatory Commission (NRC). The overall objective of the programs was to investigate the adequacy of analytical methods used to predict the performance of light water reactor (LWR) containment vessels subject to loads beyond the design basis. Five steel containment scale models and a reinforced-concrete containment model were tested. For the static internal pressurization test of the reinforced-concrete containment scale model, a number of organizations in the United States and Europe performed the pretest and posttest analyses of the scale model. This activity, referred to as a Round Robin analysis, occurred in the mid- to late-1980s.

Starting in 1991, SNL has been conducting a Cooperative Containment Research Program for LWR containments under the joint sponsorship of the Nuclear Power Engineering Corporation (NUPEC)^a of Tokyo, Japan and the NRC. This program involves the testing of two scale models: a steel containment vessel (SCV) model for an improved boiling water reactor (BWR) Mark-II containment vessel and a prestressed concrete containment vessel (PCCV) model. This report discusses the Round Robin posttest analyses of the internal pressurization test on the SCV model. The SCV model used a mixed-scale design: 1:10 for the geometry scale and 1:4 for the thickness scale. The objective of the test was to measure the failure pressure of the SCV model, to observe the failure mode and mechanisms, and to collect data on its structural response up to failure to compare with analytical predictions. The test assembly includes a bell-shaped steel contact structure (CS) at a nominally uniform distance from the SCV model. The uniform gap between these two structures permits the SCV model to undergo deformation well beyond the elastic range prior to its contact with the CS. The CS, a much simplified representation of a concrete shield building in a physical plant, was intended to study the SCV model behavior after it makes contact with the CS. The SCV/CS structural assembly provides specific features of the interaction to be investigated, including closure of gap, progression of contact, and load sharing between the SCV model and the CS.

In separate efforts, NUPEC conducted a full-scale hatch test, a biaxial tensile test, and a scaled cylindrical vessel failure test. The purpose of these tests is to provide additional information on containment vessel deformation behavior to supplement the SCV model pressure test.

Eight organizations from the U.S., Europe, and Asia participated in the Round Robin pretest analysis activity to predict the response of the coupled SCV/CS assembly. Seven of those eight groups performed the posttest analyses after they were given the test data from the high pressure test. The seven groups are:

Agenzia Nazionale per la Protezione dell'Ambienti (ANPA) [Italy]
Argonne National Laboratory (ANL) [U.S.]
Bhabha Atomic Research Centre (BARC) [India]
General Dynamics Electric Boat Division (GD-EB) [U.S.]
Japan Atomic Energy Research Institute (JAERI) [Japan]
Nuclear Power Engineering Corporation (NUPEC) [Japan]
Sandia National Laboratories (SNL) [U.S.]

NUPEC and the NRC jointly invited these international organizations to participate in the Round Robin analyses which were coordinated by SNL. Each organization was provided with the same basic information, including the design drawings of the SCV model and the CS, the material properties, and certain as-built geometrical measurements of the model for the pretest analyses, and the SCV high pressure test data and the posttest metallurgical evaluation results for the posttest analyses. All participants were instructed to provide the pretest predictions and the posttest analysis results at specified locations on the SCV model to facilitate comparison and discussion of analysis results and to correlate with the test data. A Round Robin pretest analysis meeting was held October 1-2,

^a The work of the Nuclear Power Engineering Corporation is performed under the contract by the Ministry of International Trade and Industry, Japan.

1996, in Albuquerque, New Mexico, prior to the SCV high pressure test which was conducted on December 11-12, 1996. The posttest analysis meeting took place on May 20-21, 1998, also in Albuquerque, New Mexico.

This report contains the posttest analysis reports and results submitted by the seven participants. Their posttest analysis results are compared with the test data at 52 locations on the SCV model. The first 43 locations were also selected for the pretest analysis reporting. In general terms, the posttest analysis results provide a more favorable comparison with the test data than their counterparts from the pretest analyses. However, the posttest analysis results have not picked up all the high strain concentration areas indicated by the test data, because some of the local SCV model details which may act as strain risers, such as the weld seams, have not been included in the analysis models.

The SCV model is constructed of SGV480 and SPV490 steel plates. Extensive uniaxial tensile tests were performed on the specimens of these steel plates in the prefabrication stage, and participants used these material property data to construct the material models in the analyses. The SCV high pressure test data and the posttest metallurgical evaluation results suggest that some of these material properties may have been altered by the fabrication processes such as rolling and welding, especially SPV490 steel which has the characteristics of a higher hardness low-carbon martensitic/bainitic steel. The posttest metallurgical evaluation results indicate that in the SCV model, the heat from the welding process caused a localized microstructural change and reduced hardness and strength in the SPV490 steel. The reduced strength in the SPV490 heat affected zone (HAZ) has been identified as the leading factor for the location of the tear in the lower half of the equipment hatch reinforcement plate. Analysis results would suggest tear initiation in the nominally lower strength SGV480 material in the upper half of the plate. Since the full effect of the strength reduction in the SPV490 HAZ is not entirely known, this observed tear can be only approximately simulated in the analysis models.

Acknowledgments

This report would not have been possible without the cooperation and support of many individuals and groups. The Nuclear Power Engineering Corporation (NUPEC) of Tokyo, Japan, the U.S. Nuclear Regulatory Commission (NRC), and Sandia National Laboratories (SNL) are pleased to have had the participation of the following individuals and their organizations in the SCV Round Robin posttest analysis activities:

Dr. Phillip Pfeiffer: Argonne National Laboratory (ANL) [U.S.],

Mr. Giovanni Pino and Mr. Giuseppe Maresca: Agenzia Nazionale per la Protezione dell' Ambienti (ANPA) [Italy],

Dr. H.S. Kushwaha: Bhabha Atomic Research Centre (BARC) [India],

Mr. Kenneth Arpin and Ms. A. Beacham: General Dynamics Electric Boat Division (GD-EB) [U.S.], and

Dr. Jun Sugimoto: Japan Atomic Energy Research Institute (JAERI) [Japan].

These organizations received no financial support from NUPEC, NRC, or SNL, and their efforts are gratefully acknowledged.

The authors also wish to acknowledge the guidance, support, and encouragement of Dr. Hideo Ogasawara, Director and General Manager, Systems Safety Department, of NUPEC; and Dr. James F. Costello, Structural and Geological Engineering Branch, Division of Engineering Technology, Office of Reactor Research, Nuclear Regulatory Commission.

Acronyms

ANL	Argonne National Laboratory
ANPA	Agenzia Nazionale per la Protezione dell' Ambienti
BARC	Bhabha Atomic Research Centre
BWR	boiling water reactor
CS	contact structure
GD-EB	General Dynamics Electric Boat Division
HAZ	heat affected zone
JAERI	Japan Atomic Energy Research Institute
LWR	light water reactor
MCI	material change interface
MPA	Stuttgart Staatliche Materialprüfungsanstalt, Universität Stuttgart
NRC	Nuclear Regulatory Commission
NUPEC	Nuclear Power Engineering Corporation
PCCV	prestressed concrete containment vessel
RSG	rosette strain gage
SCV	steel containment vessel
SNL	Sandia National Laboratories
STG	strip strain gage

1. INTRODUCTION

1.1 Background

The Cooperative Containment Research Program at Sandia National Laboratories (SNL) is co-sponsored and jointly funded by the Nuclear Power Engineering Corporation (NUPEC)^b of Japan and the U.S. Nuclear Regulatory Commission (NRC), Office of Nuclear Regulatory Research. The purpose of the program is to investigate the response of representative scale models of nuclear containments to pressure loading beyond the design-basis accident and to compare analytical predictions to measured behavior. This is accomplished by conducting static, pneumatic overpressurization tests of scale models at ambient temperature. There are two scale models in this research program: the steel containment vessel (SCV) model and the prestressed concrete containment vessel (PCCV) model.

Prior to the pressure testing of the scale models, a number of groups were invited to participate in a Round Robin pretest analysis effort to perform predictive modeling of the response of scale models to overpressurization. There is a similar exercise on Round Robin posttest analysis for participants to improve the modeling techniques after reviewing the test data from the pressure tests. The scale models were constructed by NUPEC, which is funding SNL for planning and site preparation, review of the model design and design support, instrumentation and data collection, and reporting. The NRC is funding SNL to perform analyses of the models and conduct the tests. Both NUPEC and the NRC are funding SNL to coordinate the Round Robin pretest and posttest analysis activities.

1.2 Program Description

The first test in the Cooperative Containment Research Program consists of pressure testing a mixed-scale SCV model. The model is representative of a steel containment for a Japanese-improved Mark-II Boiling Water Reactor containment. The geometric scale is 1:10. However, because the same materials are being used for the model as for the actual plant, the scale on the wall thickness was set at 1:4 for

manufacturability and material availability. The SCV model, fabricated at the Hitachi Works, Japan, arrived at SNL on March 8, 1995, and was installed in the fragment barrier on March 22, 1995. The fragment barrier, which houses the SCV model during instrumentation and pressure tests, is designed to contain the fragments and safely vent the overpressure from a probable catastrophic failure of the model at a maximum pressure of 12.4 MPa (1800 psig). Instrumentation of the model consists of more than 800 channels of data, including strain gages, displacement transducers, and pressure and temperature sensors, as well as visual monitoring. A steel contact structure (CS) is placed over the SCV model prior to the pressure testing to represent some features of the concrete reactor shield building in the actual plant. During the high pressure test, the SCV model expands and comes into contact with the CS, resulting in deformation and failure modes which include the effects of contact from a combination of pressure and thermal growth.

The SCV model test is intended to accomplish the following specific objectives:

1. To provide experimental data for validating the predictive capabilities of analytical methods representing certain aspects of the static internal pressure response of a steel containment, first beyond the elastic range without consideration of contact with a surrounding shield structure or thermal effects, then after contact with a surrounding shield structure.
2. To provide experimental data for the evaluation of steel containments.

The high pressure test of the SCV model was conducted December 11–12, 1996, at SNL. The test is detailed in Luk et al., 1997; Matsumoto et al., 1997; and Luk et al., 1998. The portion of the test data relevant to the Round Robin analysis was released to all eight participants who joined in the Round Robin pretest analysis activities^c. Seven of the eight groups performed the posttest analyses. They are:

^b The work of the Nuclear Power Engineering Corporation is performed under the contract by the Ministry of International Trade and Industry, Japan.

^c Klamerus, E. W., "SCV High Pressure Test Data for Round Robin Analysis," Project Report No. R-SN-S-007, Rev. A, September 1997, Rev. B, January 1998, Sandia National Laboratories, Albuquerque, NM.

- Agenzia Nazionale per la Protezione dell'Ambienti (ANPA) [Italy]
- Argonne National Laboratory (ANL) [U.S.]
- Bhabha Atomic Research Centre (BARC) [India]
- General Dynamics Electric Boat Division (GD-EB) [U.S.]
- Japan Atomic Energy Research Institute (JAERI) [Japan]
- Nuclear Power Engineering Corporation (NUPEC) [Japan]
- Sandia National Laboratories (SNL) [U.S.]

1.3 Organization of Report

This report presents the posttest analysis reports and results submitted by the seven participants. Appendix A contains the comparison plots of their posttest analysis results with the test data at the 43 standard output locations and 9 additional locations: 2 for locations of high strain concentrations near the equipment hatch reinforcement plate and 7 for free-field SCV model response in the upper conical shell sec-

tion. The individual analysis reports from the participants are available in Appendix B.

The rest of the report is assembled similarly to the Round Robin posttest analysis report for the 1:6-scale reinforced concrete containment model (Clauss, 1989). Section 2 describes briefly the design and the instrumentation of the SCV model and the CS and the measured properties data on the steel materials used in the SCV model construction. A more detailed version of this description is available in Luk et al., (1998). Section 3 provides a summary of the low and the high pressure tests and some highlights of the high pressure test results. The pretest analysis predictions are compared with the test data at the 43 standard output locations in Section 4. Section 5 focuses on evaluating posttest analysis results, summarizing the posttest metallurgical evaluation results, and discussing the lessons learned from the Round Robin pretest and posttest analysis activities. Section 6 presents a summary of the Round Robin posttest analysis effort, and references are given in Section 7.

2. DESIGN AND INSTRUMENTATION OF STEEL CONTAINMENT VESSEL MODEL AND CONTACT STRUCTURE

2.1 Design of SCV Model and Contact Structure

The SCV model is scaled 1:4 in shell thicknesses and 1:10 in overall geometry from a prototype Mark-II Boiling Water Reactor (BWR) containment structure. The model is 2.9 m in diameter and 5.9 m tall, with an enclosed volume of about 21 m³. The model weighs 15,800 kg. The design pressure of the prototype containment is 0.31 MPa (45 psig).

Containment details that are included in the steel containment vessel (SCV) model include: the equipment hatch penetration and reinforcement plate (the hatch is not to scale, and the hatch cover is welded shut); the drywell head (also welded shut); and the SGV480/SPV490 material transition location. All other hatches, airlocks, and penetrations were omitted from the SCV model. In addition, the lower wetwell and wall-basemat junction has been replaced by a thick bottom head that is designed to ensure that failure will not occur there during the high pressure test, and that deformations in this area will be minimal. All internal structures not essential to the vessel deformation responses have been omitted from the model. All thickness variations in the model occur on its outer surface; the inner surface of the model is smooth.

Figure 2.1, an outline sketch of the SCV model, illustrates its sections and features such as the top flange, the knuckle region, several stiffeners, the equipment hatch with reinforcement plate, and an interface where two dissimilar steel materials come together at a butt weld. The design drawings of the SCV model are included in Appendix A of Luk and Klamerus (1996).

A special feature of the SCV test project is the contact structure (CS) which allows investigation of the response of the SCV model against an almost rigid surrounding shield structure during pressurization. It is not, however, intended to simulate the effects of the concrete shield building in physical plants. The CS, designed to remain essentially elastic until the SCV model reaches an internal pressure of approximately 10 P_o, is a bell-shaped structure (Figure 2.1) constructed of SA-516-70 steel with a nominal thickness of 38 mm. This material has a nominal yield strength of 258 MPa and a nominal ultimate strength

of 476 MPa. The bottom of the CS was welded to the top surface of the ring support girder after it was placed over the SCV model. It did not touch the surface of the model at any point prior to the high pressure test.

Four arrays of holes, 90° apart, were drilled in the CS, both to measure the gap between the CS and the SCV model to align the CS during its installation, and later to install the contact detection devices to measure the gap closure during the high pressure test. The design drawings of the CS are contained in Appendix B of Luk and Klamerus (1996).

The gap between the SCV model and the CS is designed to have a nominal size of 18 mm. After the CS was installed over the SCV model, the gap size between the CS and the SCV model was measured at each of the hole locations. The majority of the measured gap sizes lie between 18 mm and 22 mm; a minimum gap size of 13.4 mm was measured at a hole location below the equipment hatch (Luk and Klamerus, 1996).

2.2 Material Properties

The portion of the SCV model above the ring support girder consists of two materials: SGV480 steel and SPV490 steel. The material properties for these alloys are:

SGV480 steel:

- minimum yield strength: 265 MPa
- tensile strength: 480 to 590 MPa
- minimum elongation after fracture: 17%

SPV490 steel:

- minimum yield strength: 490 MPa
- tensile strength: 610 to 735 MPa
- minimum elongation after fracture:
 - 18% for 9 mm thickness
 - 25% for 17.5 mm thickness

Uniaxial tensile tests on specimens of SGV480 steel and SPV490 steel were also conducted. These specimens were taken from the actual material lots used to construct the SCV model. Tests were performed on material taken from 12 locations on the SCV model. The data on measured material proper-

ties are available in Appendix C of Luk and Klamerus (1996).

2.3 Model Instrumentation

The number and the locations of different types of instruments installed on the SCV model are described in detail in the SCV Instrumentation Plan^d. A brief summary of various types of instruments is provided in this report:

1. Single element, rosette, and strip strain gages were used to measure the strain distributions at the installation locations on the model surfaces, including both membrane and bending components of strains.
2. Variable resistance, linear displacement transducers and cable potentiometers were installed to measure the vertical and horizontal displacements of the SCV model, relative to either the interior wall of the fragment barrier or the central support column inside the SCV model.
3. Contact detection devices were used to monitor the closure of the gap between the SCV model and the CS during the high pressure test.

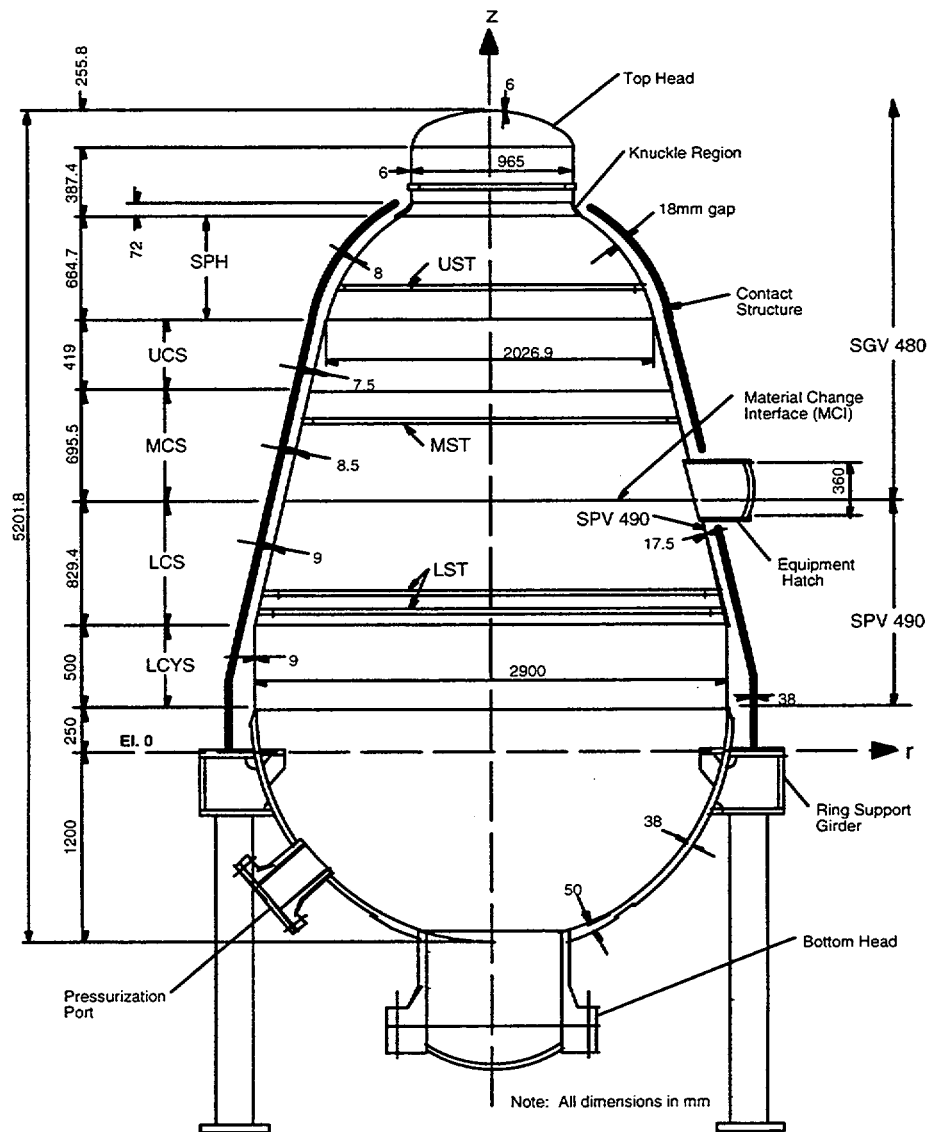
4. Pressure transducers were installed in the SCV model to record the time history of pressure.
5. Thermocouples were used to monitor the temperature variations of the inside surface of the SCV model.

2.4 Standard Output Locations

There are 43 standard output locations chosen for the pretest analysis. An instrument was installed at every standard output location to provide test data to be compared with both pretest and posttest analysis results. Table 2.1 provides a detailed description of coordinates of these locations and the type and identity of instrument.

An additional nine locations (44–52) are selected for the posttest comparisons: two located near the equipment hatch reinforcement plate and seven located in the upper conical shell section for the free-field response of the SCV model. The detailed description of these locations (44–52) is available in Appendix A.

^d Rightley M. J. and Lambert, L. D., "SCV Instrumentation Plan," Project Report No. R-SN-S-001, Rev. B, Sandia National Laboratories, Albuquerque, NM, September 1996.



Nomenclature:

<u>Location Designation</u>	<u>Description</u>
THD	top head
KNU	knuckle
SPH	spherical shell
UST	upper stiffener
UCS	upper conical shell
MST	middle stiffener
MCS	middle conical shell
MCI	material change interface
LCS	lower conical shell
LST	lower stiffeners
LCYS	lower cylindrical shell

Figure 2.1. Sketch of the steel containment vessel (SCV) model and the contact structure (CS).

Table 2.1. List of SCV Standard Output Locations for the Pretest Analysis

Category	Plot ID	Instrument ID	Inst. Type	Model Surface	Coord. System	θ, X (degrees, m)	Output Quantity
Equipment Hatch Area (Strains)	1	RSG-I-EQH-12	rosette	inside	Hatch	67.5, 0.36 ^a	max. prin. strain
	2	RSG-I-EQH-8	rosette	inside	Hatch	45, 0.36 ^a	max. prin. strain
	3	STG-O-EQH-4c	strip	outside	Hatch	0, 0.36 ^a	ext. merid. strain
	4	STG-I-EQH-2c	strip	inside	Hatch	0, 0.36 ^a	int. merid. strain
	5	SSGH-O-EQH-18	single	outside	Hatch	90, 0.36 ^a	ext. hoop strain
	6	STG-I-EQH-16c	strip	inside	Hatch	90, 0.36 ^a	int. hoop strain
Top Head Area (Strains)	7	RSG-O-THD-1	rosette	outside	Top	-, 0.00 ^b	max. prin. strain
	8	RSG-O-THD-9	rosette	outside	Top	270, 0.48 ^b	ext. hoop strain
	9	RSG-O-THD-9	rosette	outside	Top	270, 0.48 ^b	ext. merid. strain
	10	RSG-I-THD-10	rosette	inside	Top	270, 0.48 ^b	int. merid. strain
Transition Regions (Strains)	11	STG-O-UCYS-25c	strip	outside	Global	0, 3.47 ^c	ext. merid. strain
	12	SSGM-I-UCYS-27	single	inside	Global	0, 3.47 ^c	int. merid. strain
	13	STG-O-KNU-1c	strip	outside	Global	0, 3.32 ^c	ext. merid. strain
	14	STG-I-KNU-9c	strip	inside	Global	0, 3.32 ^c	int. merid. strain
	15	SSGM-O-MST-1	single	outside	Global	0, 2.10 ^c	ext. merid. strain
	16	SSGM-I-MST-7	single	inside	Global	0, 2.10 ^c	int. merid. strain
	17	SSGM-O-MCI-2	single	outside	Global	0, 1.60 ^c	ext. merid. strain
	18	RSG-I-MCI-1a	rosette	inside	Global	0, 1.60 ^c	int. merid. strain
	19	SSGM-O-LST-17	single	outside	Global	0, 0.80 ^c	ext. merid. strain
	20	SSGM-I-LST-25	single	inside	Global	0, 0.80 ^c	int. merid. strain
Free-Field (Strains)	21	RSG-O-UCS-17	rosette	outside	Global	45, 2.49 ^c	ext. merid. strain
	22	RSG-I-UCS-18	rosette	inside	Global	45, 2.49 ^c	int. merid. strain
	23	RSG-O-UCS-17	rosette	outside	Global	45, 2.49 ^c	ext. hoop strain
	24	RSG-I-UCS-18	rosette	inside	Global	45, 2.49 ^c	int. hoop strain
	25	RSG-O-LCS-5	rosette	outside	Global	45, 1.45 ^c	ext. merid. strain
	26	RSG-I-LCS-6	rosette	inside	Global	45, 1.45 ^c	int. merid. strain
	27	RSG-O-LCS-5	rosette	outside	Global	45, 1.45 ^c	ext. hoop strain
	28	RSG-I-LCS-6	rosette	inside	Global	45, 1.45 ^c	int. hoop strain
	29	RSG-I-SPH-2	rosette	inside	Global	45, 3.13 ^c	int. merid. strain
	30	RSG-I-SPH-2	rosette	inside	Global	45, 3.13 ^c	int. hoop strain
	31	RSG-I-UCS-16	rosette	inside	Global	270, 2.49 ^c	int. merid. strain
	32	RSG-I-UCS-16	rosette	inside	Global	270, 2.49 ^c	int. hoop strain
	33	RSG-I-LCS-11	rosette	inside	Global	270, 1.25 ^c	int. merid. strain
	34	RSG-I-LCS-11	rosette	inside	Global	270, 1.25 ^c	int. hoop strain
General (Disp.)	35	VCP-I-THD-11	rheostat	inside	Top	-, 0.00 ^b	vertical disp.
	36	HCP-O-UCYS-43	rheostat	outside	Global	45, 3.57 ^c	horizontal disp.
		HCP-I-UCYS-39	rheostat	inside	Global	45, 3.57 ^c	horizontal disp.
	37	HCP-I-KNU-17	rheostat	inside	Global	0, 3.32 ^c	horizontal disp.
	38	VCP-I-KNU-18	Rheostat	inside	Global	0, 3.32 ^c	vertical disp.
39	HCP-I-MCI-16	Rheostat	inside	Hatch	-, 0.00 ^a	horizontal disp.	
Equipment Hatch Area (Strains)	40	RSG-I-EQH-45	Rosette	inside	Global	105.2, 1.569 ^c	int. merid. strain
	41	RSG-I-EQH-45	Rosette	inside	Global	105.2, 1.569 ^c	int. hoop strain
	42	RSG-I-EQH-44	Rosette	inside	Global	74.6, 1.569 ^c	int. merid. strain
	43	RSG-I-EQH-44	Rosette	inside	Global	74.6, 1.569 ^c	int. hoop strain

Note: a: θ_H, R_H (H = Hatch)

b: θ_T, R_T (T = Top Head)

c: θ_G, Z_G (G = Global)

3. SUMMARY OF INTERNAL PRESSURIZATION TEST

The conduct of the low and the high pressure tests of the SCV model is described in detail in the Luk et al., 1997; Matsumoto et al., 1997; and Luk et al., 1998. A brief summary of these tests is provided in this report.

3.1 Low Pressure Testing

Two low pressure tests of the SCV model were conducted:

- leak and instrumentation test (0.2 P_d) (October 3, 1996)
- low pressure test (1.5 P_d) (November 7, 1996)

The leak and instrumentation test was conducted to check the functionality of the pressurization system, the instruments, and the data acquisition system. The SCV model was subjected to three cycles of pressure loadings in the test: first cycle to 0.1 P_d and the other two cycles to 0.2 P_d. In each cycle, the pressure was held constant for about 40 minutes to complete all necessary functionality checks. The low pressure test provided a performance check on all operating systems at a higher pressure level than the leak and instrumentation test while the SCV model still behaved elastically. This test also served as a rehearsal for the high pressure test.

3.2 High Pressure Testing

The high pressure test of the SCV model was conducted December 11–12, 1996. This test was allowed to proceed only after the functionality checks of all operating systems were completed because this test was to undergo a monotonic pressure rise and the cycle of unloading and reloading was not desirable. The pretest analyses performed at SNL (Porter et al.,

1996) provided a guide to the pressurization sequence for this test which is described in detail in the Luk et al., 1997; Matsumoto et al., 1997; and Luk et al., 1998.

After approximately sixteen and a half hours of continuous, monotonic pressurization using nitrogen gas, the high pressure test was terminated when a tear developed at a pressure of 4.66 MPa (676 psig) or roughly six times the design pressure. Rapid venting of the SCV model was observed, and the pressurization system, operating at capacity (1300 scfm), was unable to maintain pressure in the SCV model.

Posttest visual inspection of the interior of the SCV model revealed a large tear, approximately 190 mm long, adjacent to the weld at the edge of the equipment hatch reinforcement plate (Fig. 3.1). The tear, graphically shown in Fig. 3.2, appears to have initiated at a point roughly 30 mm below the material change interface in the SPV490 shell and propagated in both directions along the weld seam before it stopped. Interestingly, while the right side of the equipment hatch did not tear, significant necking was observed at a location symmetric with the tear.

In addition, a small meridional tear, approximately 55 mm long, was found in a vertical weld (at an azimuth angle of 201°) underneath a semi-circular opening in the middle stiffener above the equipment hatch (Fig. 3.3). It appears that this small tear might have occurred first but did not grow, and the pressurization system was able to compensate for any leakage through this tear. This tear also had a counterpart at a similar, diametrically opposed detail. While no tear developed at this latter location, necking in the weld was observed.

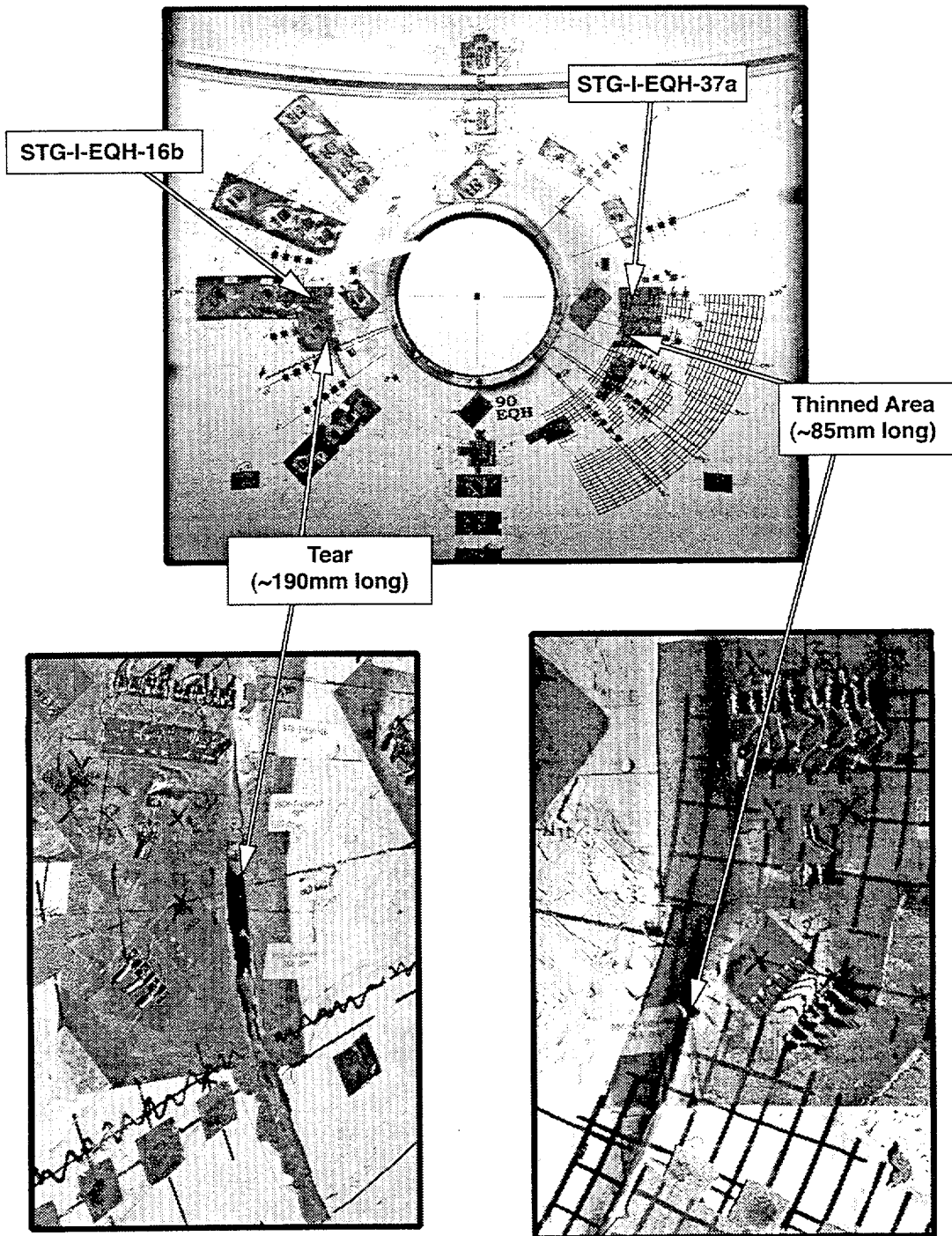
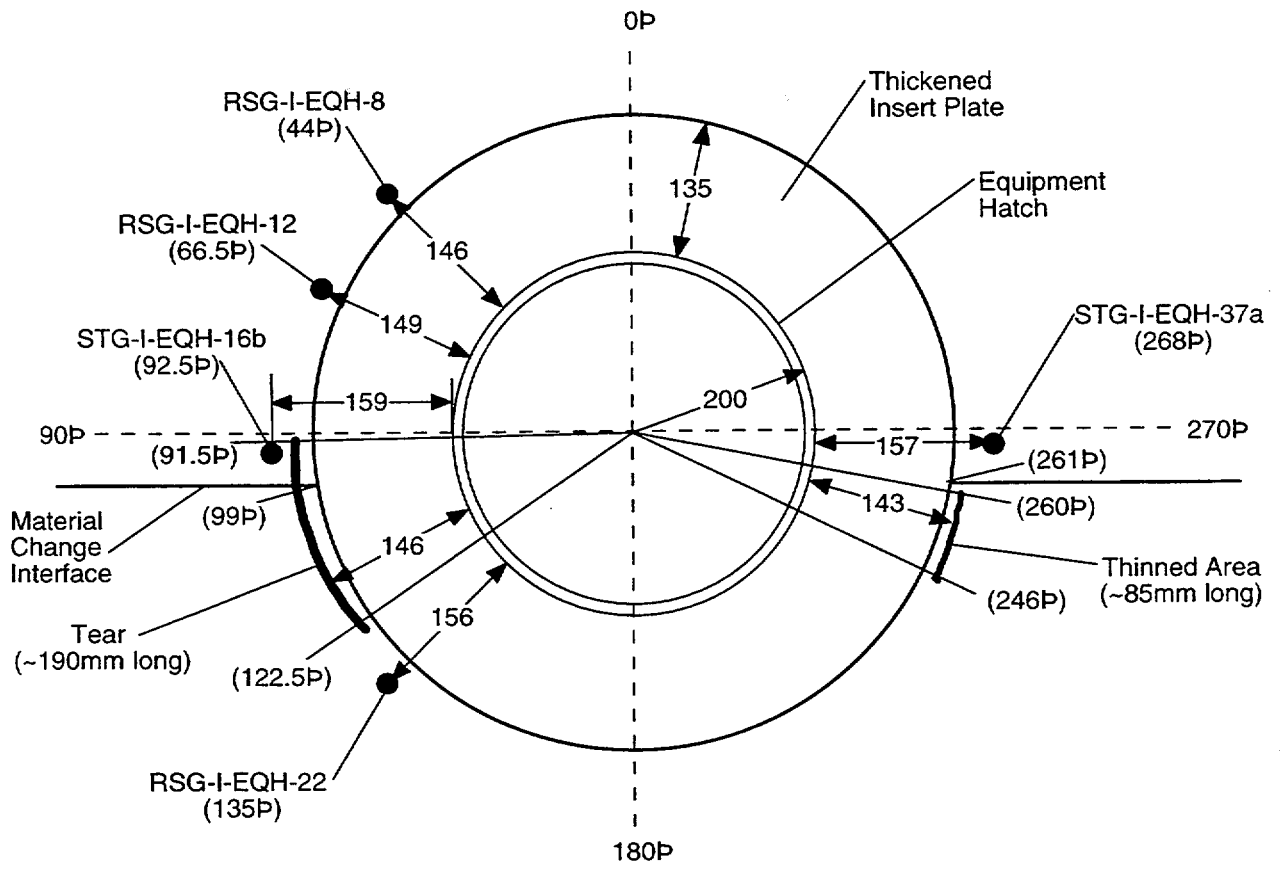


Figure 3.1. Posttest interior view of the equipment hatch.



(inside view)

Note: All dimensions in mm
 STG: strip strain gage
 RSG: rosette strain gage

Figure 3.2. Interior view of the equipment hatch.

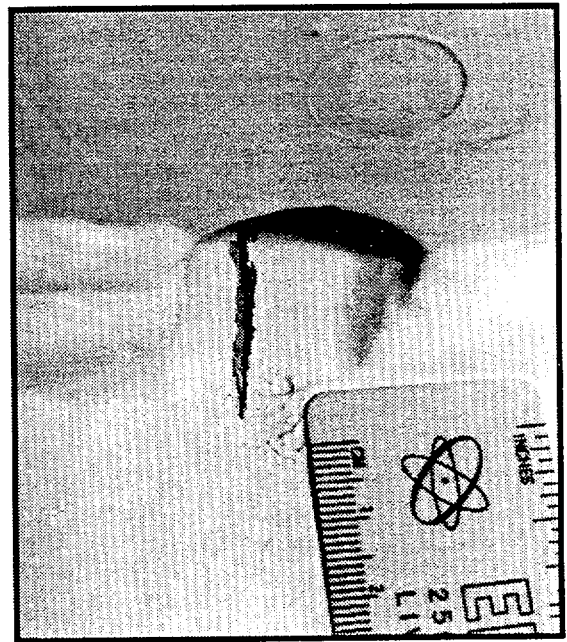
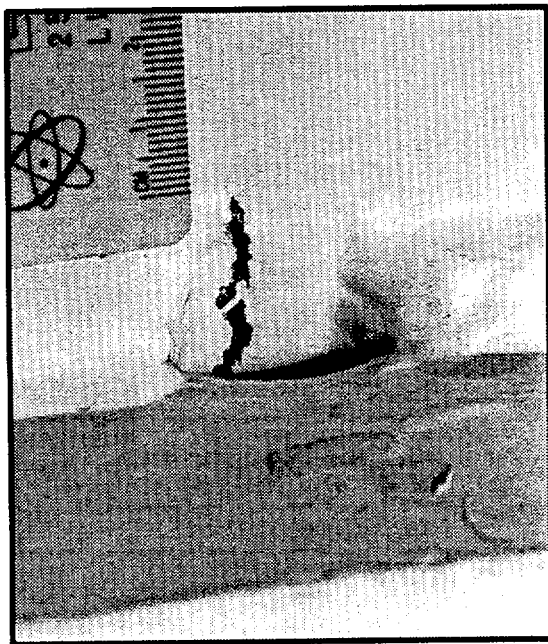
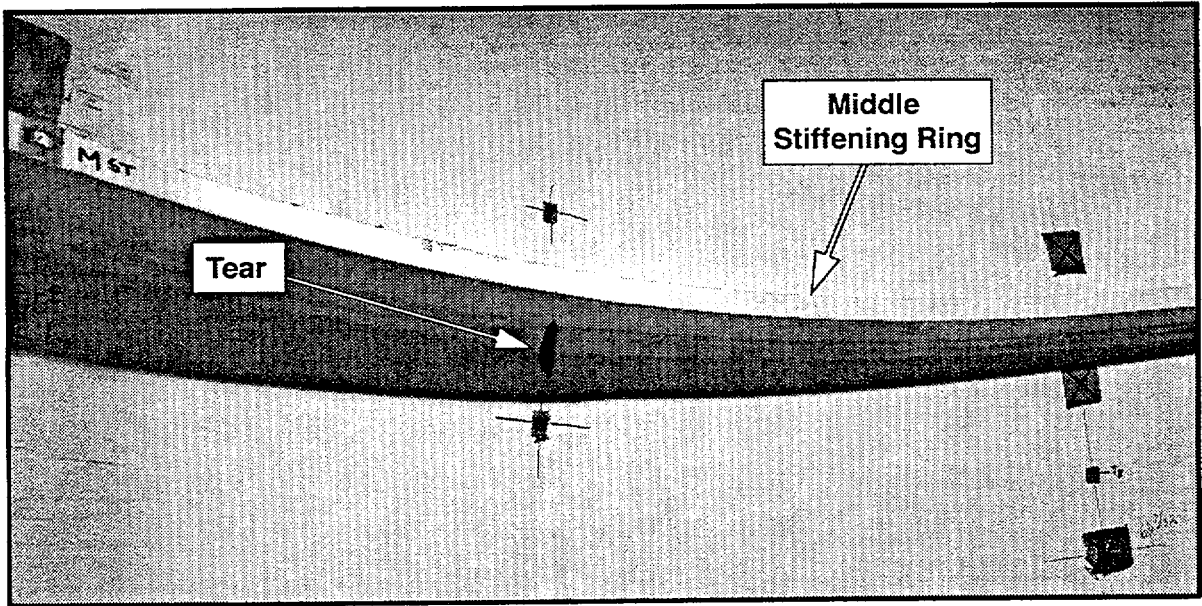


Figure 3.3. Posttest interior view of the small tear at the middle stiffening ring.

4. PRETEST ANALYSIS PREDICTIONS VS. EXPERIMENTAL DATA

Eight organizations participated in the SCV Round Robin pretest analyses (Luk and Klamerus, 1996). They performed independent finite element analyses to provide the pretest predictions of the structural behavior of the steel containment vessel (SCV) model during the high pressure test. Selected pretest predictions are compared to the experimental data from the high pressure test in this section. The comparisons focus on the major milestones in terms of the pressure and the locations on the SCV model for the first yield and its first contact with the contact structure (CS), the free-field model response, and the failure pressure and location.

4.1 Milestones

All participants were given the same information package for their independent pretest analyses. To obtain a first-order comparison of participants' pretest predictions of the structural behavior of the SCV model, the pressure and the location for the first yield and the first contact between the SCV model and the CS were chosen as the major milestones (Luk and Kalmerus, 1996). These two comparison indicators were chosen to demonstrate the effects of different modeling approaches and input parameters.

Comparison of the pretest analysis predictions of these two milestones to the test data is shown in Table 4.1. Based on the test data from strain gages, the SCV model experienced its first yielding at an azimuth angle of 45° just below the lower stiffening ring at a pressure of 1.65 MPa. At a slightly higher pressure of 1.79 MPa, two locations around the equipment hatch also started to yield. As shown in Table 4.1, the participants predicted that the pressure at which first yield occurred would range from 1.0 to 3.0 MPa. Only ANL and MPA predicted first yield would occur near the equipment hatch, while others predicted it would happen around the knuckle region. None of the participants mentioned that the lower cylindrical shell section would be a probable location for first yield.

The presence of the CS over the SCV model allowed contact to occur between the two structures during the high pressure test. Four arrays of contact detection devices were installed at 90° apart to record the progression of local contacts. The first contact signal was registered by one of these devices located at an azimuth angle of 0° and 1.72 m above the ring sup-

port girder (at an elevation of the equipment hatch) and at a pressure of 4.12 MPa. However, the data recorded by the strip strain gage, STG-O-KNU-1c, installed on the exterior of the SCV model below the knuckle region, suggest that local contact might occur there at a lower pressure of 3.44 MPa. As indicated in Standard Output Location #13, this strain gage failed to function at this pressure, and the post-test inspection of the SCV model revealed that the lead cable attached to this strain gage was crushed. Most probably, the SCV model underwent a considerable amount of vertical growth, resulting in a local contact of the knuckle region with the CS. Six of the eight participants predicted that the first contact would occur near the knuckle region. The predicted pressure for its occurrence ranged from 3.2 to 4.0 MPa.

4.2 Global Structural Response

It is important to investigate the global structural behavior of the SCV model that is not affected by the local structural or geometrical discontinuities. Standard Output Location #24 was chosen as representative of the global response of the SCV model. This location is situated in the upper conical shell section at an elevation of 2.49 m above the ring support girder and at an azimuth angle of 45°. As seen in Figures 4.1 and 4.2, this spot is significantly far away from the equipment hatch, the two stiffening rings, and the meridional weld seams. A rosette strain gage, RSG-I-UCS-18, was installed at this location on the inside surface of the SCV model to record the pressure history of internal hoop strain at this spot.

The internal hoop strains recorded by this rosette gage are plotted with the pretest analysis predictions by participants in Figures 4.1 and 4.2 for the zero and the nonzero friction cases, respectively. The test data indicate that this local area of the SCV model behaved elastically in the initial phase of the pressurization process until the pressure was increased to about 2.4 MPa, then the SCV model started to yield and undergo plastic deformation. The slope of the strain vs. pressure plot was significantly reduced at a pressure of about 4.0 MPa, indicating that local contact between the SCV model and the contact structure might occur at this pressure level.

As evidenced in these two figures, all pretest analysis predictions by participants showed an onset of yielding at a pressure of 3.0 MPa or above. There were many discussions about the probable causes to account for the discrepancies of the SCV model free-field response between the test data and the pretest analysis predictions. ANL suggested that the residual stresses induced in the SGV480 steel plate during the model fabrication process might have some effect on the local structural behavior. The effect of residual stresses was analyzed and reported in the pretest analysis (Luk and Klamerus, 1996), Appendix B-1. The pretest predictions by BARC are the closest to the test data for both zero and nonzero friction cases. A detailed review of the pretest modeling approach by BARC (Luk and Klamerus, 1996) reveals that the material data with the minimum value were used as the material model of SGV480 steel plate, instead of the data set for the local structural section with appropriate thickness. This finding seems to suggest that this structural section may behave like a material with a slightly lower strength than the prefabricated steel plate.

4.3 Failure Predictions

The high pressure test of the SCV model was terminated at a pressure of 4.66 MPa or approximately six

times the design pressure (Matsumoto et al., 1997; Luk et al., 1998). The posttest model inspection revealed a large tear, about 190 mm long, adjacent to the weld at the outside edge of the equipment hatch reinforcement plate (see Fig. 3.2). The tear appears to have initiated at a point roughly 30 mm below the material change interface in the SPV490 shell and propagated in both directions along the weld seam before it stopped. The posttest metallurgical evaluation concludes that the tear was the result of local plastic deformation and ductile shear fracture (Van Den Avyle and Eckelmeyer, 1998). The evaluation results further indicate that no contributing flaws in the SCV model wall were noted at the tear location and that in the SCV model the heat from the welding process resulted in reduced Rockwell B hardness and strength in the heat affected zone very close to the tear.

The participants provided the pretest predictions of the failure pressure and location that are reproduced in Table 4.2 (Luk and Klamerus, 1996). Both GD-EB and SNL predicted that the model failure occurred at a local thinned section near the equipment hatch reinforcement plate at a pressure level very close to the test failure pressure. However, the predicted failure mechanisms by both groups differ from the findings of the posttest metallurgical evaluation.

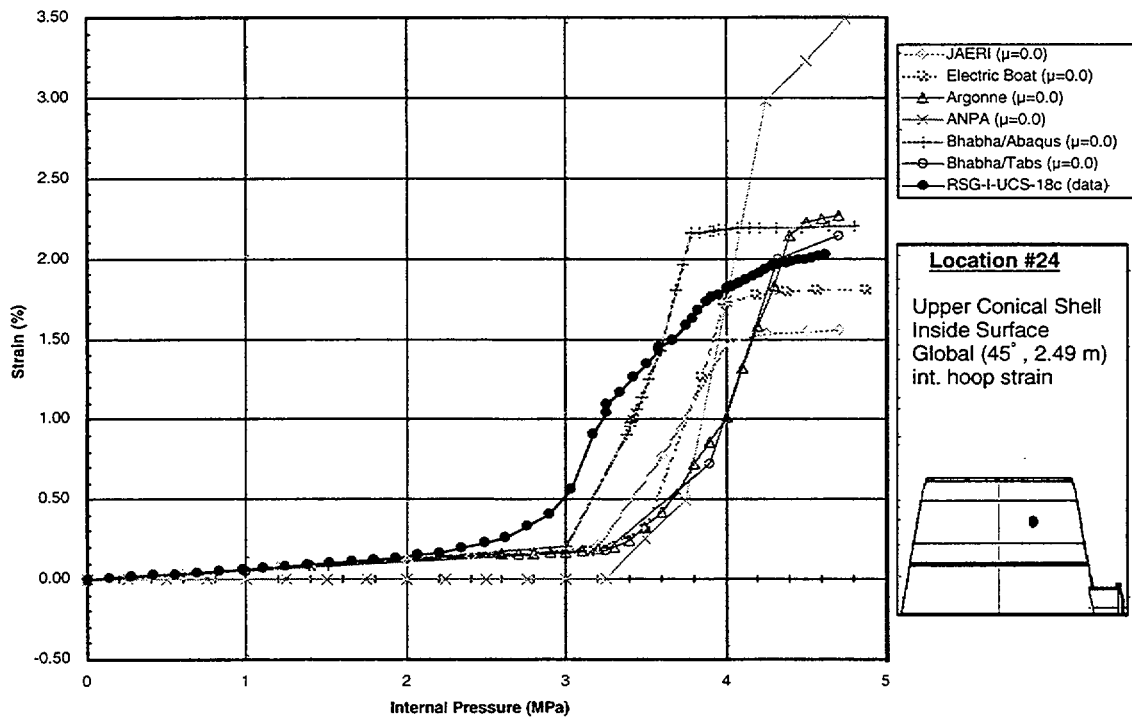


Figure 4.1. Standard Output Location #24 (zero friction case).

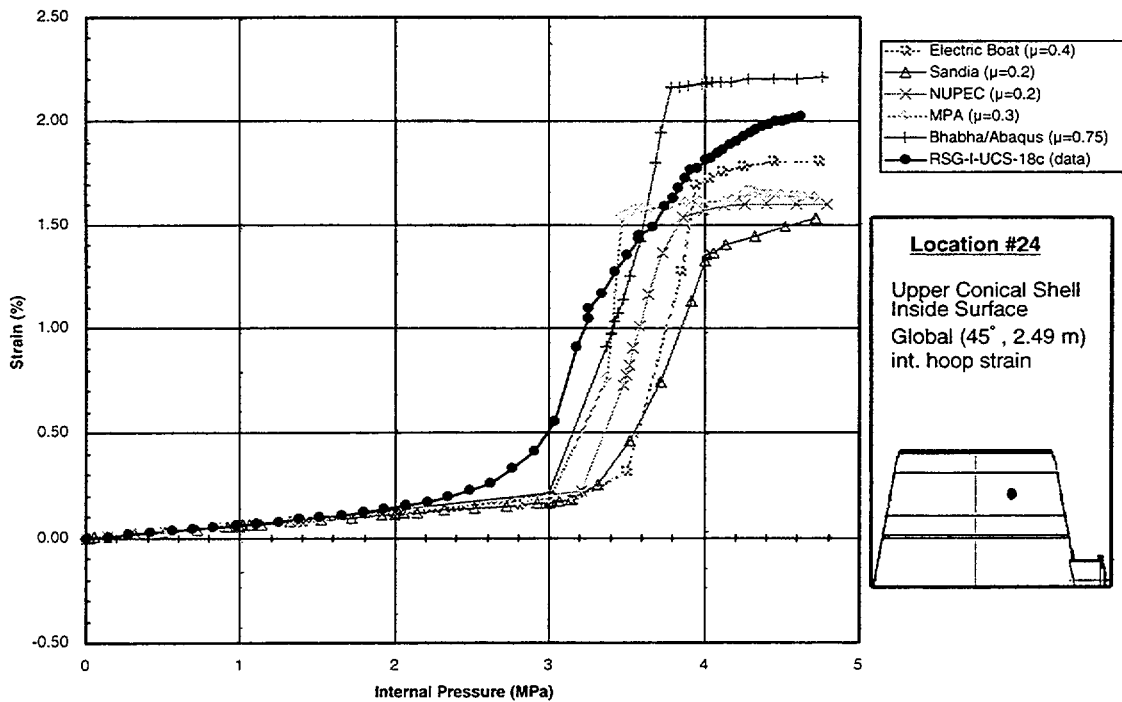


Figure 4.2. Standard Output Location #24 (nonzero friction case).

Table 4.1. Locations and Pressures of First Yield and First Contact between the SCV Model and the CS

Participant	First Yield		First Contact between SCV Model and CS	
	Pressure (MPa)	Location	Pressure (MPa)	Location
ANL	2.6	Bottom of equipment hatch and reinforcing plate	4.4	Upper conical shell
ANPA	3.0	Upper portion of spherical shell	3.5	Not stated in analysis report
BARC: ABAQUS	1.8	Below knuckle region	3.4	Knuckle region
TABS/NISA	2.0	Top spherical shell	3.5	Between knuckle region and top spherical shell
GD-EB	1.0	Knuckle region	3.2	Knuckle region
	1.1	Locally thin area around equipment hatch		
JAERI	2.8	Around knuckle region and top head	4.0	Upper and middle conical shells and around knuckle region
NUPEC	2.1	Below knuckle region	3.5	Knuckle region
SNL	2.0	Knuckle region	3.2	Knuckle region
MPA	2.5	Near equipment hatch	3.5	Upper and middle conical shells
High pressure test Data	1.65	Azimuth of 45°; 0.78 m above ring support girder (just below lower stiffening ring)	4.12	Azimuth of 0°; 1.72 m above ring support girder (at elevation of equipment hatch)
	1.79	equipment hatch @ 0° and 270°		

Table 4.2. Predicted Failure Pressure and Mechanisms

Name of Participant Organization	Numerical Code Used	Analytical Model Used in Failure Prediction	Failure Pressure	Failure Location	Failure Mechanism/Criteria
ANL	NEPTUNE	Solid model of SCV model and CS	5.5 MPa 4.9 MPa (high confidence [$>98\%$] that there is a low probability for failure)	Just above the knuckle region	Uniaxial ultimate strain (plastic failure strain) of 9.9%
ANPA	MARC	3-D shell model of SCV model, no CS and rigid surface for CS	No plastic instability at 10 MPa; local buckling of torospherical head at 10.87 MPa	Top head region	Local buckling
BARC	ABAQUS	3-D shell model with SCV model and CS based on as-designed configurations	11.49 MPa	Top head region	Strain at top head regions reaches ultimate strain
	TABS/NISA	2-D axisymmetrical model with SCV model and CS, based on some as-built configurations such as average thickness and average gap	11.5 – 12.0 MPa	Top head region at elevation 10 cm above the junction between the top head and the top cylinder	Imply possibility of in-plane axisymmetrical buckling
GD-EB	ABAQUS	Shell submodel to address the effect of local thinning	4.7 MPa	Local thinned section around equipment hatch	Minimum ultimate strain of 8% (reduced by a series of reduction factors to account for the variation and unknowns in the as-built SCV model)
JAERI	ABAQUS	Shell element model of SCV model and CS based on as-designed configuration	10.81 MPa	Top head region	Numerical instability due to yielding in the top head region
NUPEC	ABAQUS	Two submodel analyses - equipment hatch and knuckle region, using as-designed configuration	7.3 MPa 7.3 – 11.8 MPa 11.8 MPa	Near equipment hatch, below knuckle joint, and below top head flange joint. Top head apex	Maximum surface strain value
SNL	ABAQUS	Equipment hatch submodel with thinned section	4.5 MPa	Local thinned section next to equipment hatch reinforcement plate	Ductile rupture. SPV490 steel material reaches a plastic strain that in the uniaxial-stress tensile test led to necking
MPA	ABAQUS	3-D shell for half of SCV and CS; no failure analysis was performed	N/A	N/A	N/A

5. POSTTEST EVALUATIONS

Seven of the original eight organizations participated in the posttest analysis. For the posttest analysis, the standard output locations have been expanded to include locations representing free-field model responses and high-strain concentrations near the equipment hatch reinforcement plate. All participants were given the test data at these locations and the posttest metallurgical evaluation results (Van Den Avyle and Eckelmeyer, 1998). Although they were asked to provide the posttest analysis results at all standard output locations, participants were given leeway to determine the scope of their own posttest analysis effort and to choose the content of their posttest analysis report (Appendix B of this document).

The posttest analysis results submitted by the seven participants have been compiled, one plot for each standard output location (Appendix A). The test data are also included in each plot to facilitate comparisons. The comparison plots at all standard output locations are available in Appendix A. Discussion of the posttest analysis results at some chosen locations is covered in this section. A special section is devoted to discussing the posttest metallurgical evaluation results that provide insightful information to explain the observed tear near the equipment hatch reinforcement plate. In addition, the lessons learned from the collective effort of all participants from both pretest and posttest analyses are detailed in Section 5.3.

5.1 Compilation of Posttest Analysis Results from Participants

The comparison plots of the participants' posttest analysis results at all standard output locations are available in Appendix A. The discussion on the plots is partitioned into various subgroups in accordance with the different categories of analysis results:

- Equipment Hatch Area - Standard Output Locations #1-6, 40-45
- Free-Field Response - Standard Output Locations #21-34, 46-52

^c Klamerus, E. W., "SCV High Pressure Test Data for Round Robin Analysis," Project Report No. R-SN-S-007, Rev. A, September 1997 and Rev. B, January 1998, Sandia National Laboratories, Albuquerque, NM.

- Top Head Area - Standard Output Locations #7-10
- Transition Regions - Standard Output Locations #11-20
- General Displacements - Standard Output Locations #35-39

5.1.1 Equipment Hatch Area

The equipment hatch area received a high level of attention in the pretest analysis effort because it contains an array of contributors for strain risers due to geometrical and structural discontinuities and material change. This area, again, has become one of the focal locations for the posttest evaluation because a large tear, about 190 mm long, developed near the outside edge of the equipment hatch reinforcement plate, resulting in the termination of the high pressure test.

In the plots at Standard Output Locations #1-6, there is a general agreement between the test data and the analysis results, with the exception of ANPA's results. The obvious discrepancy is that the SCV model started to yield at a lower pressure of about 2.5 MPa. Two observations may explain this disagreement. First, the material models used in the analyses were generated from the steel plates in the prefabricated state, while the SCV model shell underwent various fabrication processes such as rolling and welding. These fabrication processes will probably alter the material properties, but the extent of change cannot be quantified due to lack of material test data on the fabricated structural components. Second, the pretest measurement of the SCV model indicates that the local section of the equipment hatch was displaced inward 5 to 7 mm in the radial direction. This local out-of-roundness occurred when the equipment hatch was welded onto the SCV model. In the pressurization process during the high pressure test, this section probably underwent deformation to recover roundness before additional straining in the radial and meridional directions. Since this feature of the as-built SCV model configuration was not included in the finite element models by all participants, this additional deformation experienced by the SCV model was not simulated in the analyses.

The two test data, plotted in Standard Output Locations #44 and 45, were recorded by the strip strain gages, STG-I-EQH-16b and STG-I-EQH-37a, re-

spectively. They represent the highest strain concentrations at 90° and 270° (local hatch coordinates) of the equipment hatch. The analysis results are in general agreement with the test data at these two locations, except that the test data recorded by STG-I-EQH-37a in Location #45 continue to deform at a high rate beyond 4.2 MPa, leading to a final strain reading of 8.7%.

5.1.2 Free-Field Response

There is a series of rosette strain gages (RSG-I-UCS-10c, -12c, -14c, and -18c and RSG-O-UCS-9a, -11a, -13a, and -15a) installed on the interior and exterior surfaces of the SCV model at an elevation of 2.49 m above the ring support girder. Their location in the upper conical shell section, far away from the upper and the middle stiffening rings, allows their recorded strains to provide an informative perspective on the free-field response of the SCV model. The comparison plots of the test data for these gages and the posttest analysis results are available in Standard Output Locations #24 and 46–52 of Appendix A.

Because these rosette strain gages were installed at the same elevation but at different azimuth angles, they should record almost identical strain histories for an axisymmetric structure. However, the test data indicate otherwise: the pressure level for the onset of yielding ranges from 2.24 to 2.78 MPa for the interior gages and from 2.41 to 2.83 MPa for the exterior gages, as shown in Figures 5.1 and 5.2, respectively. One major reason that may account for this variation around the circumference is that the local area where the gages were placed might have a different amount of out-of-roundness. The pretest measurement results of the as-built SCV model by CBI Services, Inc., the fabricator of the CS, indicate a range of -1.8 to +2.5 mm deviation from an average model radius of 1071.2 mmf. Although this is not much out-of-roundness, this as-built feature of the SCV model configuration was not simulated in the analyses and may have had some effect on analysis results.

Obviously, the scenario of out-of-roundness cannot totally account for the wider discrepancy of the onset of yielding pressure between the test data and the posttest analysis results. A detailed review of the comparison plot for Standard Output Location #24 reveals that BARC and GD-EB used a material

model with the minimum strength for each plate thickness and produced analysis results closer to the test data. This finding suggests that the local SCV model section might possess a material property of a lower strength than the one obtained from the virgin plate. It further suggests that some reduction in material strength might occur during SCV model fabrication processes such as rolling and welding.

5.1.3 Top Head Area

In the top head area, the apex of the SCV model remained elastic during the high pressure test, and the posttest analysis results in the Standard Output Location #7 confirmed this model response. At Standard Output Locations #8, 9, and 10 (azimuth angle of 270° and local radius of 0.48 m), the test data show that the external hoop strain started to behave plastically at a pressure of 3.57 MPa and the internal meridional strain at a pressure of 3.09 MPa, but the external meridional strain stayed in the elastic domain throughout the pressurization process. There are some discrepancies between the test data and the posttest analysis results at this location.

5.1.4 Transition Regions

The transition regions include the following locations:

- Upper cylindrical shell section above the knuckle region (Standard Output Locations #11 and 12),
- Spherical shell section immediately below the knuckle region (Standard Output Locations #13 and 14),
- Middle stiffening ring (Standard Output Locations #15 and 16),
- Material change interface (Standard Output Locations #17 and 18), and
- Lower stiffening ring (Standard Output Locations #19 and 20).

There is some disagreement between the test data and the posttest analysis results from each participant at the upper cylindrical shell section above the knuckle region, especially above a pressure of about 3.5 MPa when the test data indicate that local contact between the top of CS and the SCV model occurred. This disagreement may be attributed to the fact that the participants did not simulate accurately the as-built local gap in their posttest analysis models. Similar discrepancies are observed at the spherical shell sec-

^f CBI Drawing Nos. SK1, Rev. 1, SK2, Rev. 2, and SK3, Rev. 0, June 21, 1995.

tion immediately below the knuckle region due to difficulties in interpreting and representing the as-built gap data.

At the middle stiffening ring, there is a good agreement between the test data and the posttest analysis results from participants until the pressure reached about 3.0 MPa. Then the discrepancy started to grow, becoming worse at about 3.8 MPa, when the local contact between the CS and the SCV model might occur. There is wide-spread disagreement between the test data and the participants' posttest analysis results at the material change interface. This observation may be a direct result of the complexities caused by material discontinuities and weld. Rather poor comparisons of strain results at the lower stiffening ring also occurred between the test data and individual participant's posttest analysis results. Only GD-EB and SNL provided favorable comparisons with the test data at this location.

5.1.5 General Displacements

There were two sets of vertical displacements of the SCV model for the Round Robin comparisons: the apex of the SCV model (Standard Output Location #35) and the upper spherical shell section below the knuckle region (Standard Output Location #38). The participants' posttest analysis results on the vertical displacement at the apex of the SCV model compare well with the test data, with the exception of ANL's. At the upper spherical shell section immediately below the knuckle region, SNL's and ANL's results do not compare well with the test data, while other participants have a more favorable comparison with the test data.

The time history of the horizontal displacement of the SCV model at three locations was chosen for Round Robin comparisons: the upper cylindrical shell section above the top head flange (Standard Output Location #36), the upper spherical shell section below the knuckle region (Standard Output Location #37), and the center of the equipment hatch barrel (Standard Output Location #39). The test data on the horizontal displacement at the upper cylindrical shell section above the top head flange show that the SCV model experienced a local inward displacement there. This observation, obviously, does not compare well with the participants' posttest analysis results which indicate a local outward expansion. It is quite possible that the SCV model might have a local out-of-roundness to account for this observa-

tion. At the upper spherical shell section below the knuckle region, the test data of the horizontal displacement are smaller than the posttest analysis results from participants. This discrepancy may be the direct result of a smaller as-built gap there between the CS and the SCV model. NUPEC is the only group that provided results on the horizontal displacement at the center of the equipment hatch barrel that compare favorably with the test data, because the as-built configuration of local out-of-roundness was included in the posttest analysis model.

5.2 Posttest Metallurgical Evaluation

In the posttest effort, the SCV model was visually inspected and metallurgically evaluated to characterize the local failure mechanisms at the locations of the two tears and to gain some insight into both the global and the local responses of the SCV model. Details of the posttest metallurgical evaluation are available (Van Den Avyle and Eckelmeyer, 1998).

A close-up visual inspection of the interior of the SCV model was performed shortly after the high pressure test. A similar inspection of the exterior of the SCV model became feasible after the CS was removed. Sections of the SCV model surrounding the two tears and areas of local necking and other obvious structural distress were removed for fractographic analysis and metallurgical evaluation. The evaluation procedure included optical microscopy using a scanning electron microscope, Rockwell B hardness tests, and fracture surface observations. Evaluation results indicate that the tears produced in the SCV model wall adjacent to the equipment hatch reinforcement plate and at the semi-circular opening in the middle stiffening ring were the result of local plastic deformation and ductile shear failure. No contributing flaws in the SCV model wall were noted at these tear locations (Van Den Avyle and Eckelmeyer, 1998).

An important finding from the posttest metallurgical evaluation is that changes in the grain structure were observed and a significant reduction in the Rockwell B hardness was found in the heat affected zone (HAZ) of the SPV490 material surrounding the weld seam of the equipment hatch reinforcement plate. Based on the well-established correlation between Rockwell B hardness and tensile strength (*ASM Metals Handbook*, 1961), these results indicate a sizable reduction in tensile strength along with a corresponding, though less well-defined, reduction in the yield strength of the material. It is believed that the

heat from the welding process of the SCV model resulted in a localized microstructural alteration and a reduced hardness of strength in the SPV490 HAZ. These findings offer a possible explanation for the observed pattern of strain concentrations around the weld seams of the equipment hatch reinforcement plate in the SPV490 shell, instead of the SGV480 shell that has a lower material strength in the prefabricated state. When the SCV model was pressurized, plastic deformation occurred preferentially in the softer areas of the SPV490 HAZ, eventually resulting in the shear failure there.

5.3 Lessons Learned

In the process of comparing the pretest and the post-test analysis results with the test data, a few observations were made and are described as follows:

1. Great effort was expended on conducting material property tests for the SGV480 and SPV490 steel plates in the prefabricated state. Material models based on these test data were used by all participants in their finite element models. However, the SCV model fabrication processes such as rolling and welding might change some of these properties. If these altered properties were not incorporated in the analysis models, the analysis results would not be able to correlate with the test data.
2. Most of the analysis models were based on the design configurations of the SCV model and the CS. This modeling approach provides a practical way to predict and simulate the structural response of the SCV model. However, some as-built model features such as local out-of-roundness, wall thickness variations, and gap size between the SCV model and the CS, if not included in the finite element model, may cause discrepancies between the analysis results and the test data.
3. Since the two tears were initiated and propagated along weld seams which were not represented specifically in the finite element models, it is very difficult for the analysis model to produce results resembling the localized phenomena such as the two tears.

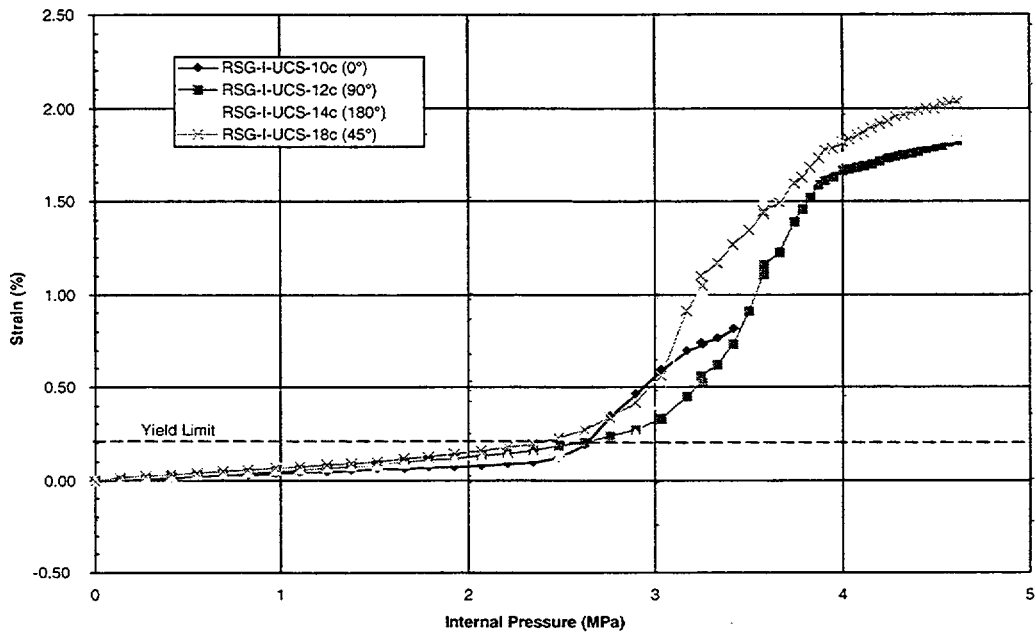


Figure 5.1. Free-field SCV model response recorded by interior gages in upper conical shell section.

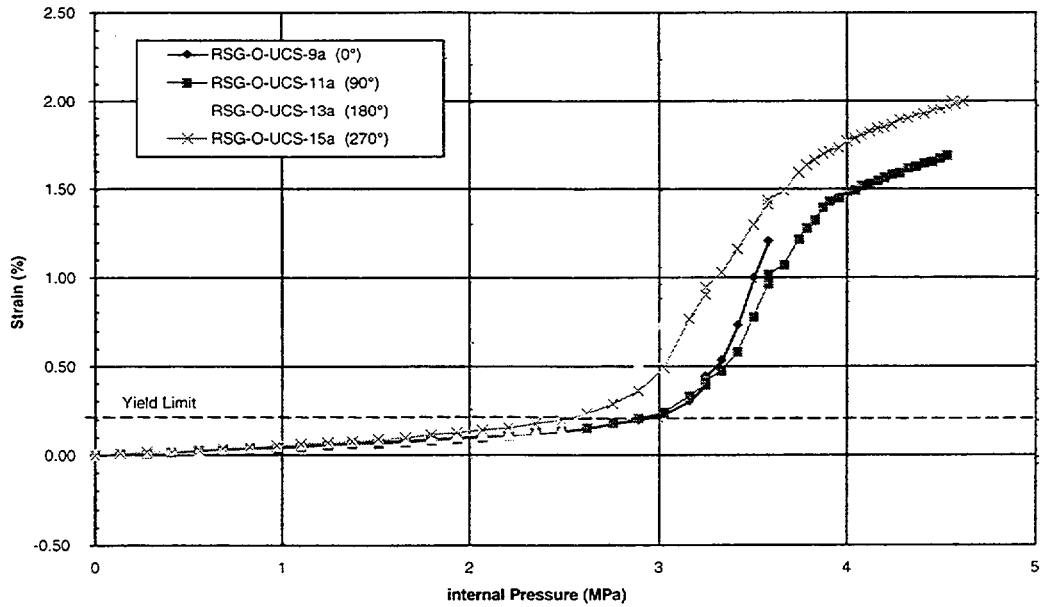


Figure 5.2. Free-field SCV model response recorded by exterior gages in upper conical shell section.

6. SUMMARY

The continuing support and cooperation of the Round Robin participants is greatly appreciated. The participants performed the pretest and the posttest analyses on a tight schedule and limited resources, and the analysis results included in the Round Robin Pretest Analysis Report (Luk and Klamerus, 1996) and this report reflect what could be accomplished within the imposed limitations. An important benefit of the Round Robin activity was obvious at the pretest and the posttest meetings, when experts from the participating organizations who used different codes to conduct independent analyses shared their modeling approaches, analysis results, and knowledge.

In general terms, the pretest and the posttest analysis results provided by the participants have compared fairly well with the test data. Most participants chose to use the design configuration of the SCV model, as a practical matter, to construct the finite element models. The analysis results so generated have provided a reasonably good representation of the general structural behavior of the SCV model, except in some local areas where the as-built configuration differs from the design dimensions. Some of the local details of the SCV model such as the weld seams were not included in the analysis models. Unfortunately some of these local discontinuities are also the strain risers.

Extensive uniaxial tensile tests were performed on the specimens of SGV480 and SPV490 steel plates in the prefabrication state, and participants used these material property data to construct the material models in the analyses. The SCV high pressure test data and the posttest metallurgical evaluation results suggest that some of these material properties may be altered by fabrication processes such as rolling and welding, especially for SPV490 steel which has the

characteristics of a higher-hardness, low-carbon martensitic/bainitic steel. The posttest metallurgical evaluation results indicate that in the SCV model the heat from the welding process caused a localized microstructural change and reduced hardness and strength in the SPV490 steel. The reduced strength in the SPV490 HAZ has been identified as the leading factor for the tear at the equipment hatch reinforcement plate. Since the full effect of the strength reduction in the SPV490 HAZ is not entirely known, this observed tear can be only approximately simulated in the analysis models.

In the pretest analysis effort, most participants experienced numerical stability difficulties in simulating the contact between the SCV model and the CS (Luk and Klamerus, 1996). The purpose of installing the CS over the SCV model is to allow contact between the two structures during the SCV high pressure test and collect data to improve the numerical contact algorithms in the finite element codes. As it turned out, the SCV high pressure test was terminated before the SCV model made global contact with the CS. Therefore, only a limited set of contact data was recorded.

One of the important issues in the Round Robin analysis activities is to predict in the pretest effort and to simulate in the posttest phase the failure mode and mechanisms of the SCV model. Since the tear at the equipment hatch reinforcement plate occurred in a local area whose details were not included in the pretest analyses and whose material strength is not entirely known in the posttest analyses, it is difficult to accomplish this task with a high level of confidence. This matter is further complicated by the lack of a failure criterion established on a physical basis.

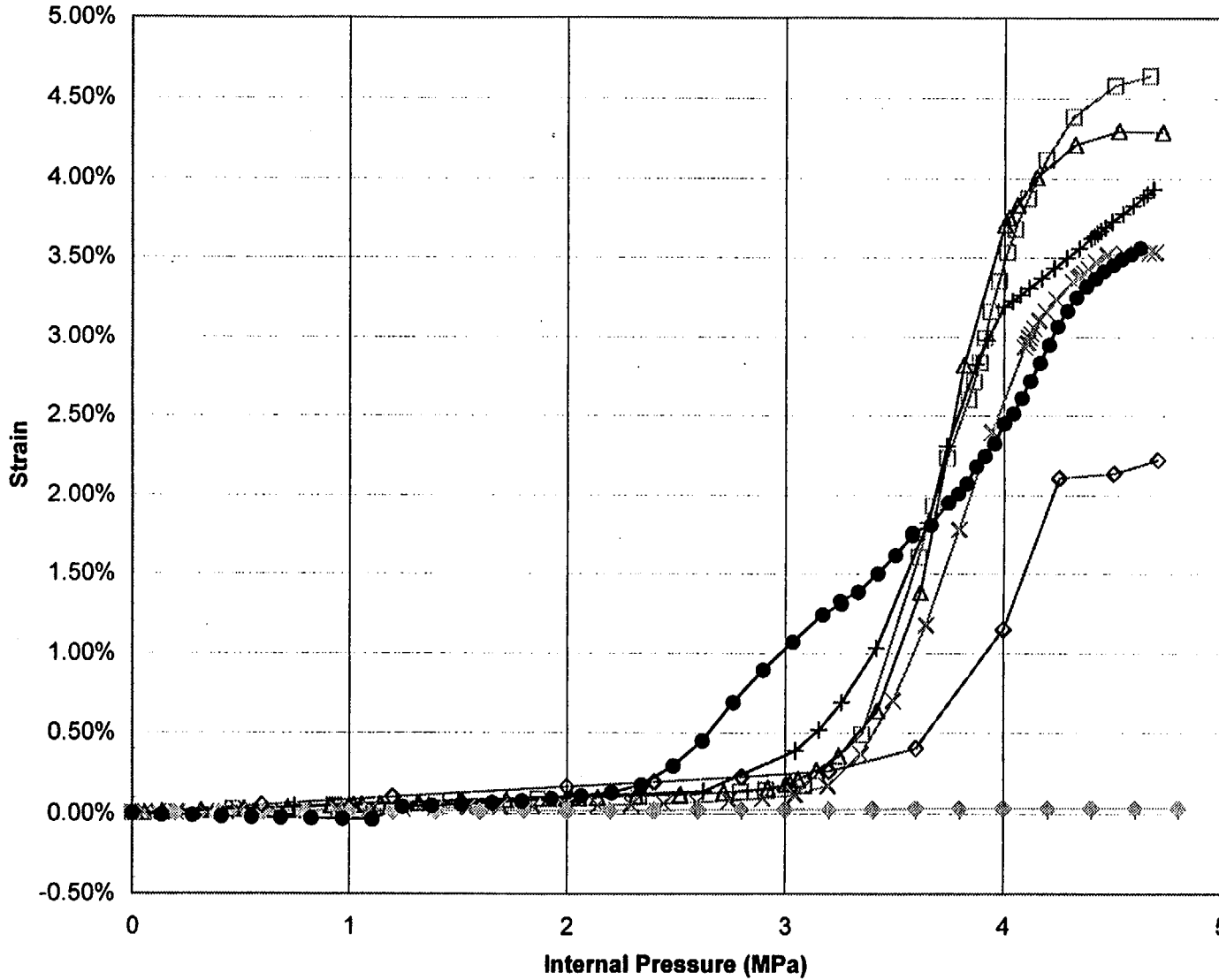
7. REFERENCES

- ASM Metals Handbook. 1961. 8th ed., Vol. 1. "Properties and Selection of Metals," p. 1236.
- Clauss, D.B. 1989. *Round Robin Analysis of the Behavior of a 1:6-Scale Reinforced Concrete Containment Model Pressurized to Failure: Posttest Evaluation*. NUREG/CR-5341, SAND89-0349. Albuquerque, NM: Sandia National Laboratories.
- Luk, V.K. and E.W. Klamerus. 1996. *Round Robin Pretest Analysis of a Steel Containment Vessel Model and Contact Structure Assembly Subject to Static Internal Pressurization*. NUREG/CR-6517, SAND96-2899. Albuquerque, NM: Sandia National Laboratories.
- Luk, V.K., M.F. Hessheimer, G.S. Rightley, D.L. Lambert, and E.W. Kalmerus. 1998. *Design, Instrumentation, and Testing of a Steel Containment Vessel Model*. NUREG/CR-5679, SAND98-2701. Albuquerque, NM: Sandia National Laboratories.
- Luk, V.K., M.F. Hessheimer, T. Matsumoto, K. Komine, and J.F. Costello. 1997. "Testing of a Steel Containment Vessel Model," *Proceedings of the 14th International Conference in Structural Mechanics in Reactor Technology*, Vol. 5, pp. 73-79, Lyon, France, August 17-22, 1997.
- Luk, V.K., J.S. Ludwigsen, M.F. Hessheimer, T. Matsumoto, K. Komine, and J.F. Costello. 1998. "Results of Steel Containment Vessel Model Test," *Proceedings of 1998 ASME/JSME Joint Pressure Vessels and Piping Conference*, San Diego, California, July 26-30, 1998.
- Matsumoto, T., K. Komine, J.F. Costello, V.K. Luk, and M.F. Hessheimer. 1997. "Pressurization Test of a 1/10 Steel Containment Vessel Model," *Proceedings of the Workshop on Severe Accident Research in Japan (SARJ-97)*, Yokohama, Japan, October 6-8, 1997.
- Matsumoto, T., K. Komine, S. Arai, V.K. Luk, M.F. Hessheimer, and J.F. Costello. 1997. "Preliminary Results of Steel Containment Vessel Model," *Proceedings of the 14th International Conference in Structural Mechanics in Reactor Technology*, Vol. 5, pp. 81-87, Lyon, France, August 17-22, 1997.
- Porter, V.L., P.A. Carter, and S.W. Key. 1996. *Pretest Analysis of the Steel Containment Vessel Model*. NUREG/CR-6516, SAND96-2877. Albuquerque, NM: Sandia National Laboratories.
- Van Den Avyle, J.A. and K.H. Eckelmeyer. 1998. *Posttest Metallurgical Evaluation Results for SCV High Pressure Test*. SAND98-2702. Albuquerque, NM: Sandia National Laboratories.

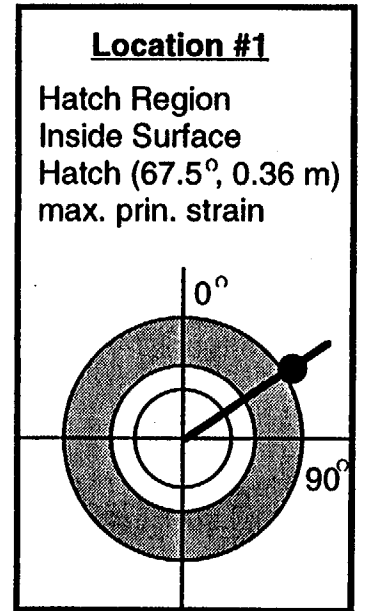
Appendix A

Compilation of Analysis Results from Participants

Standard Output Location #1



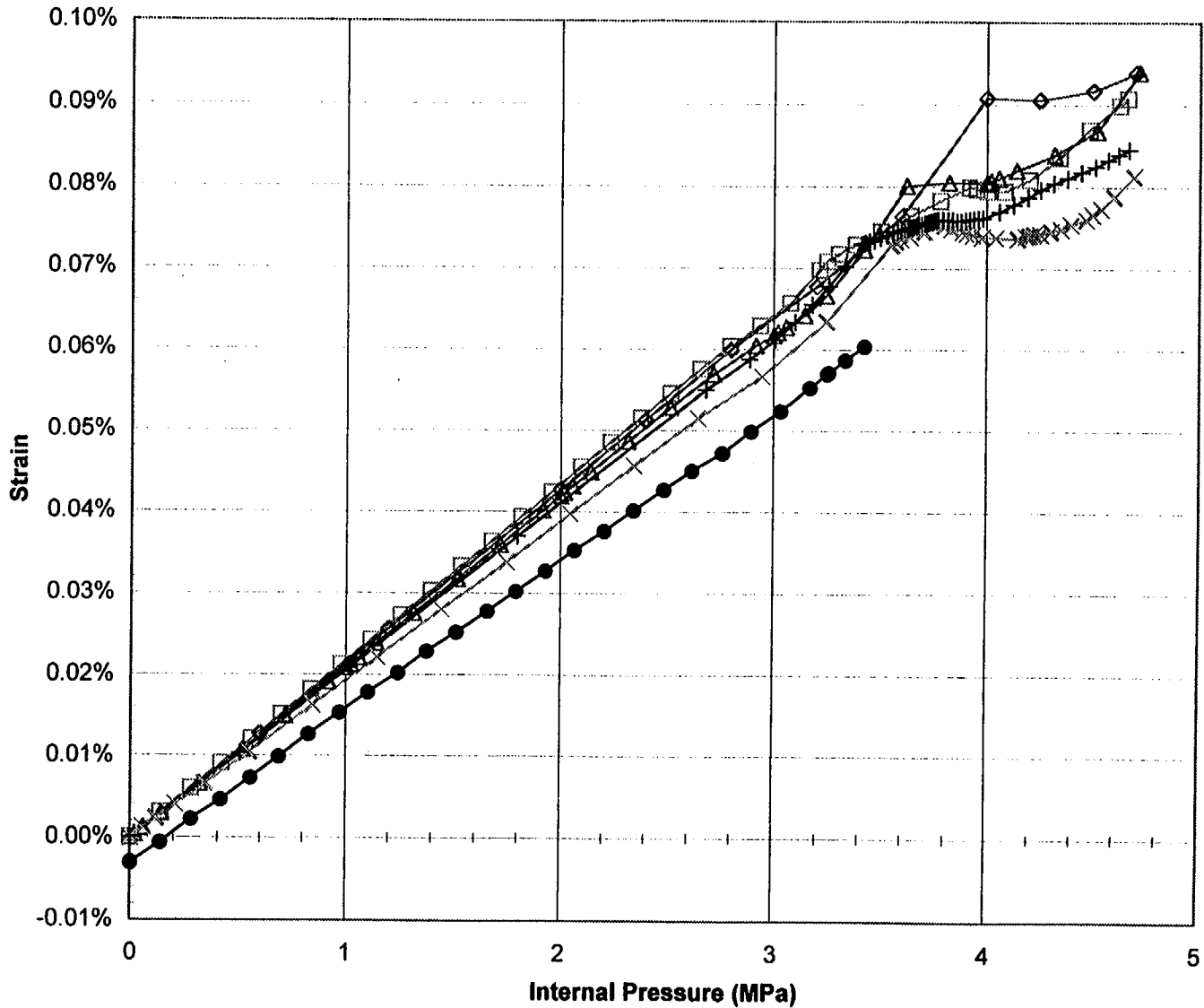
- Electric Boat
- △ Sandia
- × NUPEC
- † BARC
- ◆ ANPA
- ◇ JAERI
- RSG-I-EQH-12 (data)



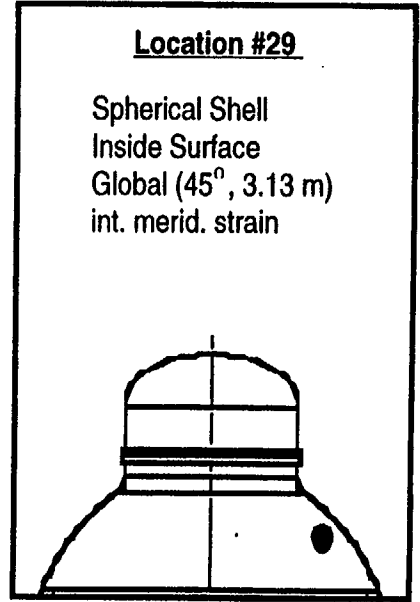
A-3

NUREG/CR-5678

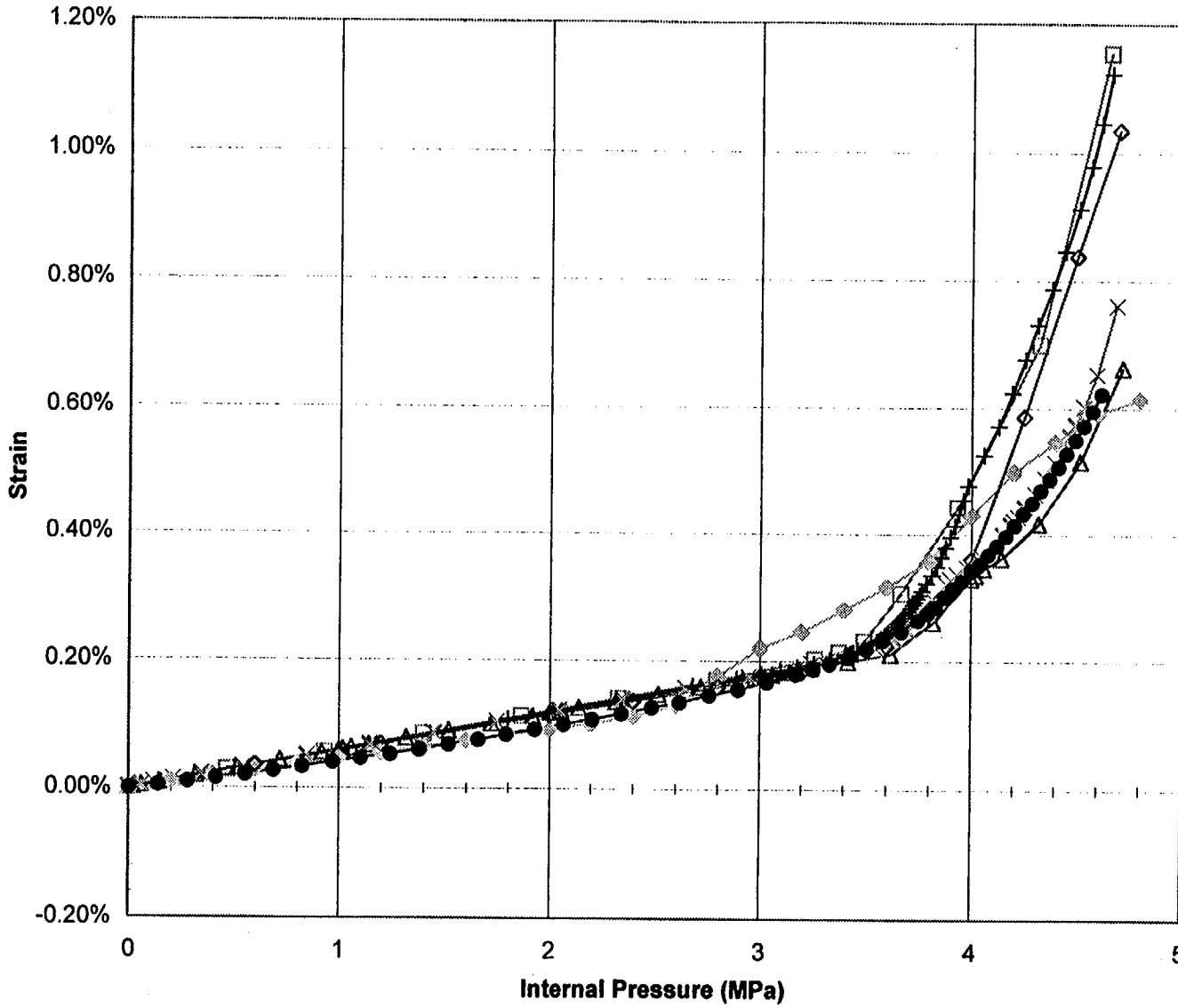
Standard Output Location #29



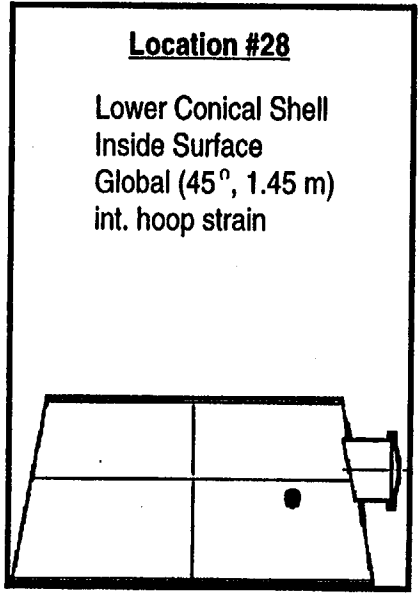
- Electric Boat
- △ Sandia
- × NUPEC
- + BARC
- ◇ JAERI
- RSG-I-SPH-2a (data)



Standard Output Location #28



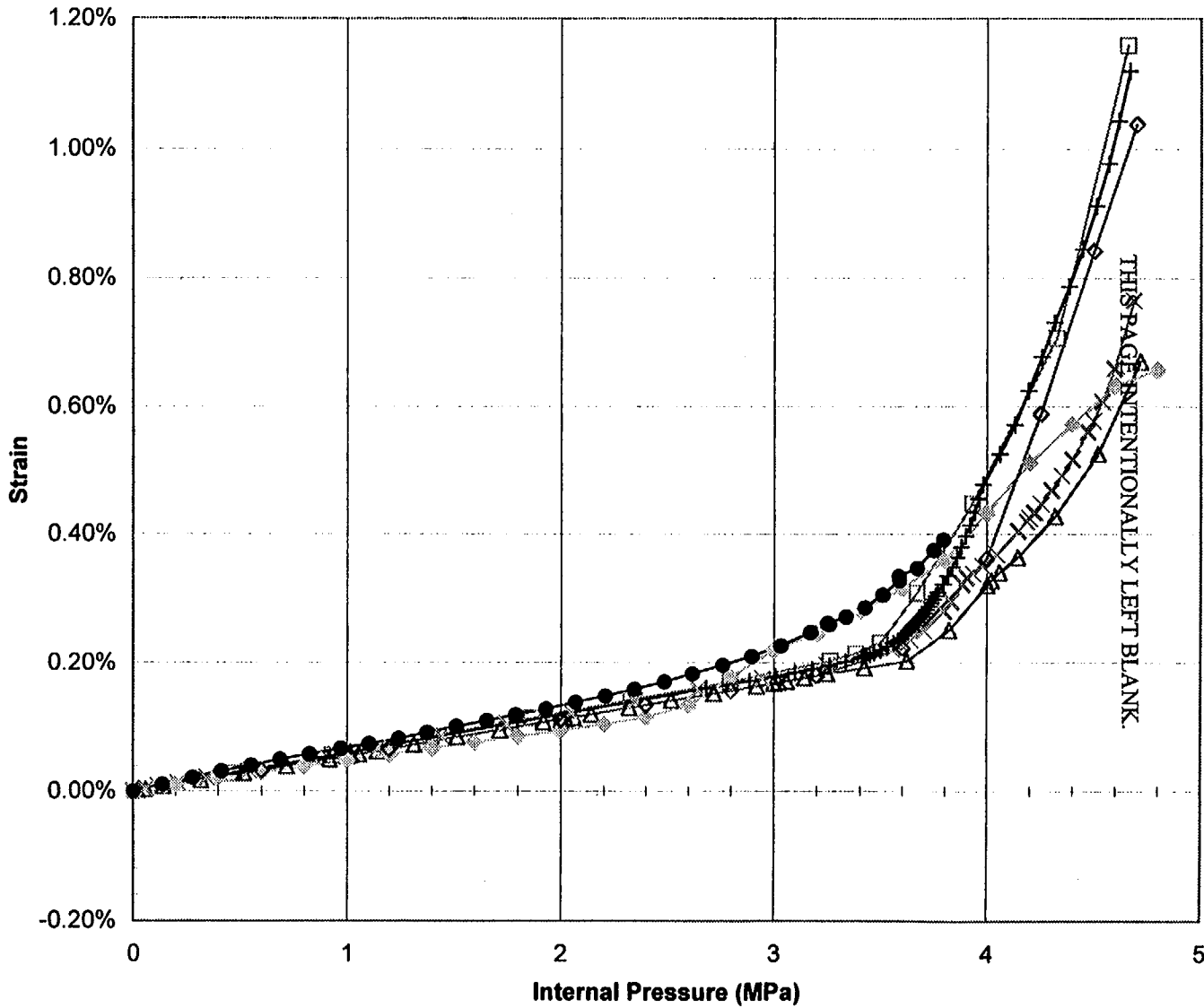
- Electric Boat
- △ Sandia
- × NUPEC
- + BARC
- ◇ ANPA
- ◇ JAERI
- RSG-I-LCS-6c (data)



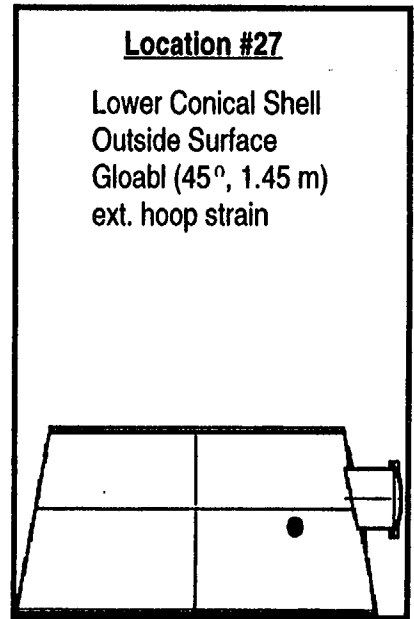
A-5

NUREG/CR-5678

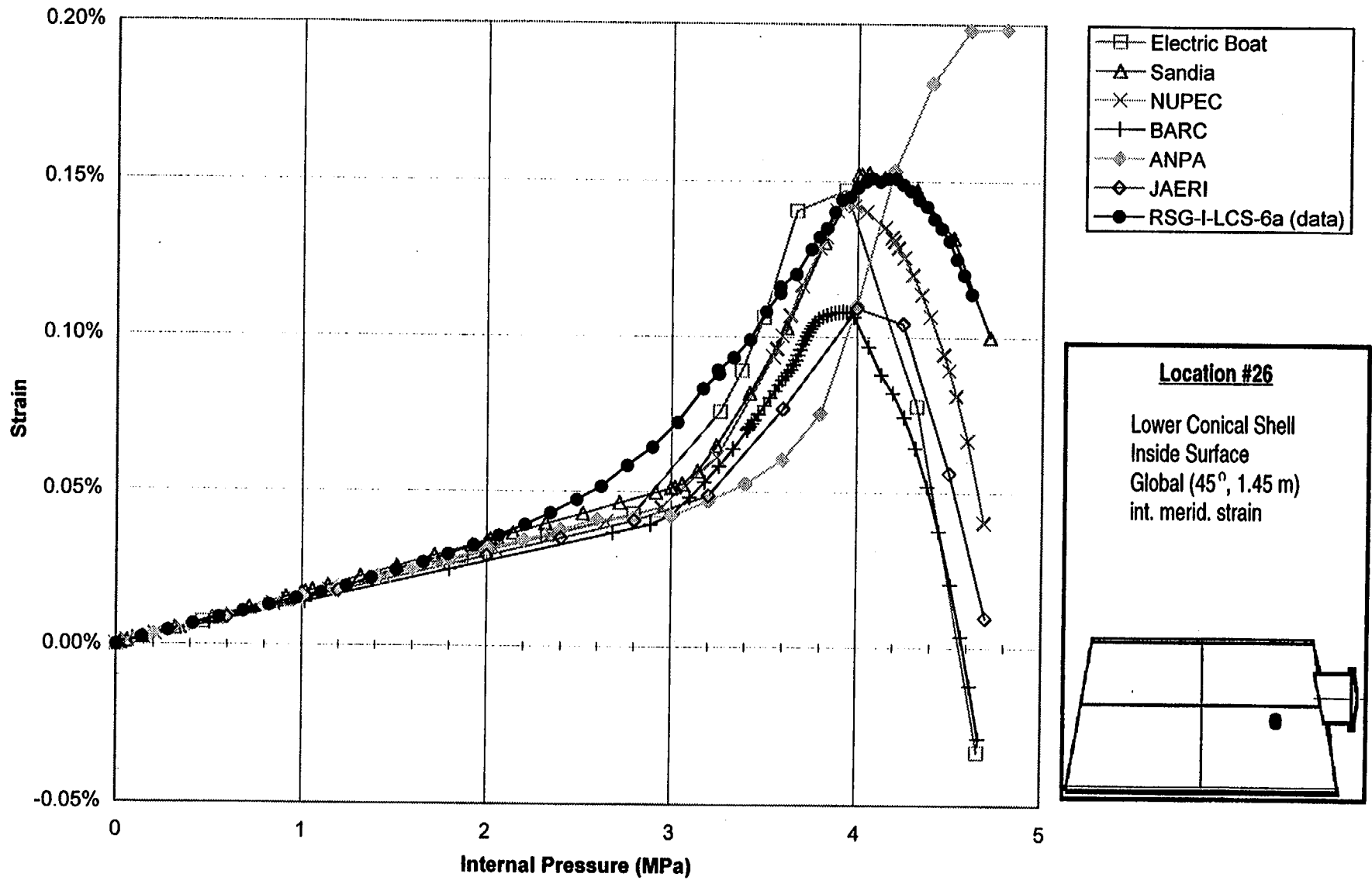
Standard Output Location #27



- Electric Boat
- △ Sandia
- × NUPEC
- ⊕ BARC
- ◆ ANPA
- ◇ JAERI
- RSG-O-LCS-5a (data)



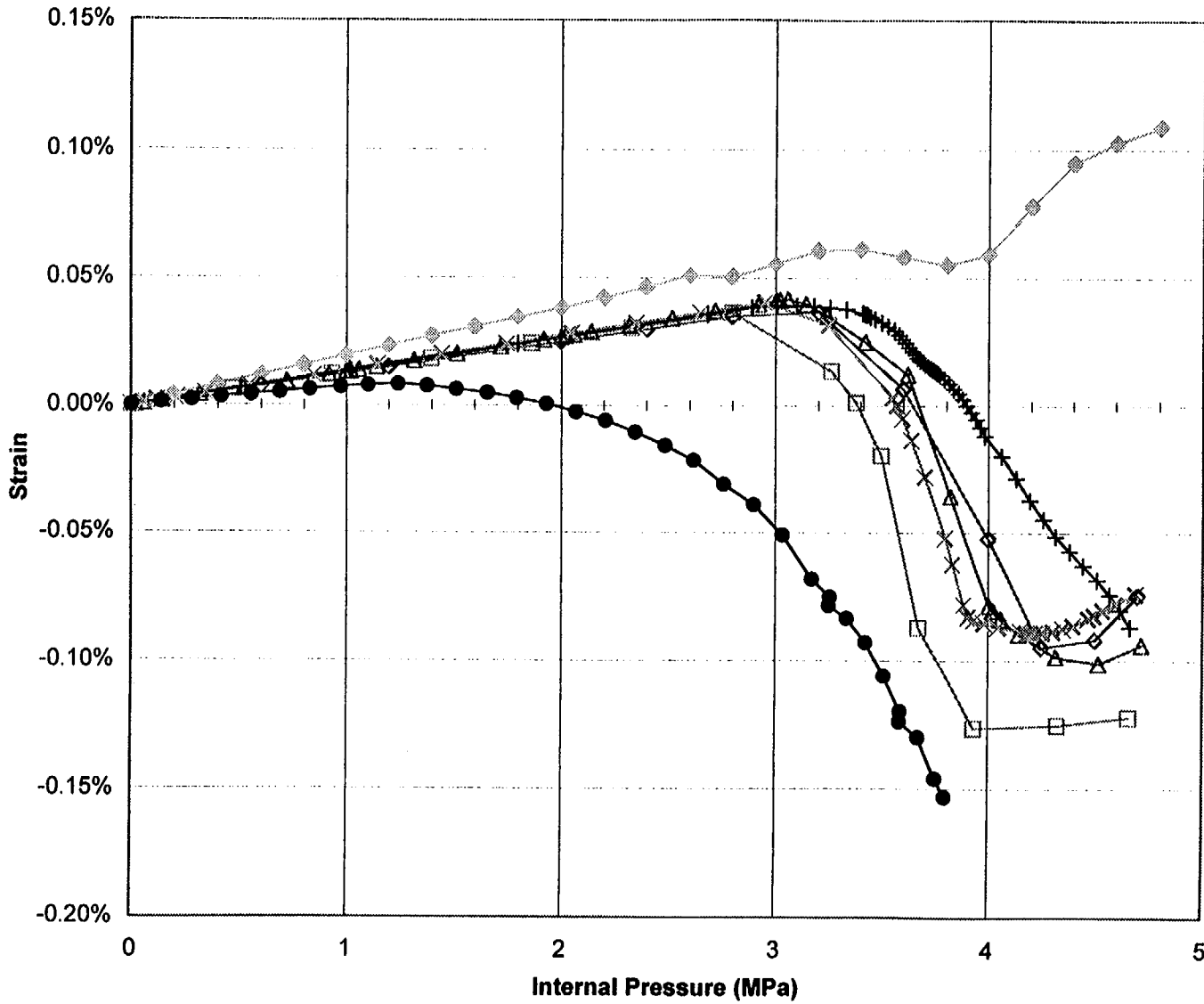
Standard Output Location #26



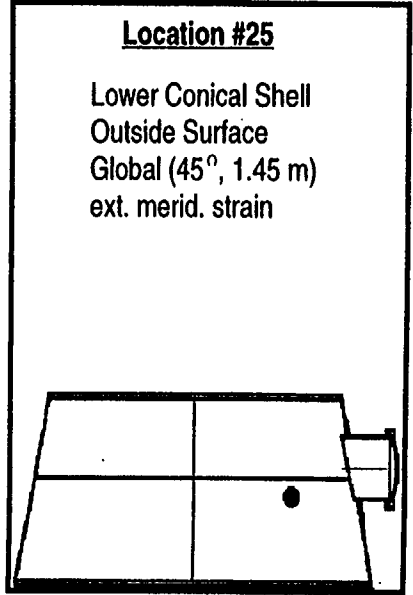
A-7

NUREG/CR-5678

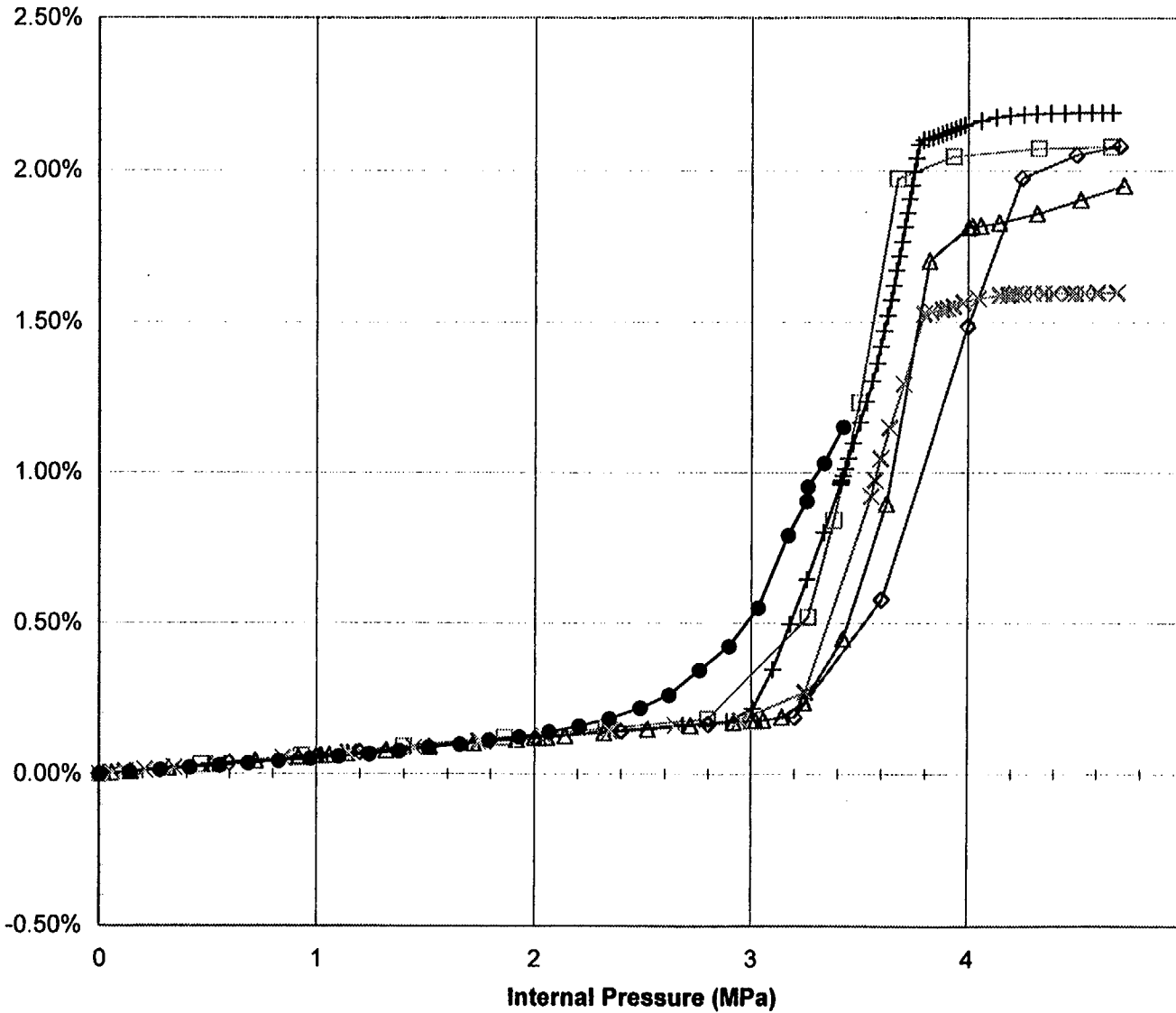
Standard Output Location #25



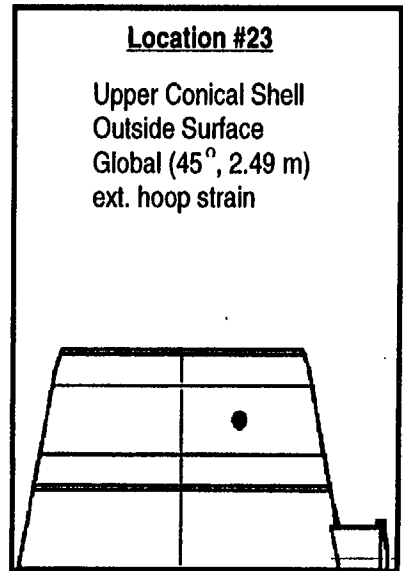
- Electric Boat
- △ Sandia
- × NUPEC
- + BARC
- ◇ ANPA
- ◊ JAERI
- RSG-O-LCS-5c (data)



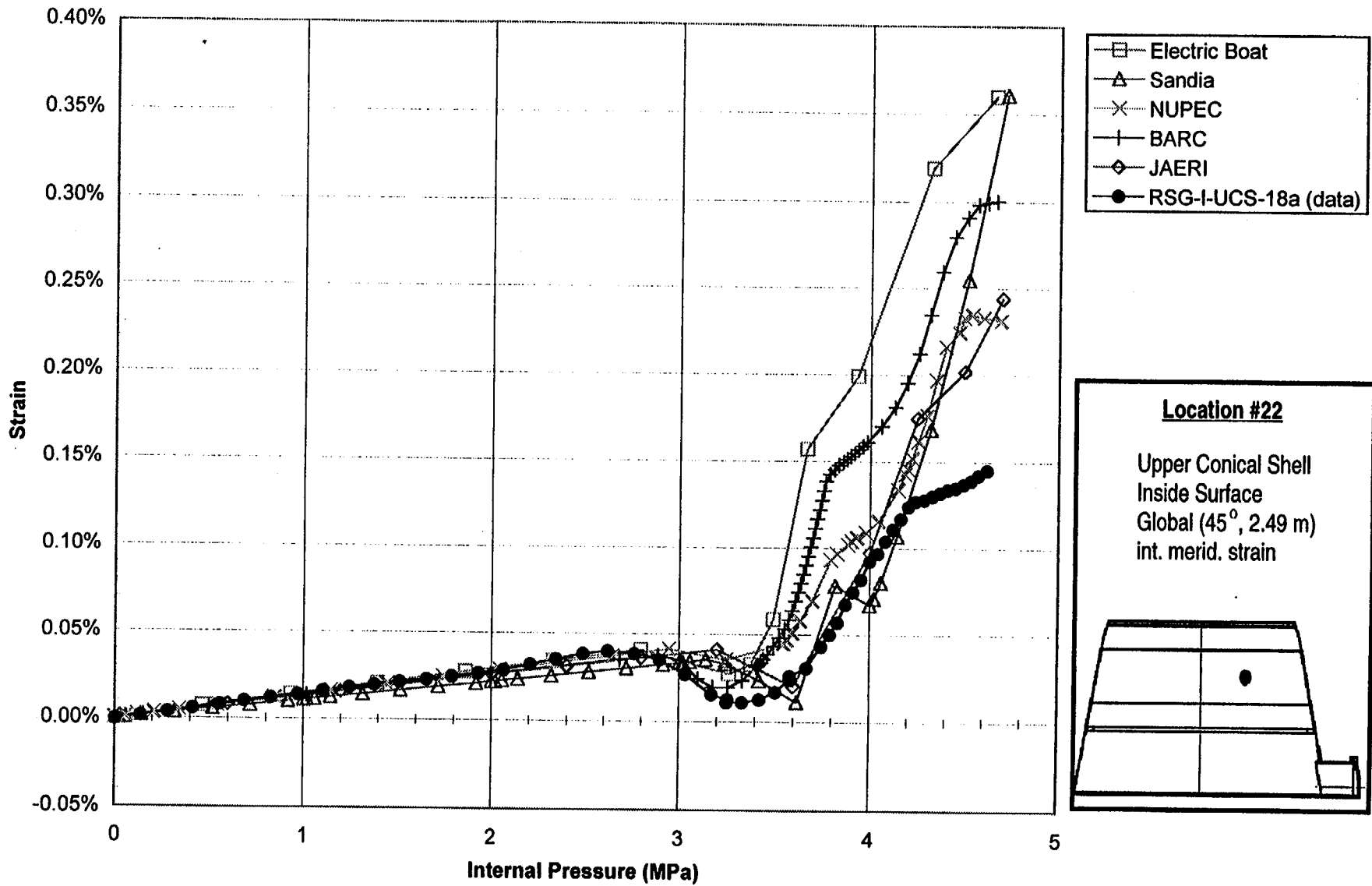
Standard Output Location #23



- Electric Boat
- △ Sandia
- × NUPEC
- † BARC
- ◇ JAERI
- RSG-O-UCS-17a (data)



Standard Output Location #22

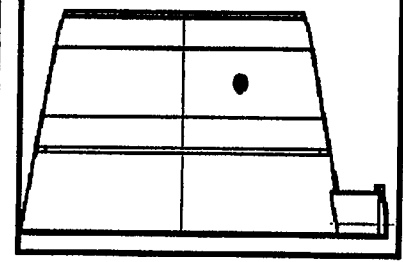


A-11

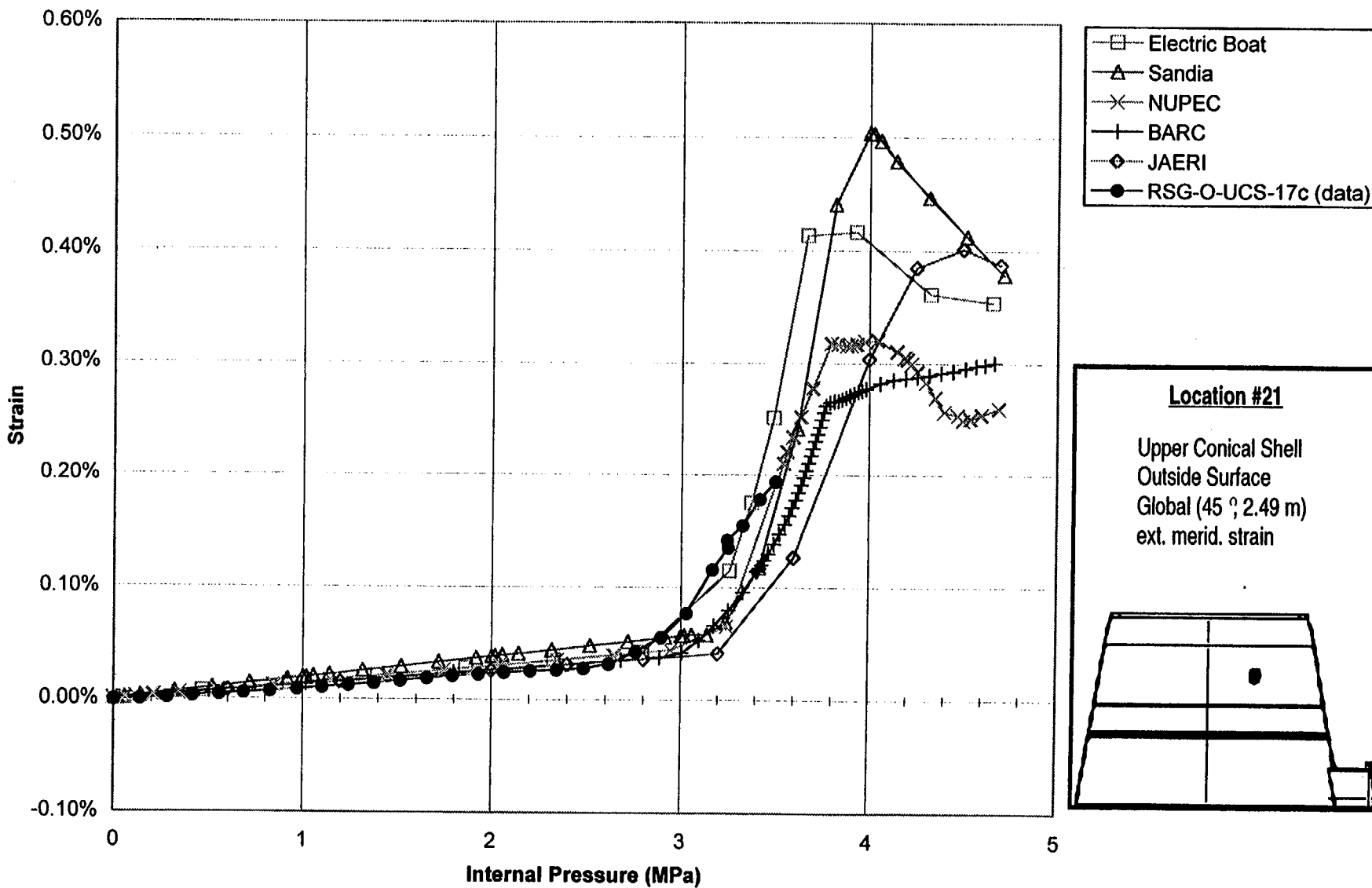
NUREG/CR-5678

Location #22

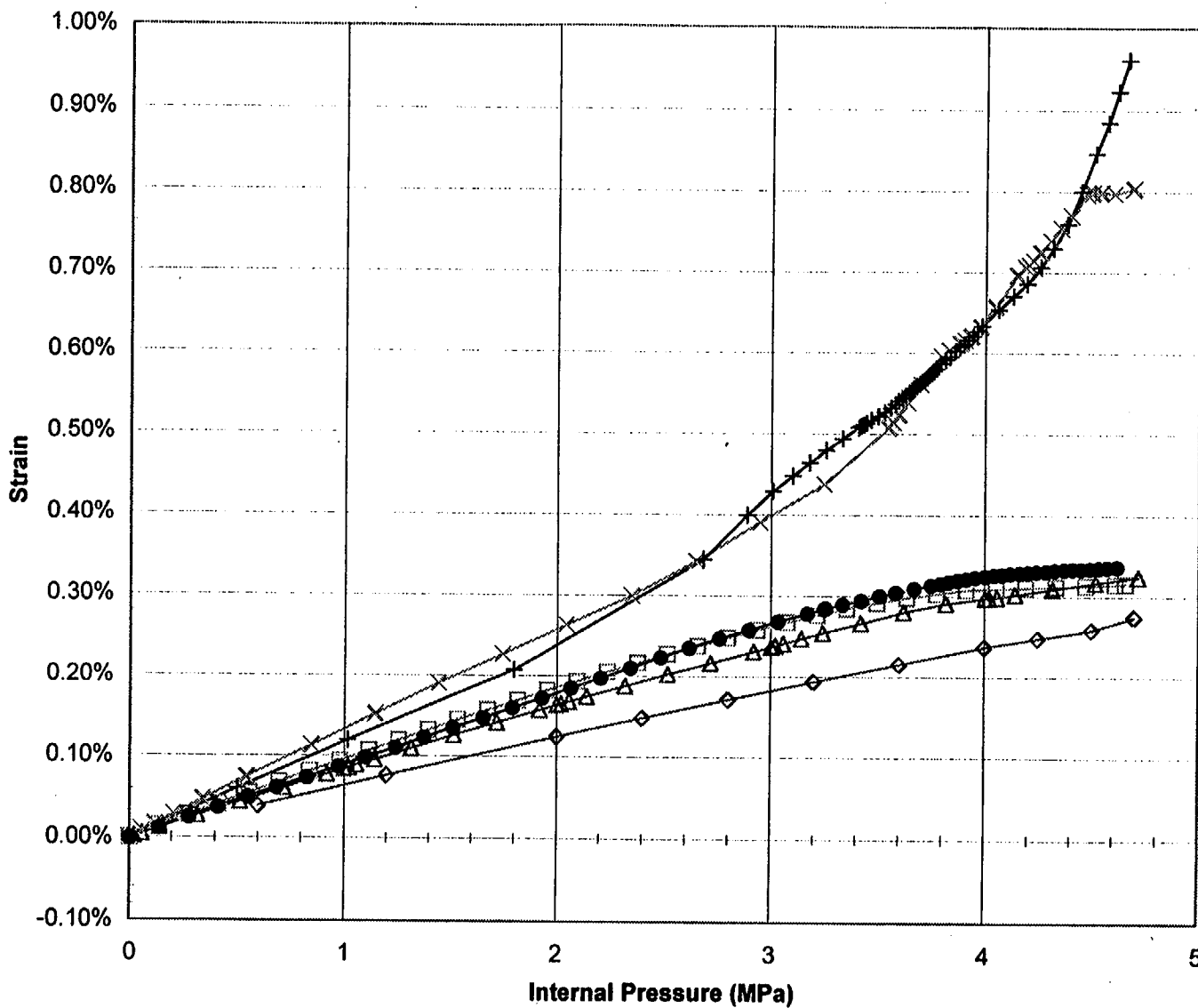
Upper Conical Shell
 Inside Surface
 Global (45°, 2.49 m)
 int. merid. strain



Standard Output Location #21



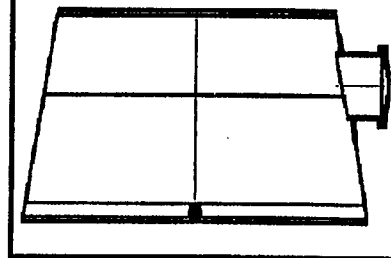
Standard Output Location #20



- Electric Boat
- △ Sandia
- × NUPEC
- + BARC
- ◇ JAERI
- SSGM-I-LST-25 (data)

Location #20

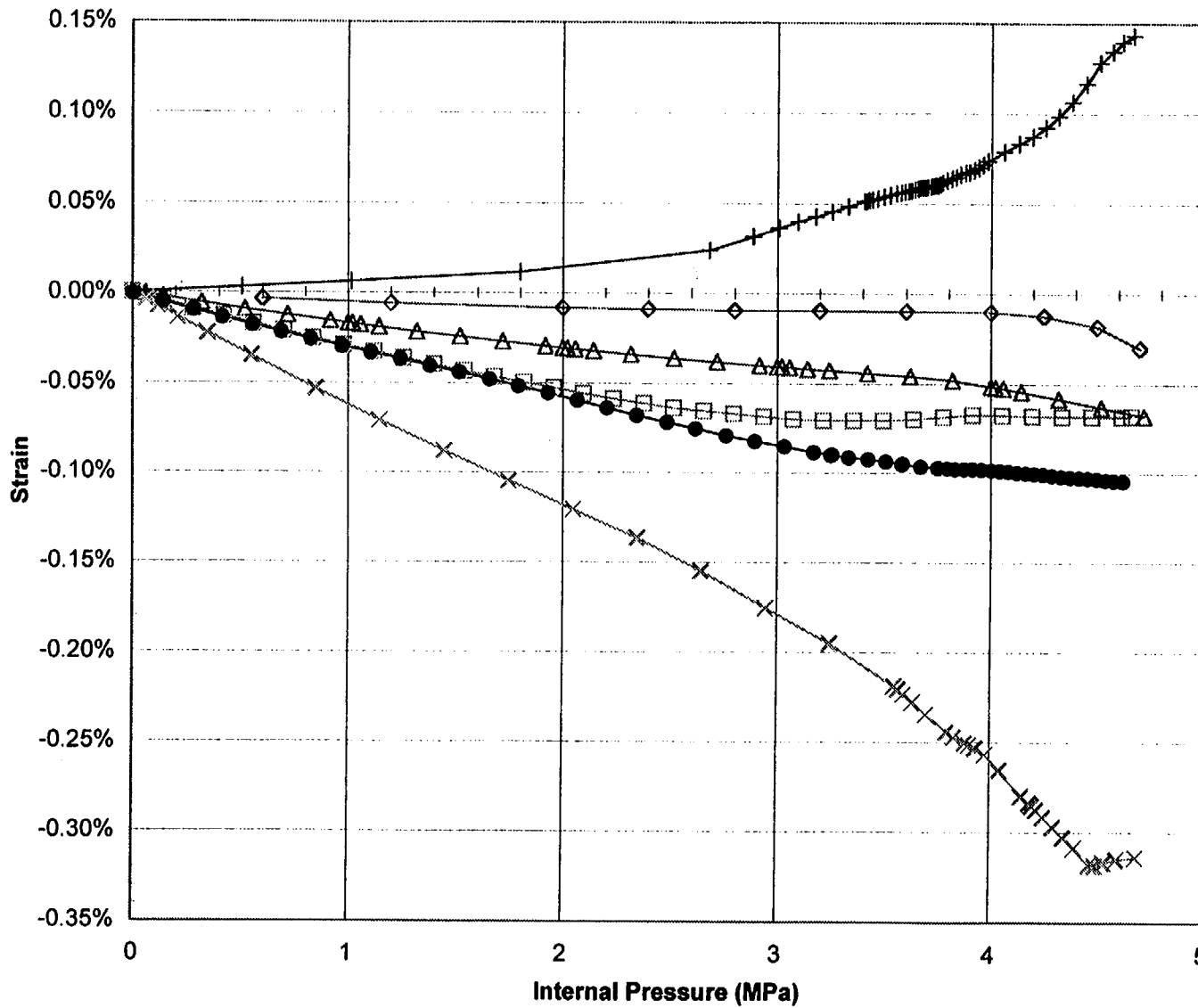
Lower Conical Shell
 Inside Surface
 Global (0°, 0.80 m)
 int. merid. strain



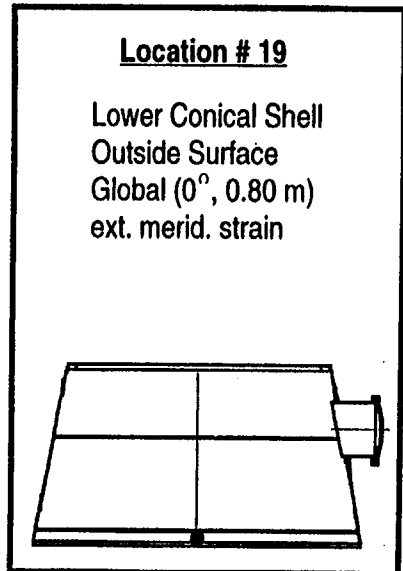
A-13

NUREG/CR-5678

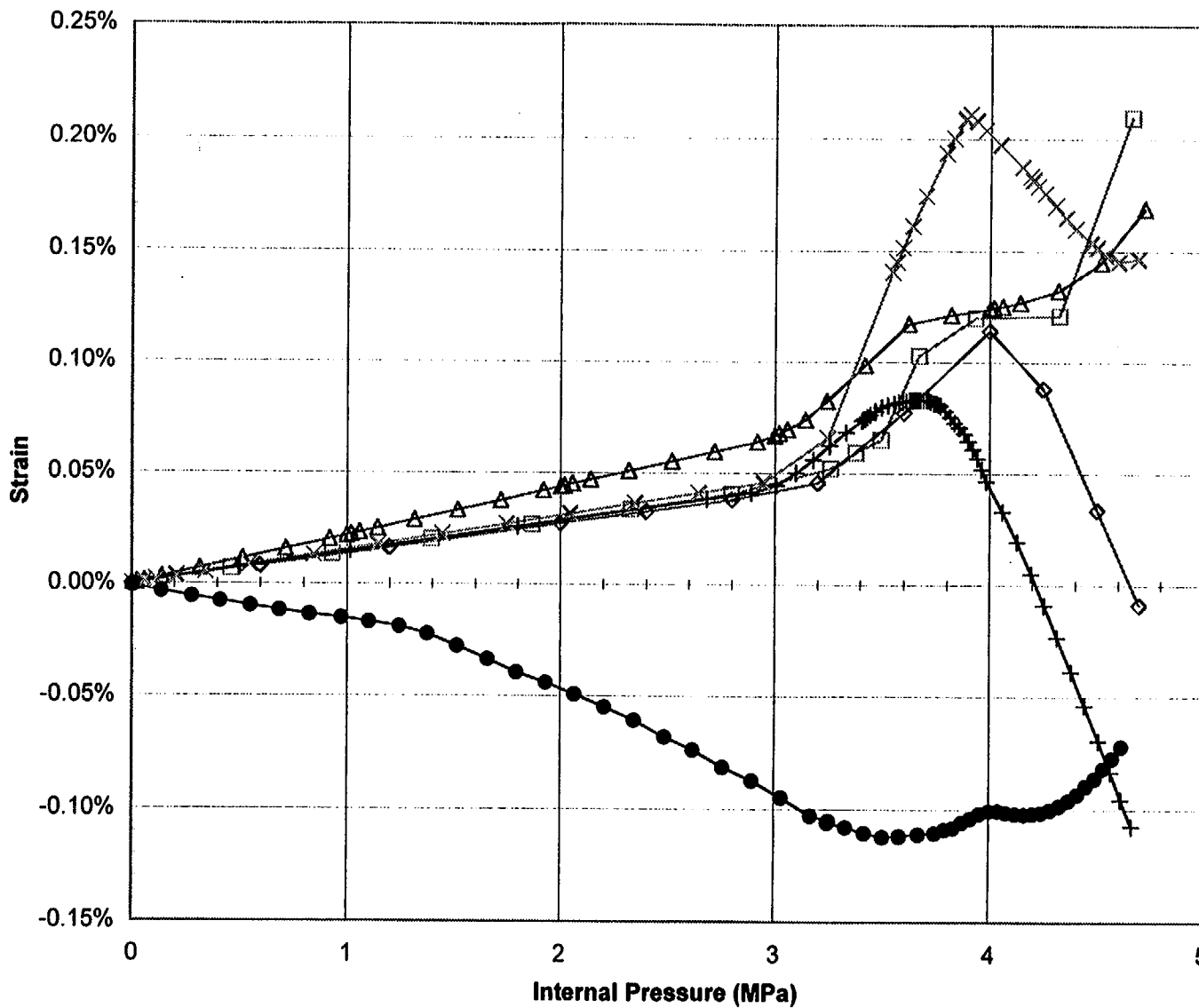
Standard Output Location #19



- Electric Boat
- △ Sandia
- × NUPEC
- + BARC
- ◇ JAERI
- SSGM-O-LST-17 (data)



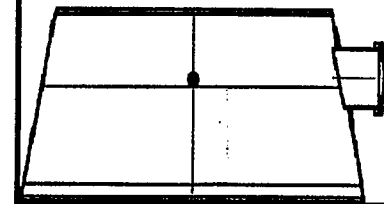
Standard Output Location #18



- Electric Boat
- △ Sandia
- × NUPEC
- + BARC
- ◇ JAERI
- RSG-I-MCI-1a (data)

Location # 18

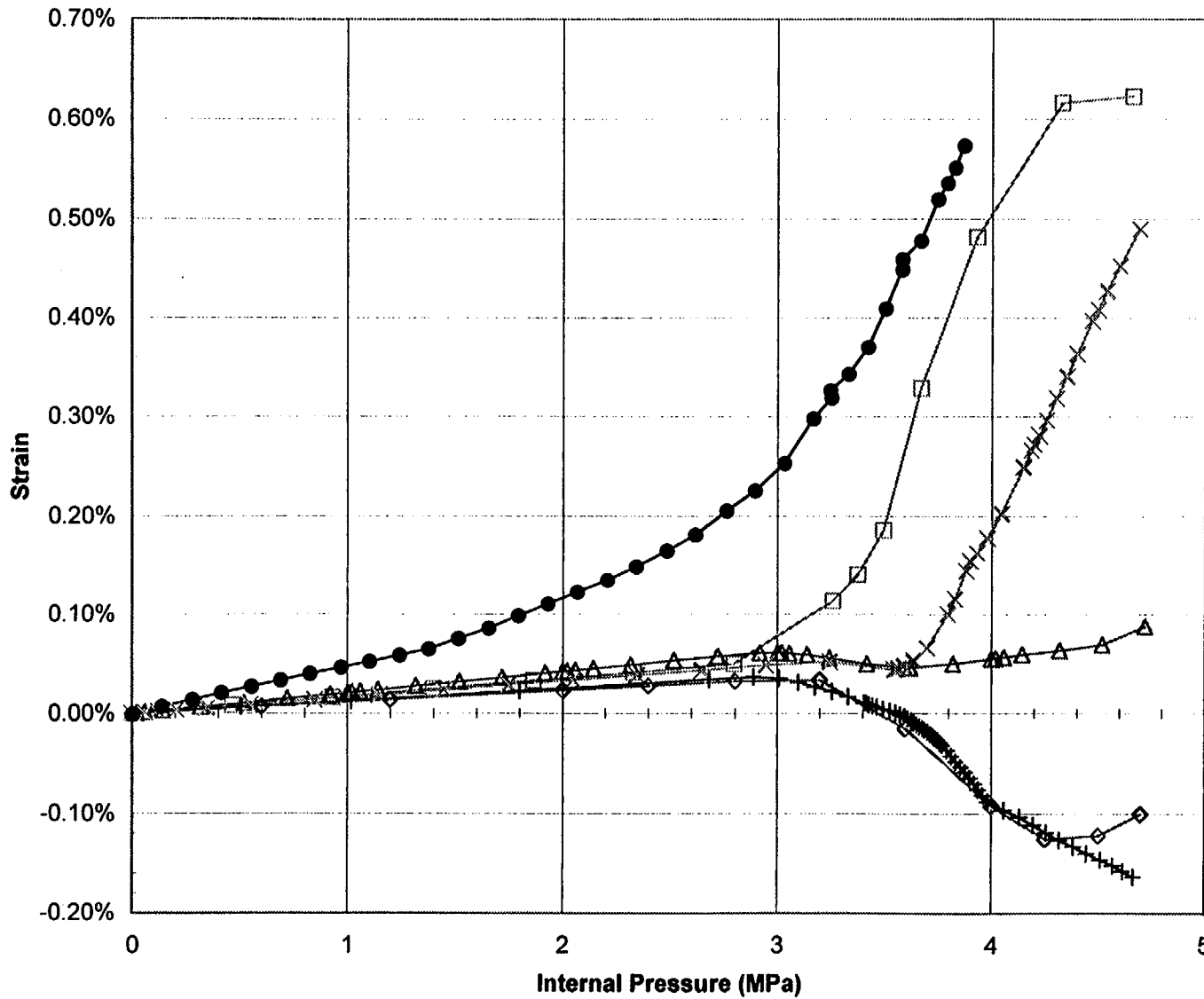
Middle Conical Shell
 Inside Surface
 Global (0°, 1.60 m)
 int. merid. strain



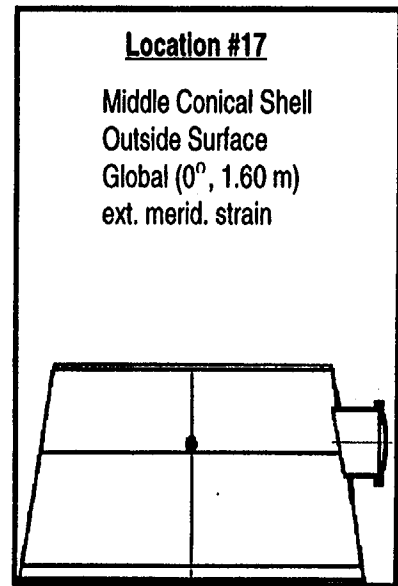
A-15

NUREG/CR-5678

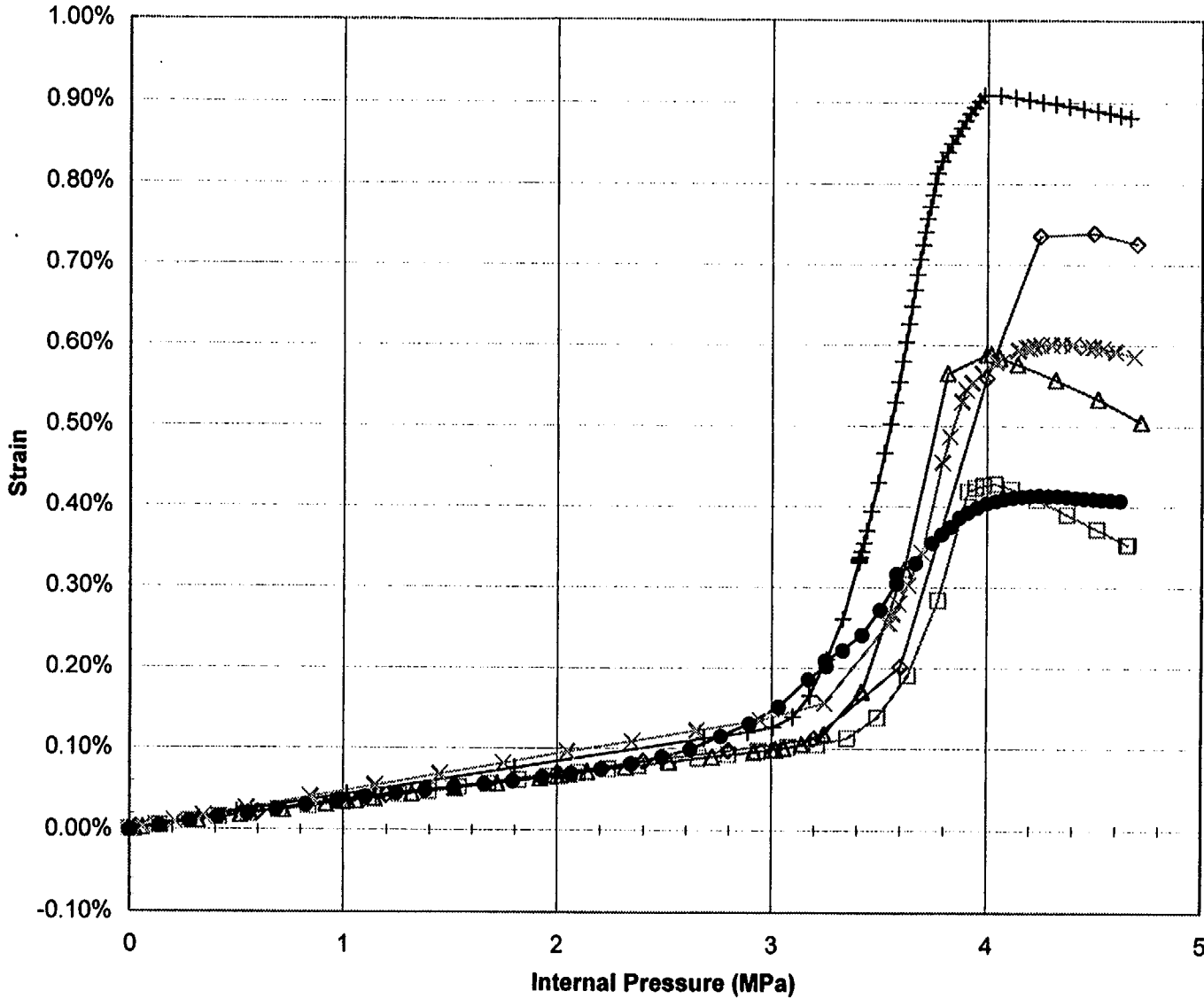
Standard Output Location #17



- Electric Boat
- △ Sandia
- × NUPEC
- + BARC
- ◇ JAERI
- SSGM-O-MCI-2 (data)



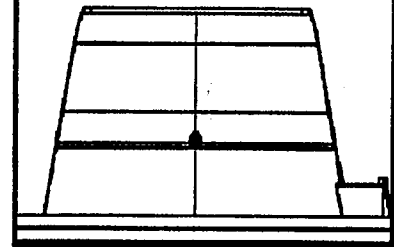
Standard Output Location #16



- Electric Boat
- △ Sandia
- × NUPEC
- + BARC
- ◇ JAERI
- SSGM-I-MST-7 (data)

Location #16

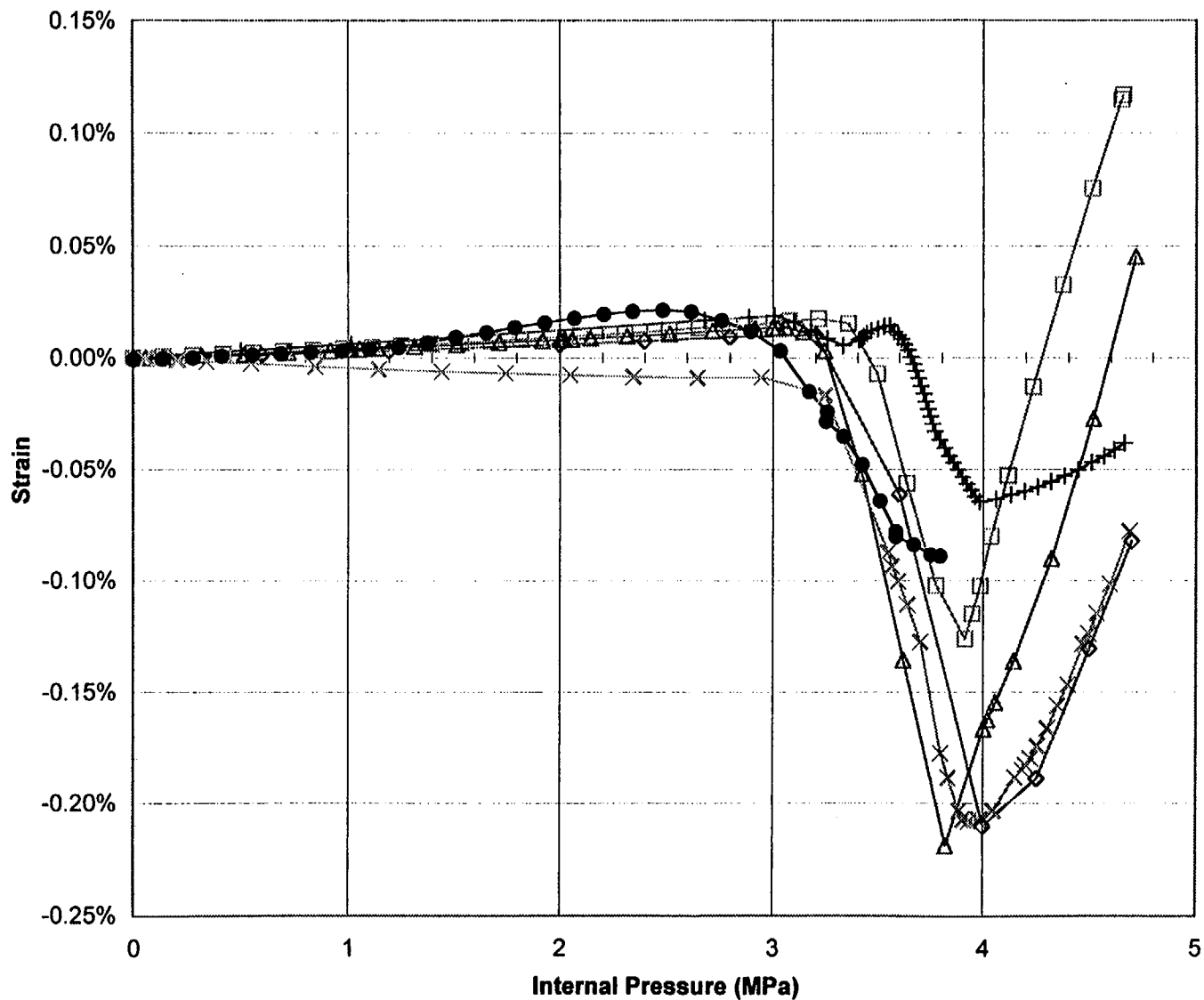
Middle Conical Shell
 Inside Surface
 Global (0°, 2.10 m)
 int. merid. strain



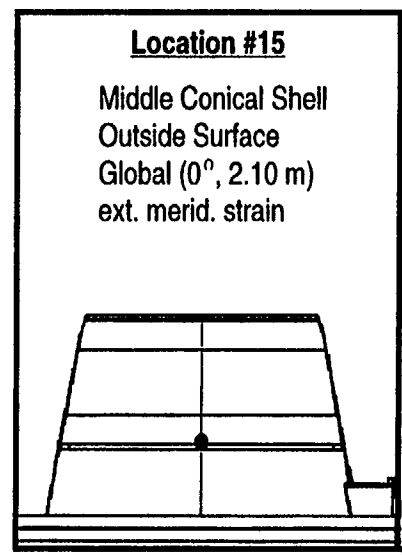
A-17

NUREG/CR-5678

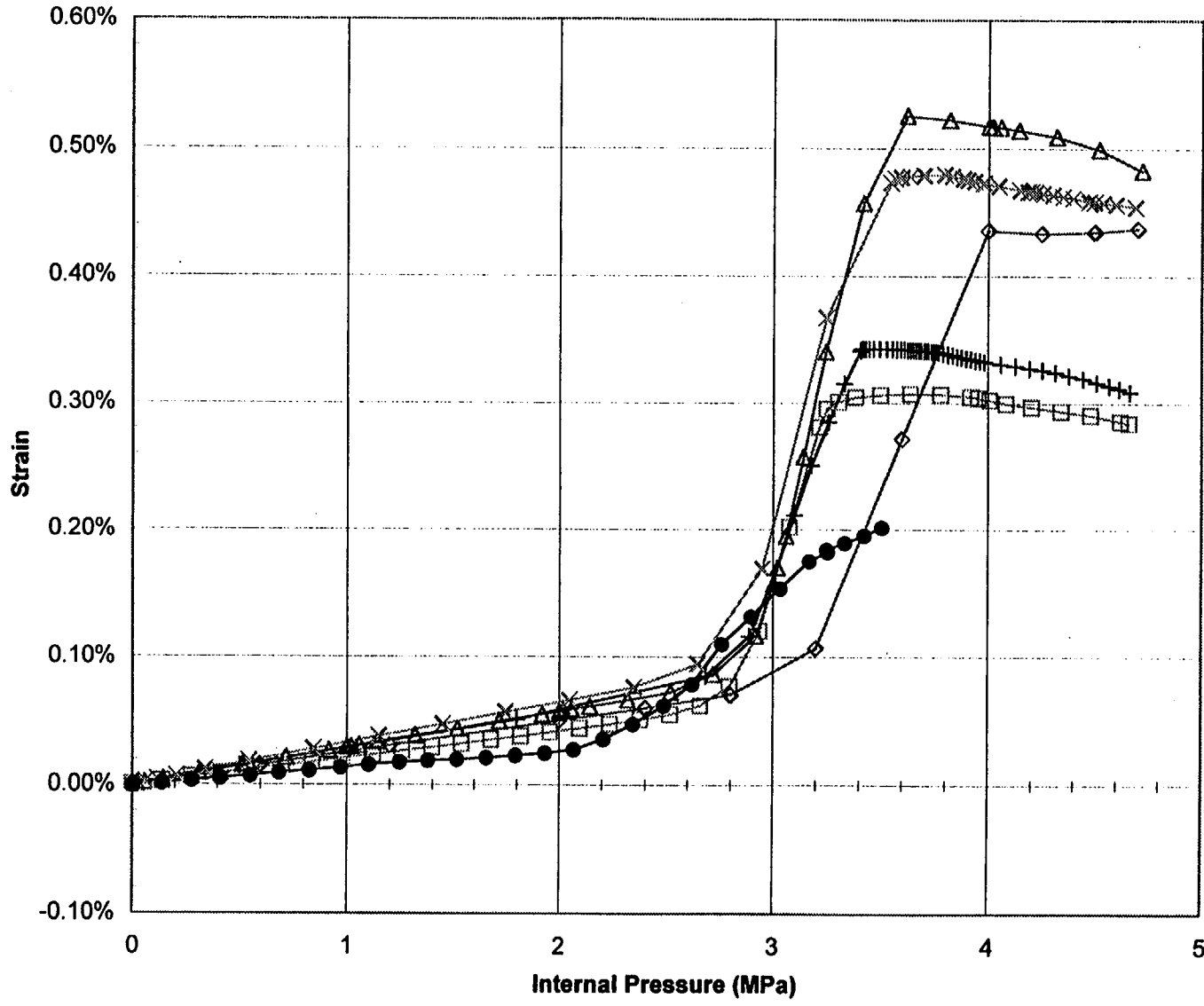
Standard Output Location #15



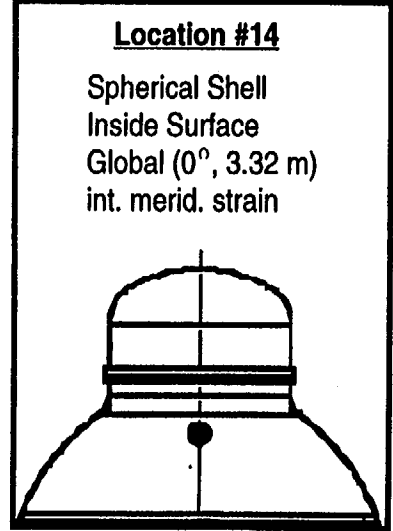
- Electric Boat
- △ Sandia
- × NUPEC
- + BARC
- ◇ JAERI
- SSGM-O-MST-1 (data)



Standard Output Location #14



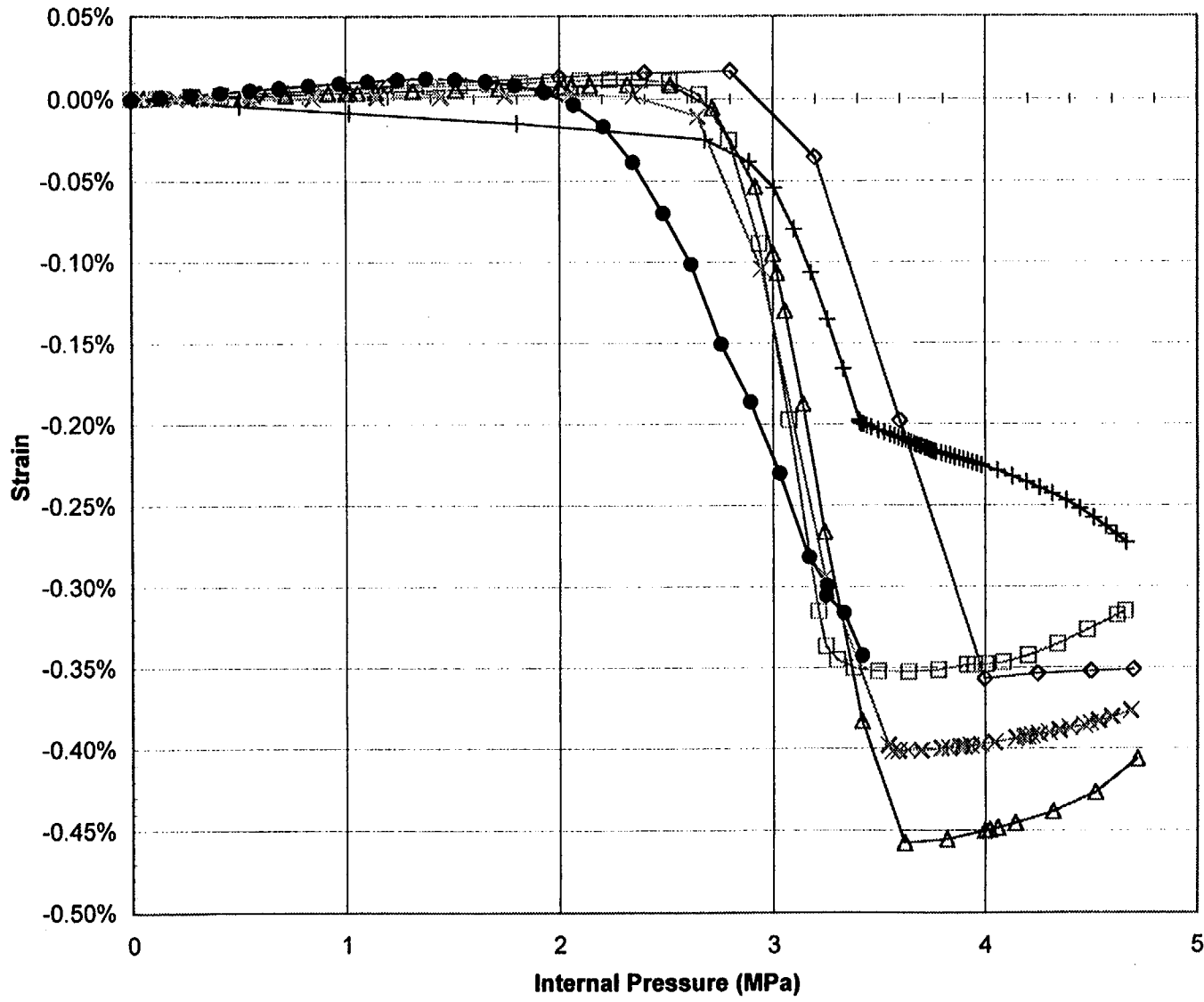
- Electric Boat
- △ Sandia
- × NUPEC
- + BARC
- ◇ JAERI
- STG-I-KNU-9c (data)



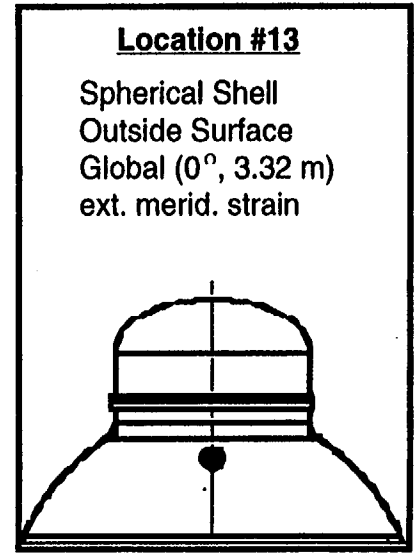
A-19

NUREG/CR-5678

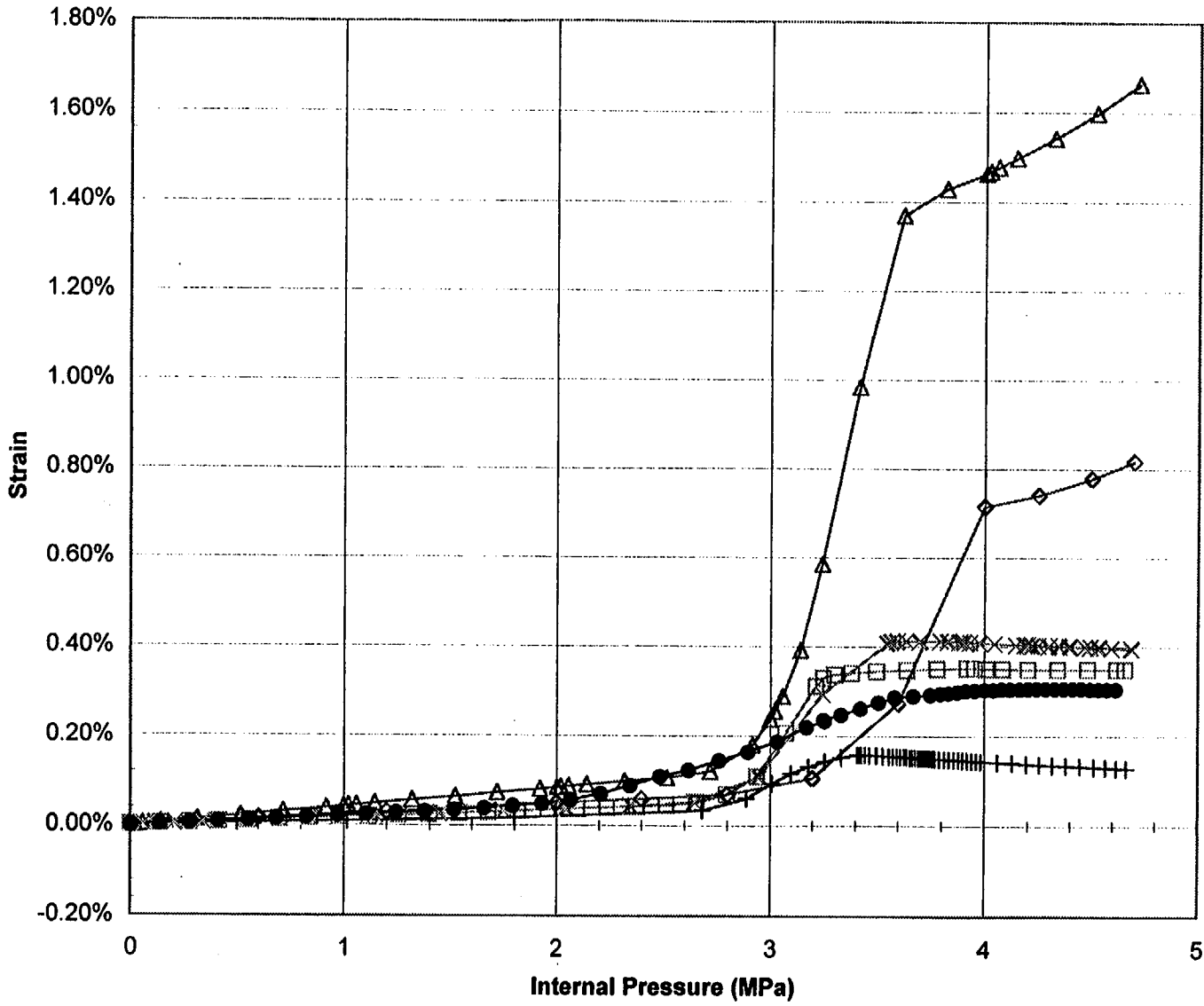
Standard Output Location #13



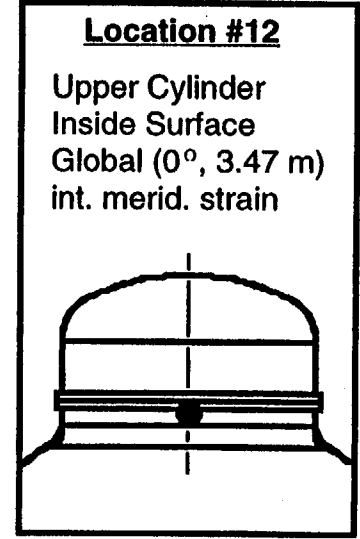
- Electric Boat
- △ Sandia
- × NUPEC
- + BARC
- ◇ JAERI
- STG-O-KNU-1c (data)



Standard Output Location #12



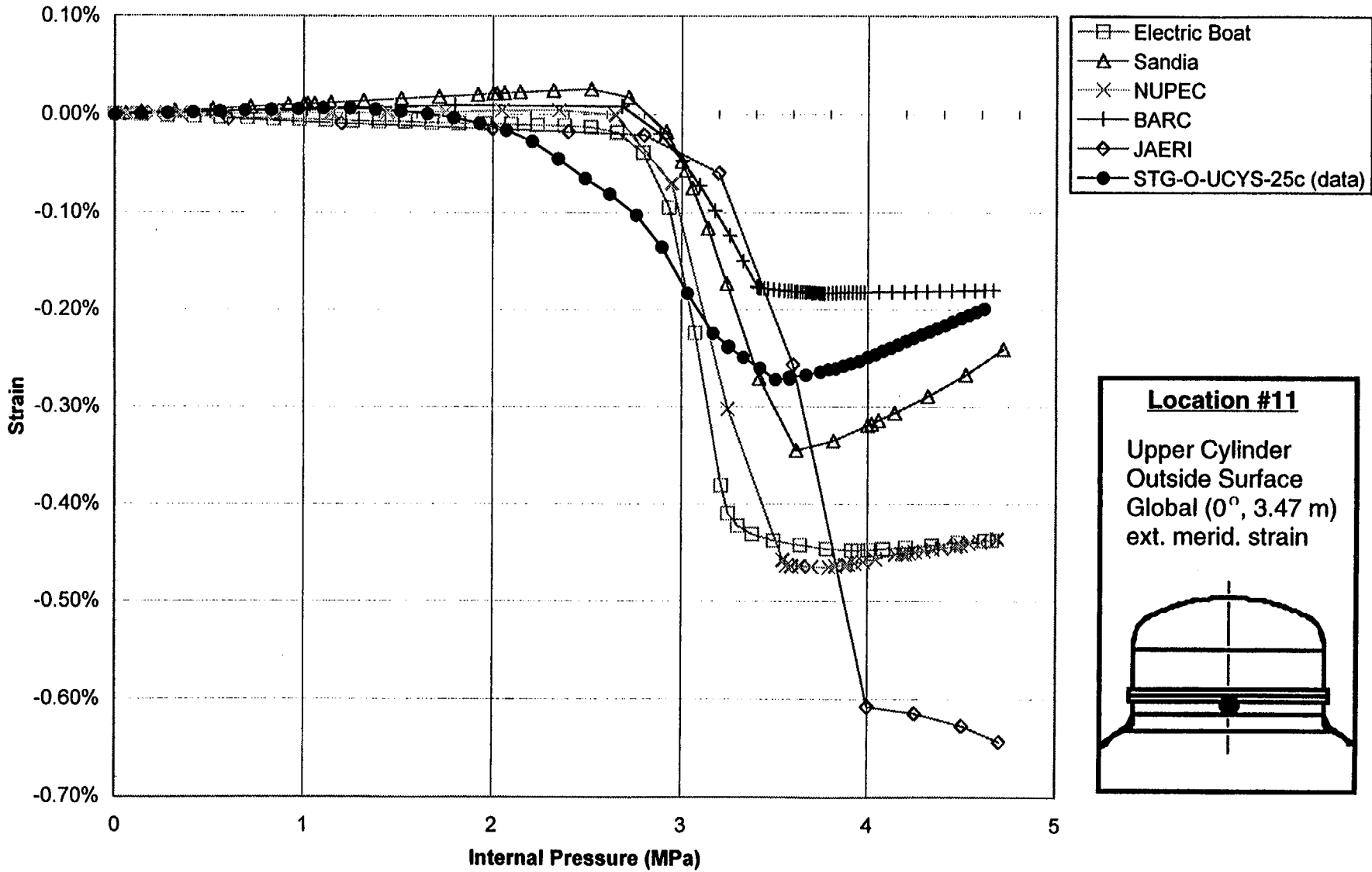
- Electric Boat
- △ Sandia
- × NUPEC
- + BARC
- ◇ JAERI
- SSGM-I-UCYS-27 (data)



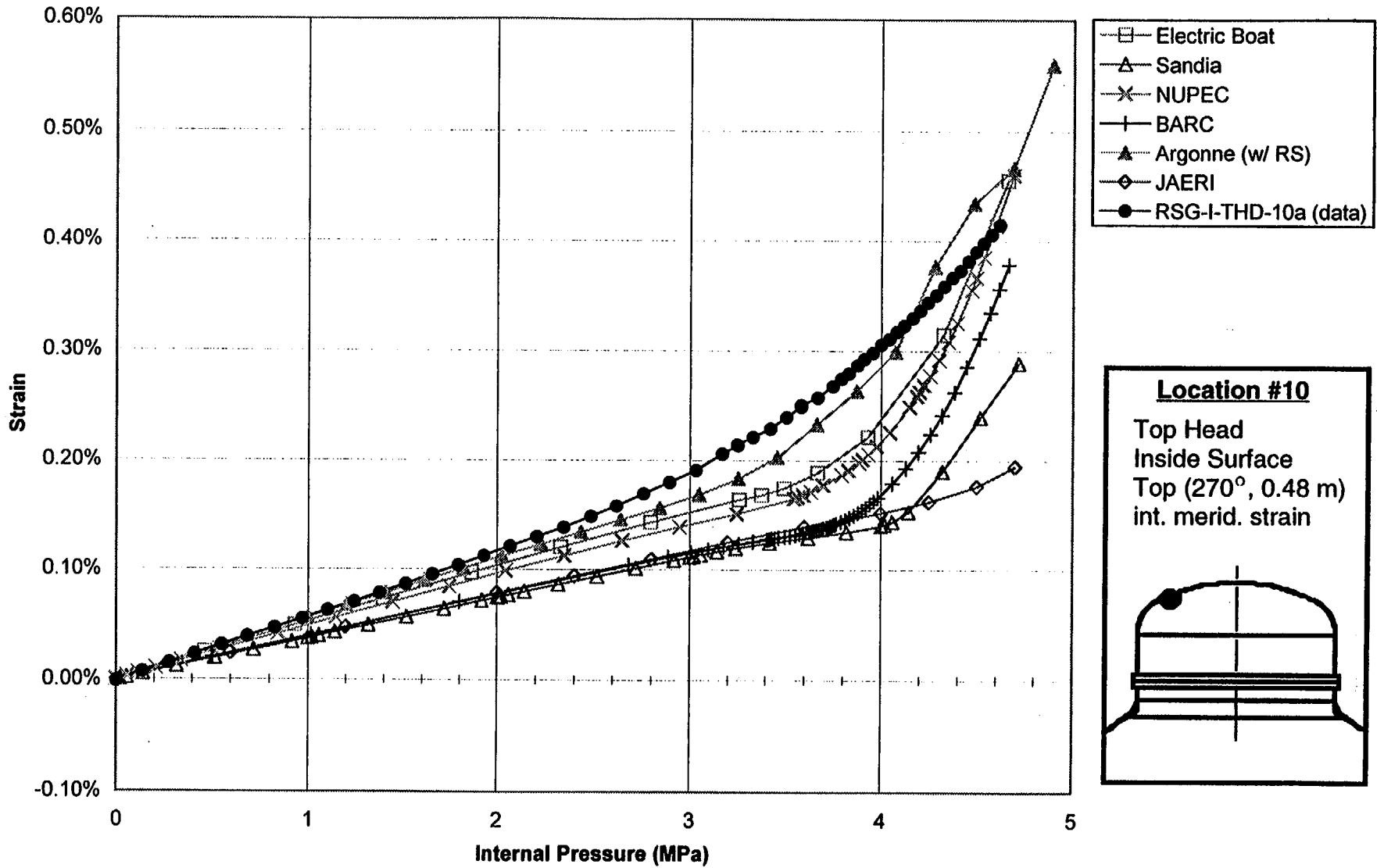
A-21

NUREG/CR-5678

Standard Output Location #11

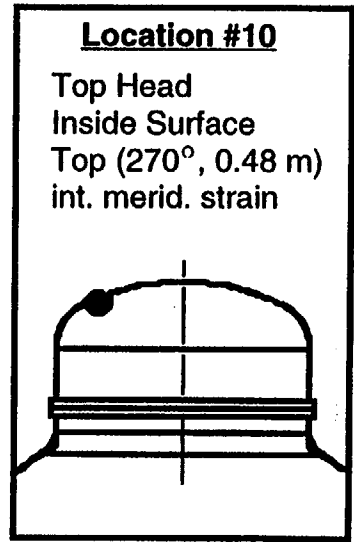


Standard Output Location #10

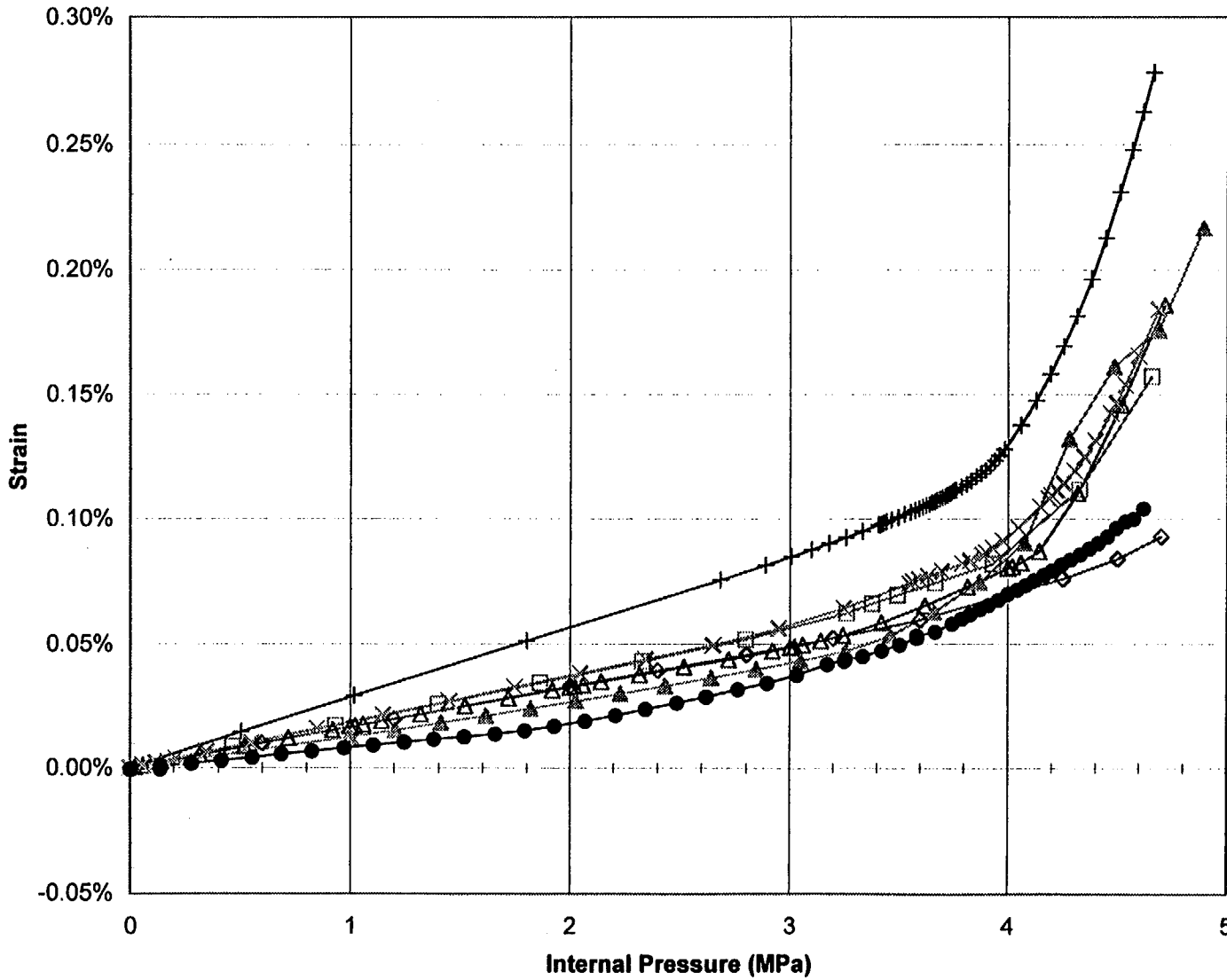


A-23

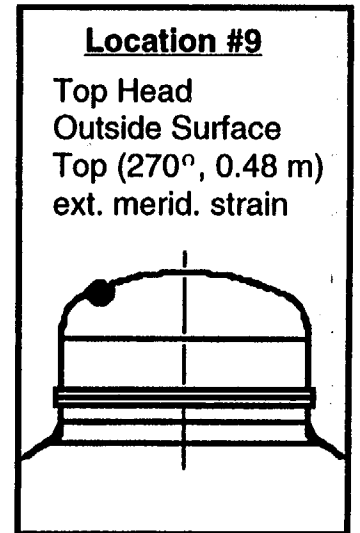
NUREG/CR-5678



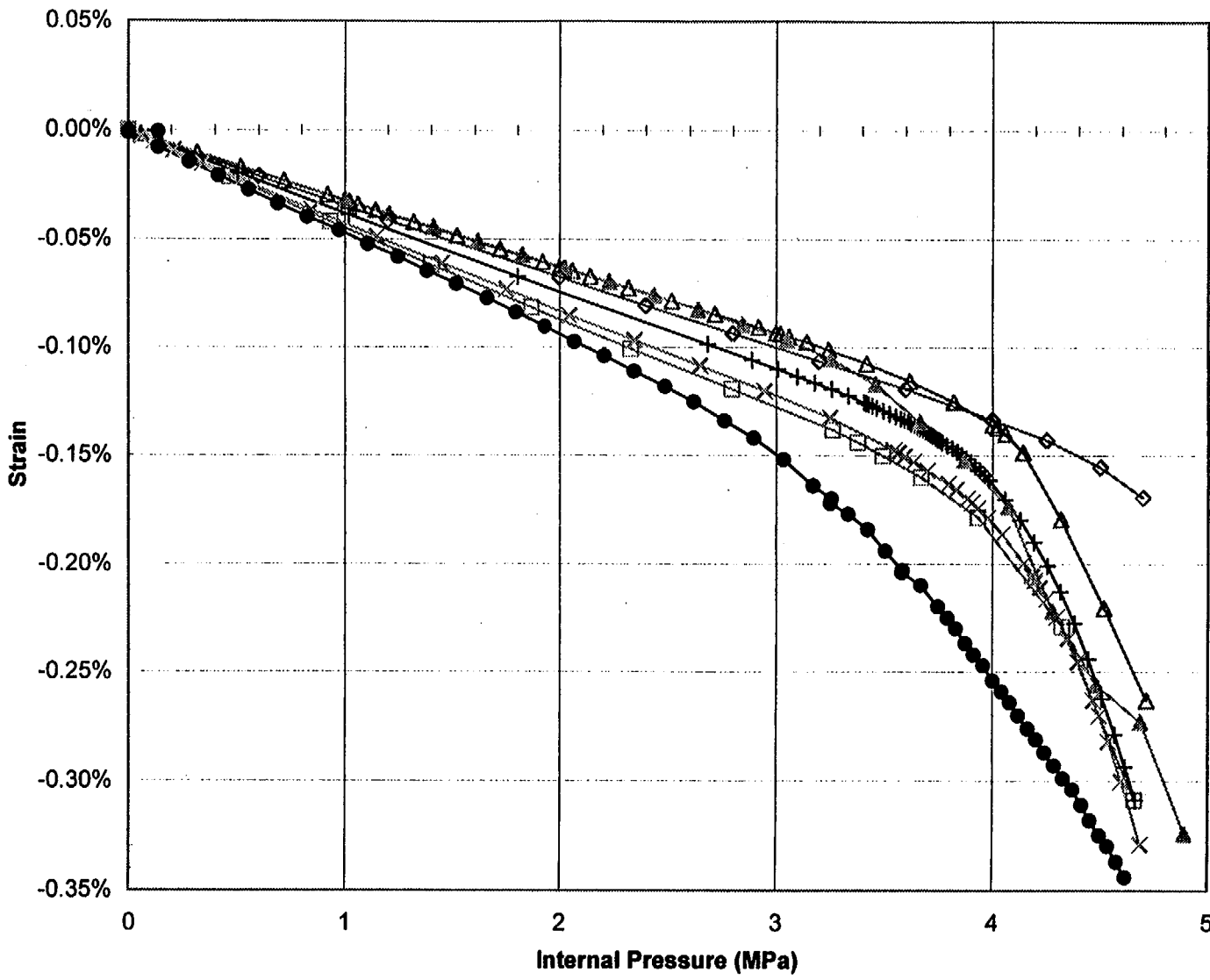
Standard Output Location #9



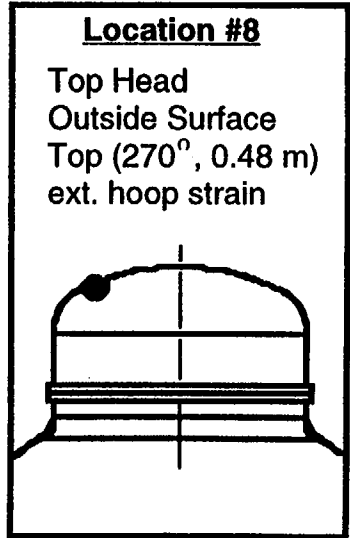
- Electric Boat
- △ Sandia
- × NUPEC
- + BARC
- ▲ Argonne (w/ RS)
- ◇ JAERI
- RSG-O-THD-9c (data)



Standard Output Location #8



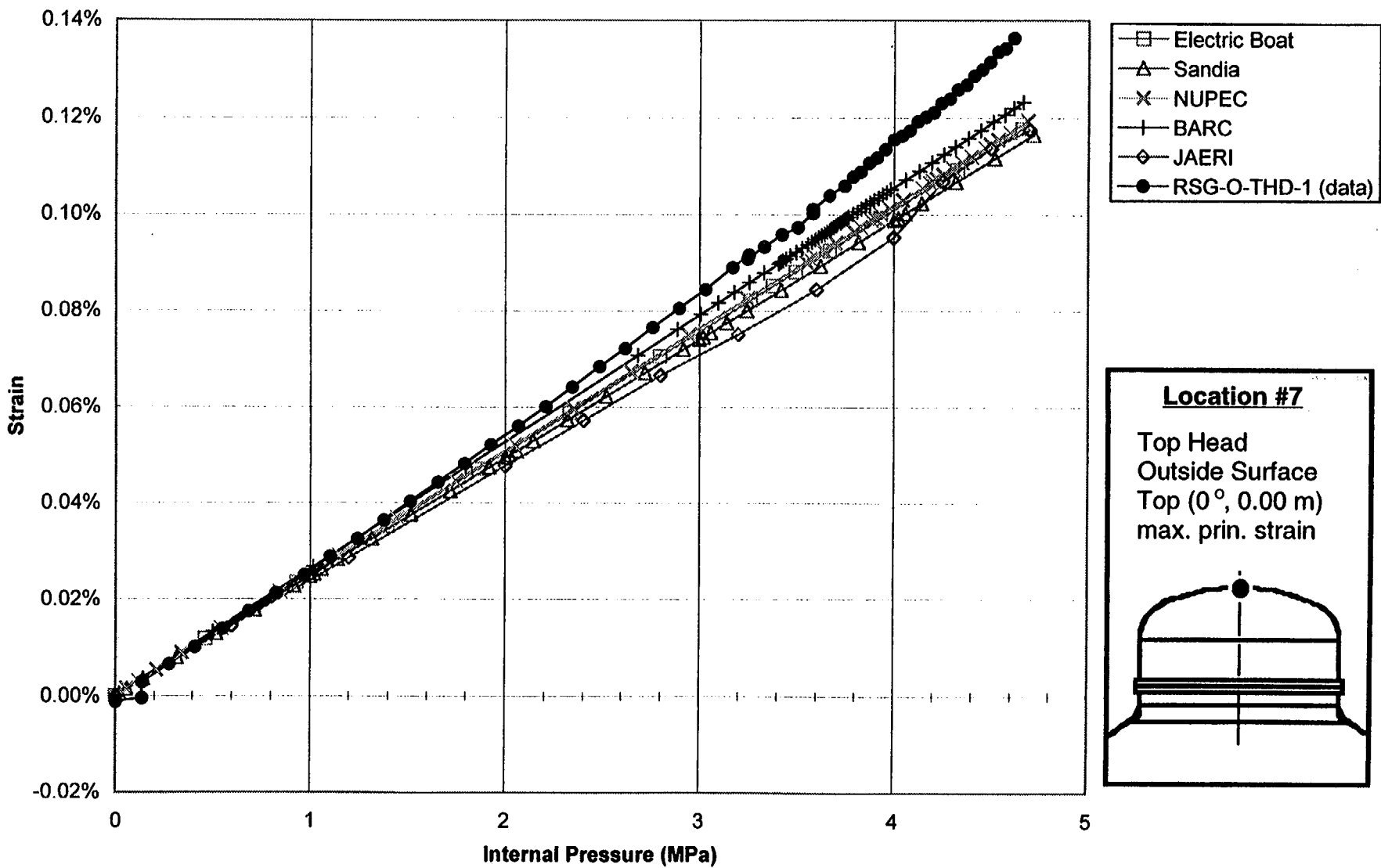
- Electric Boat
- △ Sandia
- × NUPEC
- ⊕ BARC
- ▲ Argonne (w/ RS)
- ◇ JAERI
- RSG-O-THD-9a (data)



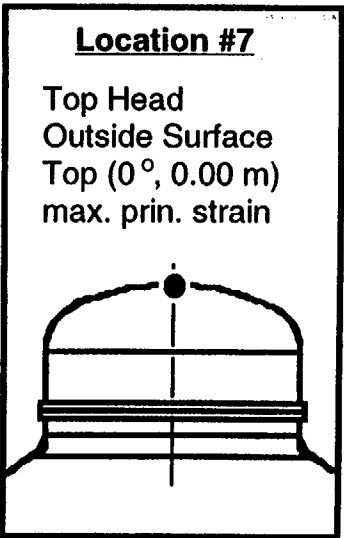
A-25

NUREG/CR-5678

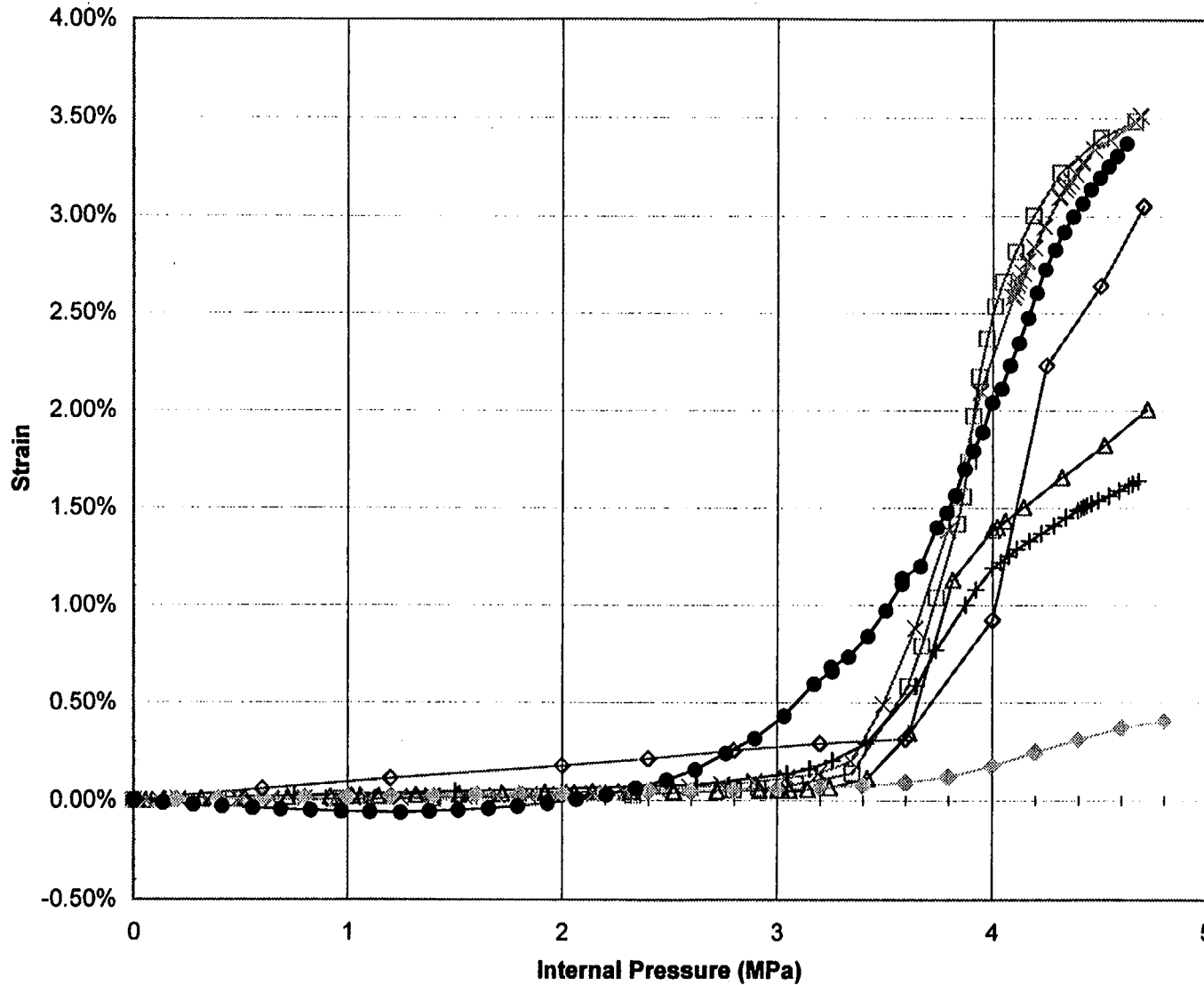
Standard Output Location #7



- Electric Boat
- △ Sandia
- × NUPEC
- + BARC
- ◇ JAERI
- RSG-O-THD-1 (data)



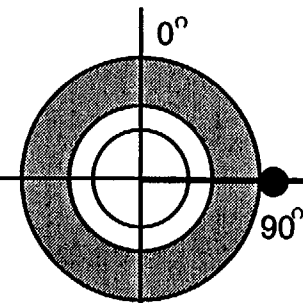
Standard Output Location #6



- Electric Boat
- △ Sandia
- × NUPEC
- † BARC
- ◇ ANPA
- ◇ JAERI
- STG-I-EQH-16c (data)

Location #6

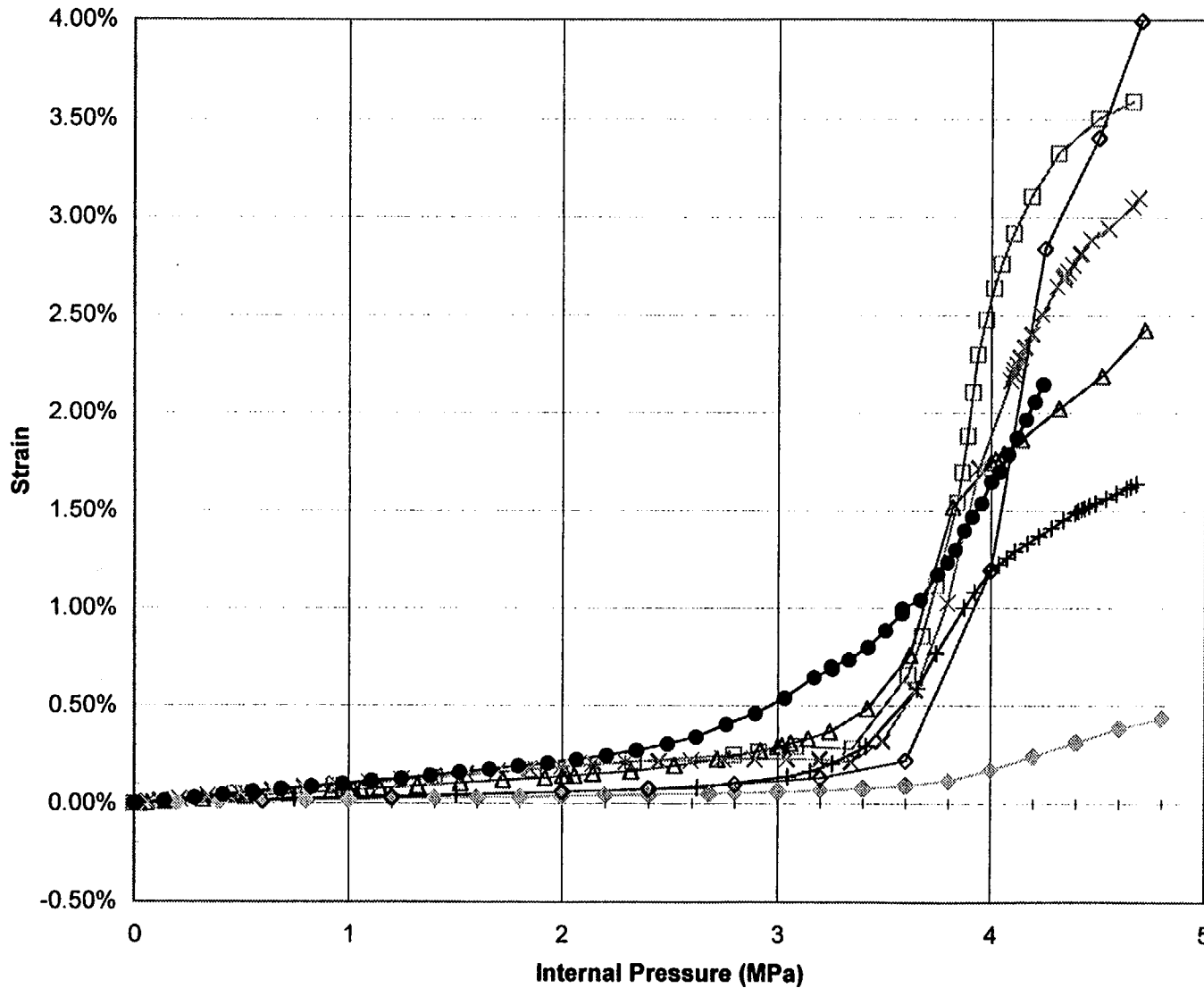
Hatch Region
 Inside Surface
 Hatch (90°, 0.36 m)
 int. hoop strain



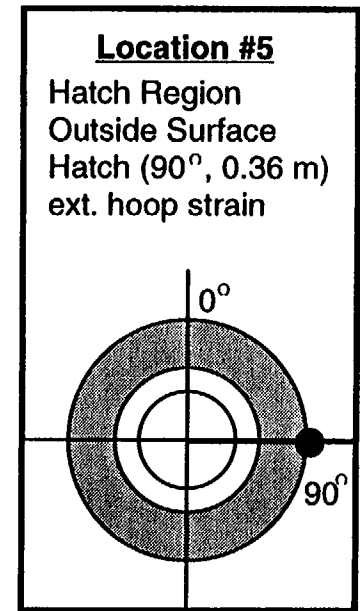
A-27

NUREG/CR-5678

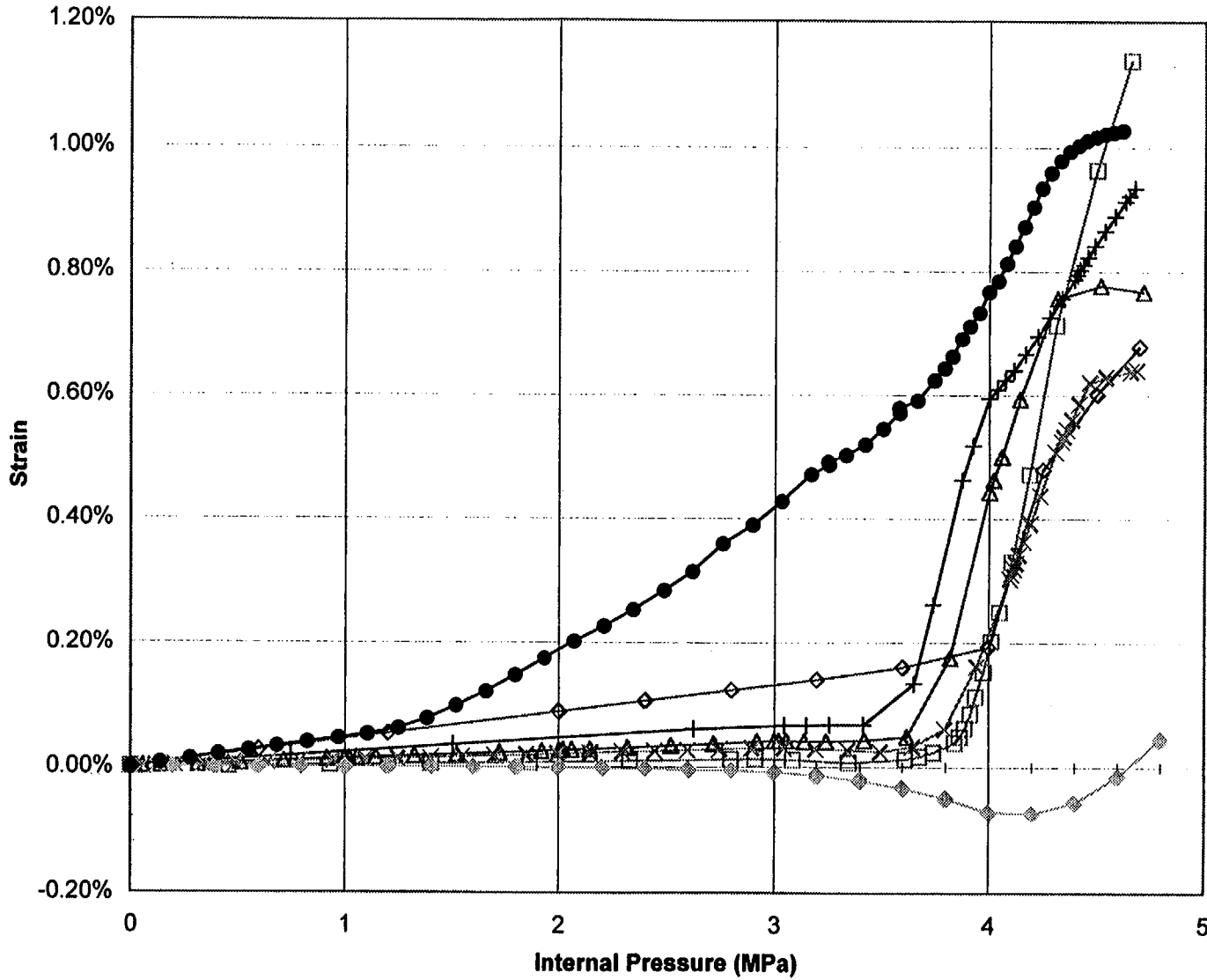
Standard Output Location #5



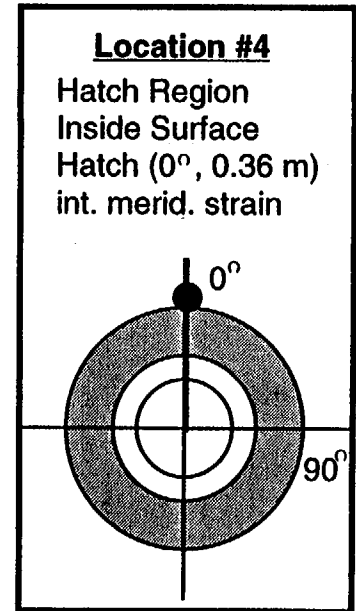
- Electric Boat
- △ Sandia
- × NUPEC
- † BARC
- ◇ ANPA
- ◊ JAERI
- SSGH-O-EQH-18 (data)



Standard Output Location #4



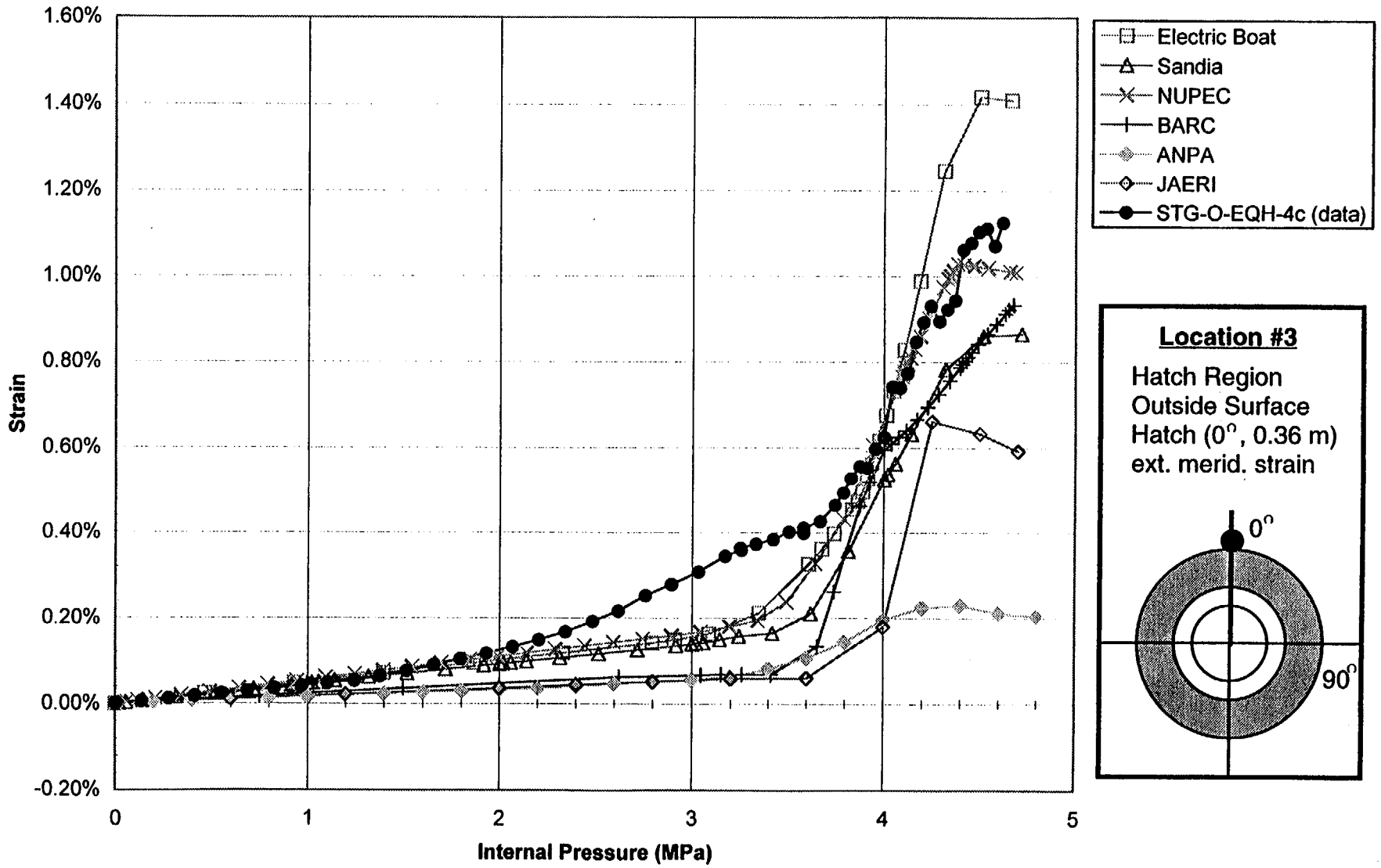
- Electric Boat
- △ Sandia
- × NUPEC
- † BARC
- ◇ ANPA
- ◇ JAERI
- STG-I-EQH-2c (data)



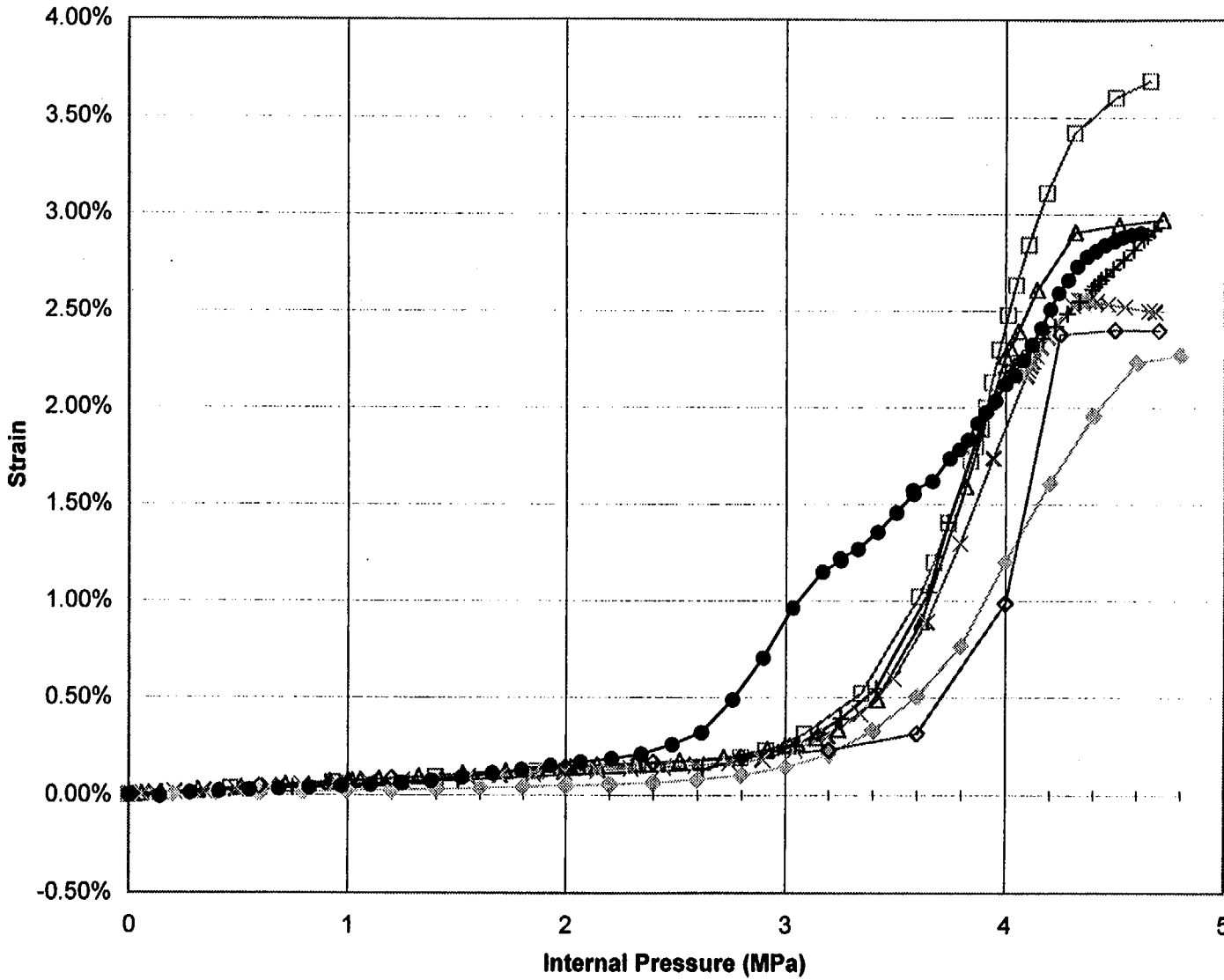
A-29

NUREG/CR-5678

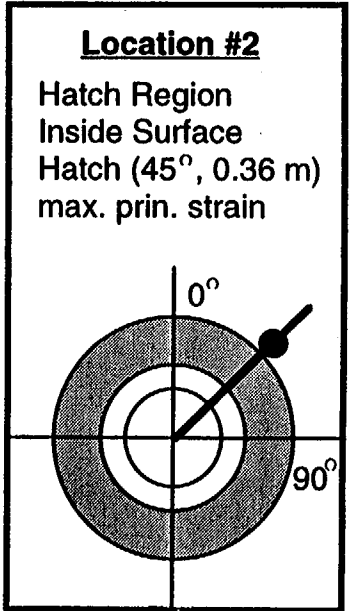
Standard Output Location #3



Standard Output Location #2



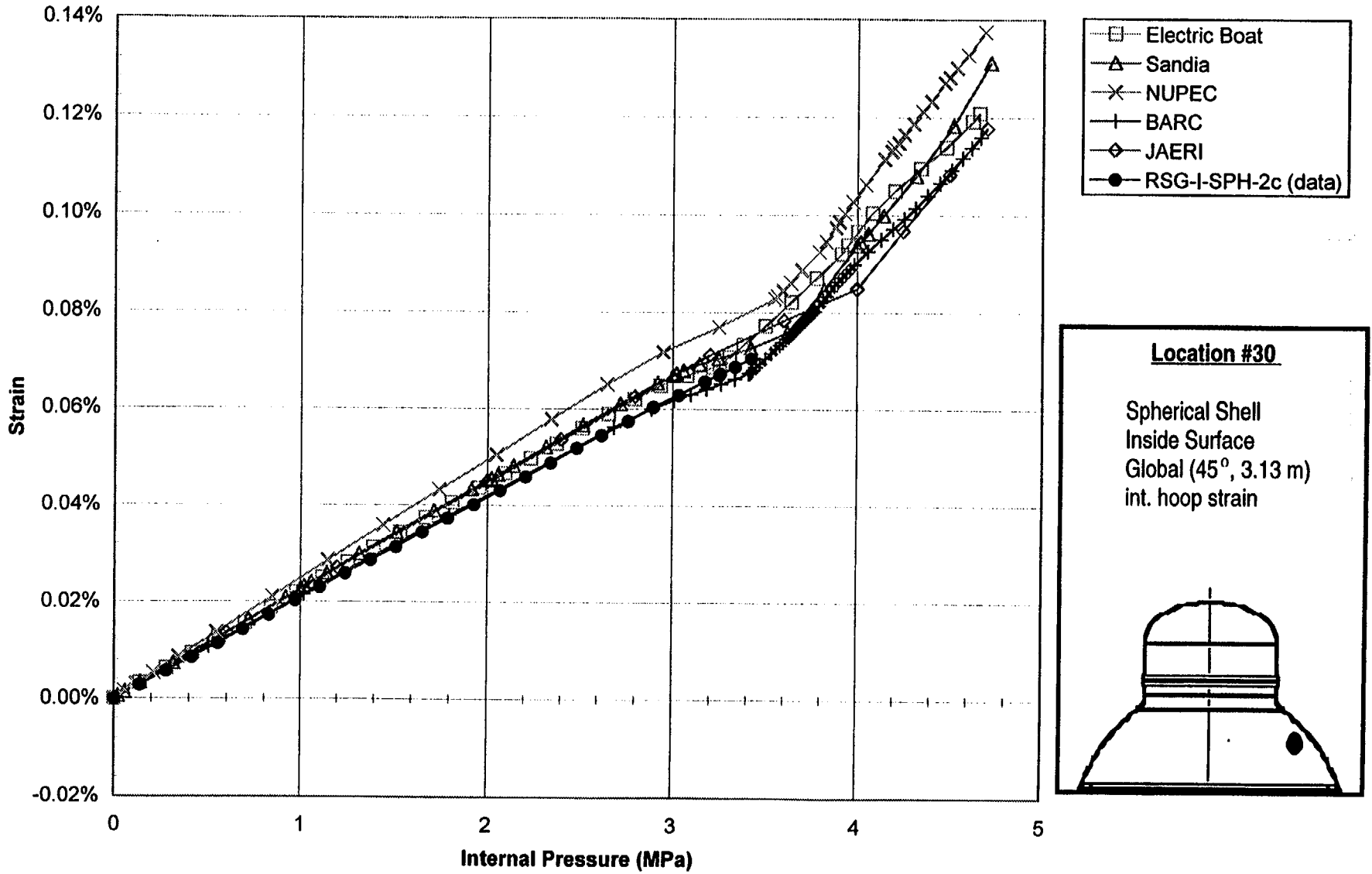
- Electric Boat
- △ Sandia
- × NUPEC
- + BARC
- ◇ ANPA
- ◇ JAERI
- RSG-I-EQH-8 (data)



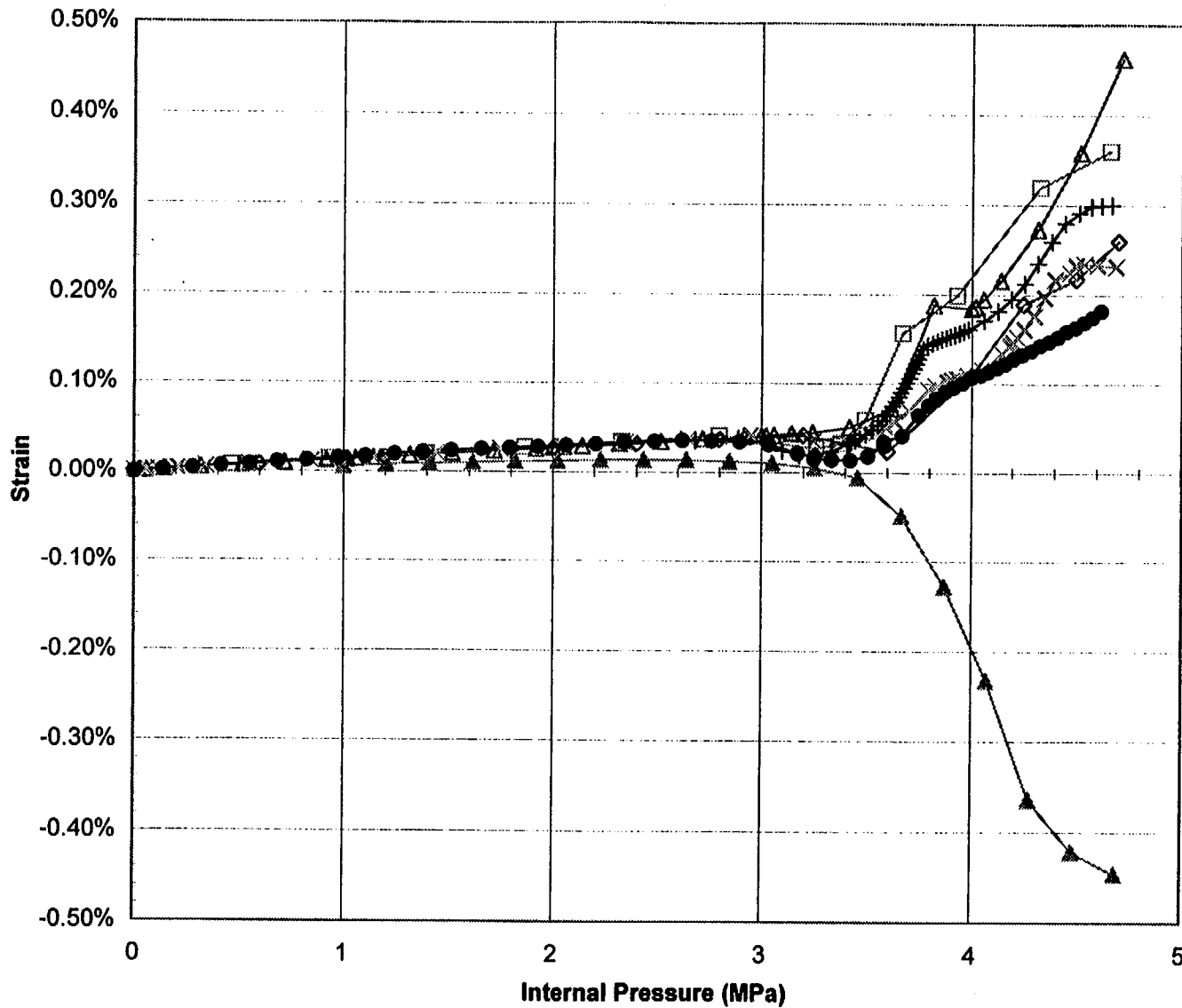
A-31

NUREG/CR-5678

Standard Output Location #30



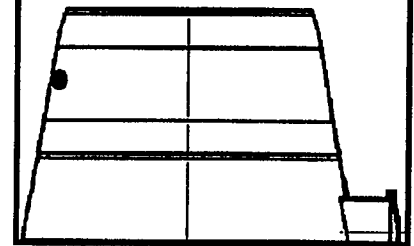
Standard Output Location #31



- Electric Boat
- △ Sandia
- × NUPEC
- ⊕ BARC
- ▲ Argonne (w/ RS)
- ◇ JAERI
- RSG-I-UCS-16a

Location #31

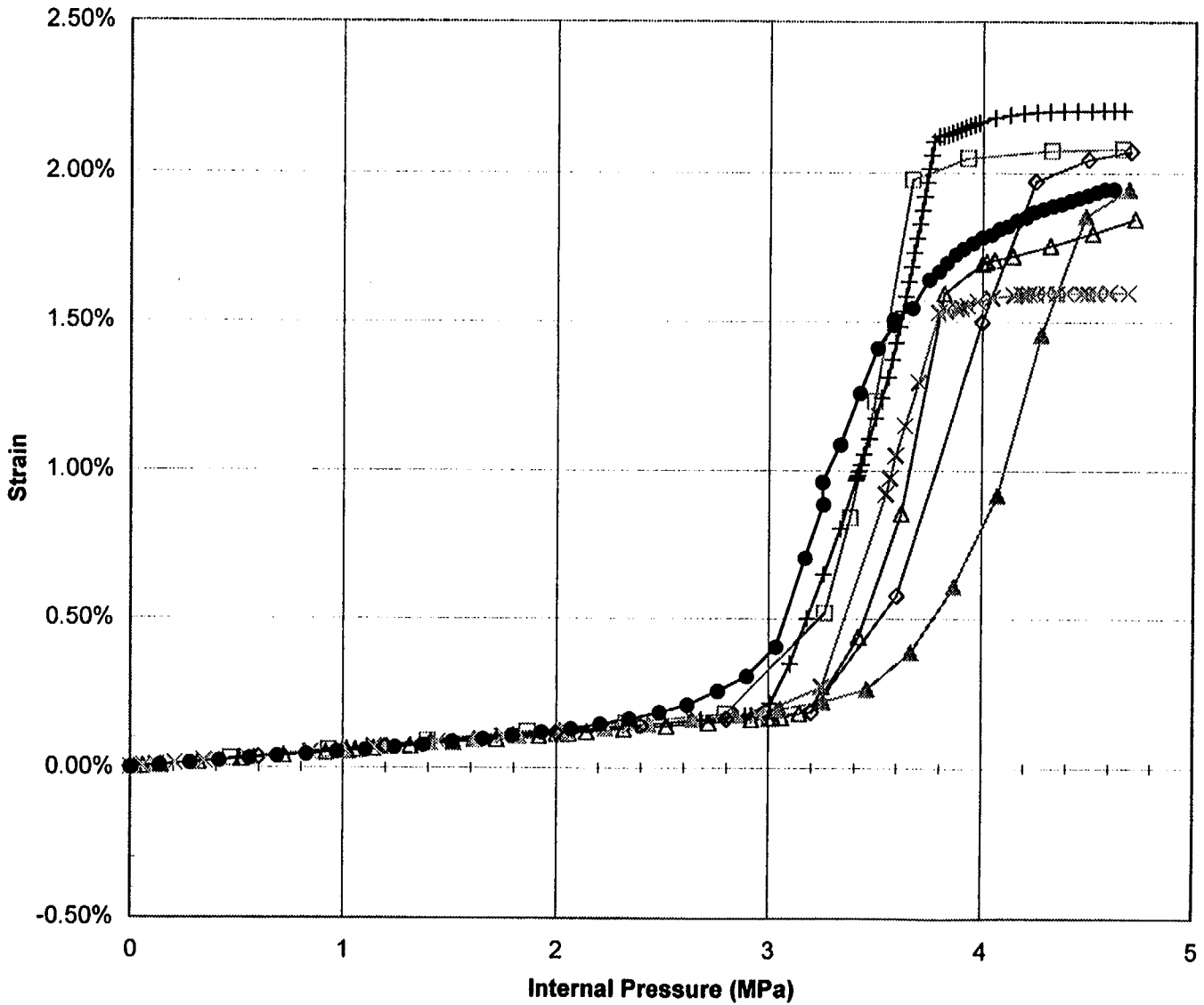
Upper Conical Shell
 Inside Surface
 Global (270°, 2.49 m)
 int. merid. strain



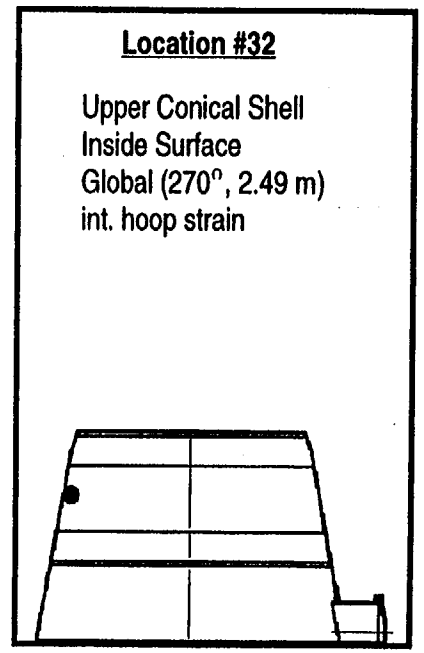
A-33

NUREG/CR-5678

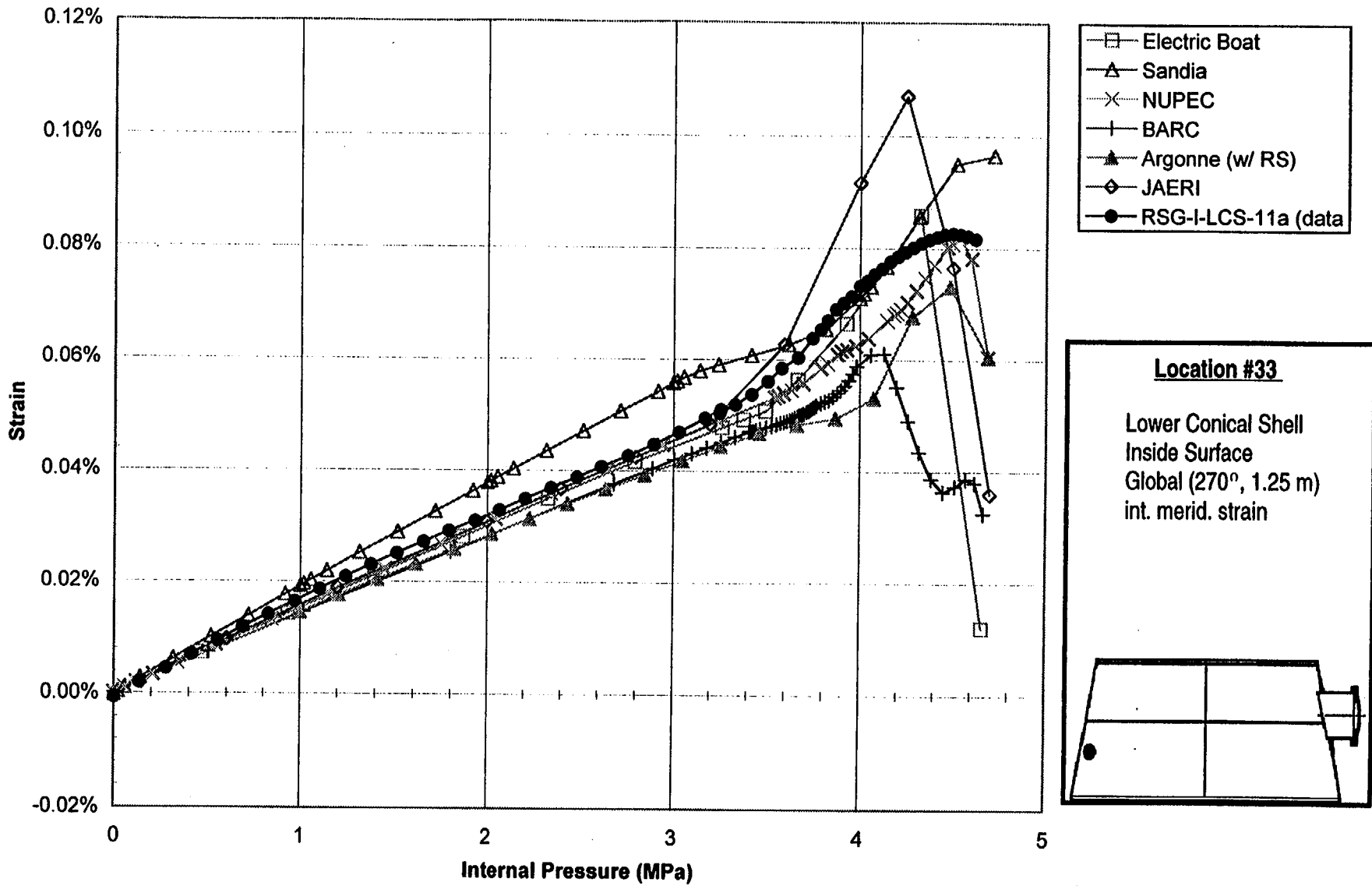
Standard Output Location #32



- Electric Boat
- △ Sandia
- × NUPEC
- + BARC
- ▲ Argonne (w/ RS)
- ◇ JAERI
- RSG-I-UCS-16c (data)



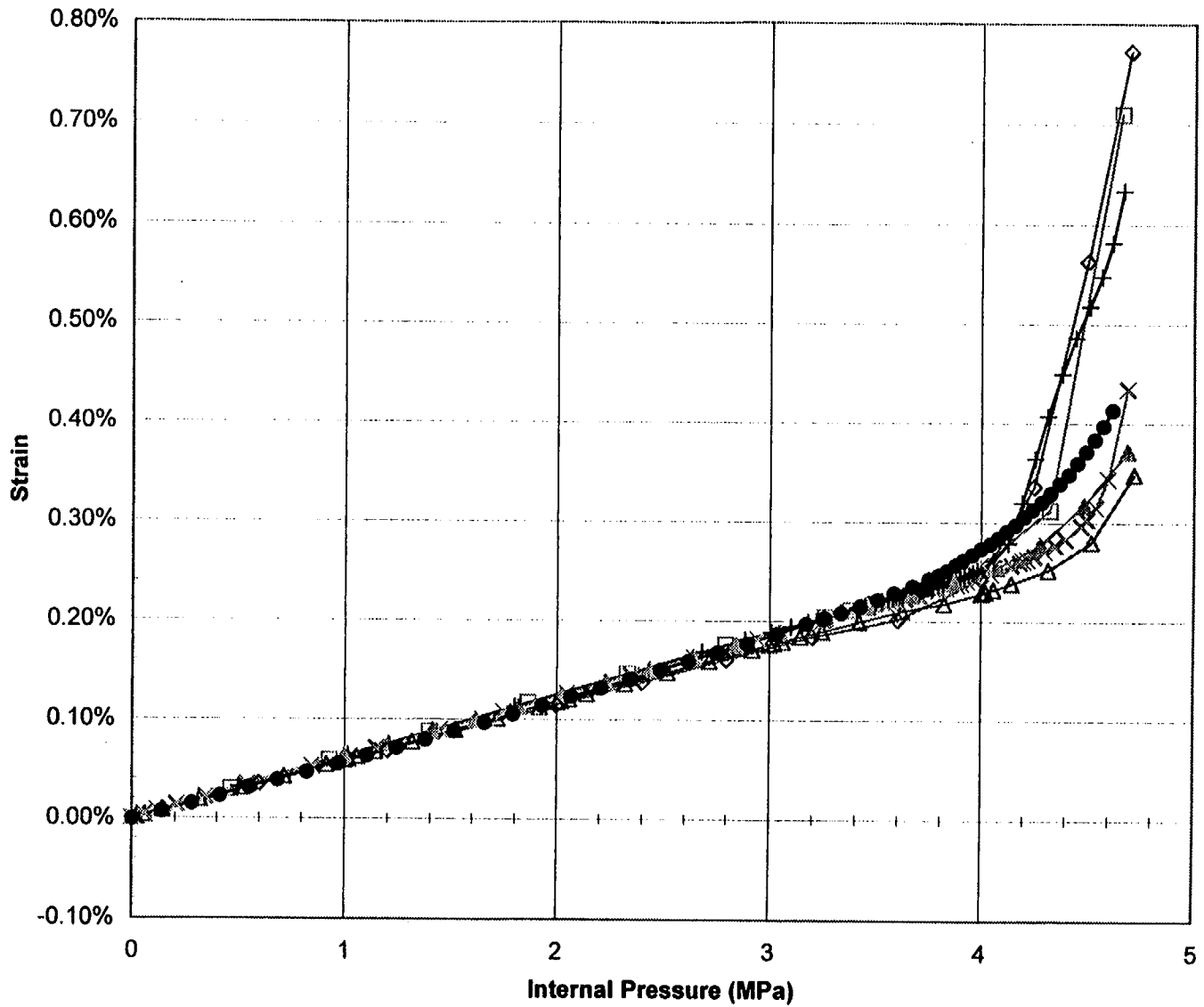
Standard Output Location #33



A-35

NUREG/CR-5678

Standard Output Location #34



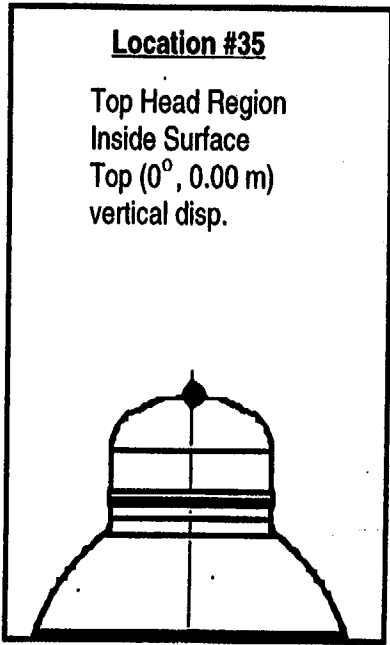
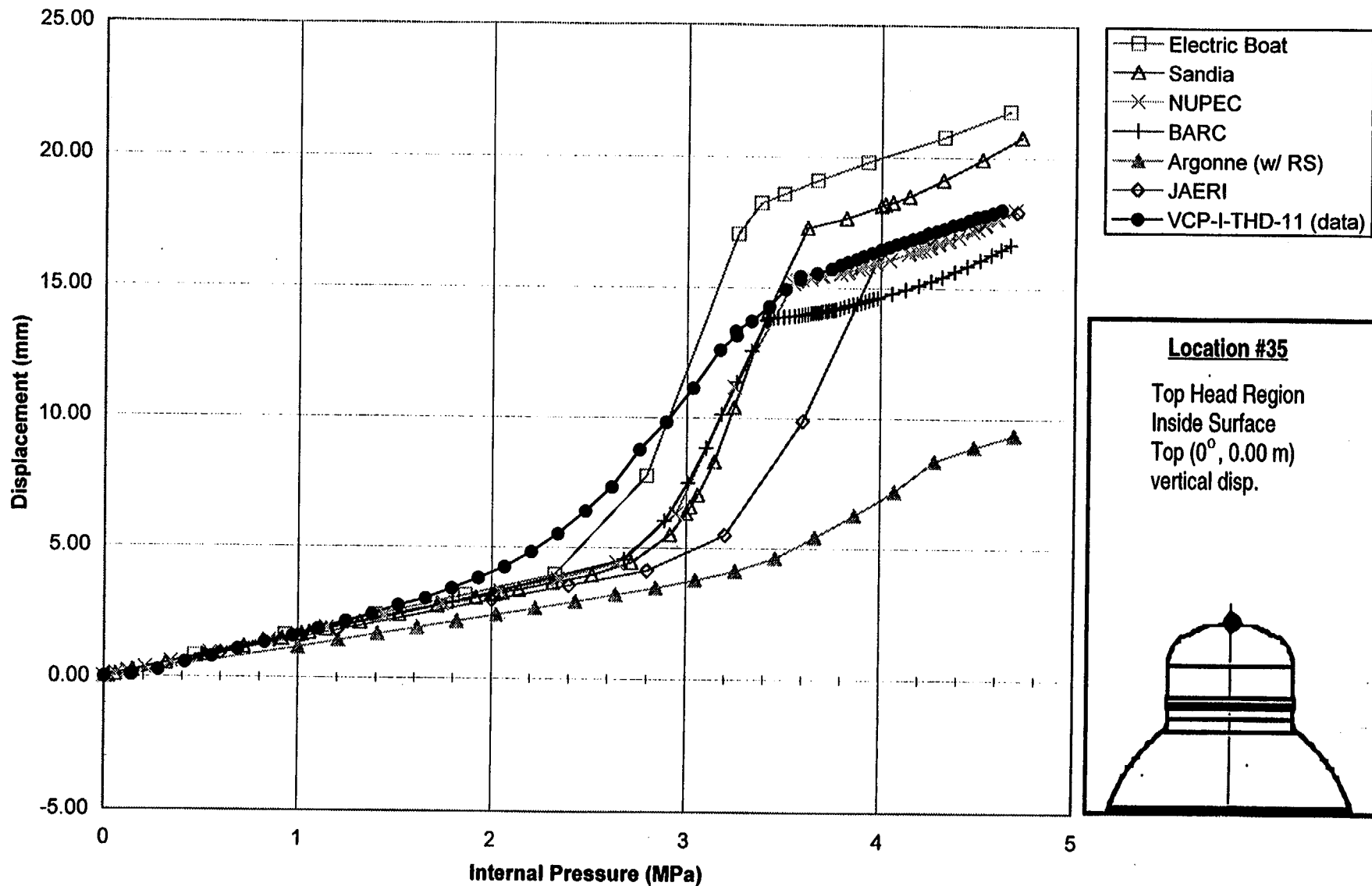
- Electric Boat
- △ Sandia
- × NUPEC
- + BARC
- ▲ Argonne (w/ RS)
- ◇ JAERI
- RSG-I-LCS-11c (data)

Location #34

Lower Conical Shell
 Inside Surface
 Global (270°, 1.25 m)
 int. hoop strain

The schematic shows a cross-section of a lower conical shell. A horizontal line represents the inside surface. A vertical line indicates the global location at 270 degrees. A dot on the left side of the shell indicates the location of the internal hoop strain sensor.

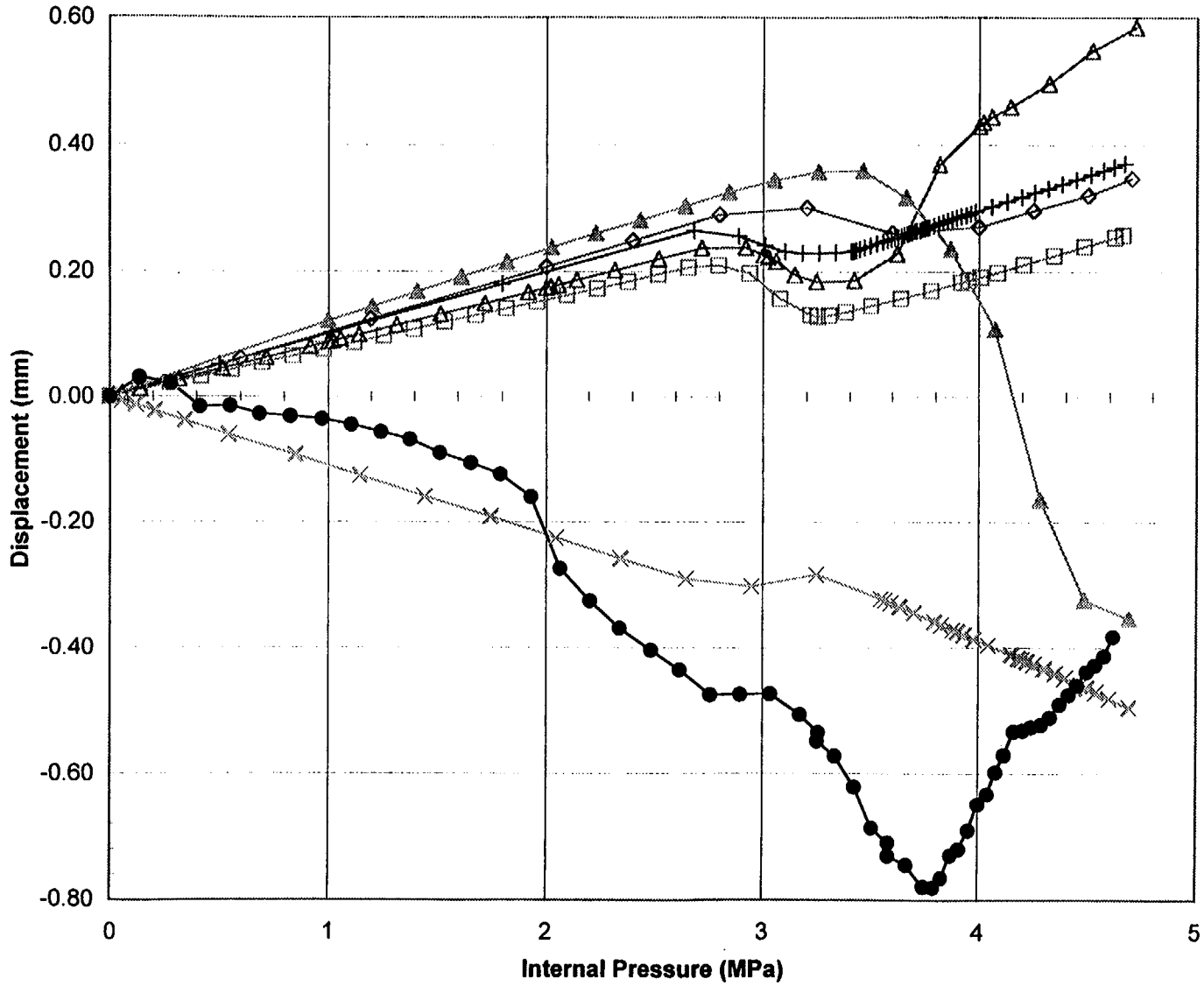
Standard Output Location #35



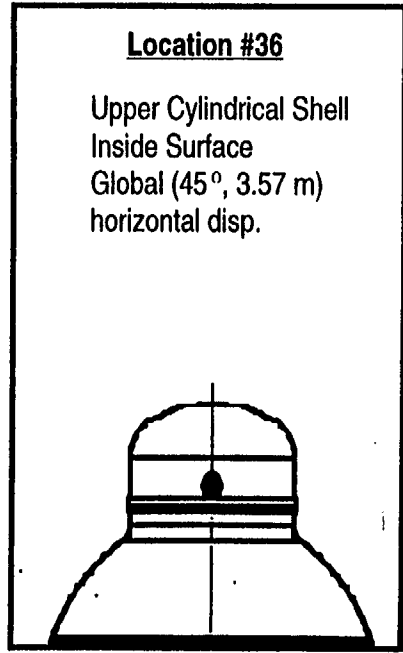
A-37

NUREG/CR-5678

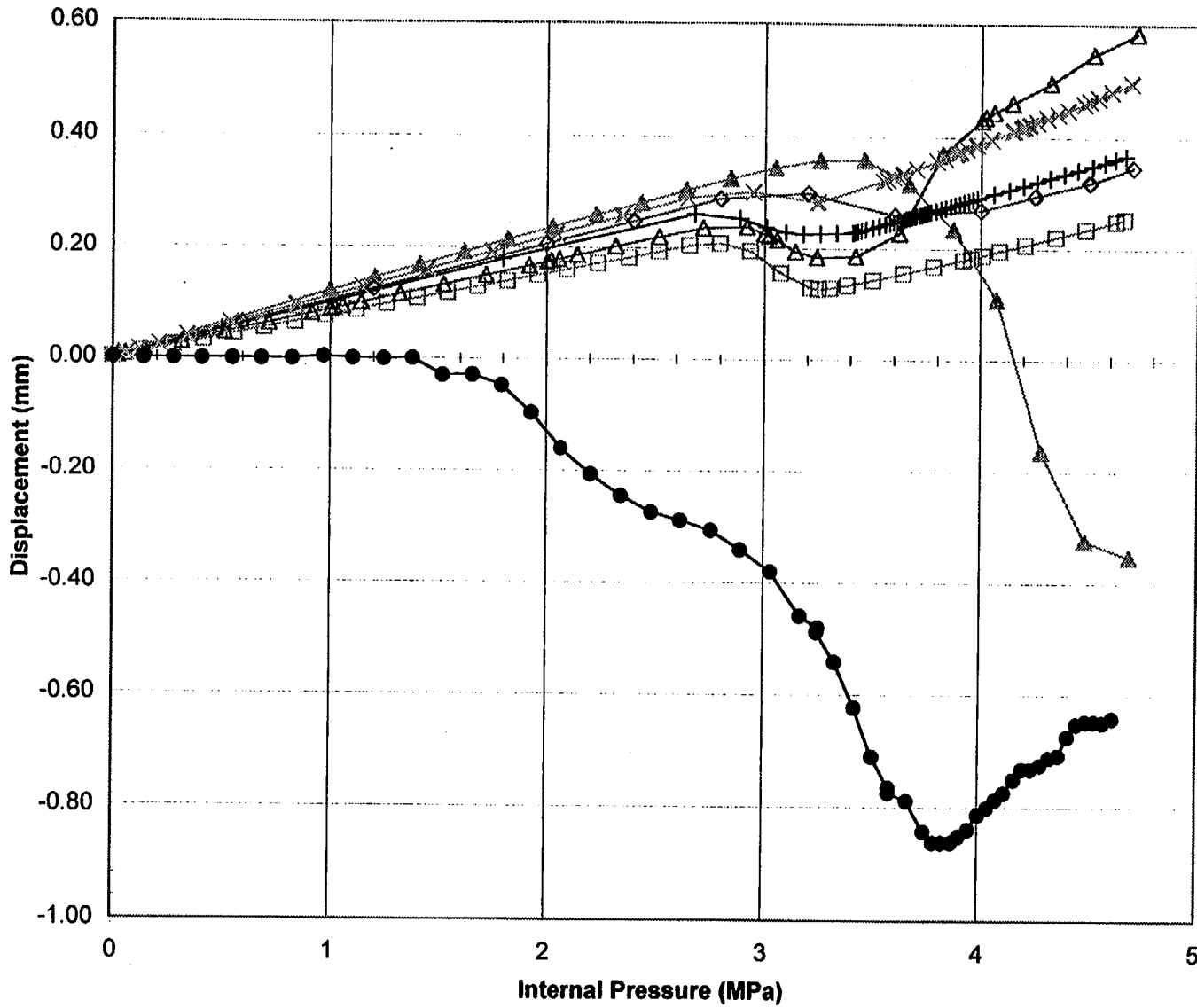
Standard Output Location #36-inside



- Electric Boat
- △ Sandia
- × NUPEC
- + BARC
- ▲ Argonne (w/ RS)
- ◇ JAERI
- HCP-I-UCYS-39 (data)



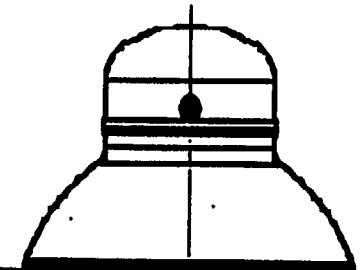
Standard Output Location #36-outside



- Electric Boat
- △ Sandia
- × NUPEC
- + BARC
- ▲ Argonne (w/ RS)
- ◇ JAERI
- HCP-O-UCYS-43 (data)

Location #36

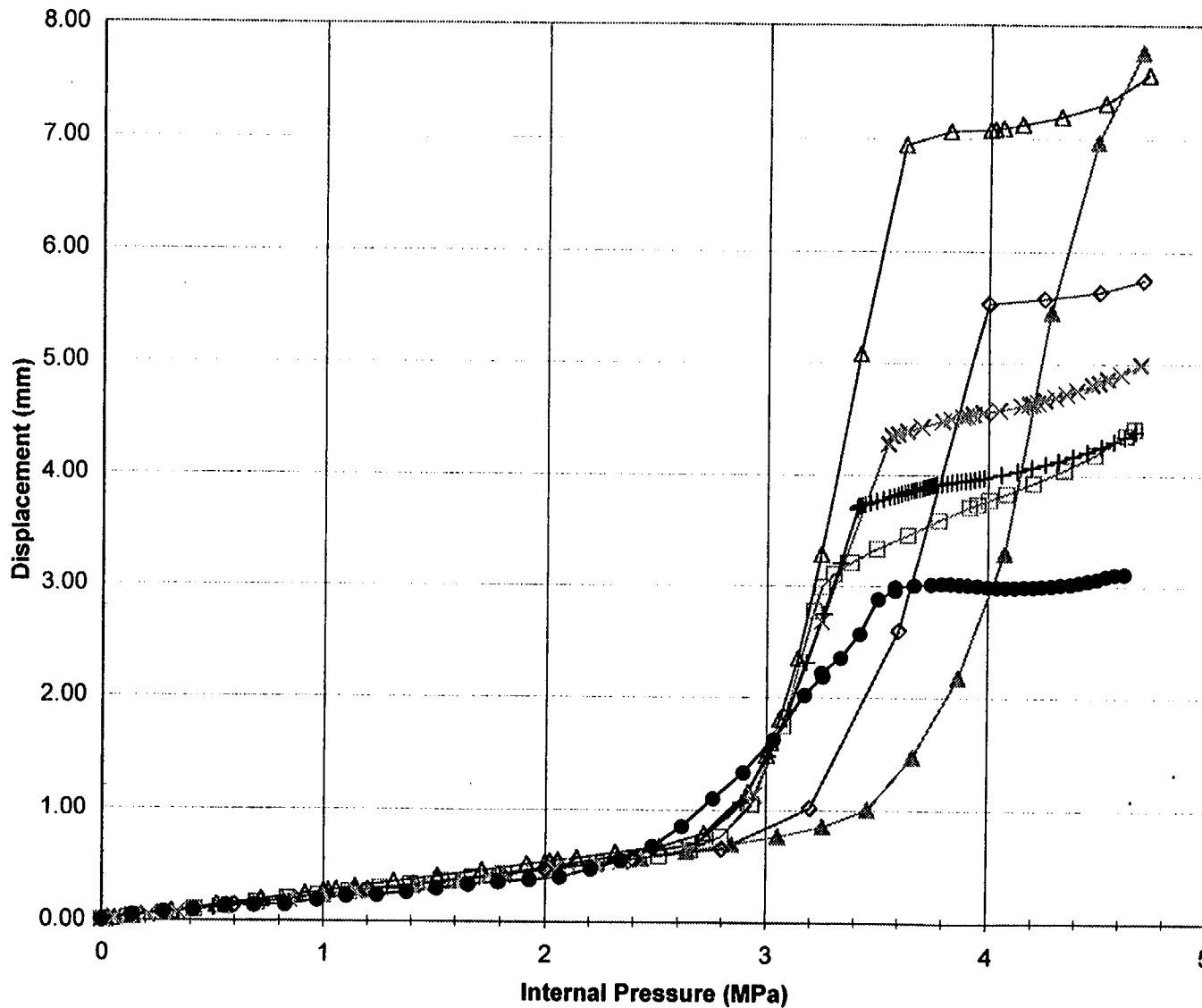
Upper Cylindrical Shell
 Outside Surface
 Global (45°, 3.57 m)
 horizontal disp.



A-39

NUREG/CR-5678

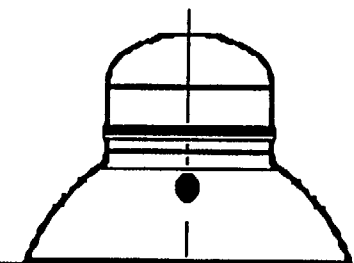
Standard Output Location #37



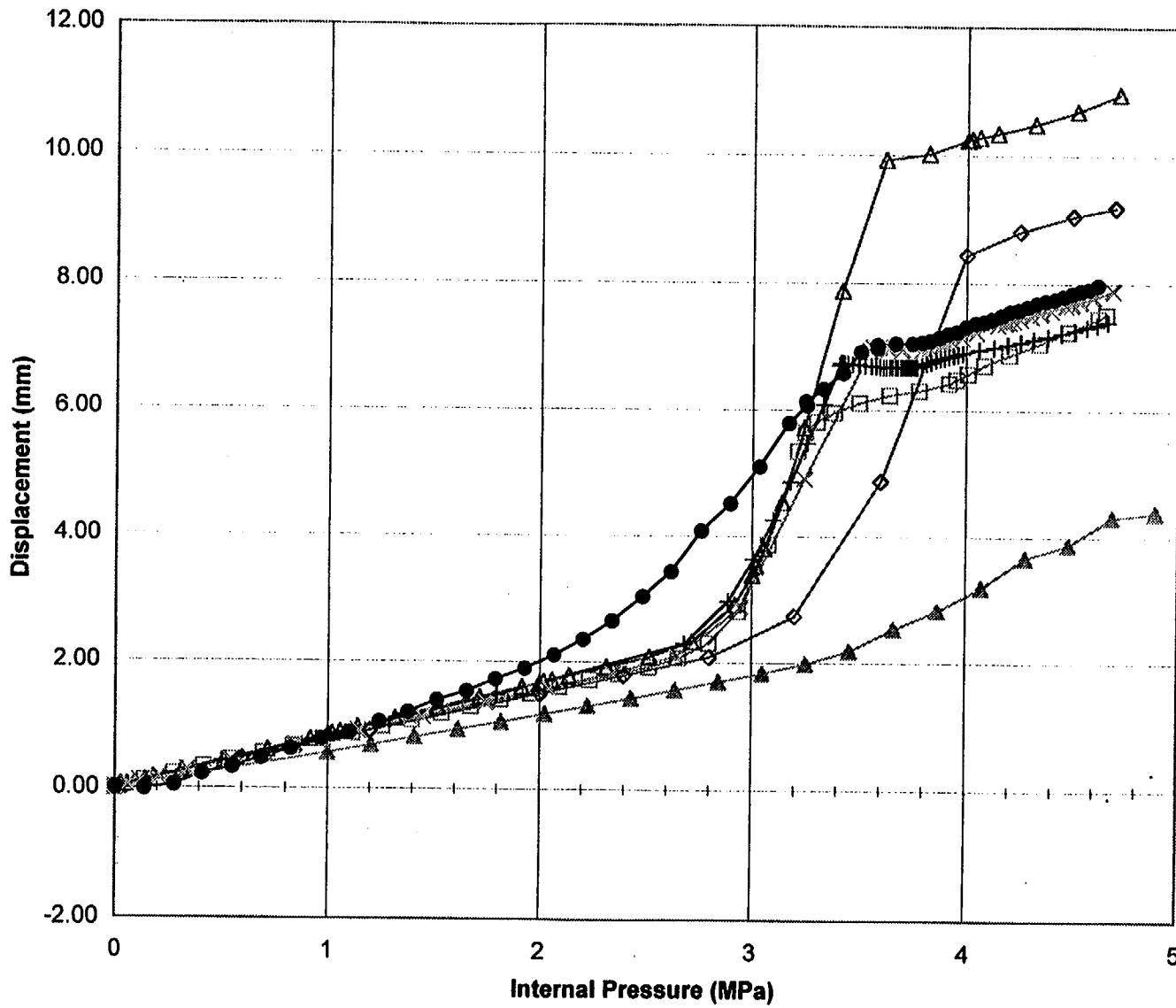
- Electric Boat
- △ Sandia
- × NUPEC
- BARC
- ▲ Argonne (w/ RS)
- ◇ JAERI
- HCP-I-KNU-17 (data)

Location #37

Spherical Shell
 Inside Surface
 Global (0°, 3.32 m)
 horizontal disp.



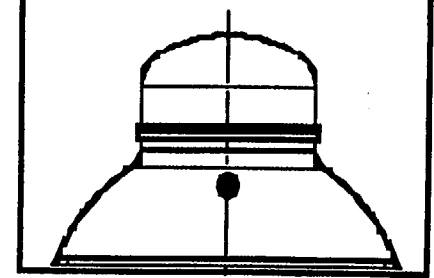
Standard Output Location #38



- Electric Boat
- △ Sandia
- × NUPEC
- † BARC
- ▲ Argonne (w/ RS)
- ◇ JAERI
- VCP-I-KNU-18 (data)

Location #38

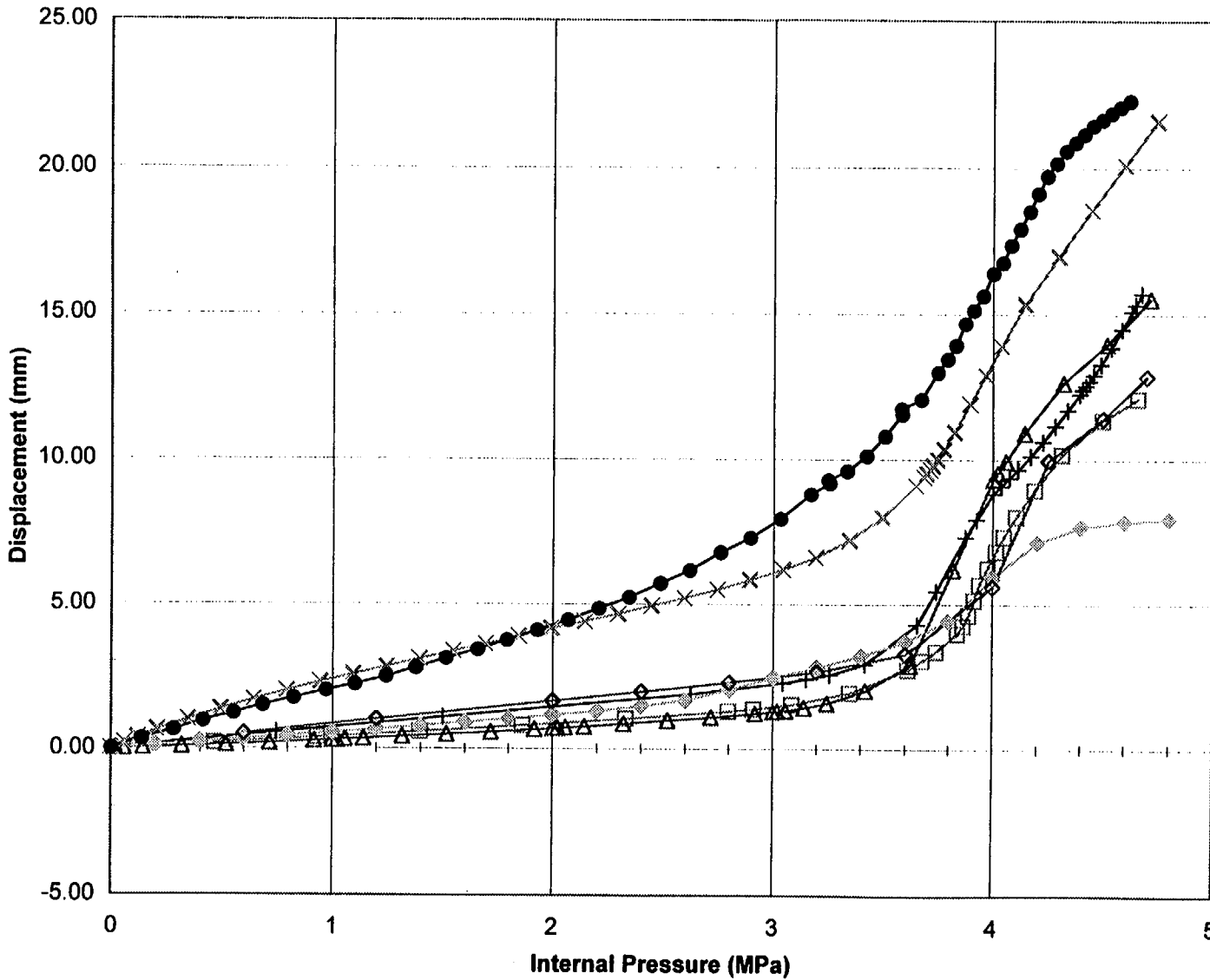
Spherical Shell
 Inside Surface
 Global (0°, 3.32 m)
 vertical disp.



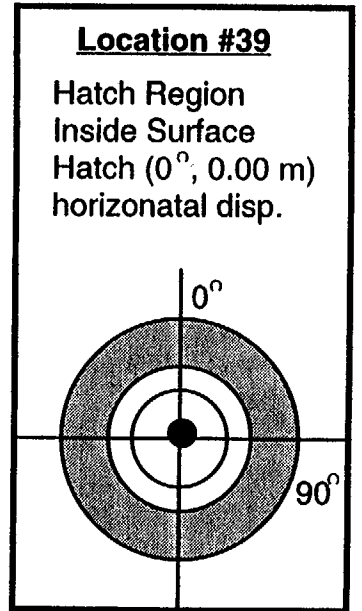
A-41

NUREG/CR-5678

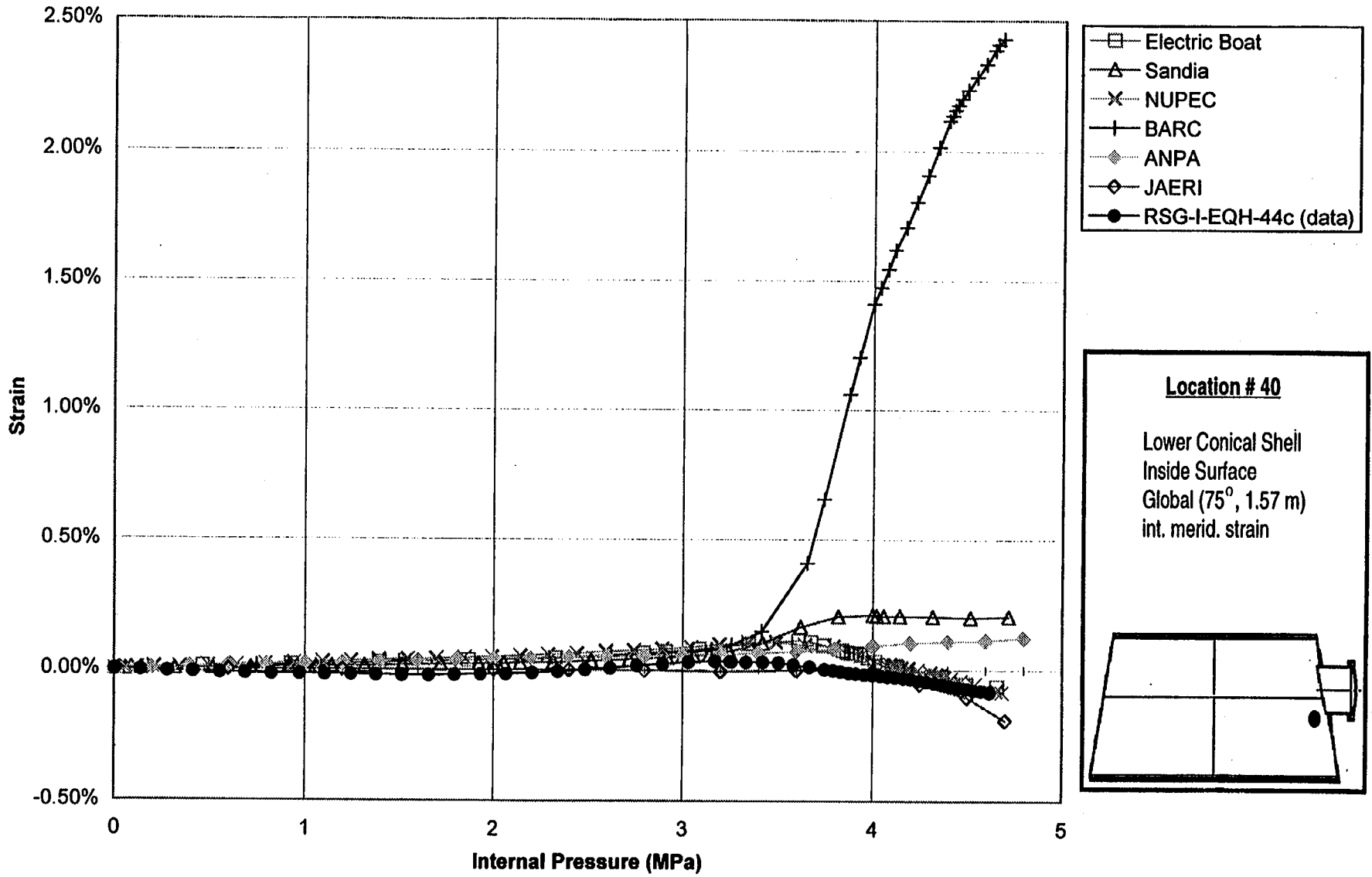
Standard Output Location #39



- Electric Boat
- △ Sandia
- × NUPEC
- + BARC
- ◇ ANPA
- ◇ JAERI
- HCP-I-MCI-16 (data)



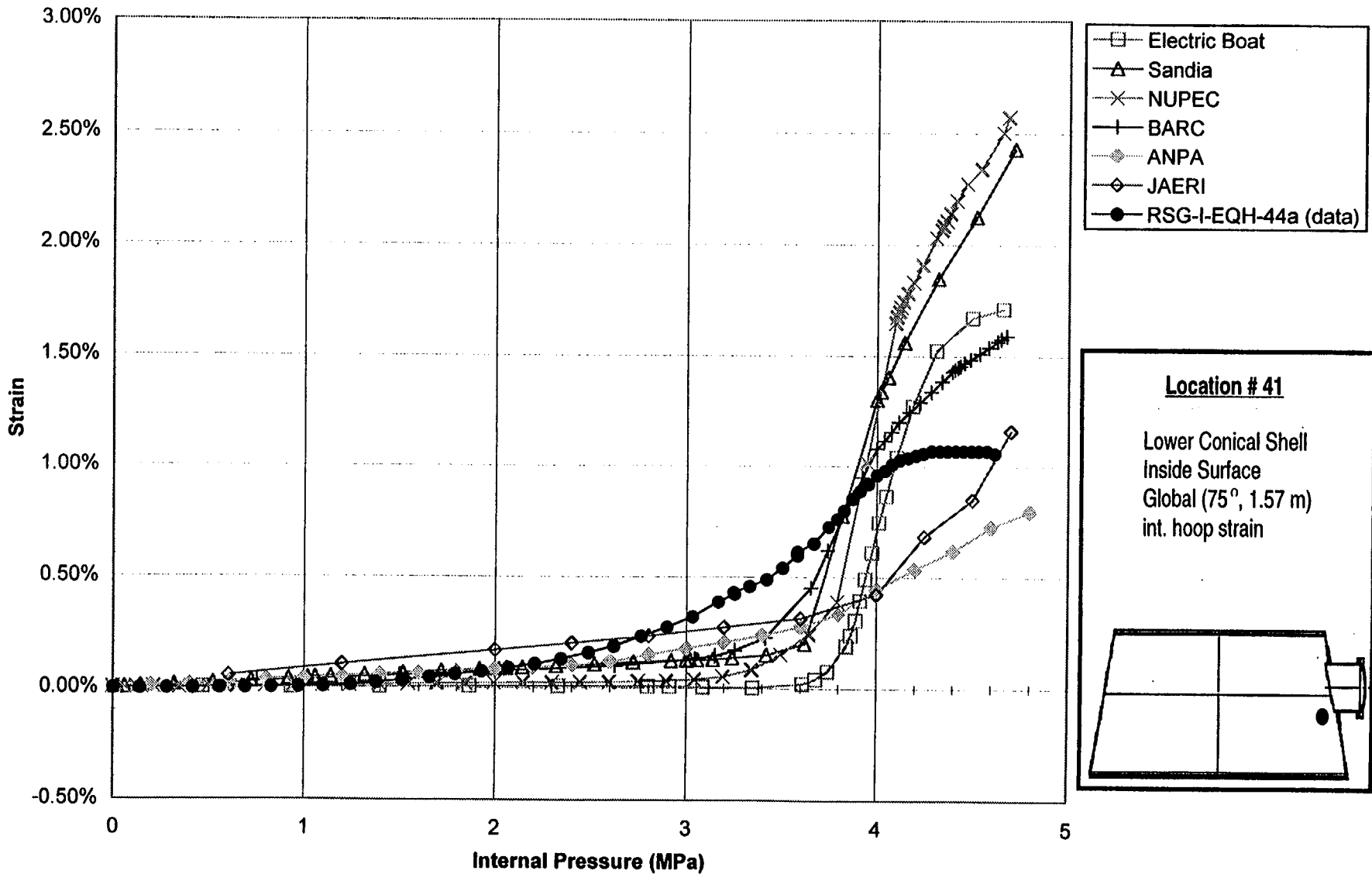
Standard Output Location #40



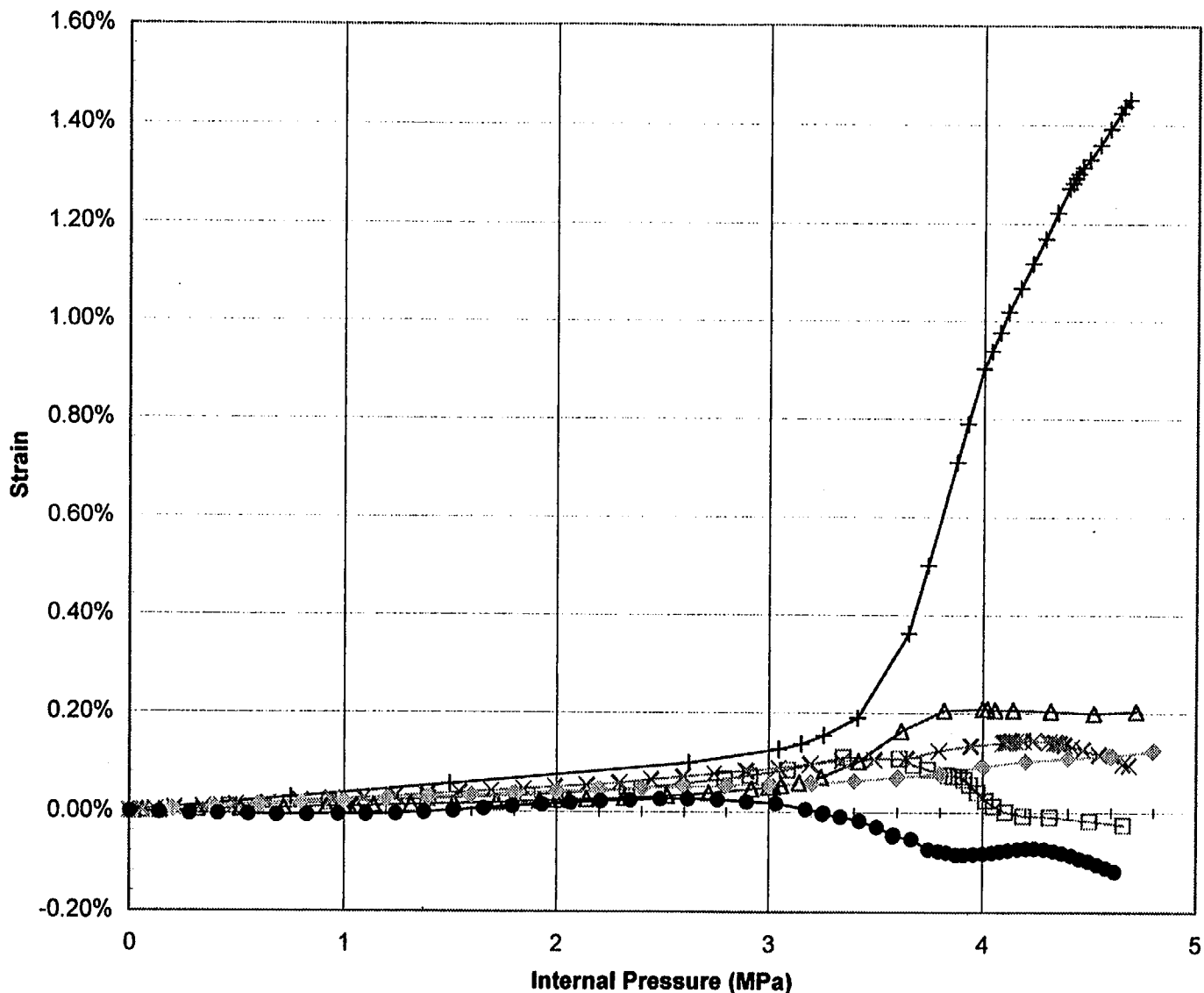
A-43

NUREG/CR-5678

Standard Output Location #41



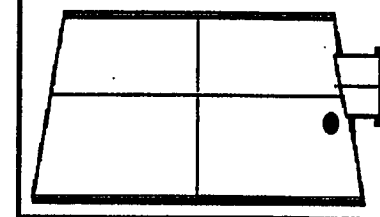
Standard Output Location #42



- Electric Boat
- △ Sandia
- × NUPEC
- ⊕ BARC
- ◇ ANPA
- RSG-I-EQH-45c (data)

Location # 42

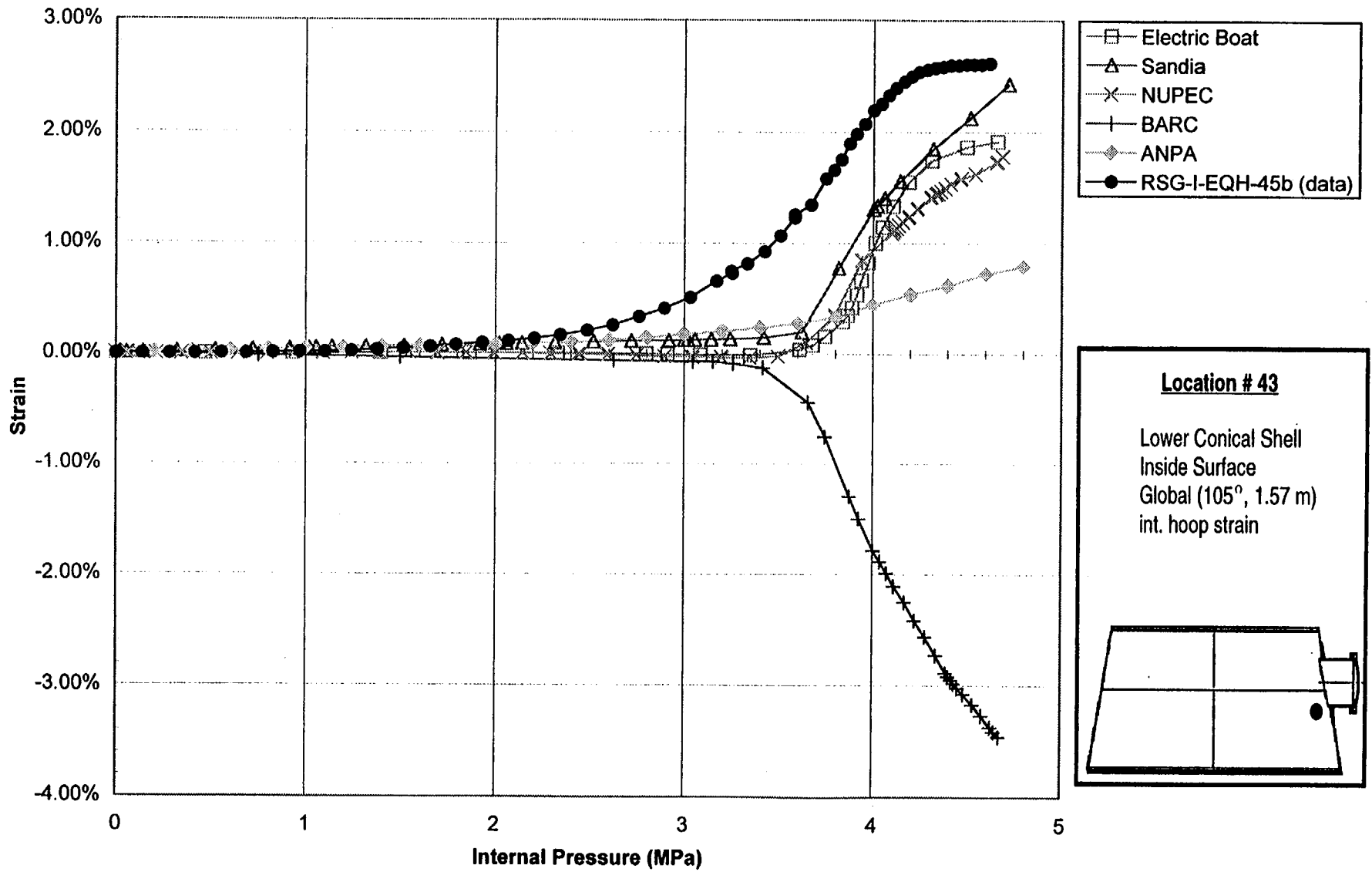
Lower Conical Shell
 Inside Surface
 Global (105°, 1.57 m)
 int. merid. strain



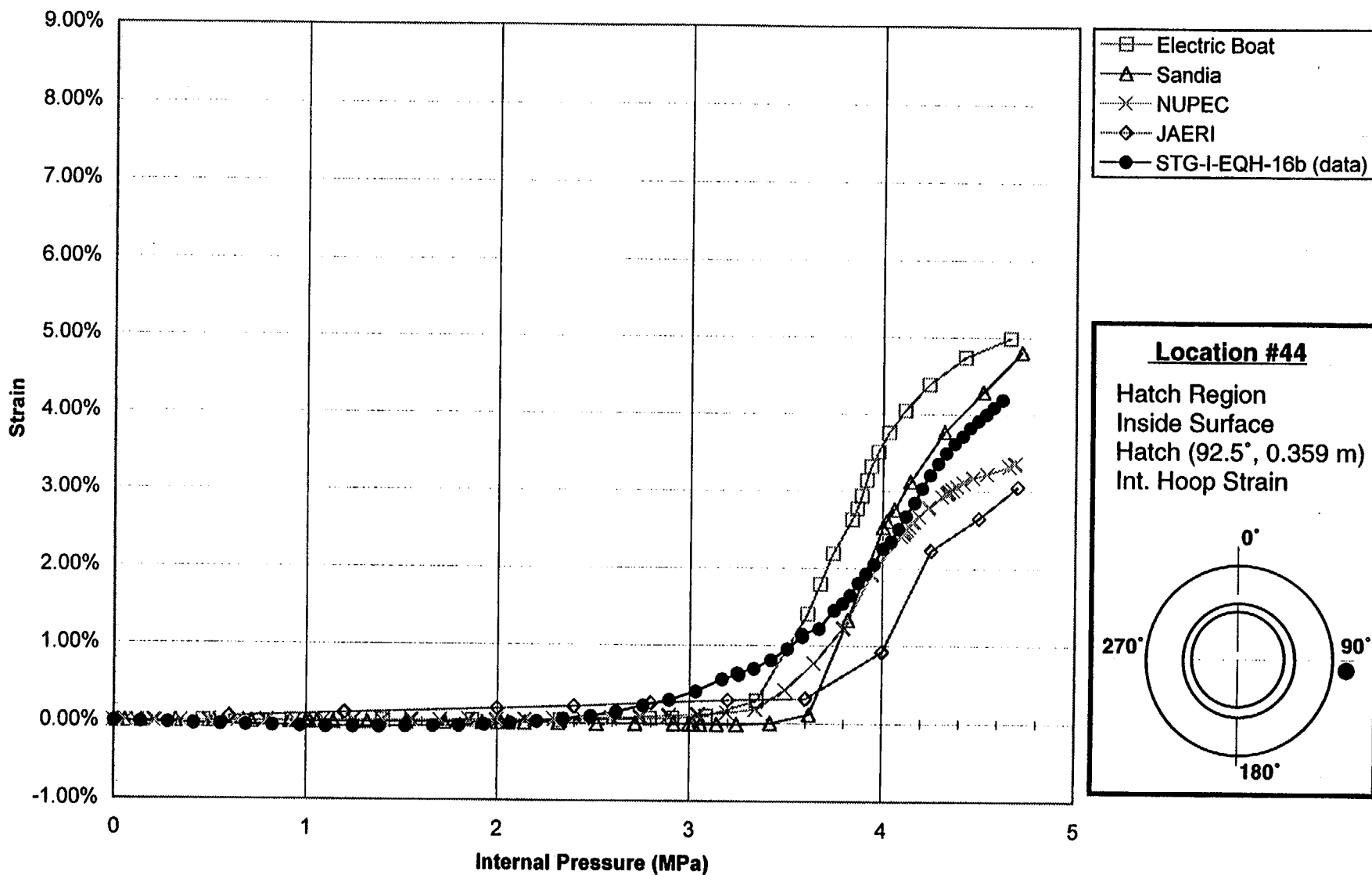
A-45

NUREG/CR-5678

Standard Output Location #43



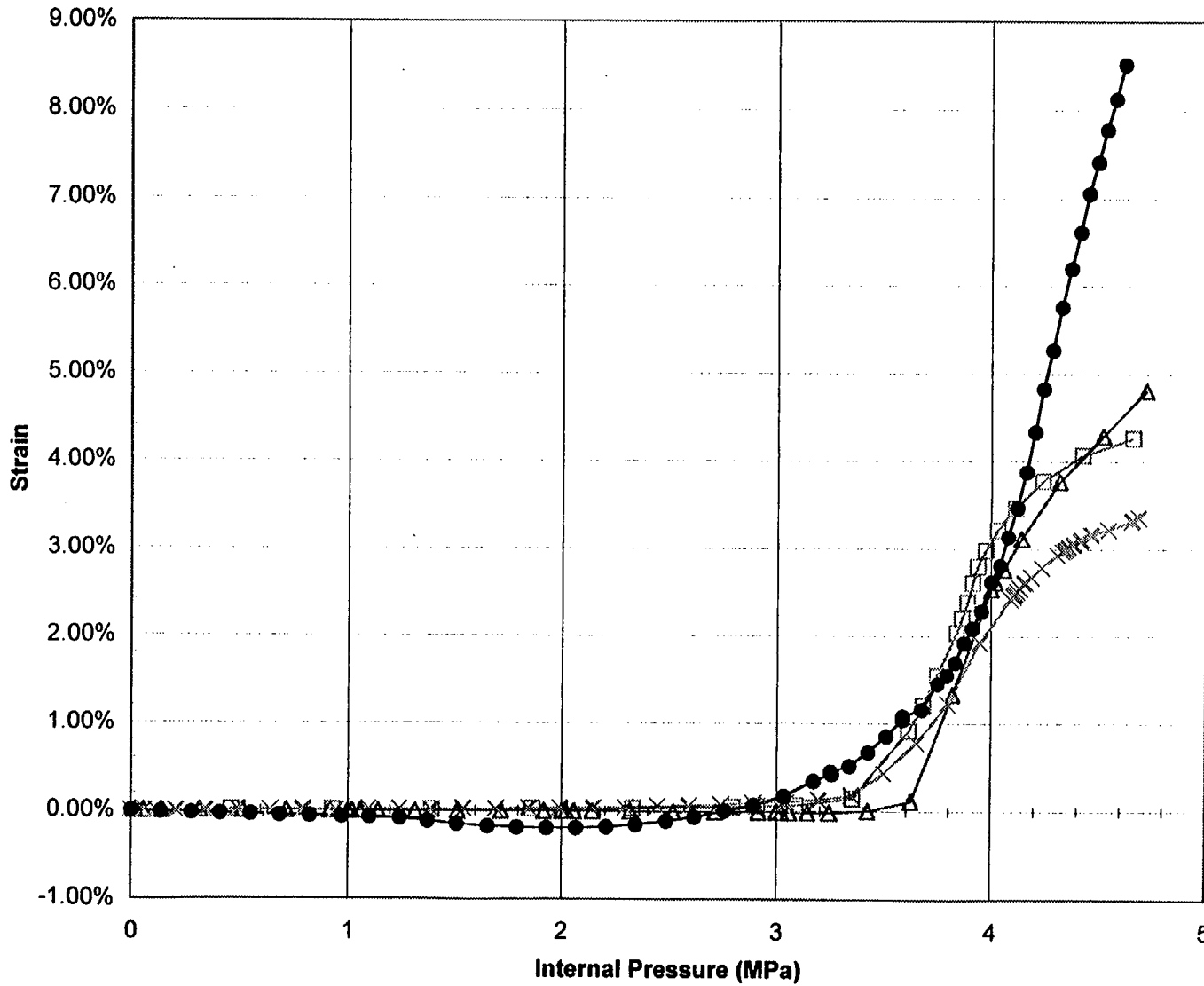
Posttest Output Location #44



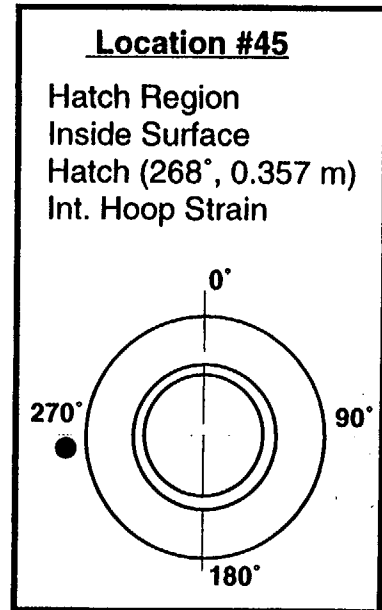
A-47

NUREG/CR-5678

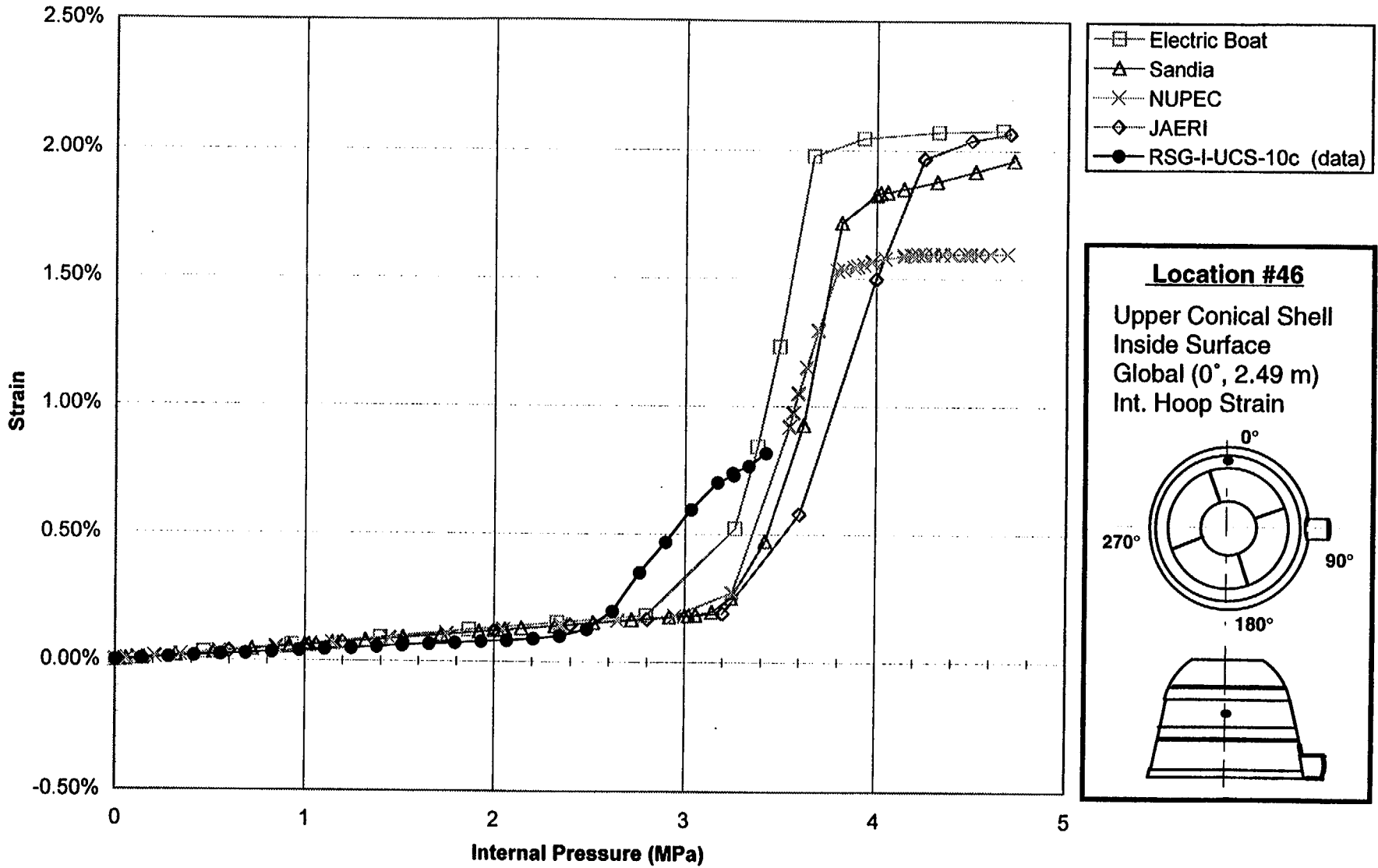
Posttest Output Location #45



- Electric Boat
- △ Sandia
- × NUPEC
- STG-I-EQH-37a (data)



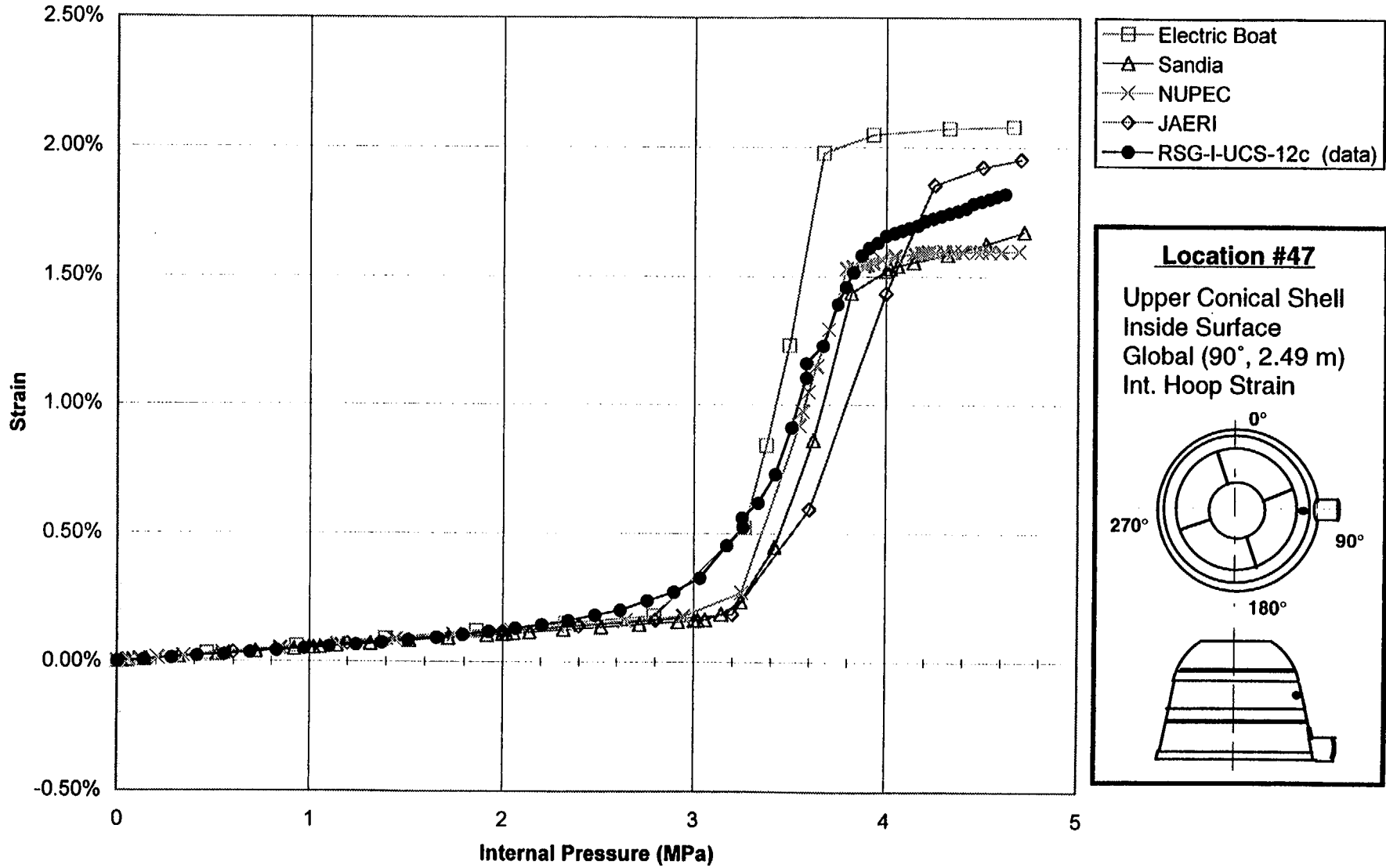
Posttest Output Location #46



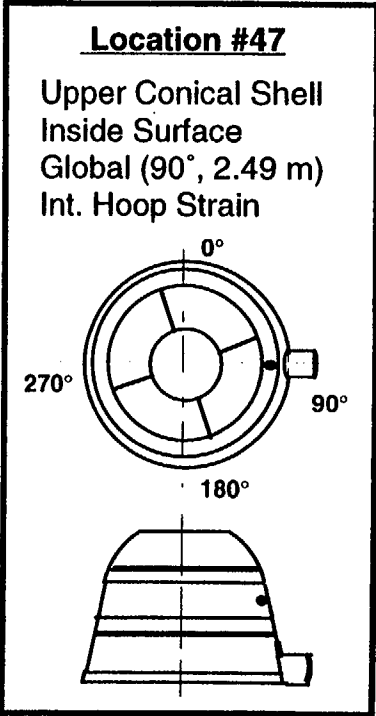
A-49

NUREG/CR-5678

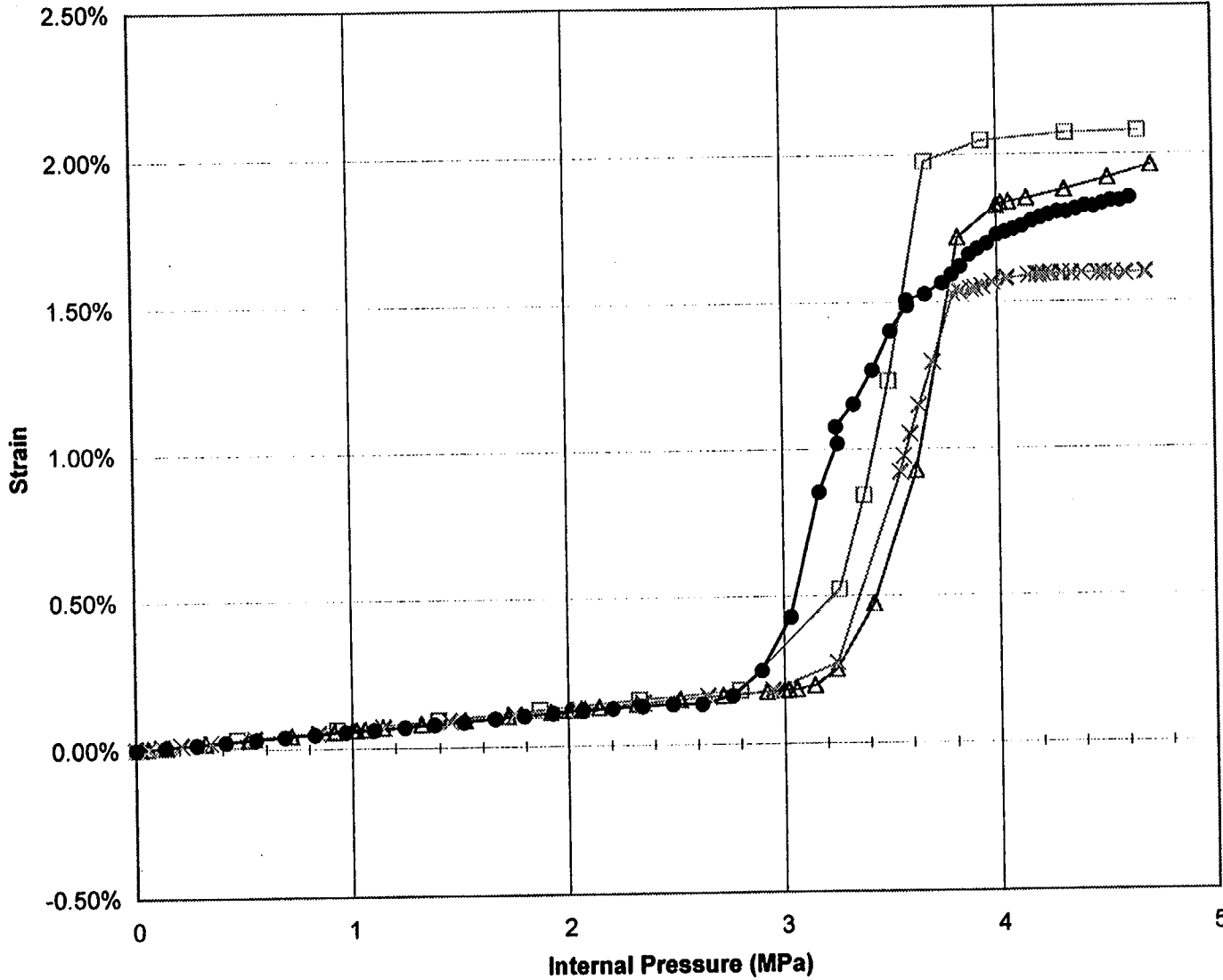
Posttest Output Location #47



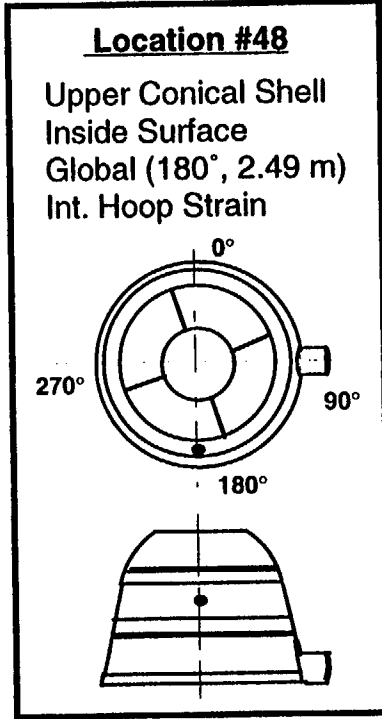
- Electric Boat
- △ Sandia
- × NUPEC
- ◇ JAERI
- RSG-I-UCS-12c (data)



Posttest Output Location #48



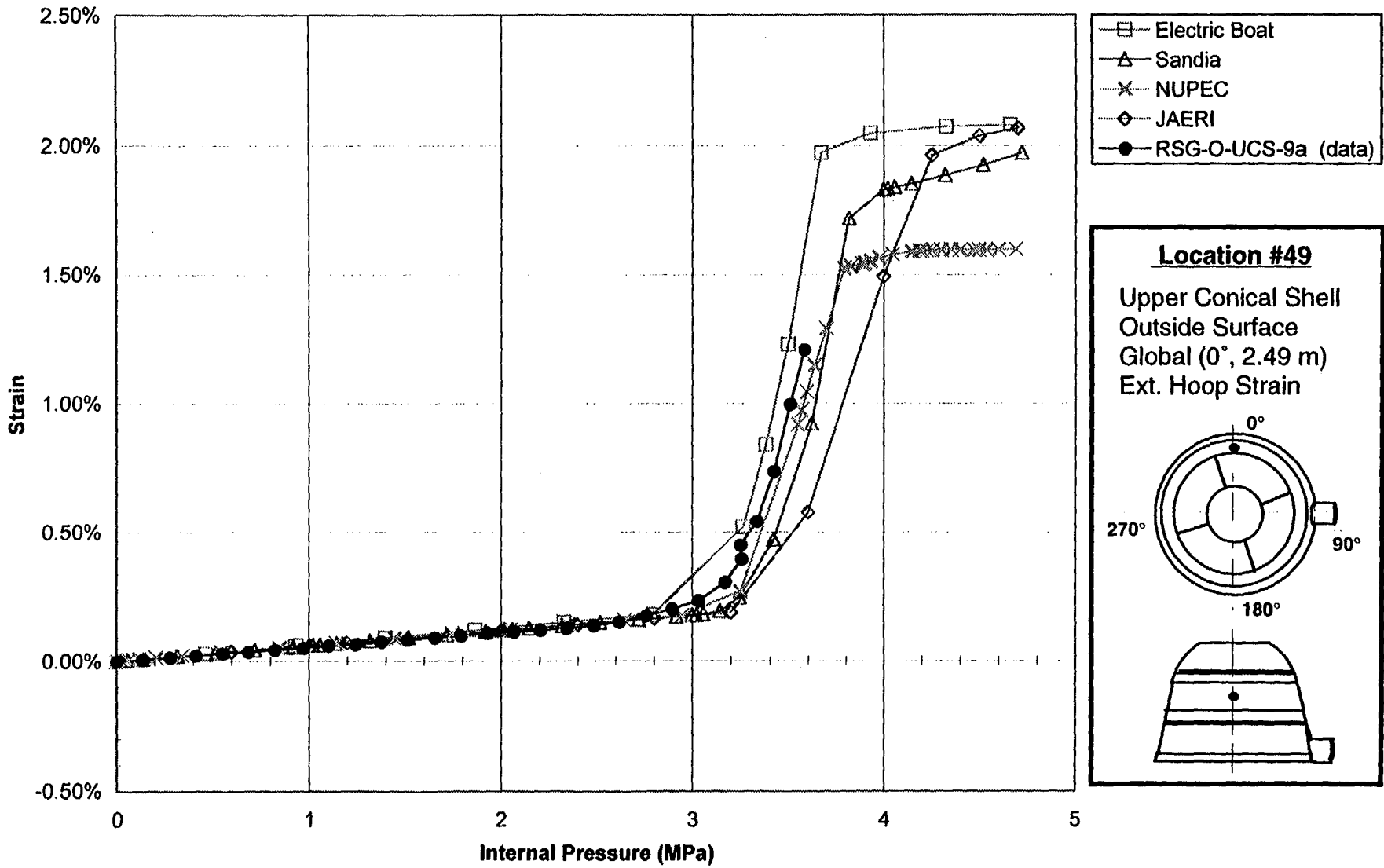
- Electric Boat
- △ Sandia
- × NUPEC
- RSG-I-UCS-14c (data)



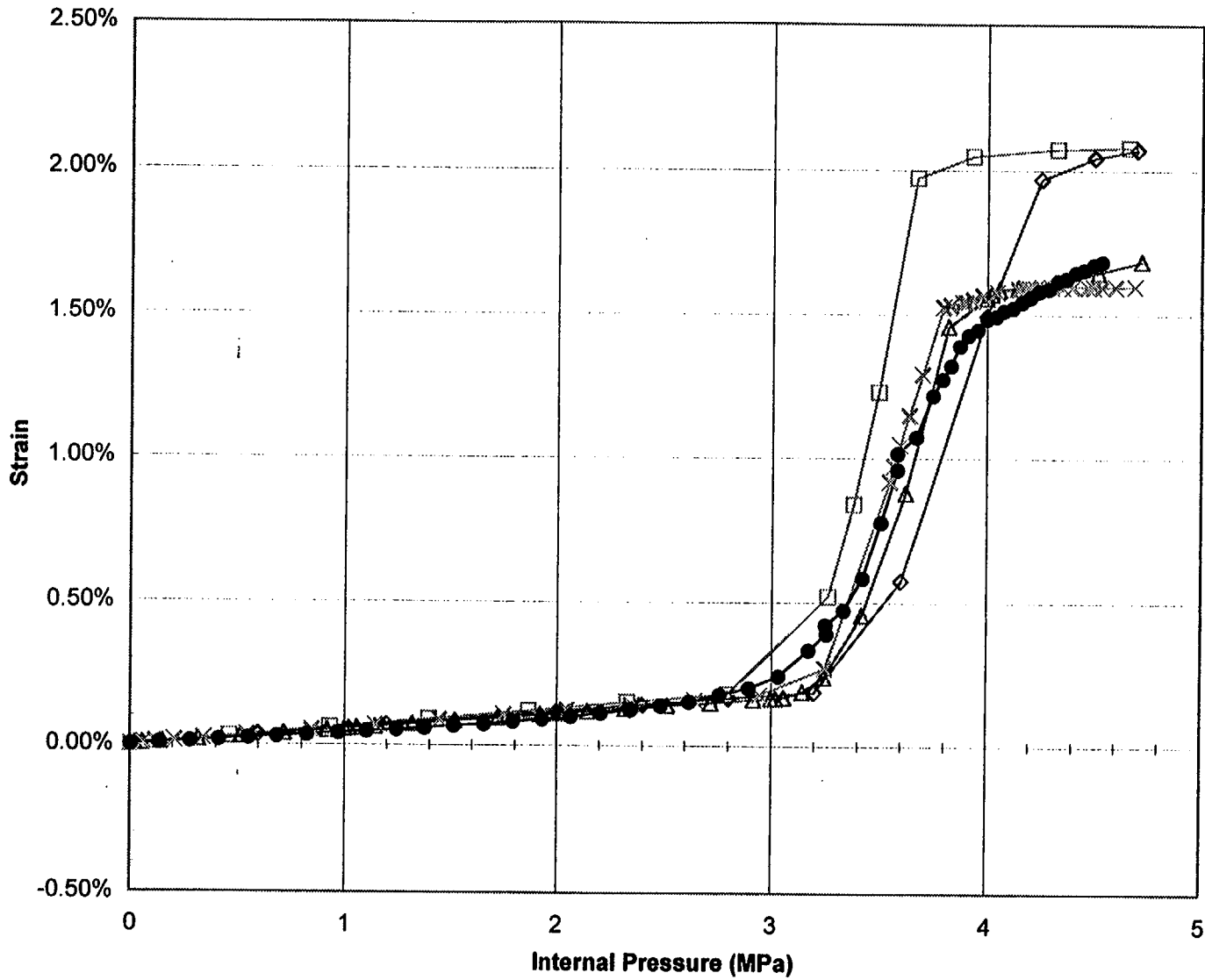
A-51

NUREG/CR-5678

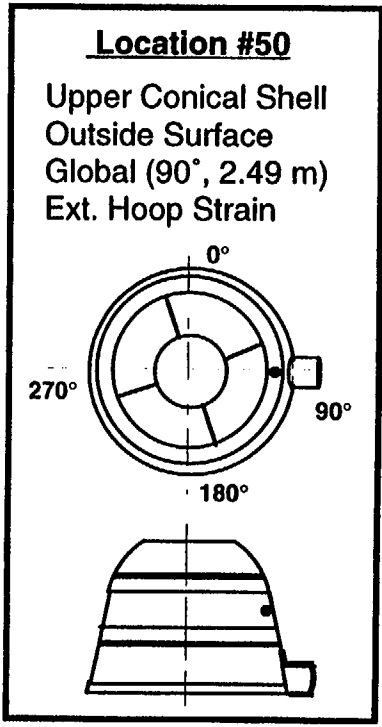
Posttest Output Location #49



Posttest Output Location #50



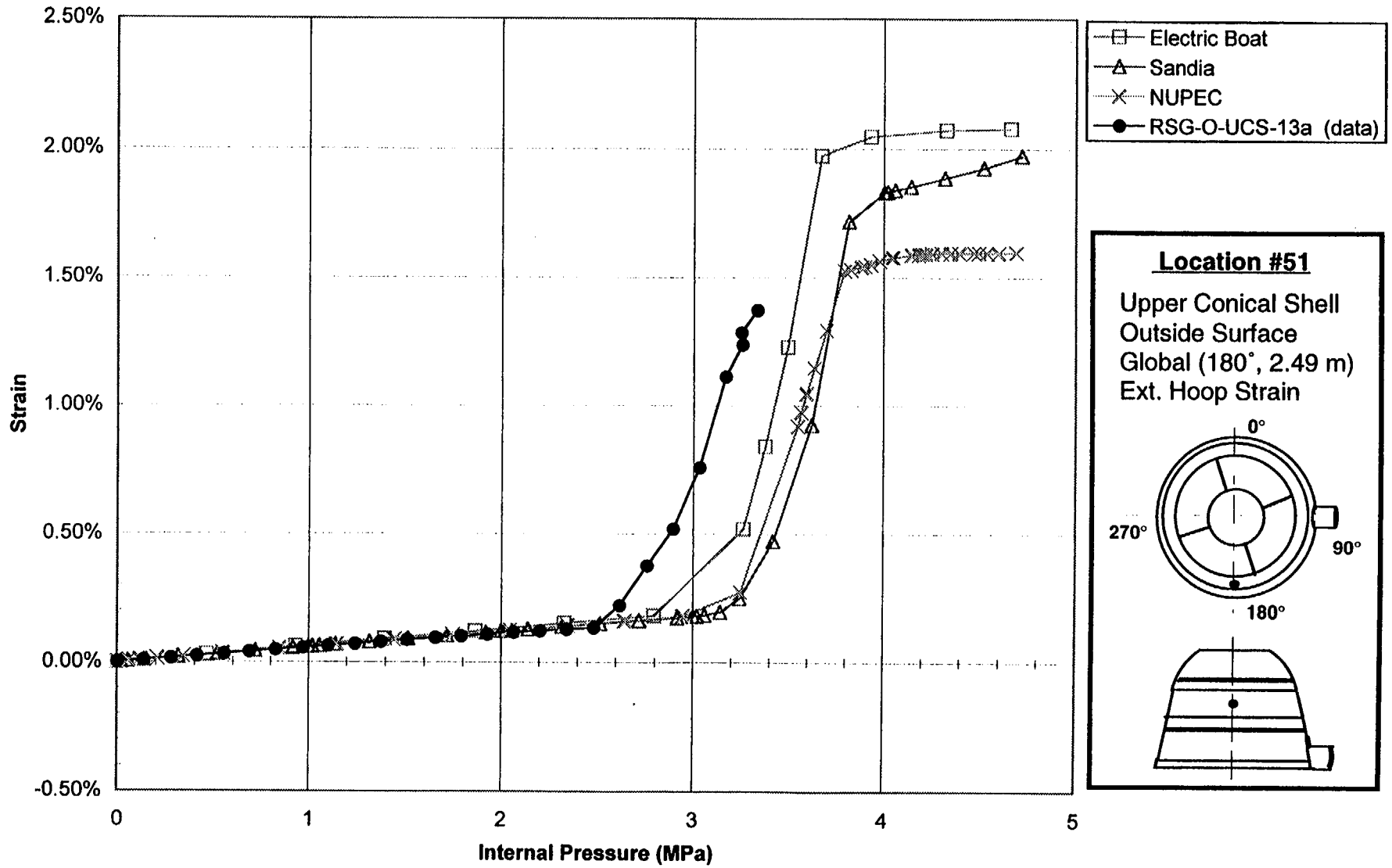
- Electric Boat
- △ Sandia
- × NUPEC
- ◇ JAERI
- RSG-O-UCS-11a (data)



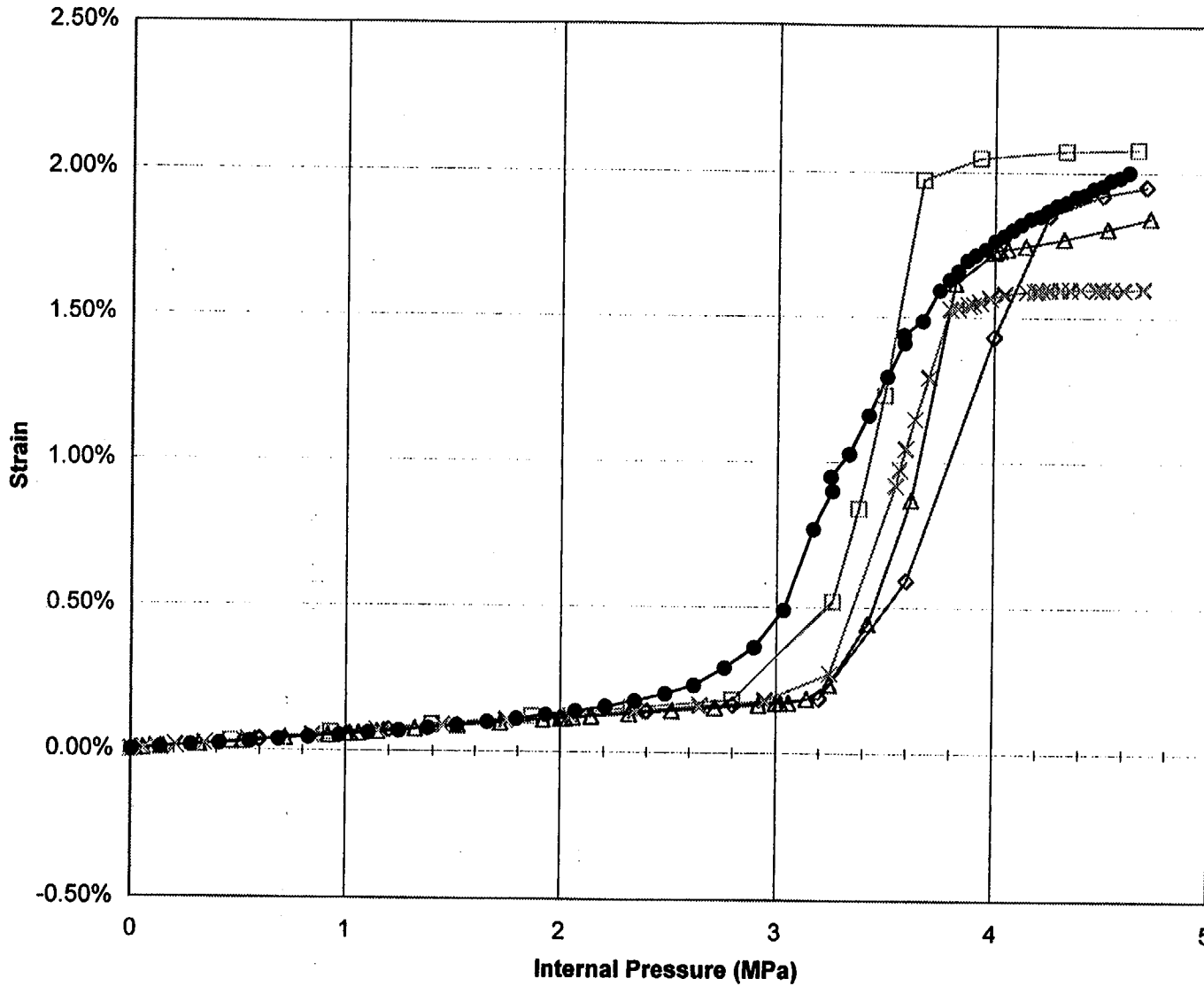
A-53

NUREG/CR-5678

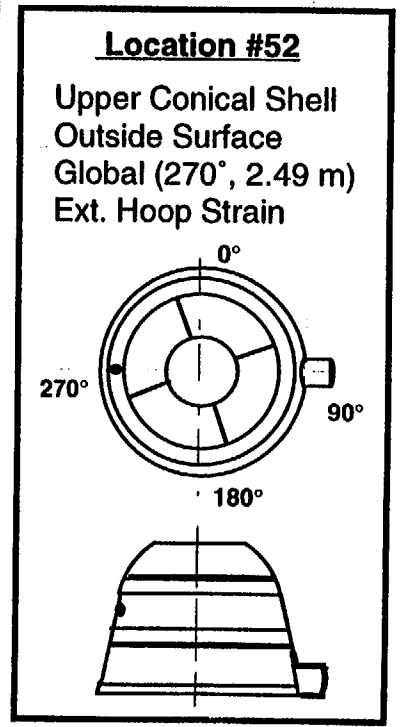
Posttest Output Location #51



Posttest Output Location #52



- Electric Boat
- △ Sandia
- × NUPEC
- ◇ JAERI
- RSG-O-UCS-15a (data)



A-55

NUREG/CR-5678

Appendix B

Round Robin Participants' Analysis Reports and Results

Appendix	Participant	Page #
B-1	Agenzia per la Protezione dell' Ambienti (ANPA) Italy	B-3
B-2	Argonne National Laboratory (ANL) U.S.	B-29
B-3	Bhabha Atomic Research Centre (BARC) India	B-49
B-4	General Dynamics Electric Boat Division (GD-EB) U.S.	B-113
B-5	Japan Atomic Energy Research Institute (JAERI) Japan	B-169
B-6	Nuclear Power Engineering Corporation (NUPEC) Japan	B-221
B-7	Sandia National Laboratories (SNL) U.S.	B-275

Appendix B-1

Agenzia per la Protezione dell'Ambienti (ANPA)

Italy

POST-TEST EVALUATION
OF A STEEL CONTAINMENT VESSEL STRENGTH

Giuseppe Maresca - Giovanni Pino

ANPA
Agenzia Nazionale per la Protezione dell'Ambiente
Via Brancati 48 - 00144 Rome - ITALY

February 98
(first edition)

SNV9.DOC

INTRODUCTION

In the present note, the experimental data obtained from the test carried out at SNLs are discussed. To understand the behavior shown by the vessel under pressurization, new analyses have been performed. They include detailed analyses of the regions which have been damaged during the test as well as improved repetitions of analyses already performed.

A preliminary post-test evaluation was carried out in July 97 (1). It was based on the results of previous analyses affected to some extent by inaccuracies. Anyway, the review of that analysis confirmed our initial belief, of a rupture originated by high triaxiality. However, two questions remained unexplained. First, the computed strains, although comparable with the gage measurements, were too small to justify the rupture also assuming high triaxiality. Second, the analysis results provided a plasticization starting with some delay with respect to the test data (2). To justify the rupture, it was hypothesized in (1) by us a grains growth in the weld HAZ, causing a reduction of the rupture limit according to the Stroh failure mechanism (3). However, further studies showed that, to get a sufficient reduction in the failure limit, too large modifications of the grain size should have occurred.

The situation became clear as soon as the data, from post test investigations (hardness tests), were made available by SNLs (4). Test data indicate that the rupture took place in the SPV490 region, near the junction between the vessel shell and the reinforcement plate. The examination of samples extracted in the rupture location showed that large plasticization preceded the rupture. In fact, by the local thinning of the shell, a local equivalent plastic strain of about 60%, just before the rupture, can be inferred. Notice that equivalent plastic strains of 2% were measured on the shell at the strain gage location close to the rupture. Thus, according to these results, it has been hypothesized by ANPA:

- 1) that a ductile rupture took place,
- 2) that the rupture was caused by excessive local distortion, necking and void growth
- 3) that the relevant local deformation was caused by a local reduction of the yielding point as well as of the ultimate stress in a limited zone,
- 4) that this zone coincides with the heat affected zone of the weld between the vessel shell and the hatch reinforcement plate,
- 5) that the reduction of the yielding is to be attributed mainly to the low carbon content of the SPV490 steel not allowing, in the HAZ, the formation of a martensitic structure during heating and subsequent quenching in the course of welding,
- 6) that the residual stresses in the weld region also contributed to lower the local yield point,
- 7) that local triaxiality has not been relevant in determining the failure strain while biaxiality has been determinant according to the Ghosh failure criterium for sheets (5).

To validate the above hypotheses a new analysis has been performed introducing a local reduction in the yielding point as well as in the ultimate stress of the SPV490 material. This reduction, which has been evaluated on the basis of the hardness data provided by SNLs, has been applied, in the 3-D hatch model (6, 7), to a narrow strip of the SPV490 shell material surrounding the reinforcement plate. Because of this modification, the hatch model provides now, at a given pressure, deformations, all around the hatch region, which are greater than the ones previously computed. This partially explains the experimental fact of an anticipated deviation from linearity of some measured strain-pressure curves with respect to calculations. However, to fully reproduce the experimental behavior of the experimental curves a further modification in the input data has been required. In fact, in our previous calculations, the non proportional elastic fraction of the stress-strain curves was neglected. By modifying the adopted stress-strain curve, in order to take into account the deviation from linearity in the elastic field, results in good agreement with the experimental data are finally obtained.

It is worth to notice that, the local reduction of the yield point of the material, produces also strong local strains in the HAZ according to the mechanism illustrated below.

In the considered zone the yield point is reached before than in other zones. Because of this, as soon as a plastic strain of about 0.2 % is reached in the other zones of the vessel shell, the deformation in the HAZ has already passed the instability value for the cylindrical geometry. Starting from this point, local necking begins and, to preserve equilibrium, greater deformations are to be expected in the other zones of the vessel shell, being the HAZ now unable to provide the equilibrium stress. The local deformation becomes totally controlled by the deformation in the surrounding zones and by plastic volume conservation. Being the meridional strain negligible, a plane strain condition is obtained in the HAZ and locally the deformation is strongly amplified because of the lower yield point and ultimate stress. In fact the stiffness of the surrounding zones prevent the thinning of the shell at the boundary of the HAZ and so the thinning required by volume conservation becomes concentrated (and therefore amplified) in the center of the HAZ.

A similar behavior, with a machined local thickness reduction substituting the local yield level reduction, has been used by ANPA to raise the strains in experimental tests performed at the ISPRA JRC laboratories on SA 537 class 1 cruciform specimens.

To demonstrate the above mechanism, an analysis has been performed on a plane strain model of the junction between the vessel shell and the reinforcement plate. Notice that a very dense mesh is required to represent the necking behavior. (Really a much more dense mesh should be required if one wishes to represent the stress pattern in a necked zone, for example the Bridgmann distribution of the stresses in the necked region of a tensile specimen.)

Using the results of the 3-D hatch model an average deformation in the shell, near the reinforcement plate, of about 1% can be deduced for the pressure of 4.66 MPa. The same average deformation is applied to the junction model. This is obtained imposing a growing displacement in the circumferential direction to one end of the junction model, while the other end is fixed. Under these conditions, a strong necking is obtained in the HAZ with a local equivalent plastic strain of about 60 %. The corresponding applied displacement is 1.5 mm which provides an average circumferential strain of 1% on the junction model length of 260 mm.

Because of the very dense mesh required to point out this behavior, it is not possible to represent this effect in the 3-D hatch zone model. The consequence is that the strains close to the reinforcement plate obtained by the 3-D hatch zone model are to some extent underevaluated. In fact, the mesh in this model make the shell stiffer than it really is. This explains why this model provides near the rupture a circumferential strain of only about 0.8 % while the strain measured in the same location is about 1%.

Finally the damage located near one of the weld relief holes in the MST ring has been considered. Also in this case a plane strain model has been used to investigate the reason of the local necking of the shell. The obtained results show that, when an average circumferential strain of 1% is applied, local necking really occurs. This is because the hole reduces locally the circumferential stiffness of the ring allowing greater deformations of the vessel shell facing the hole with respect to the remaining shell whose stiffness is increased by the ring. Also in this case volume conservation in a plane strain condition must take place. The thinning of the shell at the boundary of the hole facing zone is prevented by the more stiff region which surrounds the material facing the hole. The thinning, therefore, must be concentrated (and so amplified) at the center of the examined region. Notice that the analysis shows also a necking of the stiffener in the hole region. This necking really took place during the test as it can be seen from the photo picture of the damaged region provided by SNLs (4). In this analysis no modification in the characteristic of the material (SGV480) has been applied. However the Rockwell tests performed at SNLs indicate an increase in the hardness of the SGV480 material both in the fusion zone of weld and in the HAZ. Because of this, the local damage in the SGV480 material cannot be explained only through the local softening caused by the hole in the reinforcement ring. It is possible that residual tension effects must also be considered in this case. In fact they also contribute to thin the thickness of the shell region in front of the hole because of relevant tension exerted in the meridional direction and produced by weld retirement. This

mechanism is expected to compensate the greater stiffness of the material in the fusion zone and in the HAZ, although specific computations have not been made to prove this statement.

MATERIAL DATA

Data provided by SNLs refer to 12 locations on the vessel. The data have been treated according to the procedure described below.

The original SNLs file LOCn.TXT has been adjusted into a file MATn.DAT to be treated by a BASIC computer program, MATBAS, in order to produce for each location a single true stress - logarithmic plastic strain curve (MARn.DAT) and the corresponding input file for the MARC code (MASn.DAT). The MATBAS program performs all the elaborations described in (8).

The yield point is obtained by the above procedure assigning the initial yield stress and computing the corresponding strain simply dividing the assigned yield stress by the assigned Young's module. Because of this, the non proportional fraction of the elastic stress-strain curve is neglected. To correctly reproduce the results of the strain measurements, however, this fraction must be represented in the computer model. To this purpose the MARC input has been modified lowering the yield stress to a fictitious value which corresponds to the beginning of the non-proportional elastic fraction.

To reproduce the lowering in the yield point produced by metallurgical modifications in the weld HAZ all the SPV 490 curve has been multiplied by a factor 0.85.

RESIDUAL TENSION EFFECT

In order to explain the anticipation in yielding which is apparent in the strain measurements the only yield point reduction in the weld HAZ is not sufficient. Therefore it has been hypothesized by us that also the residual tension in the weld has an effect in order to anticipate the start of the local yielding. Consider a welding directed along the meridional direction. A residual meridional tensile stress will exist in the fusion zone while, proceeding in the direction normal to the weld line a meridional compressive stress will exist at some distance from the weld. Because of this, in a cylindrical geometry, the equivalent strain is provided by :

$$\sigma_{eq} = \sqrt{\sigma_c^2 + \sigma_m^2 - \sigma_c \cdot \sigma_m}$$

with $\sigma_m = \frac{1}{2}\sigma_c + \sigma_r$, being σ_r the residual stress.

Substituting to σ_m its expression it results:

$$\sigma_{eq} = \sqrt{\frac{3}{4}\sigma_c^2 + \sigma_r^2}$$

Therefore, the circumferential stress at the yield point is

$$\sigma_c = \frac{2}{\sqrt{3}} \cdot \sqrt{\sigma_y^2 - \sigma_r^2}$$

and it is reduced, with respect to the condition of no residual stress, by a factor $f = \sqrt{1 - \frac{\sigma_r^2}{\sigma_y^2}}$.

MODIFIED 3-D HATCH ZONE MODEL

The only modifications in the 3-D hatch zone model with respect to the model reported in (6) and (7) are the introduction of the non proportional elastic fraction in the SPV490 and SGV480 material and the lowering of the SPV 490 stress-strain curve in a narrow strip all around the reinforcement plate. To introduce this latest modification a narrow strip around the reinforcement plate has been created in the mesh (fig. 1). The lowering has been obtained multiplying all the ordinates of the SPV 490 curve by a factor 0.85.

The introduction of the non proportional elastic fraction of the stress-strain curve has been applied only to the material of the vessel shell and has not been applied to the material of hatch and of the reinforcement plate.

LOCAL PLANE STRAIN MODEL OF THE JUNCTION

To investigate local necking effects the junction between the vessel shell and the reinforcement plate has been represented by a plane strain model (fig. 2). A lowered SPV 490 curve has been used in this case. The non proportional elastic fraction has not been represented in this case.

LOCAL PLANE STRAIN MODEL OF THE SHELL FACING THE HOLE IN THE MST

A fraction (100 mm) of the stiffener and of the vessel shell has been represented (fig. 3). In the model one end (at the symmetry plane) is fixed while the other one is loaded by an increasing displacement.

CONTACT STRUCTURE MODEL

The position of the Contact Structure has been reviewed on the basis of the comparisons performed in (7). We have concluded that the reason of apparently anticipated touching of the vessel shell against the contact structure is due to the way the reinforcement plate has been modelled. In fact, in each one of our models a curvature in the horizontal plane has been assigned to the plate, such to avoid a discontinuity in the curvature of the conical shell. Because of this a vertical strip of the plate, located at the center of the plate, is displaced towards the outside with respect to reality and this is the reason of the apparent anticipated touch. Therefore the position of the Contact Structure with respect to the vessel was correctly represented in (7) and has not been changed in the present model.

PRESSURE LOADING

The modified 3-D hatch zone model has been loaded up to 5 MPa by 25 pressure steps. A uniform pressure step of 0.2 MPa has been used. The contact is obtained at a pressure of 4 MPa.

ANALYSIS RESULTS

Results from the new 3-D hatch zone analysis are reported in Figs. 4 - 10. These figures refer to the nodes 7294, 7277, 6959, 6799, 283, 282, 8, 2435, 5449, 5154 and 5151 of the modified 3-D hatch zone model.

The correspondence between these nodes and the plot locations is illustrated in tab. 1. In tab. 2 the coordinates of these nodes are also indicated in order to allow the estimation of their distance from the gage locations.

TAB. 1
Plot representative nodes in the modified 3-D hatch zone model

Global	Plot	Instrument	Variable ⁽²⁾	x ⁽¹⁾ (mm)	y ⁽¹⁾ (mm)	Outside	Middle	Inside
195	3	STG-O-EQH-4c	ems	-335.7	414	7294	7278	7277
195	4	STG-I-EQH-2c	ims	-335.7	414	"	"	"
948	2	RSG-I-EQH-8	mps	-81.14	308.6	6976	6960	6959
186	1	RSG-I-EQH-12	mps	-3.103	191.8	6816	6800	6799
942	5	SSGH-O-EQH-18	ehs	24.3	54	283	3269	282
942	6	STG-I-EQH-16c	ihs	24.3	54	"	"	"
831	40	RSG-I-EQH-44c	ims	7.8	-10	9-2436	3423-3747	8-2435
831	41	RSG-I-EQH-44a	ihs	7.8	-10	"	"	"
831	42	RSG-I-EQH-45c	ims	2.8	-10	"	"	"
831	43	RSG-I-EQH-45b	ihs	2.8	-10	"	"	"
2154	39	HCP-I-MCI-16	hd	-335.7	54	6064	-	5449
128	25	RSG-O-LCS-5	ems	344	-129	5154	5340	5151
128	26	RSG-I-LCS-6	ims	344	-129	"	"	"
128	27	RSG-O-LCS-5	ehs	344	-129	"	"	"
128	28	RSG-I-LCS-6	ihs	344	-129	"	"	"

Notes:

(1) The coordinates x and y are measured with respect to a reference frame whose origin is located at the triple point on the outer vessel surface. The y direction corresponds with the local meridional one while the x direction with the circumferential one. To get the coordinates from the Hatch reference frame coordinates the following transformation is applied:

$$x = R \times \sin\theta - x'_0$$

$$y = R \times \cos\theta - y'_0$$

where

$$x'_0 = R_p \times (1 - (y'_0 / R_p)^2)^{1/2} = 335.7 \text{ mm}$$

$$y'_0 = 1,579 - 1,633 = -54 \text{ mm}$$

$$R_p = 340 \text{ mm}$$

(2) The adopted symbols are explained below:

- ims = internal meridional strain
- ems = external meridional strain
- mps = maximum principal strain
- ihs = internal hoop strain
- ehs = external hoop strain
- hd = horizontal displacement

TAB. 2
Coordinates of the plot representative nodes
in the modified 3-D hatch zone model

Nodes	x" (mm) ⁽¹⁾	y" (mm) ⁽¹⁾	x (mm)	y (mm)
15	348.7	-51.68	0	0
7294	~ 0	363.4	-348.7	415.1
6976	257.5	257.5	-91.20	309.2
6816	333.5	136.0	-15.20	187.7
283	369.0	1.909	20.30	53.59
9	402.3	-51.68	53.60	0
2436	398.9	-84.39	50.20	-32.71
6064	10	~ 0	-338.7	51.68
5154	582.0	-185.0	233.3	-133.3

Notes:

(1) the coordinates x" and y" refer to a reference frame with the origin at about the intersection of the vessel vertical axis with the hatch horizontal axis.

In the figures strains are plotted versus time. To get the pressure (MPa) the time value must be multiplied by 0.2.

The strain data at nodes 8 and 2435 (Fig. 8) should be compared with the response of gauge RSG-I-EQH-44a (loc. 41) (2). Notice that, in the analysis, the circumferential strain reached at the failure pressure (4.66 MPa) is 0.8 % against an experimental value of about 1%. A worse agreement is obtained comparing the same results with the response of the gauge RSG-I-EQH-45b (loc. 43) (2). In this case a strong underestimation is provided by the analysis. This could be explained by the inadequacy of the model to represent the local necking as well as by a possible underestimation of the local lowering in the yield point occurred near the weld. Moreover, it must be noticed that the lowering of the SPV 490 stress-strain curve has been applied in the model only to a narrow region around the reinforcement plate. No lowering has been carried out in the region near the gage location just below the material change line.

The results from the analysis of the local junction plane strain model are reported in figs. 11-13. Fig. 11 shows the necking obtained at an average circumferential strain of 1%. The necking at an average circumferential strain of about 2.1 % is shown in fig. 12. Fig. 13 provides a plot of the strain in the necked region as the average circumferential strain increases.

Finally the main results obtained with the local plane strain model of the vessel shell facing the hole in the MST are reported in figs. 14, 15 and 16. Also in this case the obtained necking is reported (fig. 14 and 15) as well as the history of the circumferential strain (fig. 14).

Notice the necking in the stiffener to be compared with the photopicture reported in fig. 4 of reference 4.

CONSEQUENCES FOR THE ANALYSIS

At least for us, it was very difficult to foresee the results provided by the experiment. In general the analysis is able to provide accurate results only if the rupture mechanism is already implicitly represented in the analysis itself. When the possibility of the rupture mechanism is not directly included in the model the analysis can lead to misunderstanding. It is therefore important to know what should be expected in each specific case.

An effort has been made by ANPA to correctly represent the true stress - true strain relationship in the material. Since the beginning of the experiment some advances have been obtained by us as far as it concerns the modeling of the material behavior, specially in the post-necking region. However this was ineffective to represent the material in the non-proportional elastic region. The obtained results show that also this region is important in order to obtain accurate results in the plastic field, specially in the case that average strains are not too large.

CONSEQUENCES FOR THE DESIGN

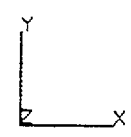
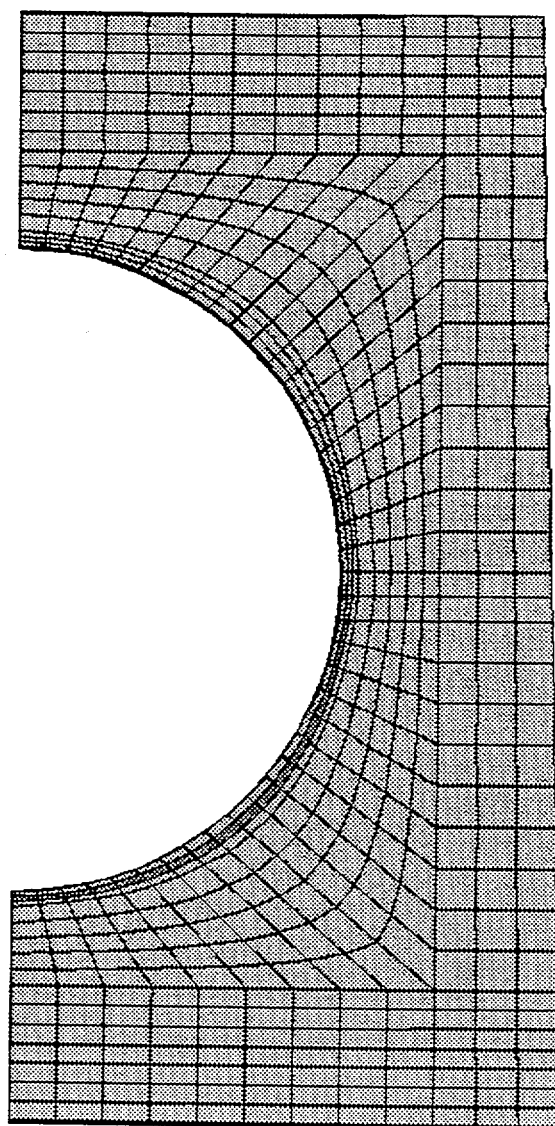
Relevant indications can be gained by the performed activity. In the design of new power stations great attention is paid to the behavior of containment in the case of a severe accident. The ultimate strength of the containment determines the maximum pressure which can be allowed inside the structure and, indirectly, the heat which can be removed by passive means. Independently from the present activity, all the analyses indicate that the strength is controlled by local effects near geometry or material discontinuities. It is therefore important to improve the local design in order to improve the overall vessel strength. The results obtained in the Sandia experiment show that the post weld behavior of the material must be fully understood. Moreover, a post weld heat treatment should always be made everywhere relevant discontinuities occur in the vessel shell. Local changes in the shell stiffness should also be avoided as far as possible. For example the holes in the stiffeners appear to have caused a local strain concentration in the shell. It is expected by us that a local reinforcement of the stiffener at the hole places could prevent this problem; however a detailed investigation should be performed to confirm this statement.

FINAL REMARKS AND ACKNOWLEDGMENTS

Further investigations should be carried out to get a full comprehension of the rupture mechanisms occurred during the test. However we can conclude that the main features of the experimental behaviour of the vessel have been explained. We feel to thank Sandia National Laboratories, NRC and NUPEC for the opportunity we have received to attend this benchmark.

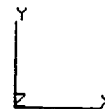
REFERENCES

1. G. Maresca , G. Pino "Preliminary Post-Test Evaluation of a Steel Containment Vessel Strength". ANPA, July 97
2. R-SN-S-007, rev. B "SCV High Pressure Test Data for Round Robin Analysis". SNLs, Jan 23, 1998.
3. A. N. Stroh "A Theory of the Fracture of Metals". *Advances in Physics*. Vol.6, p.418, 1957.
4. R-SN-S-009, rev. B "Postest Metallurgical Evaluation Results for SCV High Pressure Test". SNLs, Dec 19, 1997.
5. A. K. Ghosh "A Criterion for Ductile Fracture in Sheets under Biaxial Loading". *Metallurgical Transactions* ,Vol. 7A, pp. 523-533, 1976.
6. G. Maresca, G. Pino "Triaxiality Effects at the Hatch Reinforcement Plate of a Steel Containment Vessel". ANPA - December 96.
7. G. Maresca, G. Pino "Triaxiality Effects at the Hatch Reinforcement Plate of a Steel Containment Vessel Surrounded by a Contact Structure". ANPA - to be delivered on September 97.
8. G. Maresca, G. Pino "Pre-Test Vessel Analysis (In Absence of the Contact Structure)". ANPA - July 96.



1

Fig. 1. Modified 3-D hatch zone model.
Notice the strip of SPV 490 material
with a lowered stress-strain curve.



haz (reinforcement plate - vessel shell junction)

1

Fig. 2. Plane strain model of the junction between the vessel shell and the reinforcement plate.

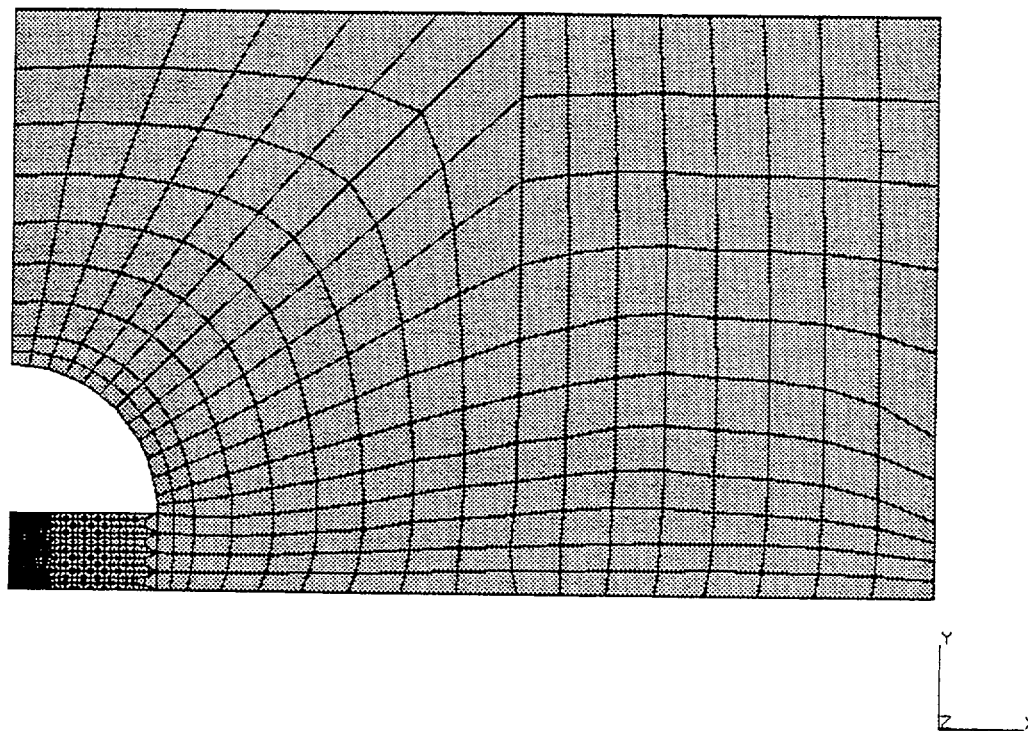


Fig. 3. Plane strain model of the shell facing the hole in the MST.

eyy (x.001)

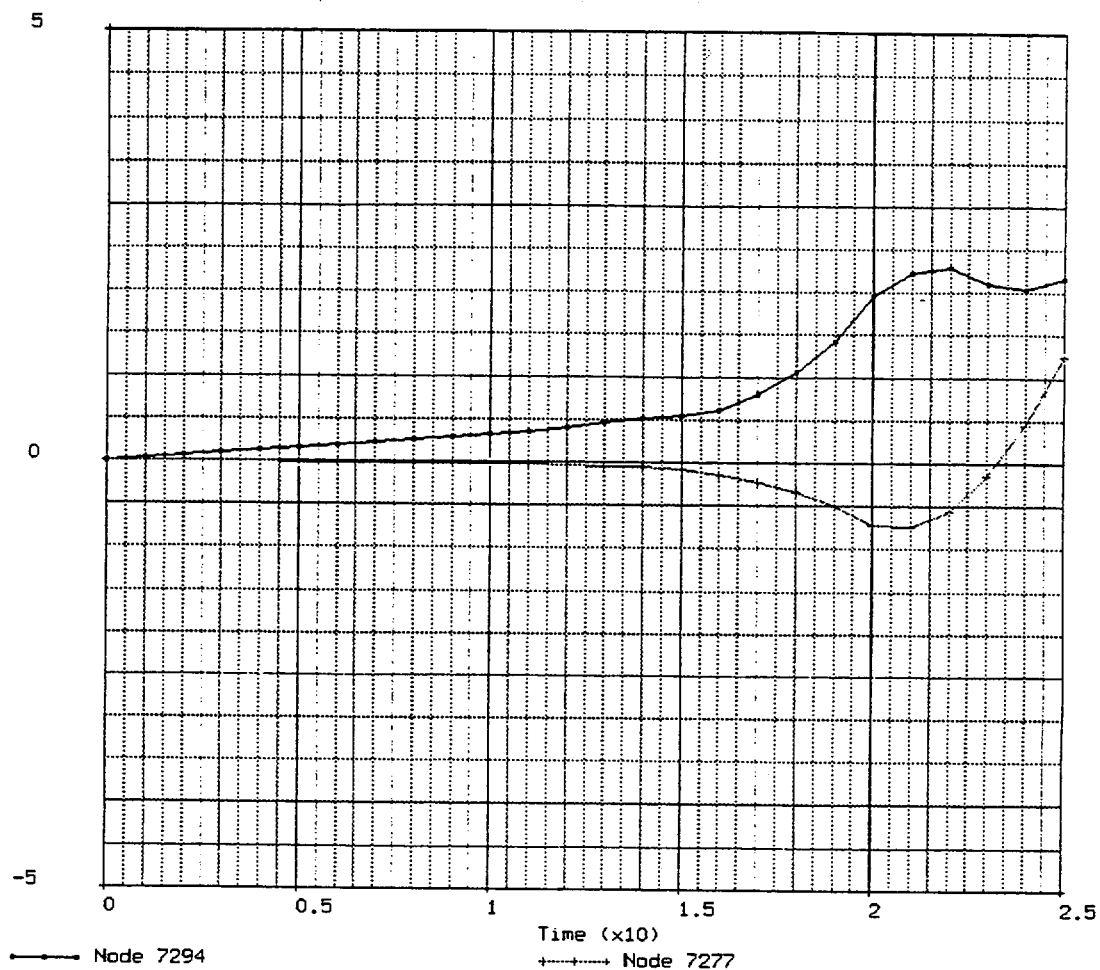


Fig. 4. Meridional strains at node 7294 (outside) and 7277 (inside).
To be compared with plots 3 and 4.

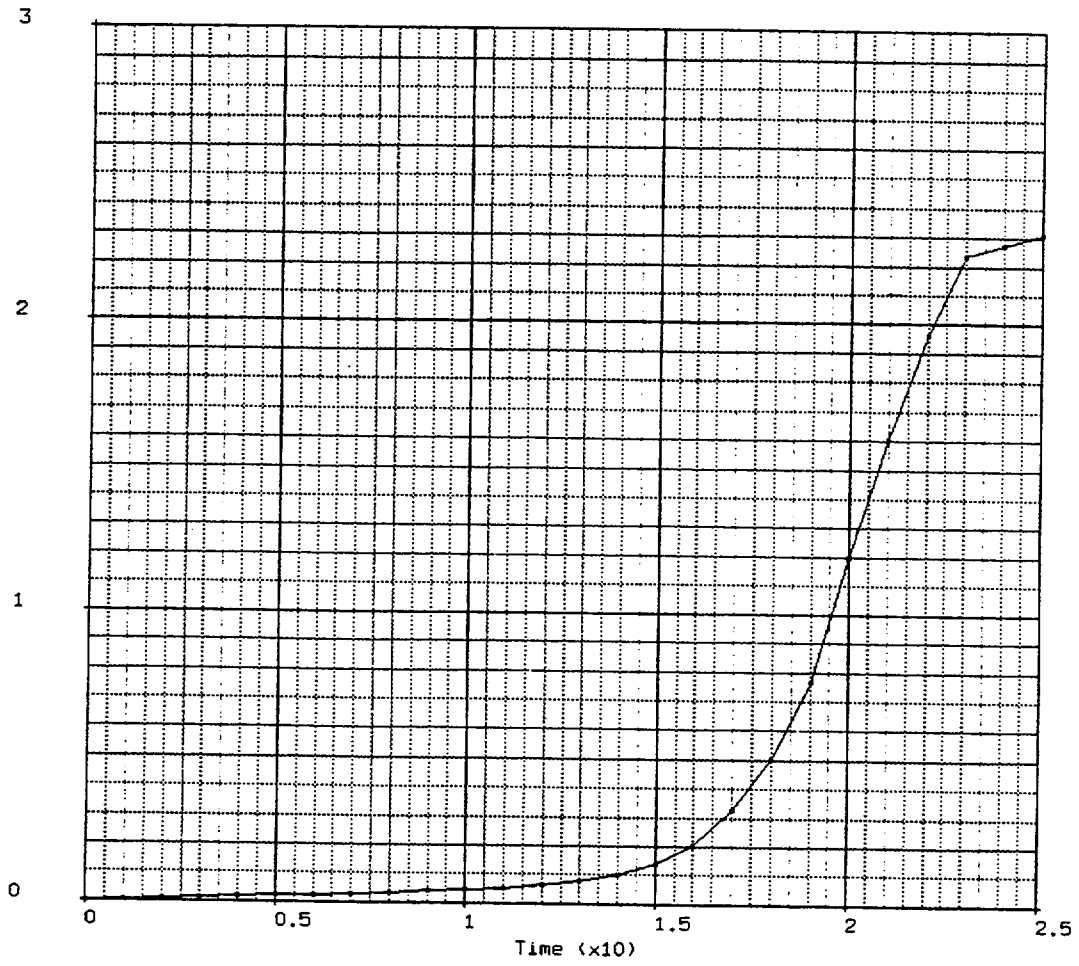


Fig. 5. Maximum principal strain (circumferential) at node 6959.
To be compared with plot 2.

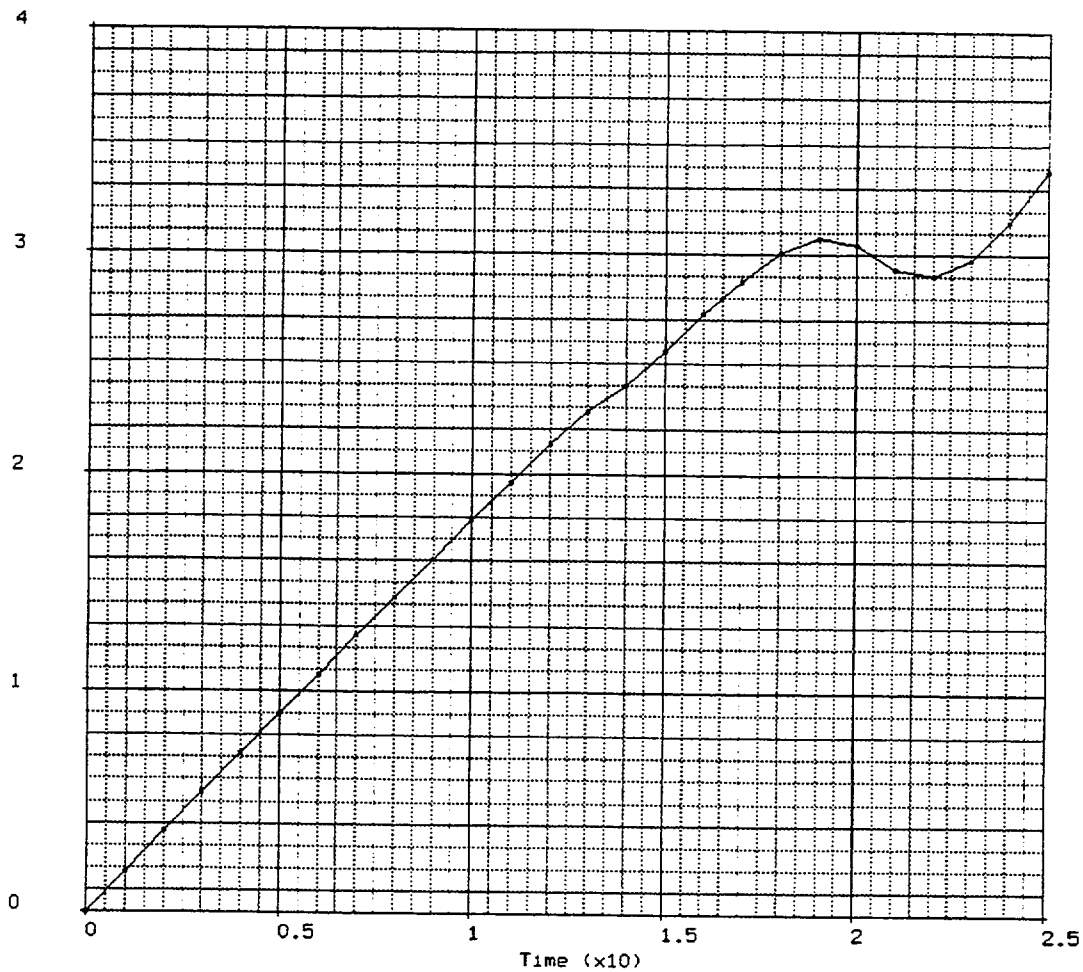
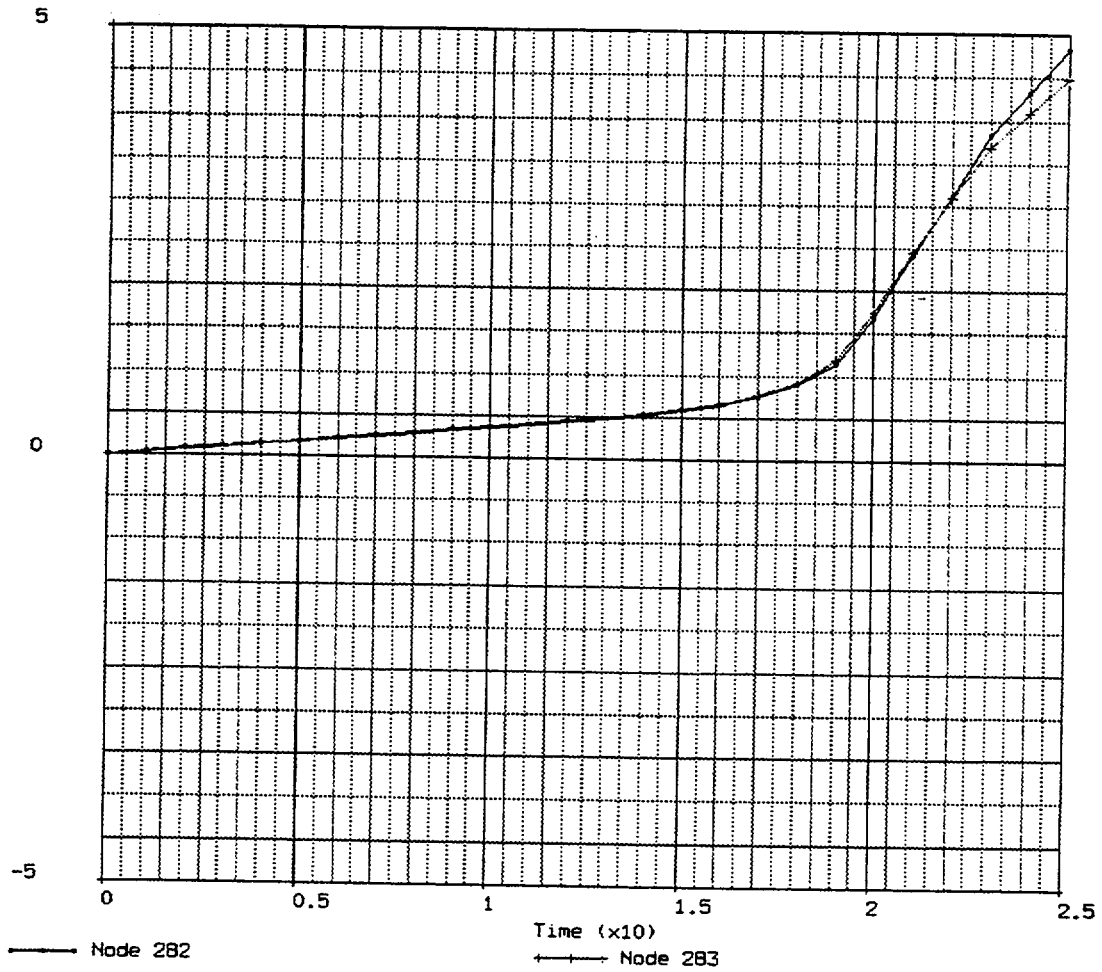


Fig. 6. Maximum principal strain (meridional) at node 6799.
To be compared with plot 1.

exx (x.001)

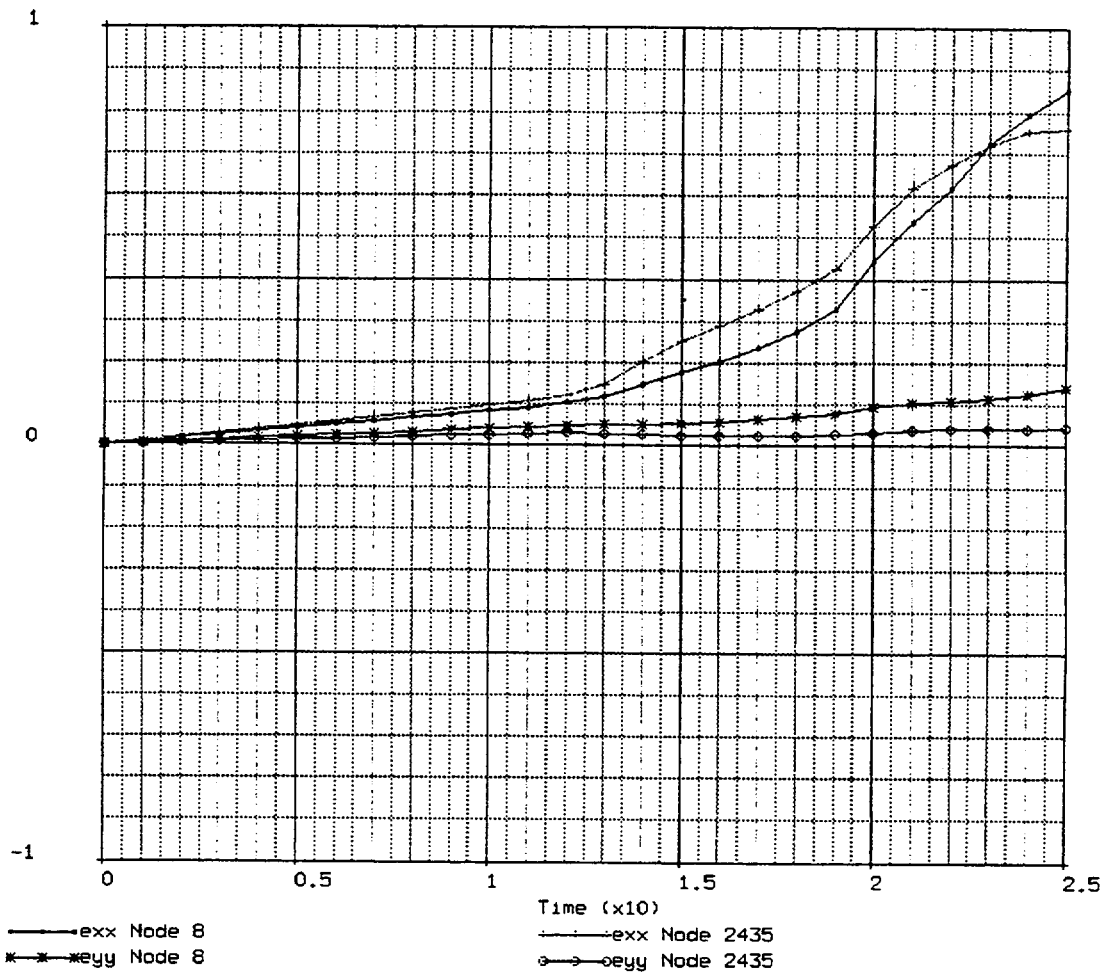
penetrazione sandia vessel - haz490 represented



1

Fig. 7. Hoop strain at nodes 282 (inside) and 283 (outside).
To be compared with plots 5 and 6.

Y (x.01)



1

Fig. 8. Hoop and meridional strains at nodes 8 (inside) and 2435 (inside). To be compared with plots 40 and 41. The same curves are representative of plots 42 and 43.

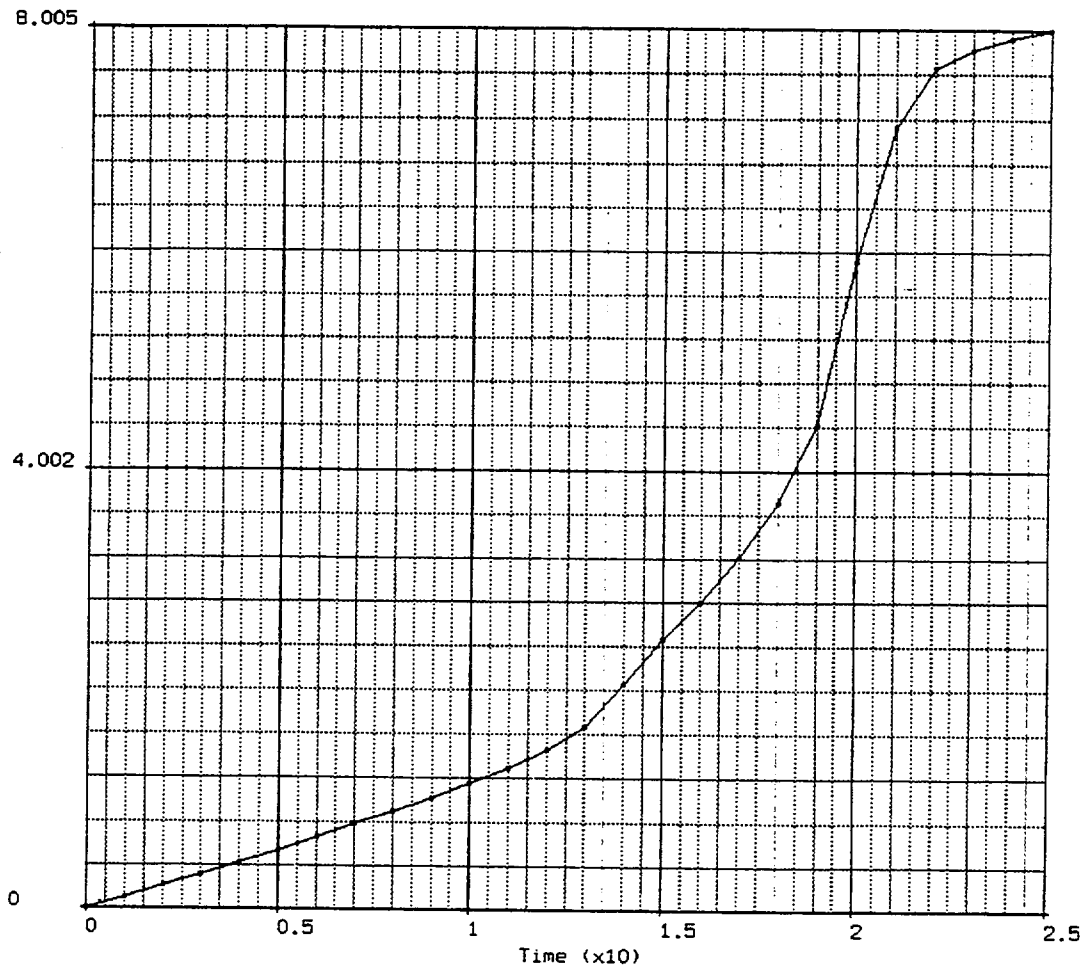
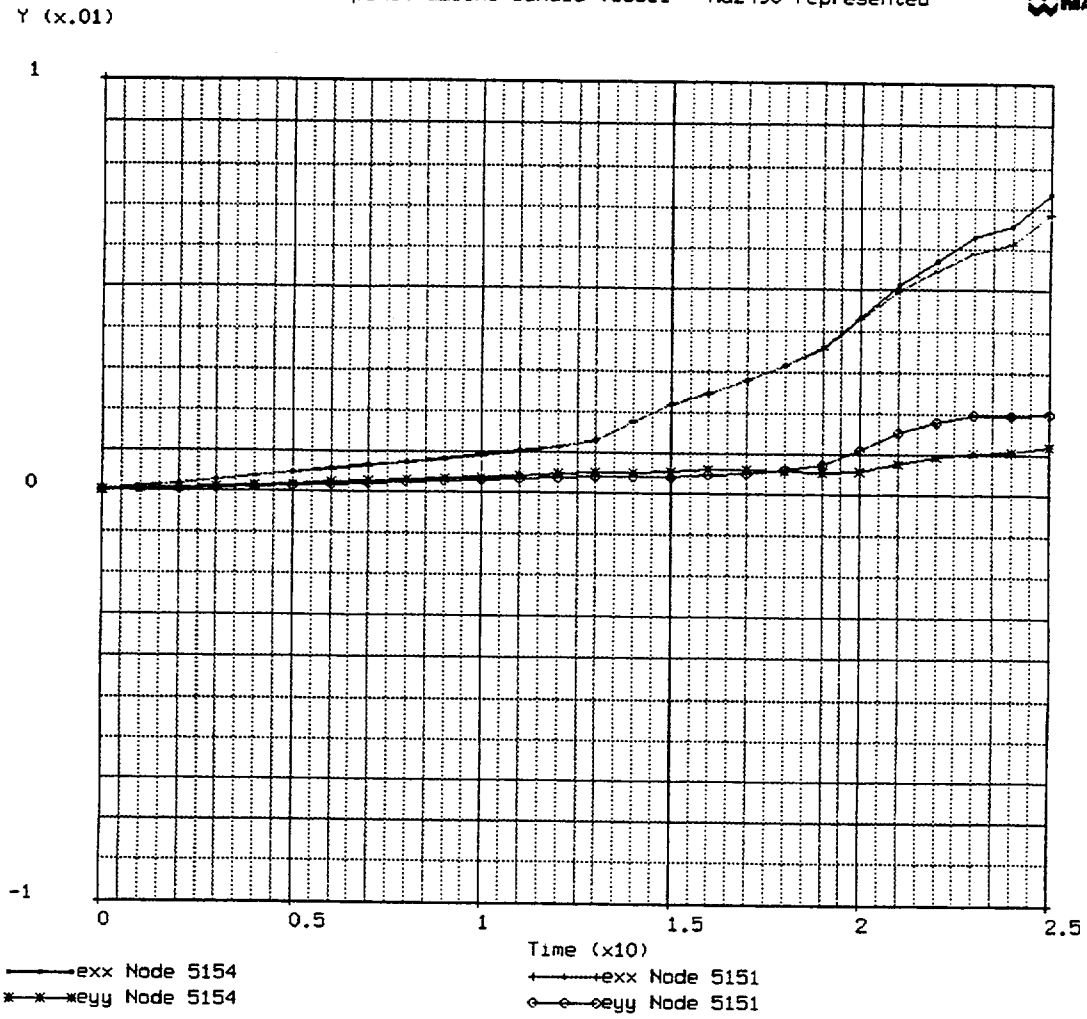


Fig. 9. Horizontal displacement (mm) at node 5449 (inside).
To be compared with plot 39



1

Fig. 10. Hoop and meridional strains at nodes 5154 (outside) and 5151 (inside).
 To be compared with plots 25, 26, 27, 28.

Inc : 26
Time : 0.000e+00

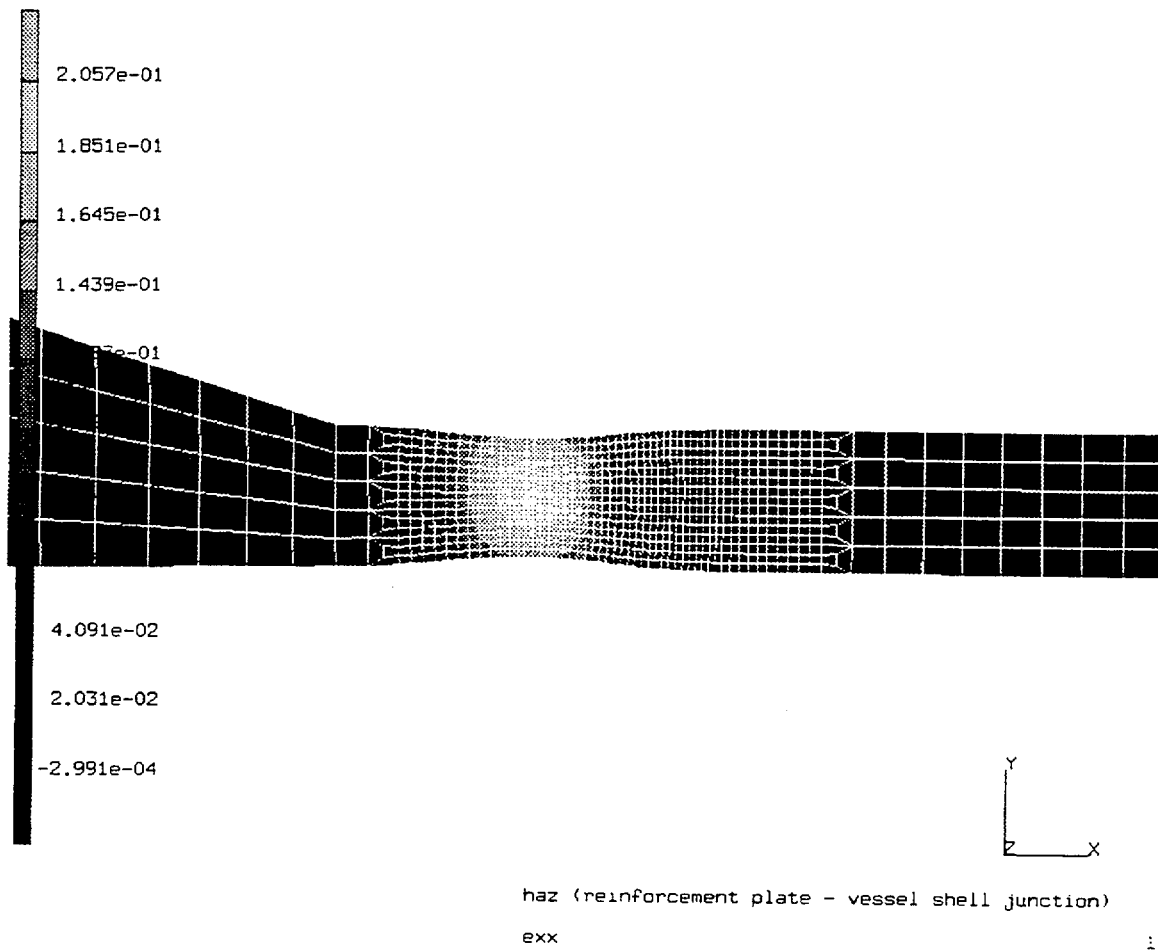


Fig. 11. Deformation of the plane strain junction model showing the local necking.
Average circumferential strain: 1%.

Inc : 54
Time : 0.000e+00

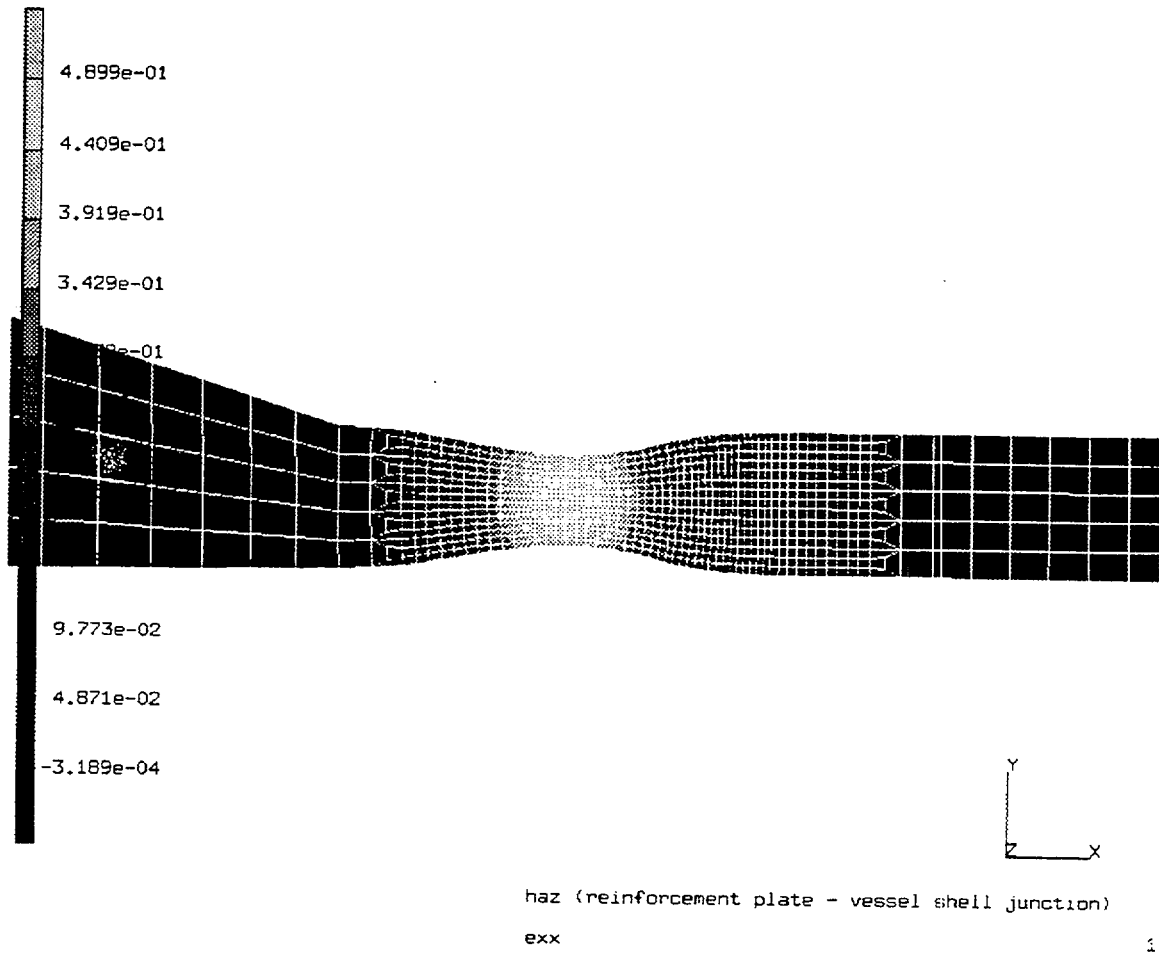
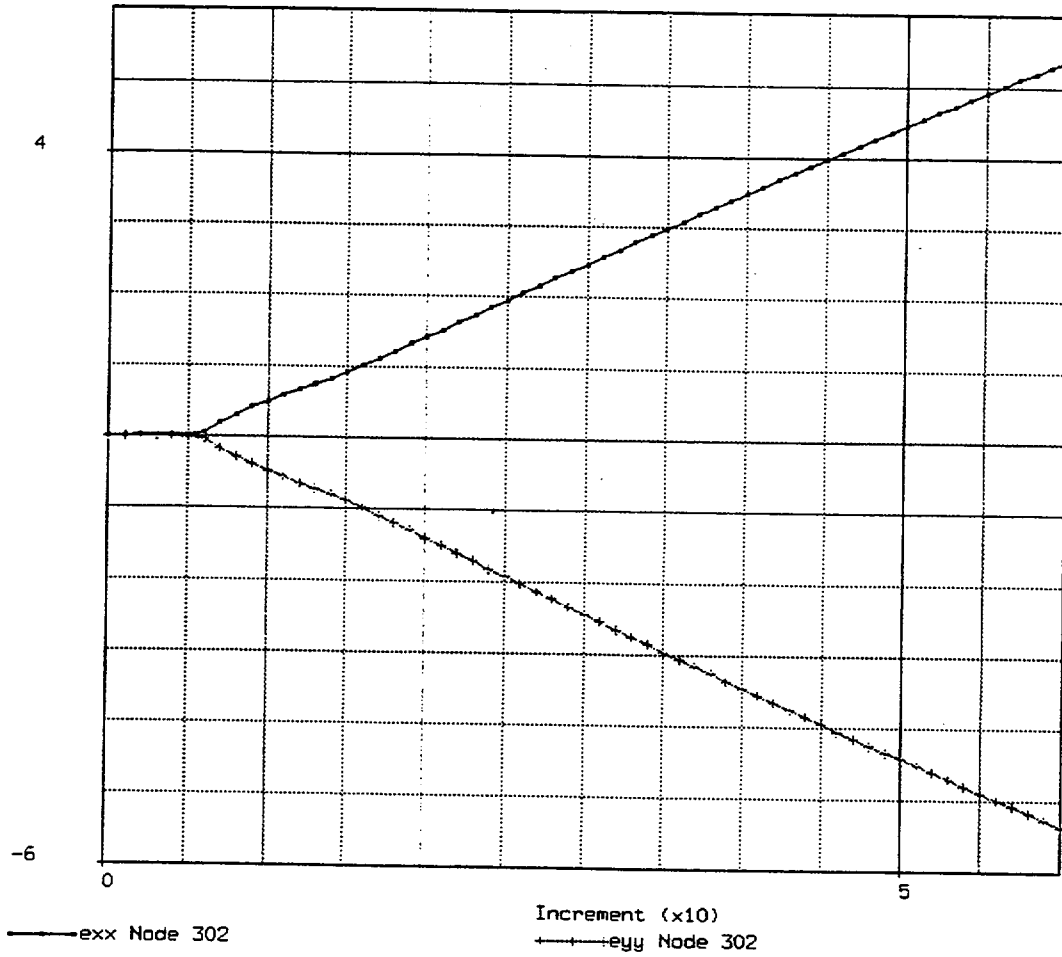


Fig.12. Deformation of the plane strain junction model showing the local necking.
Average circumferential strain: 2.1 %.

Y (x.1)

haz (reinforcement plate - vessel shell junction)

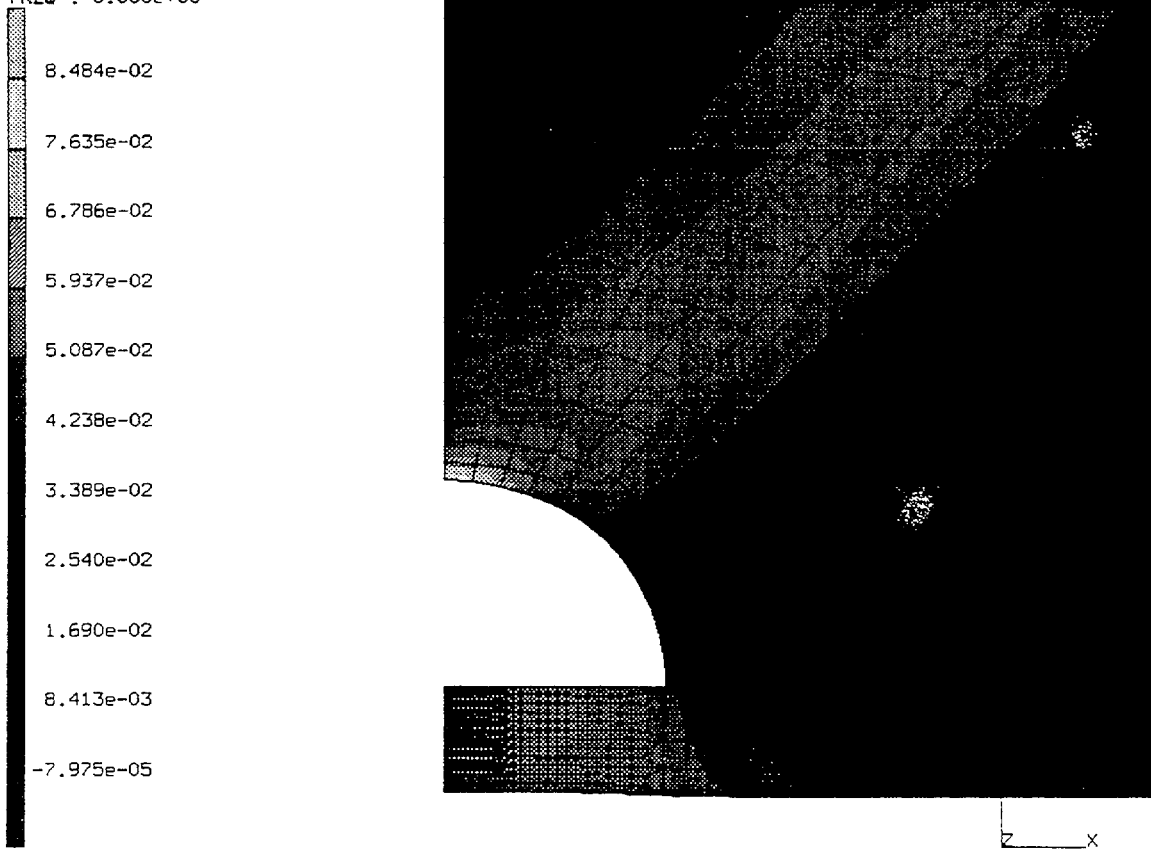


1

Fig. 13. History of the circumferential and of the radial strain at the center of the neck. Node 302. To get the average strain multiply the increment number by 0.1 and divide by 260.

INC : 10
SUB : 0
TIME : 0.000e+00
FREQ : 0.000e+00

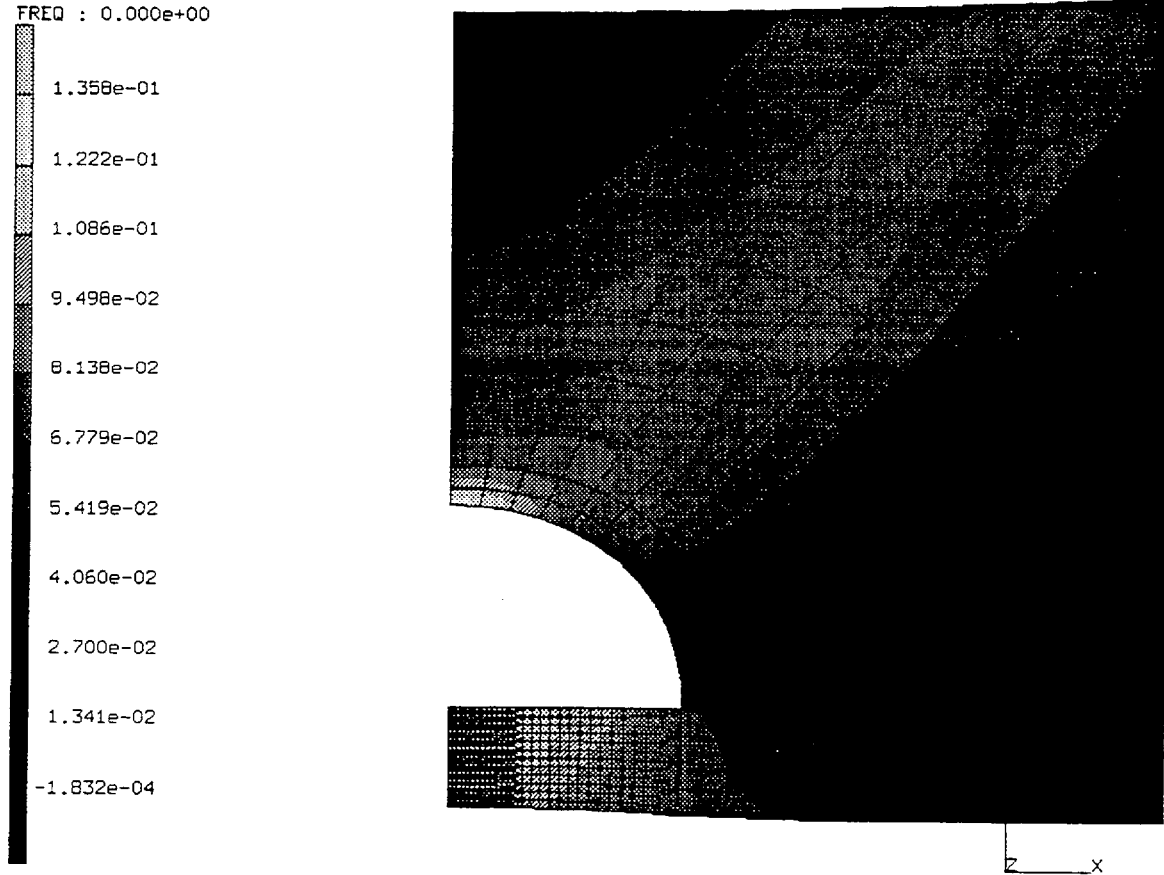
MARC



stiffner local shell analysis
1st Comp of Strain

Fig. 14. Deformation of the plane strain model of the shell facing the hole in the MST.
Average circumferential strain: 1%.

INC : 20
SUB : 0
TIME : 0.000e+00
FREQ : 0.000e+00



stiffner local shell analysis
1st Comp of Strain

Fig. 15. Deformation of the plane strain model of the shell facing the hole in the MST.
Average circumferential strain: 2%.
Notice the necking of the stiffening ring.

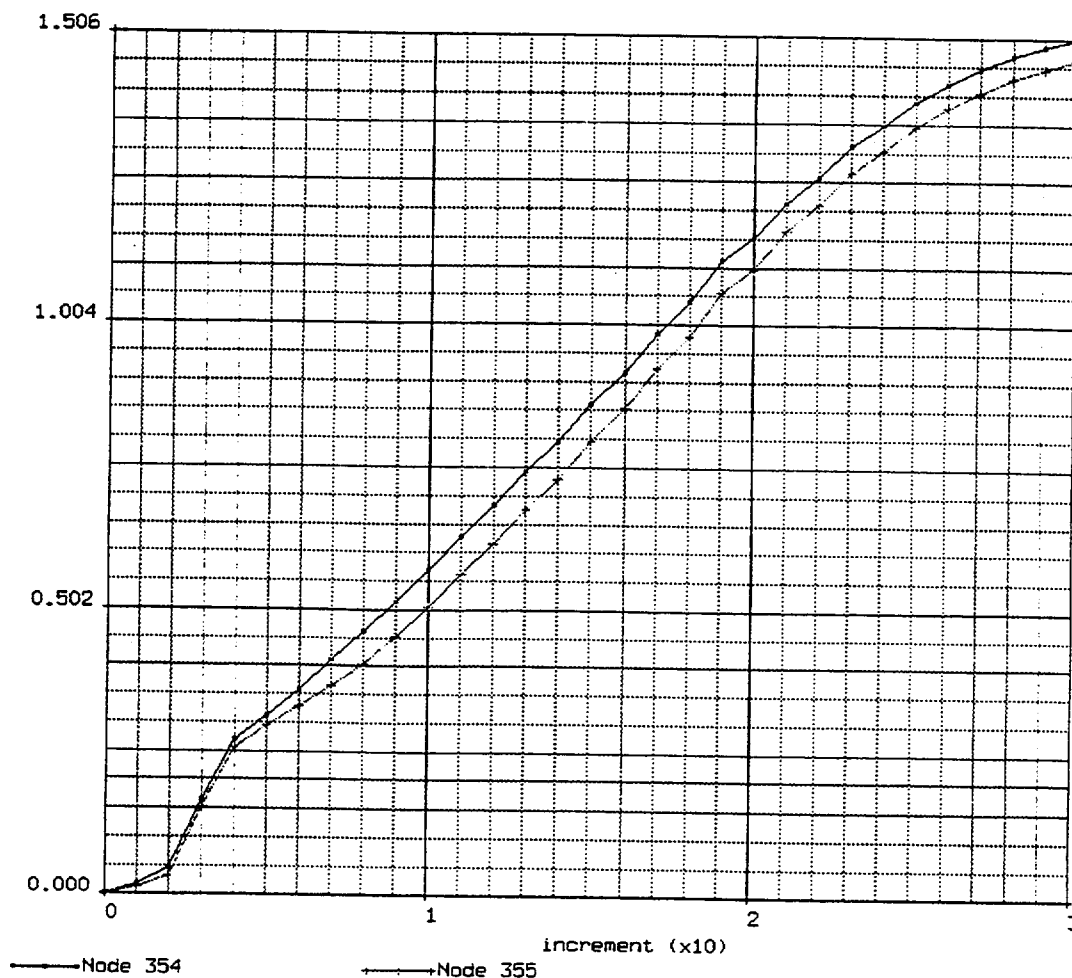


Fig. 16. History of the circumferential strain at the necked zone.
Node 354 (inside) and node 355 (outside).
To get the average strain multiply the increment number by 0.1 and divide by 100.

Appendix B-2

Argonne National Laboratory (ANL)

U.S.

Argonne National Laboratory
Round-Robin Posttest Analyses of a 1:10-Scale Steel Containment Vessel

by:

P. A. Pfeiffer, R. F. Kulak
Reactor Engineering Division, Argonne National Laboratory

1. INTRODUCTION

Pretest and posttest predictions were made by the Reactor Engineering Division of Argonne National Laboratory (ANL) for the response of the 1:10 scale Steel Containment Vessel (SCV) that was tested by Sandia National Laboratories (SNL). The SCV is a model of a prototype BWR Mark-II containment that is scaled 1:10 in overall geometry and 1:4 scale in thickness. The pretest predictions were made with a full three-dimensional model, depicted in Fig.1, using the NEPTUNE finite element code. An axisymmetric model for the free field of the SCV is shown in Fig. 2 and was used for the posttest analyses. The NEPTUNE [1, 2 and 3] code was primarily intended for 3-D fluid structure interaction problems, however additions [4] to the code were made to incorporate simulation of pressurized vessel analyses.

A review of the pretest predictions is given along with a comparison of the test results. Then the posttest analyses are described and compared with the test results and the pretest analysis. A summary of the results are presented and conclusions are given for the comparison of analytical results with the test results.

2. ANALYTICAL APPROACH

NEPTUNE is a three-dimensional finite element program that was developed to simulate the response of reactor components in 3-D space to design and beyond-design-basis loads. The code has evolved over the years to address safety issues. Since the code was developed to solve a variety of problems, the current version is a general purpose 3-D finite element code primarily suited for nonlinear problems. An important feature of NEPTUNE is its ability to handle nonlinear problems, which often occur during beyond-design basis loads. The element formulations can properly treat large deformations (i.e. geometric nonlinearities), and the rate-type material models can handle large material strains (i.e. material nonlinearities). A Von Mises elastic-plastic constitutive material law is utilized for yielding and post yielding of material. The failure model used, is based on a Davis triaxial factor for multiaxial state of stress in combination with Von Mises

elastic-plastic constitutive law. Explicit solution algorithms are used to economically solve short duration transient problems, and a dynamic relaxation (DR) method is utilized to simulate quasi-static problems.

The numerical algorithm for the explicit time integration is described in the pretest report. An elastic-plastic analysis was performed and failure is assumed to occur when the effective plastic strain reaches the ultimate strain. When an elastic-plastic analysis is utilized, the effect of multiaxial stress needs to be accounted for in the analysis. Manjoine [5] discusses the effect of multiaxial stress on the uniaxial stress-strain behavior. Reference [6] also discusses the effect of multiaxial stress on failure. Essentially, the ductility of a material can vary under a multiaxial state of stress, which in turn may reduce the plastic strain at which the material will fail. Manjoine proposed a formulation for the ductility ratio based on the Davis triaxial factor. The Davis triaxiality factor, TF_D , is equal to the sum of the principal stresses divided by the octahedral shearing stress and normalized to unity for plane stress or uniaxial tension. Thus,

$$TF_D = \frac{\sigma_1 + \sigma_2 + \sigma_3}{\frac{1}{\sqrt{2}} \left[(\sigma_1 - \sigma_2)^2 + (\sigma_2 - \sigma_3)^2 + (\sigma_3 - \sigma_1)^2 \right]^{1/2}} \quad (1)$$

where σ_1 , σ_2 and σ_3 are the principal stresses. The ductility ratio is defined as

$$c = \frac{\text{effective von mises strain}}{\text{tensile elongation}} \quad (2)$$

and the ductility ratio can be described by the triaxiality factor as

$$c = 2^{(1-TF_D)}, c_{\max} \leq 2.0 \quad (3)$$

Therefore, under multiaxial stress states the equivalent uniaxial strain is

$$\epsilon_u = \frac{\epsilon_{\text{eff}}}{c} \quad (4)$$

where ϵ_{eff} is the calculated effective Von Mises strain and ϵ_u is the strain to be compared with, i.e. uniaxial or tensile elongation data. The value of TF_D under uniaxial stress is 0 and thus $c = 1.0$, and the value of TF_D under a biaxial state of stress ($\sigma_1 = \sigma_2$) is 2.0, and thus, $c = 0.5$. Therefore under a biaxial state of stress ($\sigma_1 = \sigma_2$), the strain to failure is reduced by 50%. This is important when the strain to failure is the dominating failure mode under multiaxial stresses.

3. PRETEST VESSEL RESPONSE AND FAILURE DUE TO PRESSURIZATION

The load is a pressure incrementally applied to the inside surface of the SCV. Initially the vessel model was run elasticity to determine when the yield stress will be reached under internal pressure. That value is approximately 2.6 MPa internal pressure with yielding near the bottom connection of the equipment hatch and the vessel. The vessel model was then analyzed for an elastic-plastic response. A pressure of 2.6 MPa is applied in the first load step, and 0.1 MPa increments are used thereafter for each load step. The model was pressurized incrementally up to failure, which occurred at 5.5 MPa. At each load step, static equilibrium was checked for convergence. Static equilibrium was obtained for load steps 1 through 29 (i.e. internal pressure = 5.4 MPa).

Yielding of the vessel occurred first at the bottom of the equipment hatch sleeve and the vessel reinforcing plate ($\theta_H = 180^\circ$, $R_H = 200$ mm in the hatch coordinate system) for a pressure of 2.6 MPa. At a pressure of 2.8 MPa yielding occurs all around (360°) the knuckle at the top (elev. 3.431 m) and the bottom (elev. 3.354 m). Contact between the CS and SCV occurs at 4.4 MPa at an elevation of 2.402 m. The vessel model fails at an internal pressure of 5.5 MPa at the location just above the knuckle in the 6 mm thick upper cylindrical shell. The uniaxial ultimate strain (plastic failure strain) is reduced to 9.9% strain because of the biaxial state of stress in the shell; the value of c in Eqs.3 and 4 is approximately 0.5.

The predicted failure pressure of 5.5 MPa was within 18% of the actual failure pressure of 4.66 MPa. The predicted maximum pressure with high confidence (>95%) that there is a low probability of failure (HCLPF) was calculated for a pressure of 4.9 MPa, which is within 5% of the actual failure pressure. The predicted failure location was at the knuckle in the upper cylindrical shell of the top head. The failure ratio of the vessel at impending failure is shown in Fig. 1. The failure ratio is defined by the current effective Von Mises strain divided by the ultimate strain at failure given in Eq. 4. Thus a value of ratio = 1.0 indicates failure. The results in Fig.1 indicate that the next "most likely" failure location was at the equipment hatch. This location was very near the actual failure location of the test. When the predicted failure location, that is the knuckle in the upper cylindrical shell, reached a failure ratio of 1.0, the hatch location indicated a failure ratio of approximately 0.90. Perhaps due to grinding, the thinned out section, which was a 9.0 mm nominal wall thickness ground down to 7.5 mm, that is located in this area would cause the prime failure location to shift to this location. The pretest analysis used the nominal thickness of 9.0 mm. Additionally, the failure pressure would be reduced because of the 16.7% reduction in thickness at this location. The analysis with a local reduced thickness was not done due to budget and time constraints.

Strains and displacements for the model are given in Figs. 3 through 13, the strains are shown in Figs. 3 through 9 and the displacements are depicted in Figs. 10 through 13. The locations are the same as the standard output locations

requested by SNL, the location number is given in the legend and title of the figures. However, the displacement plots are for the nodes in the finite element model which are the centerline deflections of the plate elements, i.e. approximately the average of the inside and outside deflections of the plate. Additionally the test data at the standard output location and two posttest analysis results are provided in Figs. 3 through 13. The posttest analyses are described in the next section.

4. POSTTEST VESSEL ANALYSES

4.1 Model Description

The finite element description of the posttest model is shown in Fig. 2. The model is a 40° sector representation of the SCV and CS which does not include the equipment hatch. The main purpose of the model is to analyze the free field response of the SCV to internal pressurization. The overall model contains 698 nodes (3 degrees of freedom) and 407 elements. The SCV consists of 156 quadrilateral plate elements for the steel shell and 20 bar elements for the 5 stiffeners (i.e. 4 bar elements for each stiffener). The CS consists of 116 quadrilateral plate for the steel shell and 115 contact elements which are located between the CS nodes and the SCV nodes. The model contains 199 translational nodes and 199 rotational nodes in the SCV and 150 translational nodes and 150 rotational nodes in the CS.

The model is subjected to a fixed boundary condition (no translation or rotation allowed) at the bottom which is the 0.000 m elevation for the SCV and CS. Also, boundary conditions are applied along the vertical edges of the SCV and CS that allow only radial deflections and bending in the meridional direction, so the model will respond axisymmetrically.

The pretest analysis was performed using the material test data provided by SNL. However, that data had some unusual values for Young's modulus. Therefore, the material data was adjusted from the values used in the pretest analysis for the posttest analyses. The change was to make Young's modulus equal to 2.1×10^{11} Pa for all of the steel in the SCV and CS, originally the value of Young's modulus varied from 1.2×10^{11} Pa to 2.1×10^{11} Pa. The data was provided for the different materials and thickness', and the pretest report describes the correlation's of the test specimens. The yield and ultimate strength and failure strain for the different materials and thickness were not changed for the posttest analyses. The results of the posttest analysis are shown in Figs. 3 through 13, and are labeled as "No Residual" in the plots.

4.2 Residual Stresses Due to Forming of Vessel

A steel containment structure is made by welding individual plates together to form the sections that make up the complex shaped vessels. The individual plates

are bent into the desired shape through a forming operation that results in some elastic spring back and residual stresses. Generally, the effect of metal forming residual stresses can be reduced or virtually eliminated by thermally stress relieving the vessel. In the SCV no stress relieving was done and thus the residual stresses due to manufacturing may be important. The residual stresses could possibly affect the response of the vessel to internal pressurization. When the level of residual stresses is significant it will affect the vessel's response; such as the yielding pressure and possibly the failure pressure.

The plate forming operation incorporates plastic bending with elastic spring back that can leave considerable residual stresses in the formed plate. The strain in a plate when bent at a radius R is shown in Fig. 14. Note that the inner surface is in compression and the outer surface is in tension. The resulting stresses are shown in Fig. 15 for the bent plate assuming an perfectly plastic material after yielding, the inner portion dimensioned by 2λ is still elastic. A strain hardening material was utilized in the resulting stress determination for the posttest analysis. After the elastic spring back has occurred, the plate is bent at a radius R^* with the residual stress profile depicted in Fig. 16. Note that the inner surface is now in tension and the outer surface is in compression. Also the maximum residual stress will occur near the center of the wall. Reference [7] describes in detail the analysis and results of a pressure vessel with residual stresses present due to the forming process, under internal pressurization up to failure.

Since the SCV is mainly made with small thickness, the residual stresses due to forming are not significant. The lower part of the vessel (9mm, 8.5 mm, 8mm and 7.5 mm thickness) develops a plastic strain due to forming in the range of 0.38% to 0.40% strain. The upper part of the vessel (top head 6mm thickness) develops a plastic strain due to forming in the range of 0.38% to 0.91% strain. The effect of these residual stresses due to forming are discussed in the next section. The results of this posttest analysis are shown in Figs. 3 through 13, and are labeled as "Residual Stress" in the plots.

4.3 Comparison of Posttest, Pretest and Test Results

The posttest results concentrated on the free field response of the vessel in regards to the strain and displacement versus internal pressure. Failure of the vessel was predicted adequately in the pretest analysis and was not addressed in the posttest analyses. The test results indicated the vessel had yielded at a lower pressure than the pretest analyses predicted for some of the standard output locations. The main concern was why the vessel had yielded at a lower pressure than predicted. The avenue pursued in the posttest analyses was to consider the residual stresses that were present due to forming of the vessel. The residual stresses due to the welding process and the heat affected zone (HAZ), which could reduce the yield and tensile strength, were not considered in this investigation. An axisymmetric model of the free field section of the SCV was chosen as an initial analysis tool to address the residual stress effect on the response to internal pressurization. The

posttest model was also used to determine why the elastic response of the SCV seemed to deviate from the test results in certain sections. Due to budget and time constraints a full 3D model with the hatch was not analyzed in the posttest investigation.

The hoop and meridional strains in the top head are given in Figs. 3, 4 and 5. In Fig. 3 the hoop strain of the pretest results match the test data in the elastic region, with the plastic response diverging. The results of the posttest do not agree with the elastic response as well, but the general trend is a good fit of the test data. The posttest results, with the residual stresses, gives a better agreement than the posttest results with no residuals. Figures 4 and 5 depict the meridional strains, which indicate the posttest results agree with the test data much better than the pretest results. The change in Young's modulus is evident in the elastic response, for the pretest analysis $E = 1.3 \times 10^{11}$ Pa and for the posttest analyses $E = 2.1 \times 10^{11}$ Pa at the location. The results of the posttest indicate the residual stress effect, improves the agreement of the analysis with the test data.

The meridional and hoop strains in the upper conical shell are given in Figs. 6 and 7, respectively. No improvement was observed between the pretest and posttest results. In Fig. 7 the posttest results indicate a slight improvement over the pretest results when compared to the test data. The material at this location had the same Young's modulus in the pretest and posttest analysis.

The meridional and hoop strains in the lower conical shell are depicted in Figs. 8 and 9, respectively. In both figures the posttest results are an improvement over the pretest results when compared to the test data. The posttest analysis with the residual stress effect shows an improvement over the posttest results with no residual stress effect. The material at the location had a change in Young's modulus, for the pretest analysis $E = 1.2 \times 10^{11}$ Pa and for the posttest analysis $E = 2.1 \times 10^{11}$ Pa.

The vertical displacement of the top head is given in Fig. 10. The results of the posttest did not improve the comparison with the test results. This could occur because of the coarseness of the mesh near the top in the posttest model.

The horizontal displacement in the upper conical shell is given in Fig. 11. An improvement was observed in the posttest results over the pretest result when compared to the test data.

The horizontal and vertical displacement of the spherical shell are depicted in Figs. 12 and 13, respectively. An improvement was observed in the posttest results over the pretest results when compared to the test data. In the pretest results there was a problem with the contact elements and "blow by", which is a loss of the contact surface, had occurred. In the posttest model the contact was maintained, i.e. the SCV and CS remained in contact up near the knuckle location, in the pretest analysis this did not occur. However, the posttest finite element

model is possibly too coarse for an accurate response of the total contact in the spherical shell region. Thus a more detailed posttest model needs to be analyzed to resolve the differences from the test data.

5. SUMMARY OF RESULTS

The posttest evaluation of the SCV indicates that the failure pressure was adequately predicted in the pretest analysis and could be improved by including the local grinding near the hatch location. The posttest analyses indicate the residual stresses due to forming of the vessel may be part of the reason for the earlier onset of yielding in the SCV. However, the total answer may be the effect of the welding residual stresses and the heat affected zone (HAZ), which could reduce the yield and tensile strength of the material. The effect of welding was not addressed in the posttest analyses.

The pretest results, which were based on supplied material property data, at some locations had over predicted the strain in the elastic response of the vessel when compared to the test results. By changing Young's modulus to an average value of 2.1×10^{11} Pa (30×10^6 psi), which is the standard handbook value, the posttest analyses agreed very well with the test results in the elastic response. Further analyses should be done in order to address the local grinding near the hatch and the effect of welding on the material stress-strain behavior, but due to budget and time constraints the analyses were not completed.

6. ACKNOWLEDGMENT

This work was performed under the auspices of the U.S. Department of Energy, Technology Support Programs, under Contract W-31-109-Eng-38.

7. REFERENCES

- [1] R. F. Kulak, "A Finite Element Formulation for Fluid-Structure Interaction in Three-Dimensional Space", J. of Pressure Vessel Technology, Vol. 103, No. 2, 1981, pp. 183-190.
- [2] R. F. Kulak, "A Finite element Quasi-Eulerian Method for Three-Dimensional Fluid-Structure Interactions", Computers and Structures, Vol. 18, No. 2, 1984, pp. 319-332.
- [3] R. F. Kulak, "Three-Dimensional Fluid-Structure Coupling in Transient Analysis", Computers and Structures, Vol. 21, No. 3, 1985, pp. 529-542.
- [4] R. F. Kulak and C. Fiala, "NEPTUNE: A System of Finite Element Programs for Three-Dimensional Nonlinear Analysis," Nuclear Engineering and Design, Vol. 106, 1988, pp. 47-68.
- [5] M. J. Manjoine, "Creep-Rupture Behavior of Weldments," Welding Journal, Proceedings of American Welding Society, Vol. 49, 1982, pp. 505-575.
- [6] R. A. Dameron, R. S. Dunham, Y. R. Rashid and H. T. Tang, "Conclusions of the EPRI Concrete Containment Research Program," Nuclear Engineering and Design, Vol. 125, 1991, pp. 41-55.
- [7] P. A. Pfeiffer, R. F. Kulak and F. Costantini, "Residual Stress Concerns in Containment Analysis," Proceedings of Containment of Nuclear Reactors, 14th International Conference on Structural Mechanics in Reactor Technology, August 25-26, 1997, pp. 141-154.

List of Figures

1. Failure Ratio for Pretest Analysis of Steel Containment Vessel
2. Finite Element Mesh of Free Field Model
3. Standard Output Location #8, Exterior Hoop Strain in Top Head (Top 270° , 0.48m)
4. Standard Output Location #9, Exterior Meridional Strain in Top Head (Top 270° , 0.48m)
5. Standard Output Location #10, Interior Meridional Strain in Top Head (Top 270° , 0.48m)
6. Standard Output Location #31, Interior Meridional Strain in Upper Conical Shell (Global 270° , 2.49m)
7. Standard Output Location #32, Interior Hoop Strain in Upper Conical Shell (Global 270° , 2.49m)
8. Standard Output Location #33, Interior Meridional Strain in Lower Conical Shell (Global 270° , 1.25m)
9. Standard Output Location #34, Interior Hoop Strain in Lower Conical Shell (Global 270° , 1.25m)
10. Standard Output Location #35, Vertical Displacement of Top Head (Top 0° , 0.00m)
11. Standard Output Location #36, Inside Horizontal Displacement of Upper Conical Shell (Global 45° , 3.57m)
12. Standard Output Location #37, Inside Horizontal Displacement of Spherical Shell Global (0° , 3.32m)
13. Standard Output Location #38, Inside Vertical Displacement of Spherical Shell (Global 0° , 3.32m)
14. Strain Distribution Through the Wall of a Bent Plate
15. Stress Distribution Through the Wall of a Bent Plate
16. Residual Stresses Through the Wall of a Bent Plate

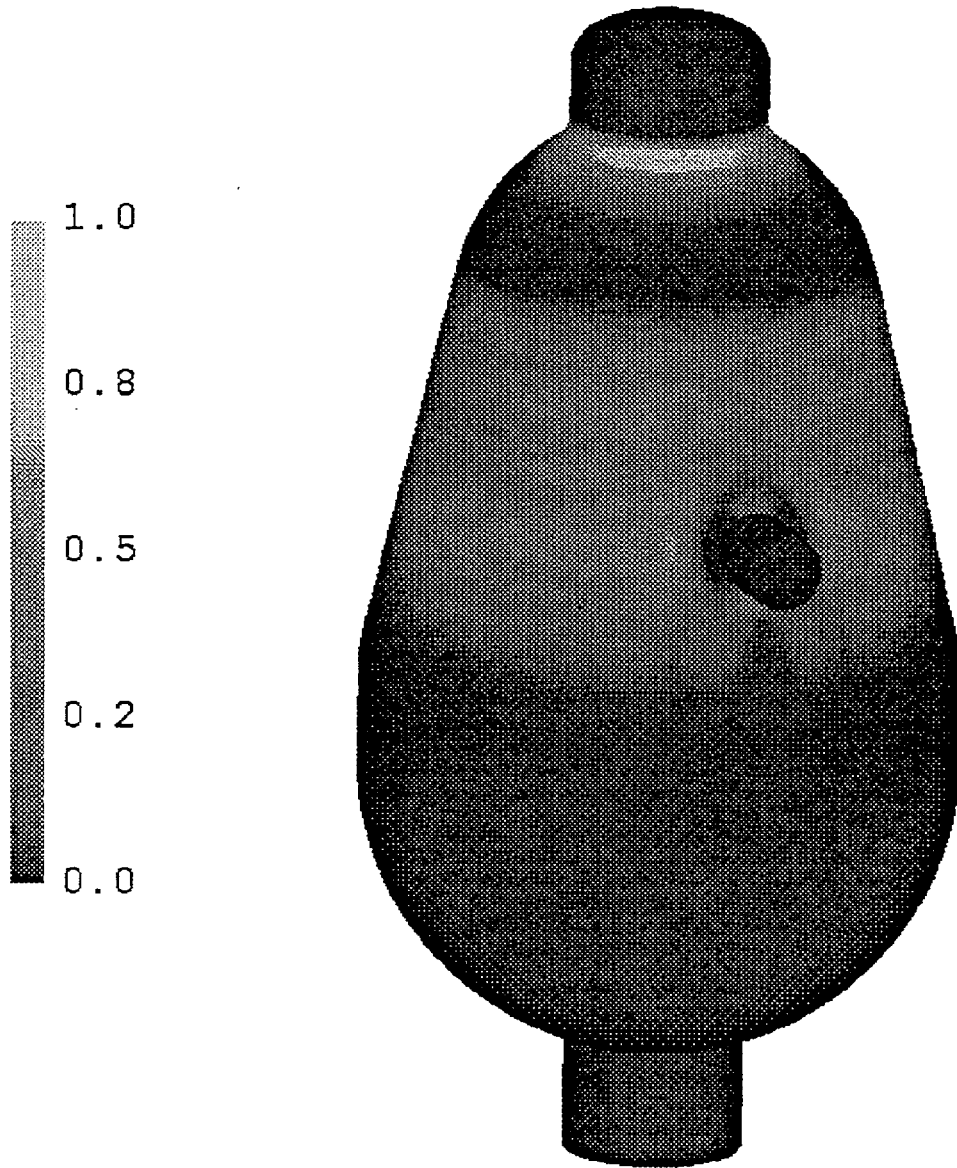


Figure 1. Failure Ratio for Pretest Analysis of Steel Containment Vessel

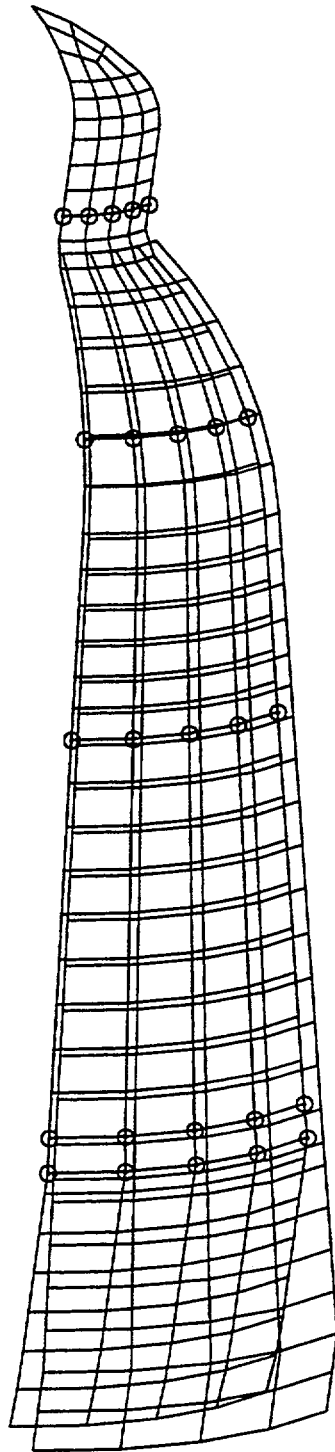


Figure 2. Finite Element Mesh of Free Field Posttest Model

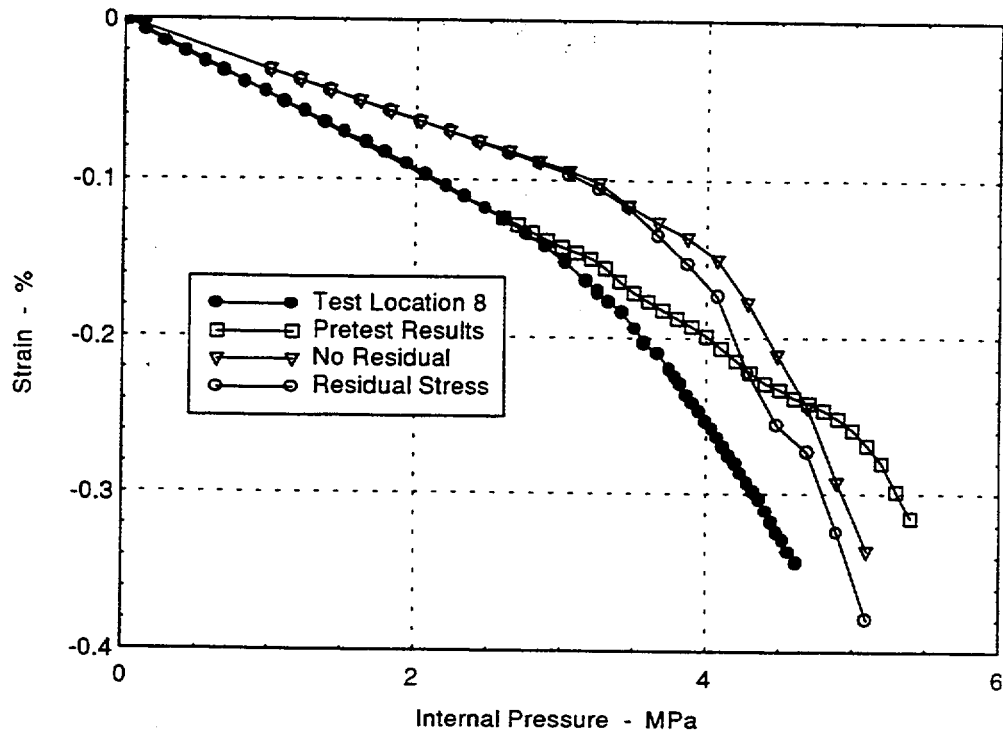


Figure 3. Standard Output Location #8, Exterior Hoop Strain in Top Head (Top 270°, 0.48m)

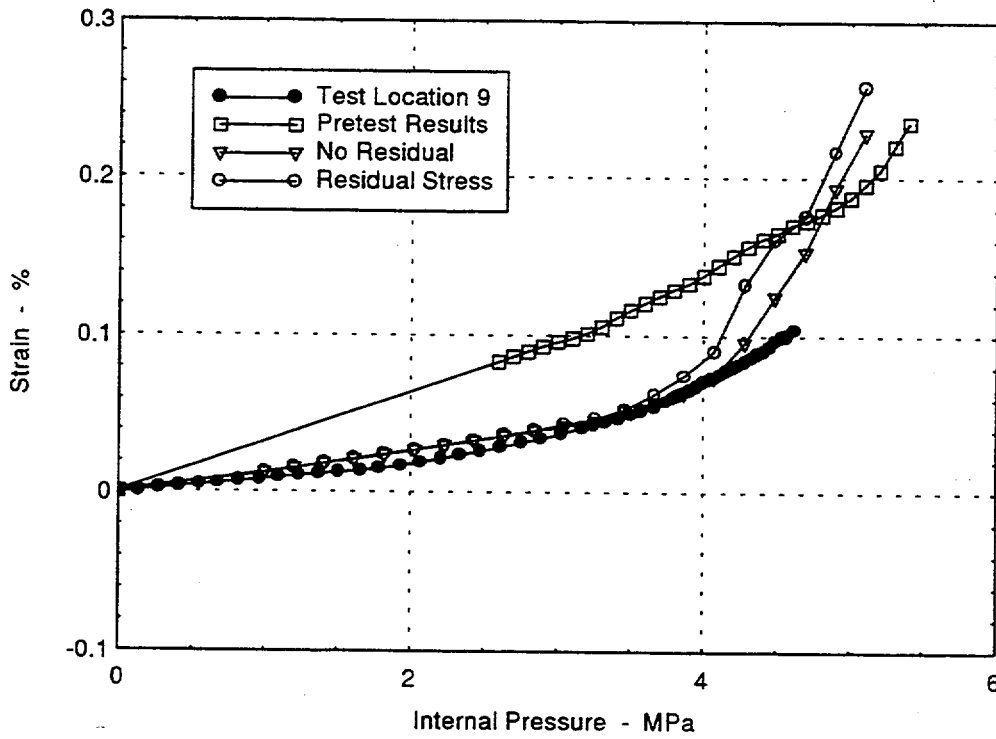


Figure 4. Standard Output Location #9, Exterior Meridional Strain in Top Head (Top 270°, 0.48m)

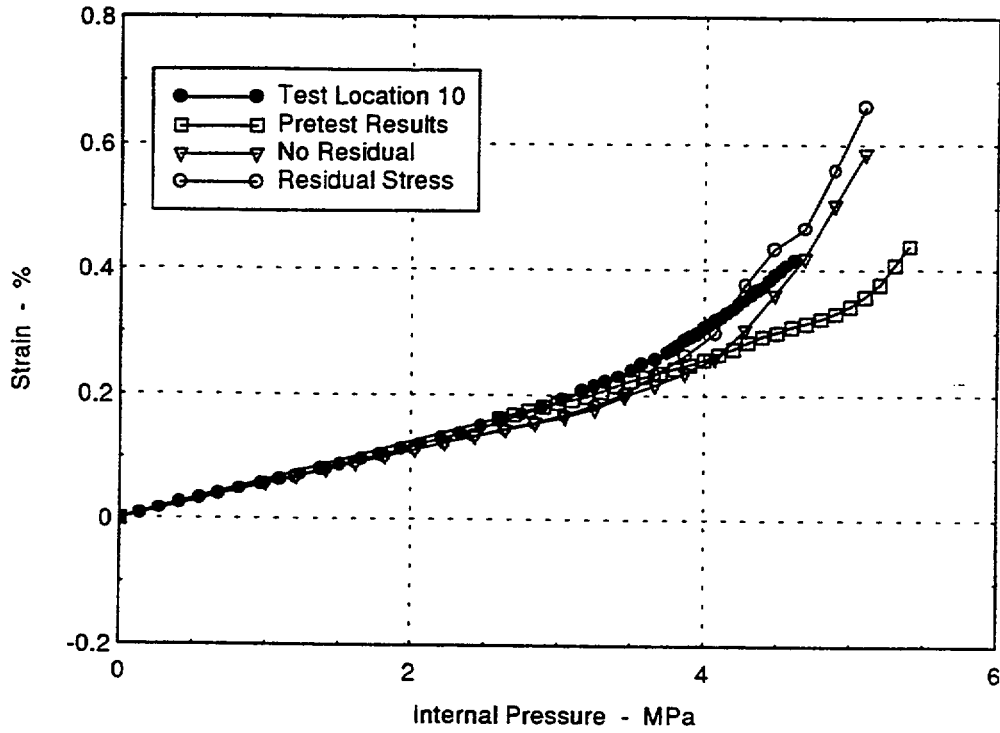


Figure 5. Standard Output Location #10, Interior Meridional Strain in Top Head (Top 270°, 0.48m)

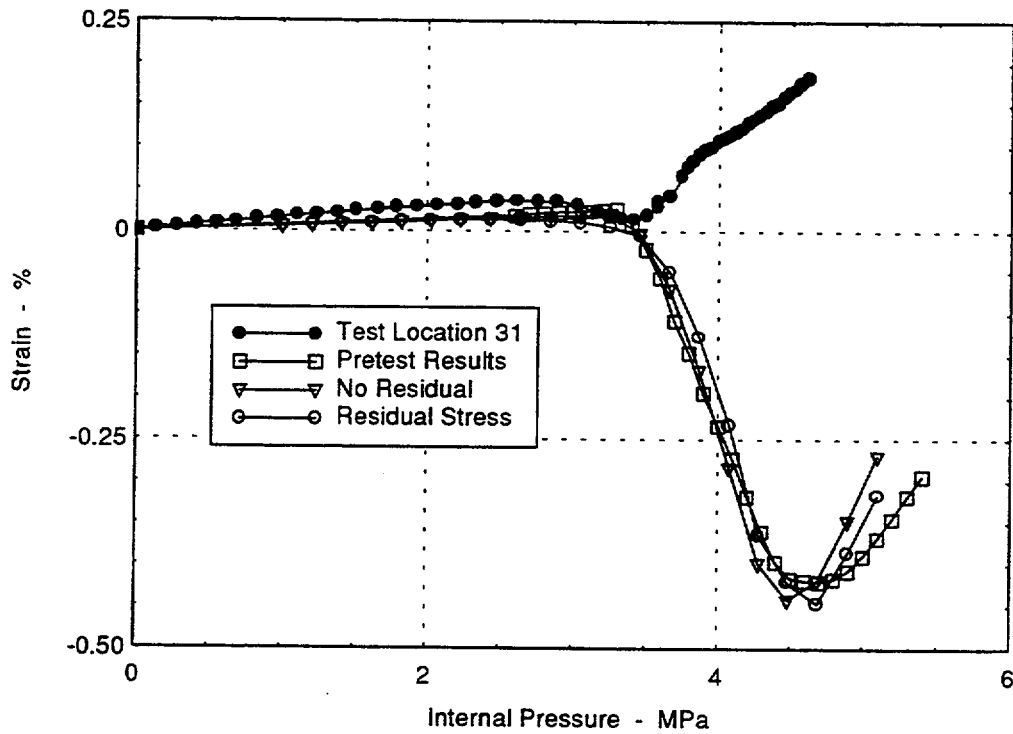


Figure 6. Standard Output Location #31, Interior Meridional Strain in Upper Conical Shell (Global 270°, 2.49m)

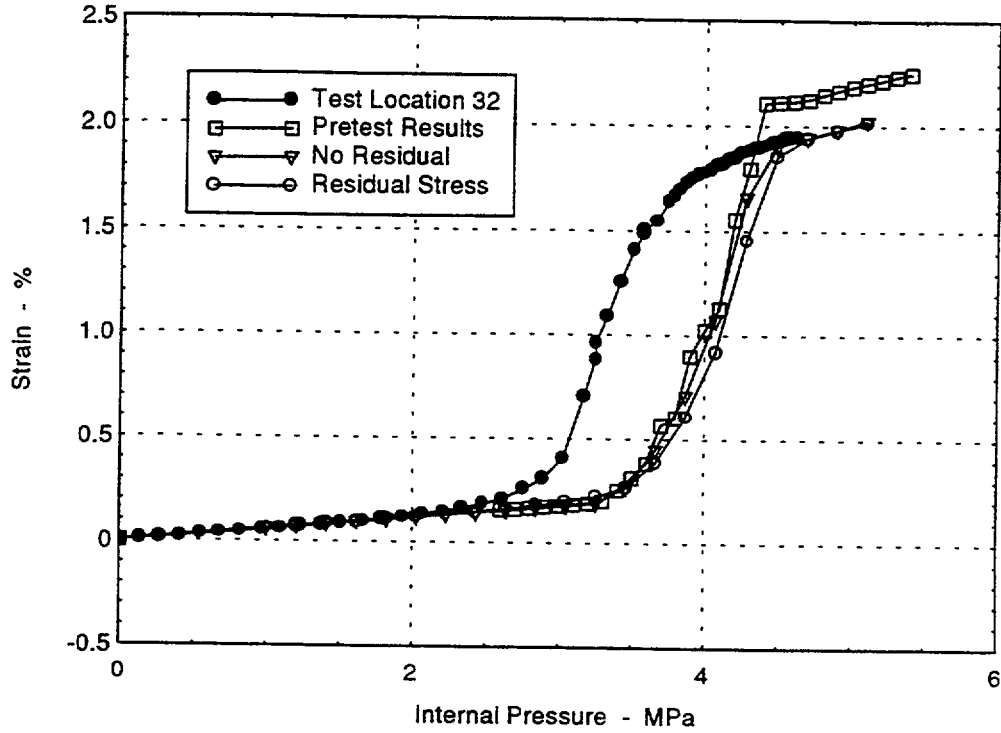


Figure 7. Standard Output Location #32, Interior Hoop Strain in Upper Conical Shell (Global 270°, 2.49m)

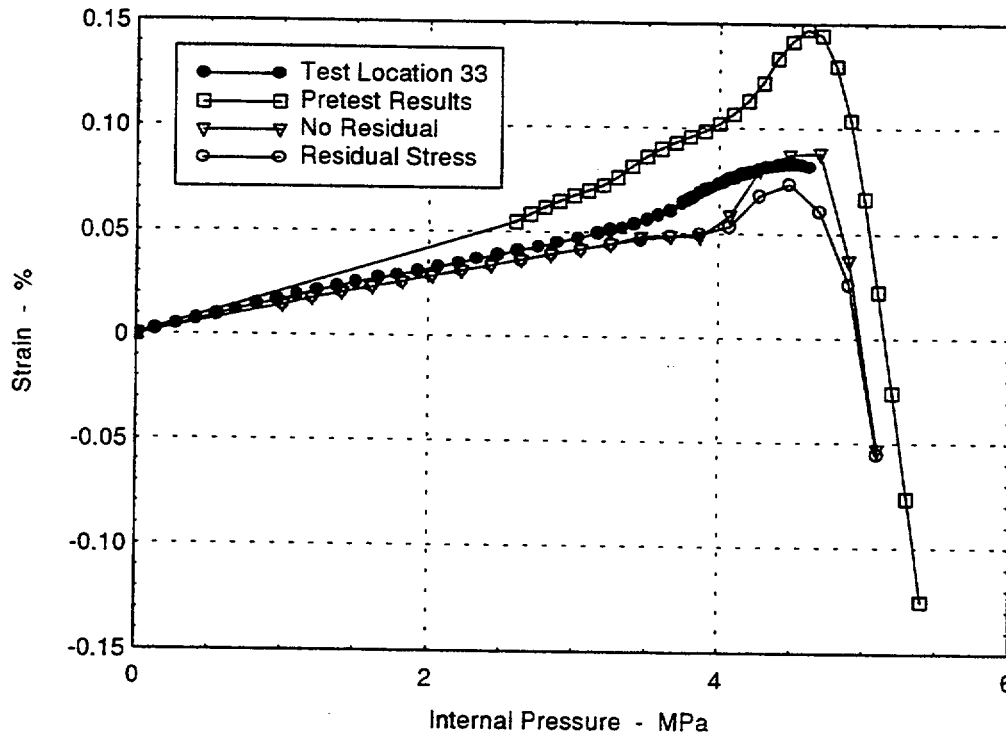


Figure 8. Standard Output Location #33, Interior Meridional Strain in Lower Conical Shell (Global 270°, 1.25m)

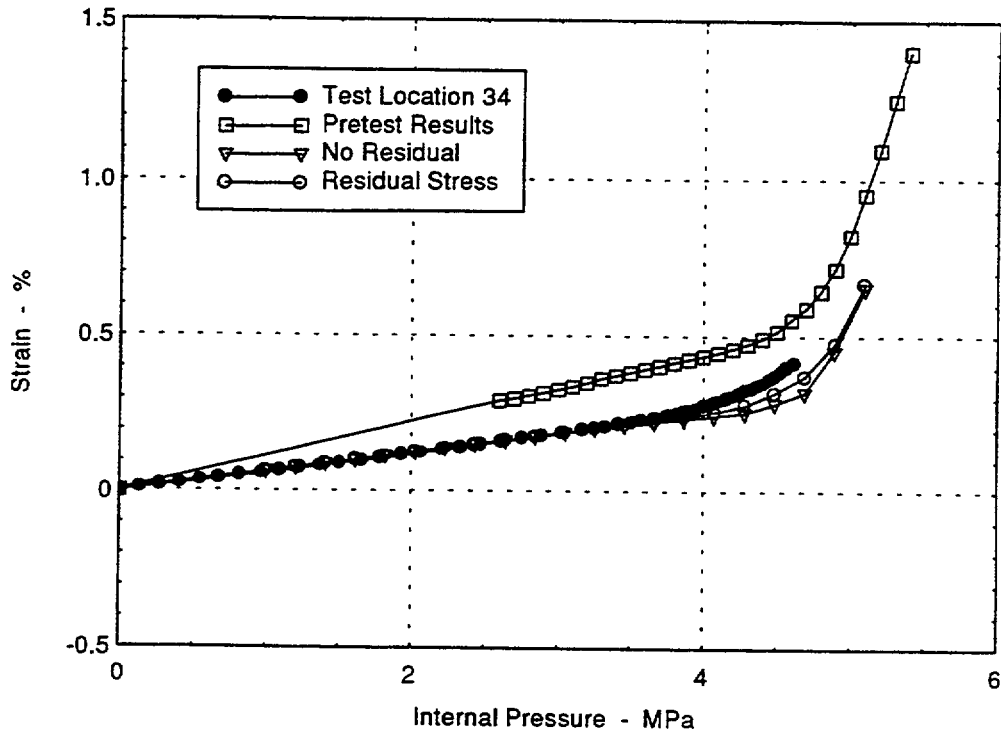


Figure 9. Standard Output Location #34, Interior Hoop Strain in Lower Conical Shell (Global 270°, 1.25m)

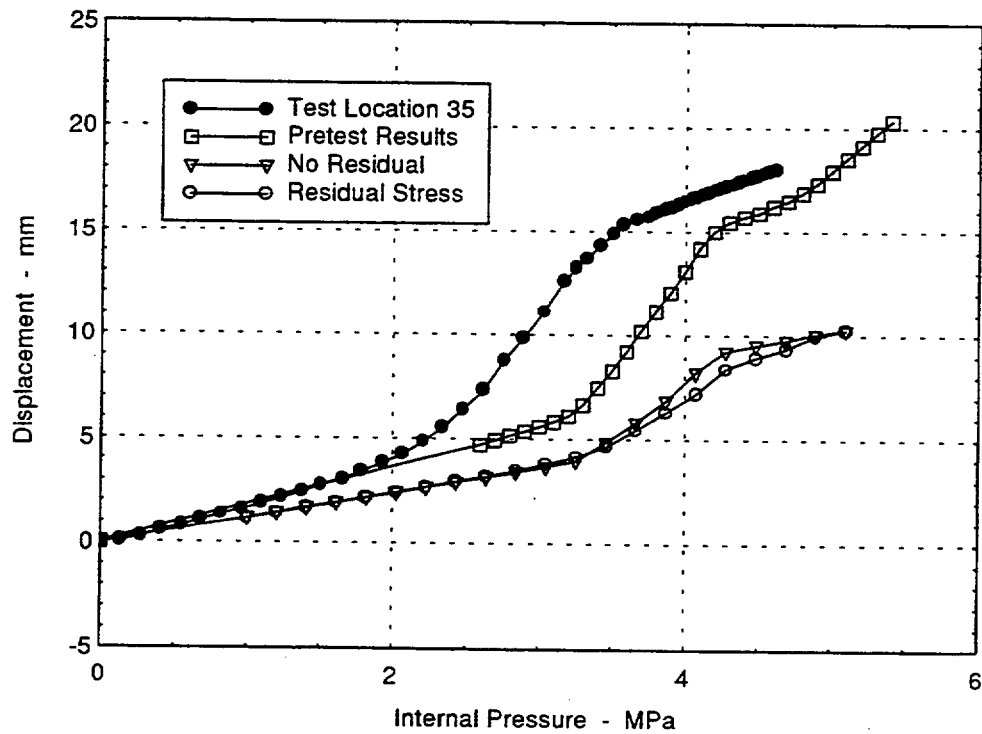


Figure 10. Standard Output Location #35, Vertical Displacement of Top Head (Top 0°, 0.00m)

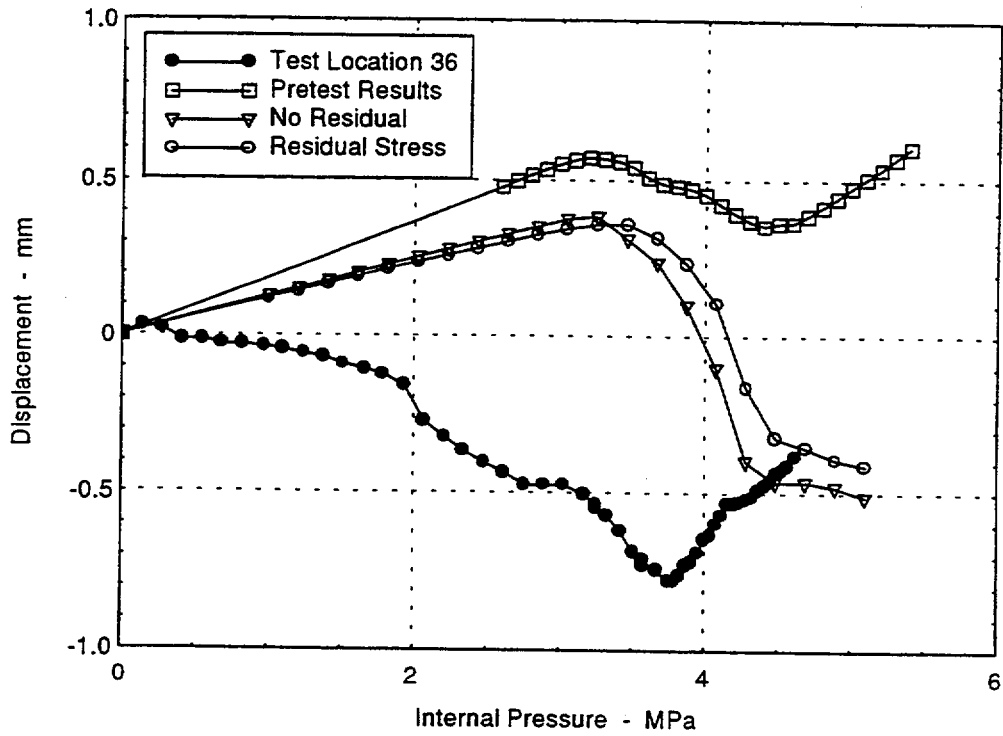


Figure 11. Standard Output Location #36, Inside Horizontal Displacement of Upper Conical Shell (Global 45° , 3.57m)

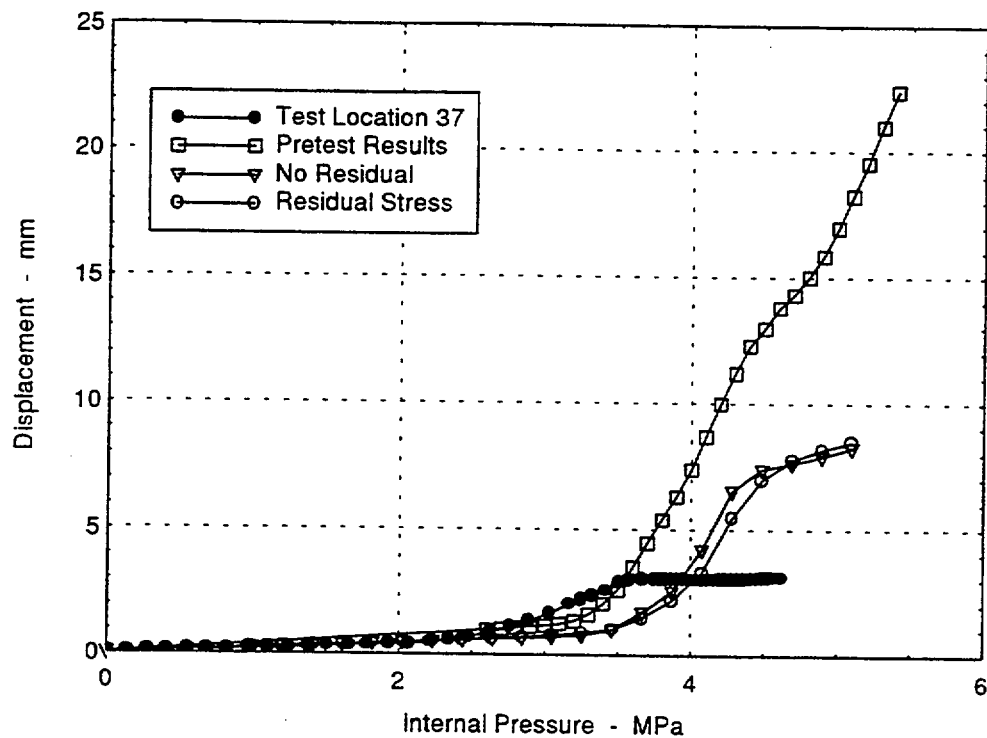


Figure 12. Standard Output Location #37, Inside Horizontal Displacement of Spherical Shell (Global 0° , 3.32m)

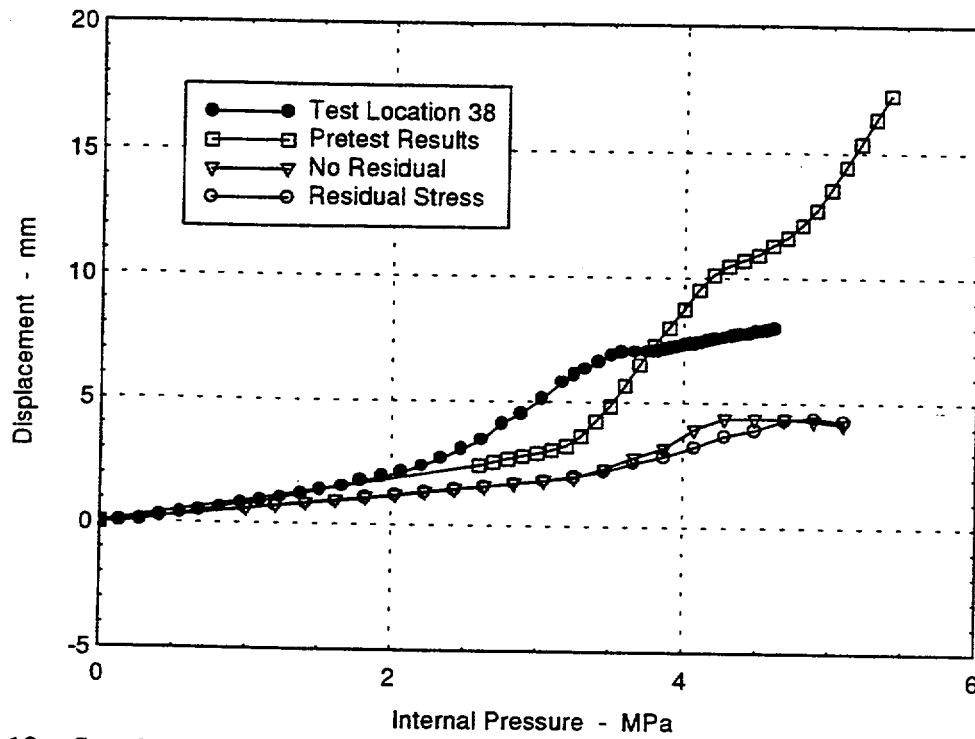


Figure 13. Standard Output Location #38, Inside Vertical Displacement of Spherical Shell (Global 0°, 3.32m)

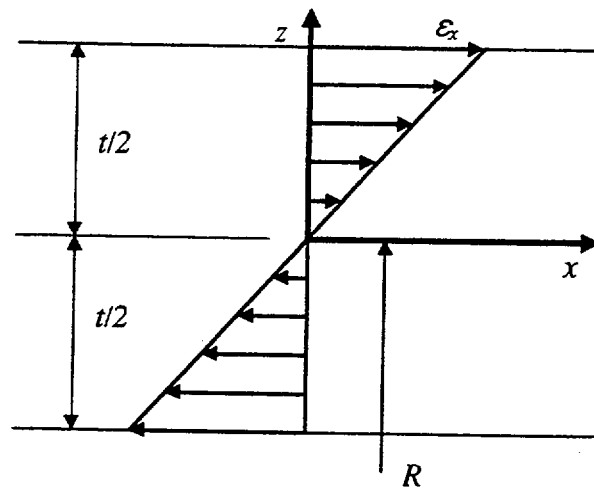


Figure 14. Strain Distribution Through the Wall of a Bent Plate

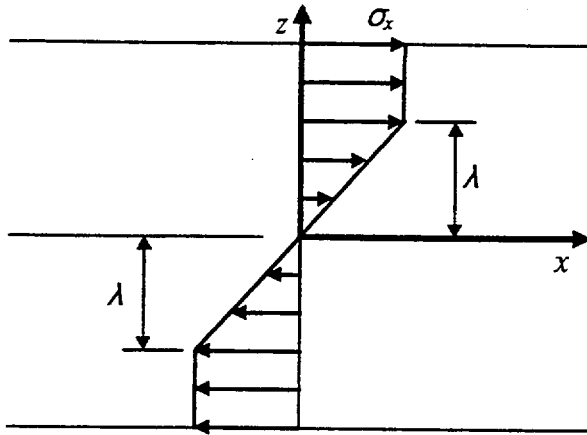


Figure 15. Stress Distribution Through the Wall of a Bent Plate

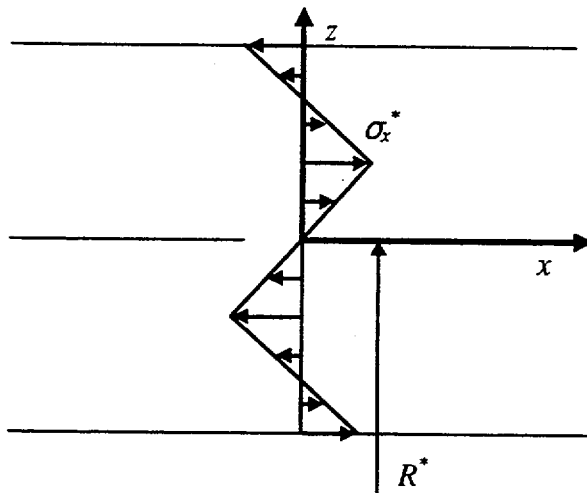


Figure 16. Residual Stresses Through the Wall of a Bent Plate

Appendix B-3

Bhabha Atomic Research Centre (BARC)

India

Post - Test Analysis Results for the High Pressure Test on Steel Containment Vessel and Contact Structure Assembly Model

***Suresh Krishnan, Vivek Bhasin, K.K.Vaze, H.S.Kushwaha
Reactor Safety Division
Bhabha Atomic Research Centre,INDIA***

1.0 Introduction

This report summarizes the post-test structural analyses results of the scale model of the Steel Containment Vessel (SCV) and Contact Structure (CS) assembly tested at Sandia National Laboratories (SNL) , USA. In our pre-test efforts, we had submitted results from a global axisymmetric model of the SCV and CS assembly. The equipment hatch was not modeled. However, during the test , a local tear appeared in the SCV near the equipment hatch opening at a pressure of about 4.66 Mpa and the test had to be stopped. This behavior has now been studied by a local shell model of the equipment hatch region with displacement driven boundary conditions derived from the global axisymmetric model.

In our pre-test analysis we had considered a co-efficient of friction of 0.75 which was very much different from those used by other analysts. Also not considered in our pre-test analysis were the changes in some of the standard output locations from those specified earlier. As a part of our post-test efforts, we have therefore repeated our global axisymmetric analysis by considering a co-efficient of friction of 0.25 between the SCV and CS and taking the new positions of the Standard Output Locations (SOL).

2.0 Global axisymmetric Analysis

2.1) Finite Element Model

The SCV and CS have been modeled using a 8 noded axisymmetric solid elements with reduced integration option (CAX8R). The gap between the SCV and CS is as per the design drawings [1]. Gap monitoring and post contact behavior is modeled using 3-noded axisymmetric interface contact elements designated as ISL22A in ABAQUS. The stiffeners and the top flange have also been modeled by CAX8R elements. The base of the model is the top flange of the ring support girder. The model is fixed at the base. All sections of SCV and the corresponding thickness changes at interfaces have been modeled (Figure 1).

The global axisymmetric analysis performed now differs from our pretest analysis in two ways

- a) Co-efficient of friction (μ) used to characterize the sliding friction between the SCV and CS is taken as 0.25 in this post-test analysis.

b) The changes in the locations of all Standard Output Locations (SOL) have been considered.

2.2) Use of NUPEC Tensile Test Data

The material properties used for the post-test global axisymmetric analyses are same as those used in our pre-test analyses. One representative true stress-true strain curve has been used in this analysis for each of the two materials. For the material SGV 480, the data for specimen R1 (6 mm thick) as given in table 6 of the design specification [1] has been used. For material SPV 490, the data for specimen R21 (9 mm thick) as given in table 14 of design specification [1] has been used. The E value considered for both the materials is 216,700 MPA and Poisson's ratio considered is 0.3 for both the materials.

2.3 Analytical Models

Both material and geometric nonlinearities have been considered. Von mises isotropic yield criteria is used. A large strain, large displacement, updated lagrangian formulation has been used to account for the geometric nonlinearities. The applied load adapts itself to shape changes in the structure as the analysis progresses. The same features were considered in our pre-test global axisymmetric analysis also.

2.4 Analysis procedure and Results

The SCV/CS assembly model is subjected to increasing internal pressure. The analysis is done by increasing the load in steps. The maximum load step was 0.5 MPa and the minimum was 0.0005 MPa. The convergence in each step was set in terms of ratio of residual force to the average force (=5.0 E-3) and the ratio of displacement correction to the incremental displacement of that load step (=1.0 E-2).

Analysis results have been presented upto a pressure of 4.67 MPa, since test was stopped at that pressure. Results of deflection v/s. pressure and strain v/s. pressure have been given at each Standard Output Location (SOL)(Figure 11 to Figure 43). In this analysis we have taken the changed positions of the standard output locations into account. Our results at SOL's 8,9 and 10 have changed considerably. In our pretest report we had given results at position (270,0.36). In this report the results at these SOL's are for the position (270,0.48).

3.0) Local Shell Model Near Equipment Hatch

3.1) Finite Element Model

To investigate the local tearing of the SCV near the equipment hatch a local shell model of the SCV was employed. This model is shown in Figure 2. Four noded shell elements with reduced integration option having 5 degrees of freedom per node (S4R5 elements) have been used in this analysis. The model has 600 S4R5 elements. For this model, all nodes on the boundary of the model have displacement driven boundary conditions derived from the global axisymmetric analysis. Symmetry Boundary conditions are applied along the edge of the model falling on the x-y plane. ABAQUS version 5.3 has been used for this analysis. This version of ABAQUS requires the user to explicitly input contact elements. Since upto a pressure of 4.66 MPA contact is not likely to affect the results significantly, it was decided not to model the contact structure in the local shell model.

3.2 Use of NUPEC Tensile Stress-Strain data

The same data as used for the global axisymmetric analysis and as described in section 2.2 of this report has been used.

3.3 Analytical Models

Same as described in section 2.3 of this report.

3.4 Analytical Procedure

Same as described in section 2.4 of this report.

3.5 Results

The finite element analysis on the local equipment hatch shell model could not proceed beyond a pressure of 4.97 MPa. At this pressure the strain at the junction of the equipment hatch reinforcement plate and the 9 mm thick Lower Conical Section (LCS) plate material had reached a strain of about 10%, which is the ultimate strain for this material (Fig.3).

In an elastic-plastic analysis, failure is said to have occurred when the effective plastic strain reaches the ultimate strain of the material. We have to take into account the effect of multiaxial stress state from uniaxial stress-strain data. Under a multiaxial stress state, we can define the equivalent uniaxial strain as

$$\epsilon_u = \epsilon_{eff} / c$$

$$c = \text{ductility ratio} = 2 \quad (1-1F)$$

TF_D = Davis Triaxiality Factor

$$= \frac{\sigma_1 + \sigma_2 + \sigma_3}{[1/2 \{(\sigma_1 - \sigma_2)^2 + (\sigma_2 - \sigma_3)^2 + (\sigma_3 - \sigma_1)^2\}]^{0.5}}$$

The value of TF_D under uniaxial stress state is 1.0 and c is 1.0. For a biaxial stress state the value of TF_D is 2.0 and is 0.5. Thus under a biaxial stress state the value of failure strain is $0.5 * 10 = 5\%$. This reduces the failure pressure from 4.97 Mpa to 4.0 Mpa (Figure 4). In this analysis , the stress state at the point of maximum equivalent plastic strain near the equipment hatch is such that the TF_D is 1.611 and c is 0.65. The failure strain is $0.65 * 10\% = 6.5\%$. This reduced failure pressure is now 4.2 MPa.

Plots of output at SOL 1 through 6 (Figure 5 to Figure 10), SOL 39 through 43 (Figure 44 to Figure 48) are additional results from the post-test analysis. In our pre-test report we had not provided results for these locations since the equipment hatch was not modelled.

4.0 Concluding Remarks

The local shell analysis of the equipment hatch region confirms a local tear in the 9 mm thick plate of the SCV at the junction of the equipment hatch reinforcement plate. In the finite element analysis uniaxial stress -strain curve was used. The analysis could not proceed beyond a pressure of 4.97 MPa, because at this pressure, the value of the equivalent strain at the junction of equipment hatch reinforcement plate and the lower conical shell section had reached the ultimate strain (10%) of the SPV 490 material .

If we consider the reduced ductility due to multiaxial stress state by the Davis triaxiality factor, the failure pressure reduced to 4.2 MPa.

The equivalent plastic strain in the SCV model just below the middle circumferential stiffener was about 2.8% at a pressure of 4.9 MPa. This is much below the ultimate pressure of the material SGV 480. So the tear formed in the model at this location could not be explained by our analysis.

5.0 References

- 1) Steel Containment Vessel Design Package (July 10 1995) and supplement No.1 of Steel Containment Design Package (September 21,1995), Sandia National Laboratories, USA.
- 2) Letter No. SO-95-099 (dated December 1,1995) " As measured data of SCV and CS", Sandia National Laboratories, USA

3) ' Round Robin Pretest Analyses of a Steel Containment Vessel Model and Contact Structure Assembly Subject to Static Internal Pressurisation ', Report R-SN-G-003, Revision A, Sandia National Laboratories, USA, 1996.

4) ' SCV High Pressure Test Data for Round Robin Analysis ', Report R-SN-S-007, Rev. A, Sandia National Laboratories, USA, 1997

5) ' Post Test Metallurgical Evaluation Results for SCV High Pressure Test ', Report R-SN-S-009, Rev. B, Sandia National Laboratories, USA.

ABAQUS

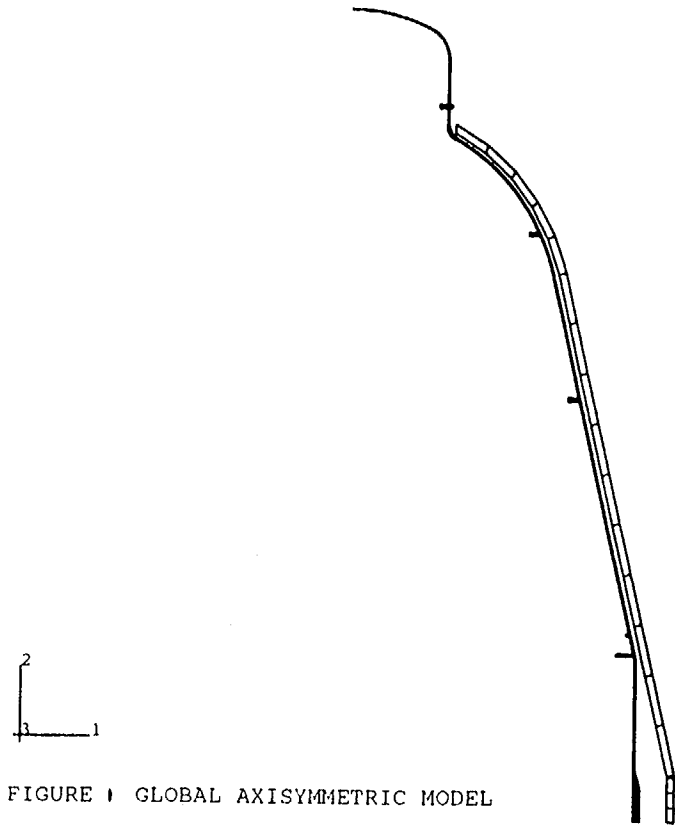


FIGURE 1 GLOBAL AXISYMMETRIC MODEL

ABAQUS

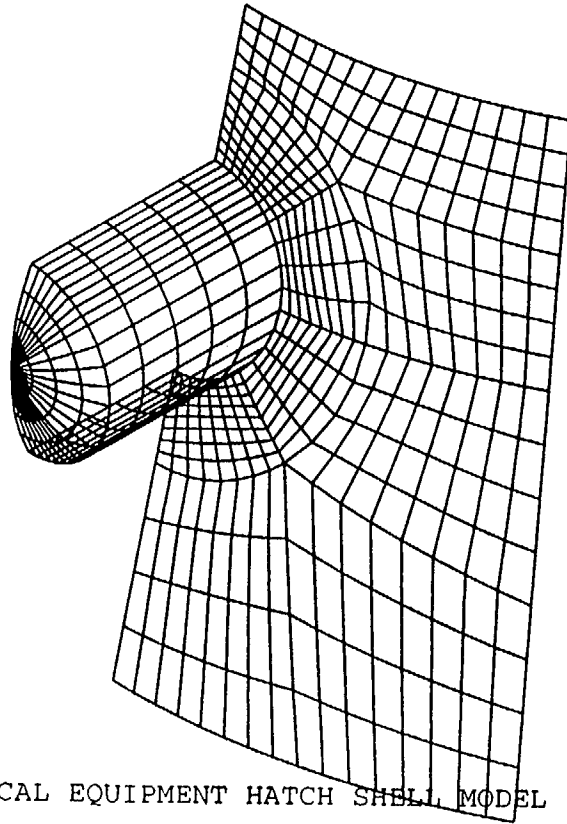


FIGURE 2 LOCAL EQUIPMENT HATCH SHELL MODEL

ABAQUS

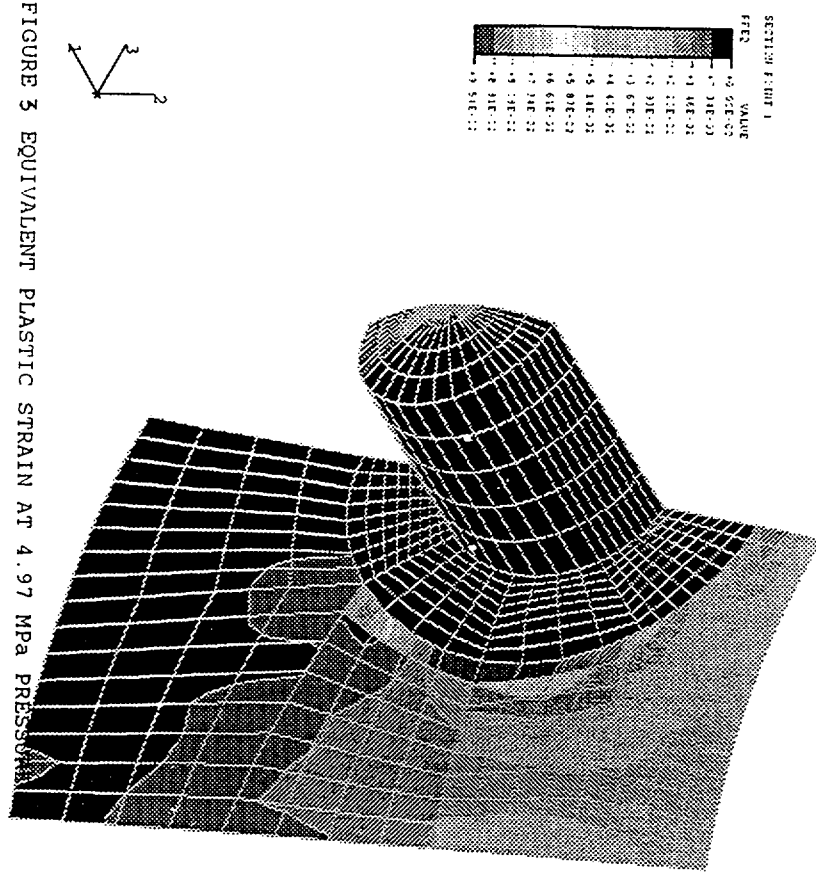


FIGURE 3 EQUIVALENT PLASTIC STRAIN AT 4.97 MPa PRESSURE

BARC (INDIA)
Post-Test Analysis
Location of Maximum Equivalent Plastic Strain

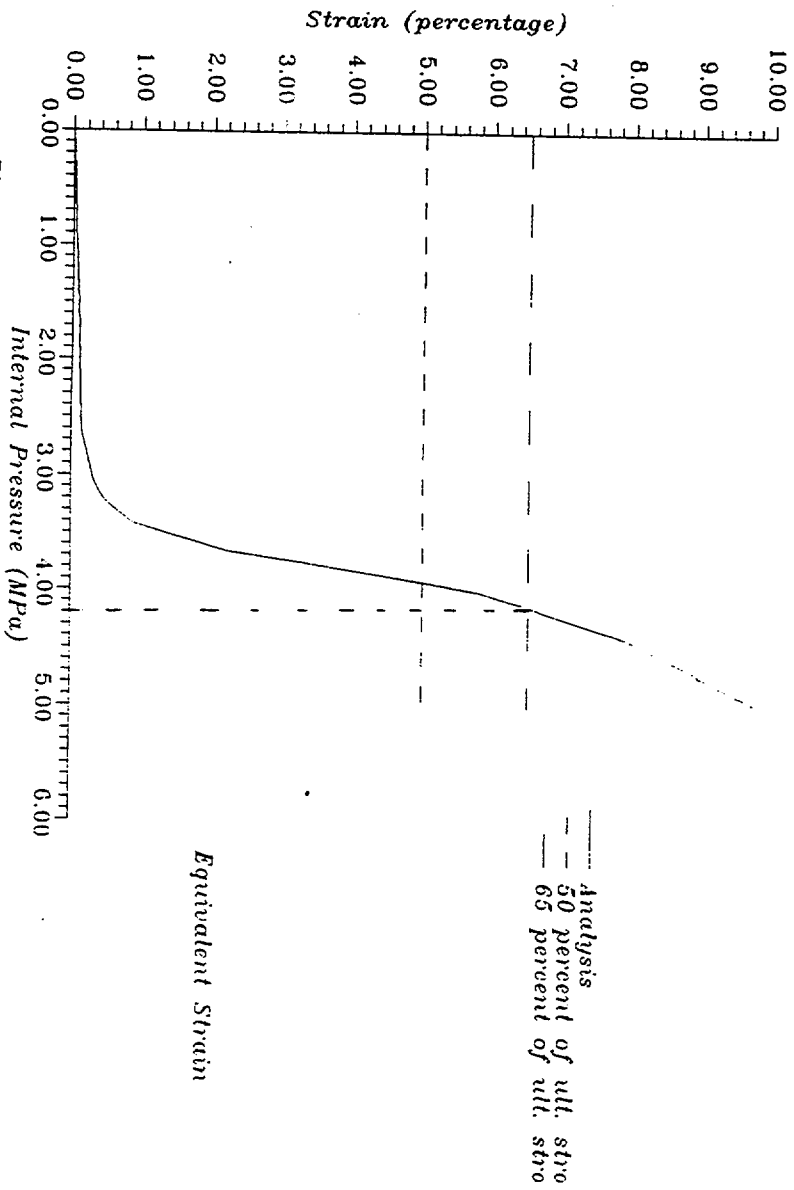


Figure 4 Local Shell Model Near Equipment Hatch

BARC (INDIA)
Post-Test Analysis
Standard Output Location 1

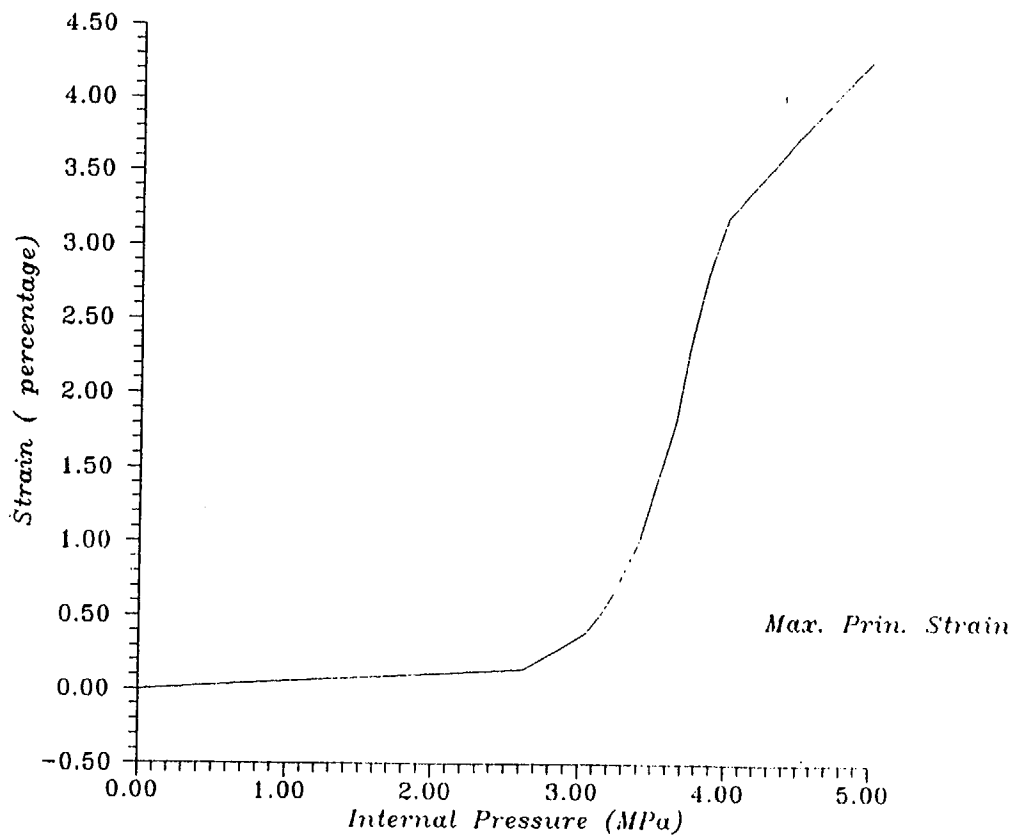


Figure 5 Local Shell Model Near Equipment Hatch

BARC (INDIA)
Post-Test Analysis
Standard Output Location 2

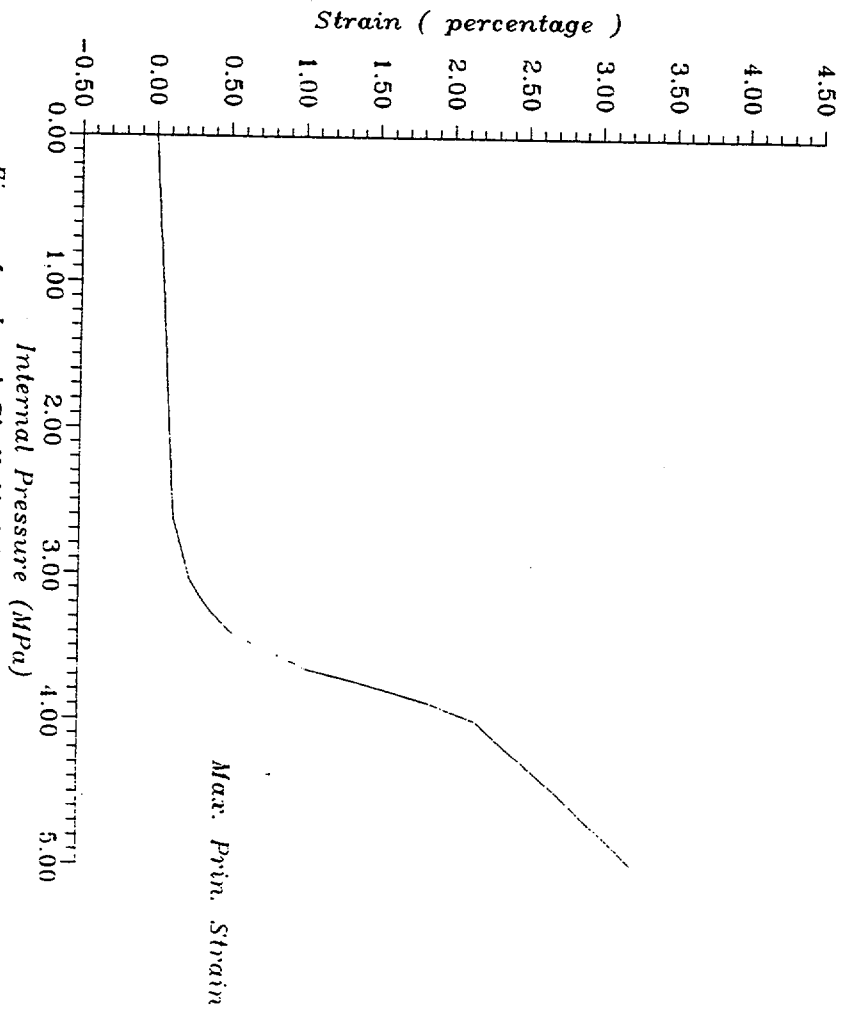


Figure 6 Local Shell Model Near Equipment Hatch

BARC (INDIA)
Post-Test Analysis

Standard Output Location 3

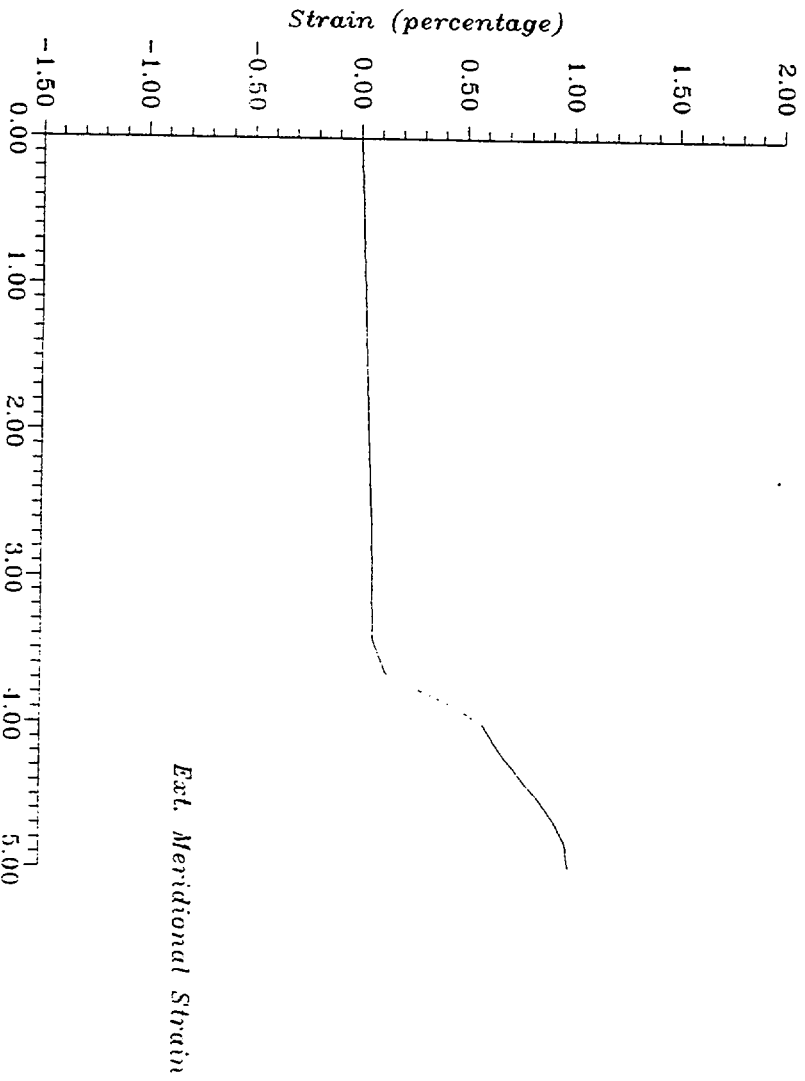


Figure 7 Local Shell Model Near Equipment Hatch

BARC (INDIA)
Post-Test Analysis
Standard Output Location 4

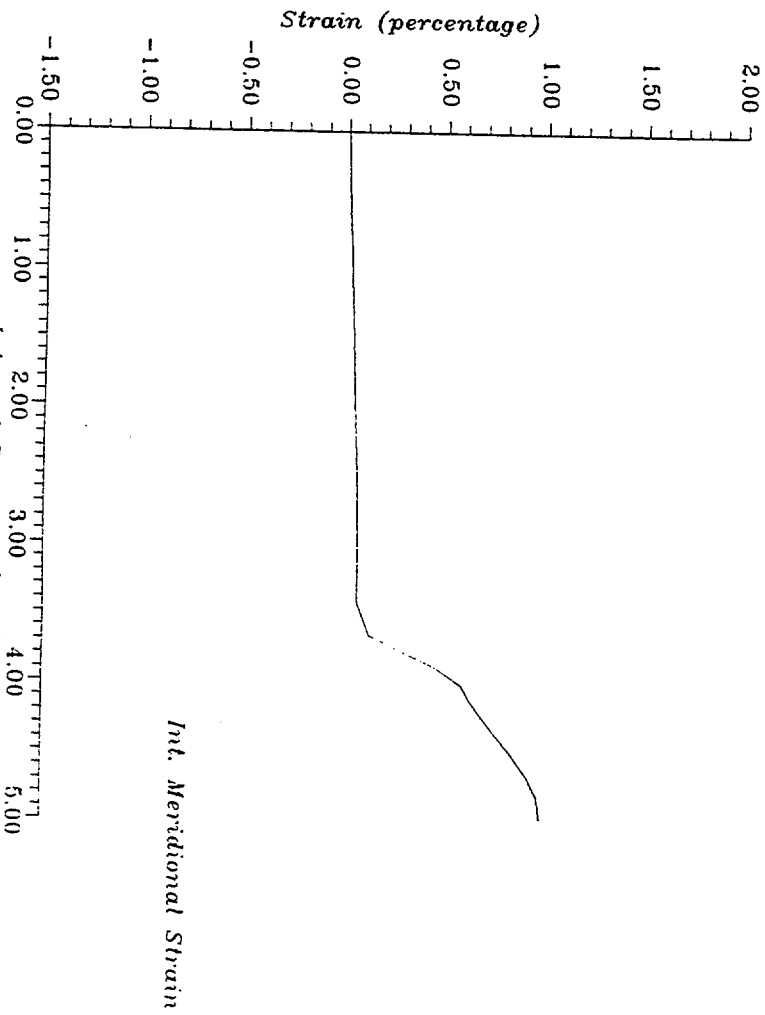


Figure 8 Local Shell Model Near Equipment Hatch

BARC (INDIA)
Post-Test Analysis
Standard Output Location 5

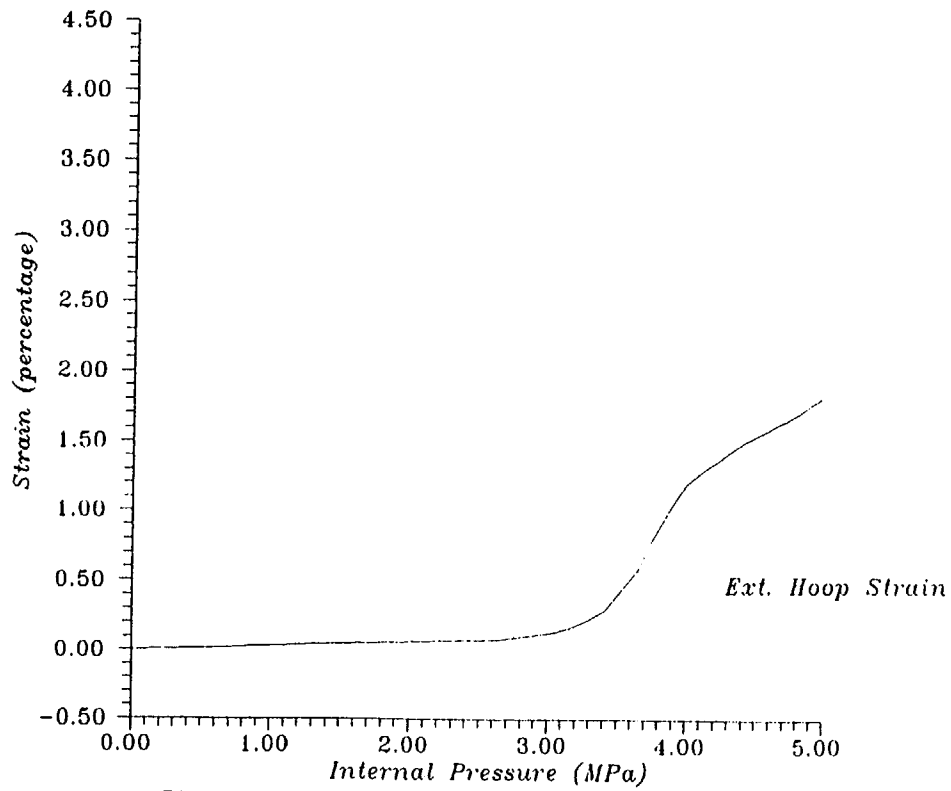


Figure 9 Local Shell Model Near Equipment Hatch

BARC (INDIA)
Post-Test Analysis
Standard Output Location 6

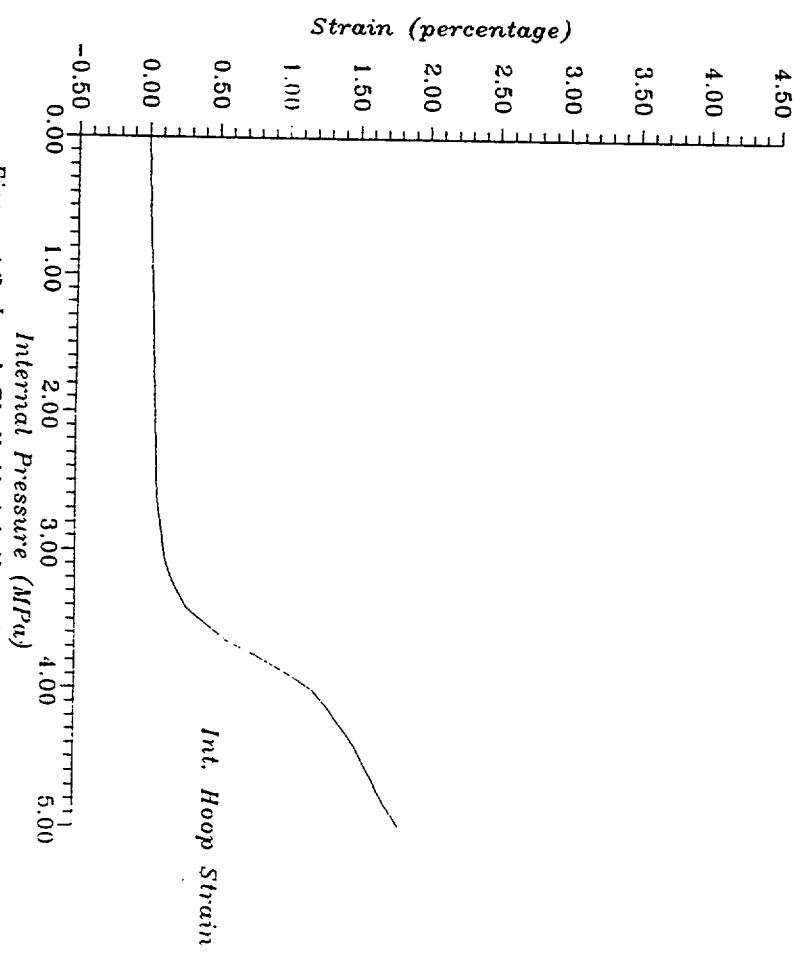


Figure 10 Local Shell Model Near Equipment Hatch

BARC (INDIA)
Post-Test Analysis
Standard Output Location 7

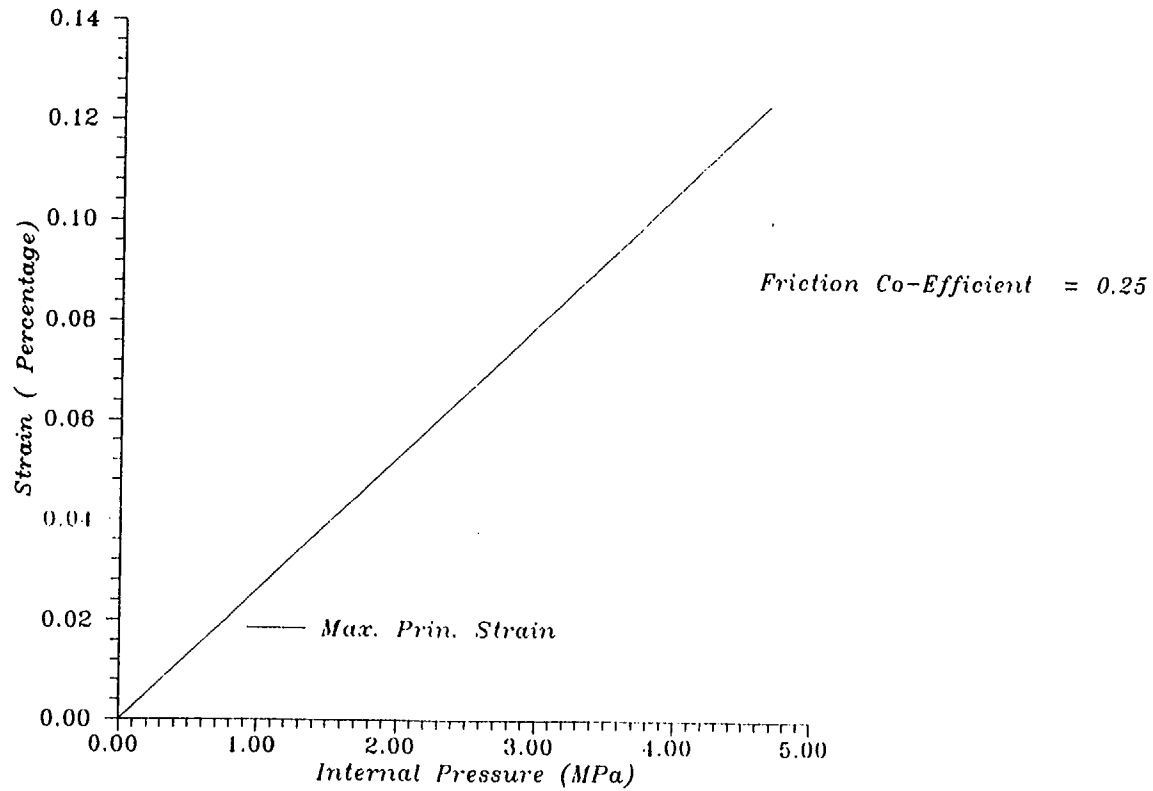


Figure 11 Global axisymmetric Model

BARC (INDIA)
Post-Test Analysis
Standard Output Location 8

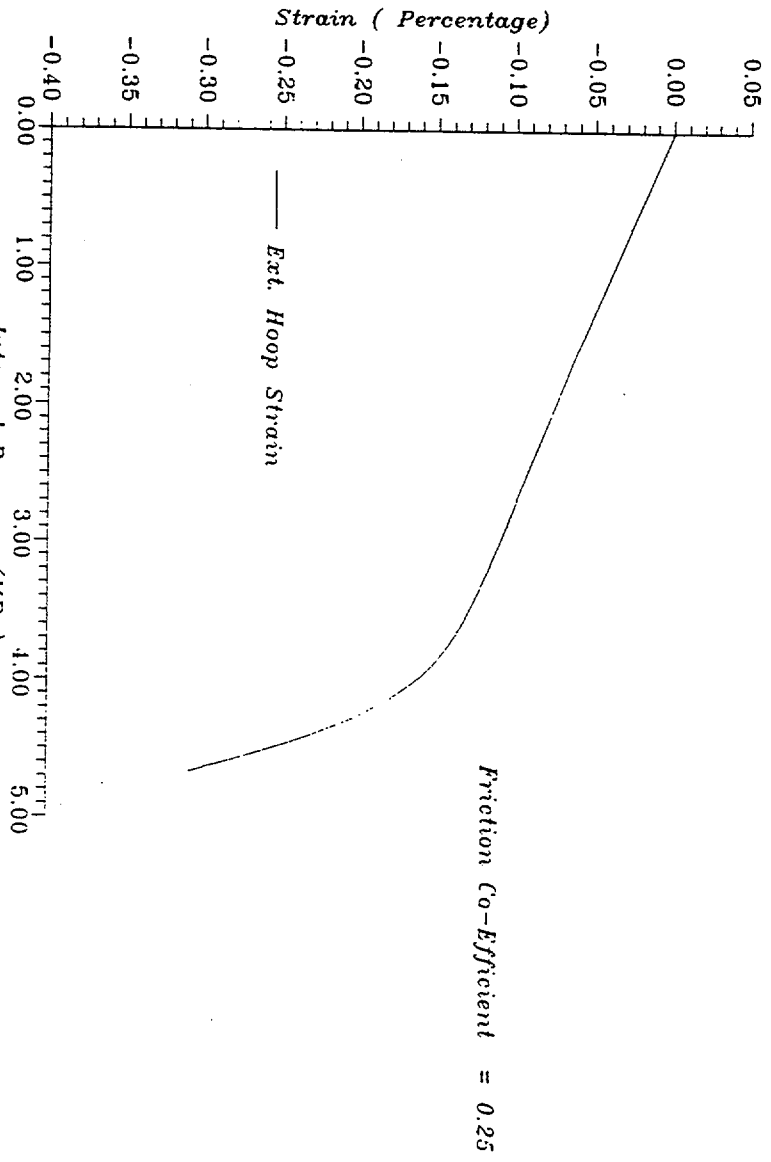


Figure 12 Global axisymmetric Model

BARC (INDIA)
Post-Test Analysis
Standard Output Location 9

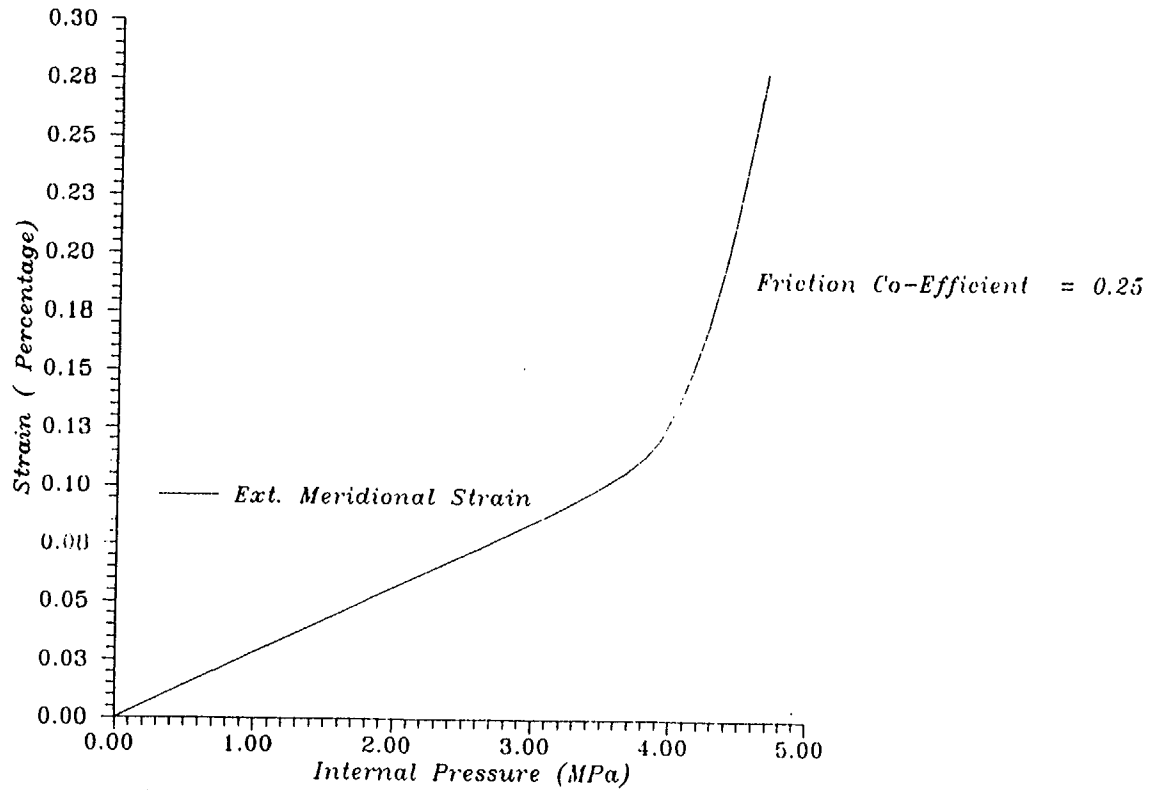


Figure 15 Global axisymmetric Model

BARC (INDIA)
Post-Test Analysis
Standard Output Location 10

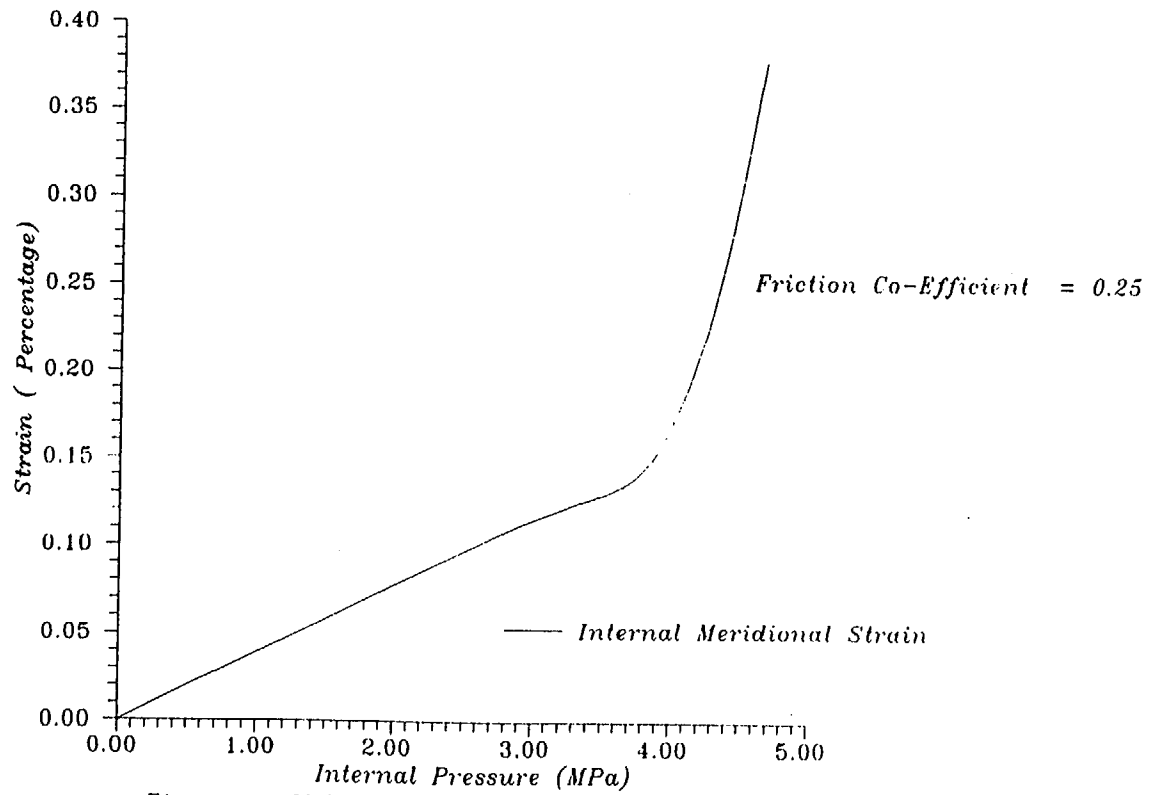
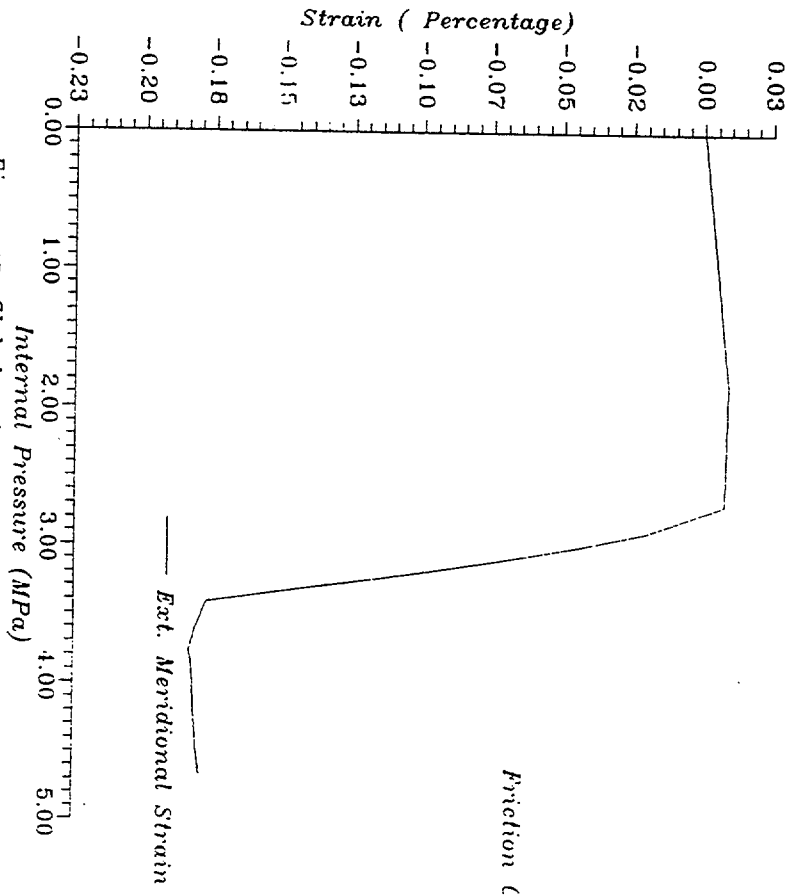


Figure 14 Global axisymmetric Model

BARC (INDIA)
Post-Test Analysis
Standard Output Location 11



Friction Co-Efficient = 0.25

Figure 15 Global axisymmetric Model

BARC (INDIA)
Post-Test Analysis
Standard Output Location 12

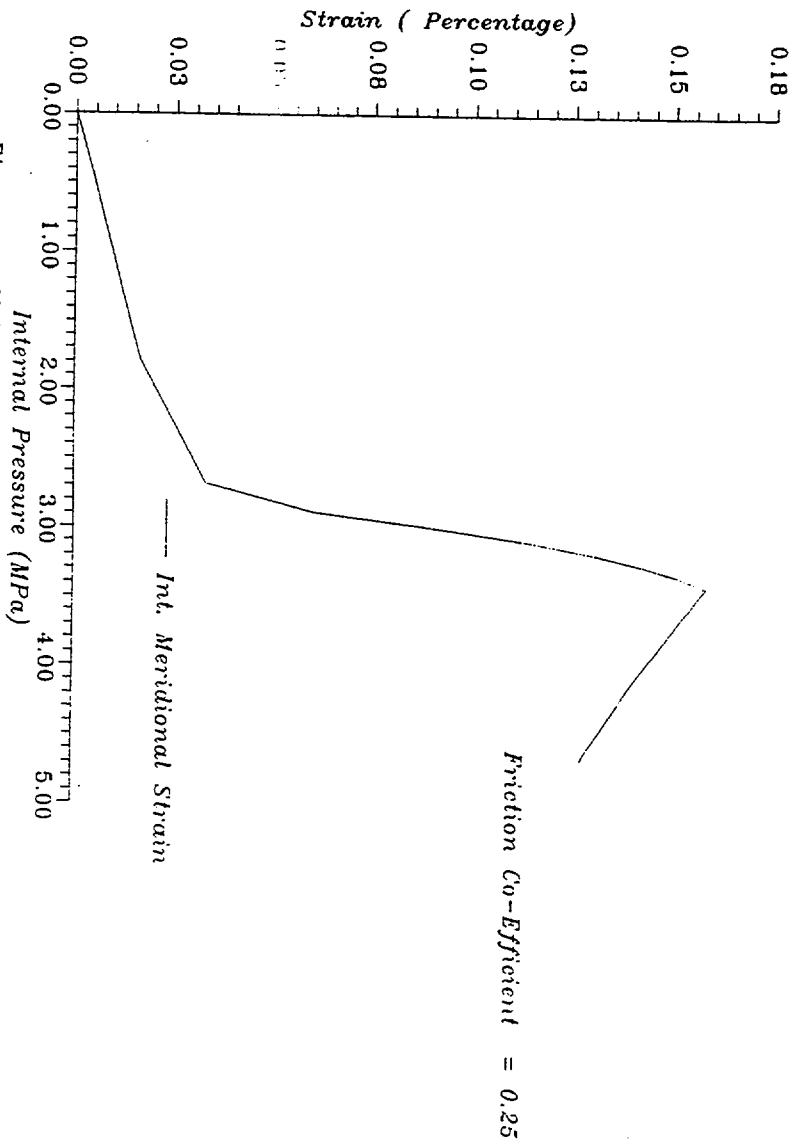


Figure 16 Global axisymmetric Model

BARC (INDIA)
 Post-Test Analysis
 Standard Output Location 13

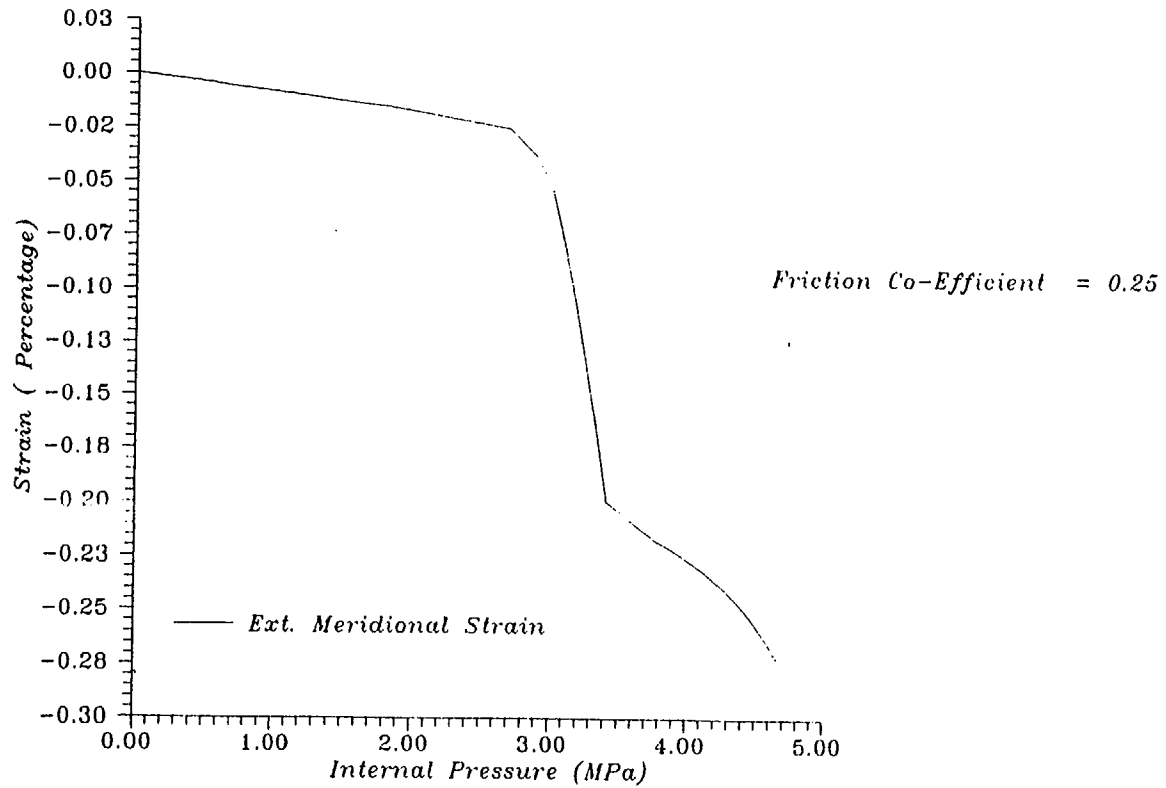


Figure 17 Global axisymmetric Model

BARC (INDIA)
Post-Test Analysis
Standard Output Location 14

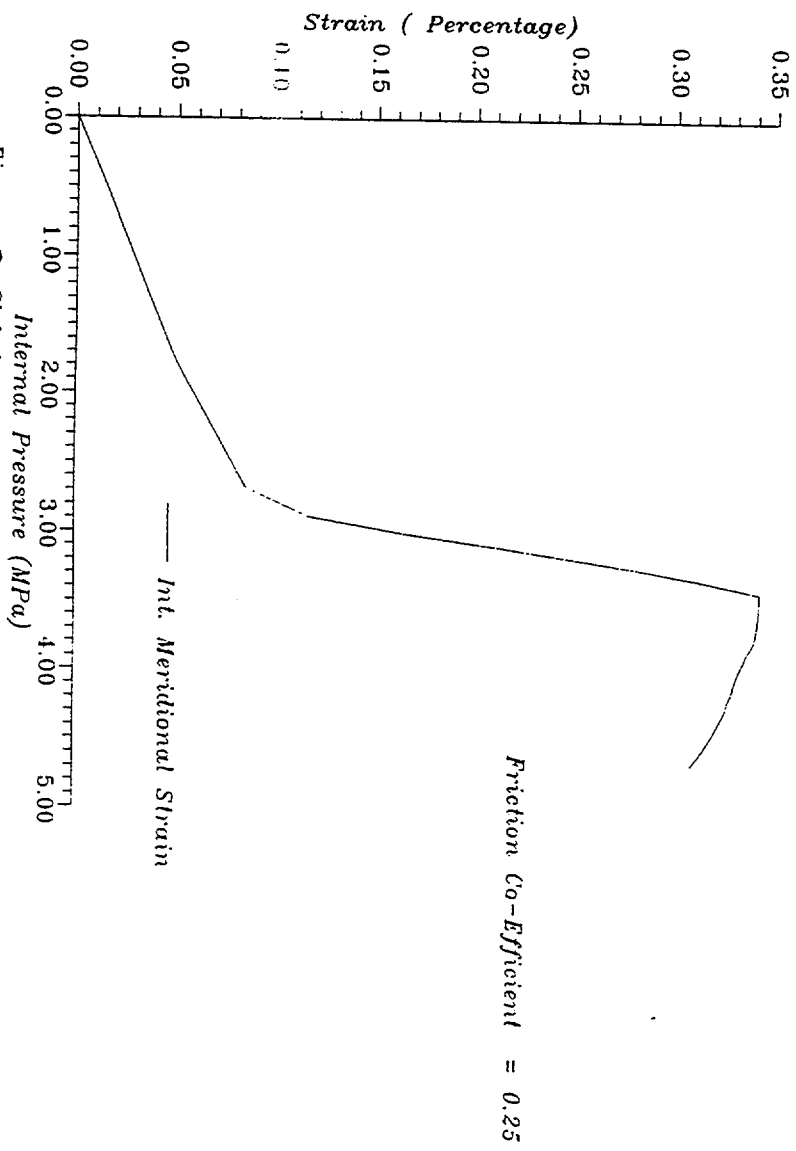


Figure 18 Global axisymmetric Model

BARC (INDIA)
Post-Test Analysis
Standard Output Location 15

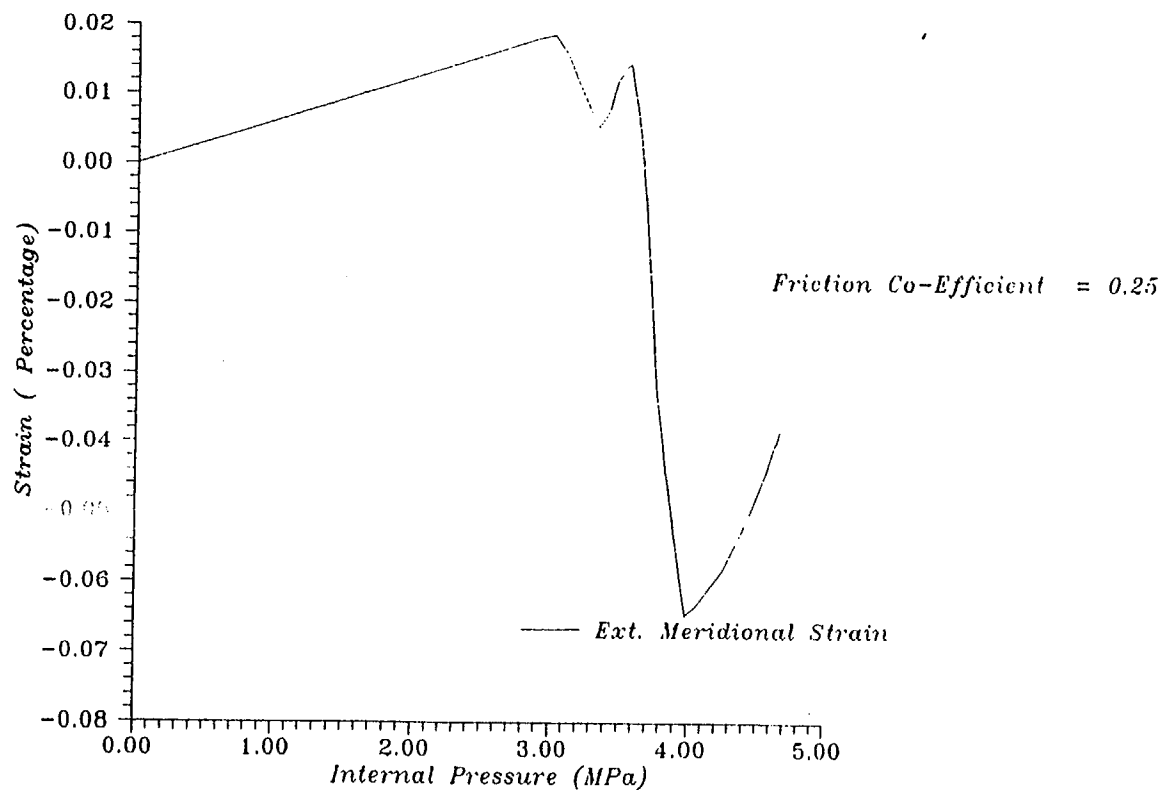


Figure 19 Global axisymmetric Model

BARC (INDIA)
Post-Test Analysis
Standard Output Location 16

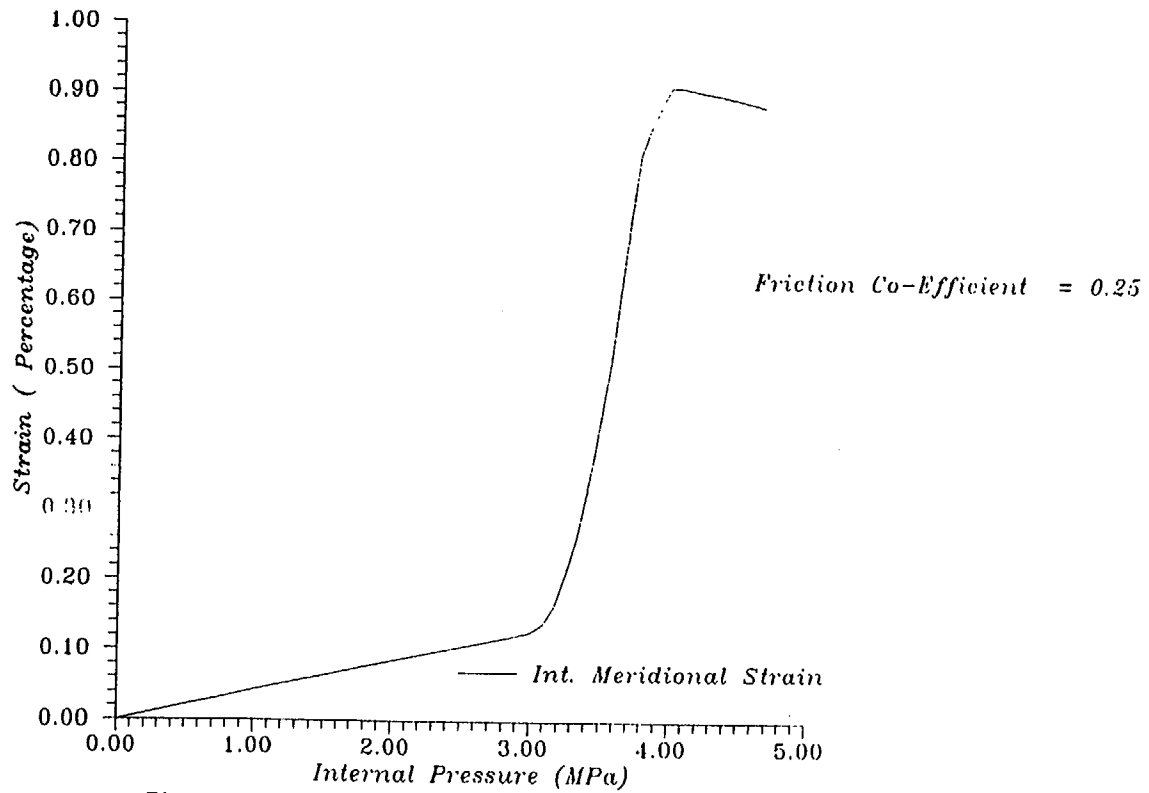


Figure 20 Global axisymmetric Model

BARC (INDIA)
 Post-Test Analysis
 Standard Output Location 17

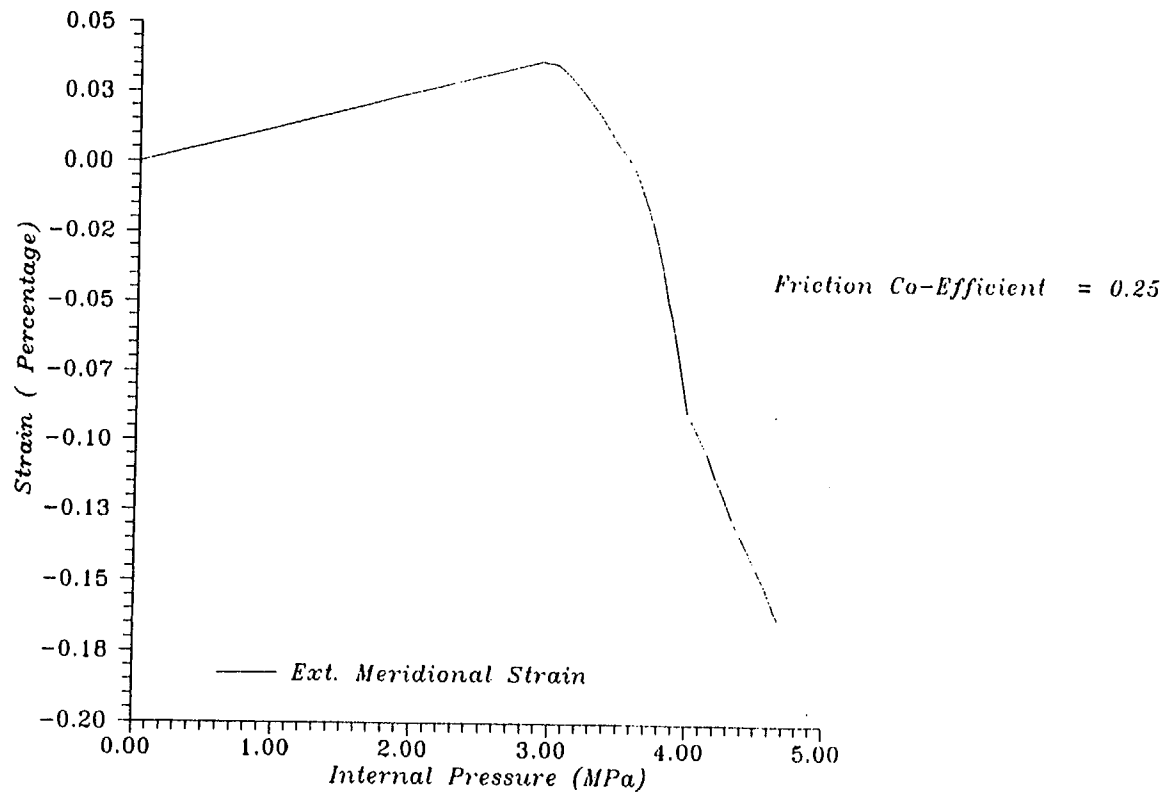


Figure 21 Global axisymmetric Model

BARC (INDIA)
Post-Test Analysis
Standard Output Location 18

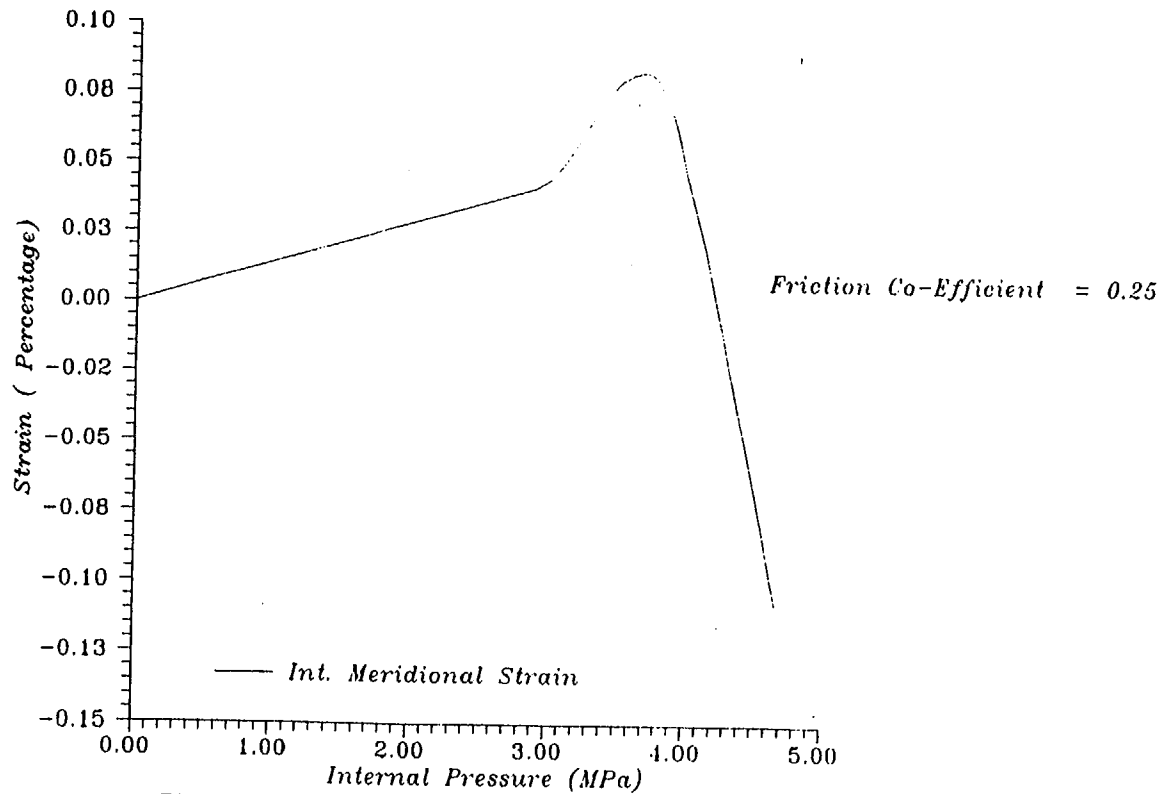


Figure 2.2 Global axisymmetric Model

BARC (INDIA)
Post-Test Analysis
Standard Output Location 19

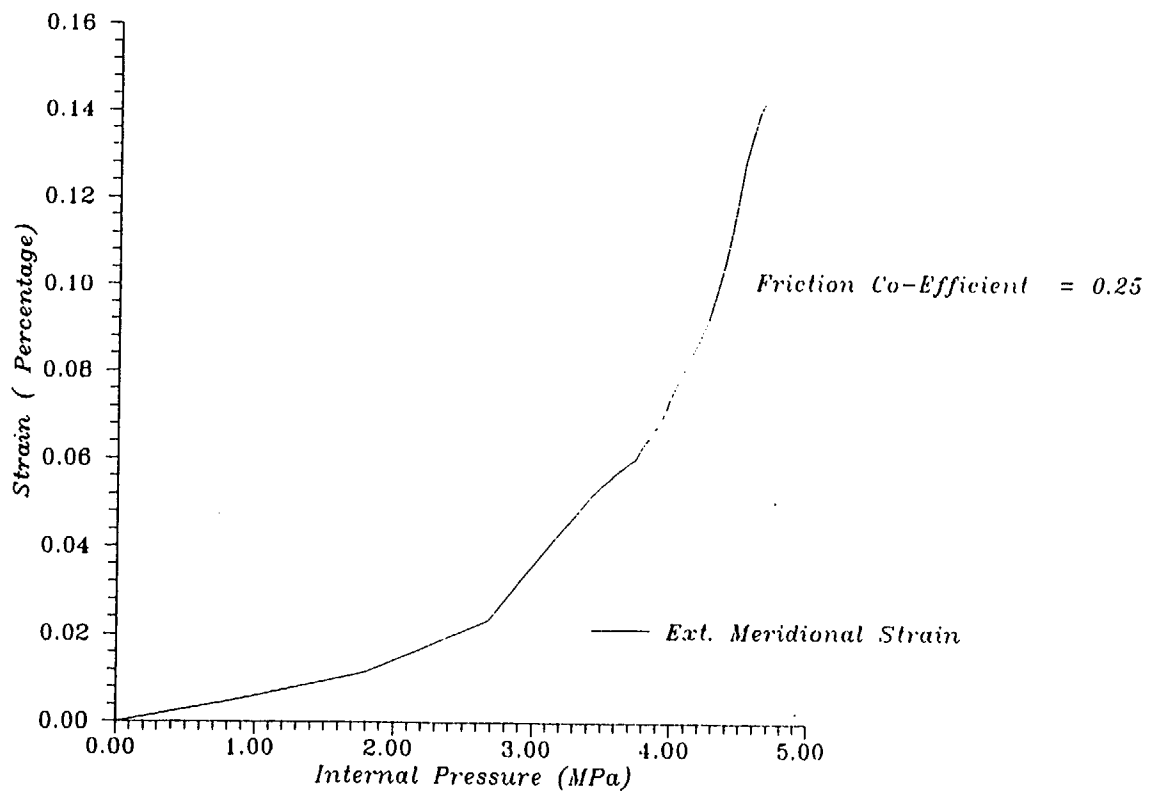


Figure 23 Global axisymmetric Model

BARC (INDIA)
Post-Test Analysis
Standard Output Location 20

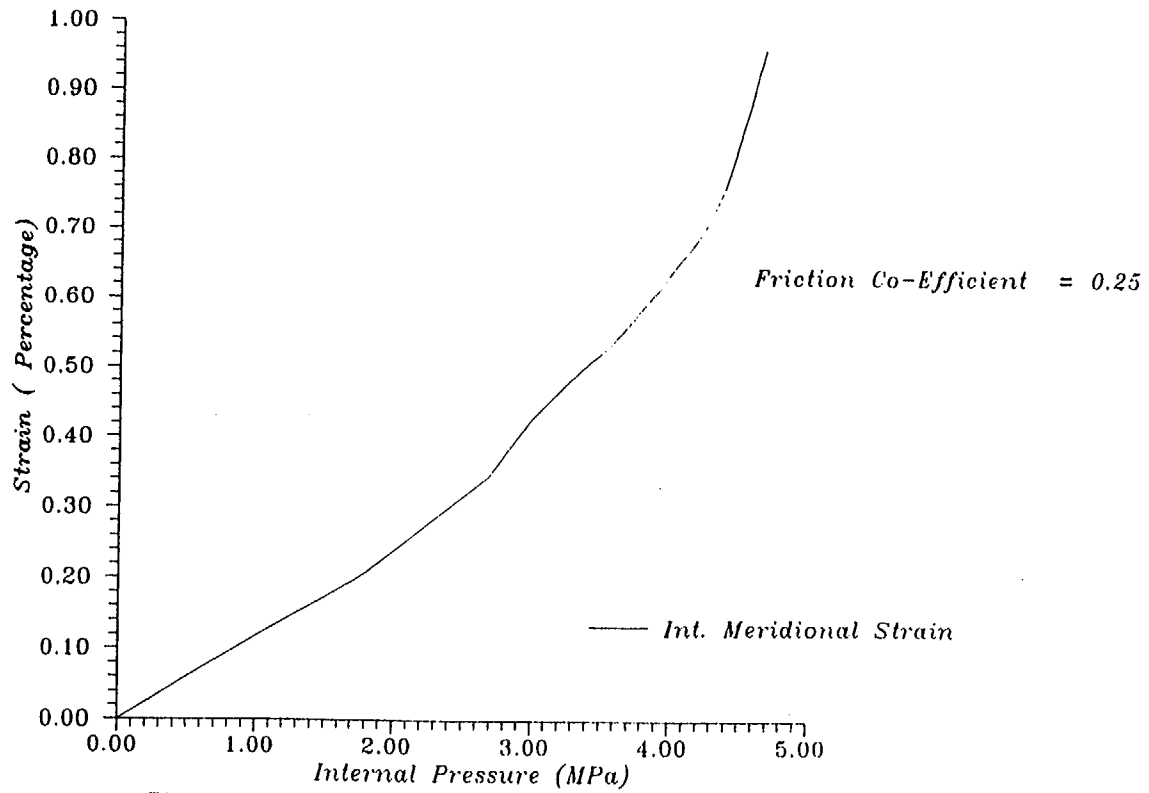


Figure 2.4 Global axisymmetric Model

BARC (INDIA)
Post-Test Analysis
Standard Output Location 21

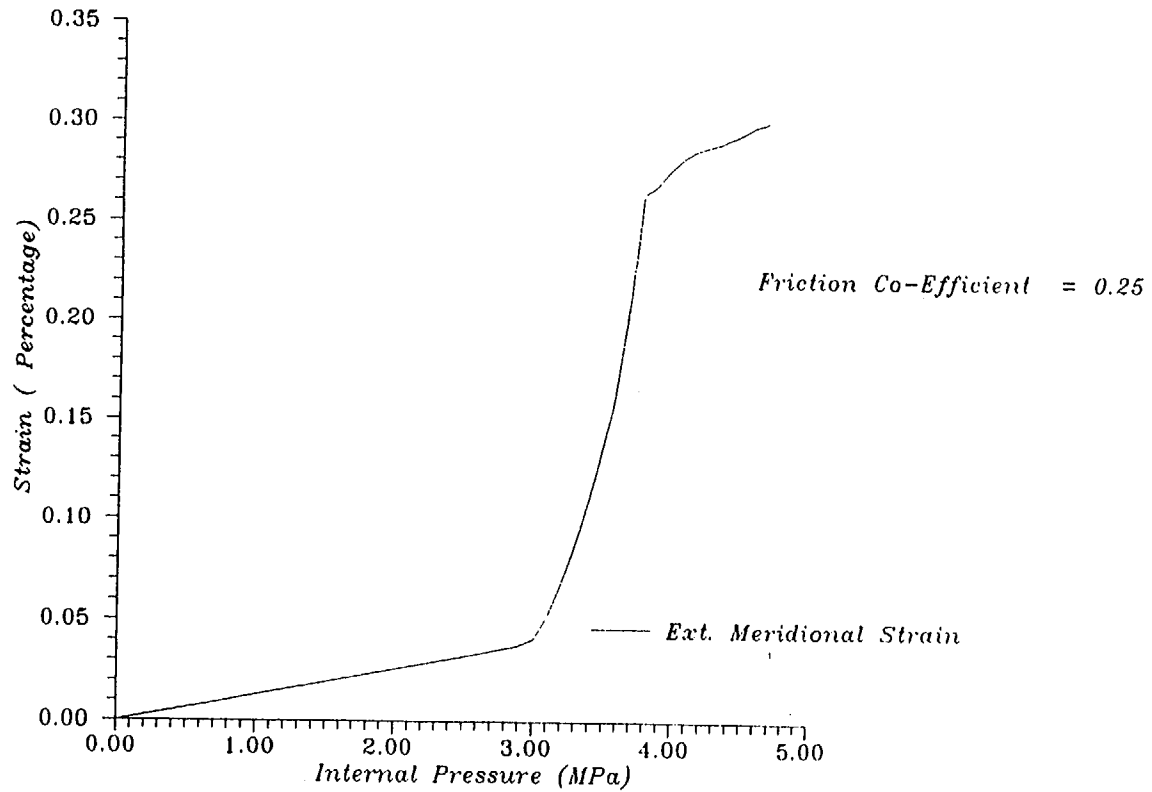


Figure 25 Global axisymmetric Model

BARC (INDIA)
Post-Test Analysis
Standard Output Location 22

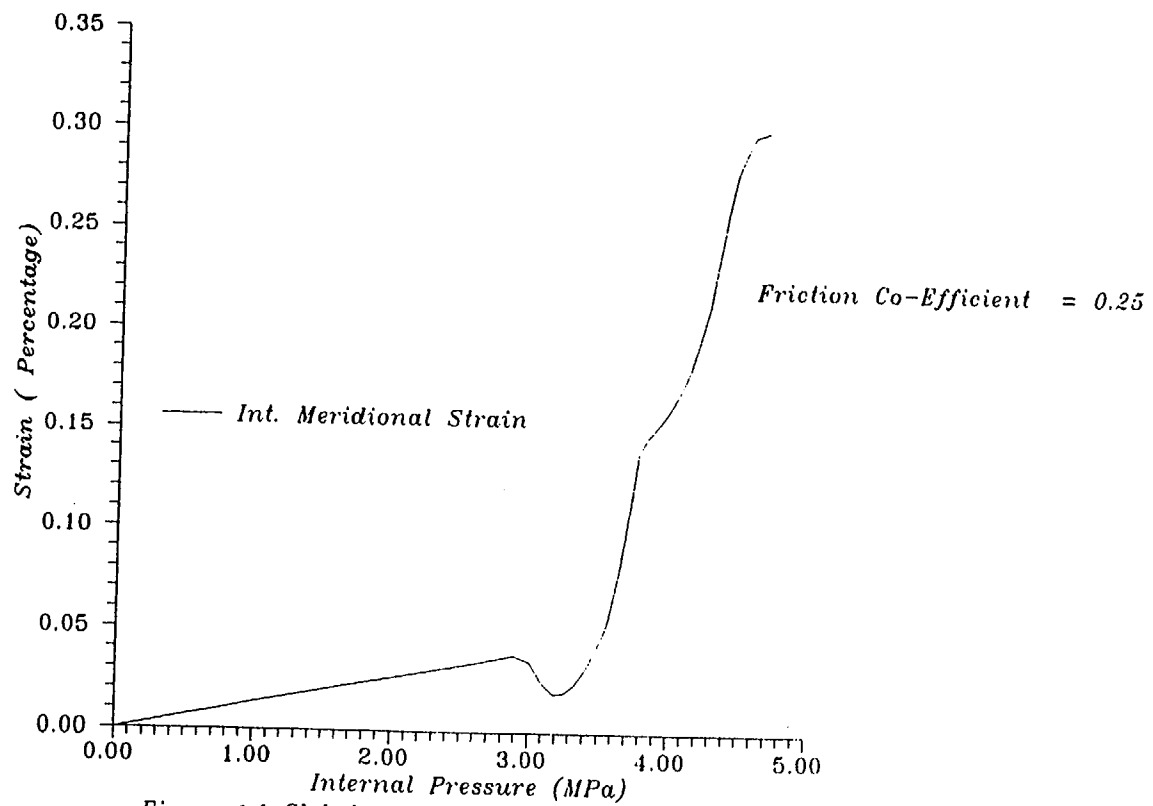


Figure 2.6 Global axisymmetric Model

BARC (INDIA)
Post-Test Analysis
Standard Output Location 23

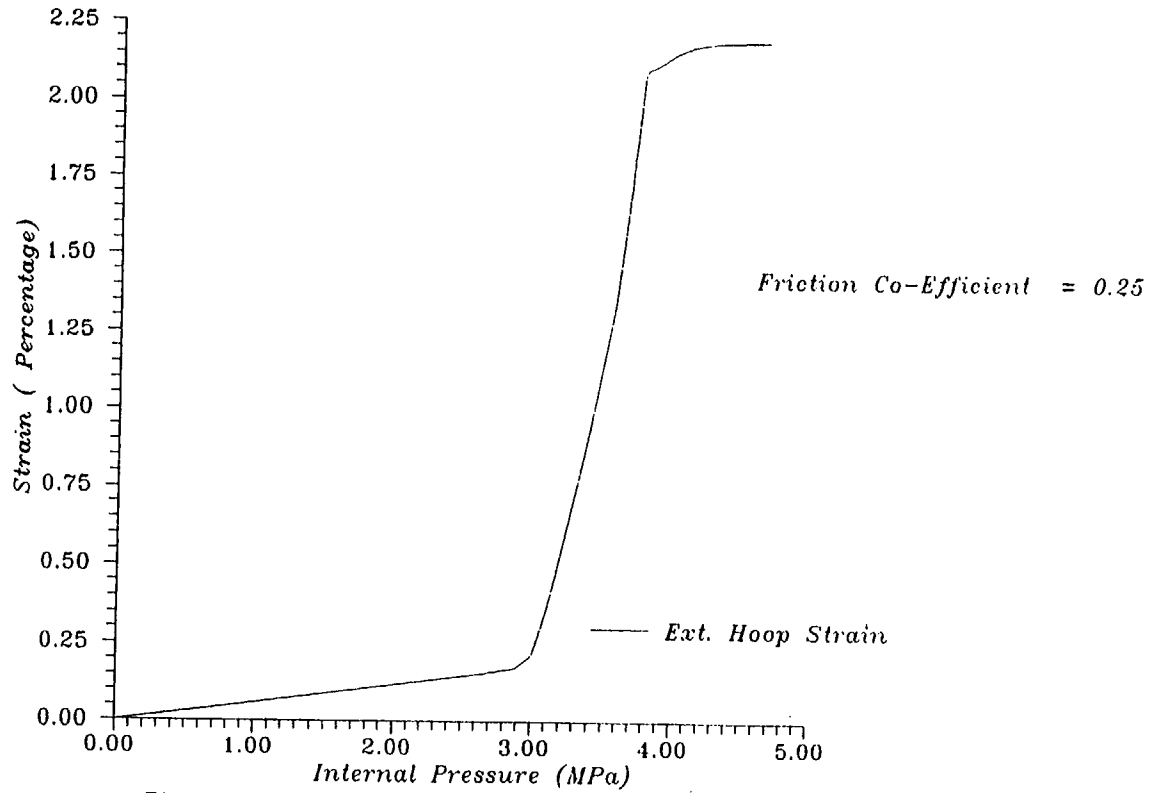


Figure 2.4 Global axisymmetric Model

BARC (INDIA)
Post-Test Analysis
Standard Output Location 24

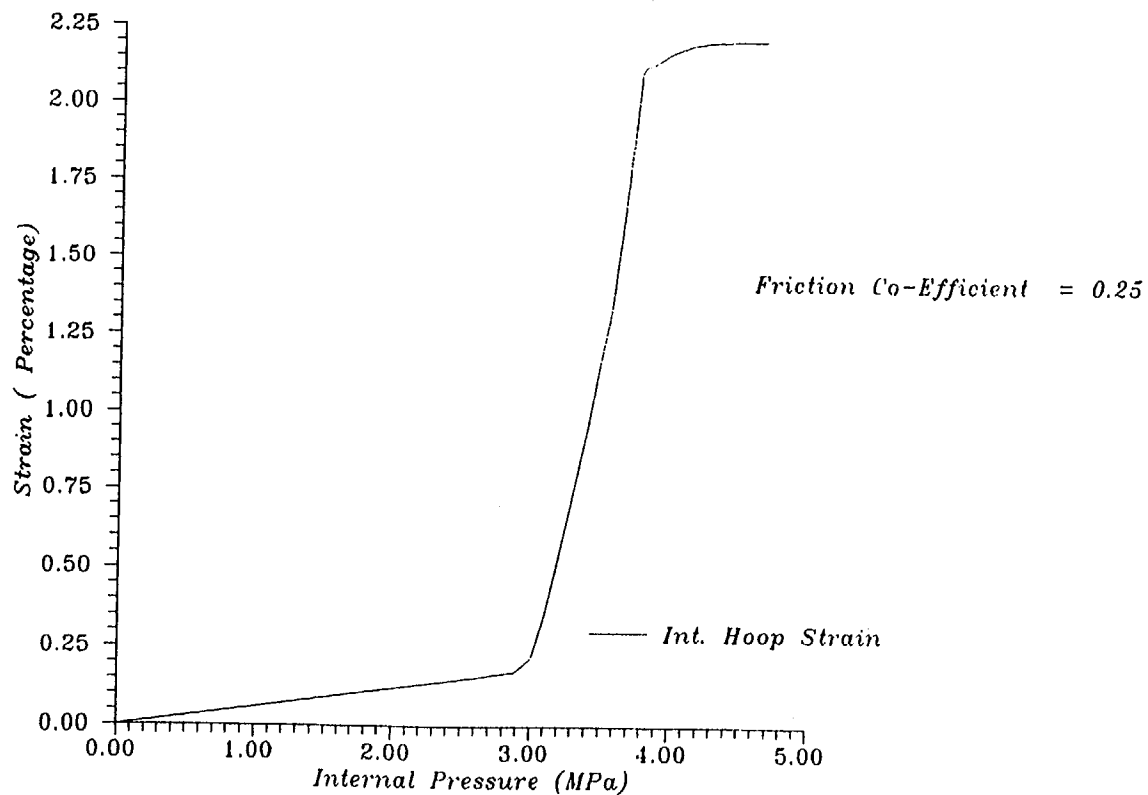


Figure 2.8 Global axisymmetric Model

BARC (INDIA)
Post-Test Analysis
Standard Output Location 25

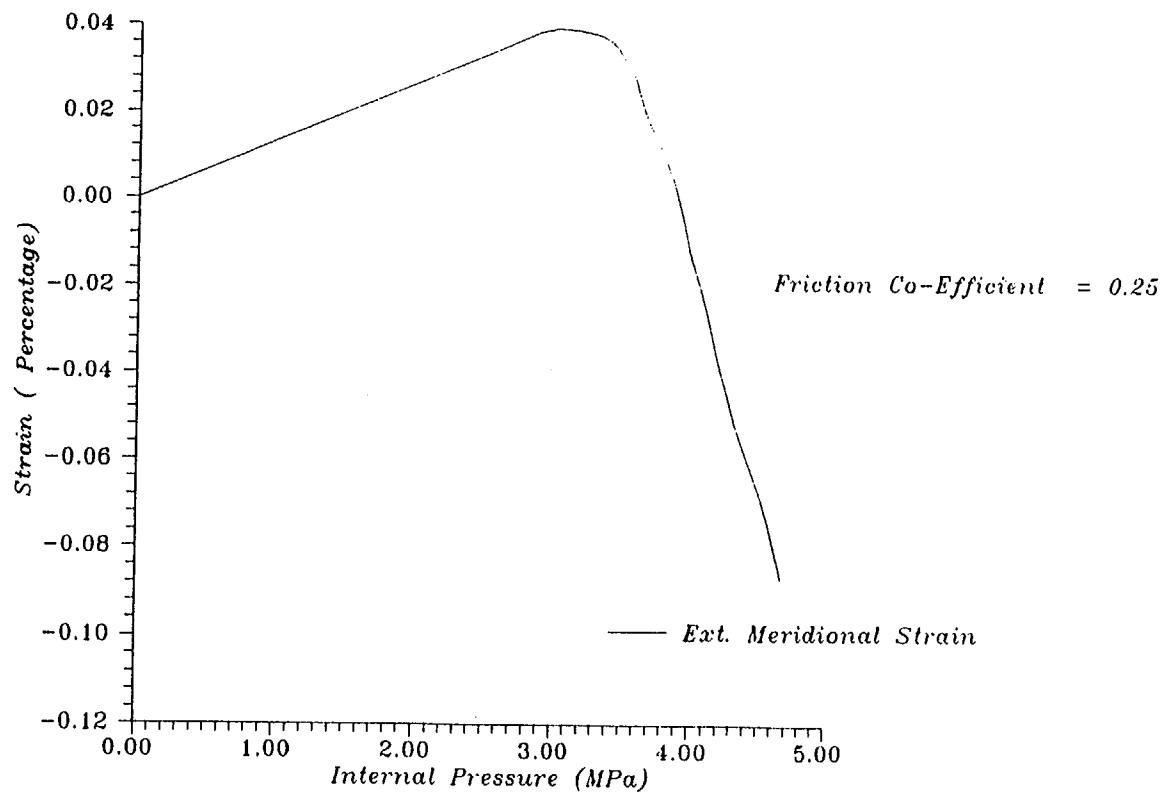


Figure 2.1 Global axisymmetric Model

BARC (INDIA)
Post-Test Analysis
Standard Output Location 26

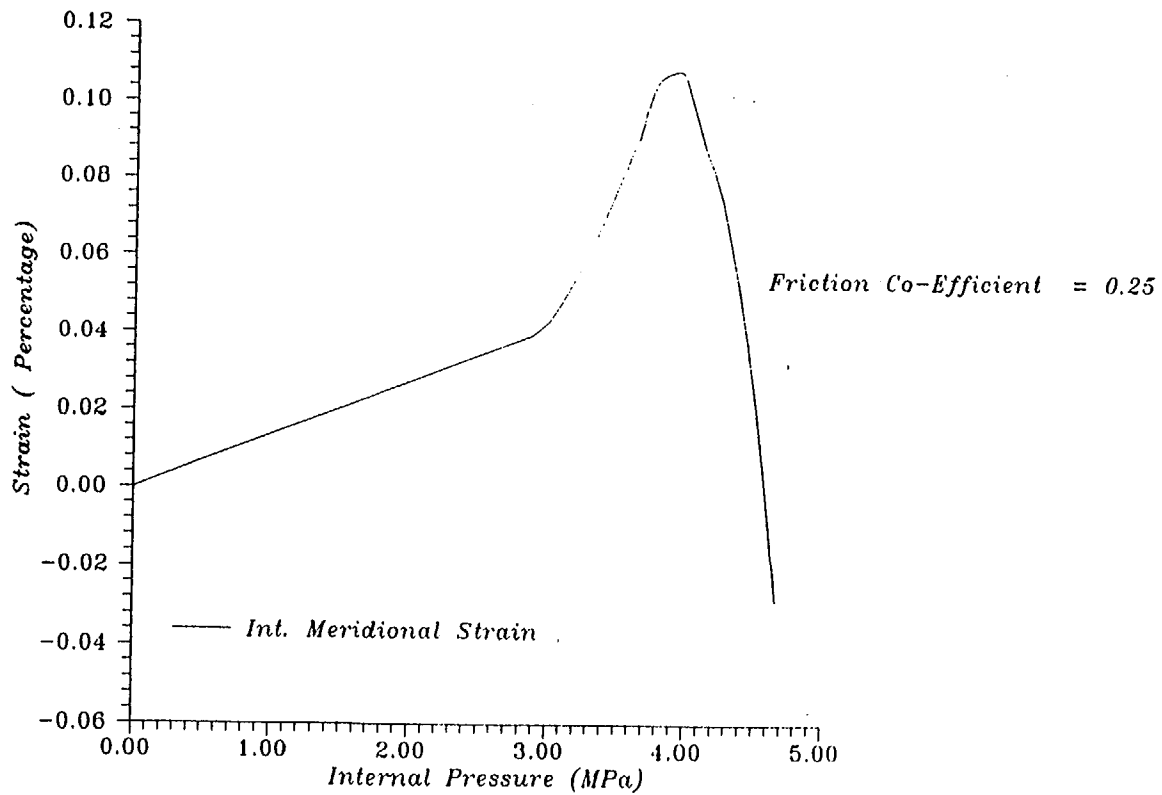


Figure 30 Global axisymmetric Model

BARC (INDIA)
Post-Test Analysis
Standard Output Location 27

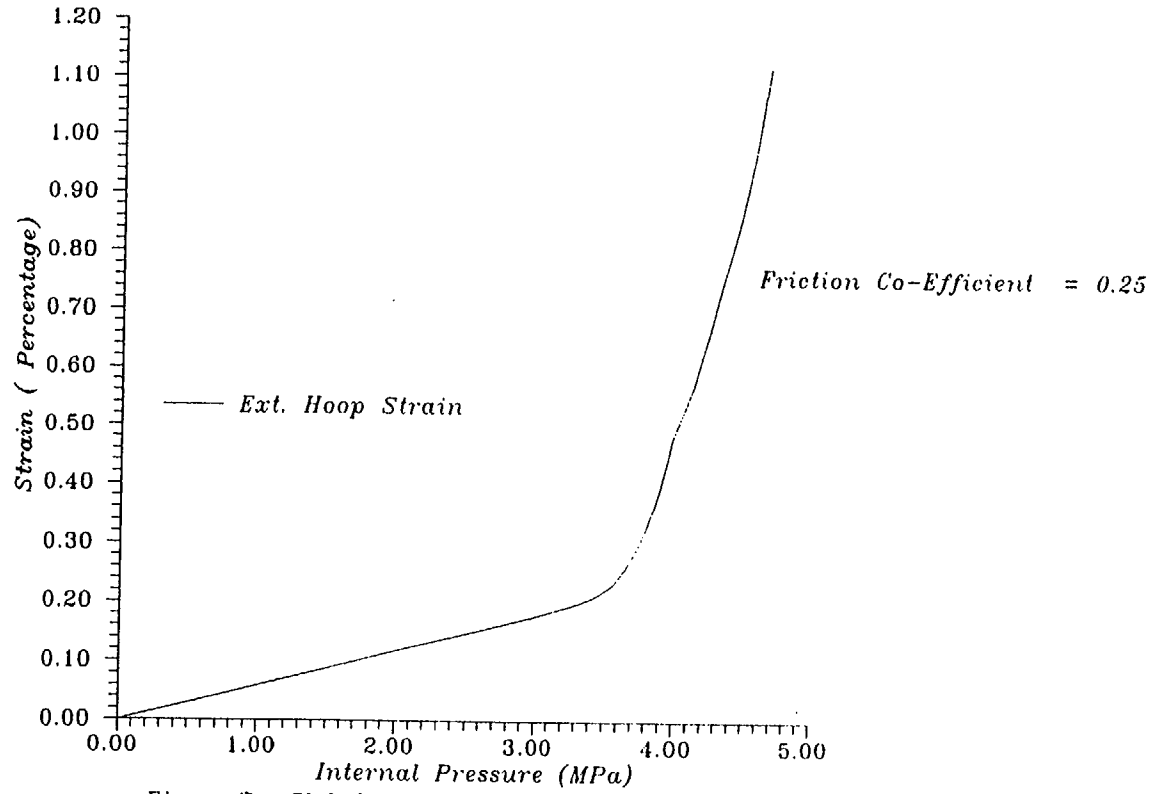


Figure 31 Global axisymmetric Model

BARC (INDIA)
Post-Test Analysis
Standard Output Location 28

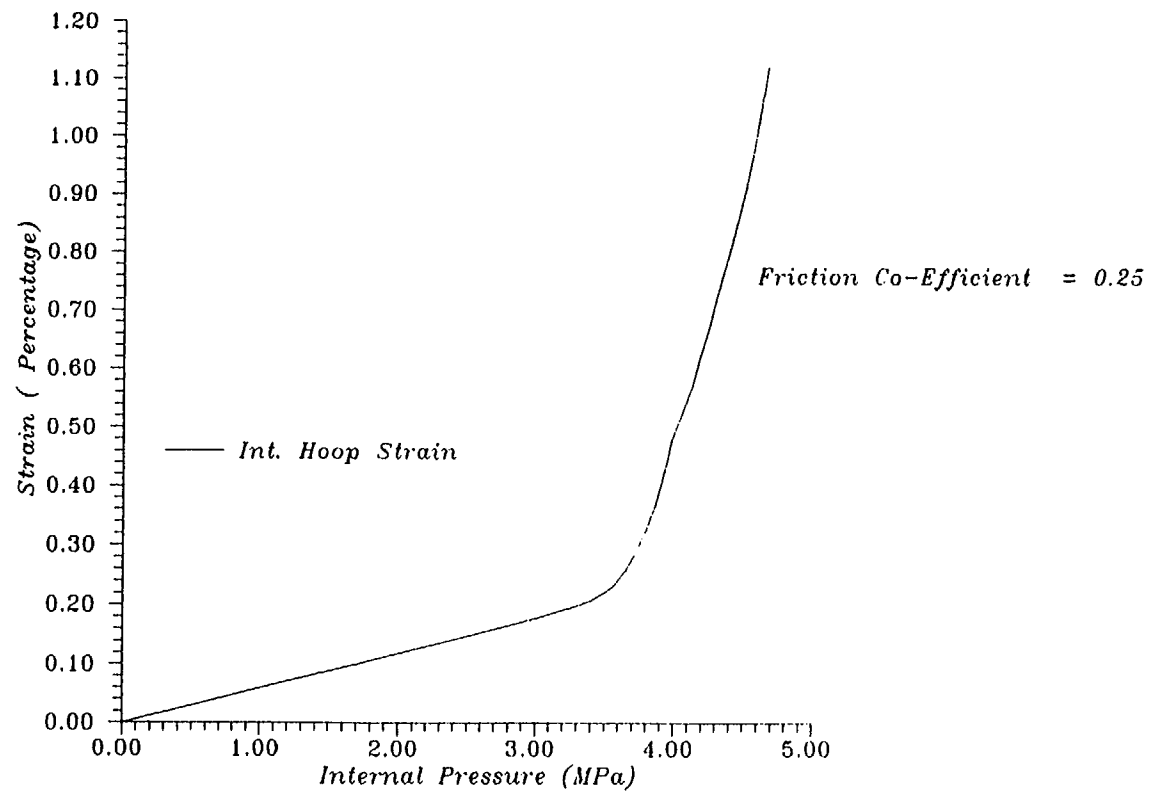


Figure 32. Global axisymmetric Model

BARC (INDIA)
Post-Test Analysis
Standard Output Location 29

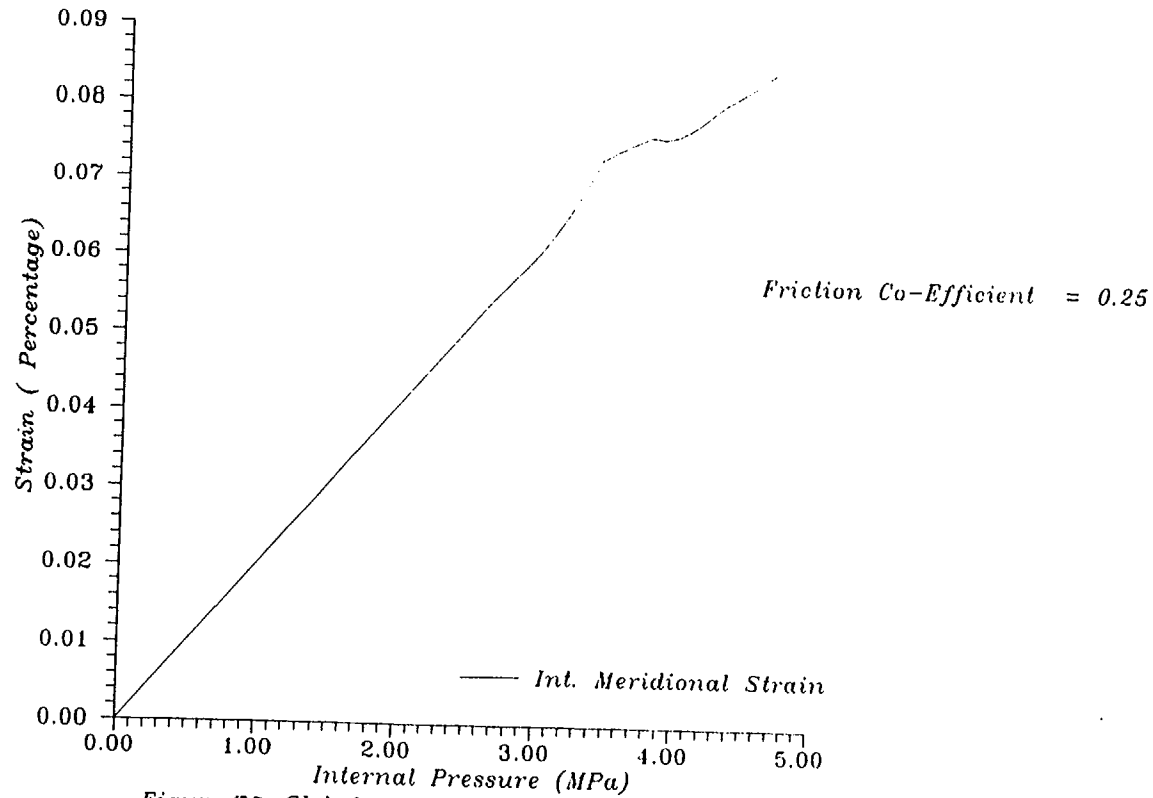


Figure 33 Global axisymmetric Model

BARC (INDIA)
Post-Test Analysis
Standard Output Location 30

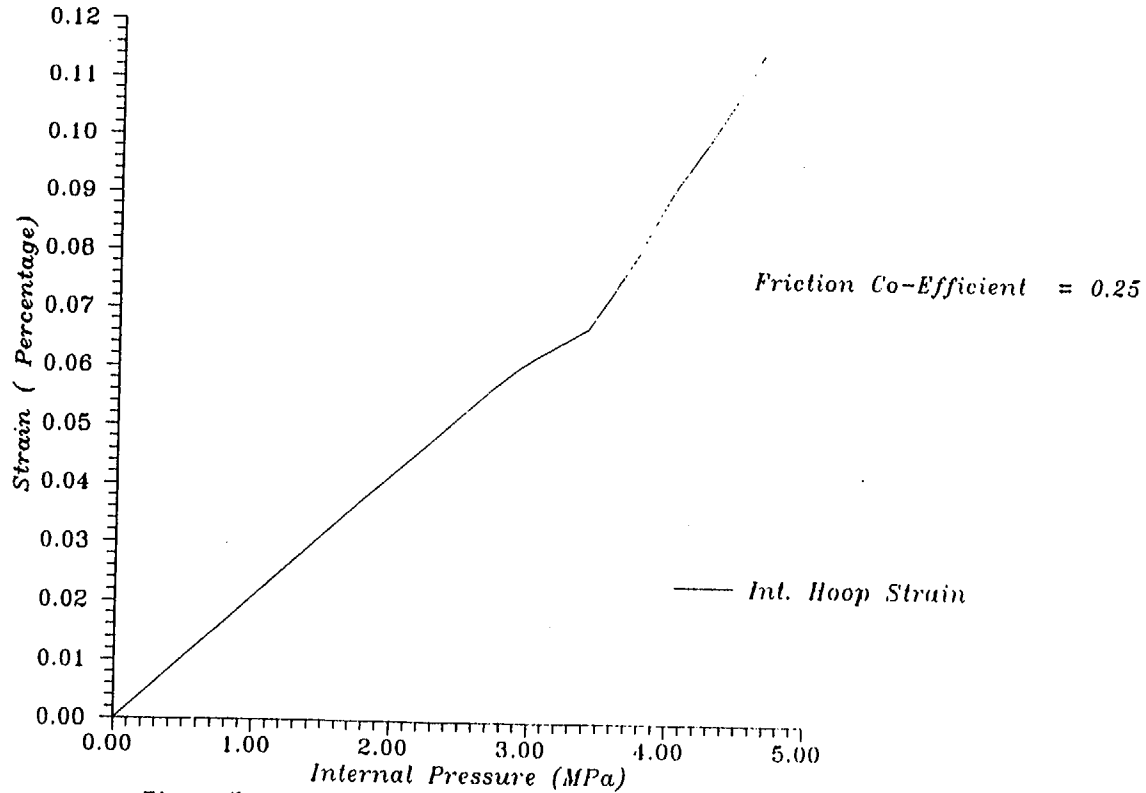


Figure 34 Global axisymmetric Model

BARC (INDIA)
Post-Test Analysis
Standard Output Location 31

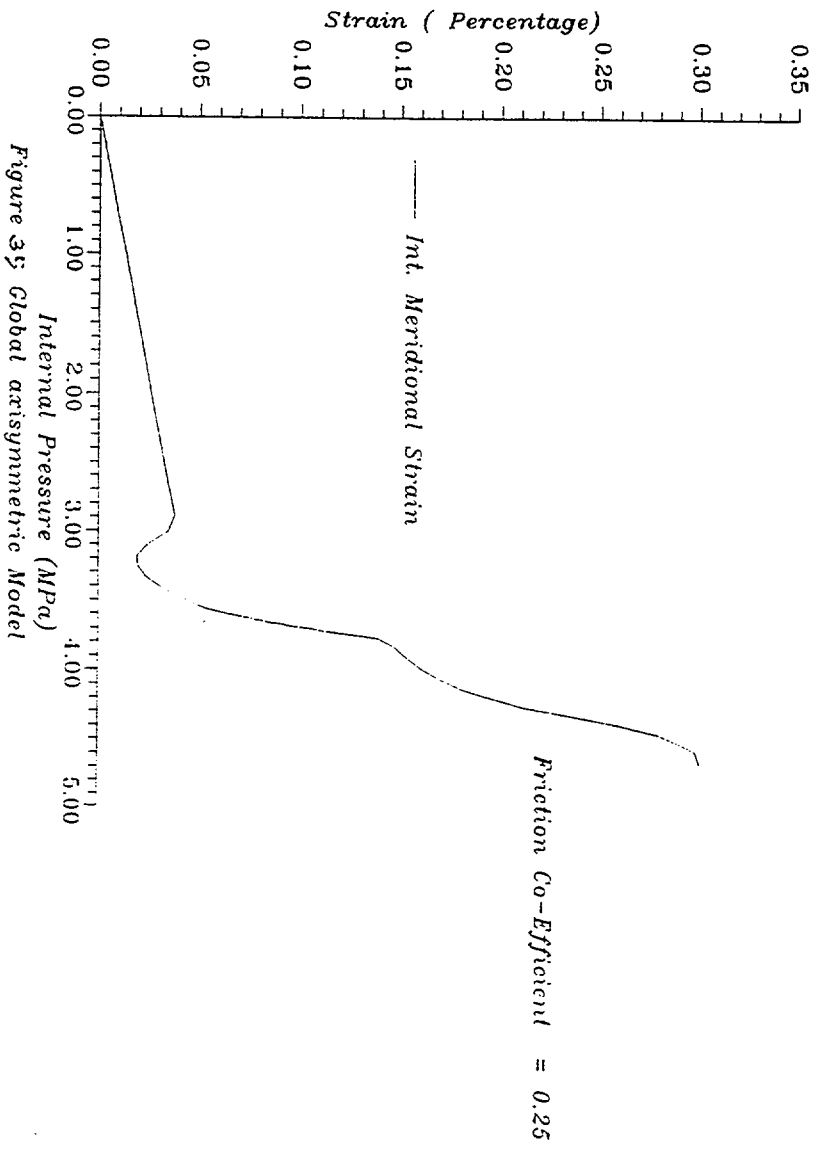


Figure 35 Global axisymmetric Model

BARC (INDIA)
Post-Test Analysis
Standard Output Location 32

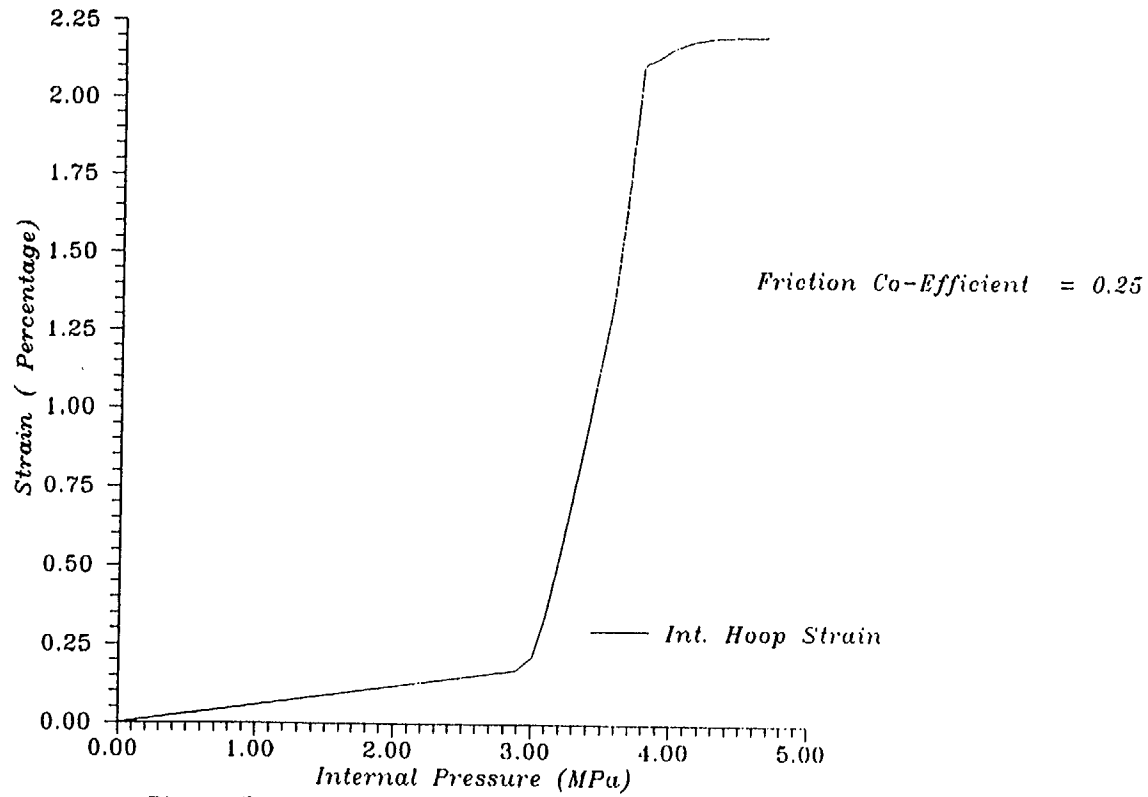


Figure 36 Global axisymmetric Model

BARC (INDIA)
Post-Test Analysis
Standard Output Location 33

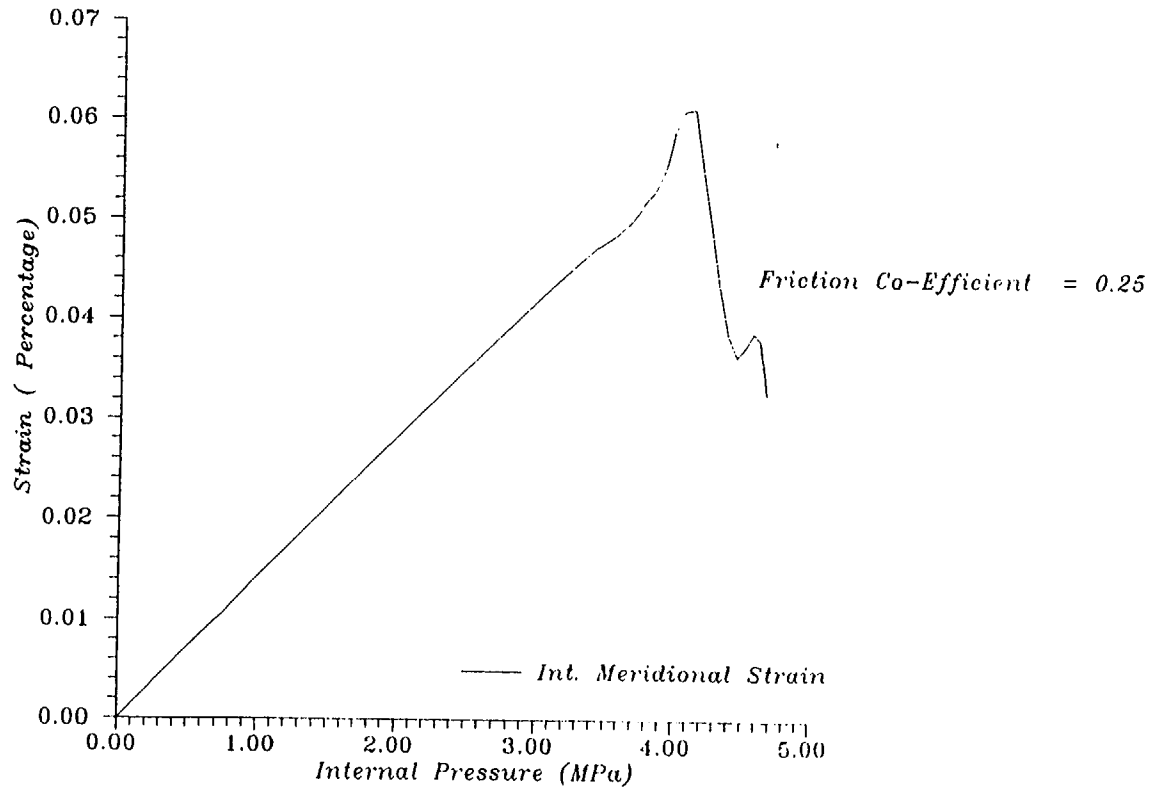


Figure 37 Global axisymmetric Model

BARC (INDIA)
Post-Test Analysis
Standard Output Location 34

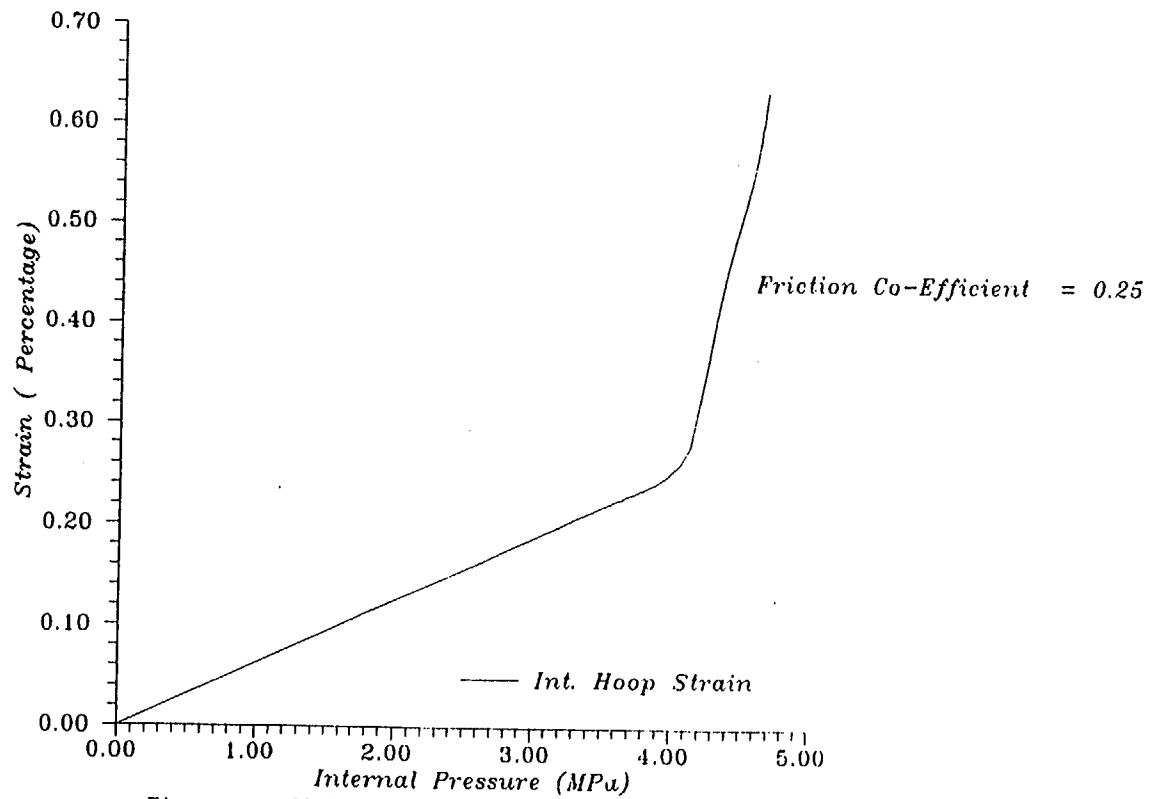


Figure 38 Global axisymmetric Model

BARC (INDIA)
Post-Test Analysis
Standard Output Location 35

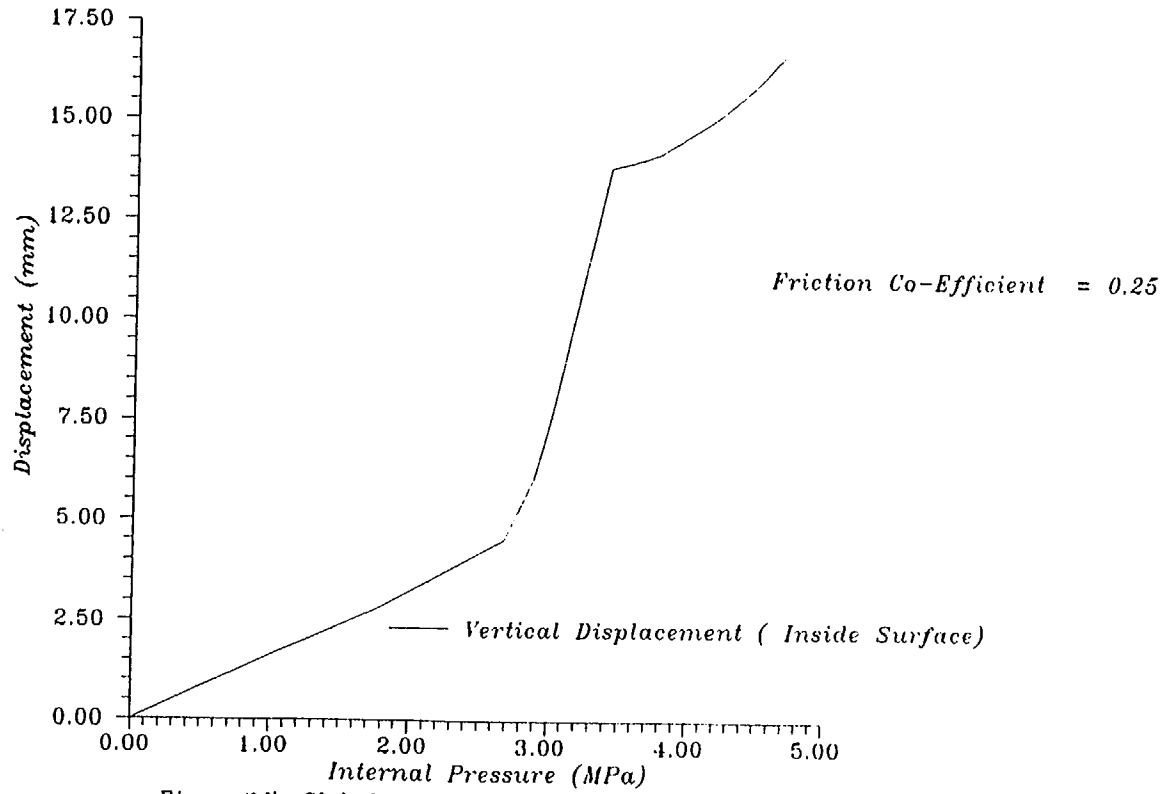


Figure 34 Global axisymmetric Model

BARC (INDIA)
Post-Test Analysis
Standard Output Location 36

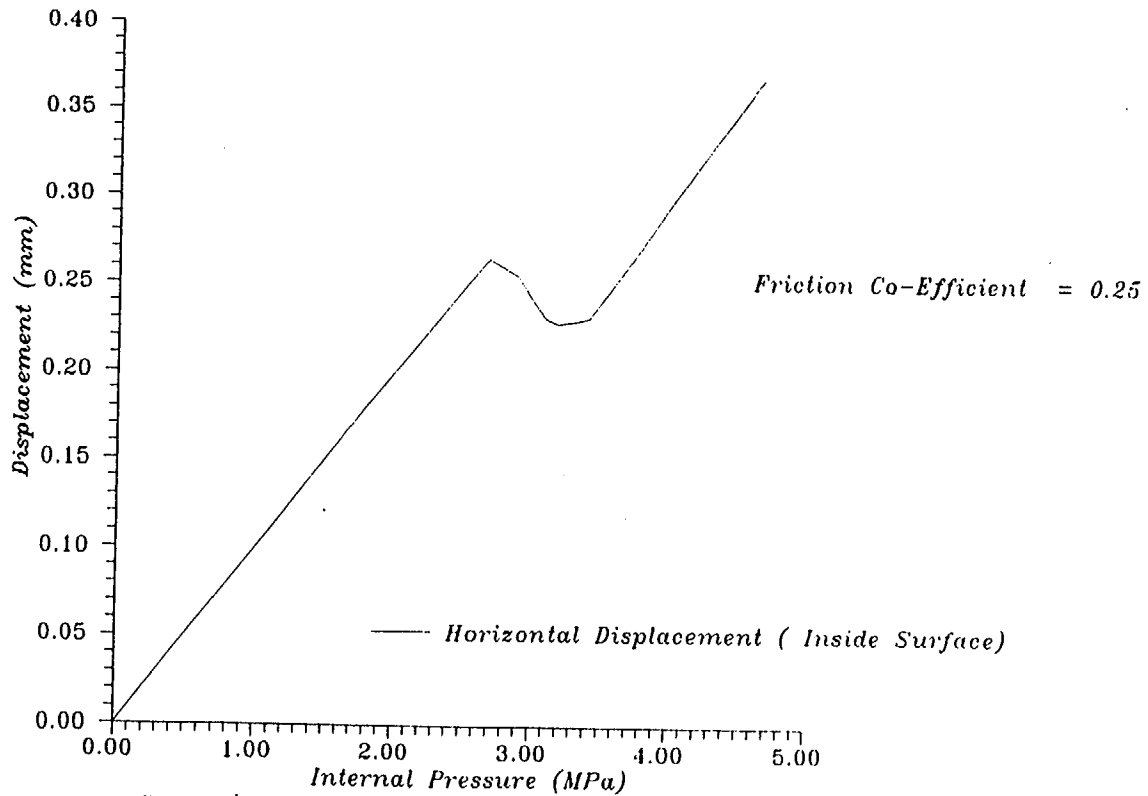


Figure 4-D Global axisymmetric Model

BARC (INDIA)
Post-Test Analysis
Standard Output Location 36

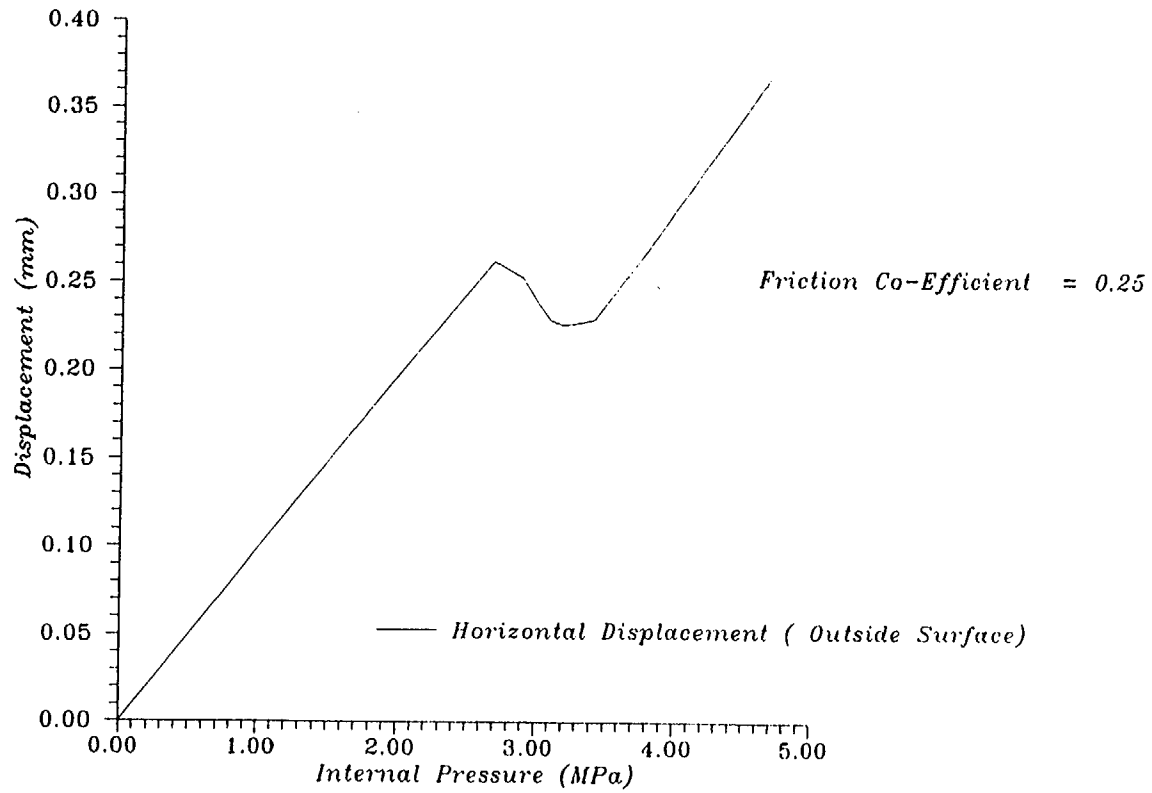


Figure 4: Global axisymmetric Model

BARC (INDIA)
Post-Test Analysis
Standard Output Location 37

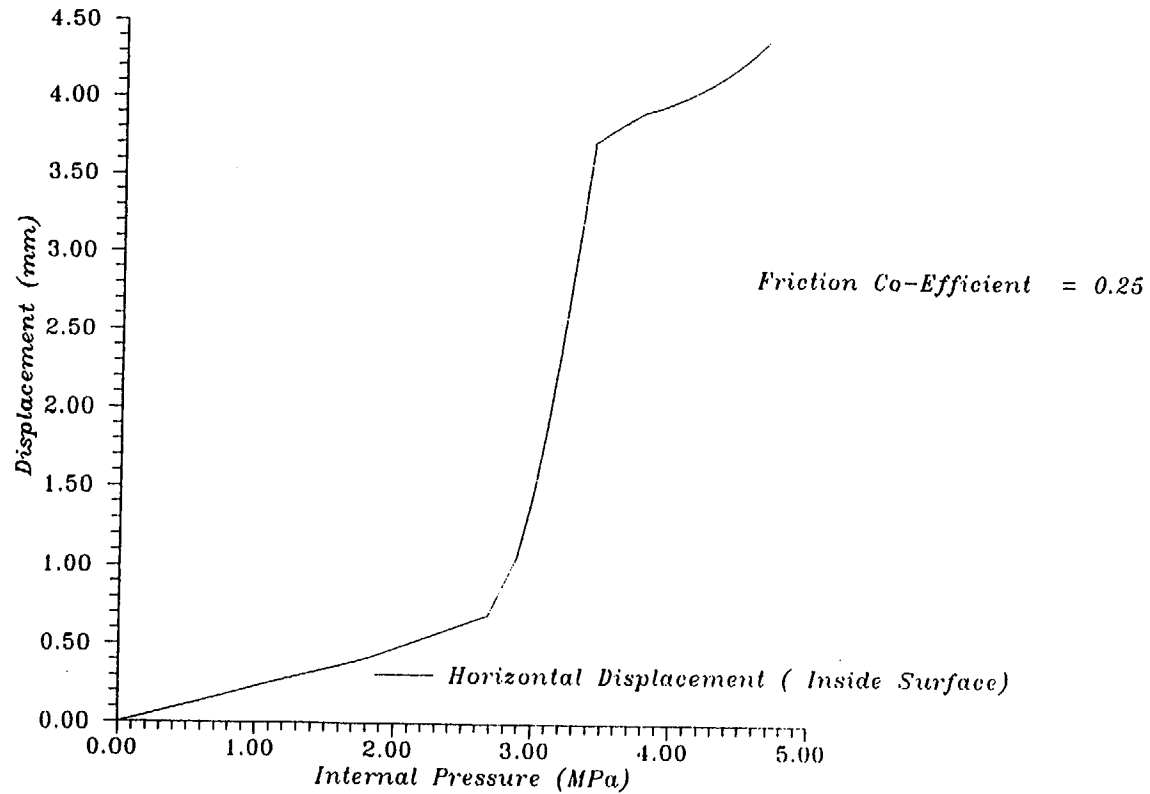


Figure 4.2 Global axisymmetric Model

BARC (INDIA)
Post-Test Analysis
Standard Output Location 38

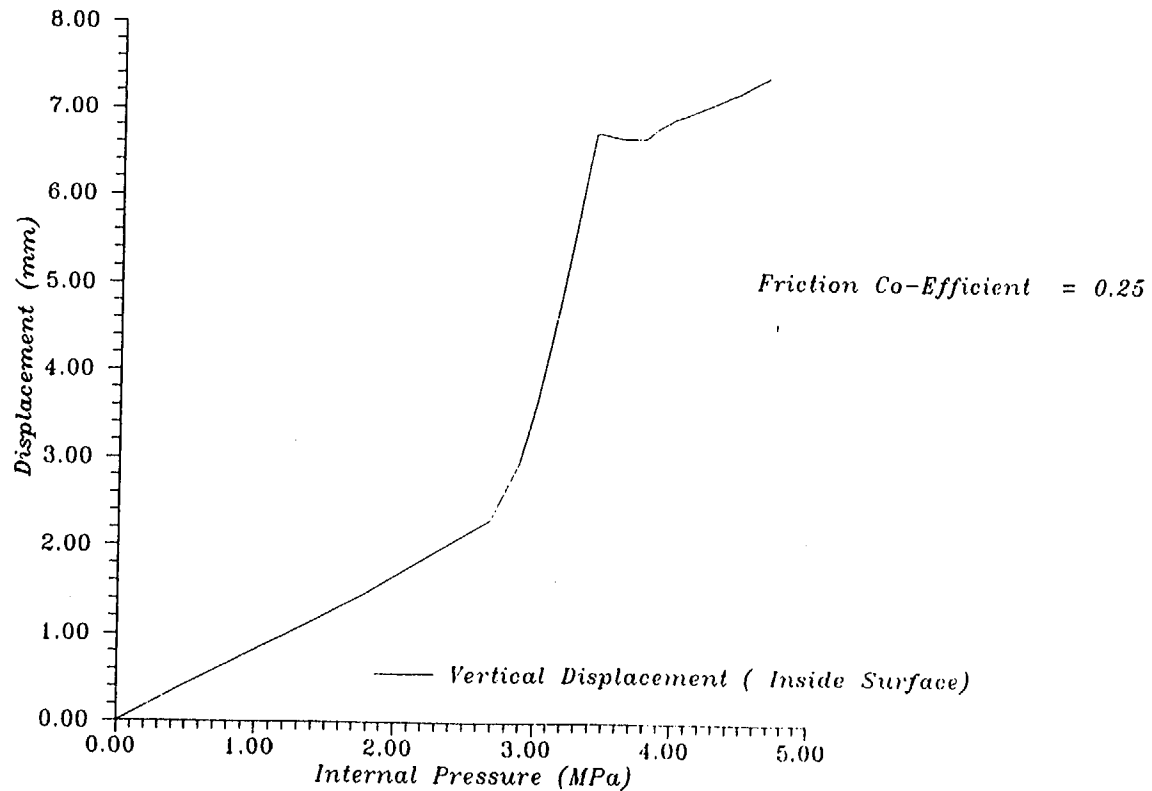


Figure 43 Global axisymmetric Model

BARC (INDIA)
Post-Test Analysis

Standard Output Location 39

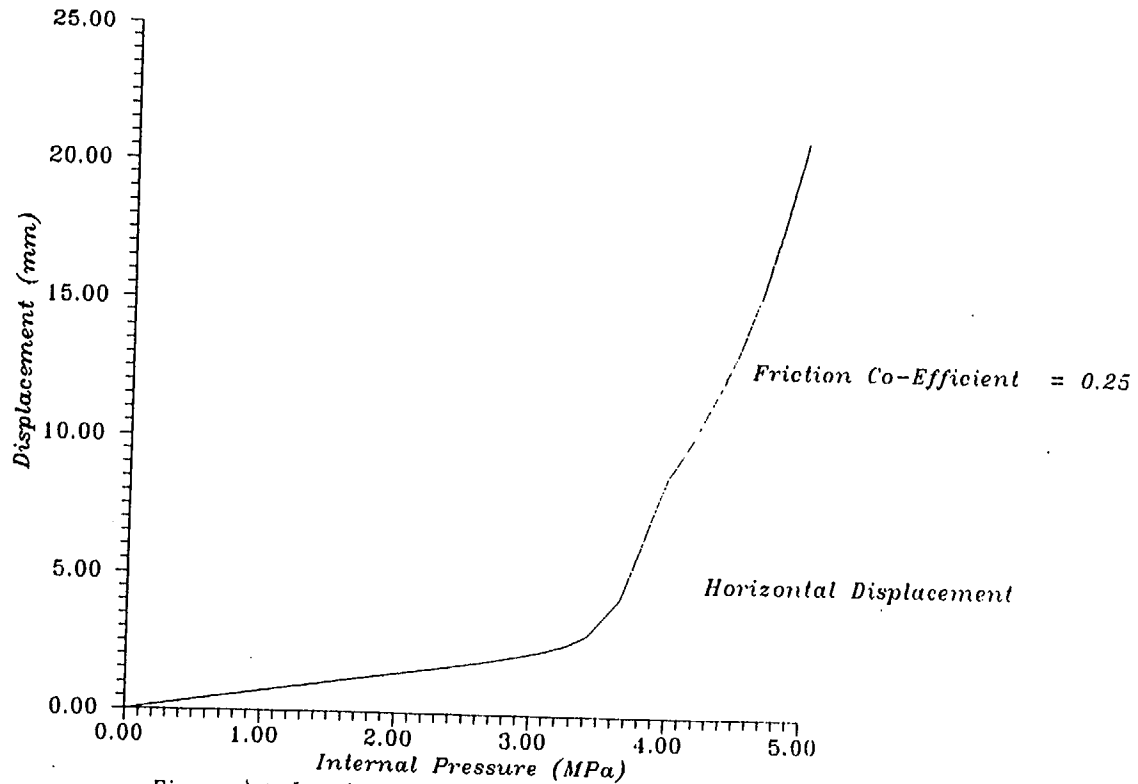


Figure 4.4 Local Equipment Hatch Shell Model

BARC (INDIA)
Post-Test Analysis
Standard Output Location 40

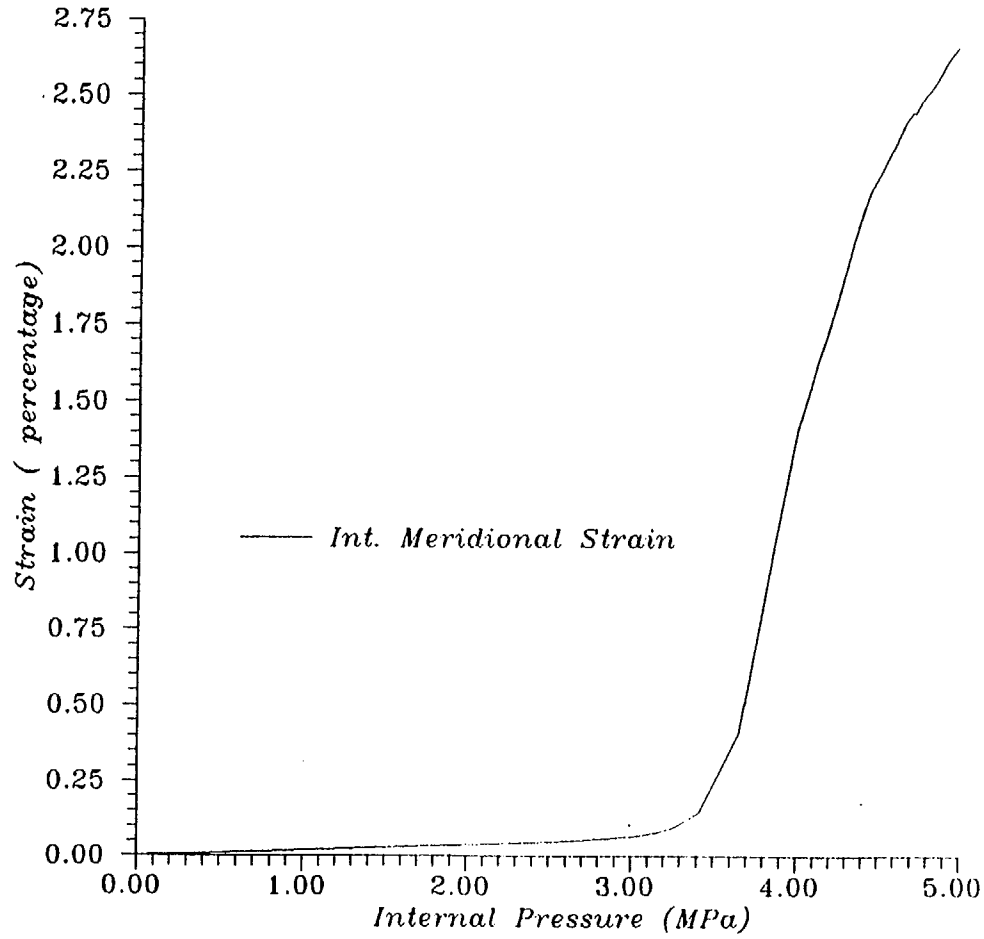


Figure 45 Local Shell Model Near Equipment Hatch

BARC (INDIA)
Post-Test Analysis
Standard Output Location 41

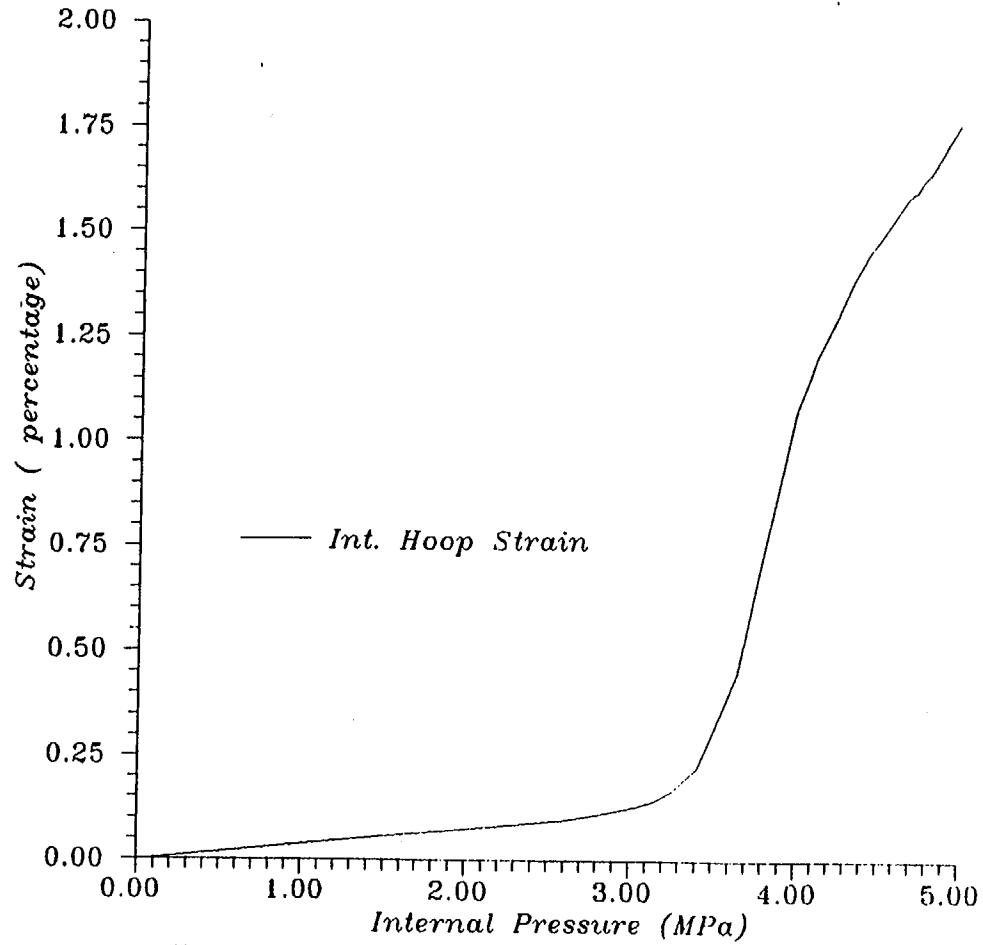


Figure 46 Local Shell Model Near Equipment Hatch

BARC (INDIA)
Post-Test Analysis
Standard Output Location 42

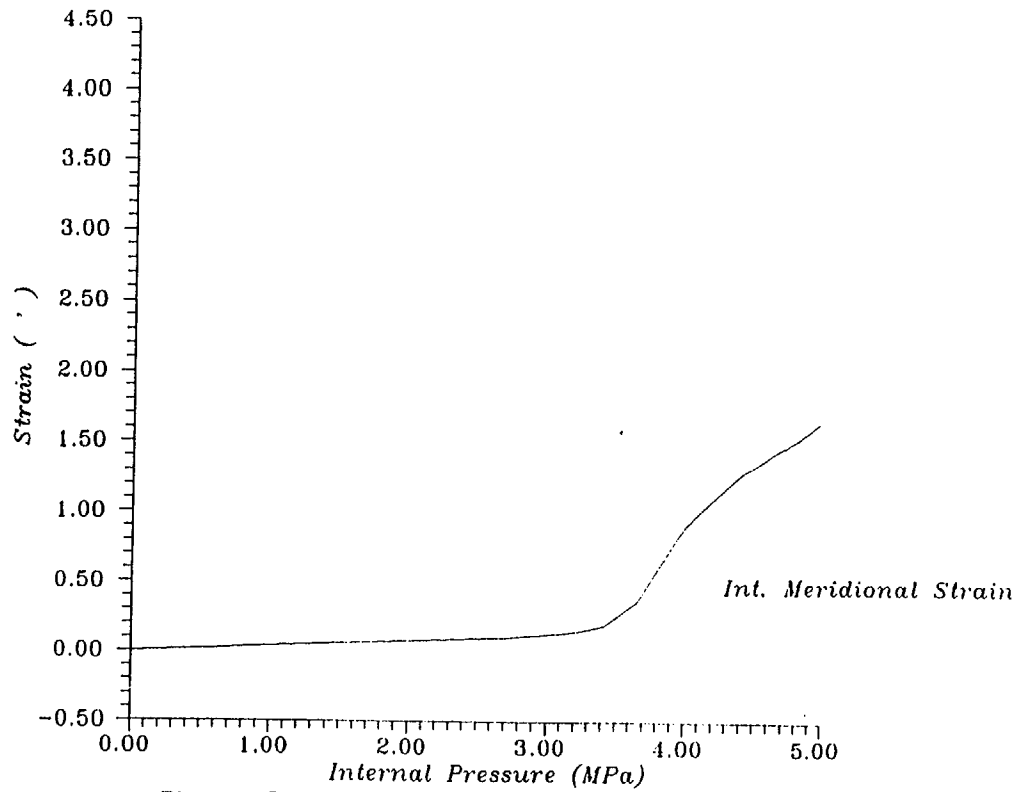


Figure 47 Local Shell Model Near Equipment Hatch

BARC (INDIA)
Post-Test Analysis
Standard Output Location 43

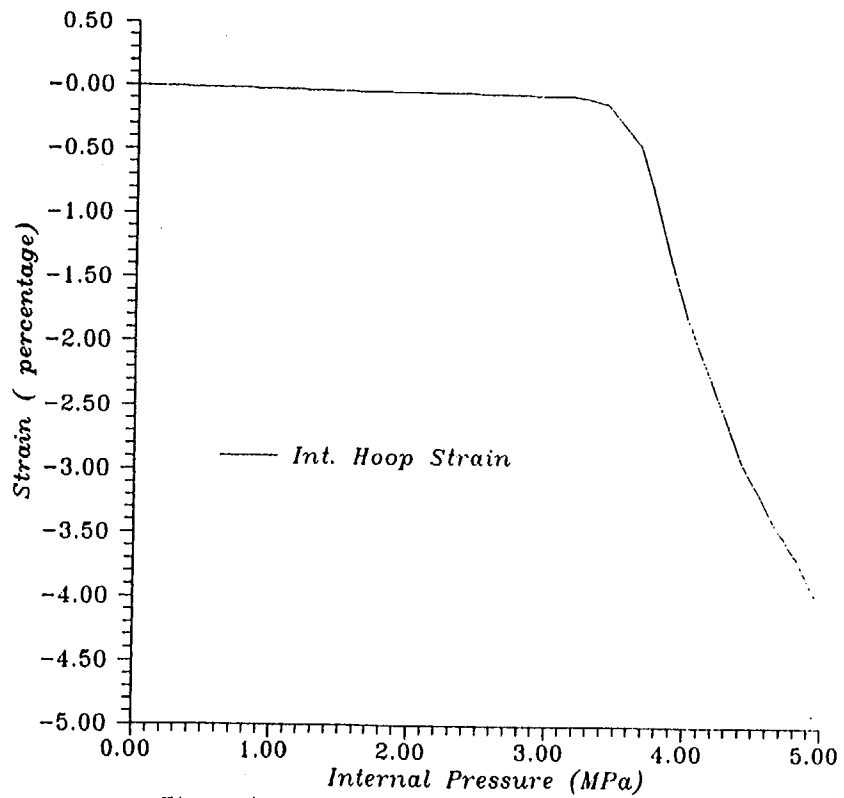


Figure 4.8 Local Shell Model Near Equipment Hatch

ABAQUS

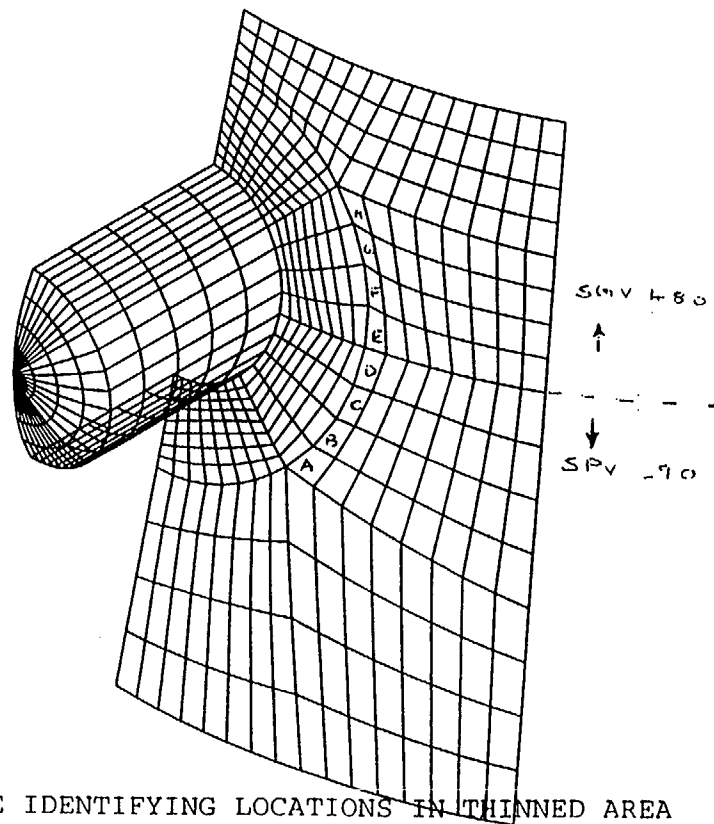


FIGURE 49 FIGURE IDENTIFYING LOCATIONS IN THINNED AREA

BARC (INDIA)
Post-Test Analysis
Thinned Area Location A

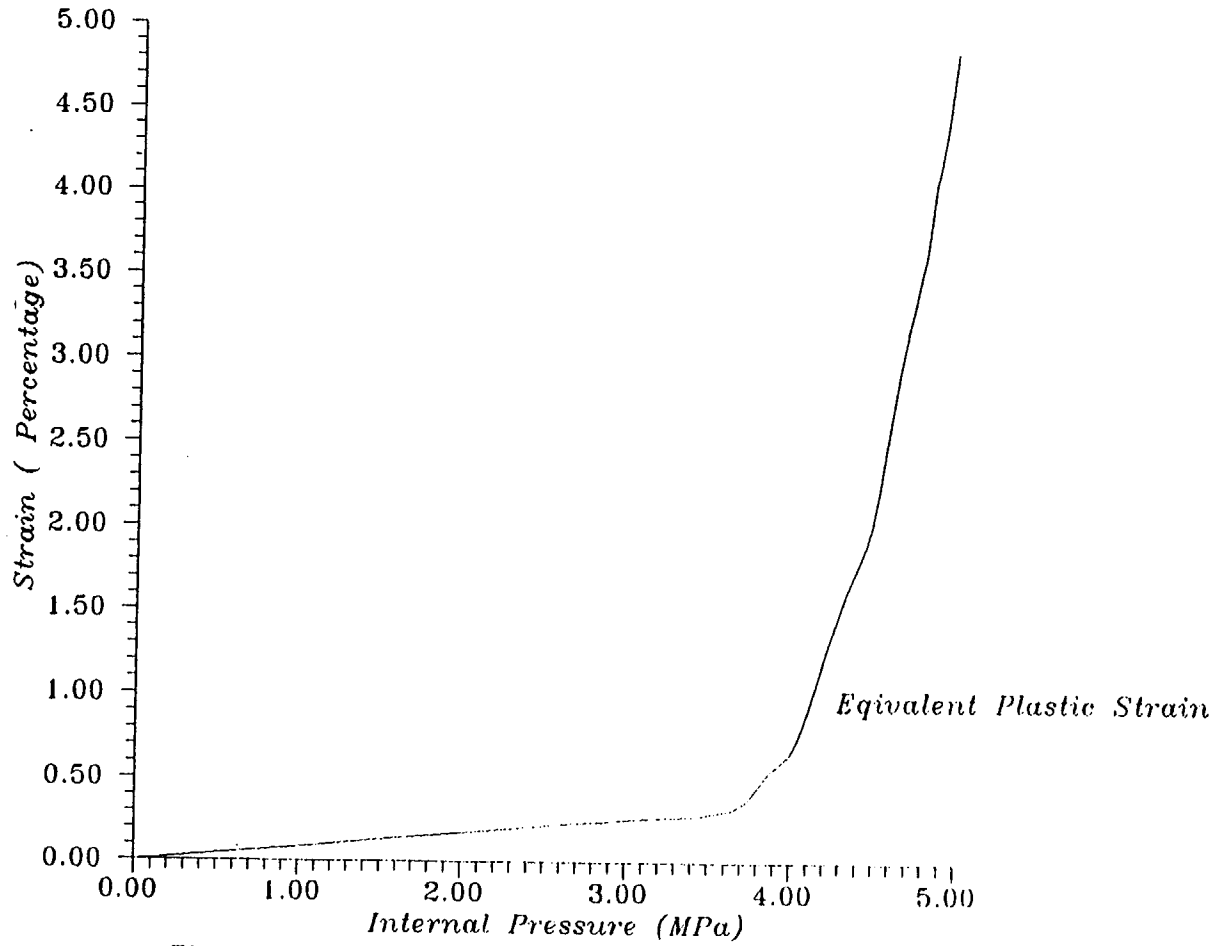


Figure 50 Local Shell Model Near Equipment Hatch

BARC (INDIA)
Post-Test Analysis
Thinned Area Location B

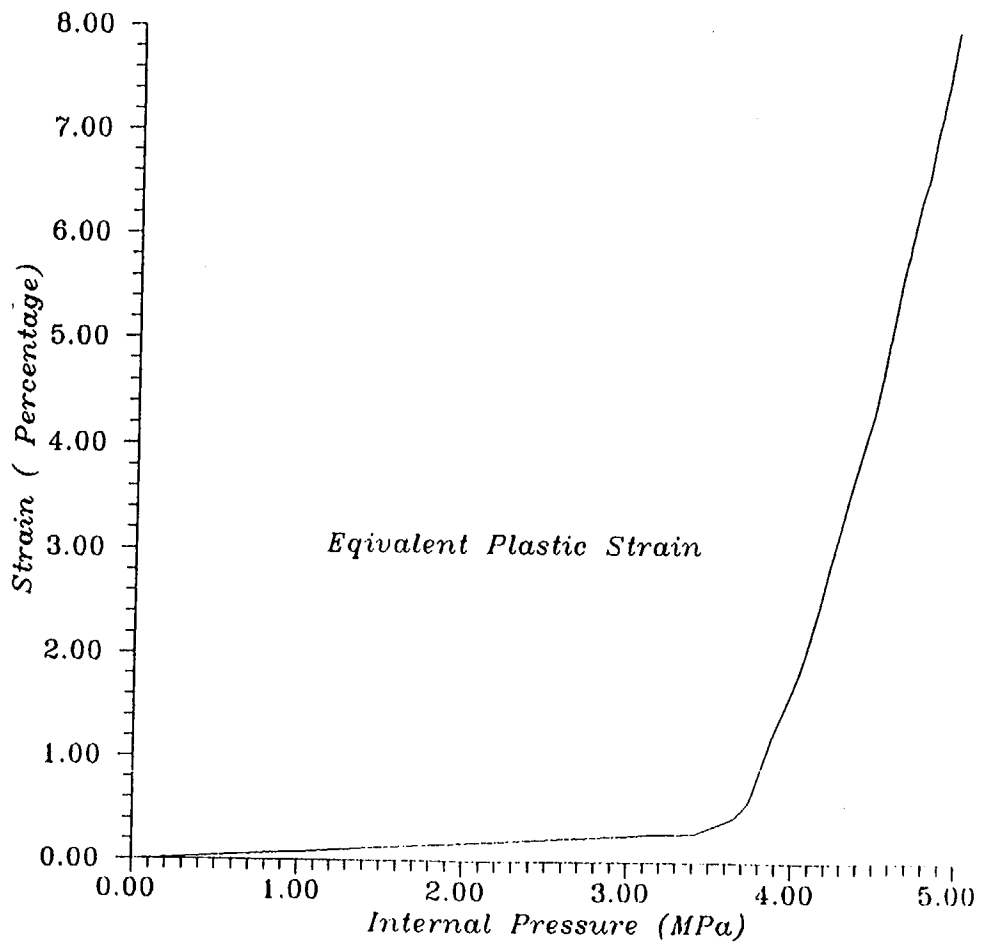


Figure 51 Local Shell Model Near Equipment Hatch

BARC (INDIA)
Post-Test Analysis
Thinned Area Location C'

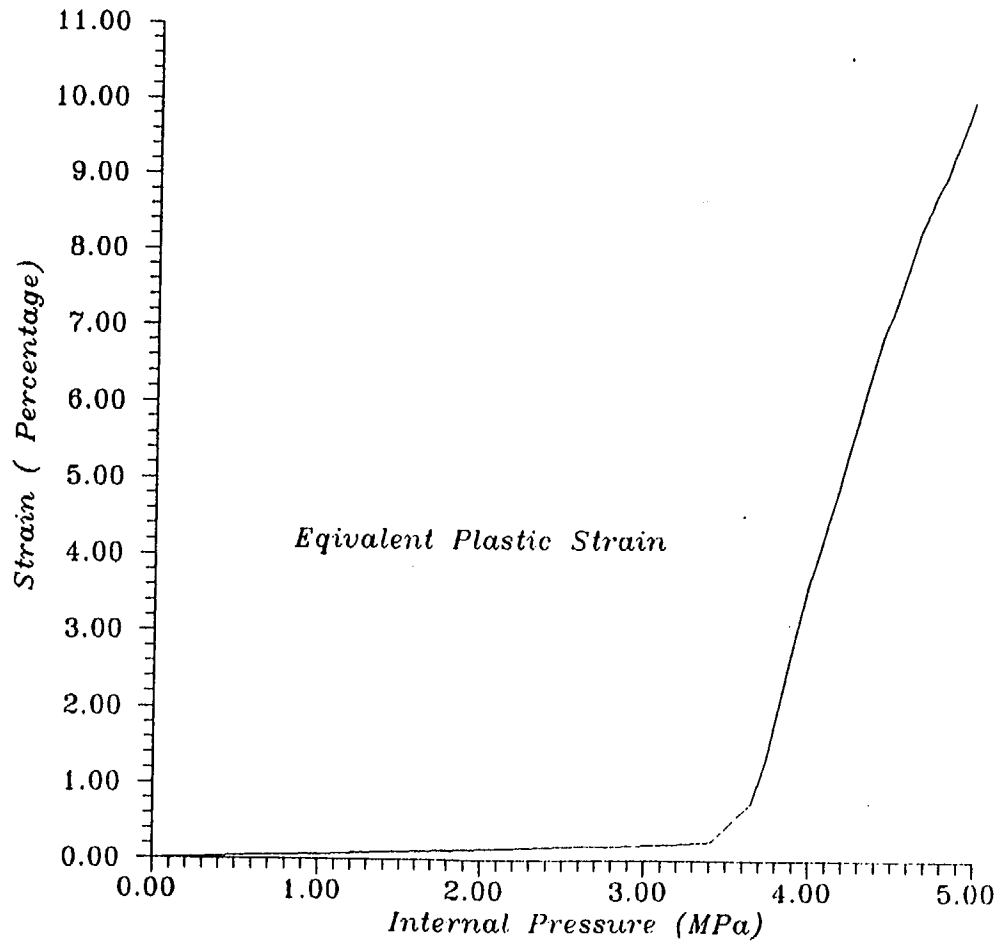


Figure 52 Local Shell Model Near Equipment Hatch

BARC (INDIA)
Post-Test Analysis
Thinned Area Location D

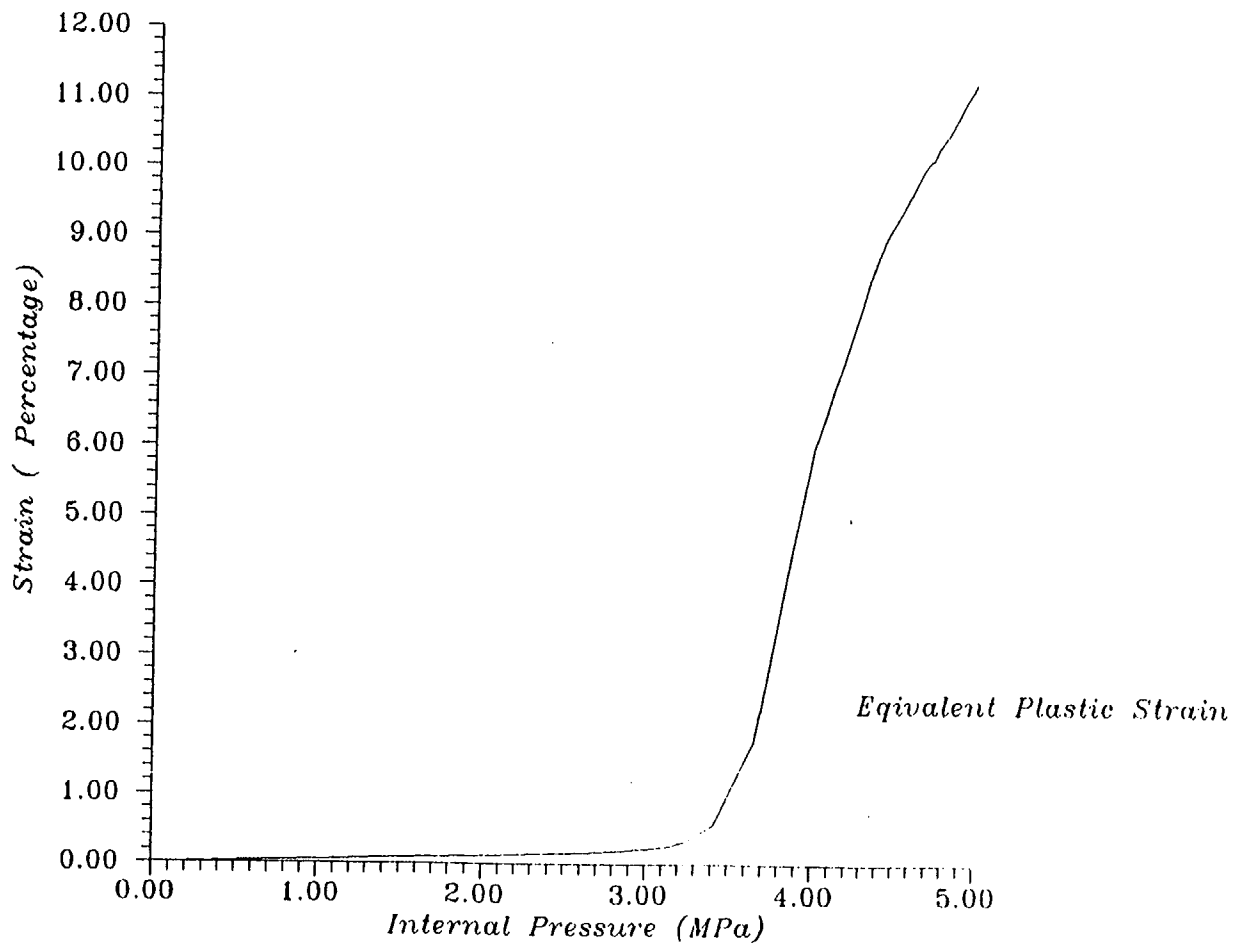


Figure 53 Local Shell Model Near Equipment Hatch

BARC (INDIA)
Post-Test Analysis
Thinned Area Location E

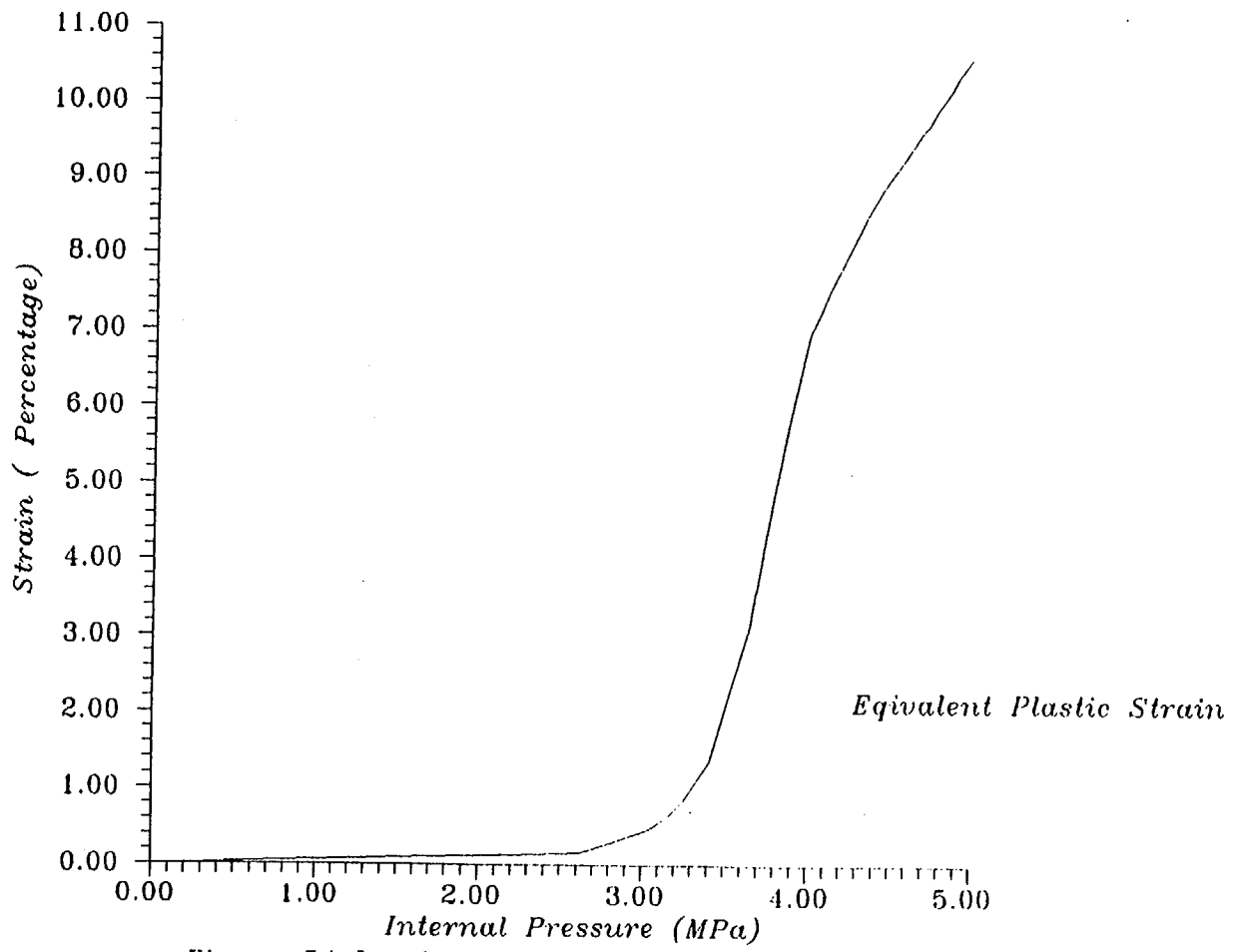


Figure 54 Local Shell Model Near Equipment Hatch

B-109

NUREG/CR-5678

BARC (INDIA)
Post-Test Analysis
Thinned Area Location F

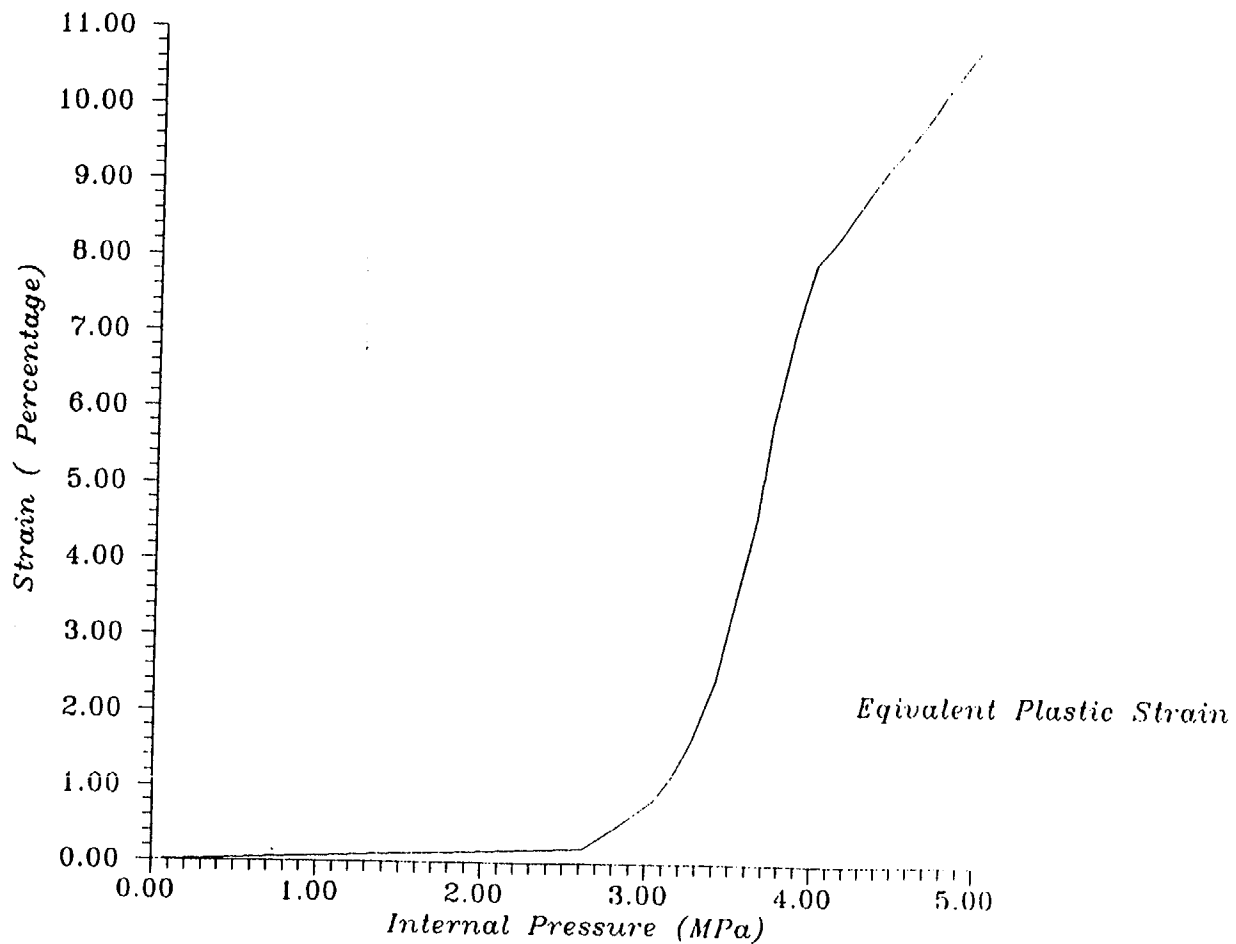


Figure 55 Local Shell Model Near Equipment Hatch

BARC (INDIA)
Post-Test Analysis
Thinned Area Location C

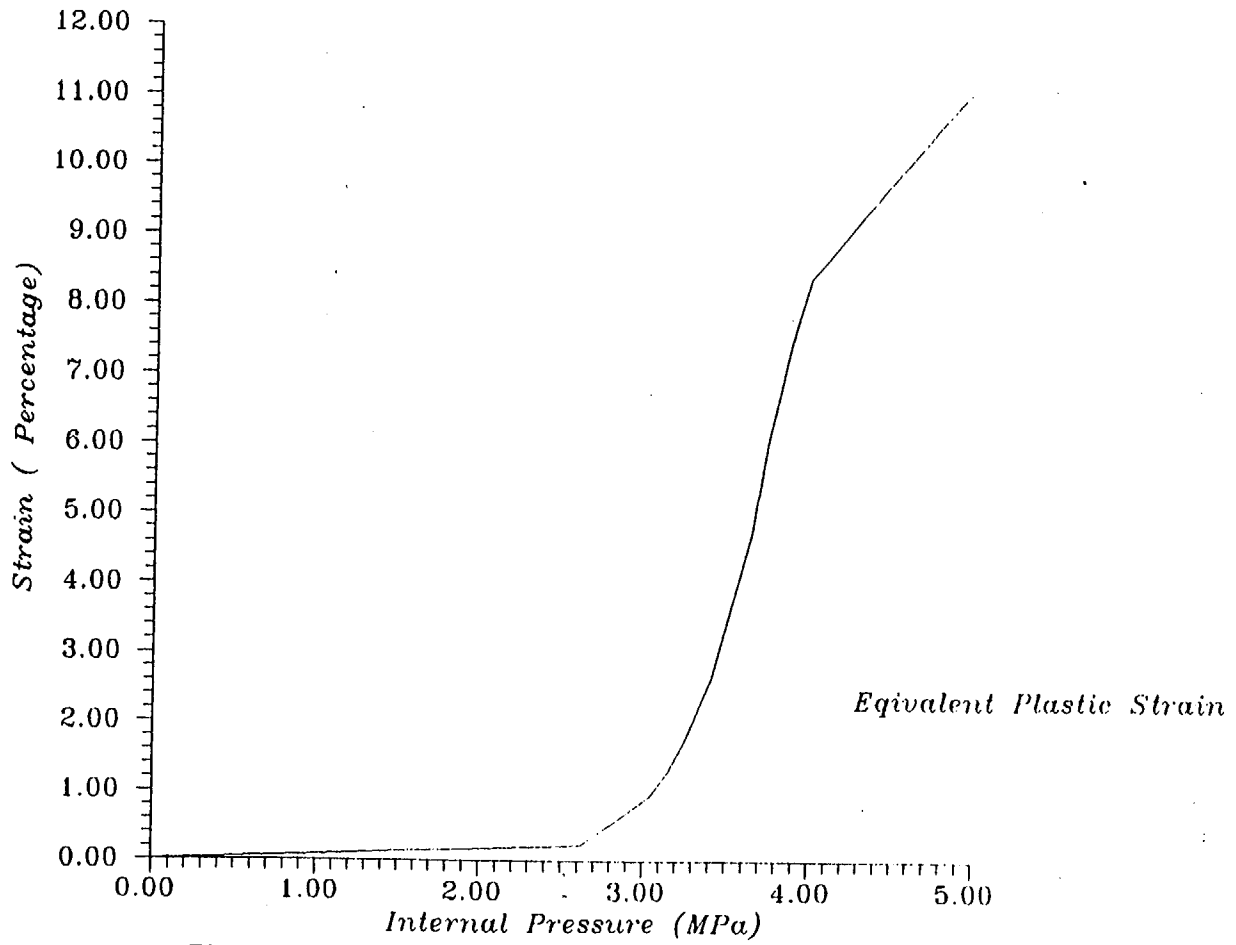


Figure 56 Local Shell Model Near Equipment Hatch

B-111

NUREG/CR-5678

BARC (INDIA)
Post-Test Analysis
Thinned Area Location H

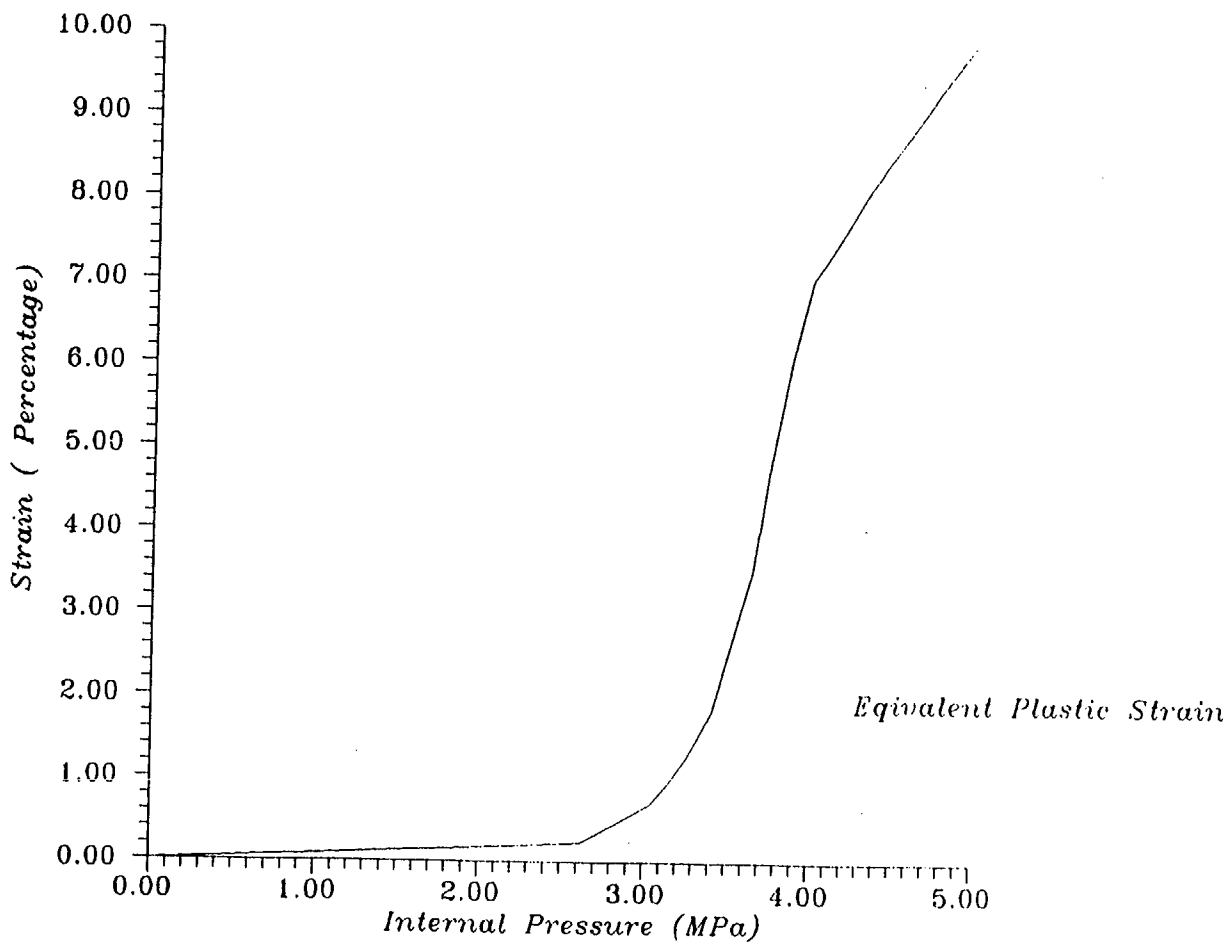


Figure 57 Local Shell Model Near Equipment Hatch

Appendix B-4

General Dynamics Electric Boat Division (GD-EB)

U.S.

ELECTRIC BOAT CORPORATION
A GENERAL DYNAMICS COMPANY

**NUPEC/USNRC STEEL CONTAINMENT VESSEL
ROUND ROBIN ANALYSIS PROGRAM**


ELECTRIC BOAT CORPORATION
POST-TEST EVALUATION OF THE
STEEL CONTAINMENT VESSEL

K. ARPIN

A. BEACHAM

T. HARRIGAN

REVIEWED BY


MINICUCCI

April 1998

ABSTRACT: This report documents Electric Boat Corporation's post-test evaluation of a steel containment vessel (SCV) as part of a research program sponsored by The Nuclear Power Engineering Corporation of Tokyo, Japan and the U.S. Nuclear Regulatory Commission. This program includes an internal pressurized test to failure of a model of a steel containment vessel enclosed by a steel contact structure. Round Robin pre-test and post-test analyses were coordinated by Sandia National Laboratories. Electric Boat Corporation employed a series of finite element models in the pre-test and post-test evaluations of the SCV. Material and geometric nonlinear analyses were performed using the ABAQUS/Standard Implicit Finite Element Program. Results of the evaluations include displacement and strain predictions for the SCV which were compared to the test response data. Pre-test failure predictions accurately identified the failure location for the most prominent tear in the vessel wall, which occurred at a pressure of 4.66 MPa (4.7 MPa predicted). Good correlation was generally observed between the test and analysis results for the pre-test predictive effort. Post-test analysis added additional insight into the effects of thickness and gap variations on the SCV response. Material properties in the Heat Affected Zone (HAZ) of welds and geometric details such as weld relief holes were demonstrated to be important when performing failure analyses.

Table of Contents:

Nomenclature	i
1.0 Purpose	1
2.0 Background	1
3.0 Pre-test Analysis Predictions	2
3.1 Response Predictions	2
3.2 Failure Prediction	7
4.0 Post-test Analysis Effort	8
4.1 Material Data	8
4.2 Parametric Investigation of Material Data	9
4.3 Parametric Investigation of Geometric Data	11
4.4 Equipment Hatch Area Response Evaluation	13
5.0 Post-test Failure Prediction	17
5.1 Equipment Hatch Area	17
5.2 Middle Stiffener Weld Relief Hole	19
6.0 SCV Standard Output Discussion	22
7.0 Conclusions	24
8.0 References	25
Appendix A Pre-test Correlation	A-1
Appendix B Post-test Correlation	B-1

Nomenclature:

C3D6	6-node linear triangular prism
C3D8	8-node linear brick
C3D8I	8-node linear brick, incompatible modes
CS	contact structure
E	Young's modulus
HAZ	Heat Affected Zone
ksi	thousand pounds per square inch
mm	millimeters
MPa	Megapascals
MPC	ABAQUS multi point constraint
NRC	U.S. Nuclear Regulatory Commission
NUPEC	Nuclear Power Engineering Corporation
P	pressure
PMAG	ABAQUS magnitude of plastic strain
psi	pounds per square inch
S3	ABAQUS 3-node triangular thin or thick shell, finite membrane strain element (Same as S3R)
S3R	ABAQUS 3-node triangular thin or thick shell, finite membrane strain element
S4	ABAQUS 4-node doubly curved thin or thick shell, fully integrated, finite membrane strain element
S4R	ABAQUS 4-node doubly curved thin or thick shell, reduced integration, hourglass control, finite membrane strain element
SCV	steel containment vessel
SNL	Sandia National Laboratories
μ	coefficient of friction

1.0 Purpose :

The purpose of this section is to describe the post-test analysis efforts performed by Electric Boat Corporation in the evaluation of the Steel Containment Vessel and Contact Structure as defined in References (1-3). Pretest response predictions are compared to test results and, where necessary, post-test analysis efforts are performed to examine deviations between test and analysis predictions.

2.0 Background :

This work is part of a multi-national analysis effort in the evaluation of the Steel Containment Vessel (SCV) and its interaction with a Contact Structure (CS). The SCV was internally pressurized resulting in an expansion of the vessel and subsequent contact between the SCV and the CS. The pressurization continued until failure of the SCV at a pressure of 4.66 MPa (676 psi). Figure 2.0.1 shows a simple schematic of the test configuration.

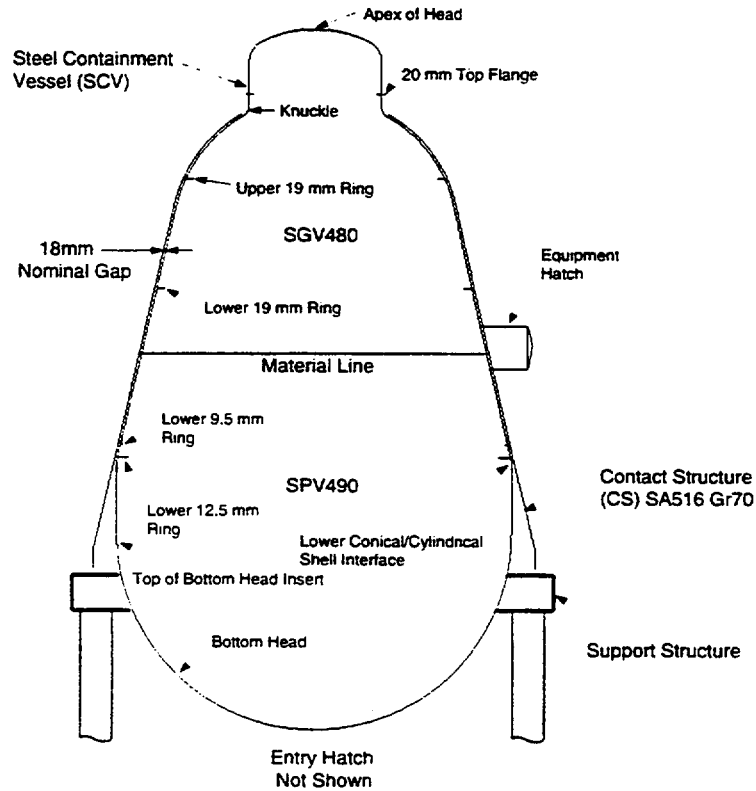


Figure 2.0.1
SCV and CS in Test Configuration

The Nuclear Power Engineering Corporation (NUPEC) of Tokyo, Japan and the U.S. Nuclear Regulatory Commission (NRC) funded all construction and test activities with Sandia National Laboratories (SNL) coordinating the "Round Robin" activities.

3.0 Pre-test Analysis Predictions :

3.1 Response Predictions :

Appendix A contains the comparison of pre-test analysis predictions and test results for the 43 gage locations defined in References (1) and (4). The test data was transmitted to Electric Boat Corporation by Reference (5). The analysis solutions with and without friction ($\mu=0.4$) are compared to the test results. A review of the results demonstrates that friction had very little effect on the SCV response results up to the failure pressure of 4.66 MPa. Also of note is that Section 5 of Reference (6) stated that the analysis results were insensitive to the level of friction as long as a reasonable level of friction was utilized ($0.2 < \mu < 0.4$) even for pressure substantially above the failure pressure. For these reasons, it has been determined that the effects of friction in this correlation effort can be safely ignored.

A review of the comparisons between the pre-test predictions and the test results shows good agreement in response behavior for the vast majority of the sensor locations. Response comparisons for the free field areas, the equipment hatch region, the transition areas, and the displacement sensors are discussed in the following paragraphs.

Examples of free field response behavior are shown in Figure 3.1.1 (Sensor Location 24 and 32) which are the inside hoop strains present in the upper conical section of the SGV480 material at two locations along the circumference. An axisymmetric model was utilized for these locations, therefore the same analysis data is used in each location. The use of mean properties (gap, plate thickness and material properties) results, in part, to a delay in the initial yielding of the material as well as an approximate ten percent underprediction of the maximum hoop strains at the time of contact with the CS. Pretest parametric investigations, as well as additional post-test evaluations (Section 4.2 and 4.3), demonstrate improved agreement with variation in model gap size, material properties and plate thickness. The variations in model material and geometric properties were within the variations observed in pre-test inspections of the SCV and CS documented in Reference (3).

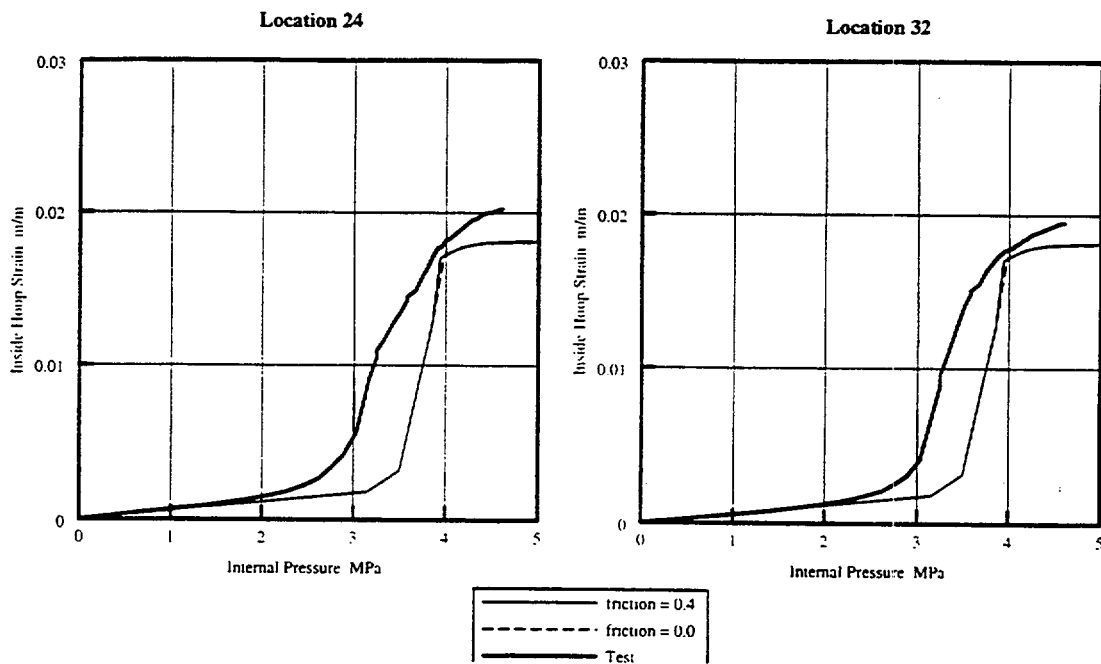


Figure 3.1.1

Typical Free Field Hoop Strain Correlation

In addition to the 43 defined sensor locations, Reference (5) included seven additional sensors at the same elevation level as Sensor 24 and 32 but at various points around the SCV circumference. Combined with the previously specified sensors

at this elevation, the hoop strains at the inside and outside surfaces are defined at five points around the circumference ($0^\circ, 45^\circ, 90^\circ, 180^\circ, 270^\circ$). The variation in test response data around the circumference (see Figure 3.1.2) illustrates the level of correlation which is obtainable using an axisymmetric model, since the hoop strains are identical around the circumference. This deviation in test response data is believed to be caused, in part, by variations in geometrical definition of the shell such as plate thickness.

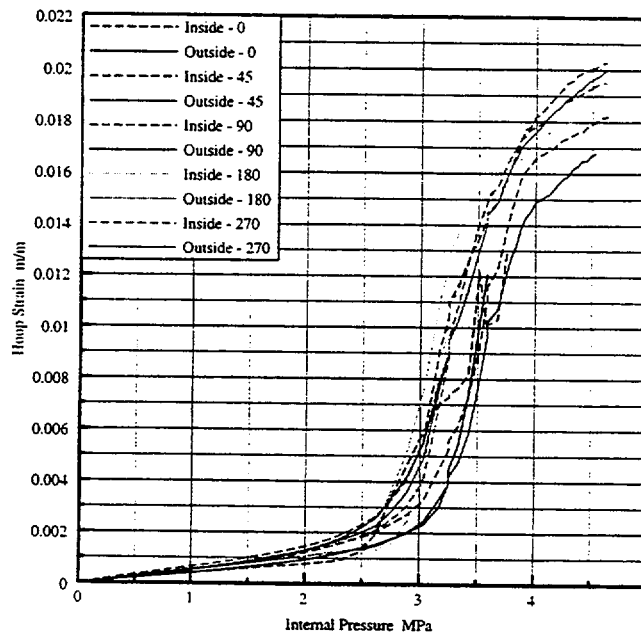


Figure 3.1.2

Test Results - Variation in Hoop Strain Around Circumference

Figure 3.1.3 shows the principal strain correlation which was obtained in the equipment hatch region. Sensor Locations 1 and 2 also show an initial delay in yielding but then over-predict the maximum strain at failure by approximately 25 percent. Other locations around the hatch show similar agreement with the exception of the additional sensors (Sensors 40-43) which were attached to the SPV490 material in the area where locally thinned plate was identified (References 3 and 4). The finite element shell model which was used to obtain the responses at this location utilized a band of elements for which the plate thickness was locally reduced to the minimum plate thickness pre-test measurement. The model nodes at the sensor locations were in this same area, resulting in significant strain levels which were not present in the test data. The location of the plate thickness variations were not accurately specified in Reference 3, therefore it is believed that the plate thickness representation was too conservative at the gage location. Improved agreement is demonstrated in the post-test analyses which utilized mean plate thicknesses (see Section 4.4).

The general behavior of the meridian bending strains at the transition sensors, with the exception of sensors 15 and 18, was simulated fairly well in the pre-test analyses. Sensors 15 and 18 are discussed later in this section. The meridian strain magnitudes at all transition sensor locations are minor with no recorded test strain exceeding 0.6 percent.

The sensors in the knuckle region are of greatest interest. Figure 3.1.4 shows meridian strains at Sensors 11 and 12 which are located above the knuckle, 4 cm below the top flange. Both sensors show that the shape of the response curve is simulated well, however, the peak strains are overpredicted. In addition, the material yields late and contact occurs at a slightly lower pressure. The comparison also shows some variation in the response for strains falling in the initial portion of the analytical plasticity curve prior to significant strain hardening. The poor curve definition in this area is most likely due to the relatively large spread in the test data and the small magnitude of the strains in this area. The improved correlation shown in the free field post-test parametric evaluations of gap size, material properties, and plate thickness would also apply to the transition areas and would account for some of these variations. It should be noted that this region is also particularly sensitive to contact between the CS and the SCV at the knuckle, as was discussed in Section 4.3 of the

Reference 6 pre-test report. In addition, the transition areas seem to be sensitive to the definition of the material curves in the perfectly plastic region prior to strain hardening.

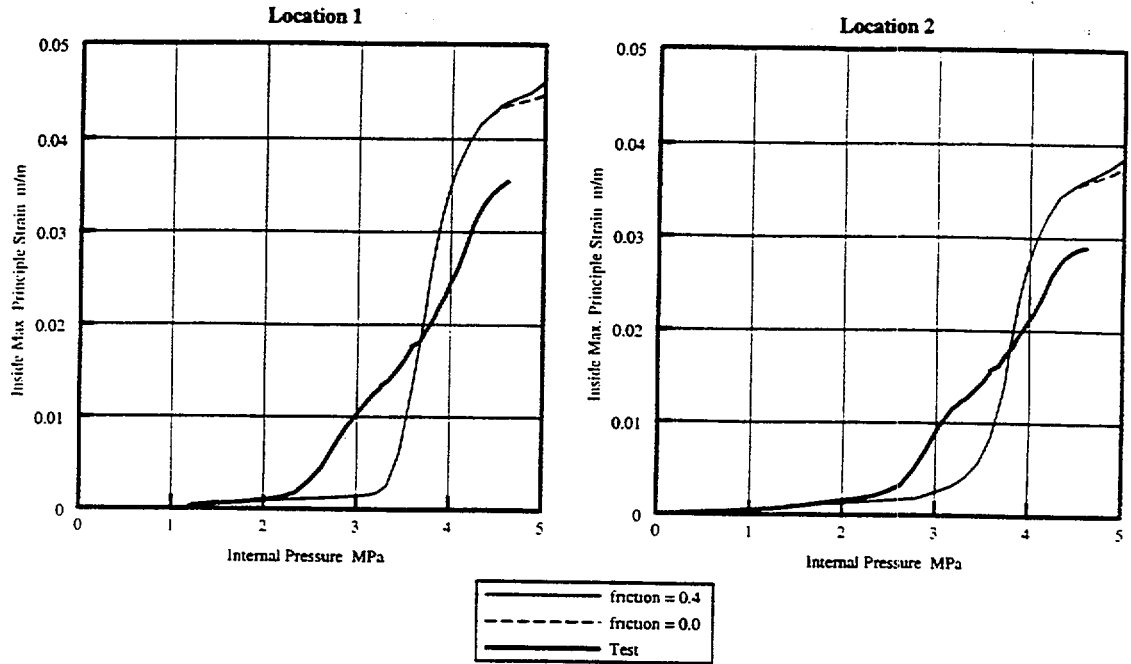


Figure 3.1.3
Principal Strain Correlation Near Equipment Hatch

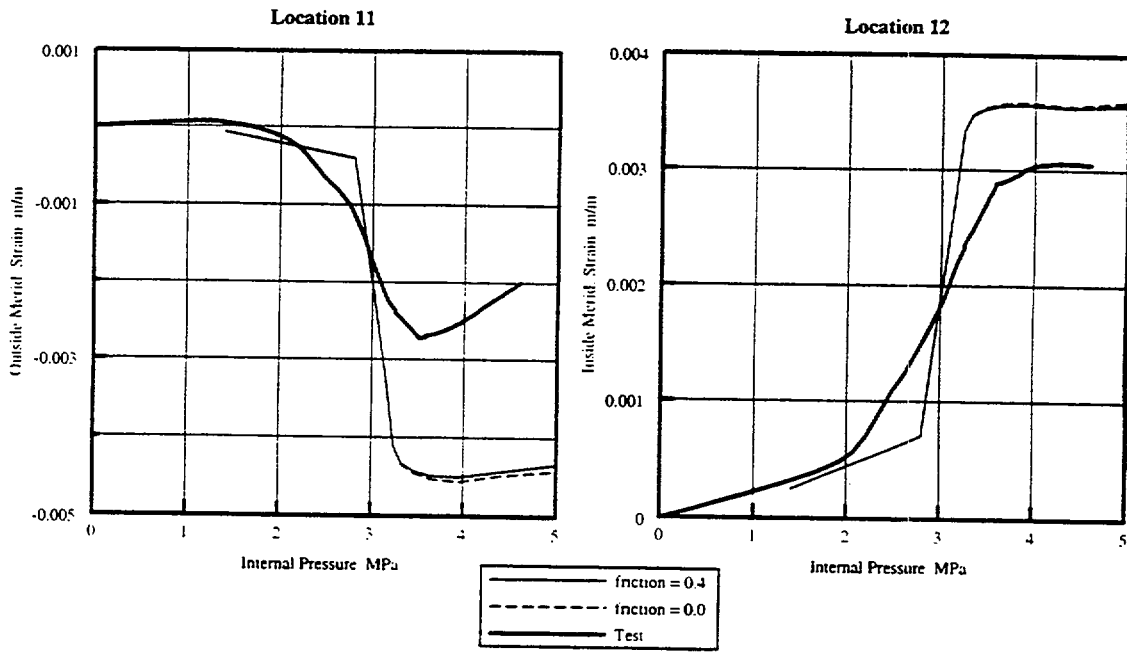


Figure 3.1.4
Typical Transition Area Meridian Strains - Just Below Top Flange

Sensor 15 showed poor correlation to the test data. A post-test review of the load incrementation utilized in the pre-test analysis showed that the increment of load was from approximately 2.8 MPa to 4.9 MPa thereby stepping past the reversal of meridian strain present at Sensor Location 15. A post-test analysis of the same model but with reduced load incrementation step size, improved the agreement significantly. The response at the Sensor 18 location also had poor correlation to test data. The outside meridian strain at the same location correlated to the same level of agreement as the other transition gages but the inside meridian strain was of opposite sign. A review of all the participant predictions shown in Reference 5 also shows similar behavior. It is believed by Electric Boat Corporation that the electrical signal was reversed resulting in a reversal of strain. Other instrumentation problems are documented in Reference 7. Therefore the test strain data was multiplied by -1.0. The improved correlation shown at sensors 15 and 18 is shown in Figure 3.1.5.

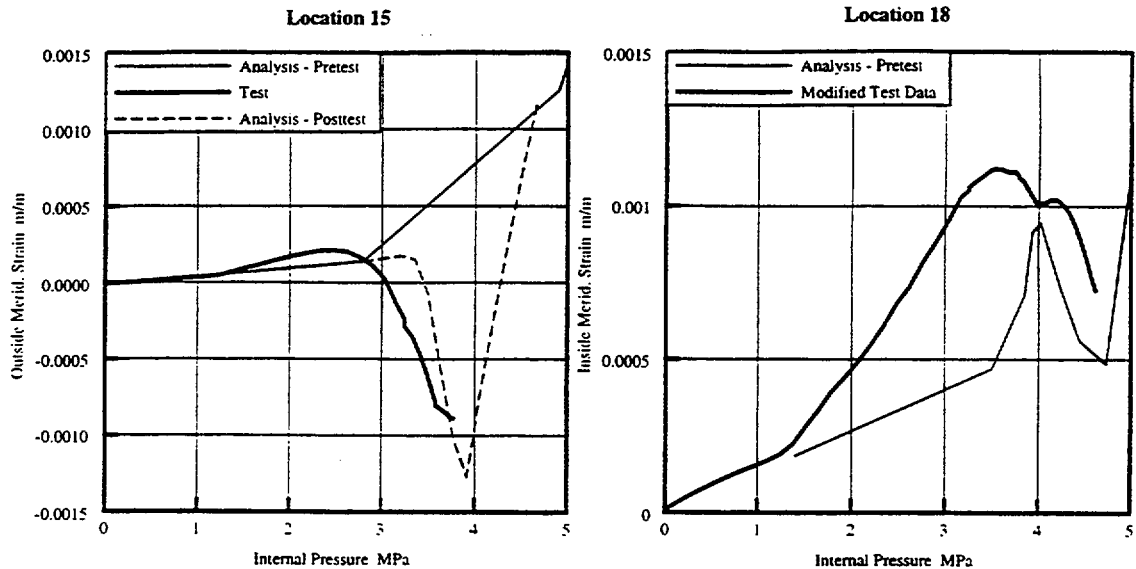


Figure 3.1.5
Improved Strain Correlation at Sensors 15 and 18

A review of the displacement sensor pre-test predictions and the test results shows good agreement in response behavior with the exception of the horizontal displacements at Sensor Locations 36 and 39. Good correlation in the vertical displacements at the apex of the head (Location 35) and at 4 cm below the knuckle (Location 38) are shown in Figure 3.1.6. The poor correlation demonstrated for the horizontal displacements above the top flange (Location 36) and at the center of the equipment hatch (Location 39) is shown in Figure 3.1.7. Similar trends in the displacement response are shown for both sensors. The displacement reversal at Location 36 as the SCV contacts the CS at the knuckle, for example, is clearly shown at approximately 3.2 MPa in the pre-test analysis data and at approximately 3.8 MPa in the test data. However, the magnitudes of the displacements do not correlate. No improvement in the correlation was gained from the post-test analyses performed. It should be noted that all the participant predictions given in Reference 5 show similar behavior at these two sensors.

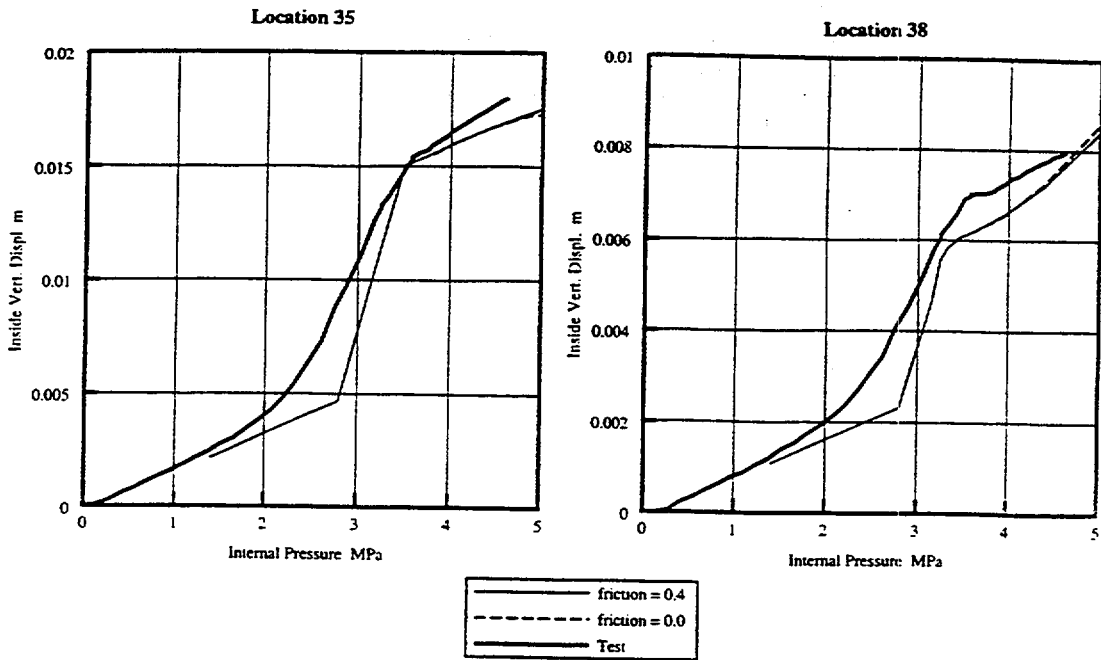


Figure 3.1.6
 Vertical Displacement Correlation at Sensor Locations 35 and 38

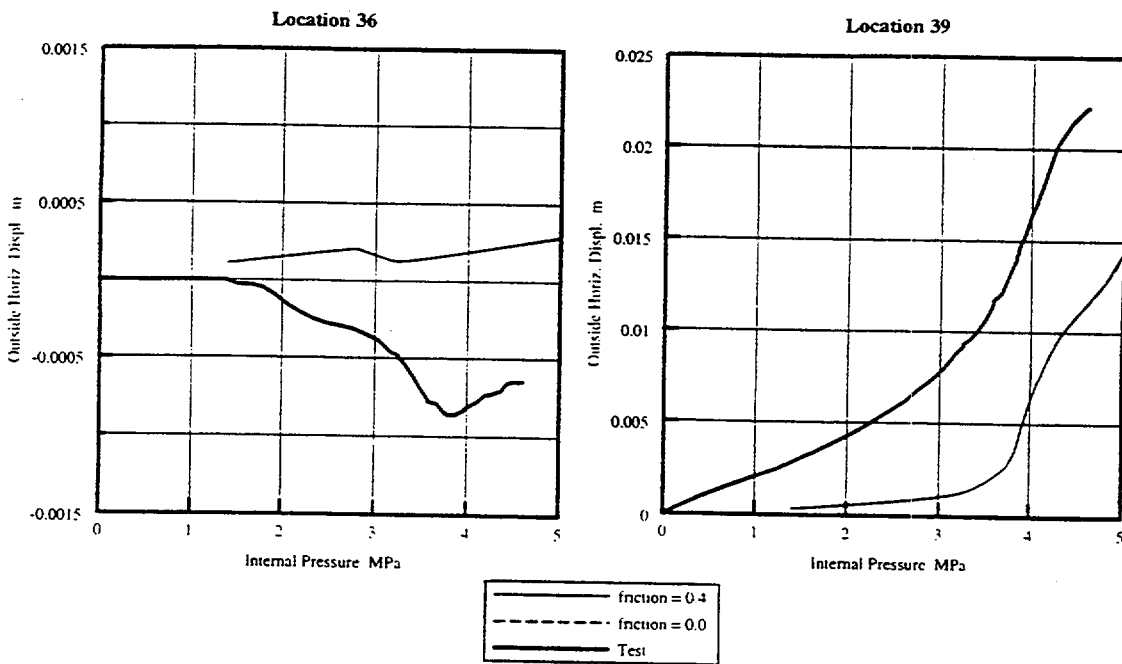


Figure 3.1.7
 Horizontal Displacement Correlation at Sensor Locations 36 and 39

3.2 Failure Prediction :

The pre-test failure prediction utilized a minimum ultimate strain reduced by a series of reduction factors to account for variations and unknowns in the as-tested SCV as the method for determining a suitable maximum pressure. It was believed that the use of reduction factors would ensure that the pressure specified was achieved. The critical area identified was the equipment hatch area below the material interface. The SPV490 base steel possessed a minimum ultimate strain of 10.0 percent. This strain was reduced by a combined reduction factor of 1.23 which included factors for gap variation, friction and as-built structural details. The resulting "failure" limit strain was therefore defined as 8.0 percent. The maximum pressure determined by allowing the peak equivalent strain to obtain this failure limit value through the thickness of the shell was 4.7 MPa (680 psi). Figure 3.2.1 shows the location of the maximum strains at a pressure of 4.7 MPa.

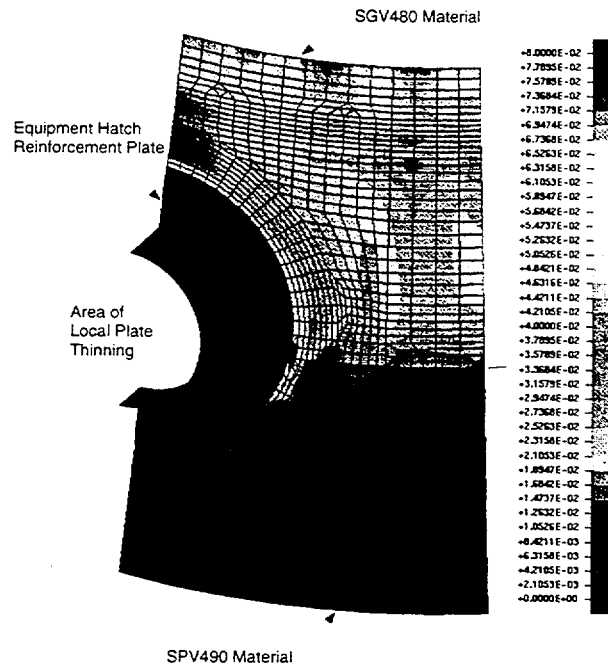


Figure 3.2.1

Deformed Fringe Contour Plot of the Locally Thinned SCV Submodel of the Equipment Hatch Area
Mid-fiber Equivalent Plastic Strain - P=4.7 MPa (680 psi) - Deformed Scale =1.0

Dry nitrogen gas at ambient temperature was added to the SCV to a maximum pressure of 4.66 MPa when leaking was noted. Reference 8 details the damage to the SCV as well as post-test metallurgical evaluations which contain valuable information utilized in the post-test failure evaluation (Section 5.0). Localized damage was observed at several locations on the SCV model. Pre-test predictions correctly identified the most significant failure location, which was a ~190 mm tear at the Equipment Hatch reinforcement plate and shell plating interface. The majority of the deformation and tearing occurred along the weld between the reinforcement plate and the lower SPV490 material, however, the localized strain also crossed the horizontal weld into the thinner, but higher, ultimate strain SGV480 material. Symmetrically on the other side of the hatch, a localized neck also formed but a tear did not occur.

A 55 mm vertical tear also occurred in the SCV wall below a weld relief hole in the lower 19 mm thick ring. Local necking also occurred at a similar relief hole 180 degrees away at the same elevation. Weld relief holes (see Figure 5.2.1) are provided in the ring stiffener to accommodate the vertical welds joining the sections of the middle conical shell. The relief hole geometry was not included in the pre-test analysis effort. Post-test analyses (Section 5.2) will investigate the effect of the relief hole on strains in the SCV shell. Local necking also formed within the vertical weld lines at the 160 and 340 degree positions which connect the two plates forming the lower conical shell (SPV490 material) but tears did not occur.

4.0 Post-test Analysis Effort :

4.1 Material Data :

A review of the pre-test predictions shows a delay in the prediction of material yielding at a majority of the sensor locations. Since mean material properties were utilized in all pre-test simulations, the sensitivity of response to material property variation was not examined. For all material locations, a minimum material property curve was developed which also included the use of minimum elastic properties. A minimum Young's Modulus (E) of 203,000 MPa (29,440 ksi) for the SGV480 steel and a minimum Young's Modulus of 214,600 MPa (31,150 ksi) for the SPV490 steel was utilized (Reference 2).

In addition, a fitting procedure utilized by Sandia National Laboratories (SNL) and the Nuclear Power Engineering Corporation (NUPEC) of Japan in the pre-test evaluation effort was also examined. As was done in the SNL pretest report, two different hardening plasticity models were utilized, the inverse hyperbolic sine function for the SGV480 steel and the power law hardening model for the SPV490 steel.

Figures 4.1.1a and 4.1.1b show a comparison of the various material data fits for two different plate thicknesses of SGV480 steel. Figure 4.1.1a (Material Location Id 3) is for a 7.5 mm thick plate utilized in the conical section of the SCV shell. As can be seen, there is only a minor difference between the mean Least Squares fit and the minimum material fit. The inverse hyperbolic sine function fit matches well at the extremes of the plot, but deviates from the test data in the moderate strain range (~2.0 to 8.0%). Figure 4.1.1b (Material Location Id 4) is for an 8.0 mm thick plate used in the spherical shell section just above the conical section shown in Figure 4.1.1a. A more significant variation between the mean and minimum properties is shown, as well as a slight lowering of the initial yield stress value as compared to Figure 4.1.1a.

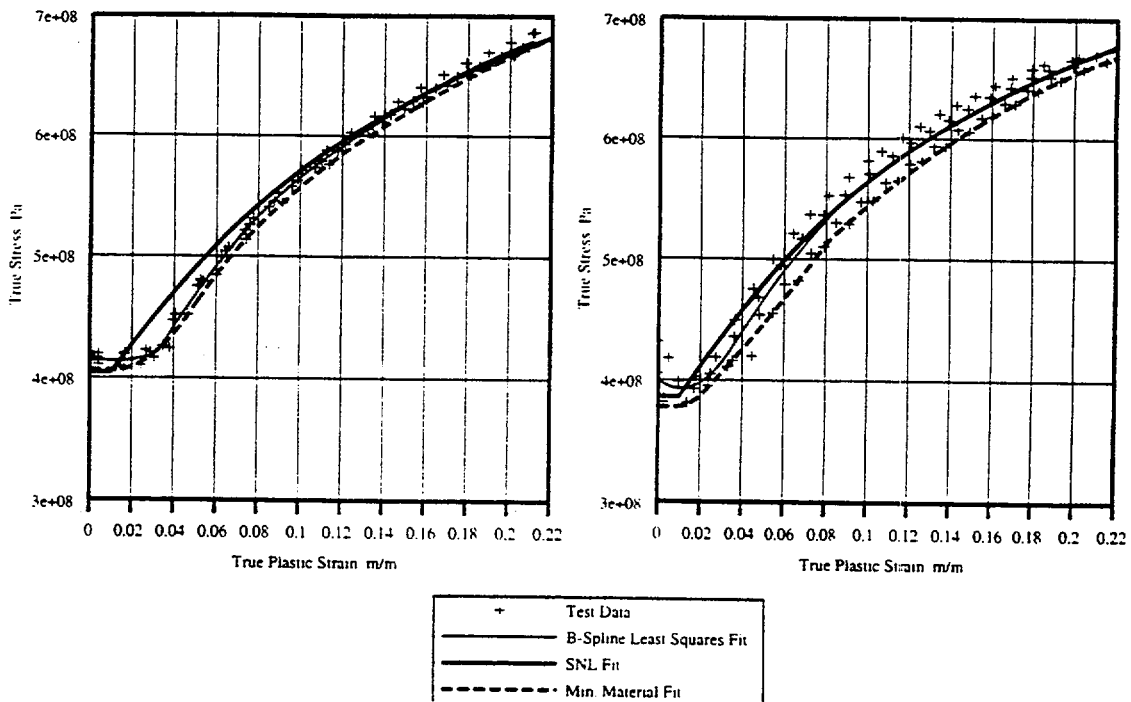


Figure 4.1.1a

Figure 4.1.1b

True Stress True Plastic Strain Data Fit
 SGV480 Steel 7.5 mm Thick Conical Shell 3 Location 3
 SGV480 Steel 8.0 mm Thick Spherical Shell Location 4

Figures 4.1.2a and 4.1.2b show a comparison of the various material data fits for two different plate thicknesses of SPV490 steel. Figure 4.1.2a (Material Location Id 11) is for a 9.0 mm thick plate utilized in the conical and cylindrical sections of the SCV shell. As can be seen, there is a noticeable difference between the mean Least Squares fit and the minimum material fit. The variation is caused by the different material properties in the two plate material directions (rolling direction and transverse to the rolling direction), with the rolling direction properties being softer. The power law hardening function fit matches the rolling direction properties at the extremes of the plot and approaches the transverse direction properties in the moderate strain range (-2.0 to 6.0%). Figure 4.1.2b (Material Location Id 12) is for a 17.5 mm thick plate used in the equipment hatch reinforcement plate. Minor variations between the mean and minimum properties are shown but the yield stress is significantly lower than the 9.0 mm thick plate.

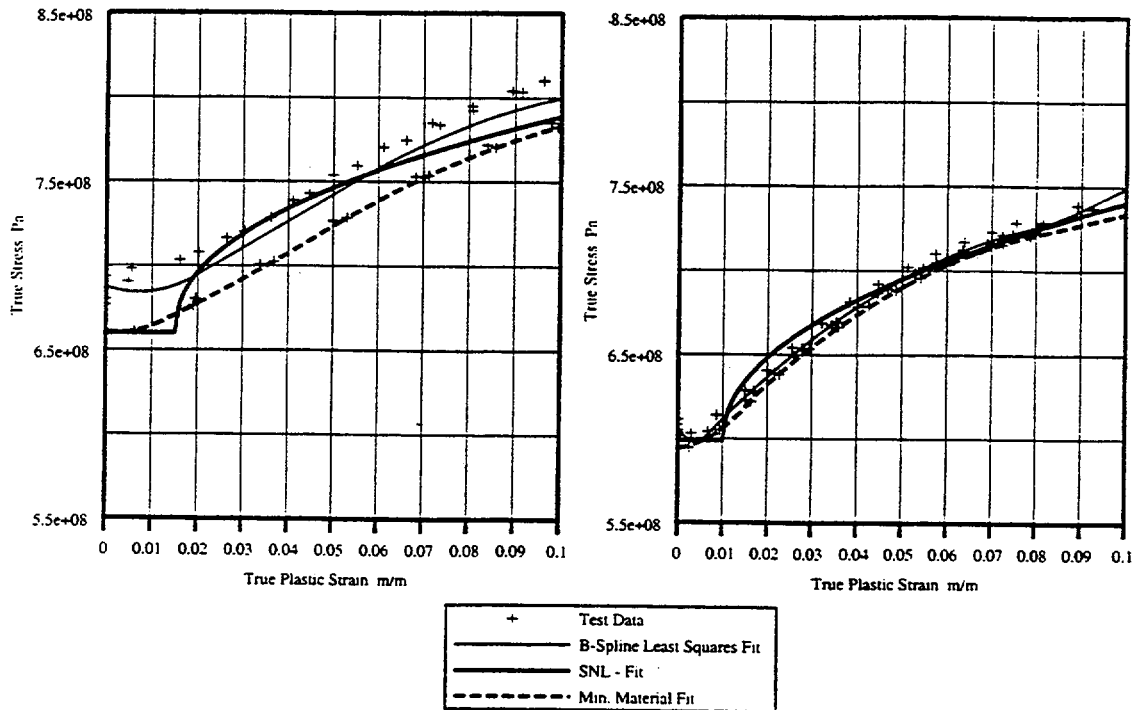


Figure 4.1.2a

Figure 4.1.2b

True Stress True Plastic Strain Data Fit
 SPV490 Steel 9.0 mm Thick Conical and Cylindrical Shell Location 11
 SPV490 Steel 17.5 mm Thick Reinforcement Plate Location 12

4.2 Parametric Investigation of Material Data :

To investigate the various material data fits, the pre-test axisymmetric model developed in Reference 6 was utilized. Specifically, the model is based on mean plate thicknesses (Reference 6, Table 4.1.1), average gap (21 mm) and a coefficient of friction (μ) equal to 0.40. The CS utilized elastic properties since the structure remains elastic up to the failure pressure of 4.66 MPa. The material properties for all the material point locations were modified to include either the minimum material properties or the functional fit of the test data. As a comparison, the mean material properties were also re-evaluated using the Reference 9 finite element program. Figures 4.2.1a and 4.2.1b show the inside and outside hoop strains present in the nominal 7.5 mm conical section of SGV480 steel. In each plot, test hoop strains which approximately bound all the hoop strains recorded around the circumference ($0^\circ, 45^\circ, 90^\circ, 180^\circ, 270^\circ$) are plotted along with the three material data fits. As can be seen, the variation in material properties has negligible effect. There is clearly more variation in the test data around the perimeter of the vessel than in the material data fitting procedure.

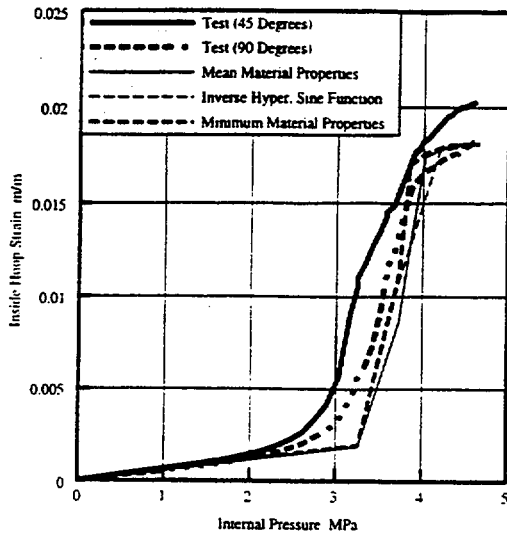


Figure 4.2.1a

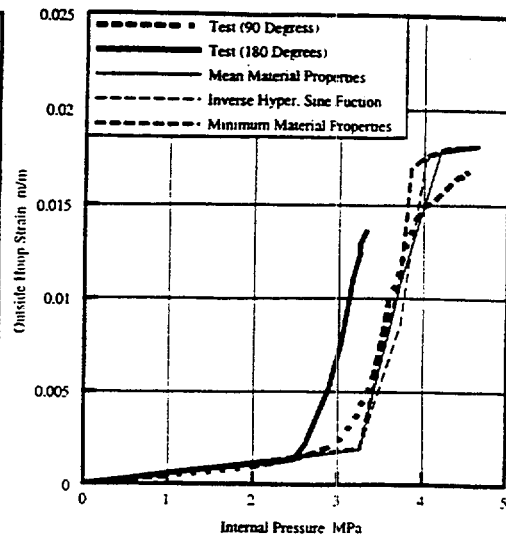


Figure 4.2.1b

Material Data Data Fit Parametric Comparison
Hoop Strains in 7.5 mm Thick Conical Section of SGV480 Steel

Figures 4.2.2a and 4.2.2b show the inside and outside hoop strains present in the nominal 9.0 mm conical section of SPV490 steel. This material showed the largest spread in material test data and hence the largest differences among the data fitting methods. This test data is the only free field paired (inside, outside) hoop strain test data available for the SPV490 material so it was used regardless of the small magnitude of strains which were present. As can be seen, the variation in material properties has only a minor effect in improving the level of correlation for the hoop strain. Agreement between the analysis prediction and test data for the inside hoop strain is very good for all material models. The power law hardening model and the minimum material properties models produce similar results for this strain magnitude. Figure 4.1.2a shows that both material data fits are nearly identical for strains less than 0.006 m/m and use a minimum material yield point.

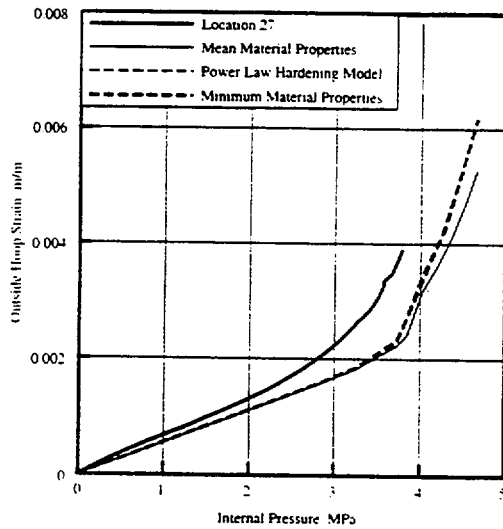


Figure 4.2.2a

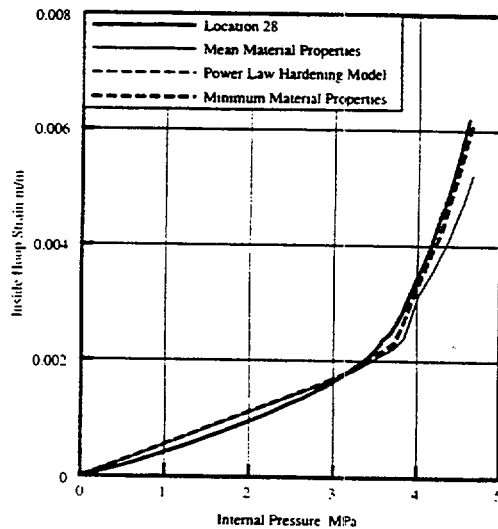


Figure 4.2.2b

Material Data Data Fit Parametric Comparison
Hoop and Meridian Strains in 9.0 mm Thick Conical Section of SPV490 Steel

4.3 Parametric Investigation of Geometric Data :

The material data parametric investigation showed there were minor improvements in correlation to test data utilizing the available material test data. Investigations into variations in response due to plate thickness deviations and gap variations were performed in the pre-test analysis report, Reference 6. Gap distance studies were performed ranging from a minimum gap of 17 mm to a maximum gap of 24 mm, which approximately bounded the actual gap variation reported in Reference 3. Variations in hoop strain after contact with the CS were most notable in the study. Plate thickness studies included a mean thickness and minimum thickness plate comparison. Table 4.3.1 shows the thicknesses used in the two investigations. Each study was performed separately to examine the effects of a single perturbation of a modelling parameter (gap, plate thickness, friction, and analytical solution strategies). Therefore, no 'worst case' condition was performed. To evaluate the effect on the SCV response, an axisymmetric finite element model was developed which was considered to be a conservative combination of modelling parameters. Specifically, the model used the minimum material properties discussed in Section 4.2, a gap distance of 24 mm, and the minimum plate thickness which may have been present. Unlike the pre-test thickness study, which used the minimum plate thickness measured around the circumference of the SCV shell at 45 degrees increments (Reference 3), this study utilizes the minimum of these measured values or design values. The highlighted values in Table 4.3.1 are the values used in the 'worst case' model.

Design Thickness (mm)	Material Location Id	Thickness Label	Minimum Thickness (mm)	Mean Thickness (mm)
6.0	1	T18, T19	6.1	6.8
6.0	2	T21	6.7	6.8
7.5	3	T11, T12, T13	7.2	7.8
8.0	4	T14, T15	7.6	7.9
8.5	5	T7, T8, T9	8.2	8.7
9.5	6	T6	9.6	9.9
12.5	7	T5	13.1	13.3
19.0	8	T10	19.2	19.5
19.0	8	T16	19.8	19.9
20.0	9	T20	20.2	20.7
16.5	10	T17	16.2	16.8
9.0	11	T1-T4	8.8	9.48
17.5	12	T22	17.6	18.0
20.0	9	T23	20.2	20.7
20.0	9	T24	20.3	20.4

Table 4.3.1 - SCV Design and Minimum/Mean As Built Plate Thicknesses

The 'worst case' model therefore represents, to the extent possible given the available information, a model which may be used to perform design calculations and should, in theory, always upper bound the test predictions. Comparisons are made, as before, to the free field strain locations present in the nominal 7.5 mm thick SGV480 steel, as well as the nominal 9.0 mm thick SPV490 material. Figures 4.3.1a and Figure 4.3.1b show the inside and outside hoop strains present in the SGV480 conical section. An improvement in agreement to the test data is apparent, however, the 'worst case' model referred to as the Min/Max Model (minimum material and thickness, maximum gap) does not upper bound the extreme test response curves shown for the complete load history. A true lower bound model would use maximum thicknesses, maximum material properties, and minimum gap values. A review of the pre-test parametric studies shows that the mean thickness, mean material, minimum gap model already lower bounds the peak strain. Therefore, those results are plotted and no lower bound model was developed. Maximum test strains are therefore bounded by the simulations, but the onset of yielding is not.

Figures 4.3.2a and Figure 4.3.2b show the free field hoop strains present in the 9.0 mm SPV490 conical section. Again improved correlation in the initial straining of the shell is demonstrated by the Min/Max Model over the Mean Model but the results do not upper bound the test results for both complete load histories. Maximum strains are, however, either equal or are conservatively predicted by the 'worst case' model. The Minimum Gap Model is not shown since contact has not occurred in the lower shell area.

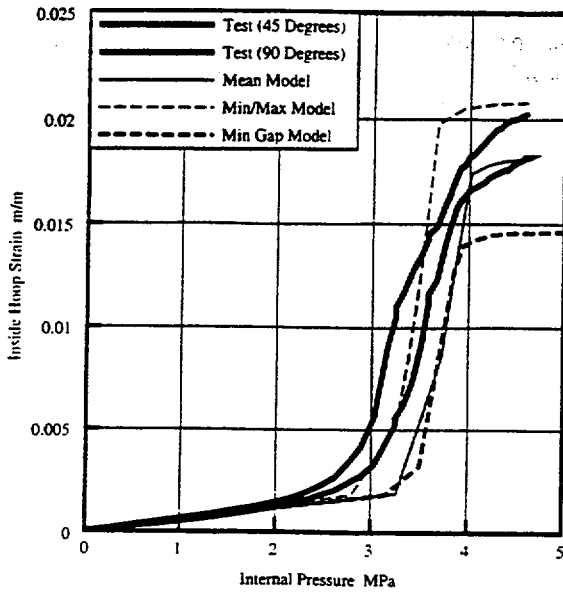


Figure 4.3.1a

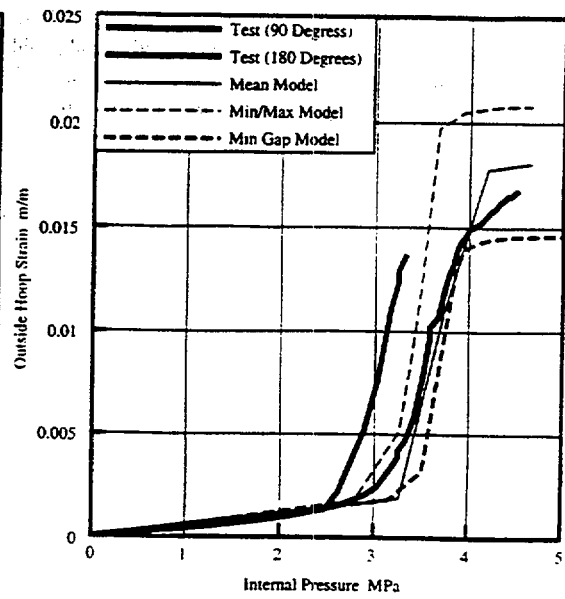


Figure 4.3.1b

Bounding Analysis Comparison
Hoop Strains in 7.5 mm Thick Conical Section of SGV480 Steel

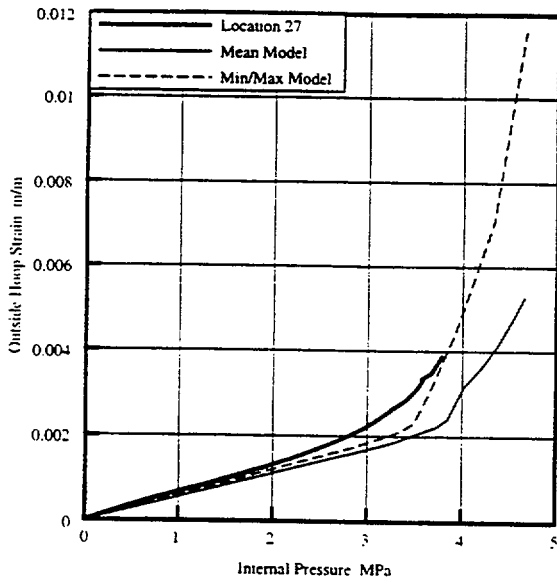


Figure 4.3.2a

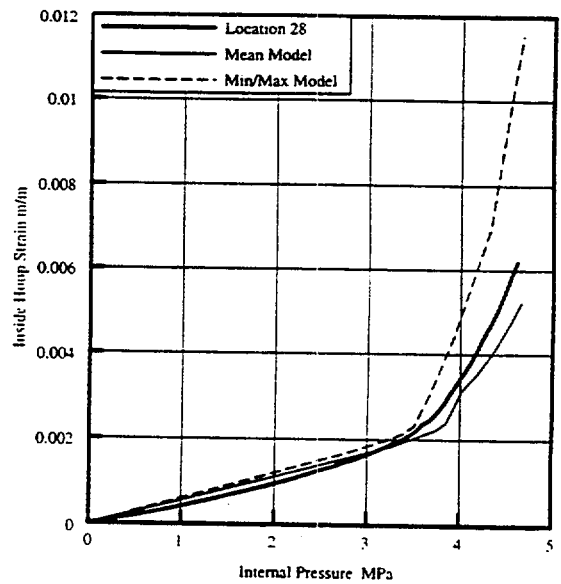


Figure 4.3.2b

Bounding Analysis Comparison
Hoop and Meridian Strains in 9.0 mm Thick Conical Section of SPV490 Steel

4.4 Equipment Hatch Area Response Evaluation :

Correlation around the perimeter of the equipment hatch reinforcement plate is consistent with other areas of the SCV with the exception of the gages which were added near the reinforcement plate / 9.0 mm thick SPV490 steel shell interface (Sensors 40-43). To improve the agreement, the shell models were modified to better represent the thinned areas identified in Reference 3. Since the plate thinning around the hatch area was not symmetric, it was necessary to expand the quarter symmetry model developed in the Reference 6 pre-test report to a half symmetry model. The global model, shown in Figure 4.4.1, is similar to the quarter symmetry model. Mean material, mean gap (21 mm in shell area, 25.7 mm around hatch) and mean thickness were used as before. The CS was treated as a linear structure, since the structure was shown to remain elastic in the pre-test report at pressures below 4.66 MPa. The main objective of the global model was to obtain edge displacements for the equipment hatch area submodels.

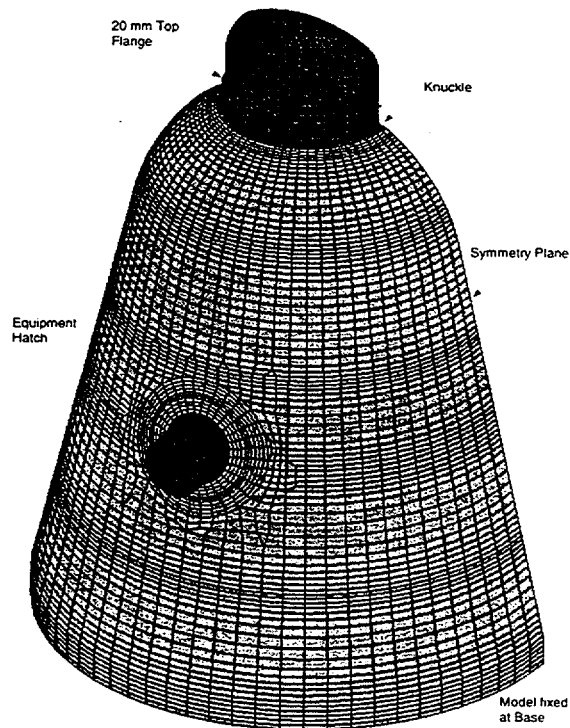


Figure 4.4.1

1/2 Symmetry Shell Model of the SCV and CS

The model was also used to examine the SCV and CS contact condition at the time of failure. Figure 4.4.2 shows a color fringe contour of the SCV / CS shell gap distances at a pressure of 4.66 MPa. The dark blue bands in the 7.5 and 8.5 mm thick SGV480 conical shell sections are clearly seen, which identify contact between the two shells. Contact also occurs in the knuckle region, but the axisymmetric solid model of the knuckle region (see Section 10.0 of the pre-test report) predicts this behavior more accurately. The lower SPV490 shell and reinforcement plate are not in contact in this simulation. Gap closure test data was not supplied in Reference 5, so no correlation to test data is possible at this time. Figure 4.4.3 shows a magnified deformed plot of the SCV at the failure pressure of 4.66 MPa. The restraint of the shell by the radial stiffeners and hatch reinforcement plate is clearly seen.

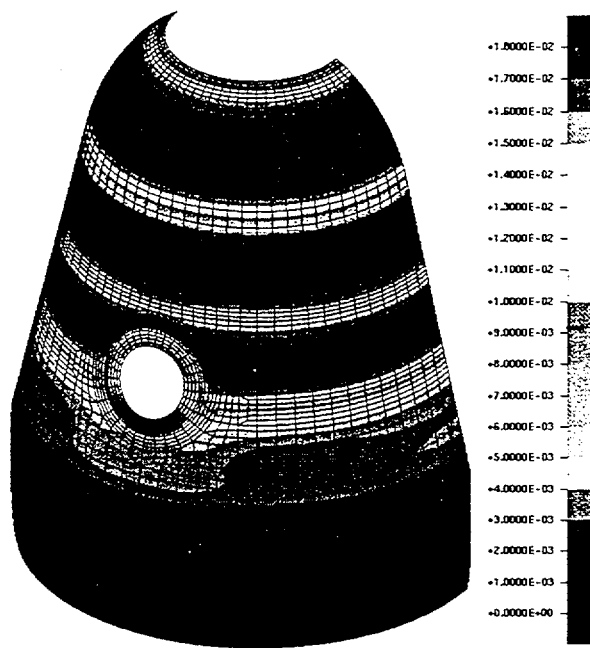


Figure 4.4.2

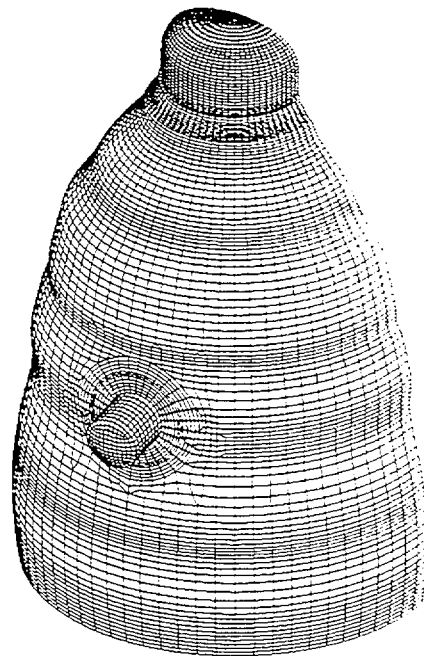


Figure 4.4.3

Gap Distance Fringe Contour at Failure Pressure - P=4.66 MPa
SCV Deformed Shape Plot - Scale=5.0

The pre-test submodel of the equipment hatch was expanded to include the full hatch. Additional model refinement was included in the areas of the shell tear and thinning near the hatch. Two variations of the submodel were used to evaluate the response in the equipment hatch area. The first is similar to the global model in which mean plate thicknesses were used. The second attempts to simulate the plate thinning caused by grinding that was identified in Reference 3. Since no specific locations were specified in Reference 3, the location was approximated based on the relative location to the hatch reinforcement plate. In addition the reduced integration finite membrane strain shells (S4R) used in the pre-test model were replaced with newly developed fully integrated finite membrane strain elements (S4). The S4 element has four integration points per element compared to the single integration point of the reduced element formulation. The element does not have hourglass modes in either the bending or membrane response, therefore hourglass control is not required. The associated three node shell, S3 is, however, identical to the S3R element previously utilized. A detailed discussion on the formulation of the element is contained in Reference 9.

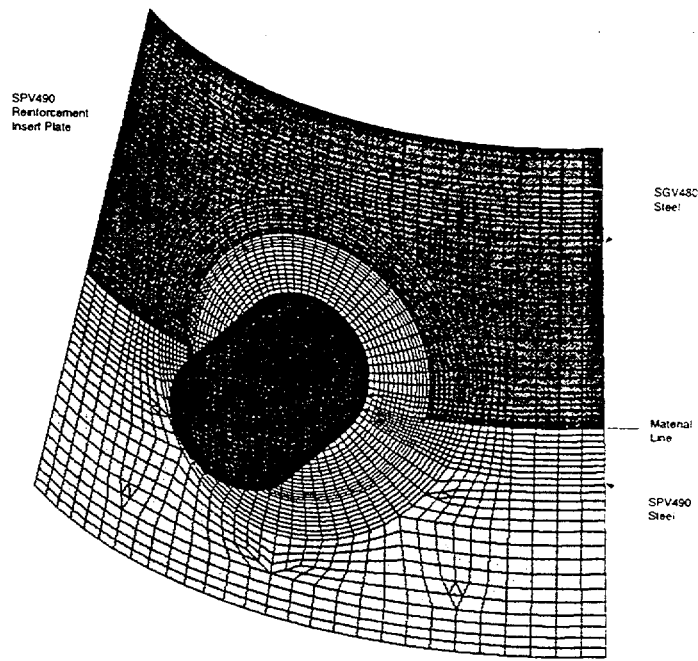


Figure 4.4.4
Submodel of Equipment Hatch Area - CS Removed for Clarity

Figure 4.4.5 shows the plate thickness used in the local plate thinning submodel. The pre-test model used a strip of elements with the minimum plate thicknesses specified in Reference 3, in order to add a level of conservatism to the failure pressure level prediction. As previously discussed, the pre-test model significantly over-predicted the strains for sensors 40 through 43. This post-test evaluation utilizes a more gradual transition from the mean plate thickness to the minimum plate thickness.

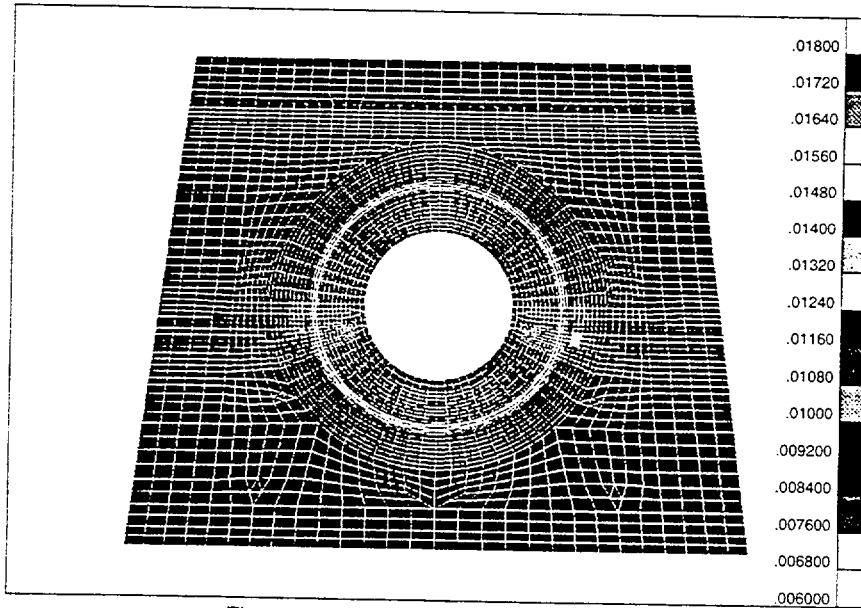


Figure 4.4.5 Submodel of Equipment Hatch Area
Plate Thickness Variations in Local Plate Thinning Model - Equipment Hatch Not Shown

Figure 4.4.6 shows the post-test results from the mean and local plate thinning models as compared to sensors 40 through 43. Correlation is significantly improved over the pre-test predictions. The meridian strains now show the strain reversal present in the test data, with the mean and local thinning models bounding the maximum test strain. Hoop strains are also improved with the best correlation coming from the use of mean plate thicknesses. The sensitivity of response to plate thickness in the area of the hatch is clearly seen through the comparison of the various simulations. Since the location of the local plate thickness was not specifically identified, improvements in correlation above what has been achieved is considered unlikely.

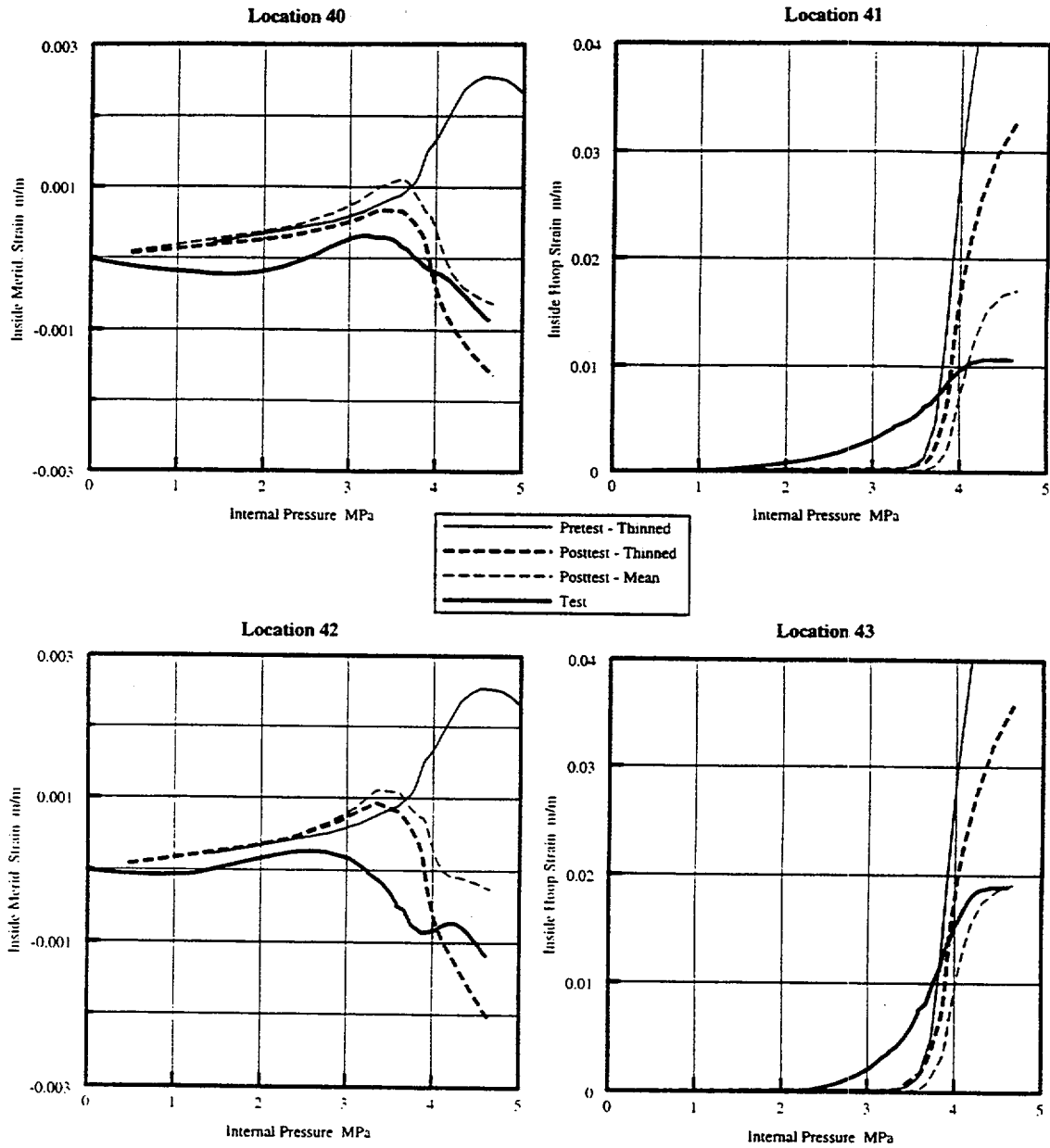


Figure 4.4.6
 Post-test Correlation at Sensors 40-43
 Mean and Local Plate Thinning Models

5.0 Post-test Failure Prediction :

5.1 Equipment Hatch Area :

Reference 8 discusses in detail the three areas of damage which occurred on the SCV shell. The most significant was an approximately 190 mm tear along the edge of the Equipment Hatch reinforcement plate. The tear originated in the SPV490 material but also propagated across the material line into the SGV480 material. Necking was also noted on the other side of the equipment hatch in a similar area. A review of the pre-test report shows a through thickness maximum strain of 8.0% at a pressure of 4.7 MPa. The post-test model which included a more gradual representation of the locally thinned area had a maximum mid-fiber strain of approximately 7.5% at the failure pressure of 4.66 MPa. The location of the maximum strain is also some distance from the model tear as shown in Figure 5.1.1.

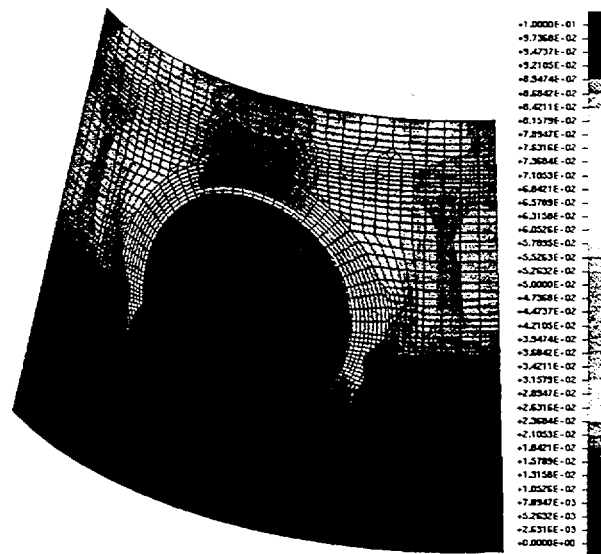


Figure 5.1.1
Post-Test Mid-Fiber Plastic Strain Magnitude at P=4.66 MPa
Locally Thinned Finite Element Model

A review of the post-test metallurgical evaluation report, Reference 8, states that the Heat Affective Zone (HAZ) of the SPV490 welds consistently showed a significantly lower hardness. HAZ material that had not been substantially deformed had an average Rockwell B hardness of 90.7 compared to the average base material of 97.4. This suggests a HAZ engineering ultimate tensile strength of approximately 625 MPa, 100 MPa lower than the base metal. This value is near the lower ultimate strength design specification. The Fusion Zone of the weld had an average hardness value of 96.2 with the final fusion regions being slightly harder (~97) and the altered early passes being slightly softer (~94). As stated in Reference 8, metallurgical analysis "indicates that the heat from the welding process resulted in localized microstructural alteration and reduced hardness and strength of the SPV490 steel plate". The extent of the softening included the HAZ, which ranged from 4 to 6 mm wide, and a narrow zone of reduced hardness base metal next to the HAZ, approximately 2 to 3 mm wide.

To approximate the effect of the reduced material properties, a material curve (true stress-true plastic strain) for the HAZ and adjacent base plate was developed. The estimated engineering ultimate stress of the HAZ (625 MPa) was converted to a true ultimate stress value of 688.0 MPa. The minimum property base metal curve was translated to match the true ultimate stress magnitude of the HAZ. Figure 5.1.2 shows a true stress - true plastic strain estimate of the HAZ material as compared to the base metal properties of the SPV490 steel. The extent of the softening ranged from 6 to 9 mm (HAZ plus adjacent base material). The maximum width of the softened material is near the width of a single element used near the equipment hatch. Therefore, a single row of elements surrounding the reinforcement plate was modified to utilize the reduced properties of the HAZ. Figure 5.1.3 identifies the finite elements which were modified.

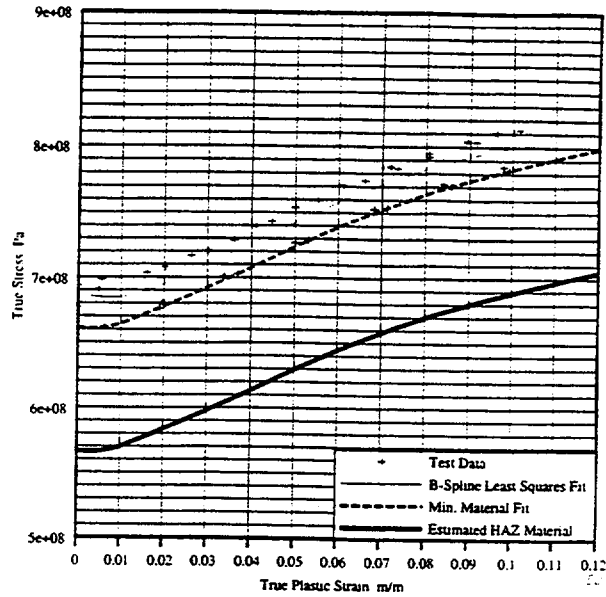


Figure 5.1.2
 True Stress True Plastic Strain
 9.0 mm Thick SPV490 Base Material and Estimated HAZ Properties

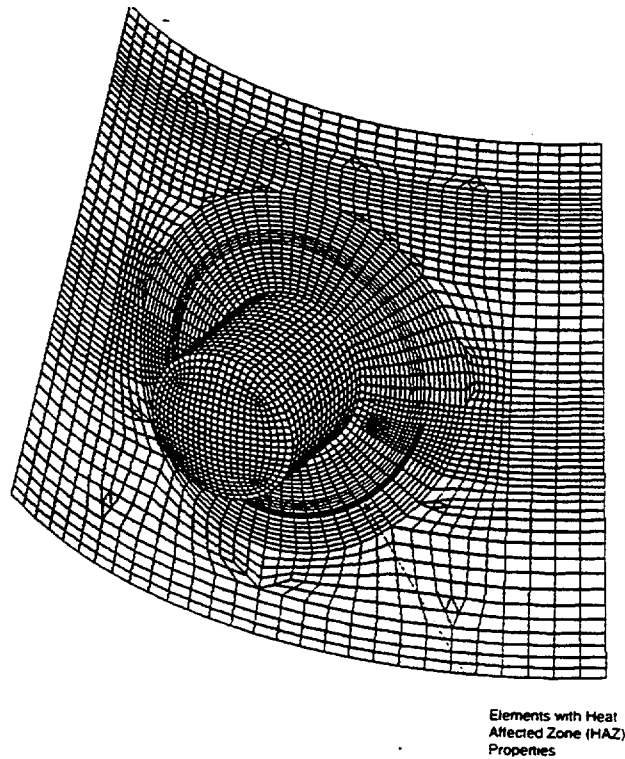


Figure 5.1.3
 Locally Thinned HAZ Finite Element Model of the SCV
 Location of Finite Elements with 'HAZ' Material Properties

Figure 5.1.4 shows the mid-fiber plastic strain magnitudes from the locally thinned finite element model with HAZ material properties. Mid-fiber strains slightly exceed the minimum ultimate strain of 10.0% (Maximum mid-fiber plastic strain 10.9%) for the SPV490 material with surface strains exceeding 13.5%. The location of the maximum strains is also more consistent with the location of the plate tear. Exceeding the ultimate strain magnitude most likely lead to uncontrolled necking in the narrow softened region until the material finally tore, resulting in the loss of pressure in the SCV. Reference 8 states that "all material deformations and fractures observed in the samples were ductile in nature. There was no evidence of material flaws, defects or brittle behavior of the base material or welds. The tears that occurred resulted from exceeding the local ductility of the alloy steel." The material model and ductile failure model utilized in this report are therefore in agreement with the test results. The numerical simulation results also support the findings of Reference 8 since "ductile failure strains" were developed in the vicinity of the tear at the failure pressure of 4.66 MPa.

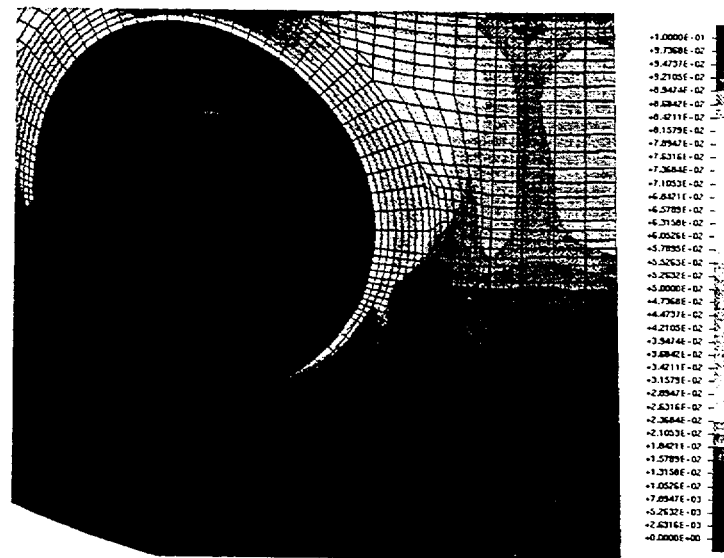


Figure 5.1.4
Post-Test Mid-Fiber Plastic Strain Magnitude at P=4.66 MPa
Locally Thinned HAZ Finite Element Model of the SCV

In addition to the above finite element model, a model was developed which included the HAZ material data, but utilized the mean plate thicknesses. The purpose of this model was to determine if the local plate thinning in the area of the tear significantly contributed to the failure of the SCV. Results from the analysis indicate approximately the same location of the high plastic strains but also an increase of the mid-fiber strains to approximately 12.5 percent. It appears, from this simple evaluation, that the SCV would have failed near the same failure pressure regardless of the local plate thinning which was present. No definitive statement can be made as to whether the thinning helped to shed strain away from the softened material due to the approximate nature of the HAZ material properties and relative coarseness of the finite element model.

Local necking which formed within the vertical weld lines in the lower conical shell (SPV490 steel) (Reference 8) also supports the theory that the softened material properties found in the HAZ and adjacent plate aided in the failure around the equipment hatch reinforcement plate. Incorporation of this material data into the pre-test predictions would have resulted in a lowering of the estimated failure pressure to below the 4.66 MPa failure pressure.

5.2 Middle Stiffener Weld Relief Hole :

Per Reference 8, a 55 mm vertical tear and local necking occurred in the vertical welds in the middle conical shell below weld relief holes in the lower 19 mm ring at 20 degrees and 21 degrees respectively. Weld relief holes are provided in the ring stiffener to accommodate the vertical welds joining the sections of the middle conical shell at these locations. A submodel of a portion of the middle conical shell and this stiffener was developed to investigate these areas. This submod-

el is shown in Figure 5.2.1. Mean model thicknesses, material properties and gap values were used. The design radius of 15 mm was used for the weld relief hole. The refined area of the SCV wall in the area of the relief hole is composed of 5376 C3D8I 8-node linear brick elements that are enhanced by incompatible modes. Incompatible deformation modes are added internally to these elements to improve their bending behavior. The remainder of the SCV wall and the stiffener is composed of 5528 C3D8 linear brick elements and C3D6 6-node linear triangular prisms. The C3D6 elements were used in mesh transition areas. A frame of 356 S4R 4-node, finite strain, reduced integration, general purpose shell elements are used solely to transfer edge displacements to the solid elements. These elements are not included in the contact surface definition. Multipoint constraint equations (MPC's) were used at the shell/solid interface to ensure continuity. The CS is represented by 1872 S4R shell elements. Pressure loads were applied to the submodel as was done for the global model. The submodel option of the ABAQUS program was used to automatically interpolate boundary displacements from the 3D half symmetry shell model described in Section 4.4 onto the submodel. In applying the edge displacements, only the translational values were applied to the perimeter elements since the interpolation scheme used in ABAQUS is inappropriate for shell rotations which are not linearly related. Rotations are therefore applied by the coupling action of the two driven nodes of a particular perimeter element. The contact interaction utilized the small sliding solution and softened contact as detailed in Section 4.1 of the pre-test analysis. The model was evaluated with a coefficient of friction of 0.4 (steel on steel in air). The CLEARANCE option in ABAQUS was utilized to set the initial clearance between the solid SCV elements and the CS shell elements equal to the mean gap of 21 mm. The CLEARANCE option was required since the midsurfaces of the SCV elements and the CS elements are separated by 21 mm in the submodel to align with the global 3D shell model. The use of solid elements through the thickness of the SCV reduces the modelled gap by one half the SCV wall thickness. Therefore, the CLEARANCE option was required to analytically restore the gap to 21 mm.

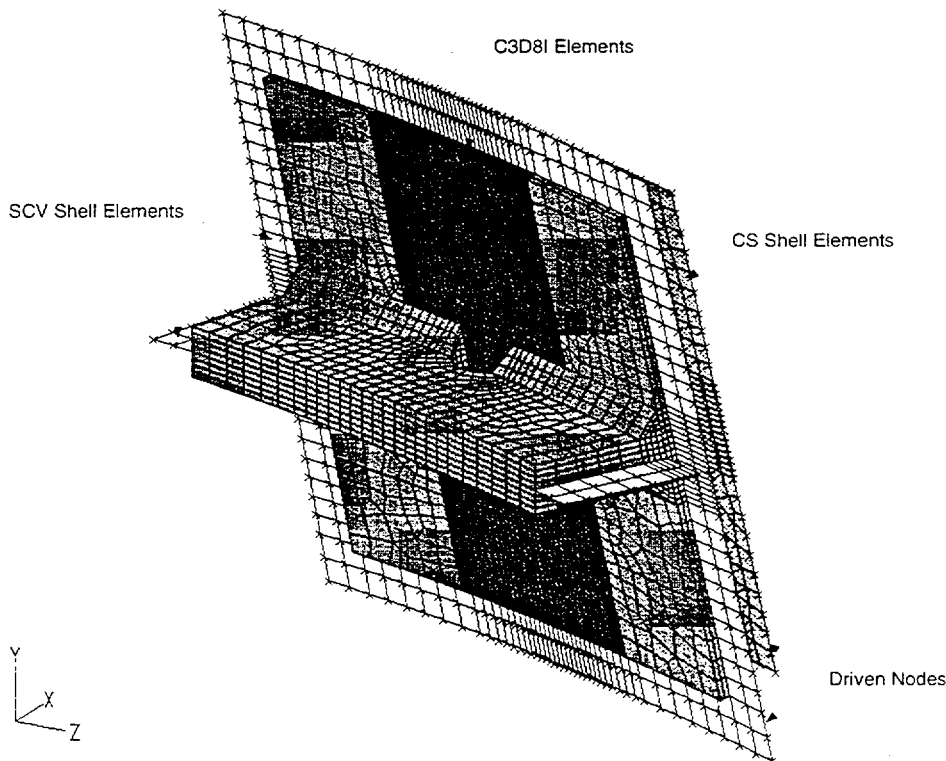


Figure 5.2.1
Solid Model of Weld Relief Hole

Figure 5.2.2 is a deformed plot showing the plastic strain magnitudes at the failure pressure of 4.66 MPa. A maximum surface strain of 11.8% was recorded in the wall of the SCV. The through thickness strains in this area are approximately 5%. The results show that the discontinuity causes significant strain concentrations in the conical shell, however, the maximum strain is significantly less than the minimum ultimate strain of 19.5% for the SGV480 material in this area. In addition, the reduction in thickness based on the analysis results was estimated to be roughly 4-5% which is less than the 12.8% reduction which occurred at the 20 degree location per Table 3 of Reference 8. The Reference 8 post-test metallurgical evaluation found no flaws which would have contributed to premature failure and no softening of the HAZ material as was shown for the SPV490 material where the tear occurred at the equipment hatch. A potential reason for the failure and necking in this area is geometric variations. For example, localized plate thinning may have occurred at the weld due to grinding. Also, the Reference 8 report shows a 32 mm weld relief hole while the calculation was based on the nominal design diameter of 30 mm. Another potential cause is that the strain state is biaxial in this area (unlike the uniaxial strain state at the hatch tear). The compressive radial strains and the tensile circumferential strains are nearly equal in the high strain region. In their pre-test analysis, using a typical material forming limit diagram for low carbon steel, SNL estimates that necking will occur at 65% of the tensile test ultimate strain for equal biaxial tension. If this method is used, the 11.8% maximum strain approaches 65% of the minimum ultimate strain or 12.7%. Further investigation of the biaxial effects would be necessary since no forming limit diagram is available for the SGV480 steel and since the biaxial strains are compressive/tensile. In summary, the analysis has shown significant strain concentrations in this area, however, more investigation would be required for a full understanding of the failure.

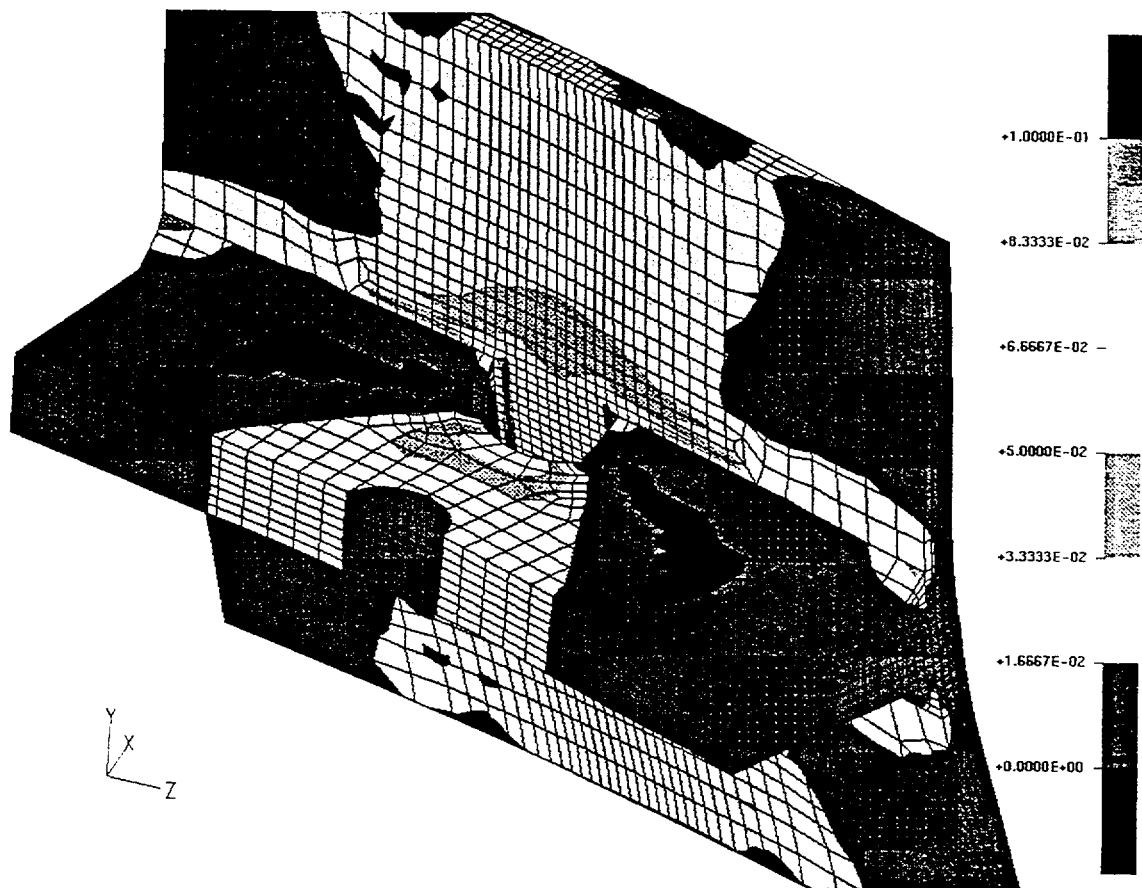


Figure 5.2.2
Plastic Strain Magnitude at P=4.66 MPa
Deformed Shape Plot - Scale=2.5

6.0 SCV Standard Output Discussion :

In Reference 1, SNL requested all participants to supply predictions at 39 sensor locations for comparison to test results. In Reference 4, the sensor locations were updated and four additional sensors were added near the equipment hatch. In Reference 5, nine additional sensor locations were supplied (two in the hatch area and seven in the upper conical shell area) for a total of 52 sensor locations. The final nine sensors were not formally given plot identification numbers as was done for the previous 43 locations. Table 6.0.1 assigns plot identification numbers for the final nine sensors with cross reference to the actual sensor designation (RSG-O-UCS-9a) supplied in Reference 5. The combined requested data consists of vertical and horizontal displacement response as well as meridian, hoop and maximum principal strain results.

Plot ID	Sensor	Output Quantity
44	STG-I-EQH-16b	Inside Hoop Strain
45	STG-I-EQH-37a	Inside Hoop Strain
46	RSG-I-UCS-10c (0°)	Inside Hoop Strain
47	RSG-I-UCS-12c (90°)	Inside Hoop Strain
48	RSG-I-UCS-14c (180°)	Inside Hoop Strain
49	RSG-O-UCS-9a (0°)	Outside Hoop Strain
50	RSG-O-UCS-11a (90°)	Outside Hoop Strain
51	RSG-O-UCS-13a (180°)	Outside Hoop Strain
52	RSG-O-UCS-15a (270°)	Outside Hoop Strain

Table 6.0.1
Plot Identification Table for Final Nine Locations

Table 6.0.2 lists the finite element models and related model information used in the post-test analysis. As in the pre-test portion of this effort, axisymmetric shell models were used to evaluate free field response, the axisymmetric solid models were used to evaluate transition areas around stiffener locations or rapid thickness changes and the half symmetry shell model and associated submodel of the hatch area were used to evaluate points in the hatch vicinity.

The axisymmetric shell post-test results were taken from the model which used the minimum material and plate thickness properties as well as the maximum gap evaluated (24 mm). The use of this model was not to improve correlation over the pre-test results, but to show the variation in response from the pre-test mean model results (Reference 6) which is possible due to variations in physical properties. Appendix B plots the results for the 52 sensor locations along with the associated test data. The pre-test results requested for sensors 1 through 43 are also included for comparison. The 3D shell submodel which used mean properties was used for the hatch area response locations. Comparisons are then possible to the pre-test model which utilized a conservative estimate of the local plate thinning which was present in the hatch area. The axisymmetric solid model post-test results are taken from the identical model used in the pre-test. The maximum load increment was limited to a smaller magnitude than the pre-test simulations to obtain greater resolution in response predictions at lower pressure levels. This improved visual agreement between the plotted analysis and test results for some sensor locations, in particular locations 15 and 16.

For the remaining nine new sensor locations, both mean and minimum type model results are included in Appendix B. For locations 44 and 45 near the equipment hatch, the mean and the post-test locally thinned model were used. For locations 46 through 52 both the post-test mean and min/max property axisymmetric shell models were used. This is similar to the pre-test mean model and post-test min/max model used for sensor locations 7-10, 17-18, 21-28 and 31-35.

Category	Sensor Location	Output Quantity	Numerical Model	Node	Grp. No.	DOF
Equipment Hatch	1	Max. Princ. Strain	3-D Shell Submodel - Mean Properties	3535	1	2
Equipment Hatch	2	Max. Princ. Strain	3-D Shell Submodel - Mean Properties	3529	1	2
Equipment Hatch	3	Ext. Merid. Strain	3-D Shell Submodel - Mean Properties	3520	1	2
Equipment Hatch	4	Int. Merid. Strain	3-D Shell Submodel - Mean Properties	3520	1	8
Equipment Hatch	5	Ext. Hoop Strain	3-D Shell Submodel - Mean Properties	3542	1	7
Equipment Hatch	6	Int. Hoop Strain	3-D Shell Submodel - Mean Properties	3542	1	7
Top Head	7	Max. Princ. Strain	Axisymmetric Shell - Min/Max Properties	1	-	4
Top Head	8	Ext. Hoop Strain	Axisymmetric Shell - Min/Max Properties	33	-	4
Top Head	9	Ext. Merid. Strain	Axisymmetric Shell - Min/Max Properties	33	-	3
Top Head	10	Int. Merid. Strain	Axisymmetric Shell - Min/Max Properties	33	-	1
Transition Region	11	Ext. Merid. Strain	Axisymmetric Solid - Knuckle	1235	-	2
Transition Region	12	Int. Merid. Strain	Axisymmetric Solid - Knuckle	664	-	2
Transition Region	13	Ext. Merid. Strain	Axisymmetric Solid - Knuckle	1423	-	2
Transition Region	14	Int. Merid. Strain	Axisymmetric Solid - Knuckle	886	-	2
Transition Region	15	Ext. Merid. Strain	Axisymmetric Solid - Middle Stiffener	2672	-	2
Transition Region	16	Int. Merid. Strain	Axisymmetric Solid - Middle Stiffener	2073	-	2
Transition Region	17	Ext. Merid. Strain	Axisymmetric Shell - Min/Max Properties	204	-	3
Transition Region	18	Int. Merid. Strain	Axisymmetric Shell - Min/Max Properties	204	-	1
Transition Region	19	Ext. Merid. Strain	Axisymmetric Solid - Lower Stiffener	522	-	2
Transition Region	20	Int. Merid. Strain	Axisymmetric Solid - Lower Stiffener	36	-	2
Free Field	21	Ext. Merid. Strain	Axisymmetric Shell - Min/Max Properties	160	-	3
Free Field	22	Int. Merid. Strain	Axisymmetric Shell - Min/Max Properties	160	-	1
Free Field	23	Ext. Hoop Strain	Axisymmetric Shell - Min/Max Properties	160	-	4
Free Field	24	Int. Hoop Strain	Axisymmetric Shell - Min/Max Properties	160	-	2
Free Field	25	Ext. Merid. Strain	Axisymmetric Shell - Min/Max Properties	218	-	3
Free Field	26	Int. Merid. Strain	Axisymmetric Shell - Min/Max Properties	218	-	1
Free Field	27	Ext. Hoop Strain	Axisymmetric Shell - Min/Max Properties	218	-	4
Free Field	28	Int. Hoop Strain	Axisymmetric Shell - Min/Max Properties	218	-	2
Free Field	29	Int. Merid. Strain	Axisymmetric Solid - Knuckle	954	-	2
Free Field	30	Int. Hoop Strain	Axisymmetric Solid - Knuckle	954	-	3
Free Field	31	Int. Merid. Strain	Axisymmetric Shell - Min/Max Properties	160	-	1
Free Field	32	Int. Hoop Strain	Axisymmetric Shell - Min/Max Properties	160	-	2
Free Field	33	Int. Merid. Strain	Axisymmetric Shell - Min/Max Properties	227	-	1
Free Field	34	Int. Hoop Strain	Axisymmetric Shell - Min/Max Properties	227	-	2
Displacement	35	Vertical	Axisymmetric Shell - Min/Max Properties	1	-	2
Displacement	36	Horizontal	Axisymmetric Solid - Knuckle	1343	-	1
Displacement	36	Horizontal	Axisymmetric Solid - Knuckle	804	-	1
Displacement	37	Horizontal	Axisymmetric Solid - Knuckle	938	-	1
Displacement	38	Vertical	Axisymmetric Solid - Knuckle	938	-	2
Displacement	39	Horizontal	3-D Shell Submodel - Mean Properties	3970	-	3
Equipment Hatch	40	Int. Merid. Strain	3-D Shell Submodel - Mean Properties	15029 14998	2	8
Equipment Hatch	41	Int. Hoop Strain	3-D Shell Submodel - Mean Properties	15029 14998	2	7
Equipment Hatch	42	Int. Merid. Strain	3-D Shell Submodel - Mean Properties	10898	2	8
Equipment Hatch	43	Int. Hoop Strain	3-D Shell Submodel - Mean Properties	10898	2	7
Equipment Hatch	44	Int. Hoop Strain	3-D Shell Submodel - Locally Thinned	3542	-	7
Equipment Hatch	45	Int. Hoop Strain	3-D Shell Submodel - Locally Thinned	12196	-	7
Free Field	46	Int. Hoop Strain	Axisymmetric Shell - Min/Max Properties	160	-	2
Free Field	47	Int. Hoop Strain	Axisymmetric Shell - Min/Max Properties	160	-	2
Free Field	48	Int. Hoop Strain	Axisymmetric Shell - Min/Max Properties	160	-	2
Free Field	49	Ext. Hoop Strain	Axisymmetric Shell - Min/Max Properties	160	-	4
Free Field	50	Ext. Hoop Strain	Axisymmetric Shell - Min/Max Properties	160	-	4
Free Field	51	Ext. Hoop Strain	Axisymmetric Shell - Min/Max Properties	160	-	4
Free Field	52	Ext. Hoop Strain	Axisymmetric Shell - Min/Max Properties	160	-	4

Table 6.0.2
Standard Output Model Identification
Sensor Locations Identified in Reference 10

7.0 Conclusions :

Based upon the results presented in this section, the following conclusions are reached:

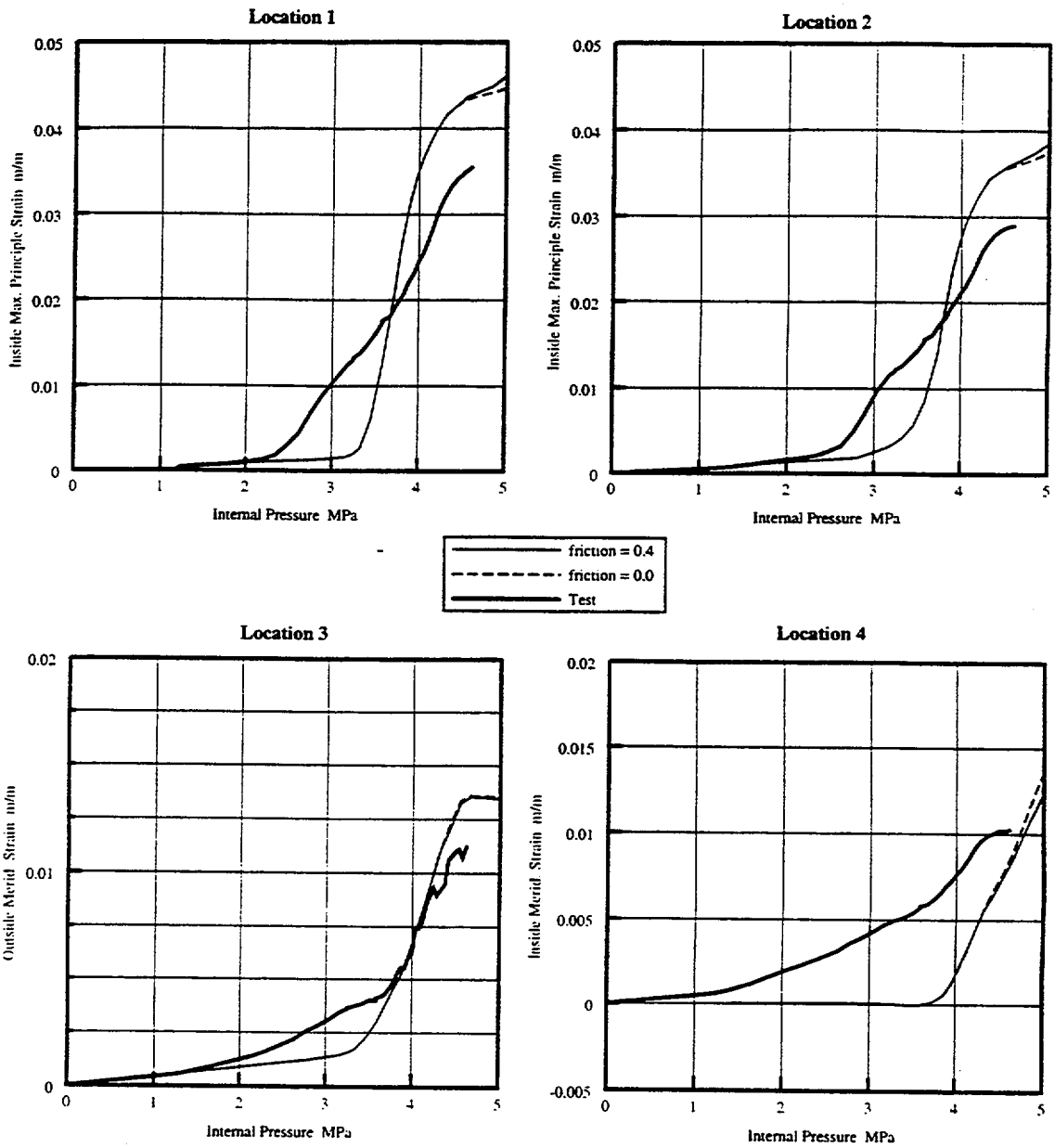
- (1) Pre-test failure predictions accurately identified the predominant failure location (Equipment Hatch Reinforcement plate boundary) and approximate failure pressure (4.66 MPa test versus 4.7 MPa pre-test prediction). Post-test evaluations determined that the failure was more likely attributed to the reduced material properties in the Heat Affected Zone (HAZ) near the SPV490 shell plate weldment and not the locally thinned plate which was also present. The material properties of the HAZ were not available for the pre-test portion of this task. The use of accurate material properties for base plate, weldment, and HAZ is critical in performing failure predictions of steel structures.
- (2) Overall good correlation was observed between test sensor data and analysis response data. The general inelastic response at the vast majority of sensor locations was accurately predicted in Electric Boat's pre-test evaluation effort. Parametric investigations of material and geometric variations that existed in the SCV demonstrated that the maximum strain at failure could be bounded by analysis predictions.
- (3) A delay in the onset of yielding was observed in the analysis results as compared to the test results for a portion of the sensor locations examined. Variations in material and geometric properties present in the SCV explain, in part, the yielding delay, but a complete upper bound response history prediction for some of the sensor locations was not obtained. Electric Boat believes this delay in yielding not to be an artifact of the solution strategy of the ABAQUS code since this program has been utilized in other predictive tasks with excellent prediction of the onset of yielding. Possible explanations may lie with the material tests performed to determine the material properties though no definitive reason for the yielding delay was determined.
- (4) Post-test analyses also examined the tear failure near the middle stiffener weld relief hole. The weld relief hole was not included in the pre-test analyses. Significant strain concentrations due to the presence of the relief hole were shown. A maximum strain of 11.8 % was predicted which is below the 19.5% minimum ultimate strain for the SGV480 material. Geometric variation such as the increased size of the relief hole (32.0 mm versus 30.0 mm design) as well as localized plate thinning such as was seen elsewhere in the vessel may have increased the actual strain magnitude above the predicted 11.8%. The strain state predicted is biaxial (unlike the uniaxial strain state at the hatch tear). A review of a typical forming limit diagram for low carbon steel shows a decrease in the tensile test ultimate strain by 65% for biaxial tension resulting in an equivalent ultimate strain of 12.7%, which is near the 11.8% predicted maximum strain. The strain state is, however, compressive/tensile and no forming limit diagram is available for the SGV480 material. Additional investigation would be required to completely understand the nature of the failure at this location.

8.0 References :

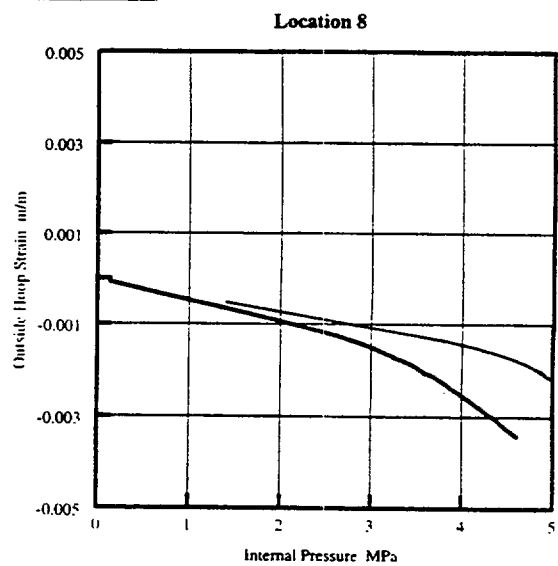
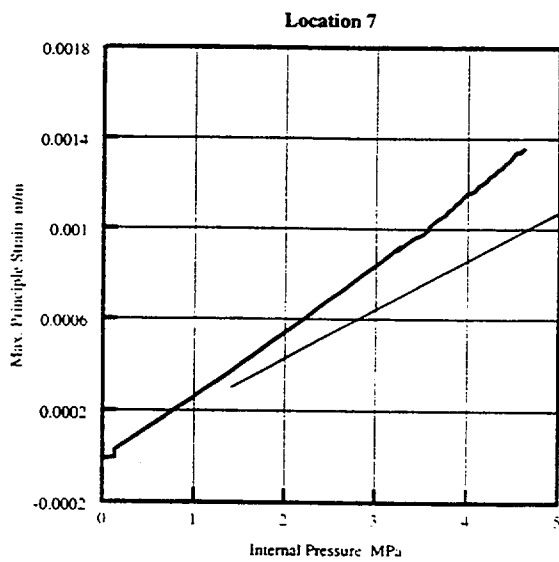
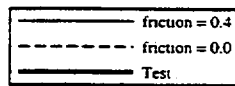
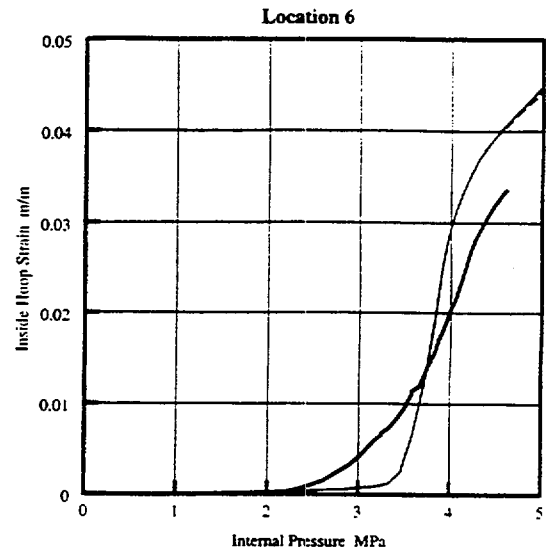
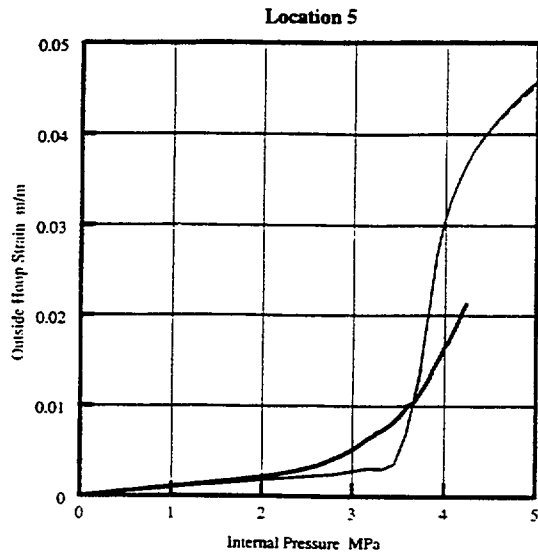
- (1) Sandia National Laboratories Submittal, 10 July 1995.
- (2) Sandia National Laboratories Submittal, 21 September 1995.
- (3) Sandia National Laboratories Submittal, 20 February 1996, SO-96-012.
- (4) Sandia National Laboratories Submittal, 9 May 1996, SO-96-041.
- (5) Sandia National Laboratories Report, R-SN-S-007 Revision No. B, "SCV High Pressure Test Data for Round Robin Analysis", 22 September 1997.
- (6) Electric Boat Corporation Report, "Electric Boat Corporation Pre-test Evaluation of the Steel Containment Vessel", May 1996.
- (7) Sandia National Laboratories Submittal, 3 February 1998, SO-98-006.
- (8) Sandia National Laboratories Report, R-SN-S-009 Revision No. B, "Posttest Metallurgical Evaluation Results for SCV High Pressure Test", 19 December 1997.
- (9) ABAQUS/Standard User's Manual, Hibbitt, Karlsson & Sorenson, Inc. Version 5.7, 1997.
- (10) Sandia National Laboratories Report, R-SN-G-003 Revision No. A, "Round Robin Pretest Analyses of a Steel Containment Vessel Model and Contact Structure Assembly Subject to Static Internal Pressurization", September 1996.

APPENDIX A
PRE-TEST CORRELATION

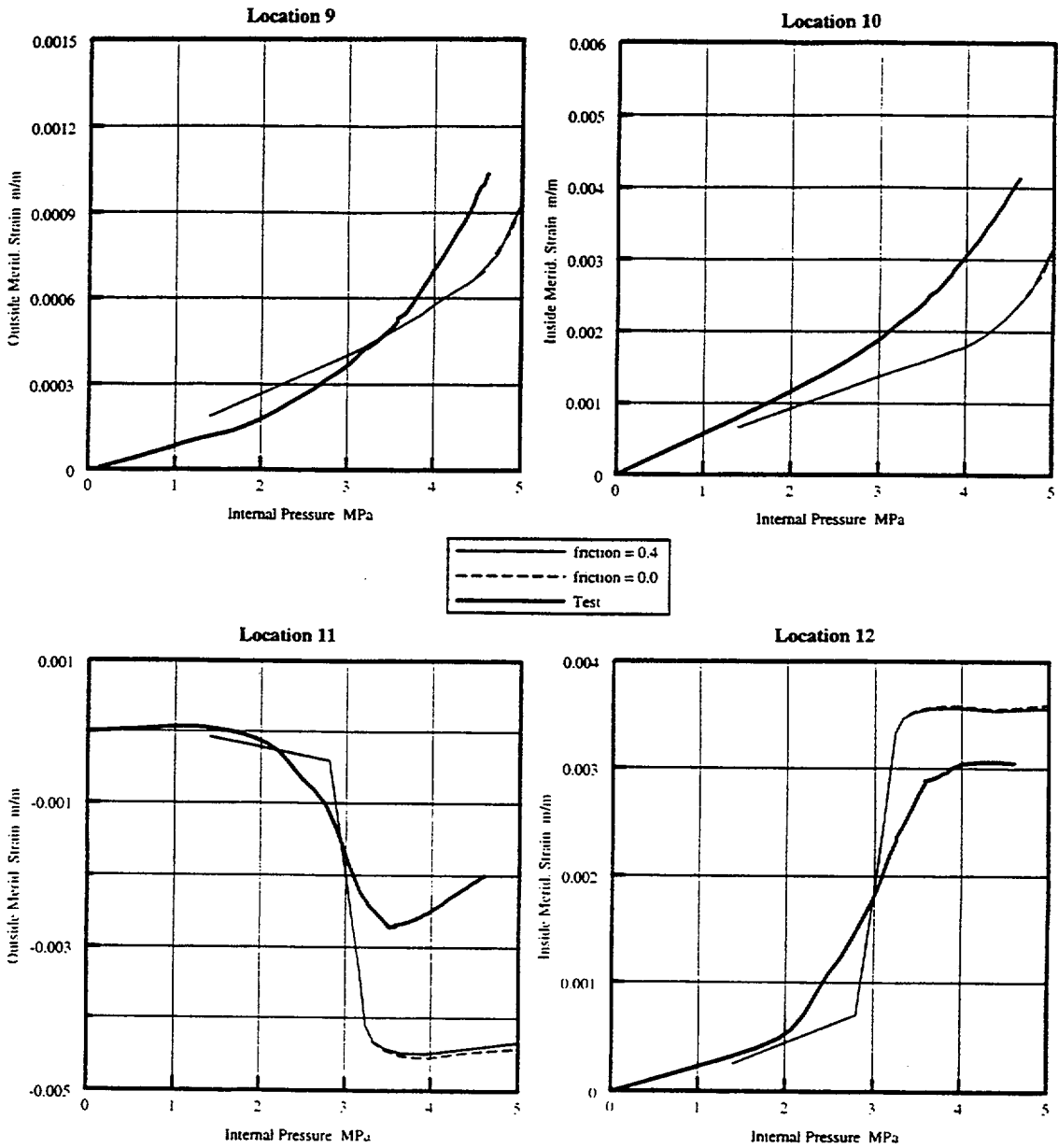
A-1 of A-12



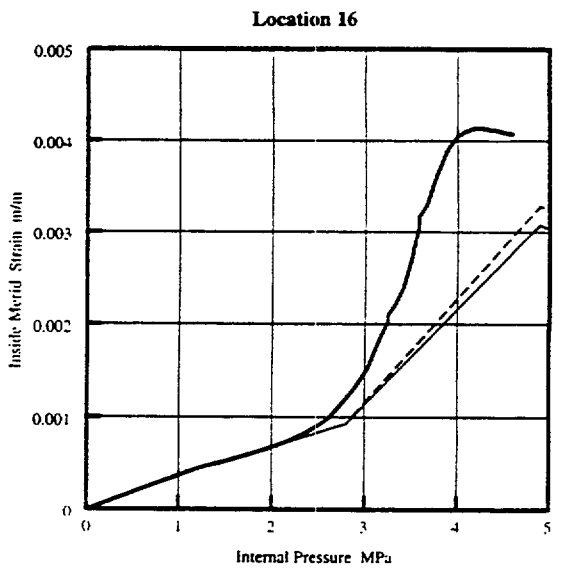
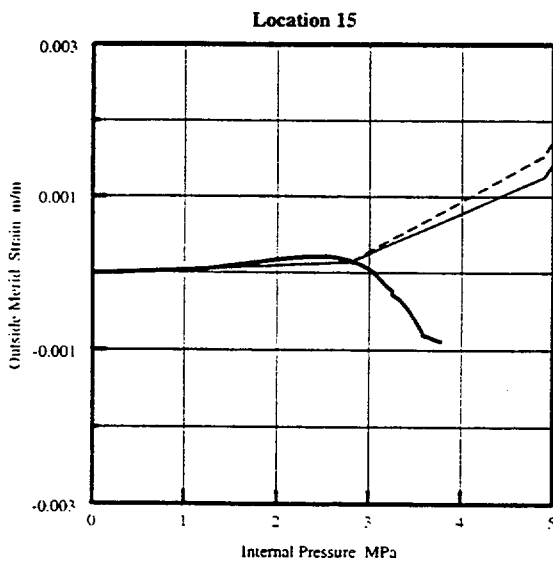
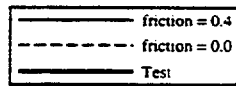
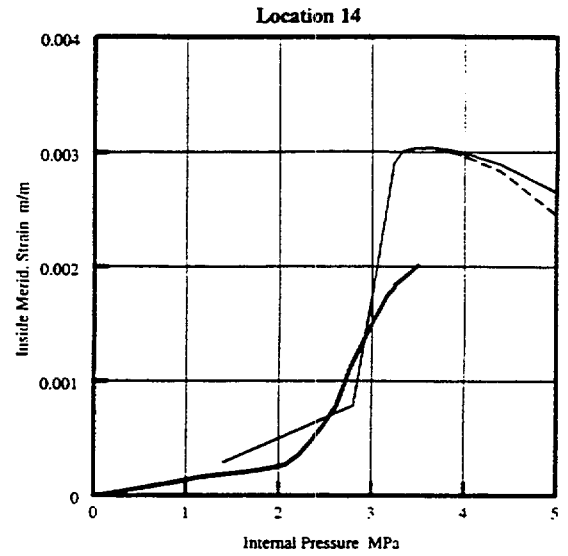
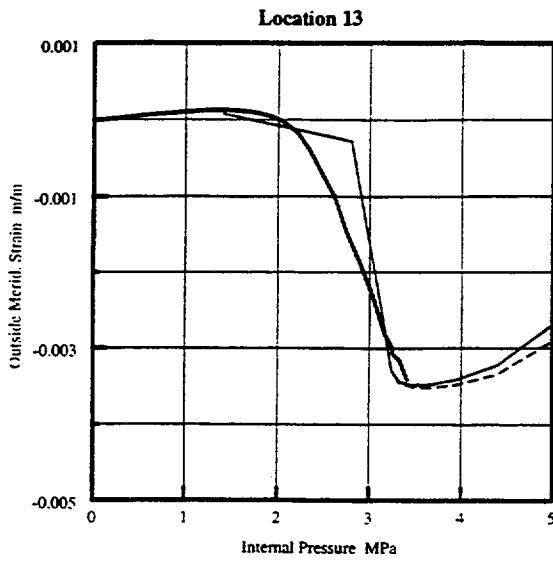
A-2 of A-12

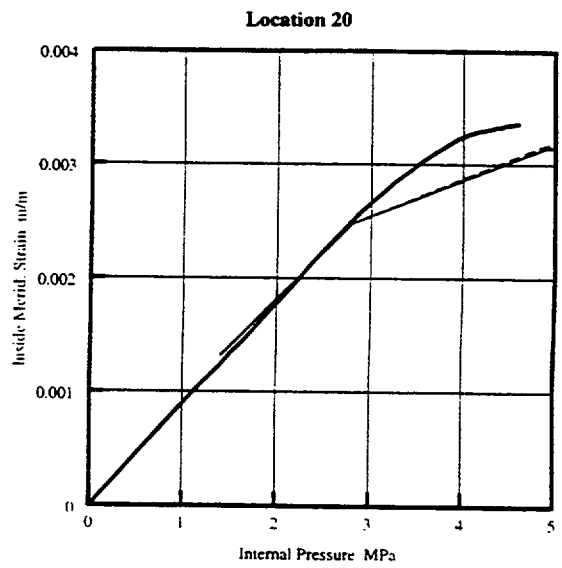
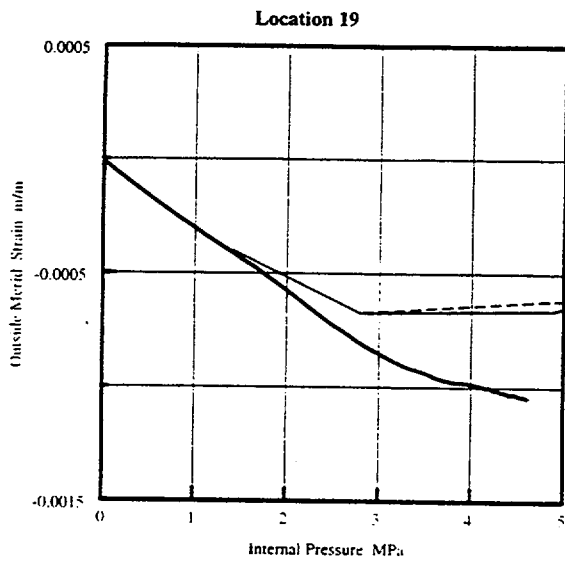
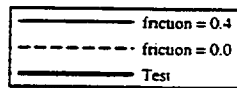
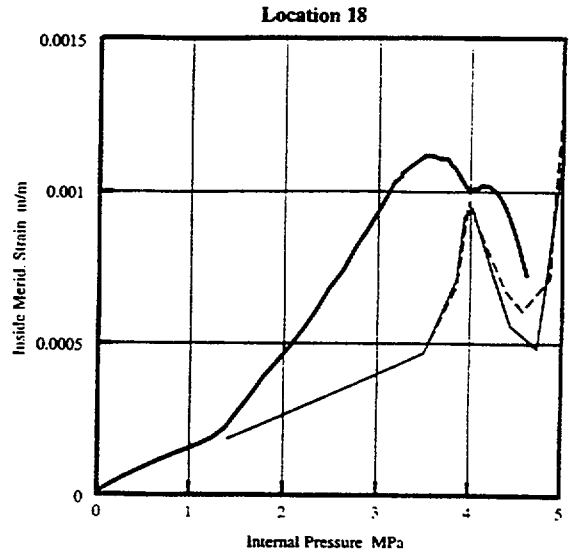
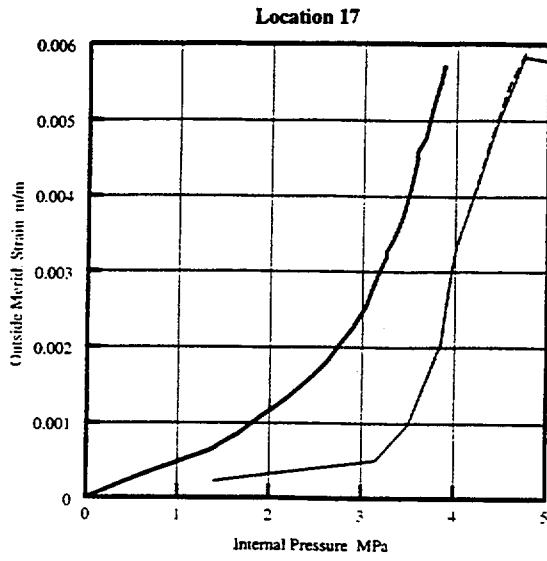


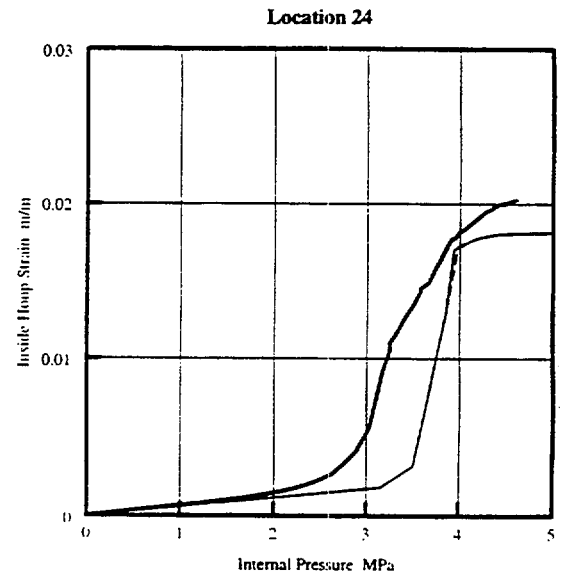
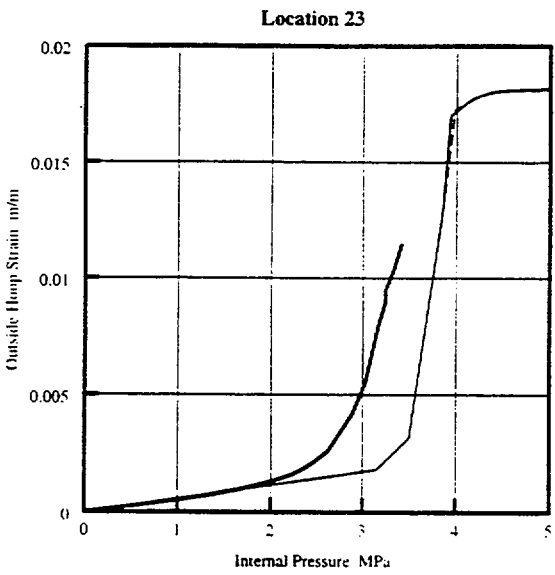
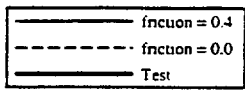
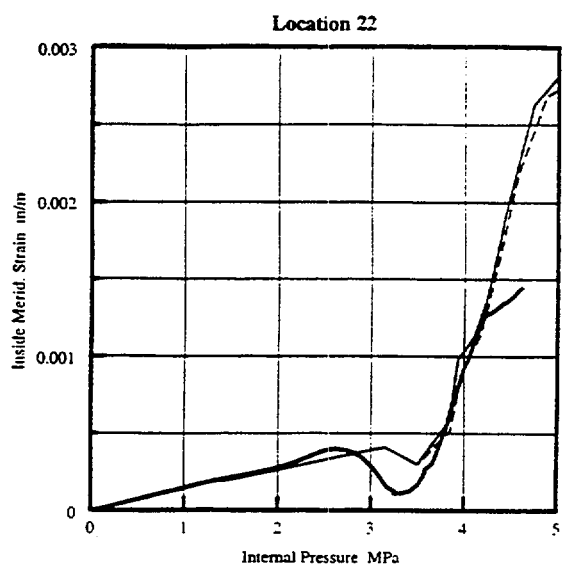
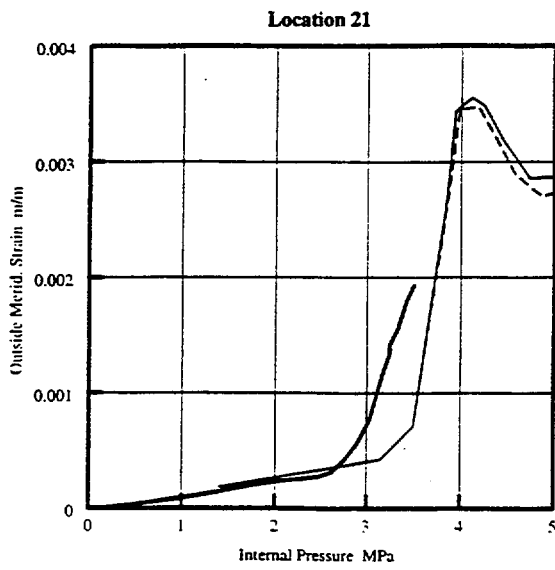
A-3 of A-12

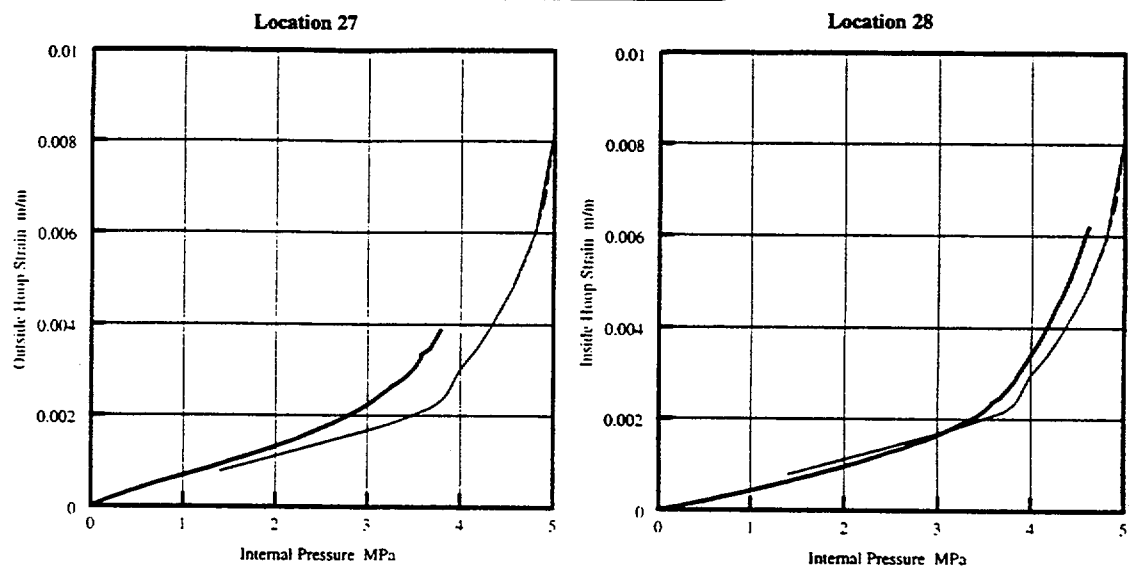
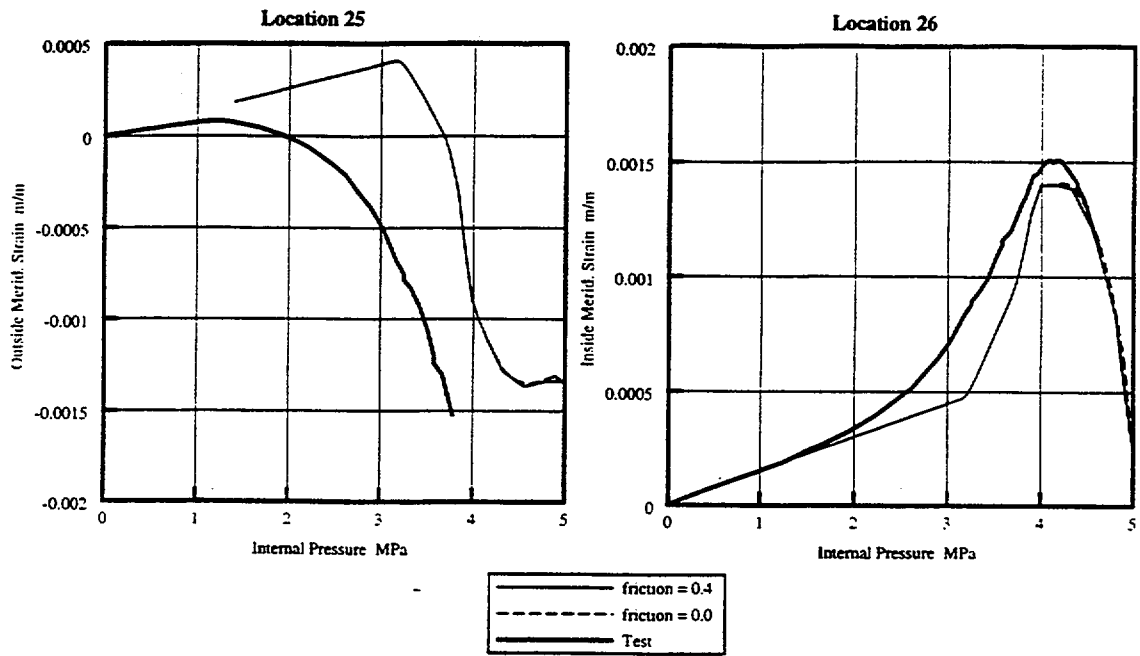


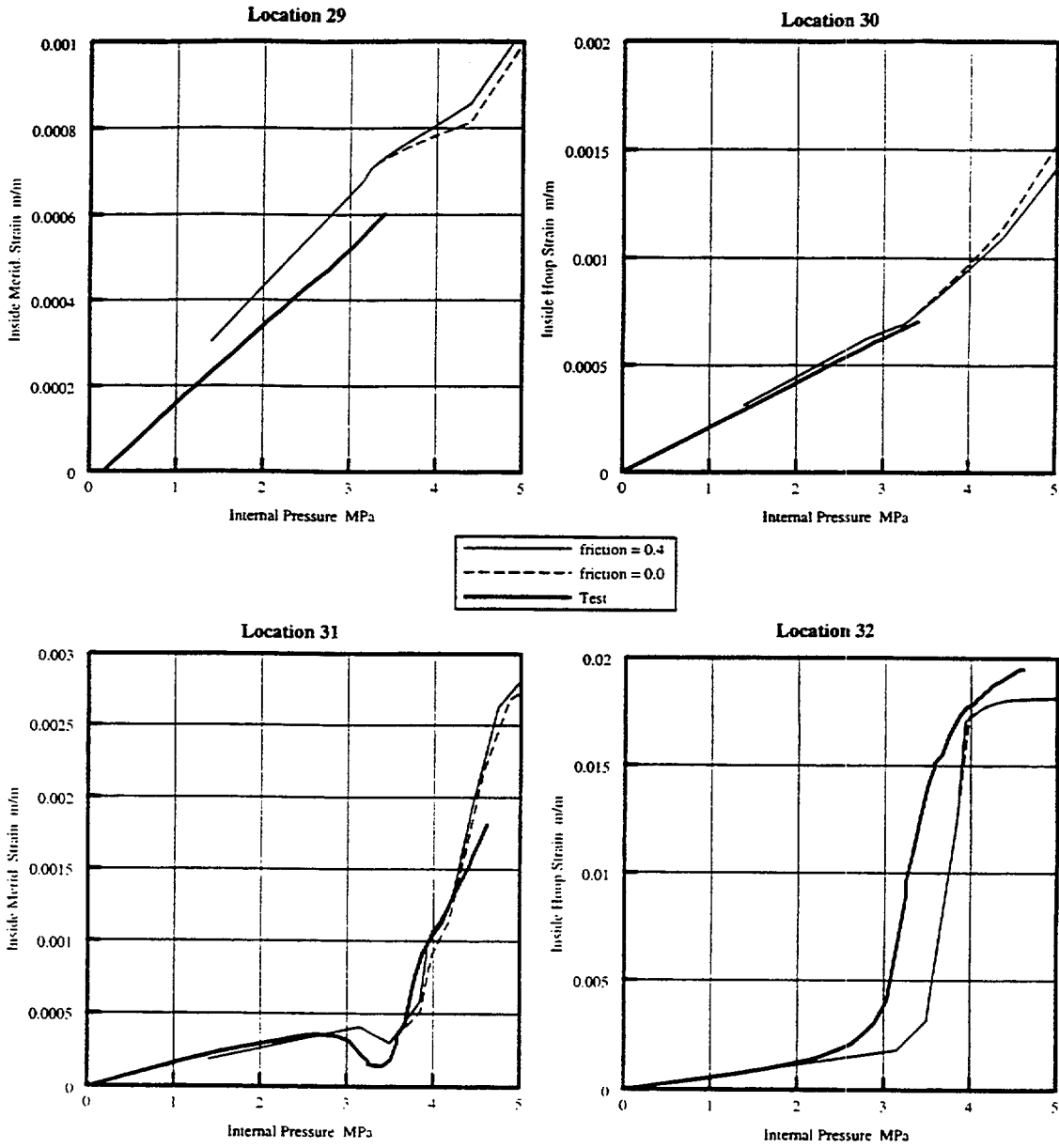
A-4 of A-12

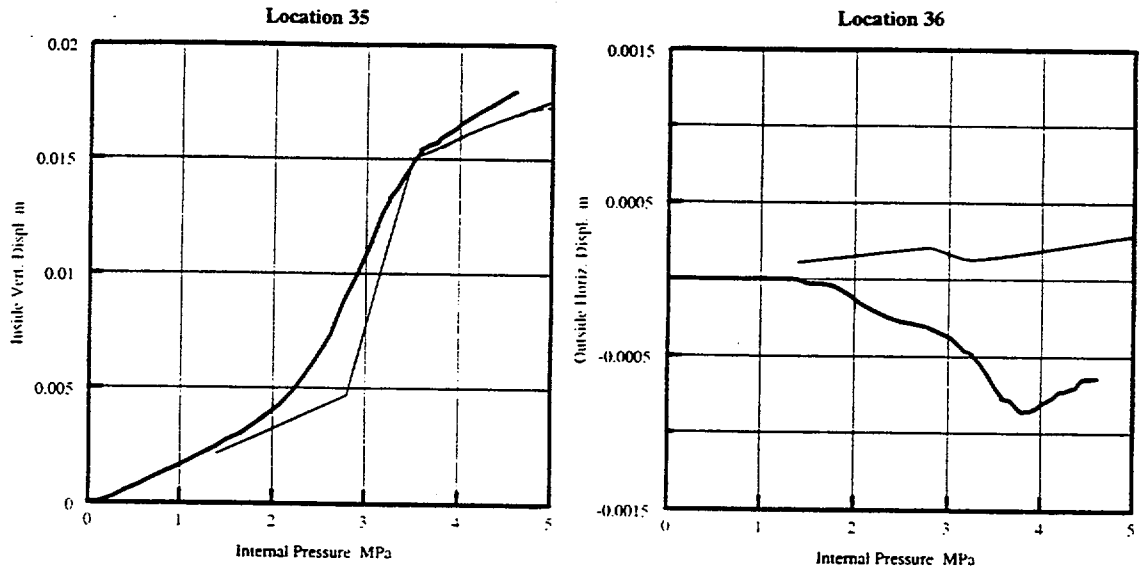
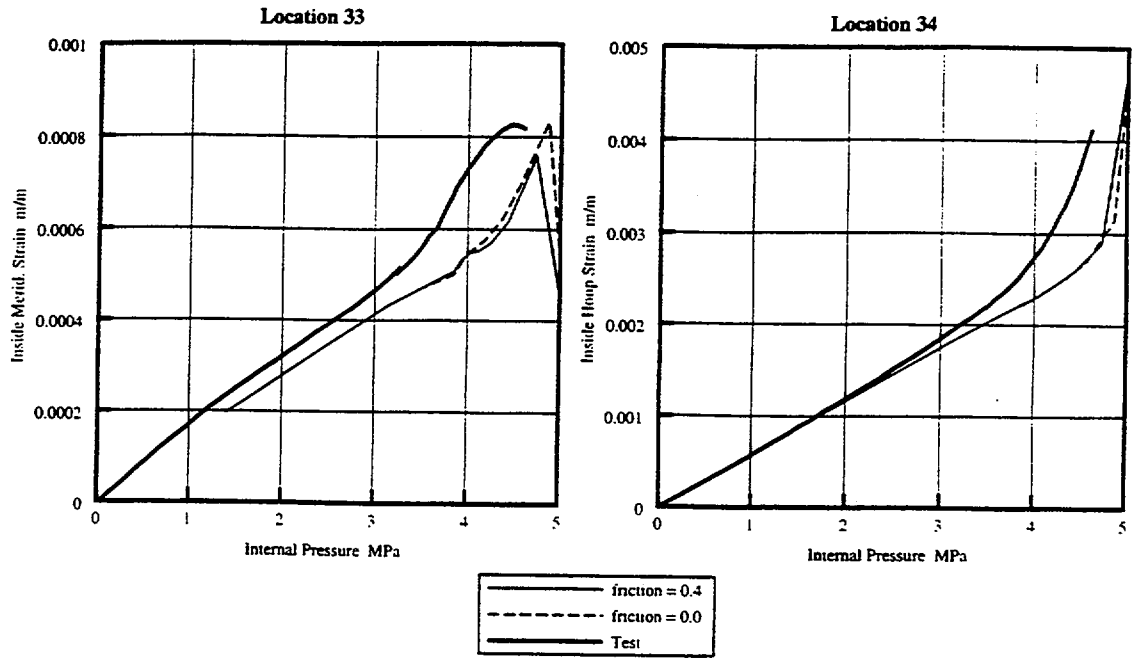


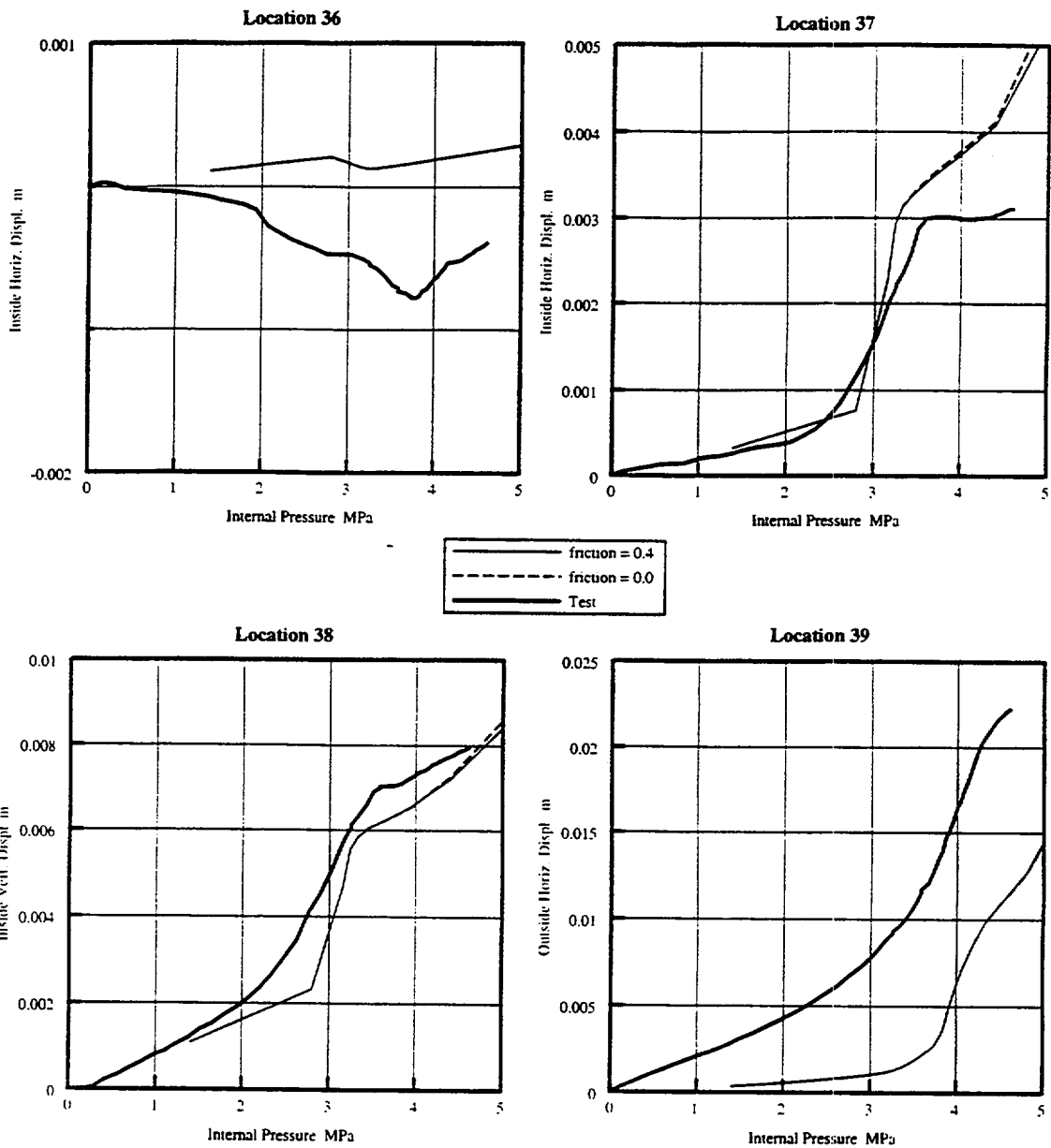




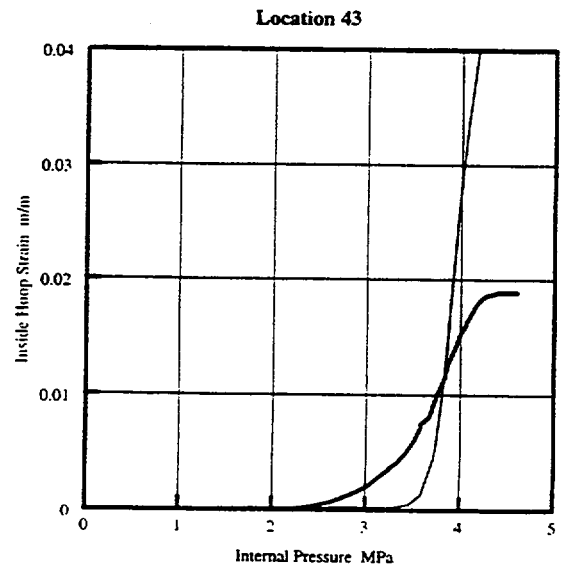
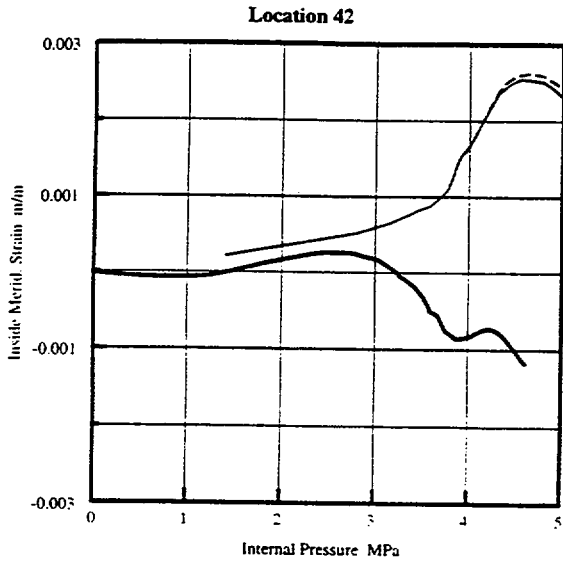
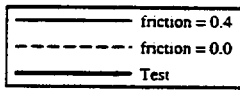
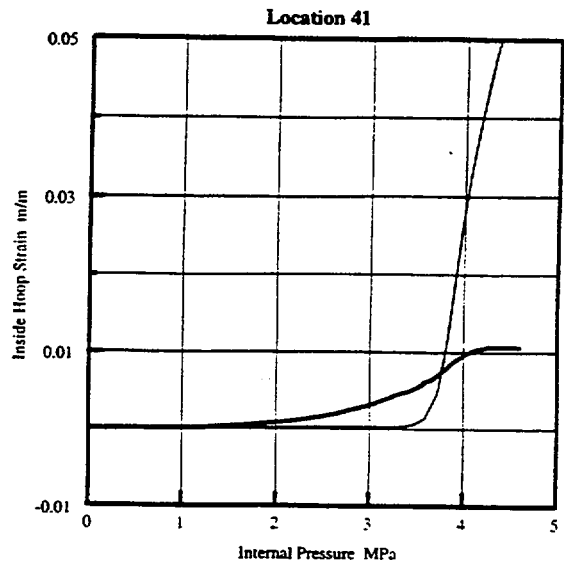
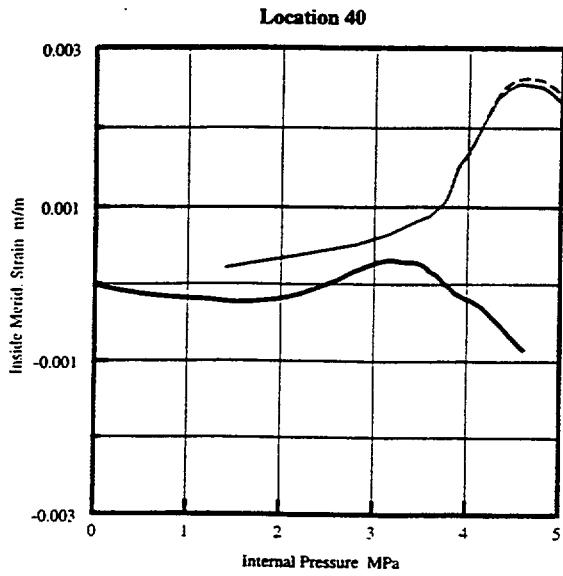






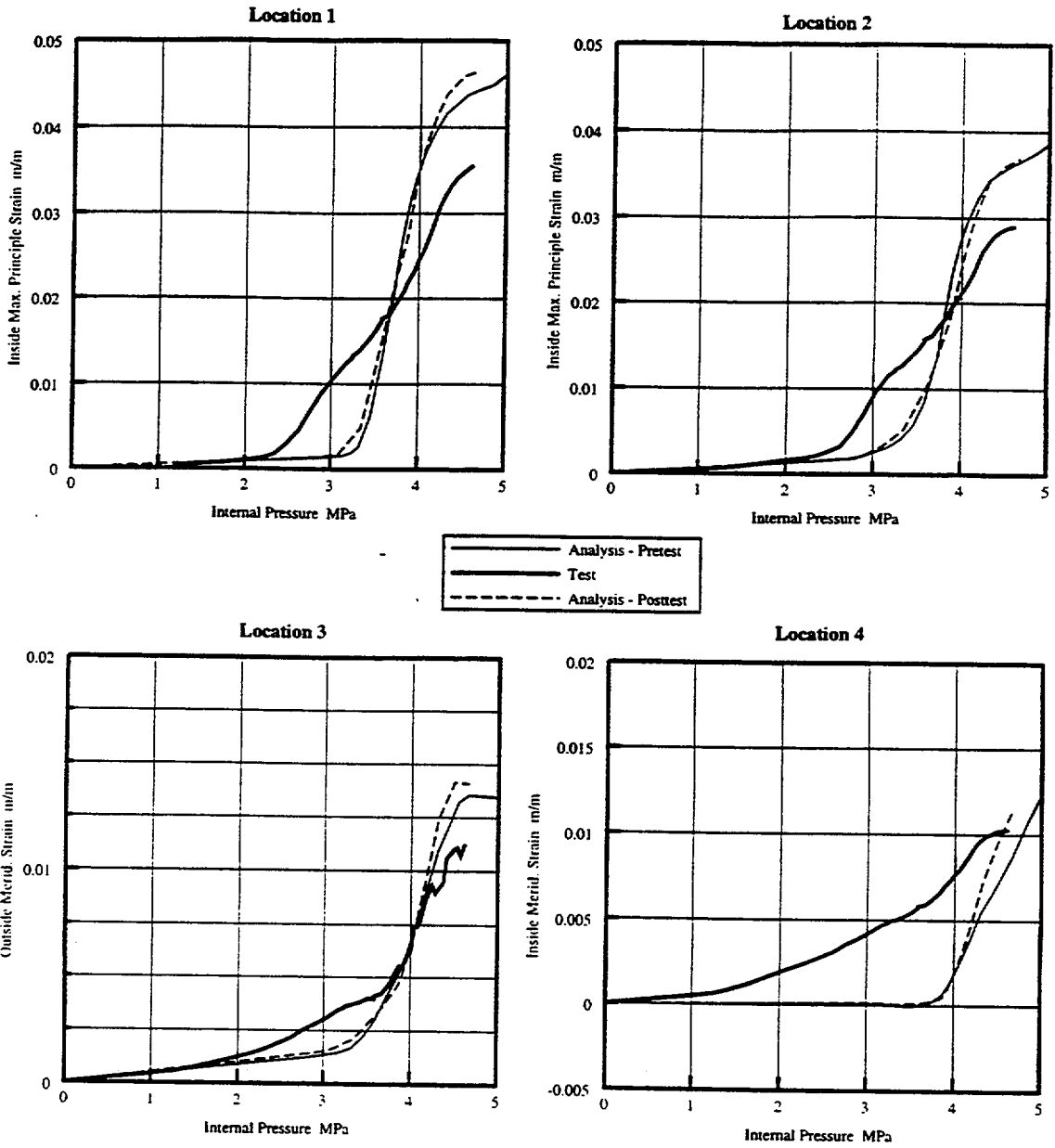


A-11 of A-12

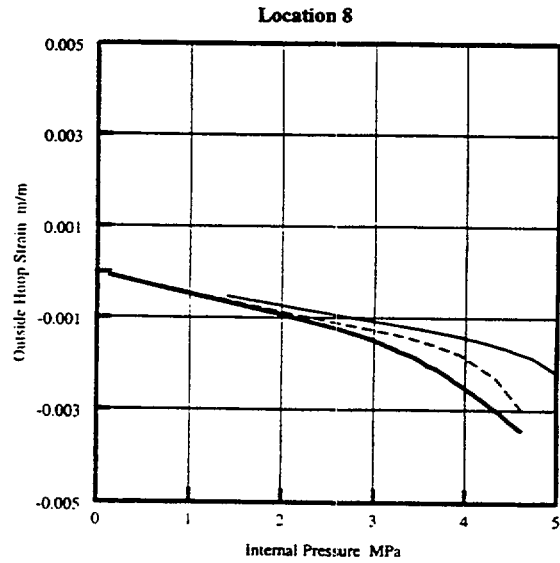
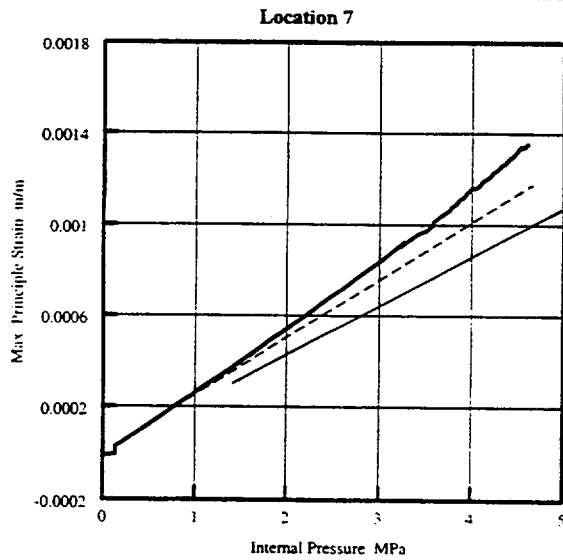
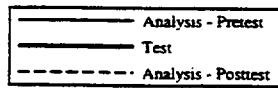
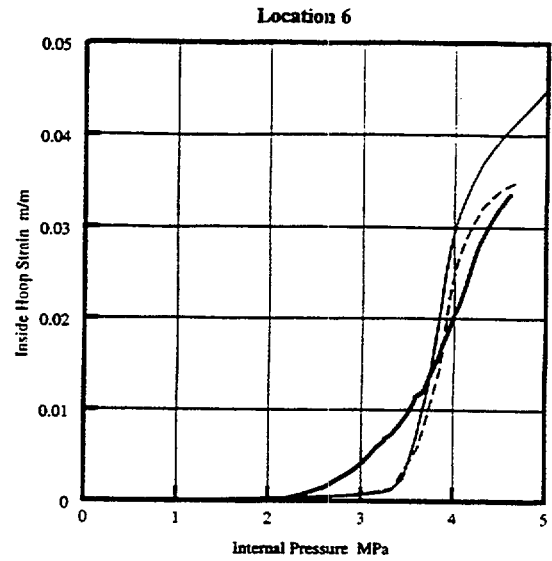
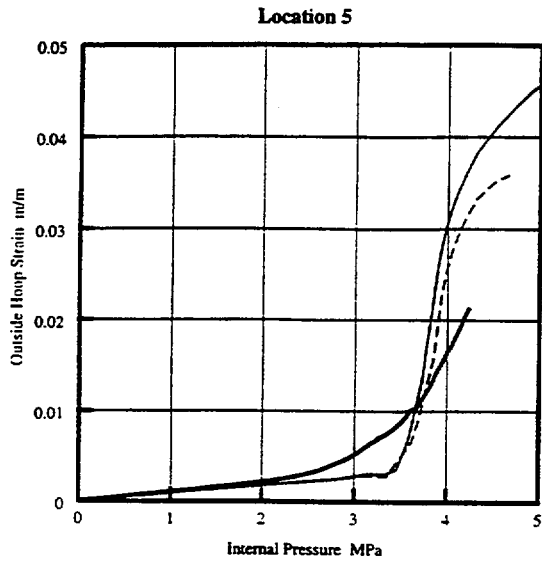


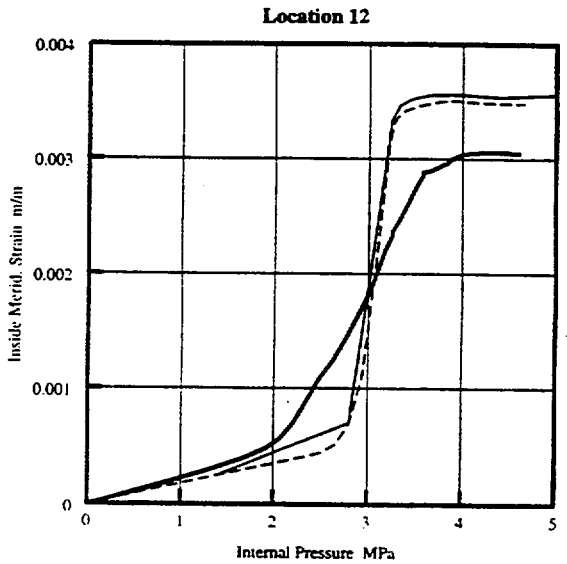
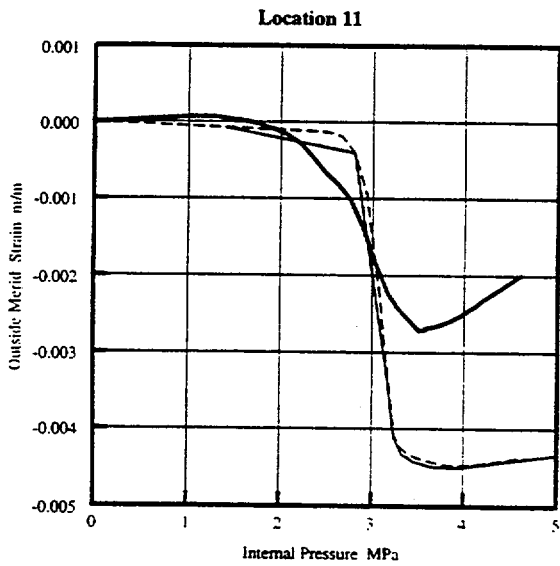
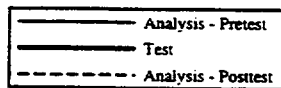
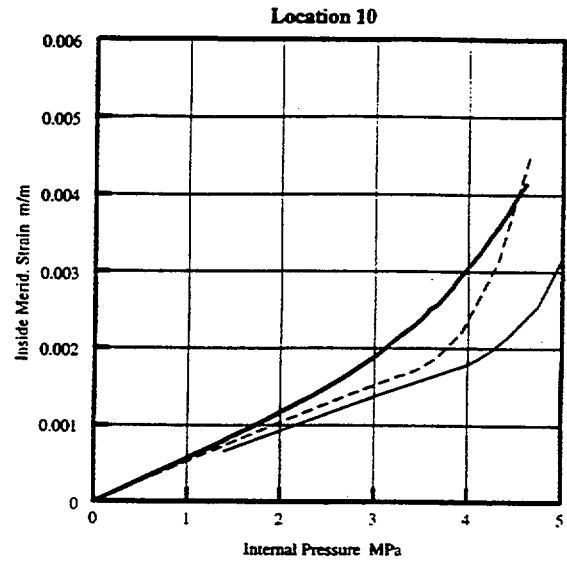
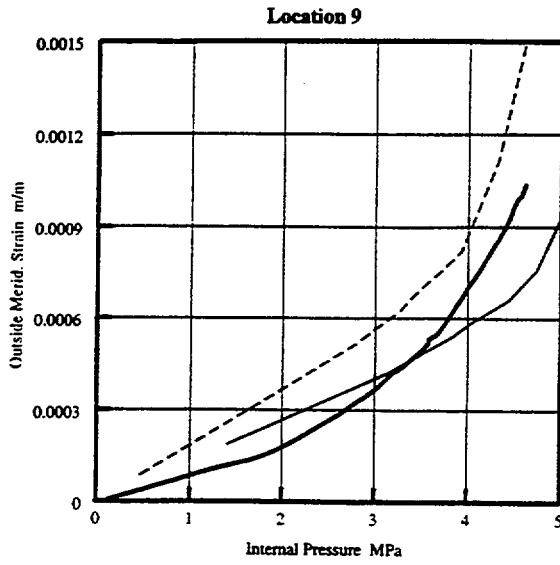
APPENDIX B
POST-TEST CORRELATION

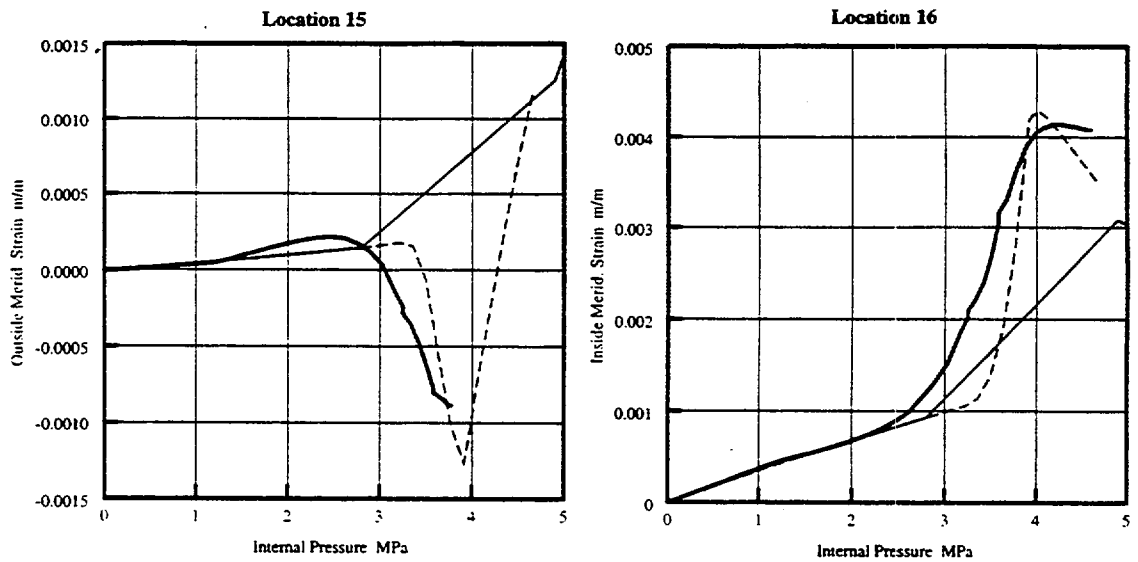
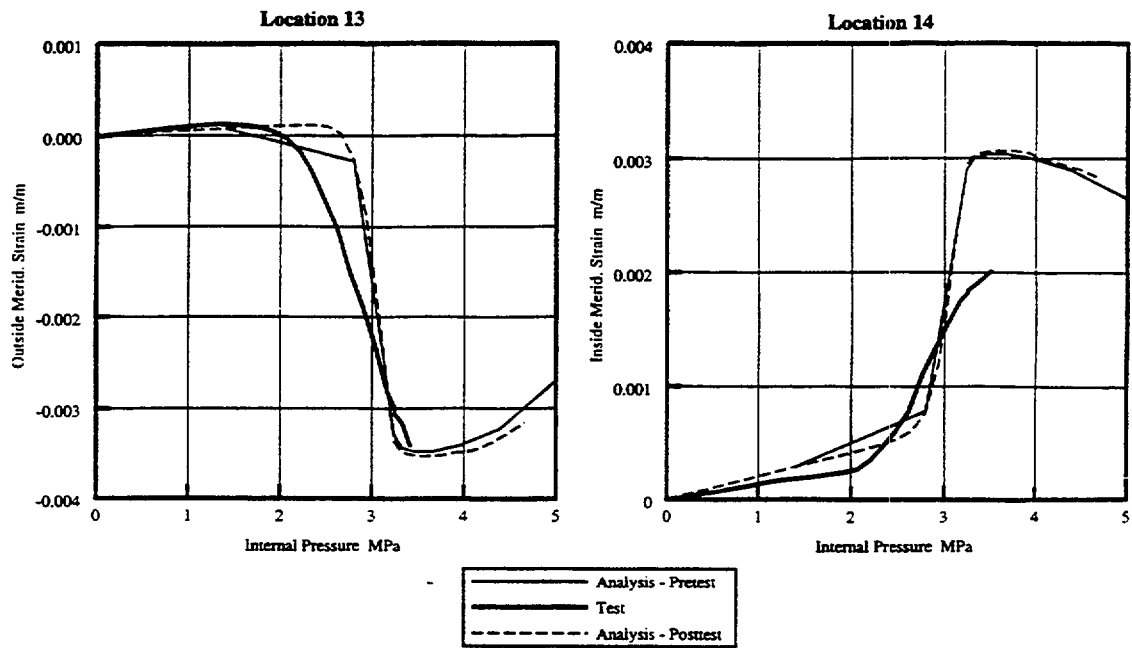
B-1 of B-15



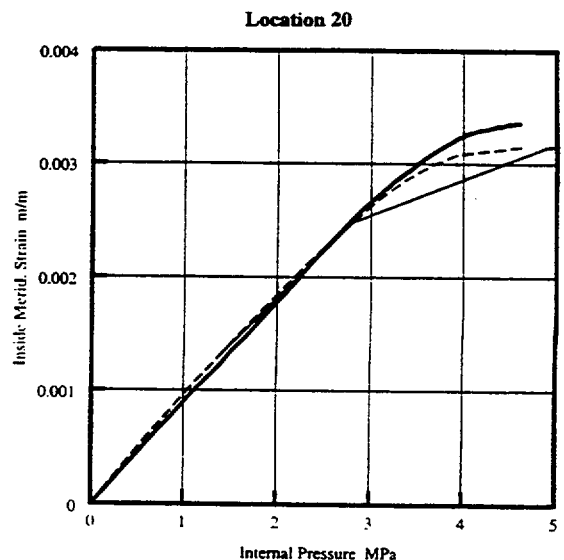
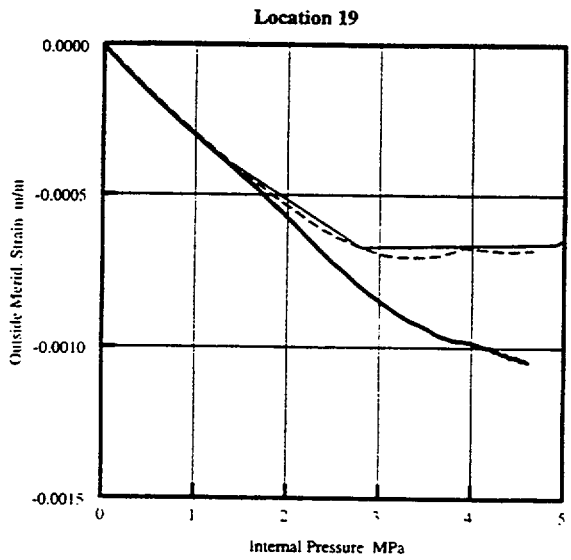
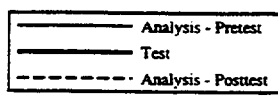
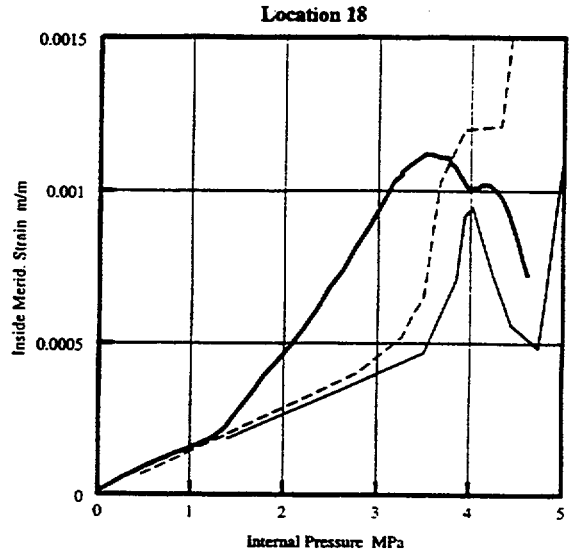
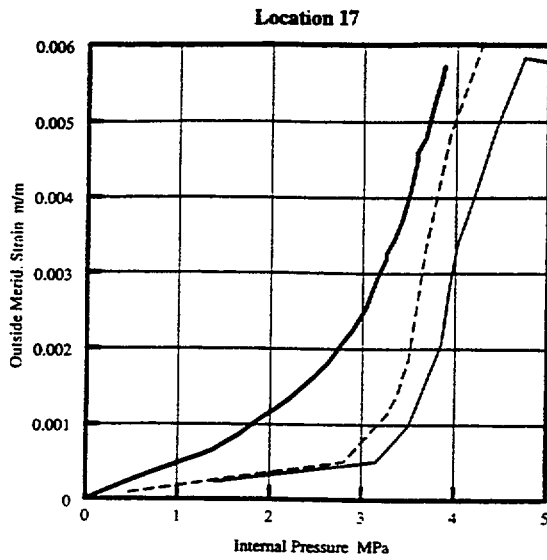
B-2 of B-15

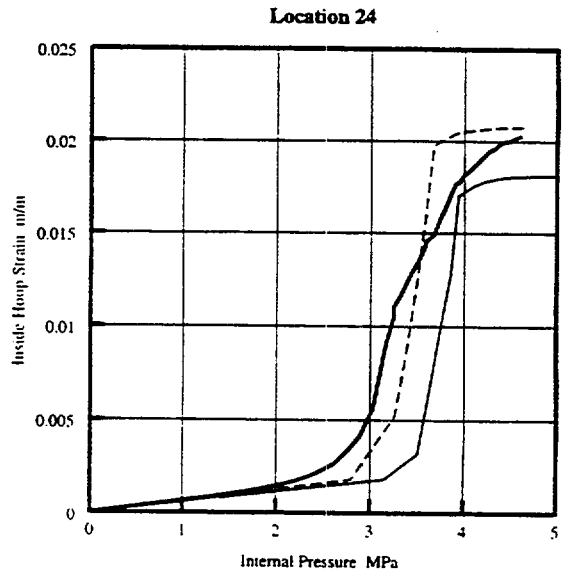
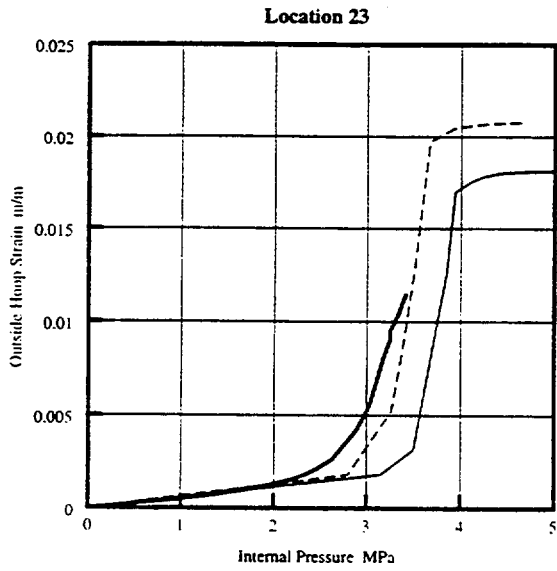
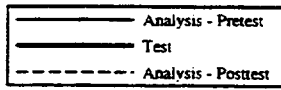
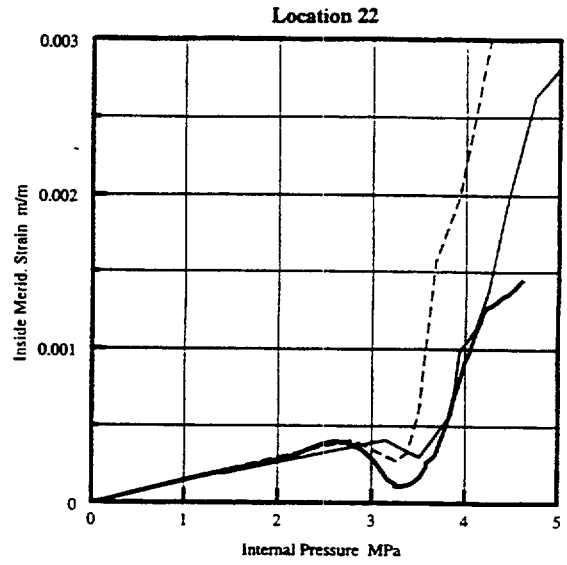
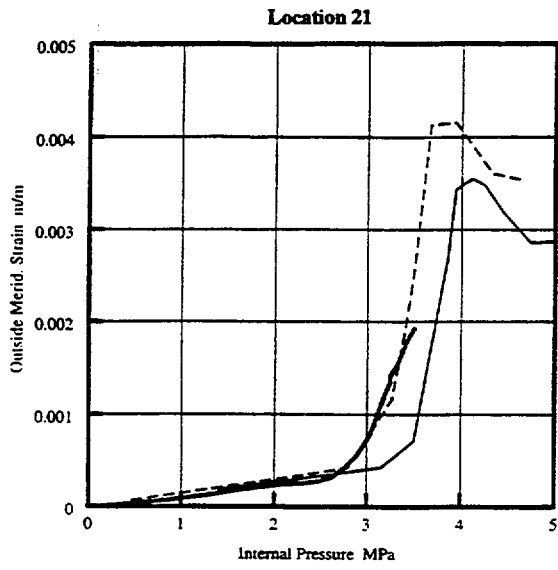




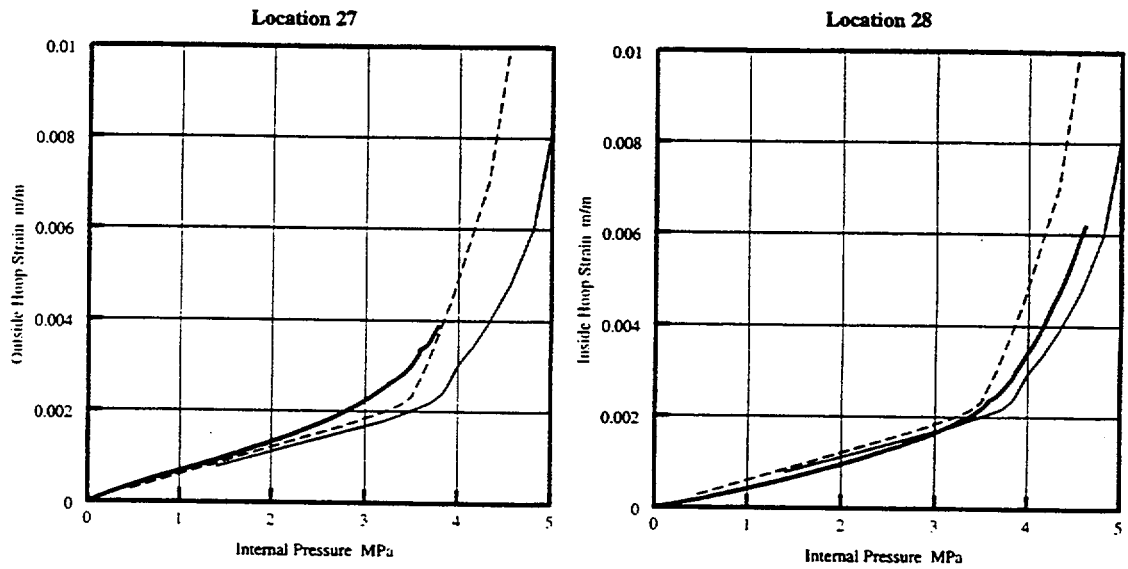
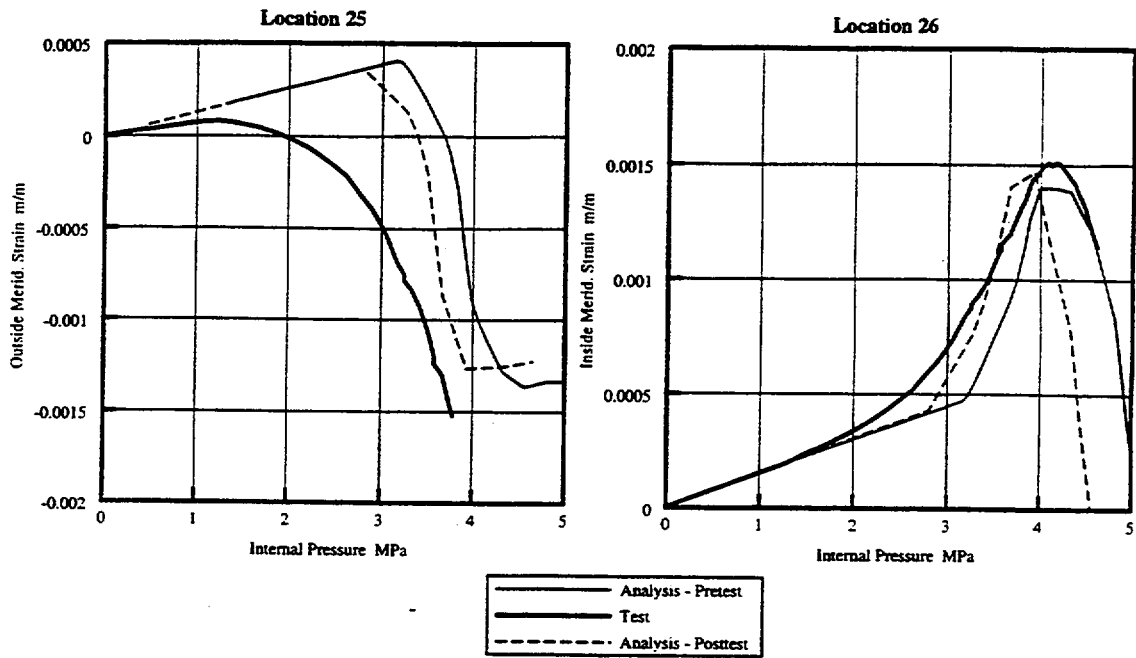


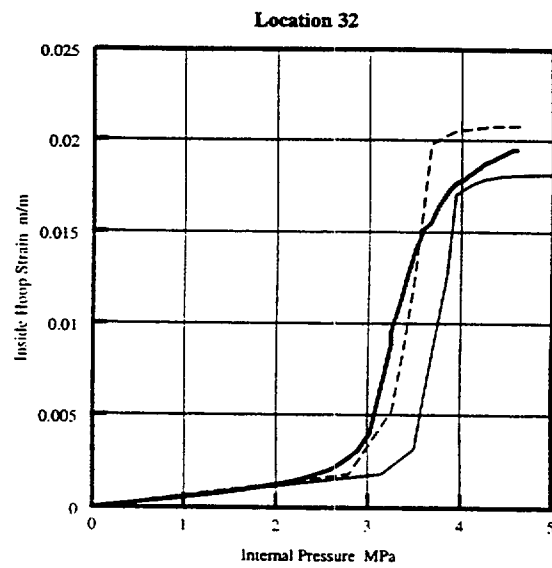
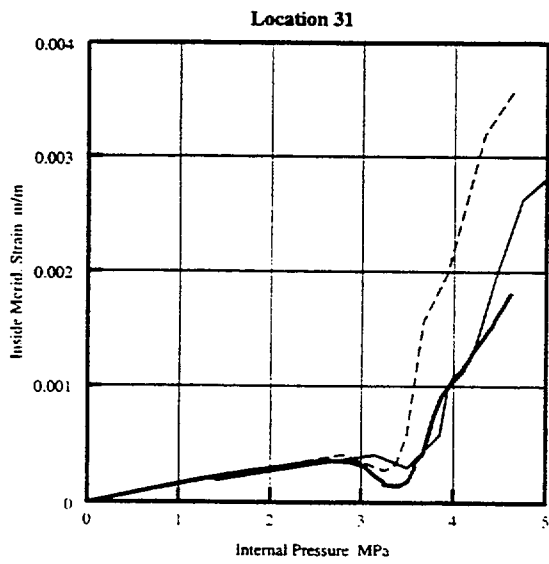
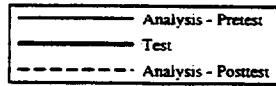
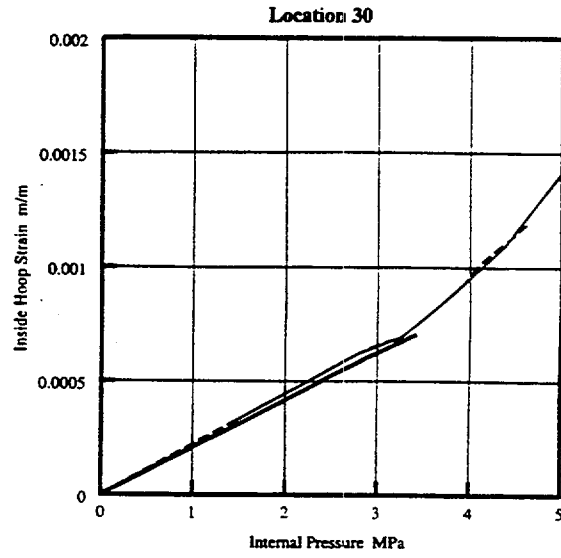
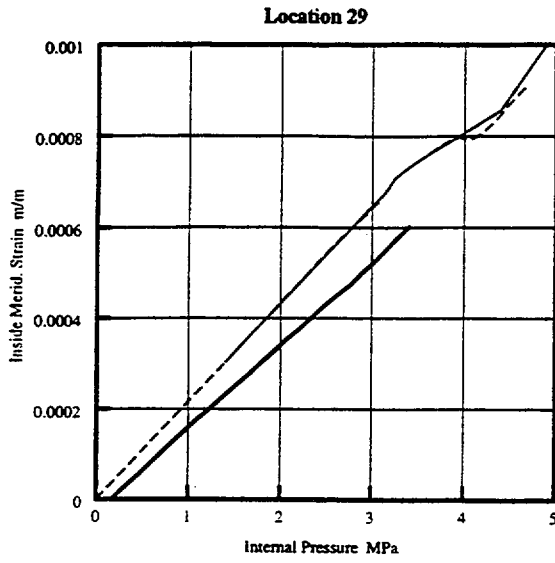
B-5 of B-15



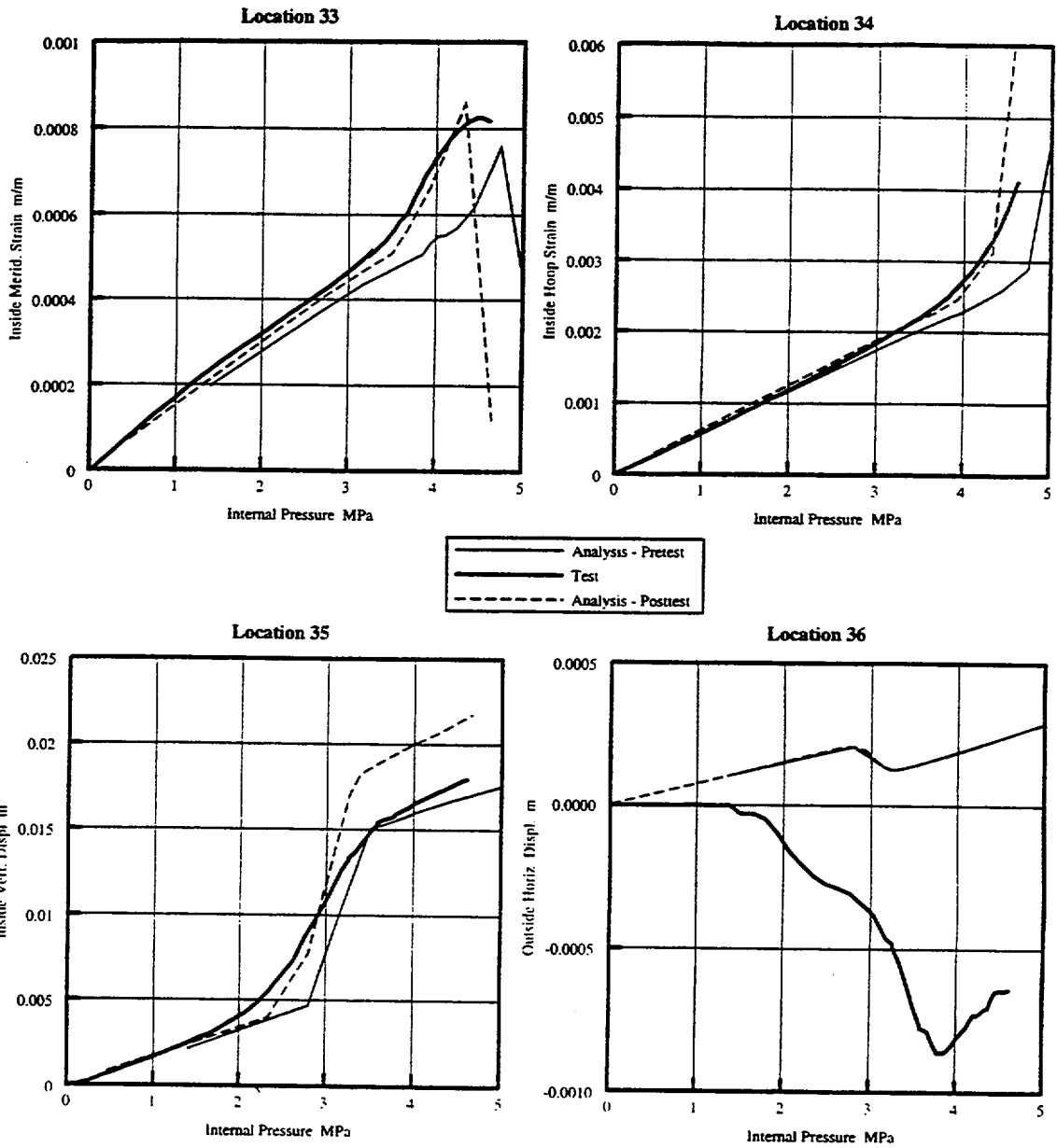


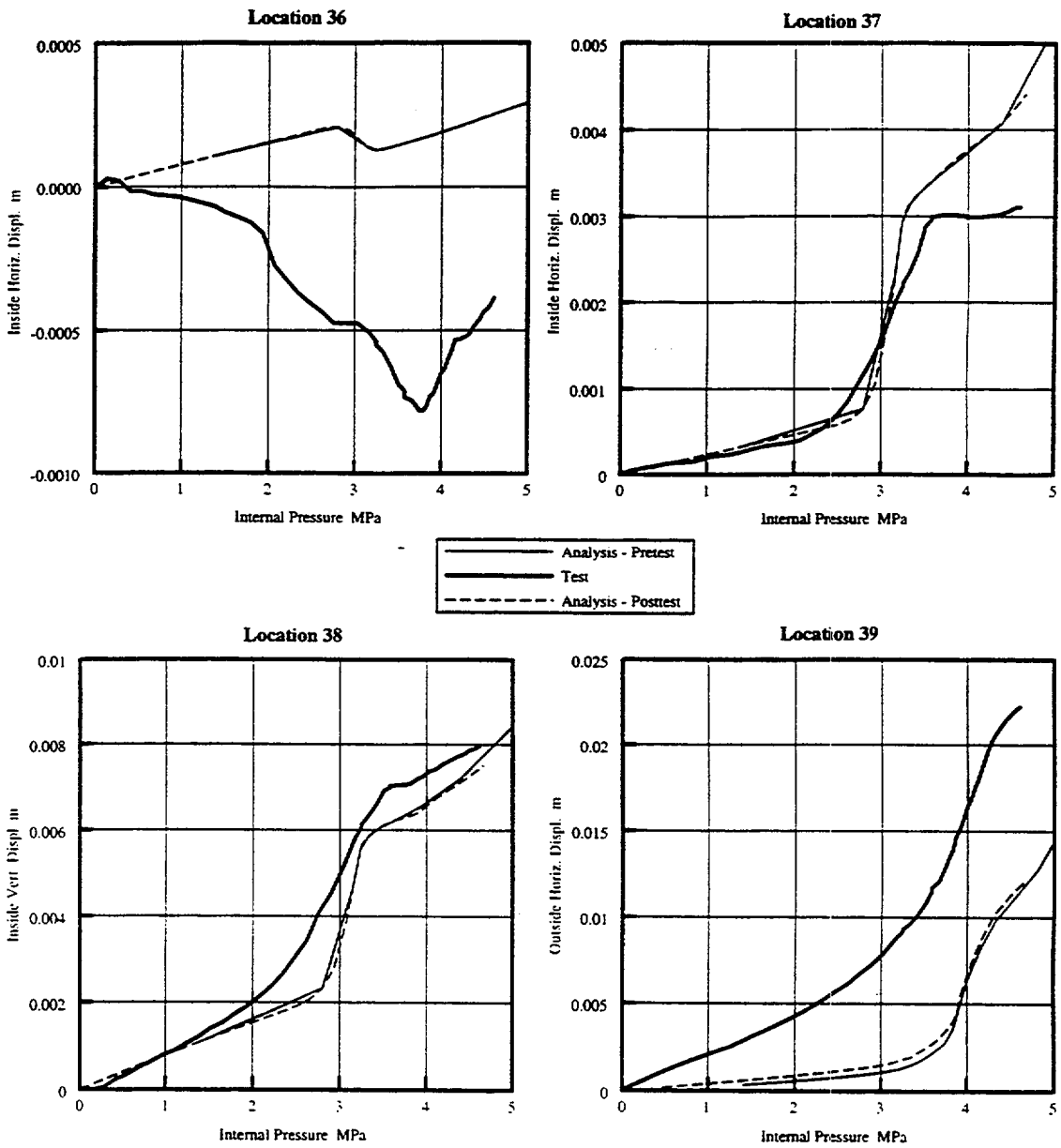
B-7 of B-15

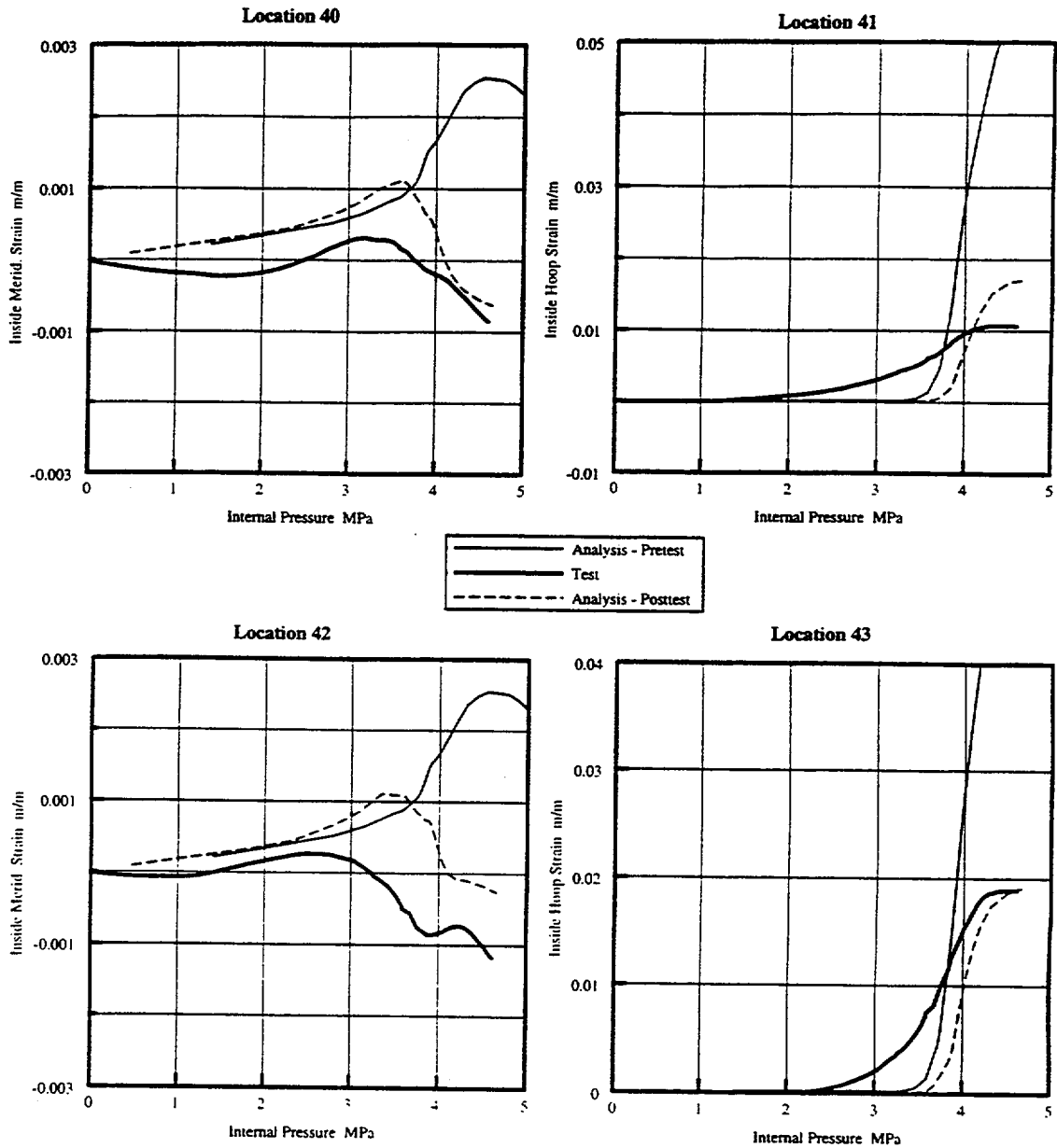




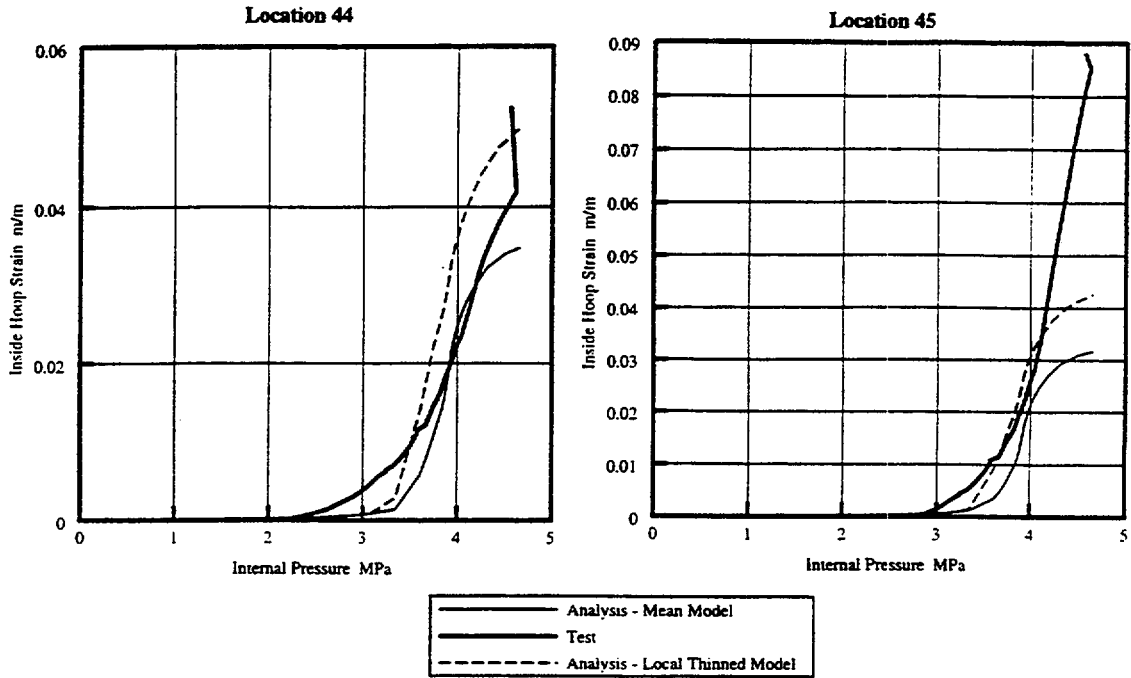
B-9 of B-15

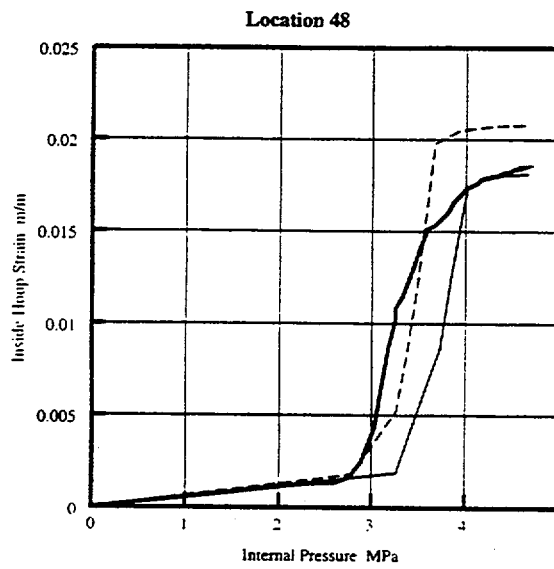
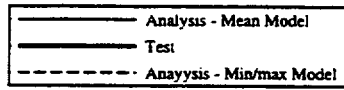
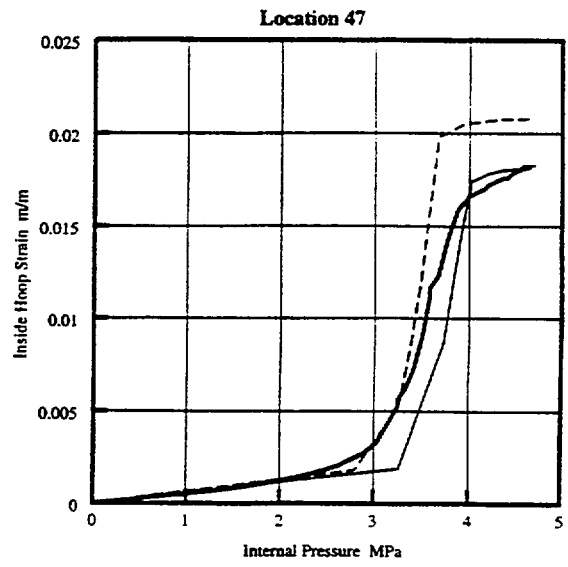
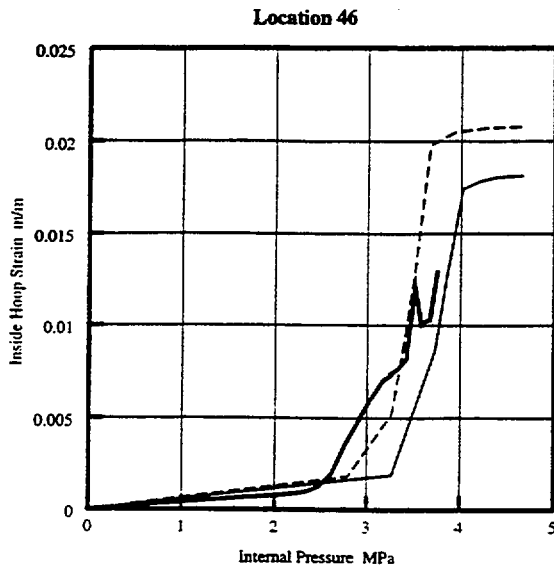




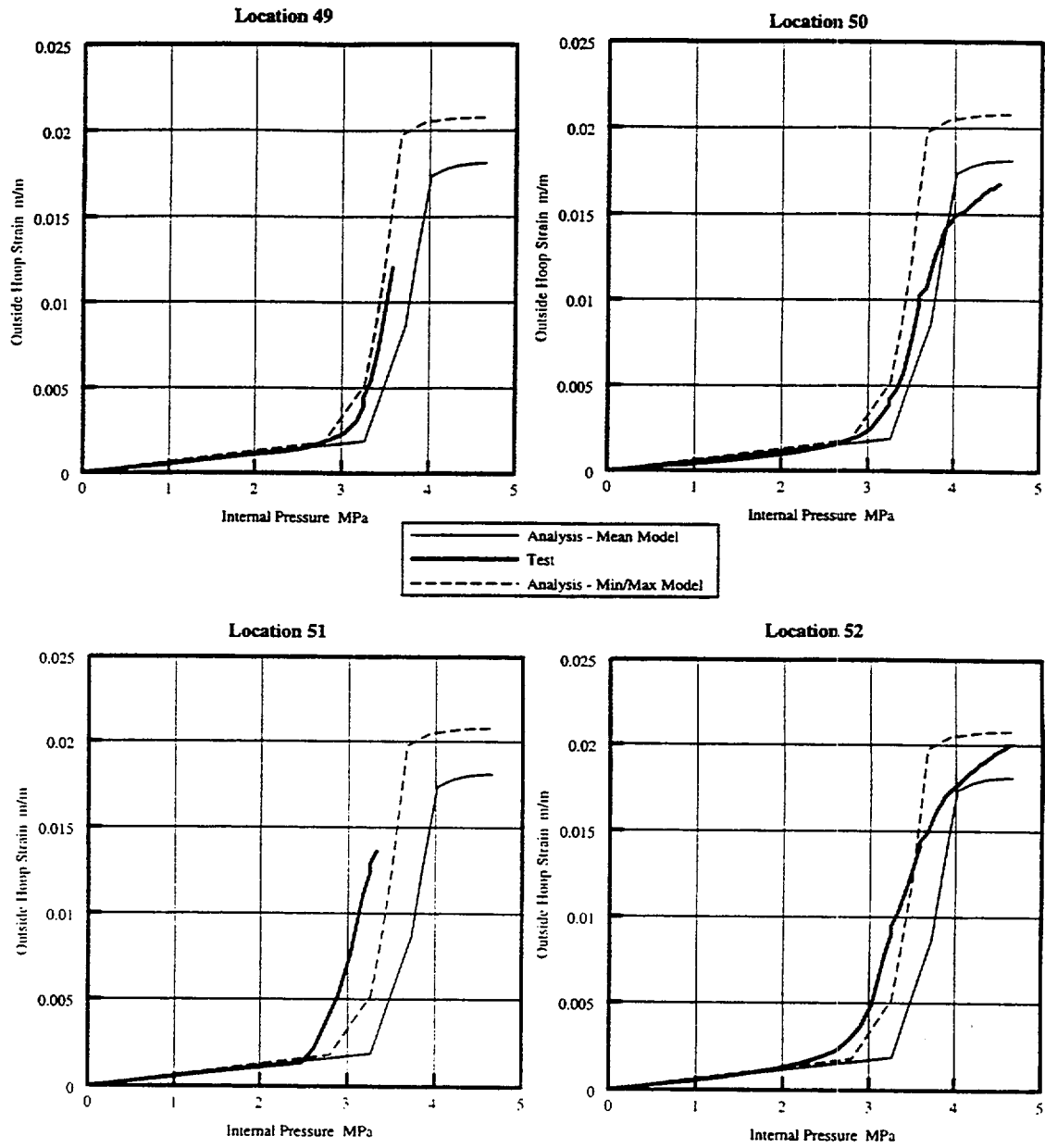


B-12 of B-15





B-14 of B-15



B-15 of B-15

Appendix B-5

Japan Atomic Energy Research Institute (JAERI)

Japan

Post-test Analysis of SCV Test by JAERI with ABAQUS

SUGIMOTO, Jun and NIYAMA, Kenji*

Japan Atomic Energy Research Institute

Tokai-mura, Ibaraki-ken, 319-1195 Japan

*Mitsubishi Research Institute, Inc.

Otemachi 2-3-6, Chiyoda-ku, Tokyo 100-8141 Japan

1. Introduction

Containment Model Tests to investigate a failure of the containment vessel has been initiated as a joint research program among Nuclear Power Engineering Corporation (NUPEC), U.S. Nuclear Regulatory Commission (NRC) and Sandia National Laboratories (SNL). For the effective pre- and post test analysis of these tests, the Round Robin analytical activities have been organized.

JAERI has performed the post-test analysis of SNL's 1/6 scale RCCV test⁽¹⁾⁽²⁾, and the pre-test analysis of this Steel Containment Vessel (SCV) test with ABAQUS code⁽³⁾. The present paper describes the results of the post-test analysis for SCV test.

2. FEM Modeling with ABAQUS

(1) FEM Mesh

A finite element code for non-linear problems, ABAQUS, was used to analyze the behavior of SCV and Contact Structure (CS). Both SCV and CS were modeled with shell elements. Most parts were modeled with 4-node shell elements. The top of the top head and hatch cover were modeled with 3-node shell elements. The total number of integration points in element section was five. Figures 1 and 2 show the FEM mesh of SCV and CS. The FEM model is 180-degree symmetric, and modeled between 270 and 90 degree directions in the global coordinate system. The part lower than the upper surface of the ring support, i.e. $z < 0$ in the global coordinate system, was not modeled in the present

analysis, because the bottom head is much thicker than the rest of the system and the deformation of this part is expected to be negligible.

Nodes for SCV model were located along the center of shell thickness so that the eccentricity due to different shell thickness could be considered. The measured gaps for as-built model were averaged for each elevation. Nodes for CS were located so that the gaps between SCV and CS were set to the averaged value.

(2) Contact Modeling

Contact between SCV and CS are modeled with small-sliding surface contact pair with friction coefficient 0. Type of contact model is hard contact model in ABAQUS.

(3) Material Properties

The SCV is made of two materials, SGV480 and SPV490, welded into one body. NUPEC conducted tensile tests of the material pieces cut from SCV. The results of the tensile tests were used for the material properties. The tri-linear curve was used to model stress-strain relation of the materials. Young's moduli were measured by NUPEC. The hardening coefficients for two materials were evaluated by the least squares method using tensile tests data after yielding point. After the stress reached tensile strength, the hardening coefficient was set to zero. The tensile test data at loc-11 was not used to evaluate hardening coefficient because Young's modulus is much different from that measured by NUPEC. Evaluated material properties are presented in Table 1. Figures 3 and 4 show the stress-strain relation, measured in the tensile tests, used in the present analysis for SGV480 and SPV490, respectively. Material properties of the CS made of SA516-70 are also presented in Table 1. The CS is assumed to be elastic in the present analysis because it is much thicker than the SCV.

Thickness for each part of the SCV model was set to averaged value measured for as-built model. Because there were no measured data for CS, thickness for the CS model was set to the design value.

(4) Boundary Conditions and Loading

The bottom of the model was completely fixed. Symmetric conditions were used as the boundary condition on the plane of symmetry.

The internal pressure was loaded to SCV in the test. The pressure level was increased in the analysis until the calculation was stopped because of numerical instability due to plastic deformation.

(5) Changes from Pre-test Model

In this post-test model, there are some changes from pre-test model.

In the pre-test model, nodes for SCV were located along internal surface of the shell to set the clearance between SCV and CS easily, while in the post-test model, they were located along the thickness center of the shell, so that eccentricity due to different thickness of the shell could be considered.

Thickness for each part of the SCV model and initial gap between SCV and CS, in the present model, were set to averaged value measured in as-built situation. Design thickness for each part of the SCV model and averaged value measured for as-built model are compared in Table 2. Initial gap size for the post-test model is presented in Fig. 5, compared with the averaged gap size measured for as-built model. In the pre-test model, initial gap size was set to the design values. They are 18mm in conical shells, and 9mm in hatch reinforcement plate. Measured gap size was almost same or slightly higher than the design value, used in the pre-test model.

3. Calculated Results

Deformations on 0-degree section in global coordinate system at some pressure levels are shown in Figs. 6 through 9. Figures 10 through 15 show distributions of equivalent plastic strain and Mises stress at some pressure levels. Clearances between SCV and CS at some pressure levels are shown in Figs. 16 and 17.

(1) Contact between SCV and CS

The first contact between SCV and CS occurred around the knuckle past at 4.00MPa. At 4.70MPa, the hatch reinforcement plate contacted with CS. As the pressure level increased, most of conical shells contacted with CS except around stiffening plate as shown in Fig. 8. In addition, SCV and CS were still open around hatch reinforcement plate just above material change interface, even at high pressure level as indicated in Fig. 17.

(2) Yielding

The first yielding occurred around the knuckle, and the hatch reinforcement plate just above material change interface of middle and lower conical shells, at 2.8MPa as shown in Fig. 10. As pressure increased, high plastic deformation were observed around the knuckle and the hatch reinforcement plate. At pressure above 4.70MPa, the maximum plastic strain was detected around the hatch reinforcement plate as shown in Figs. 11 and 12.

Finally, the calculation was terminated at 13.26MPa, because of numerical instability due to large plastic deformation in top head as indicated in Fig. 13.

4. Discussion

(1) Comparison with Pre-test Results

Figure 18 shows the standard output #35, the displacement at apex of top head. The pressure level at which the calculation was terminated in the post-test analysis due to numerical instability is higher than in the pre-test analysis. Since the material properties for both analysis were the same, this is probably due to the different shell thickness modeled as mentioned in 2(5). The final pressure at which the calculation was terminated increase from 11.61MPa in pre-test analysis to 13.26MPa in post-test analysis.

In some standard output locations, strains are limited by contacts between SCV and CS. For example, in the standard output #2 located around the hatch reinforcement plate shown in Fig. 19, the strain stopped to increase above around 4MPa. Because initial gap size are different between two models, the calculated strain reached different value in the two models after SCV contacted with CS. It is considered that the initial gap size has much influence on the strain behaviors.

In the standard output location of transition region, the results of two models gave little difference at the beginning of loading, as typically shown in Fig. 20 for the standard output #17 and #18. From these results, it is considered that the eccentricity due to the change of shell thickness used in the post-test analysis seems to has little effect on strain behaviors.

(2) Comparison with Test Results

In general, the calculations give reasonable agreement with the experiments. Some identified differences between the calculation and experiment are as follows:

At many standard outputs as typically shown in Fig. 19, the measured strain seem to be plastic only at lower pressure compared with the calculation. Tri-linear fit of material plasticity might have resulted in these behavior.

As described before, the calculated strains are limited by the contact between SCV and CS. However the strain after SCV contacted with CS are different between the calculation and the experiment as shown in Fig. 19 for the standard output location #2. The calculated maximum strain in these regions are sensitive with the initial gap size.

A pair of test results at standard output locations #17 and #18 shows that the bending occurred around this region, while in the calculation no bending occurred as shown in Fig. 20. These output location in transition region are near material interface. The calculated results show little bending at the location in both pre-test and post-test results, although the eccentricity is considered in the post-test analysis.

(3) Failure Mode

Although no failure model was included in the present model, possible failure modes are discussed here.

The calculation was terminated at 13.26MPa as shown in Fig. 13. It is predicted that the structural failure occur in the top head. At the pressure level above 8.20MPa, the plastic strain around the knuckle and in the top head exceed that around the hatch reinforcement plate as shown in Figs. 12 and 13. If the internal pressure reaches at this level, a rupture will occur in the top head region.

Another possible failure mode is a local failure. The plastic strain increase suddenly around the hatch reinforcement plate after the yielding occurred, and the equivalent plastic strain exceeded five percent at 4.70MPa as shown in Fig. 11. The maximum plastic strain was detected around the hatch reinforcement plate at that pressure level in the analysis. In this region, the shells with three different thickness connected and the initial gap between SCV and CS varied for each shells with different thickness. SCV and CS kept open in this region until the high pressure level was reached as shown in Fig. 17. The stress intensity was obtained very locally around the hatch reinforcement plate, especially just below material change interface of middle and lower conical shells as indicated in Figs. 14 and 15.

In the high pressure test for SCV, the local tear occurred around the hatch reinforcement plate and on the middle stiffening ring. The tear around the hatch reinforcement plate could be predicted by FEM analysis. Otherwise, the tear on the middle stiffening plate could not be predicted from the present model, which did not model the local thinning.

5. Conclusions

A finite element code for non-linear problems, ABAQUS, was used to analyze the behavior of Steel Containment Vessel (SCV) and Contact Structure (CS). SCV and CS were modeled with shell elements and contact between SCV and CS was modeled with small-sliding surface contact pair with zero friction coefficient. In this post-test analysis, the following modifications of the model have been made from the pre-test analysis.

- (1) Nodes for SCV were located at the thickness center of shell, instead of inside surface of shell in the pre-test model.
- (2) Shell thickness was set to averaged value for each design thickness measured in as-built test.
- (3) Initial gap size between SCV and CS was set to averaged value at each elevation measured in ad-built test.

Calculated results were compared with test results and the following conclusions have been obtained.

- (1) Calculated results generally gave reasonable agreement with the test results.
- (2) Eccentricity due to different shell thickness gave little influence on the strain behaviors.
- (3) Material Properties used in the analysis, fitted with tri-linear curve, gave different results from experiments at low pressure.
- (4) Thickness of shell had influence on the stiffness of the model.
- (5) Initial gap between SCV and CS had large influence on decided the limit strain where SCV contacts with CS.

- (6) Stress intensity was observed around the hatch reinforcement plate, and plastic strain in the region exceeded five percent at about 4.70MPa.
- (7) Structural failure was detected in the top head at above 13.26MPa.
- (8) Failure mode predicted from these analysis were local failure around the hatch reinforcement plate at about 5MPa, or rapture in the top head region at above 13MPa.

References

- (1) K. Soda and H. Kimura, "Structural Analysis of the Reinforced Concrete Containment under Extreme Static and Dynamic Pressure Loading." Second Int. Conf. Containment Design and Operation, Toronto, Canada,(1990).
- (2) J. R. Weatherby, "Posttest Analysis of a 1:6-Scale Reinforced Concrete Reactor Containment Building," NUREG/CR-5476, USNRC,(1990).
- (3) H. D. Hibbitt, "ABAQUS User's Manual," Hibbitt, Karlsson & Sorensen, Inc.,(1995).

Tab. 1 Material Properties used in Analysis

Material	Young's modulus [MPa]	Poisson's ratio	Yield stress [MPa]	Hardening [MPa]	Tensile strength [MPa]
SGV470	209900	0.30	381.7	1058.	538.5
SPV490	215800	0.30	592.4	1370.	730.3
SA516-70	210000	0.29	—	—	—

Tab. 2 Comparison between Design and Measured As-built Thickness

Design Thickness [mm]	Measured Value (Model Input) [mm]	Descriptions
6.0	6.7	top head
16.5	16.8	knuckle
8.0	7.9	spherical shell
7.5	7.8	upper conical shell
8.5	8.7	middle conical shell
9.0	9.5	lower conical shell
20.0	20.7	top flange
19.0	19.9	upper stiffener
19.0	19.5	middle stiffener
9.5	9.9	lower stiffener(1)
12.5	13.3	lower stiffener(2)
17.5	18.0	hatch reinforcement plate
20.0	20.7	hatch
20.0	20.4	hatch cover

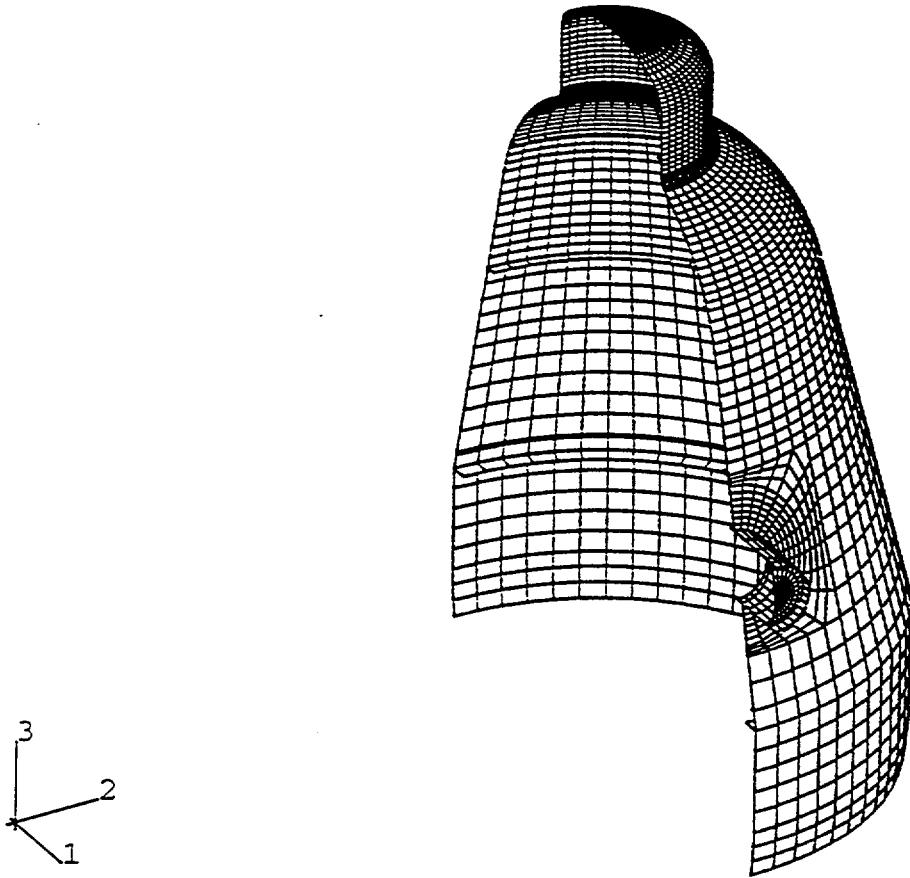


Fig. 1 FEM Mesh for SCV

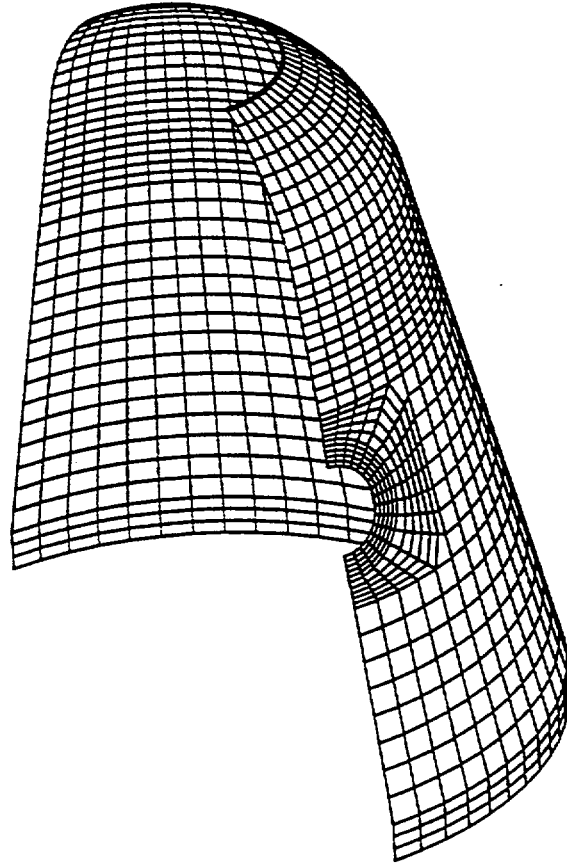
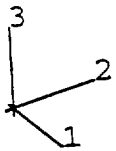


Fig. 2 FEM Mesh for CS

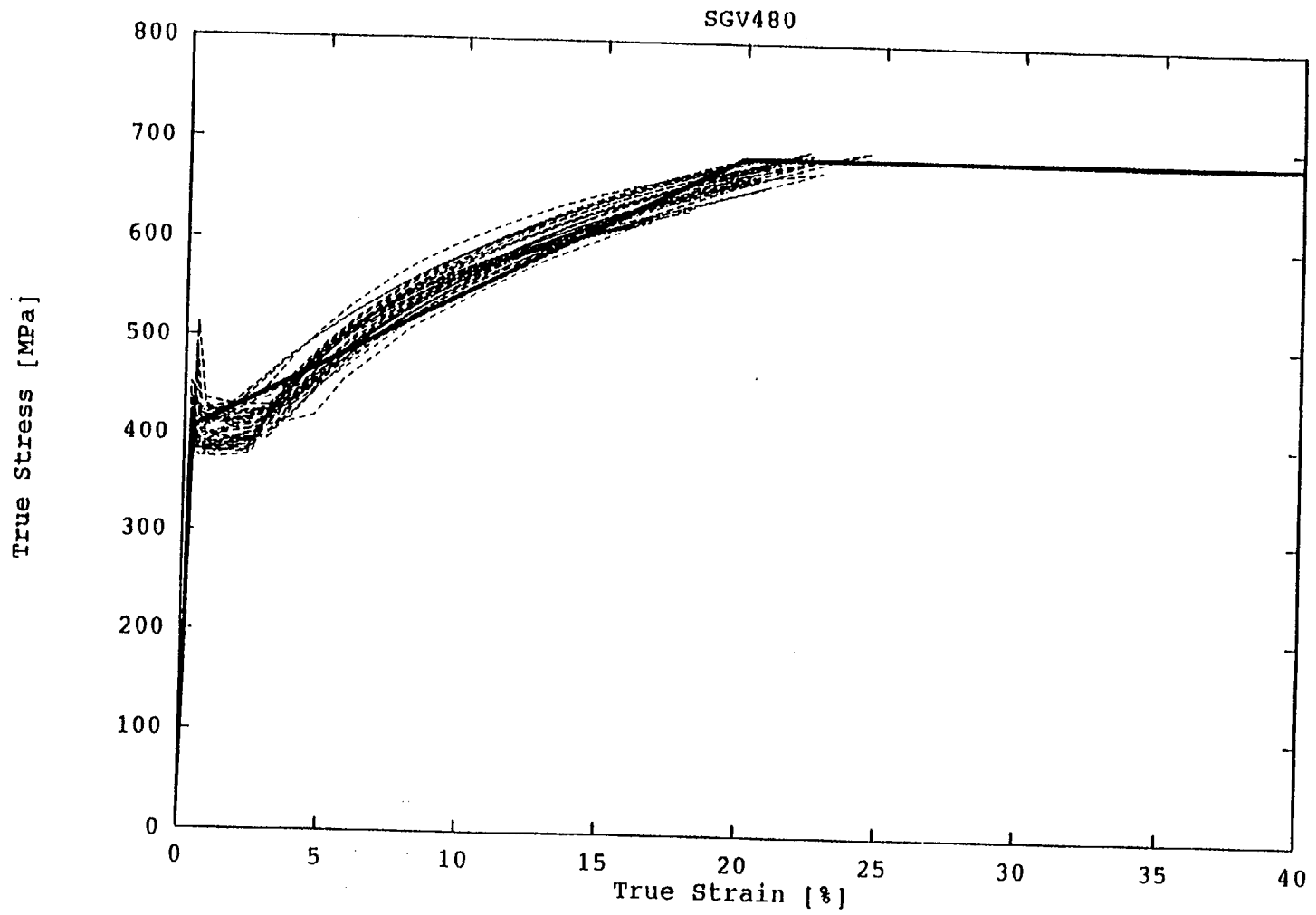


Fig. 3 Material Property for SGV480

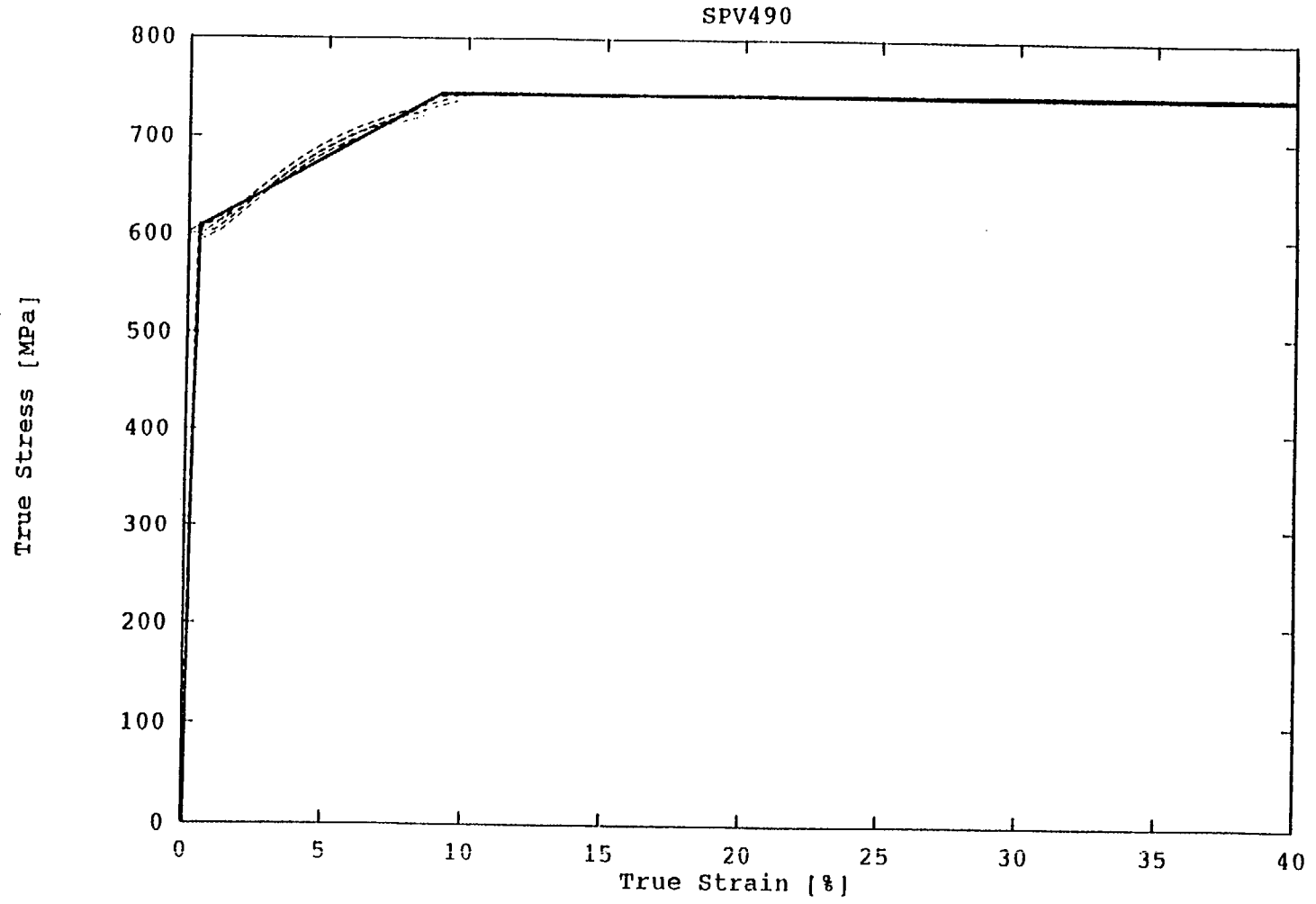


Fig. 4 Material Property for SPV490

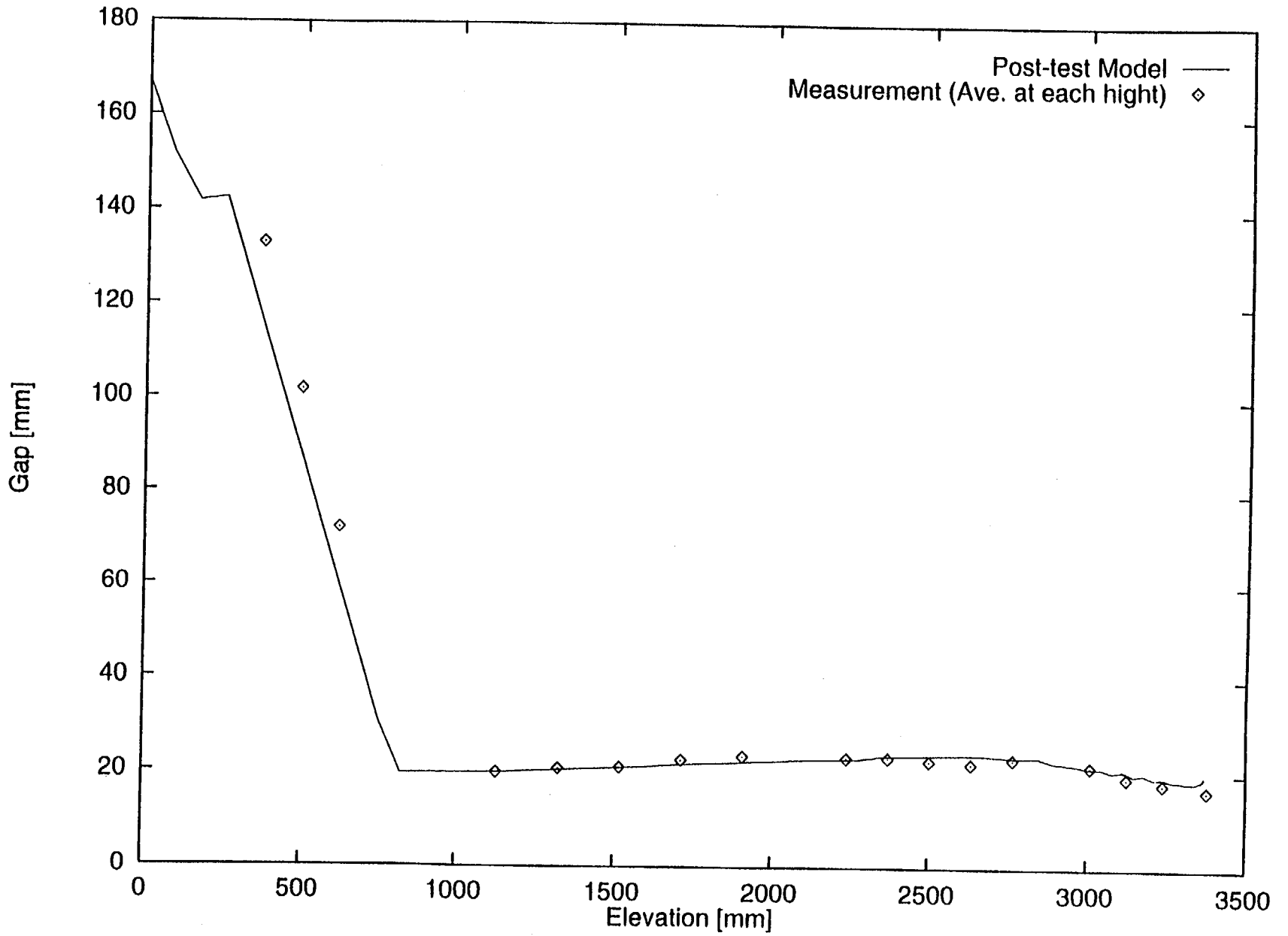


Fig. 5 Initial Gap between SCV and CS

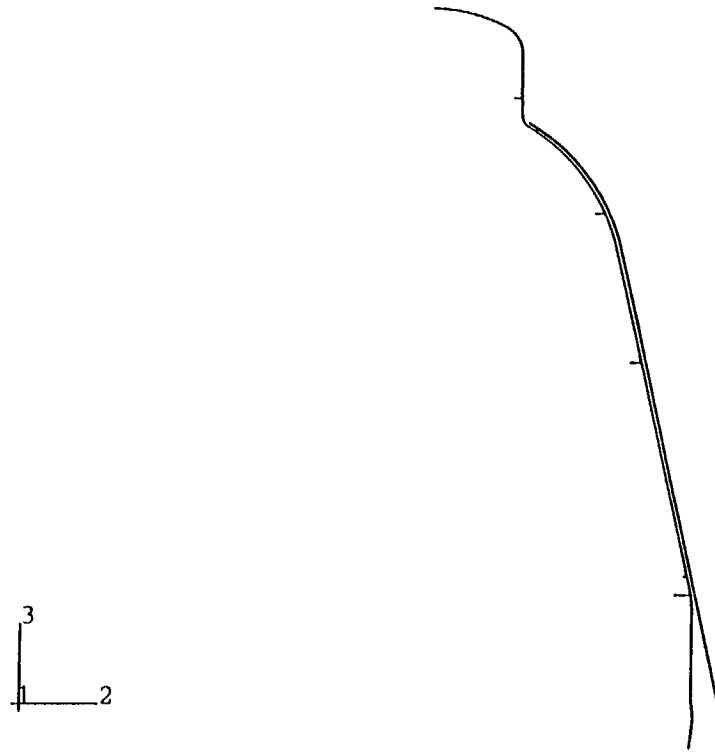


Fig. 6 Undeformed shape of SCV and CS on 0-degree Section

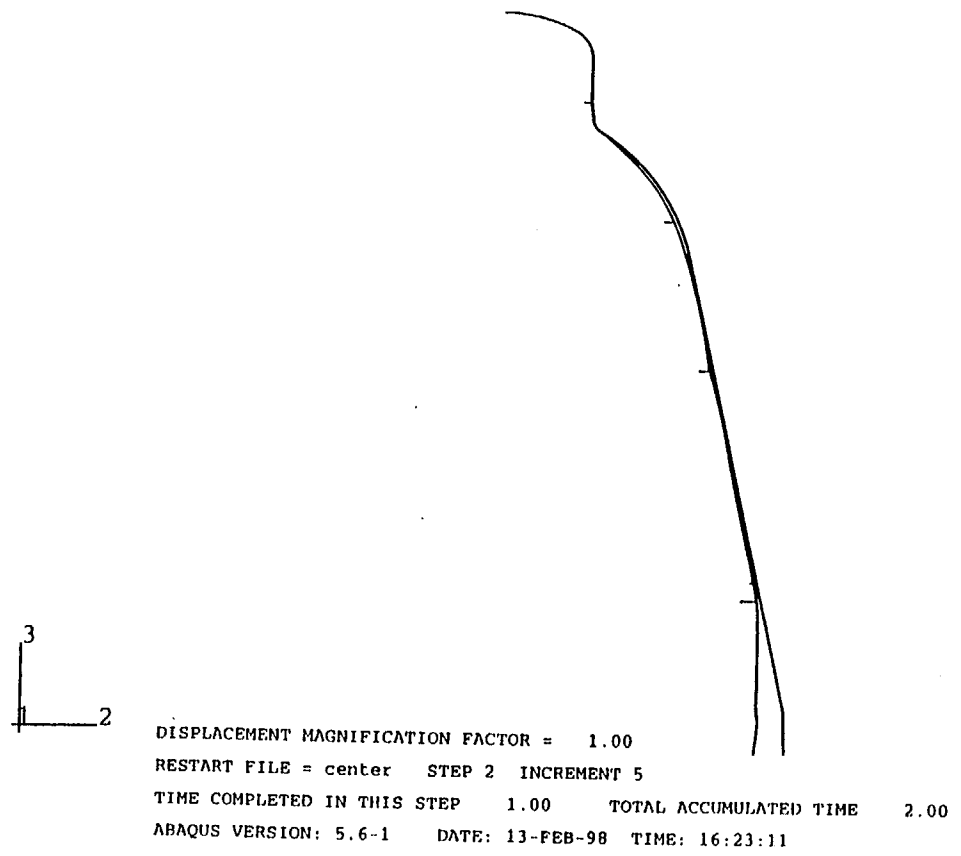


Fig. 7 Deformation on 0-degree Section at Pressure of 4.00MPa

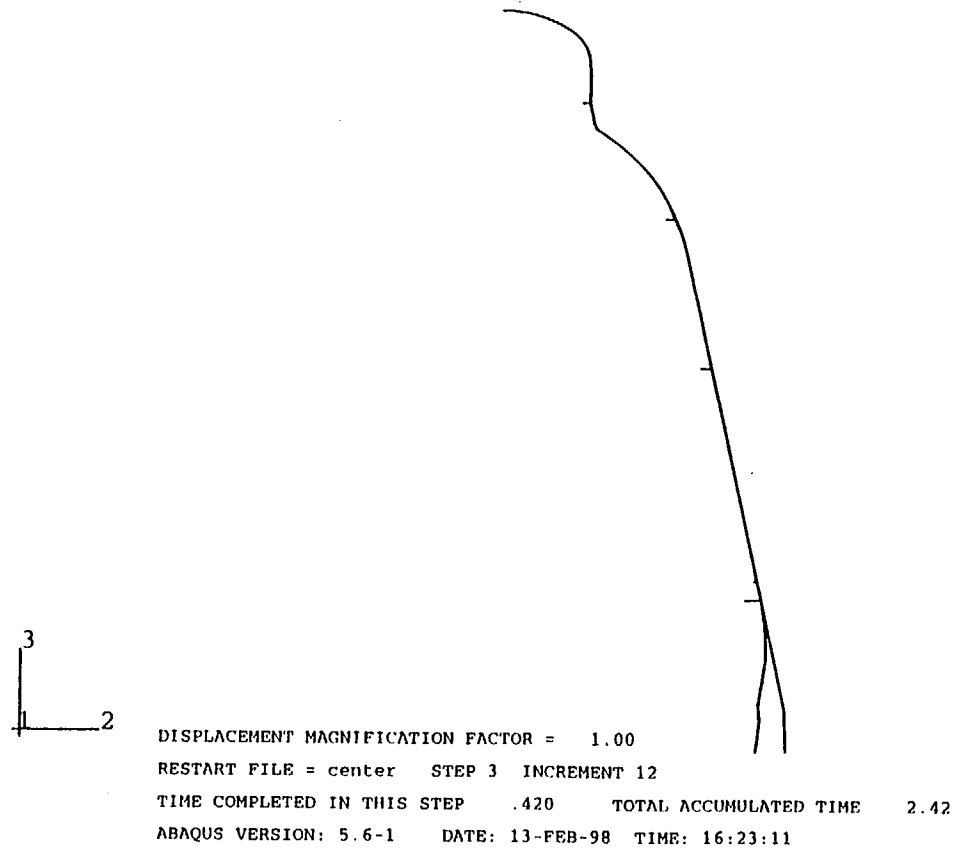


Fig. 8 Deformation on 0-degree Section at Pressure of 8.20MPa.

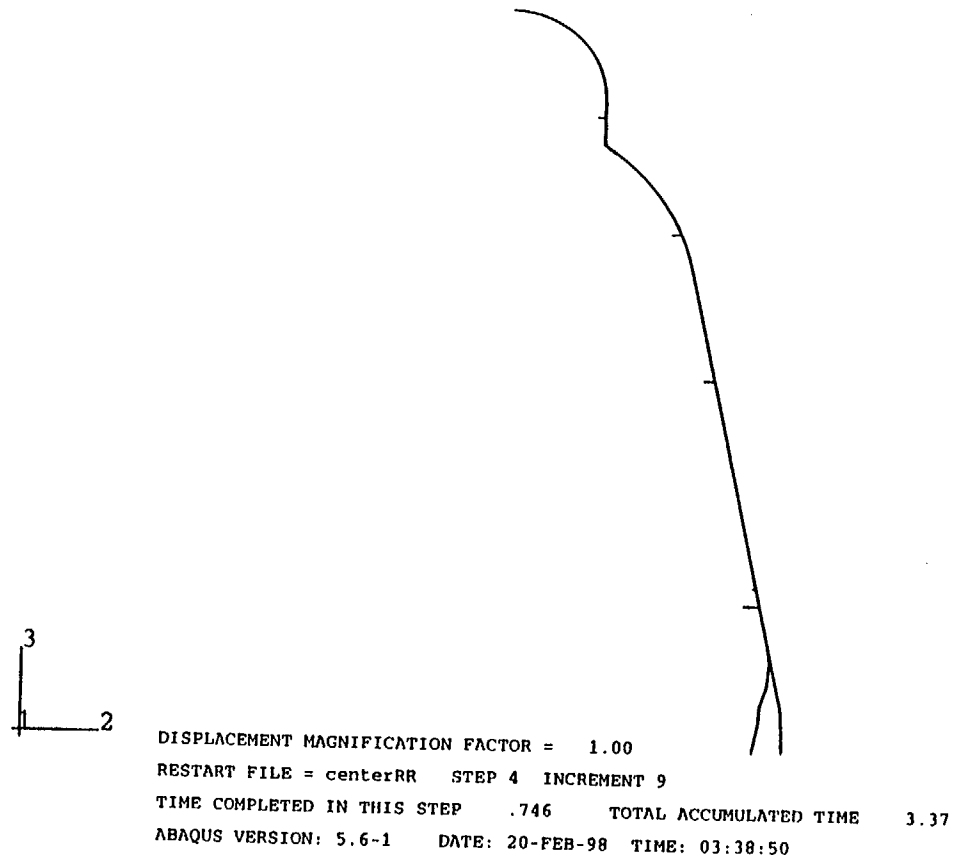
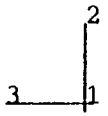


Fig. 9 Deformation on 0-degree Section at Pressure of 13.26MPa

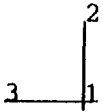


SECTION POINT :	VALUE
1	0.00E+00
2	7.03E-05
3	1.41E-04
4	2.11E-04
5	2.81E-04
6	3.52E-04
7	4.22E-04
8	4.92E-04
9	5.62E-04
10	6.32E-04
11	7.03E-04
12	7.74E-04
13	8.44E-04
14	9.14E-04

Equivalent strain
[no dimension]

DISPLACEMENT MAGNIFICATION FACTOR = 1.00
 RESTART FILE = center STEP 2 INCREMENT 2
 TIME COMPLETED IN THIS STEP .400 TOTAL ACCUMULATED TIME 1.40
 ABAQUS VERSION: 5.6-1 DATE: 13-FEB-98 TIME: 16:23:11

Fig. 10(a) Distribution of Equivalent Plastic Strain at Pressure of 2.80MPa ; inside surface



SECTION POINT 5	VALUE
1	+0.00E-02
2	+2.49E-05
3	+4.98E-05
4	+1.05E-04
5	+2.40E-04
6	+1.74E-04
7	+2.09E-04
8	+2.44E-04
9	+2.79E-04
10	+3.14E-04
11	+3.49E-04
12	+3.84E-04
13	+4.19E-04
14	+4.54E-04



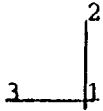
Equivalent strain
[no dimension]

DISPLACEMENT MAGNIFICATION FACTOR = 1.00
 RESTART FILE = center STEP 2 INCREMENT 2
 TIME COMPLETED IN THIS STEP .400 TOTAL ACCUMULATED TIME 1.40
 ABAQUS VERSION: 5.6-1 DATE: 13-FEB-98 TIME: 16:23:11

Fig. 10(b) Distribution of Equivalent Plastic Strain at Pressure of 2.80MPa ; outside surface

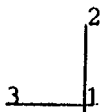
SECTION POINT :	
PDMAC	VALUE
1	+0.00E-01
2	+5.55E-01
3	+1.11E-01
4	+1.66E-01
5	+2.22E-01
6	+2.77E-01
7	+3.33E-01
8	+3.88E-01
9	+4.44E-01
10	+4.99E-01
11	+5.55E-01
12	+6.10E-01
13	+6.65E-01
14	+7.21E-01

Equivalent strain
[no dimension]



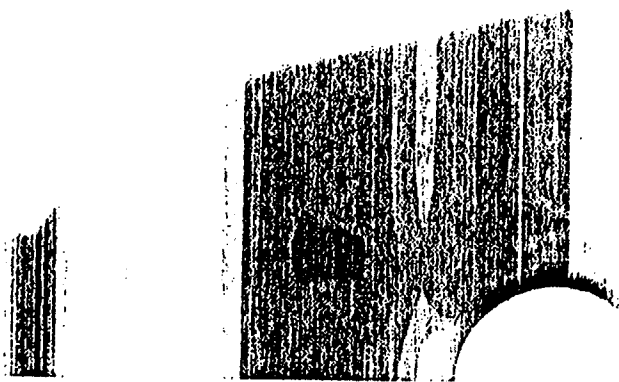
DISPLACEMENT MAGNIFICATION FACTOR = 1.00
 RESTART FILE = center STEP 3 INCREMENT 3
 TIME COMPLETED IN THIS STEP 7.000E-02 TOTAL ACCUMULATED TIME 2.07
 ABAQUS VERSION: 5.6-1 DATE: 13-FEB-98 TIME: 16:23:11

Fig. 11(a) Distribution of Equivalent Plastic Strain at Pressure of 4.70MPa ; inside surface



SECTION POINT 5	VALUE
PERAC	-0.00E-00
	-4.87E-03
	-9.74E-03
	-1.46E-02
	-1.95E-02
	-2.43E-02
	-2.92E-02
	-3.41E-02
	-3.90E-02
	-4.38E-02
	-4.87E-02
	-5.36E-02
	-5.84E-02
	-6.33E-02

Equivalent strain
[no dimension]



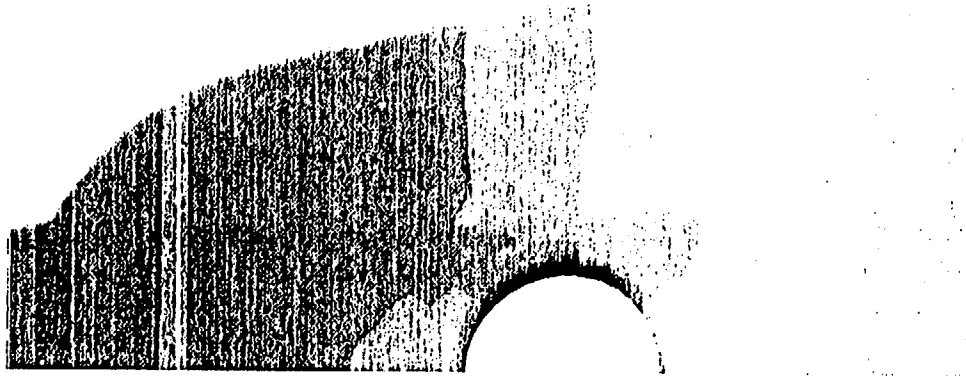
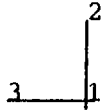
DISPLACEMENT MAGNIFICATION FACTOR = 1.00
 RESTART FILE = center STEP 3 INCREMENT 3
 TIME COMPLETED IN THIS STEP 7.000E-02 TOTAL ACCUMULATED TIME 2.07
 ABAQUS VERSION: 5.6-1 DATE: 13-FEB-98 TIME: 16:23:11

Fig. 11(b) Distribution of Equivalent Plastic Strain at Pressure of 4.70MPa ; outside surface

SECTION POINT 1

FORMS	VALUE
	-0.00E+00
	-7.48E-02
	-1.50E-01
	-2.24E-01
	-2.99E-01
	-3.74E-01
	-4.49E-01
	-5.24E-01
	-5.98E-01
	-6.73E-01
	-7.48E-01
	-8.23E-01
	-8.97E-01
	-9.72E-01

Equivalent strain
[no dimension]

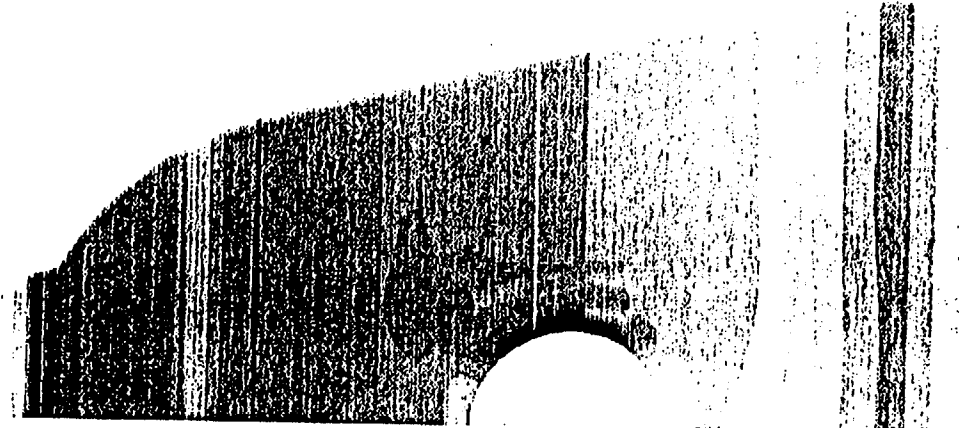
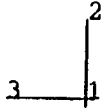


DISPLACEMENT MAGNIFICATION FACTOR = 1.00
 RESTART FILE = center STEP 3 INCREMENT 9
 TIME COMPLETED IN THIS STEP .303 TOTAL ACCUMULATED TIME 2.30
 ABAQUS VERSION: 5.6-1 DATE: 13-FEB-98 TIME: 16:23:11

Fig. 12(a) Distribution of Equivalent Plastic Strain at Pressure of 7.00MPa ; inside surface

SECTION POINT 5	VALUE
1	+0.00E+00
2	-5.81E-03
3	-1.16E-02
4	-1.74E-02
5	-2.32E-02
6	-2.90E-02
7	-3.48E-02
8	-4.06E-02
9	-4.65E-02
10	-5.23E-02
11	-5.81E-02
12	-6.39E-02
13	-6.97E-02
14	-7.55E-02

Equivalent strain
[no dimension]



DISPLACEMENT MAGNIFICATION FACTOR = 1.00
 RESTART FILE = center STEP 3 INCREMENT 9
 TIME COMPLETED IN THIS STEP .303 TOTAL ACCUMULATED TIME 2.30
 ABAQUS VERSION: 5.6-1 DATE: 13-FEB-98 TIME: 16:23:11

Fig. 12(b) Distribution of Equivalent Plastic Strain at Pressure of 7.00MPa ; outside surface

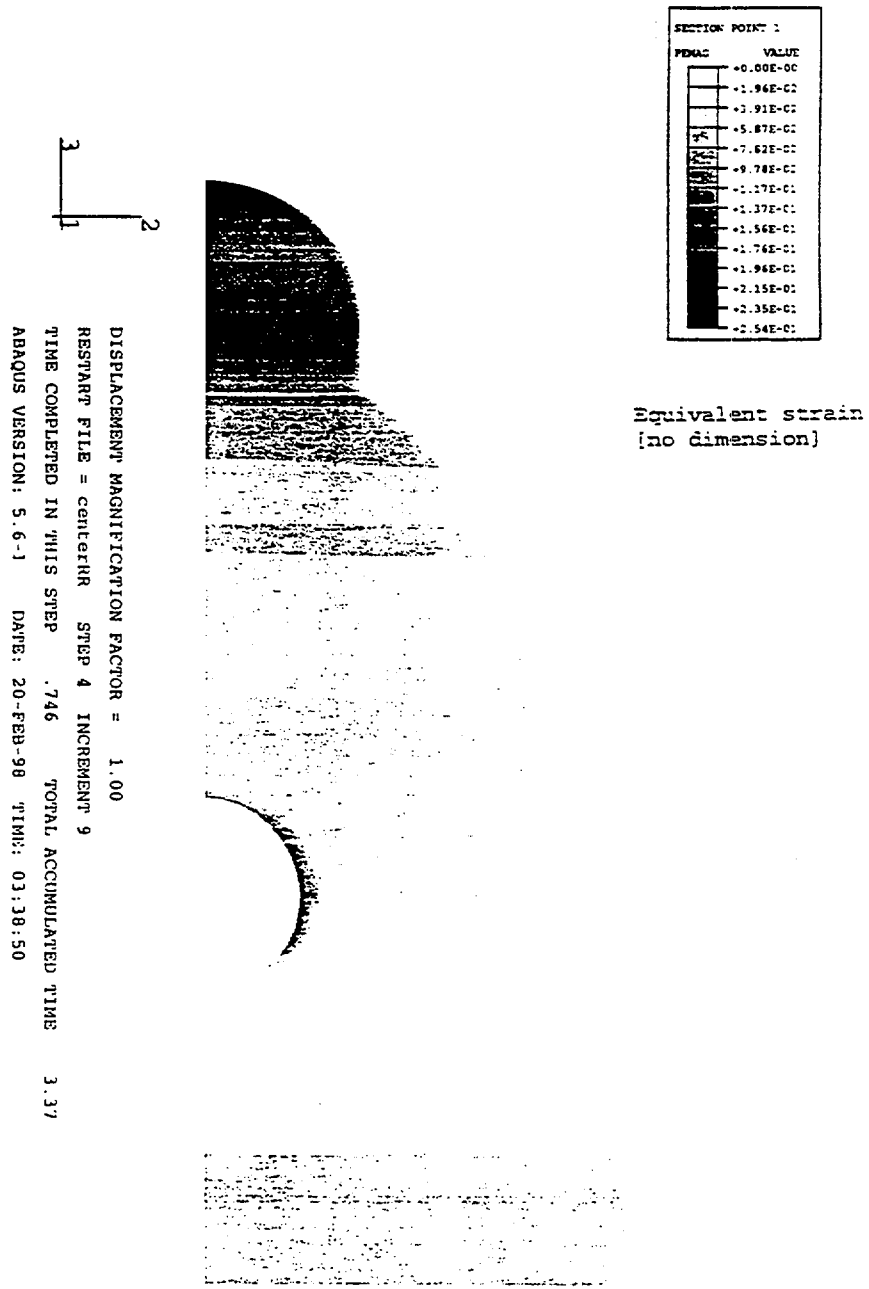
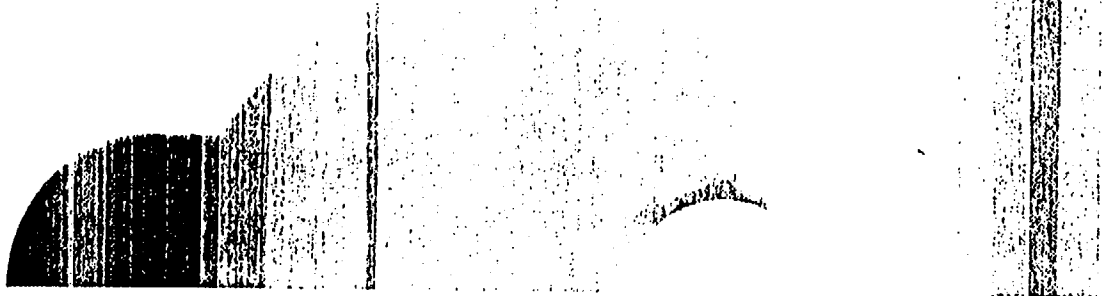
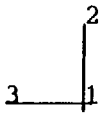


Fig. 13(a) Distribution of Equivalent Plastic Strain at Pressure of 13.26MPa ; inside surface

SECTION POINT 5	
PRINC	VALUE
1	-0.00E+00
2	-2.07E-02
3	-4.13E-02
4	-6.20E-02
5	-8.26E-02
6	-1.03E-01
7	-1.24E-01
8	-1.45E-01
9	-1.65E-01
10	-1.86E-01
11	-2.07E-01
12	-2.27E-01
13	-2.48E-01
14	-2.69E-01

Equivalent strain
[no dimension]

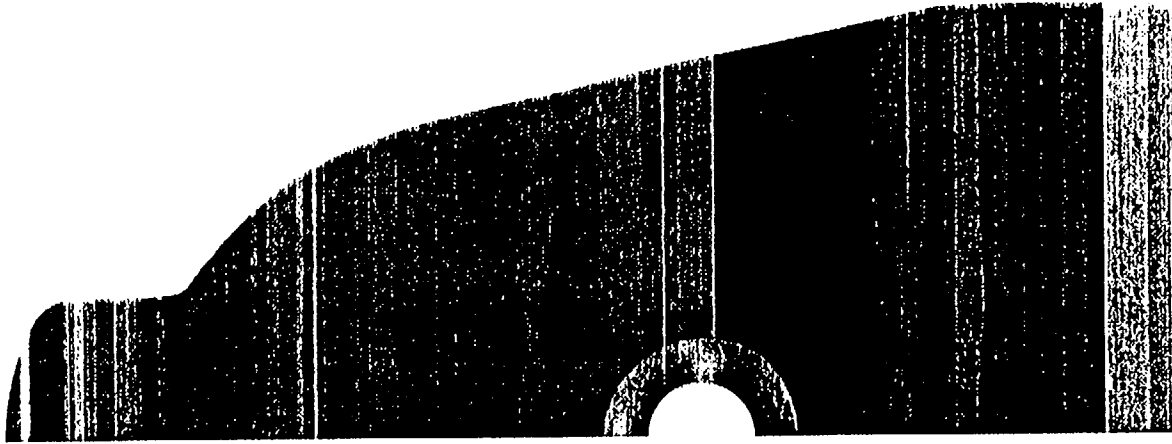
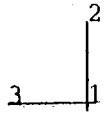


DISPLACEMENT MAGNIFICATION FACTOR = 1.00
 RESTART FILE = centerRR STEP 4 INCREMENT 9
 TIME COMPLETED IN THIS STEP .746 TOTAL ACCUMULATED TIME 3.37
 ABAQUS VERSION: 5.6-1 DATE: 20-FEB-98 TIME: 03:30:50

Fig. 13(b) Distribution of Equivalent Plastic Strain at Pressure of 13.26MPa ; outside surface

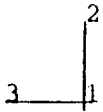
SECTION POINT :	VALUE
MISES	-4.31E+02
	-5.91E+01
	-1.12E+02
	-1.65E+02
	-2.17E+02
	-2.70E+02
	-3.22E+02
	-3.75E+02
	-4.28E+02
	-4.80E+02
	-5.33E+02
	-5.85E+02
	-6.38E+02
	-6.90E+02

Mises Stress
[MPa]



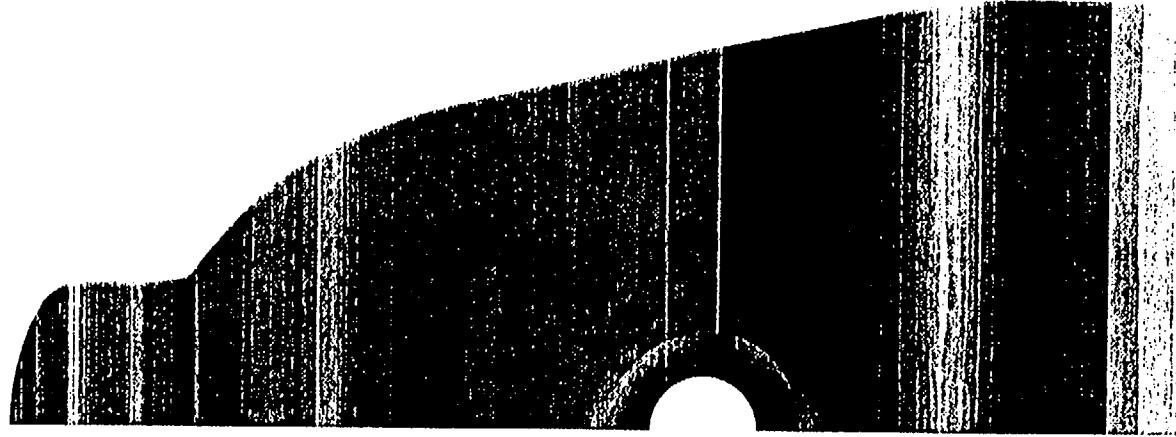
DISPLACEMENT MAGNIFICATION FACTOR = 1.00
 RESTART FILE = center STEP 3 INCREMENT 3
 TIME COMPLETED IN THIS STEP 7.000E-02 TOTAL ACCUMULATED TIME 2.07
 ABAQUS VERSION: 5.6-1 DATE: 13-FEB-98 TIME: 16:23:11

Fig. 14(a) Distribution of Mises Stress at Pressure of 4.70MPa ; inside surface



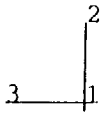
SECTION POINT 5	
MISE	VALUE
1	7.01E+01
2	5.91E+01
3	4.11E+01
4	2.63E+01
5	2.16E+01
6	2.68E+01
7	3.20E+01
8	3.72E+01
9	4.24E+01
10	4.76E+01
11	5.28E+01
12	5.80E+01
13	6.32E+01
14	6.84E+01

Mises Stress
[MPa]



DISPLACEMENT MAGNIFICATION FACTOR = 1.00
 RESTART FILE = center STEP 3 INCREMENT 3
 TIME COMPLETED IN THIS STEP 7.000E-02 TOTAL ACCUMULATED TIME 2.07
 ABAQUS VERSION: 5.6-1 DATE: 13-FEB-98 TIME: 16:23:11

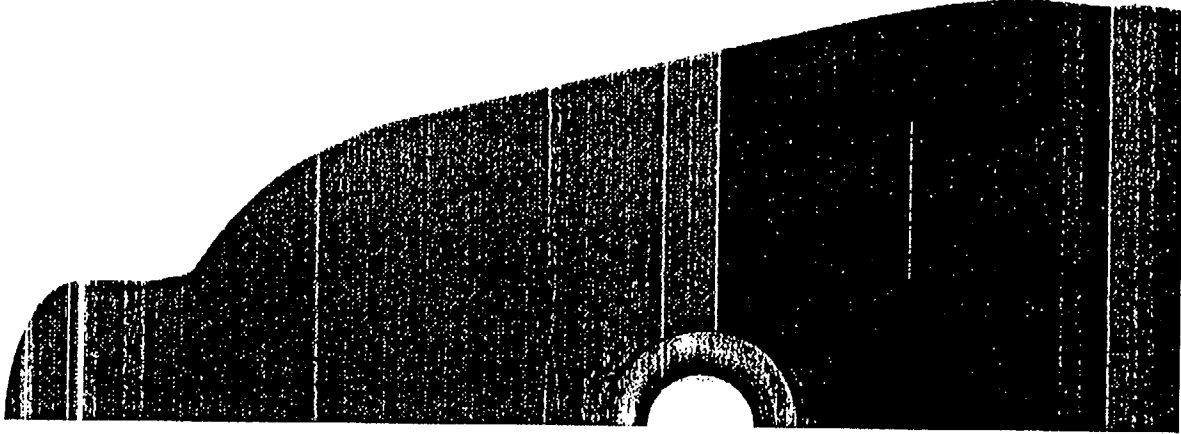
Fig. 14(b) Distribution of Mises Stress at Pressure of 4.70MPa ; outside surface



SECTION POINT :

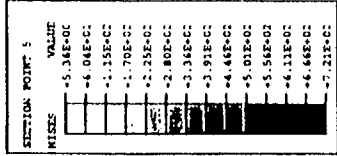
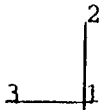
MISES	VALUE
1	-1.09E+02
2	4.74E+02
3	1.24E+02
4	-1.86E+02
5	-2.37E+02
6	-2.93E+02
7	-3.50E+02
8	-4.06E+02
9	-4.62E+02
10	-5.19E+02
11	-5.75E+02
12	-6.32E+02
13	-6.88E+02
14	-7.45E+02

Mises Stress
[MPa]

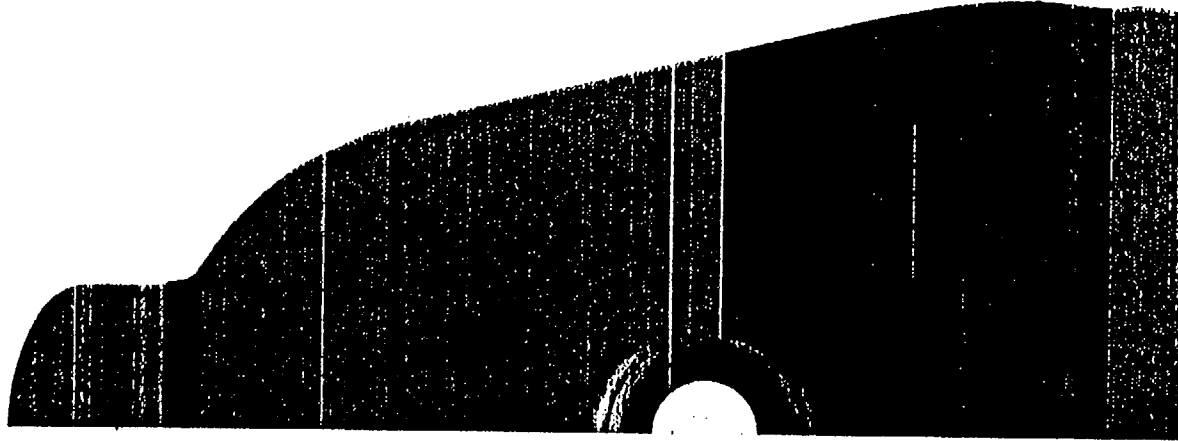


DISPLACEMENT MAGNIFICATION FACTOR = 1.00
 RESTART FILE = center STEP 3 INCREMENT 9
 TIME COMPLETED IN THIS STEP .303 TOTAL ACCUMULATED TIME 2.30
 ABAQUS VERSION: 5.6-1 DATE: 13-FEB-98 TIME: 16:23:11

Fig. 15(a) Distribution of Mises Stress at Pressure of 7.00MPa ; inside surface

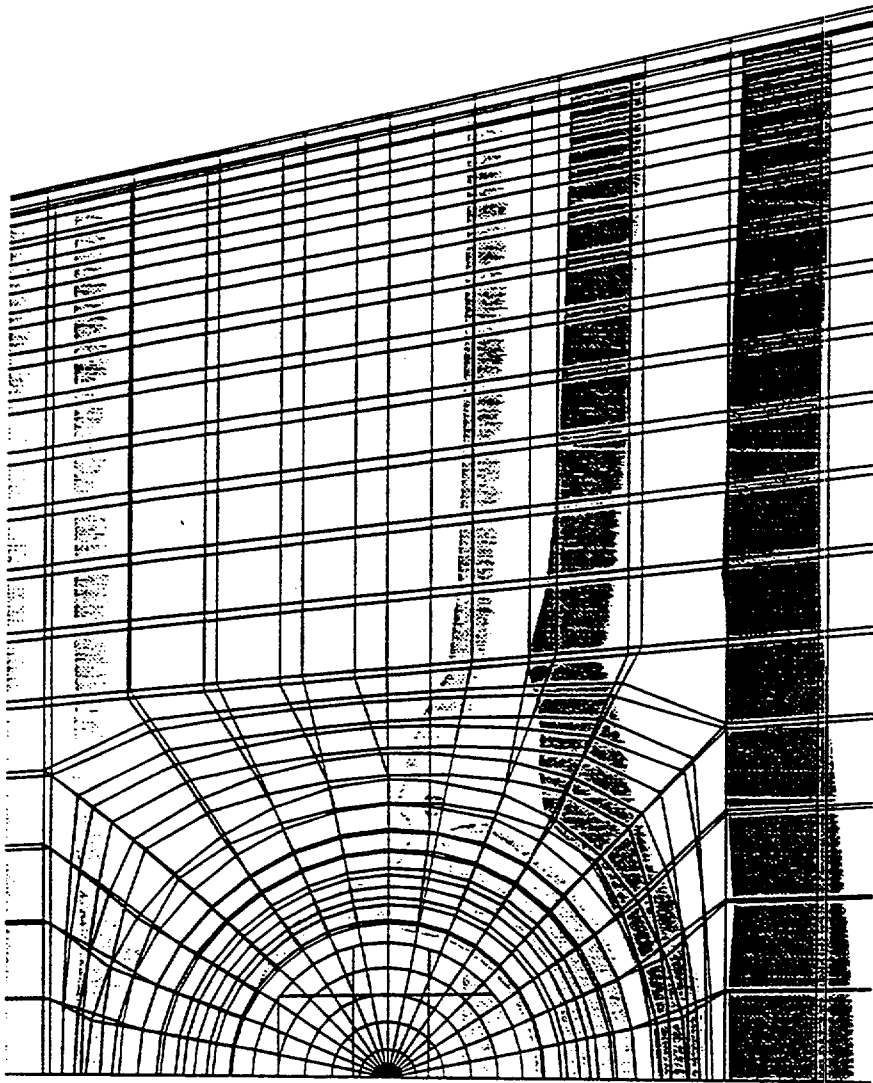


Mises Stress
[MPa]



DISPLACEMENT MAGNIFICATION FACTOR = 1.00
 RESTART FILE = center STEP 3 INCREMENT 9
 TIME COMPLETED IN THIS STEP .303 TOTAL ACCUMULATED TIME 2.30
 ABAQUS VERSION: 5.6-1 DATE: 13-FEB-98 TIME: 16:23:11

Fig. 15(b) Distribution of Mises Stress at Pressure of 7.00MPa outside surface



COPEN	VALUE
1	-4.49E-11
2	+2.00E+00
3	+4.00E+00
4	+6.00E+00
5	+8.00E+00
6	+1.00E+01
7	+1.20E+01
8	+1.40E+01
9	+1.60E+01
10	+1.80E+01
11	+2.00E+01
12	+1.41E+02

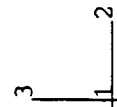


Fig. 16 Distribution of Clearance between SCV and CS at Pressure of 4.70MPa

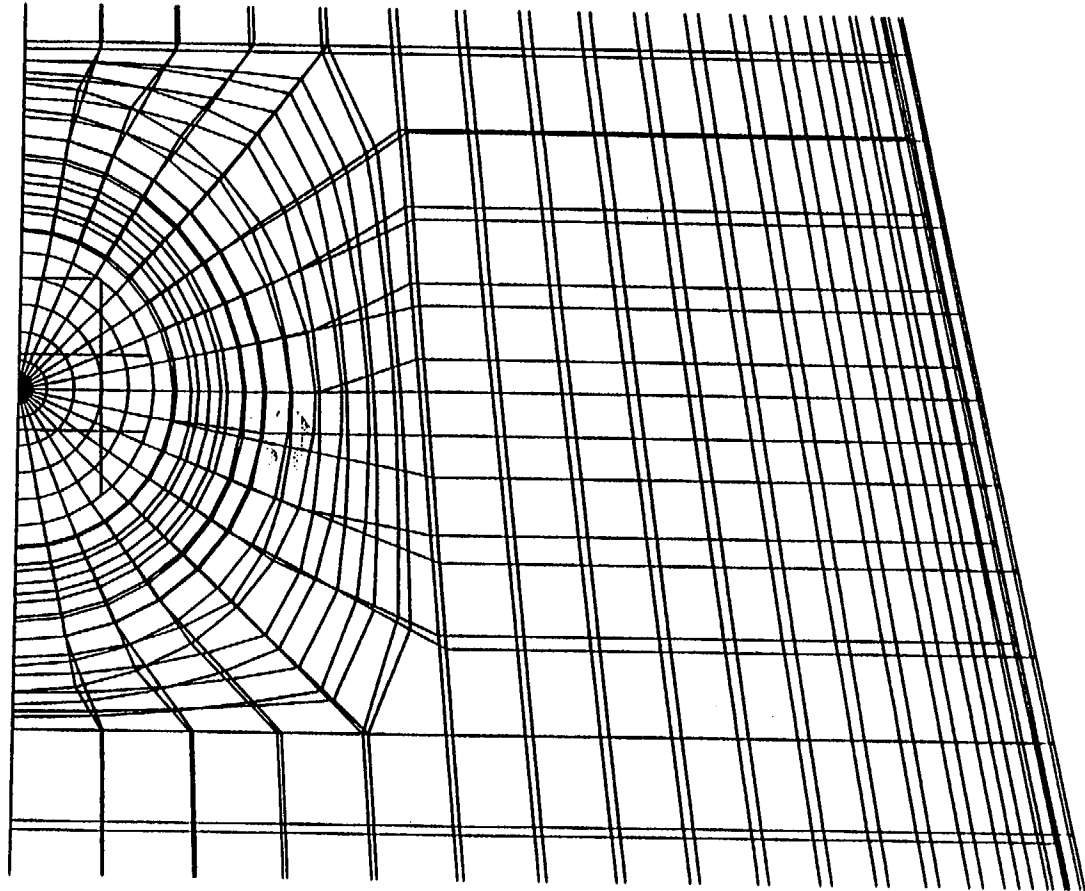
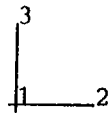
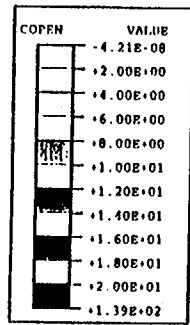


Fig. 17 Distribution of Clearance between SCV and CS at Pressure of 7.00MPa

Displacement [mm]

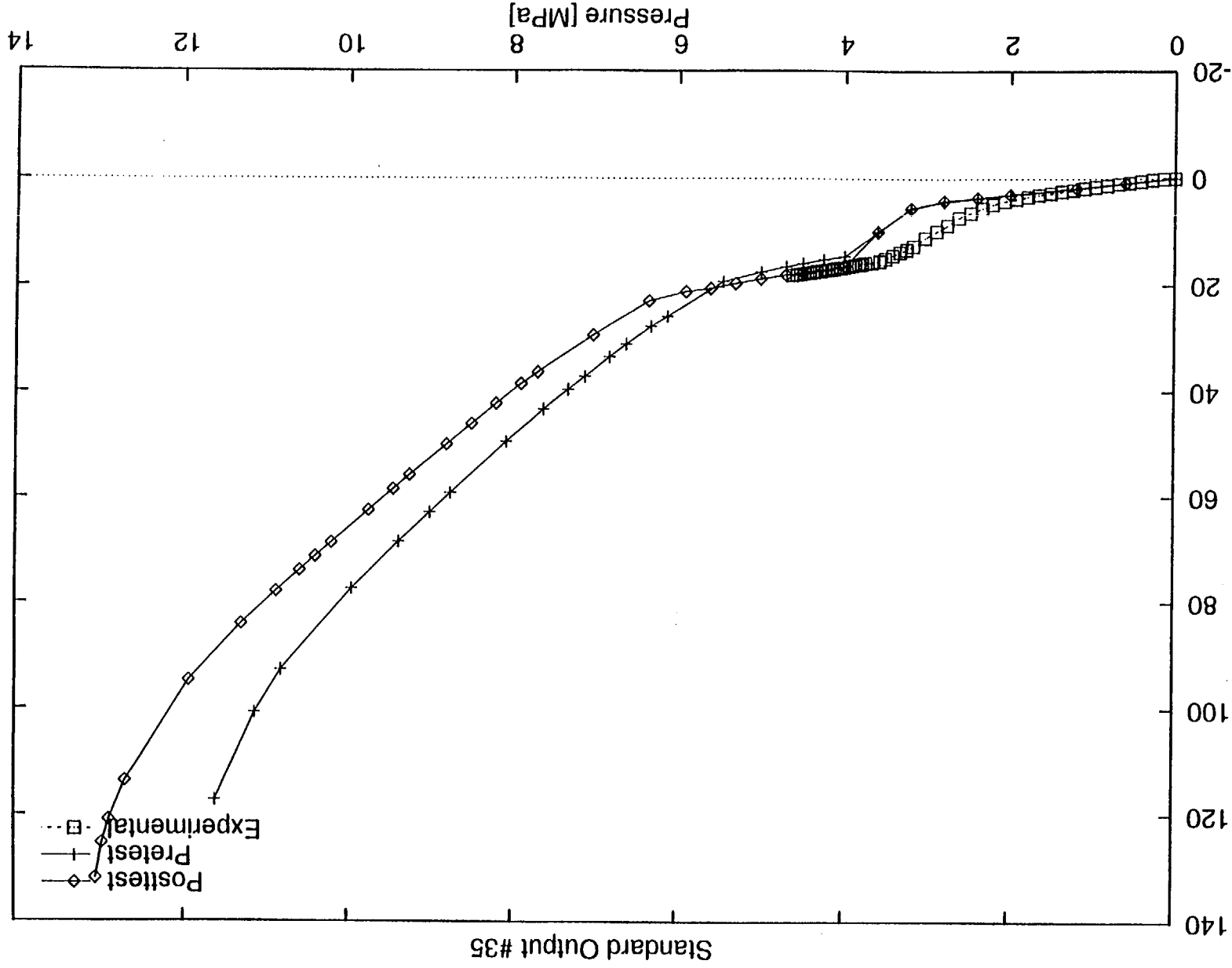


Fig. 18 Standard Output #35 : Pretest/Post-test and Experimental Results

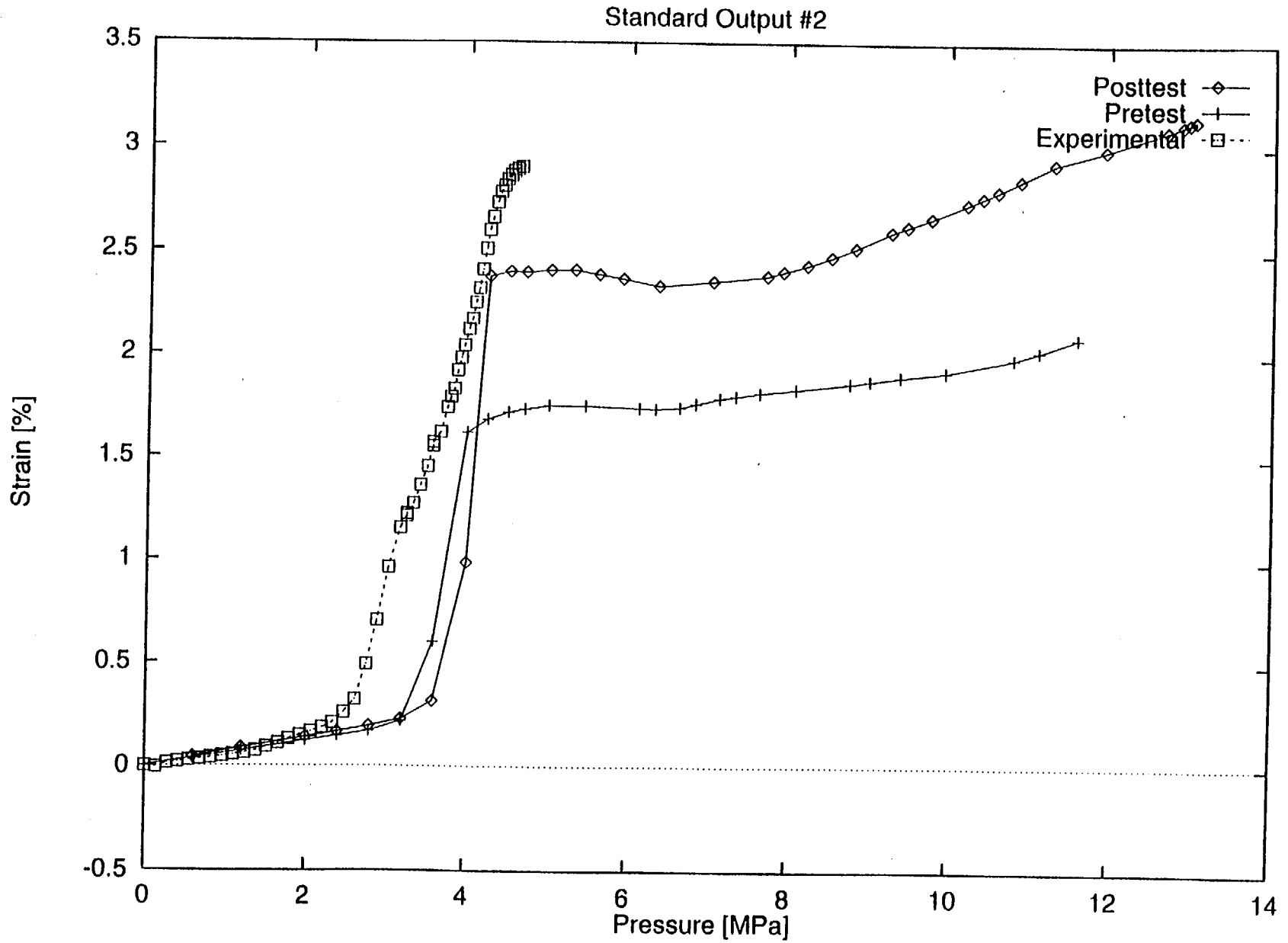


Fig. 19 Standard Output #2 ; Pretest/Post-test and Experimental Results

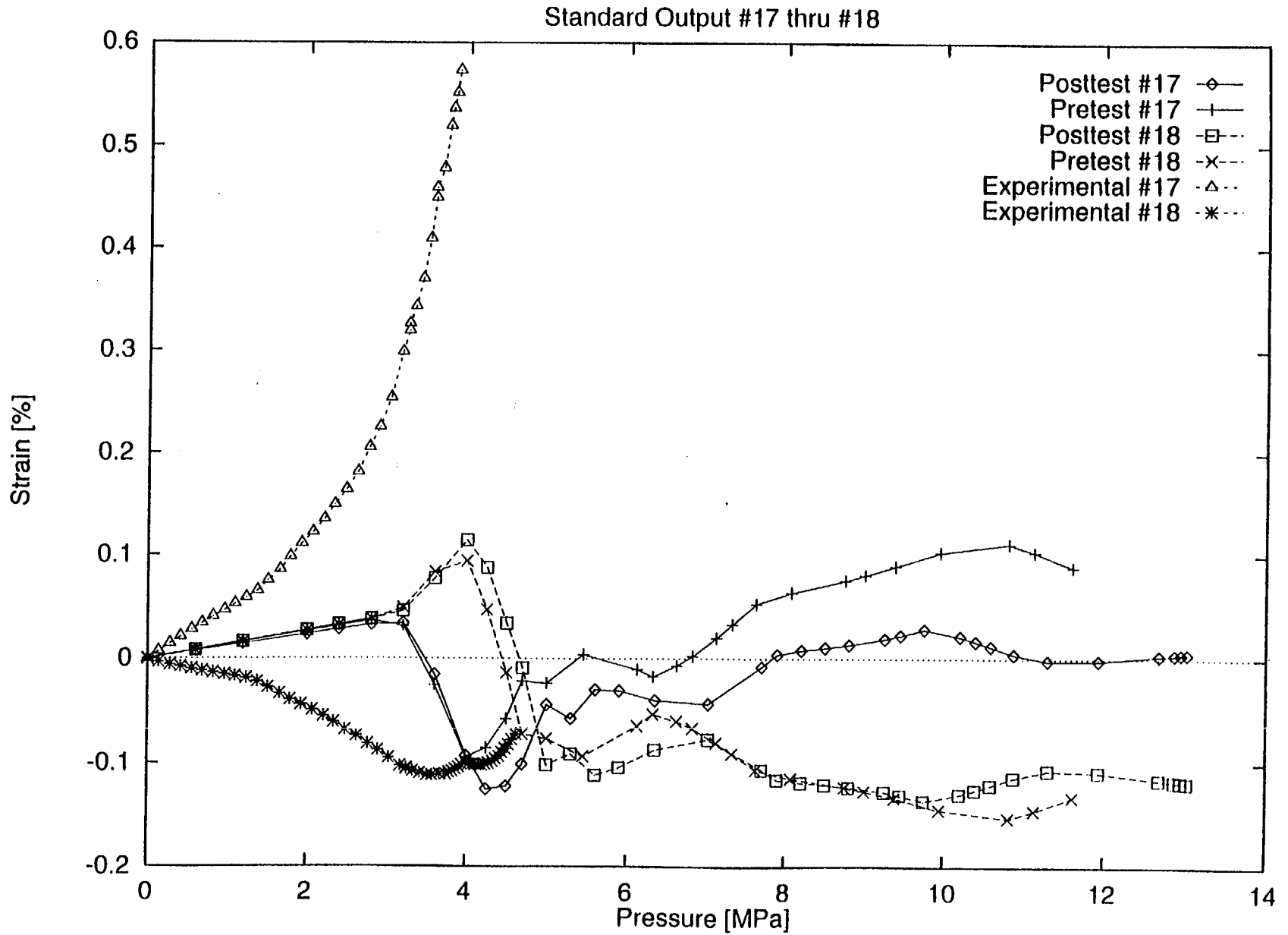


Fig. 20 Standard Output #17,18 ; Pretest/Post-test and Experimental Results

JAERI Appendix A

Posttest, Pretest, and Experimental Results at Standard Output Locations

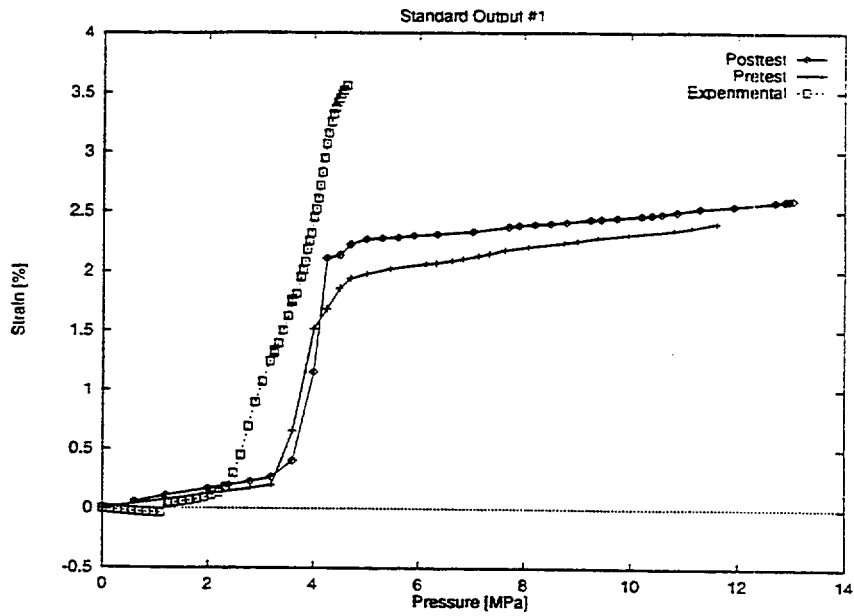


Figure A1. Standard Output #1

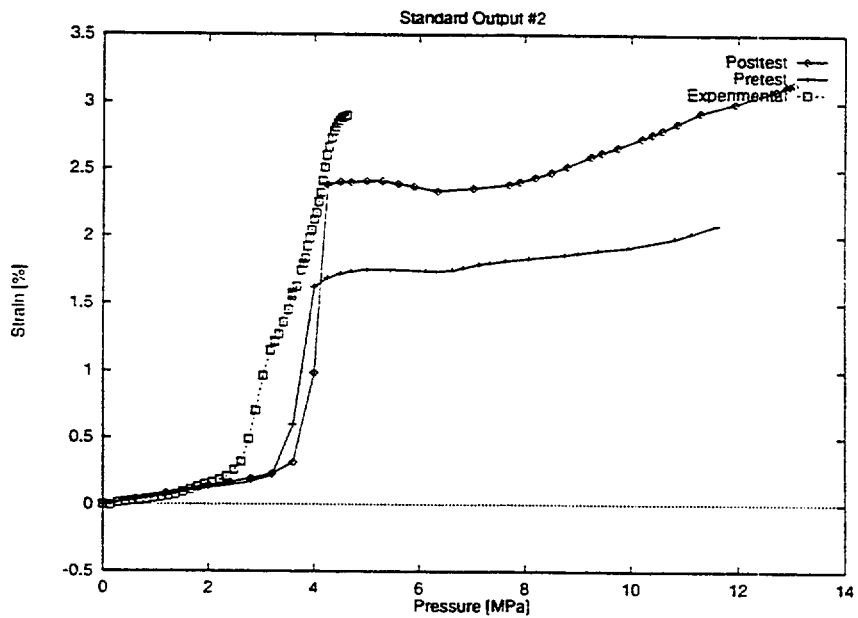


Figure A2. Standard Output #2

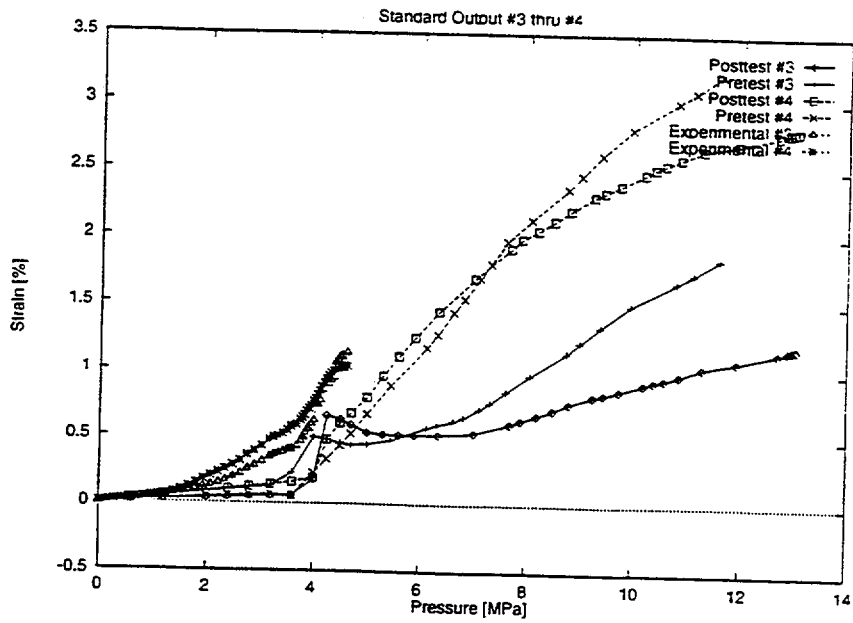


Figure A3. Standard Output #3 and #4

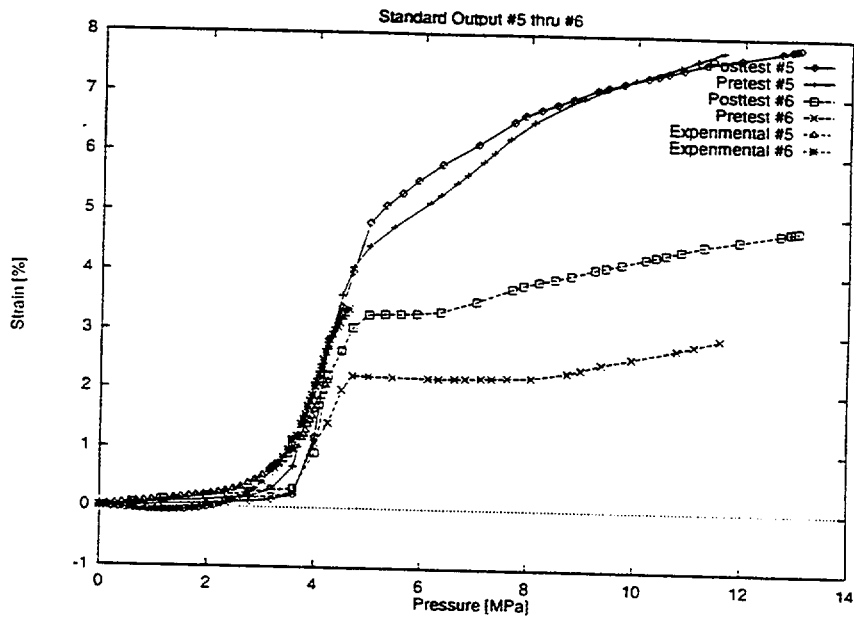


Figure A4. Standard Output #5 and #6

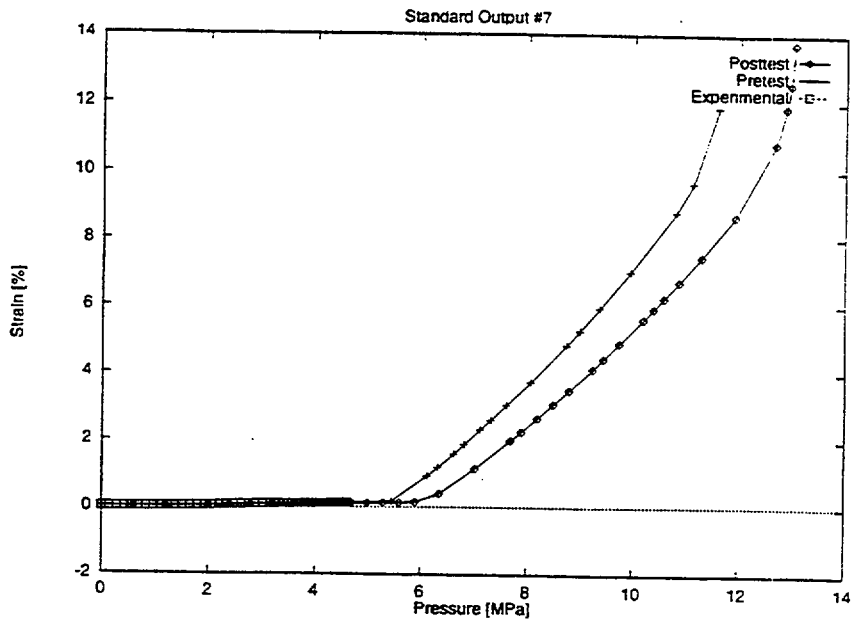


Figure A5. Standard Output #7

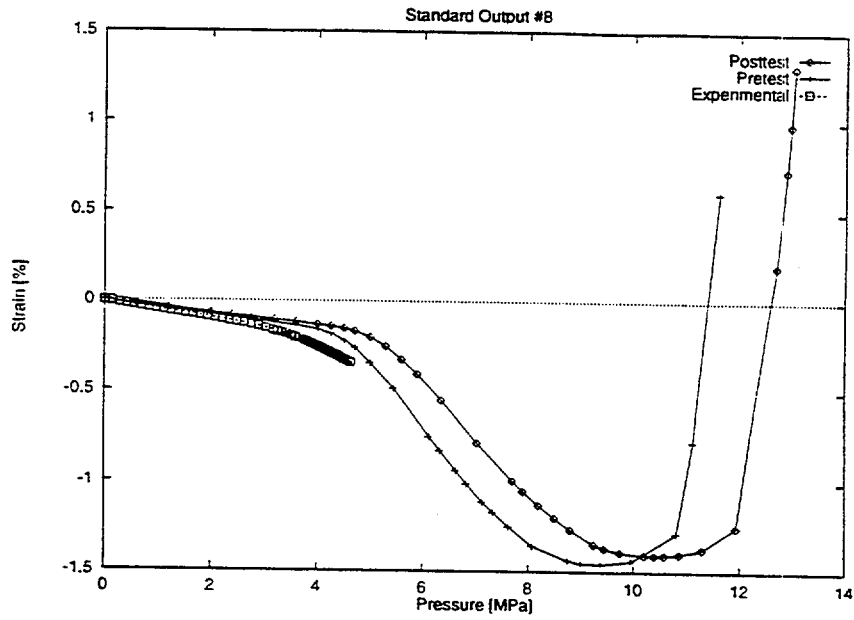


Figure A6. Standard Output #8

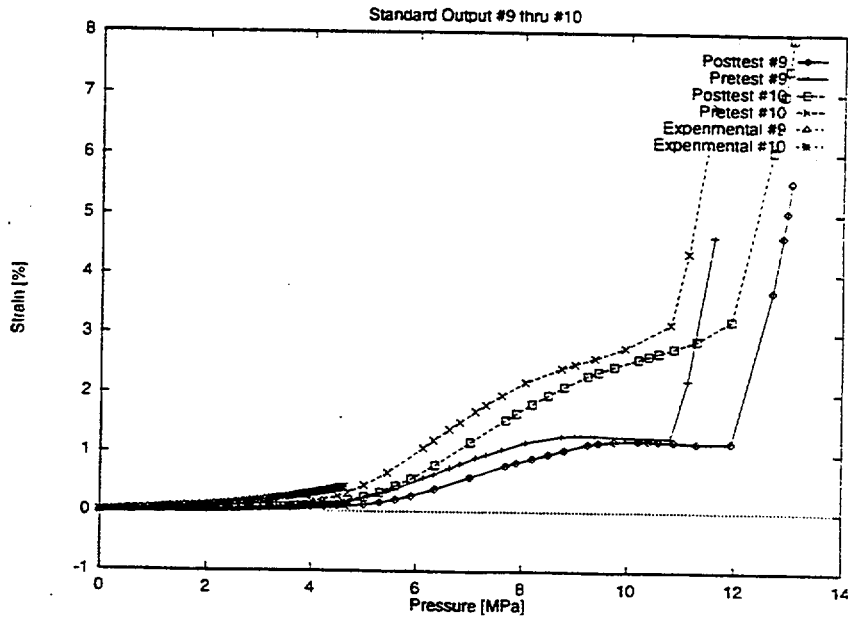


Figure A7. Standard Output #9 and #10

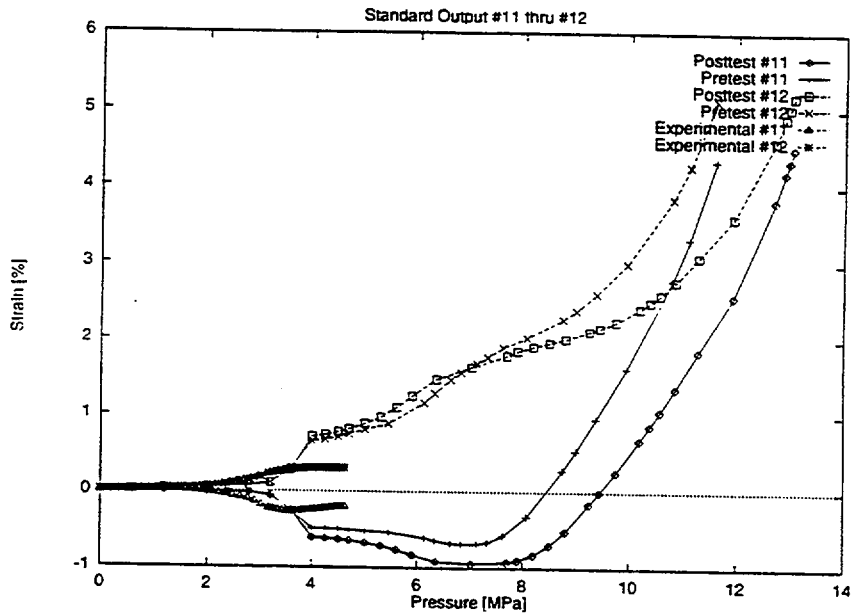


Figure A8. Standard Output #11 and #12

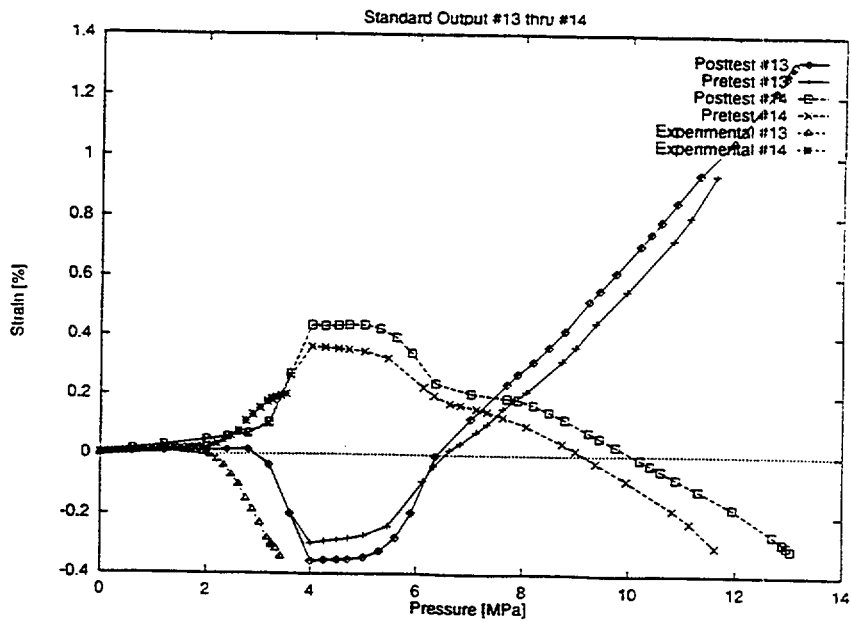


Figure A9. Standard Output #13 and #14

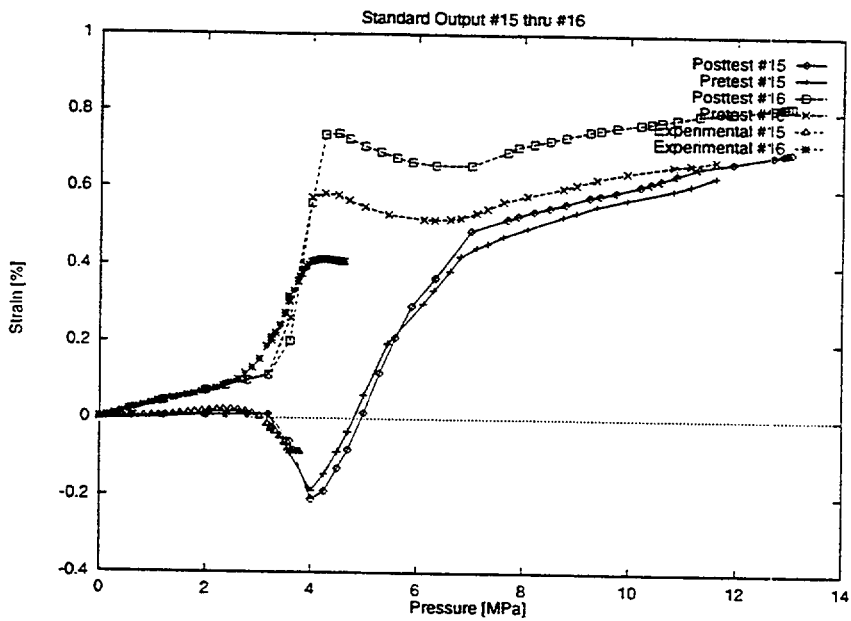


Figure A10. Standard Output #15 and #16

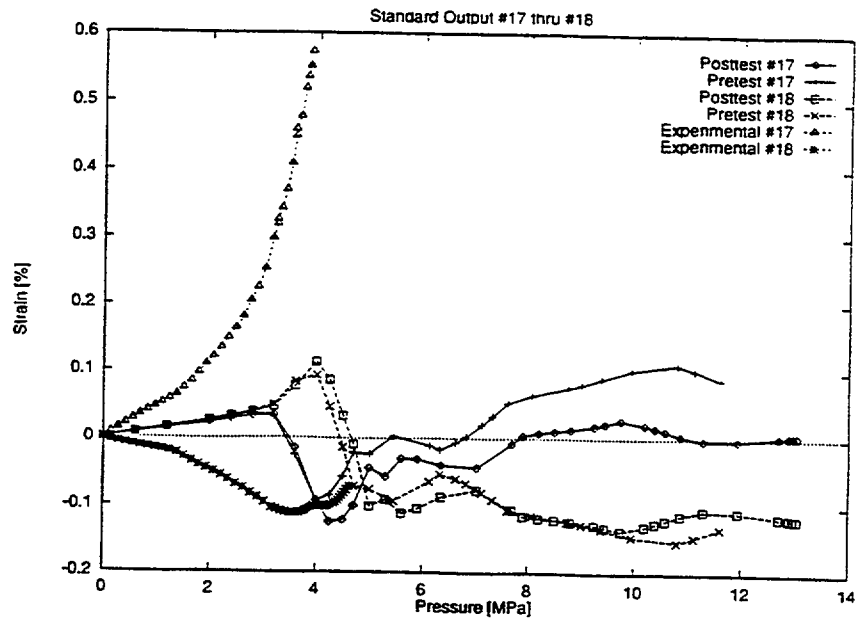


Figure A11. Standard Output #17 and #18

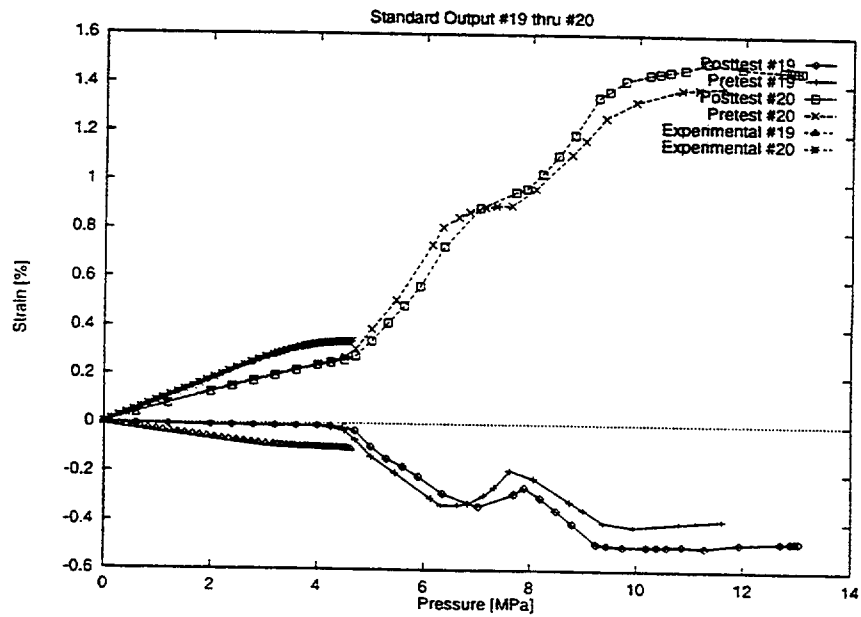


Figure A12. Standard Output #19 and #20

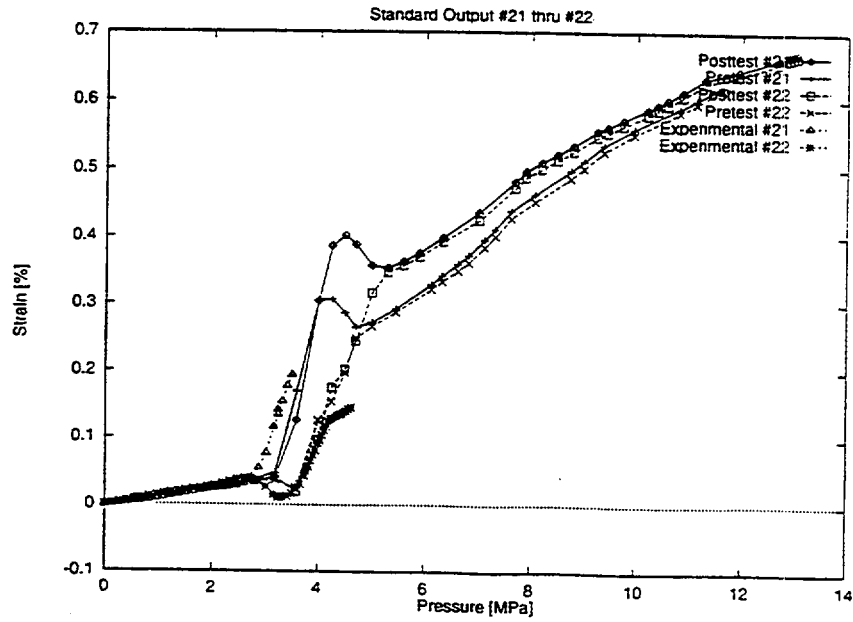


Figure A13. Standard Output #21 and #22

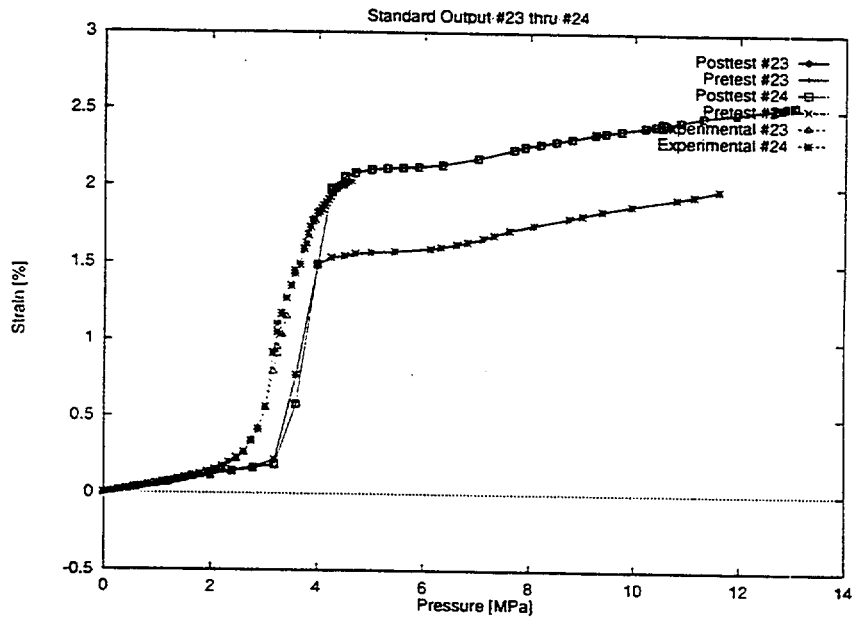


Figure A14. Standard Output #23 and #24

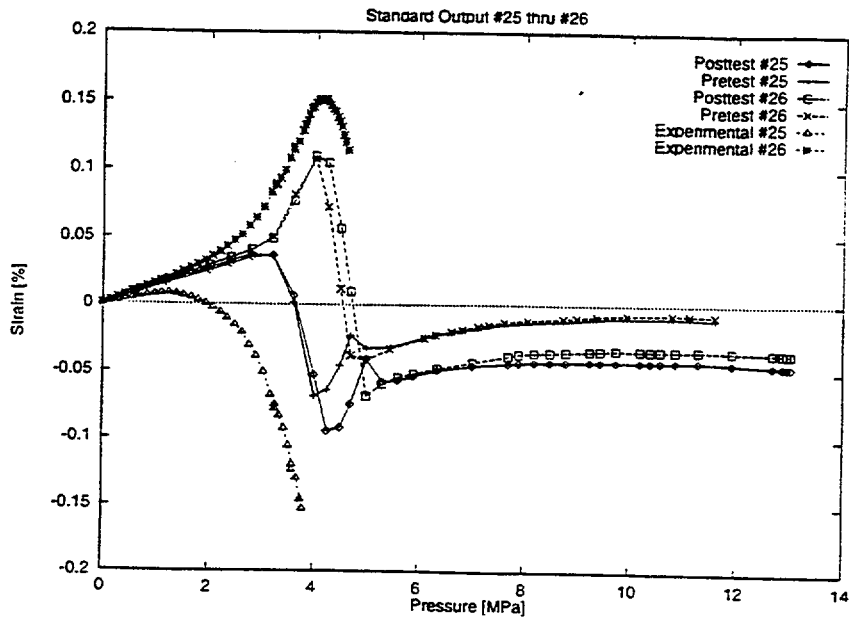


Figure A15. Standard Output #25 and #26

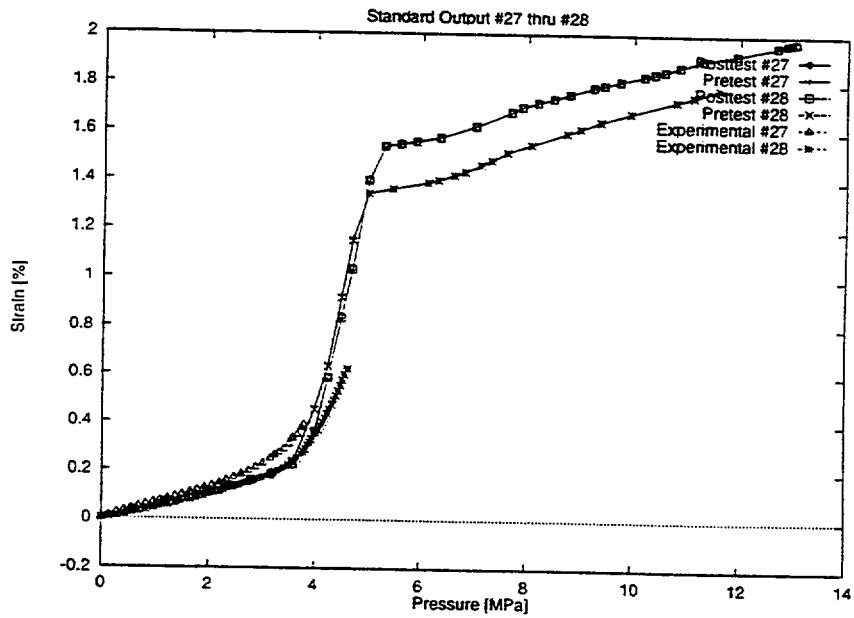


Figure A16. Standard Output #27 and #28

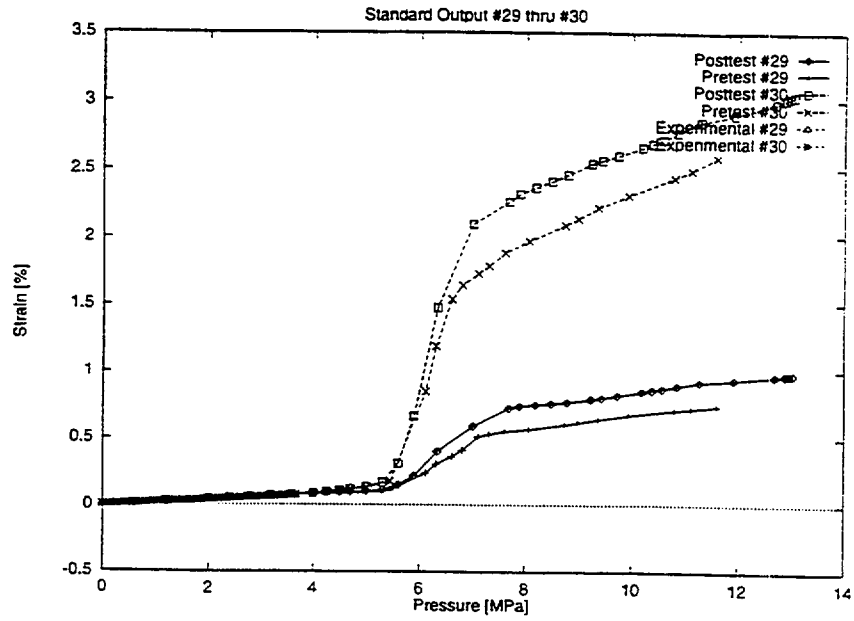


Figure A17. Standard Output #29 and #30

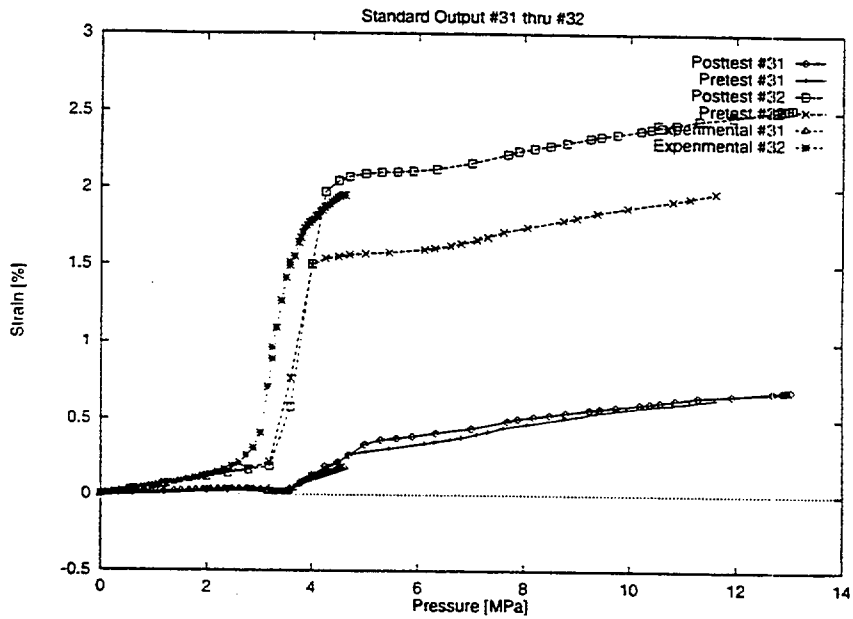


Figure A18. Standard Output #31 and #32

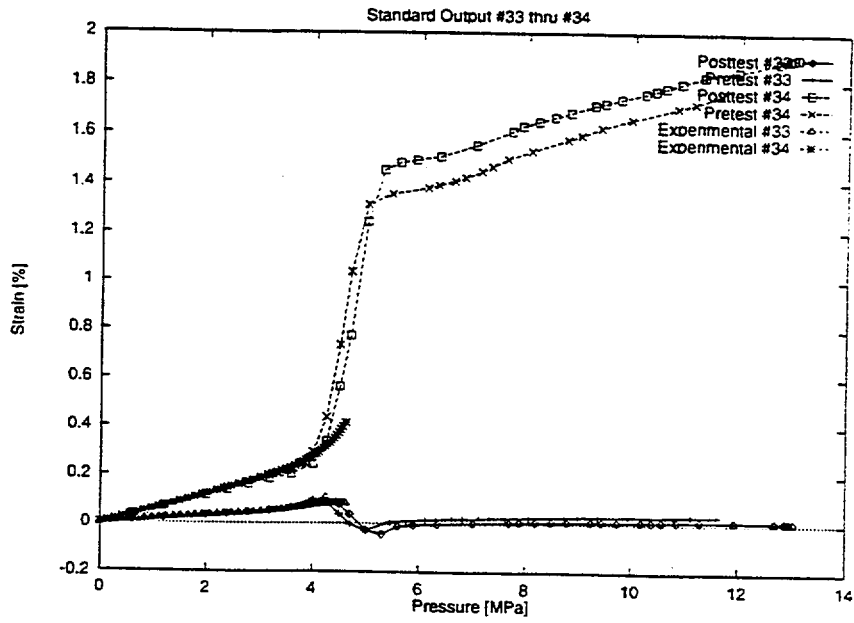


Figure A19. Standard Output #33 and #34

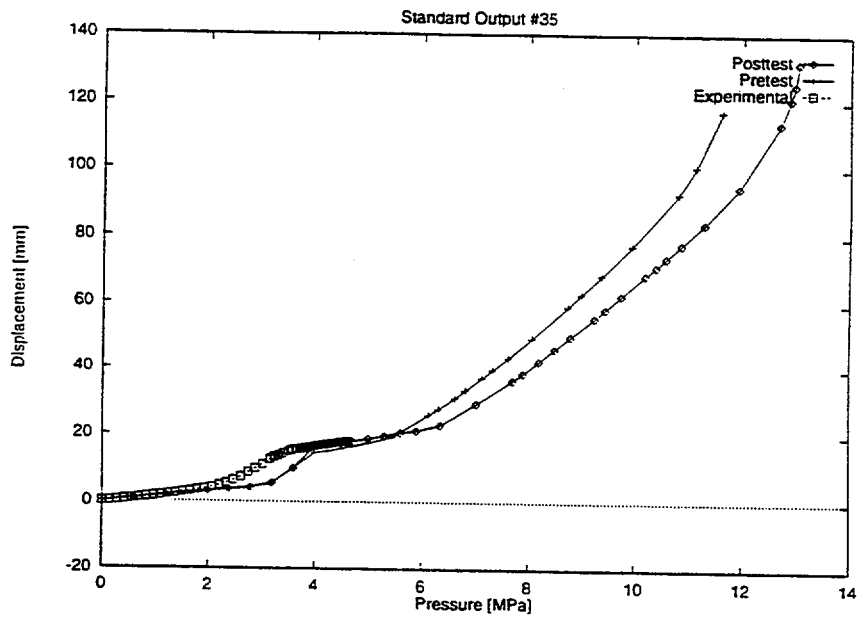


Figure A20. Standard Output #35

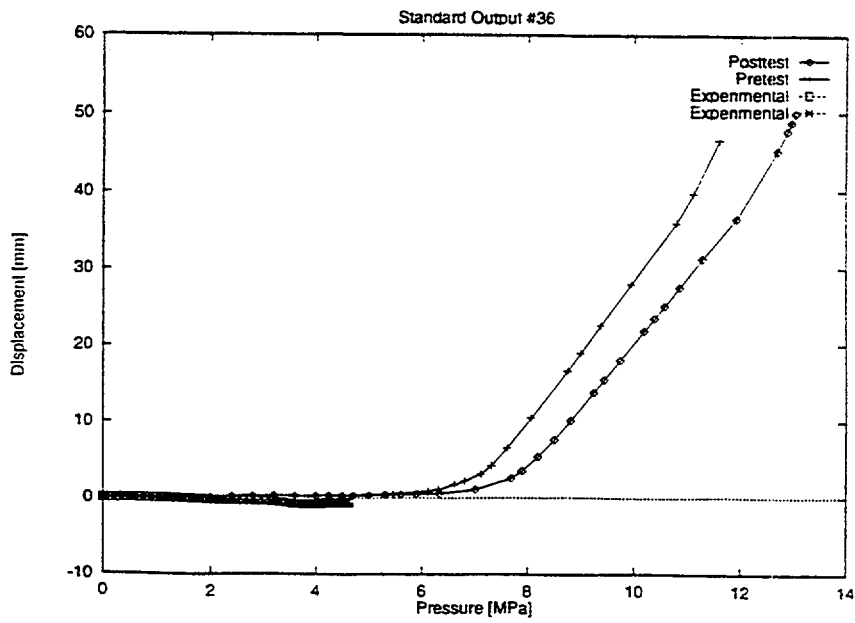


Figure A21. Standard Output #36

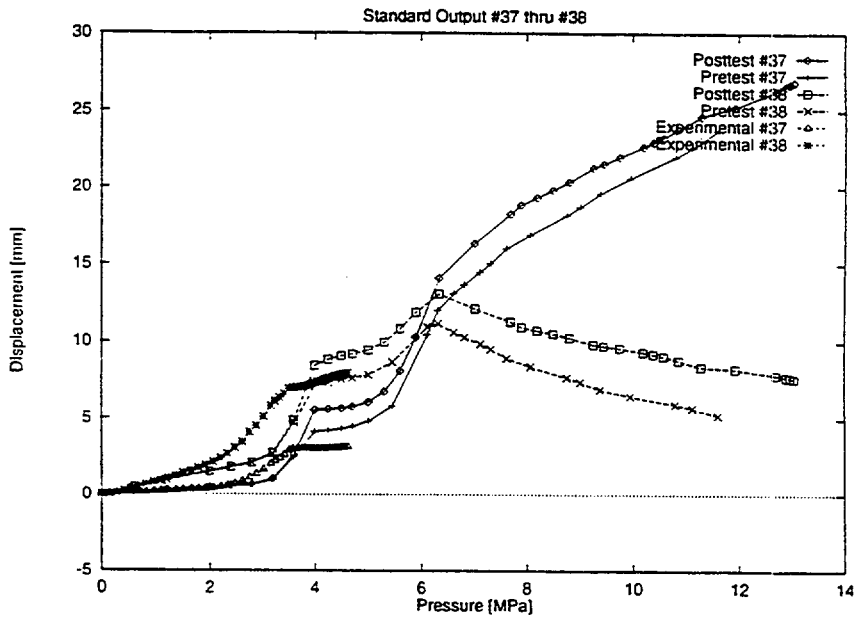


Figure A22. Standard Output #37 and #38

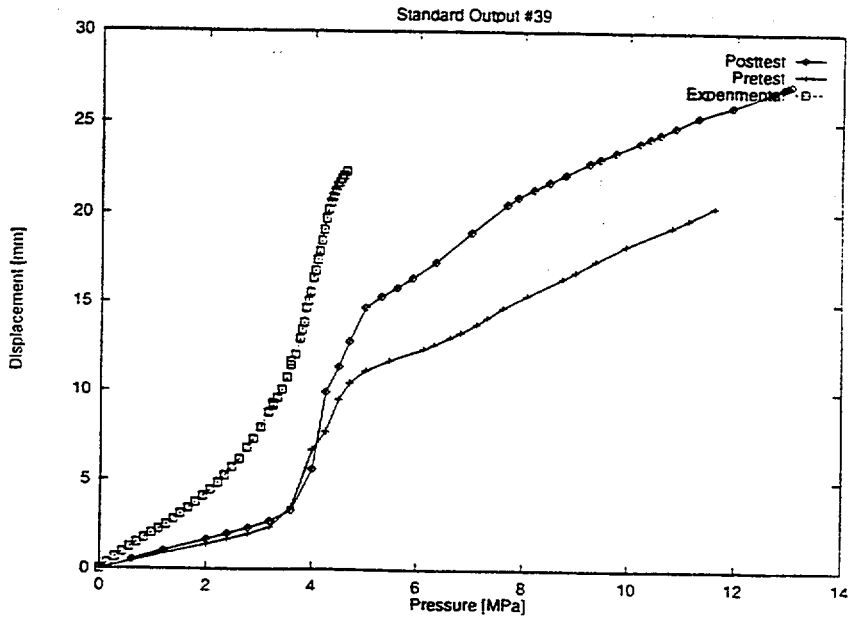


Figure A23. Standard Output #39

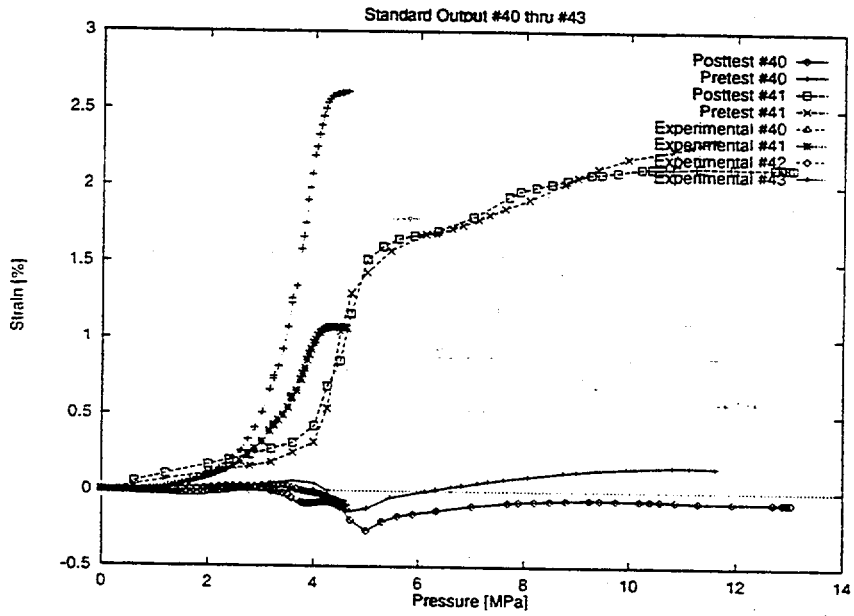


Figure A24. Standard Output #40 through #43

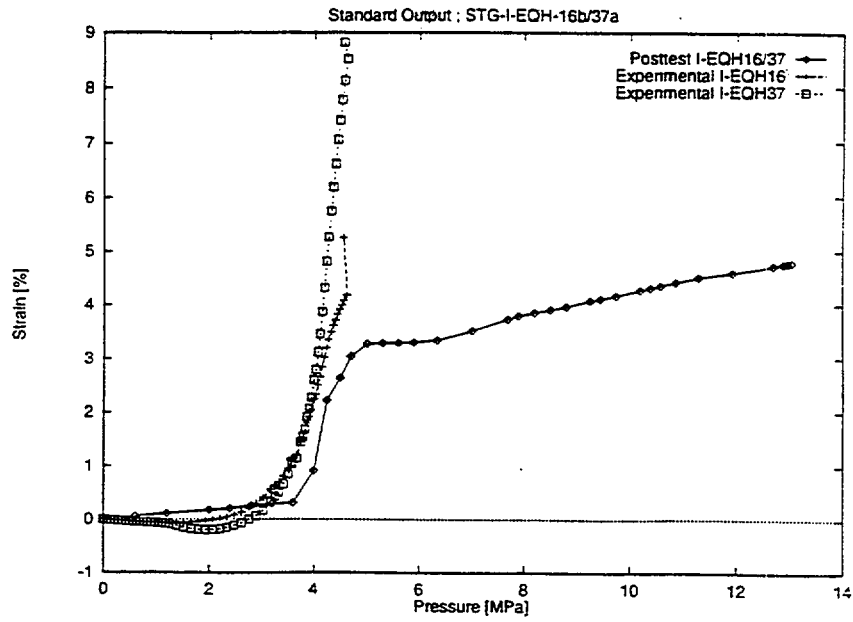


Figure A25. Standard Output I-EQH-16b/37a

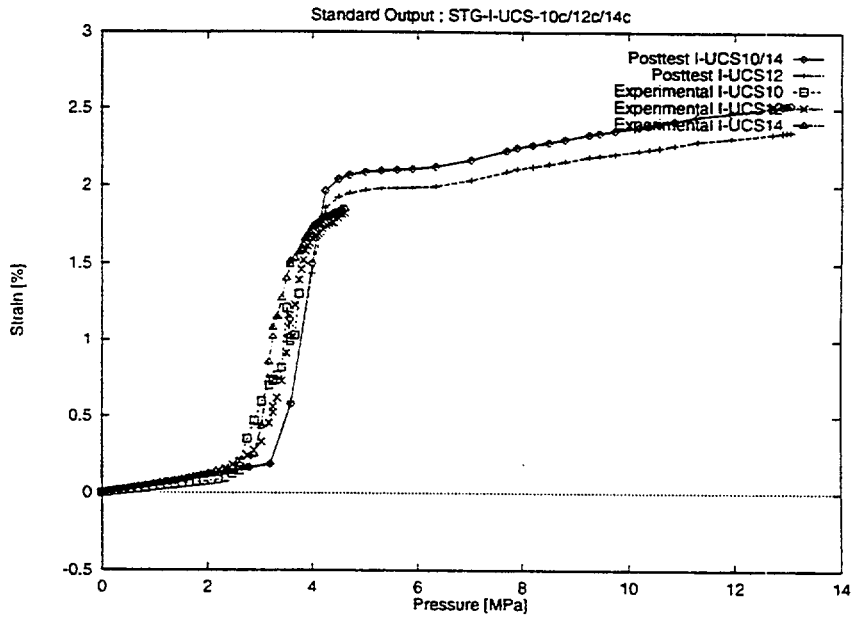


Figure A26. Standard Output I-UCS-10c/12c/14c

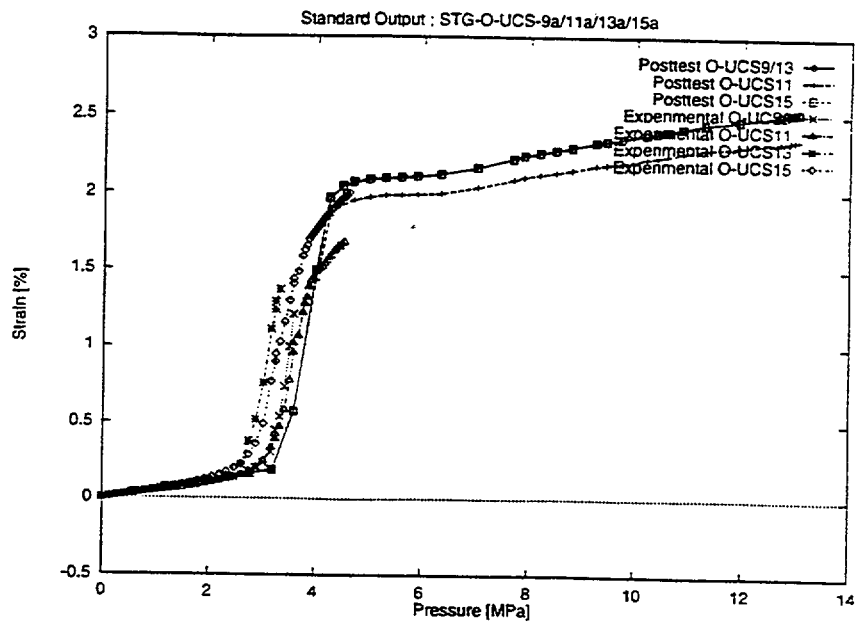


Figure A27. Standard Output O-UCS-9a/11a/13a/15a

Appendix B-6

Nuclear Power Engineering Corporation (NUPEC)

Japan

Round Robin Posttest Analysis of a 1:10-Scale Steel Containment Vessel

K. Komine* , T. Matsumoto* , S. Arai* and M. Konno**

*Nuclear Power Engineering Corporation
Fujita Kanko Toranomom Bldg.5F
17-1, 3-Chome Toranomom, Minato-ku,
Tokyo 105 Japan

**Hitachi Engineering Co., Ltd.
2-1, Saiwai-cho 3-Chome, Hitachi-shi,
Ibaraki-ken, 317 Japan

1. Introduction

The Nuclear Power Engineering Corporation (NUPEC) as an implementing organization of MITI of Japan and the U.S. Nuclear Regulatory Commission (NRC), Office of Nuclear Regulatory Research are performing a Cooperative Containment Research Program at Sandia National Laboratories (SNL). The purpose of this program is to investigate the response of representative models of nuclear reactor containment structure due to pressure loading beyond the design basis accident and to compare analytical predictions with measured data. The Steel Containment Vessel (SCV) model uses a mixed scale ; 1:10 for the geometry scale, 1:4 for the thickness scale and simulates an improved boiling water reactor (BWR) Mark-II containment vessel in Japan.

SCV model pressurization test was conducted at SNL on December 11-12 1996. This report describes the results of NUPEC's posttest analyses to grasp global behavior of SCV test model and to clarify the cause of tearing based on the test data of the SCV model pressurization test.

The posttest analyses were performed by using a finite element method analysis code, ABAQUS.

Performed posttest analyses are as follows.

- (1) Comparison of test result and pretest analyses result.
- (2) Investigation of reason for difference and of action plan for posttest analysis.
- (3) Detail analyses based on the action plan for posttest analysis.
 - a. Analysis using Fine Mesh Model
 - b. Analysis for Effect of Yield Condition
 - c. Analysis for Effect of Initial Imperfection
 - d. Analysis for Effect of Welded Portion around Equipment Hatch (E/H)
- (4) Analysis for second crack
- (5) Study for the cause of failure

2. Comparison of test result and pretest analysis result

In order to confirm the propriety of pretest analytical model and to prepare posttest analytical model, we compared the test results with pretest analysis results.

2.1 Comparison results

Standard Output Locations (SOL) are shown in Figure 2.1-1, -2, and measurement gage locations around E/H are shown in Figure 2.1-3. Also, comparison results of representative portion are shown in Figure 2.1-4 to 2.1-14.

As shown in Figure 2.1-4 to 2.1-7, with regard to SOL#6 around E/H, SOL#26,28 in lower conical shell, SOL#35 in top head, SOL#38 in knuckle region, and STG-I-EQH-16b of measurement gages, test and pretest analyses results show good fit. However, as shown in Figure 2.1-8 to 2.1-14, with regard to SOL#12 in upper cylindrical shell, SOL#17,18 in material change interface, SOL#23,24 in upper conical shell, SOL#39 in hatch cover apex, SOL#41,43 around E/H and measurement gage STG-I-EQH-37a around E/H, test and pretest analyses results show large difference.

2.2 Different Items and Assumed Reason for Difference

Different Items and assumed reasons for difference in each portion described in the above section 2.1 are shown in table 2.2-1.

Table 2.2-1 Different Items and Assumed Reason for difference

Portion	SOL No.& gage No.	Different Items	Assumed Reason for Difference
Just below Top Head Flange	SOL#12	Strain marks are reverse (Test result is positive, Analysis result is negative)	due to rough mesh of the analysis model, analytical evaluation points do not correspond to measurement point
Material Change Interface	SOL#17,18		
Equipment Hatch Cover Apex	SOL#39	Displacement of test result is larger than that of analysis result	test model has initial imperfection around E/H
around E/H	SOL#41	Strain of analysis result is larger than that of test result	effect of lower hardness at welded portion
	SOL#23,24,43	Yield pressure in test result is smaller than that in analysis result	difference of yield condition
	STG-I-EQH-37a	Strain of analysis result is larger than that of test result	effect of lower hardness at welded portion

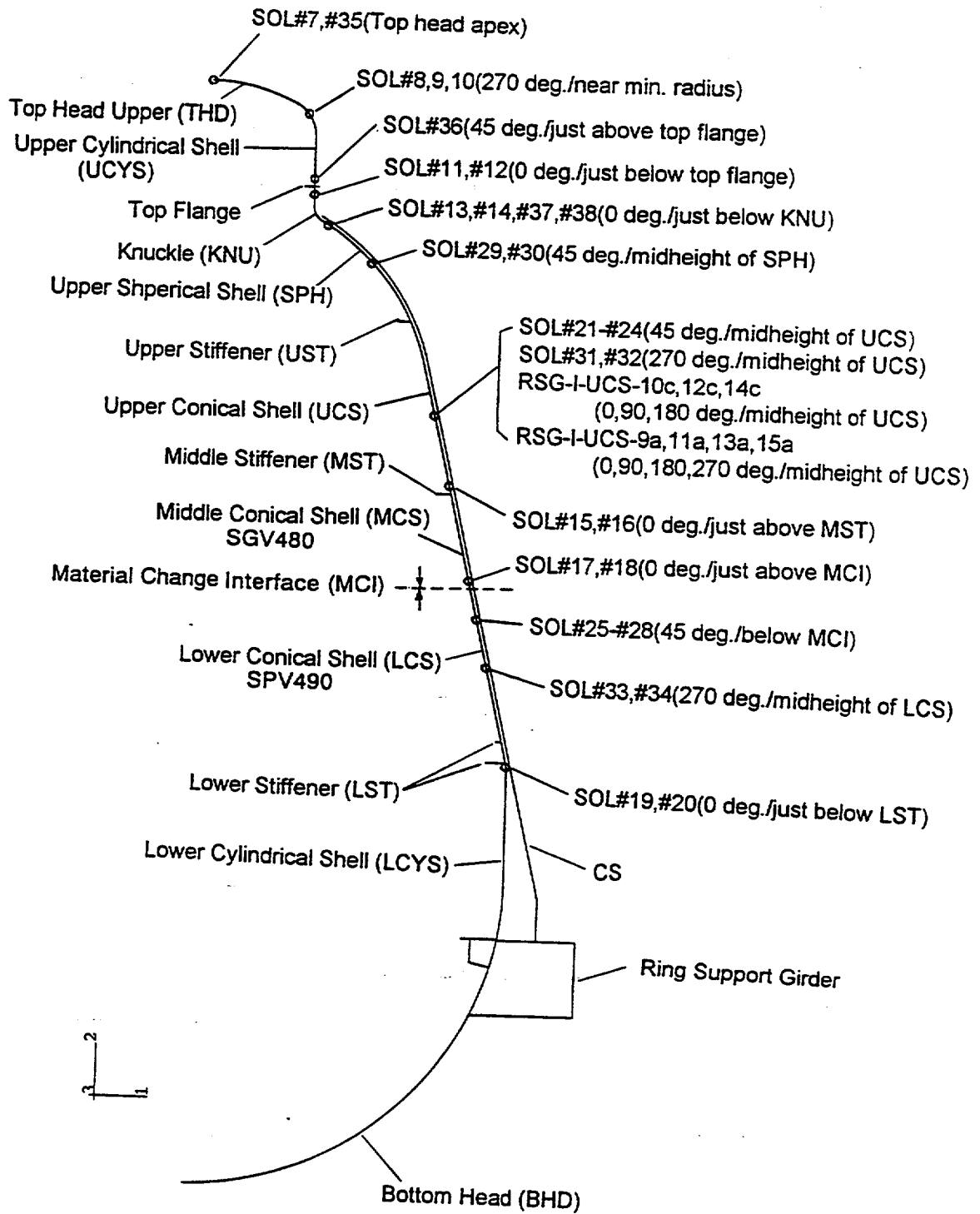


Figure 2.1-1 Standard Output Locations

4

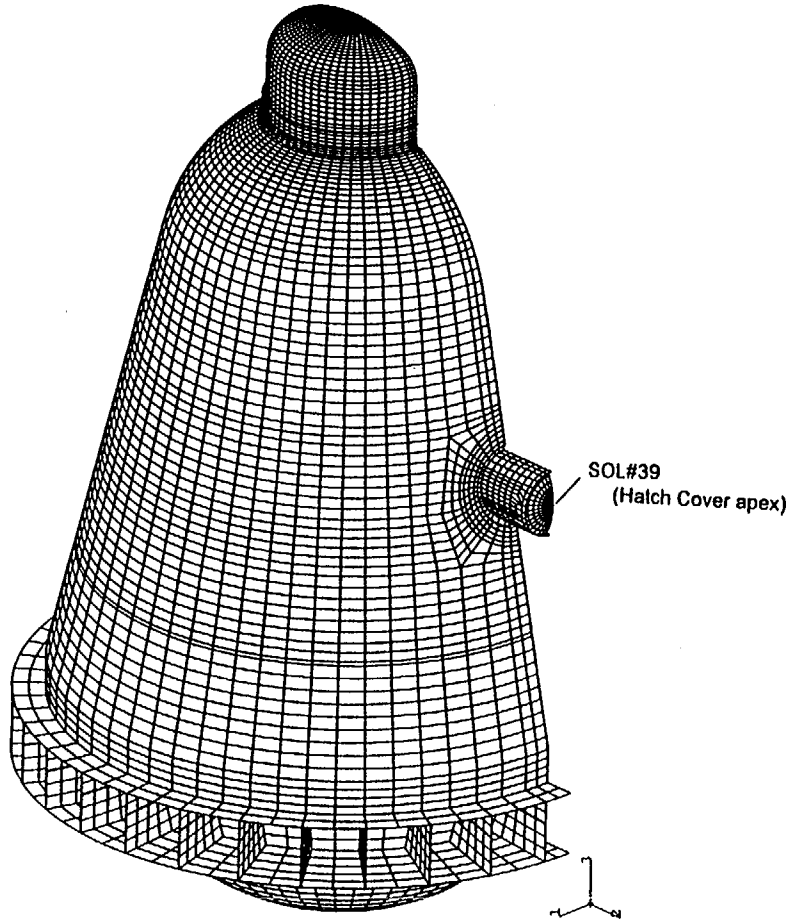


Figure 2.1-2 Standard Output Location

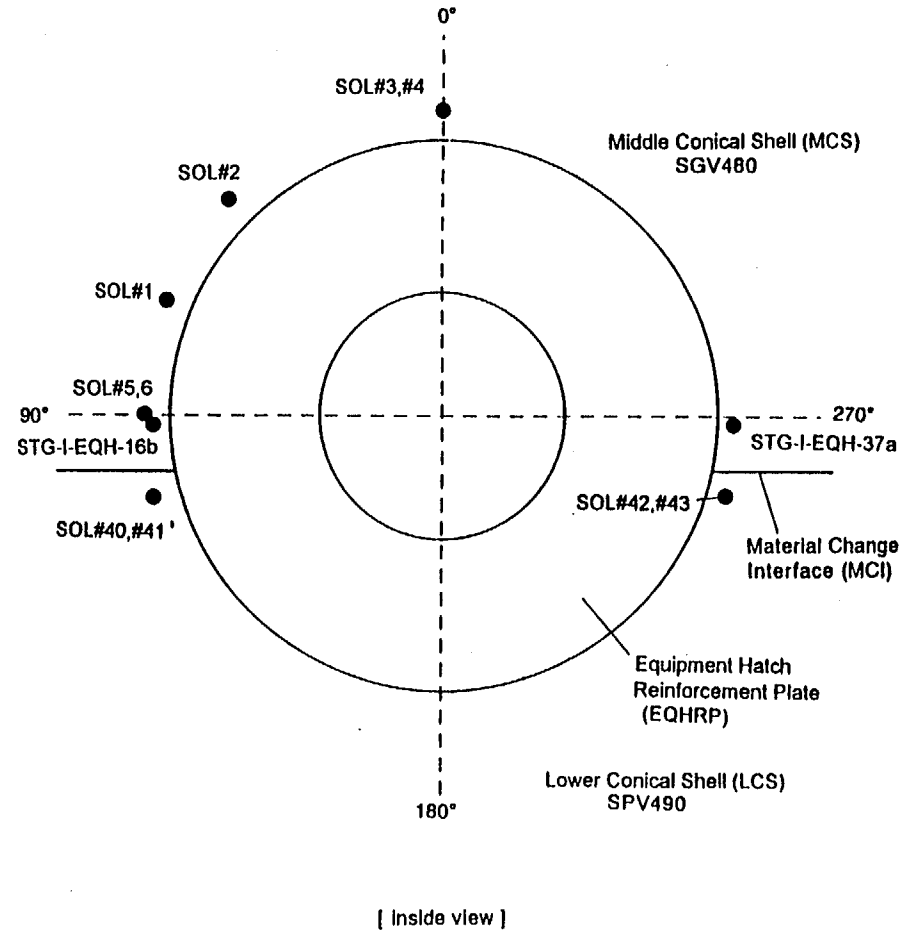


Figure 2.1-3 Standard Output Locations and measurement gage locations

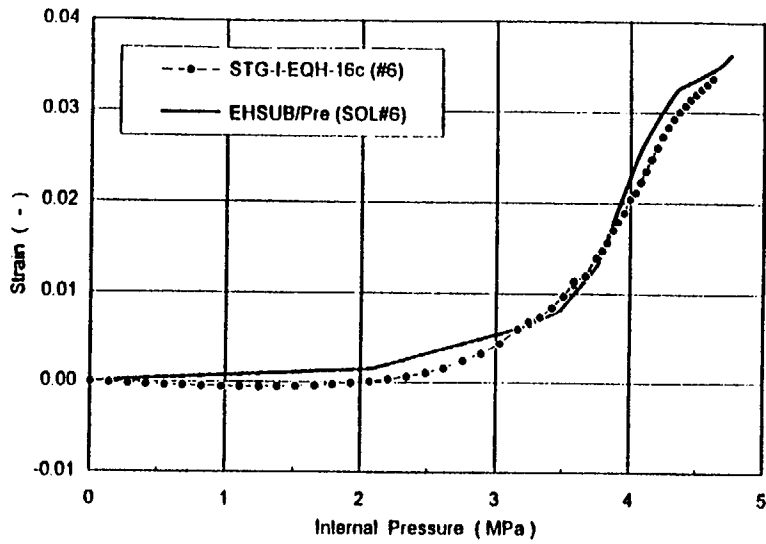


Figure 2.1-4 Comparison of Hoop Strain at SOL#6 (near Equipment Hatch) Results from SCV High Pressure Test and Pretest Analysis

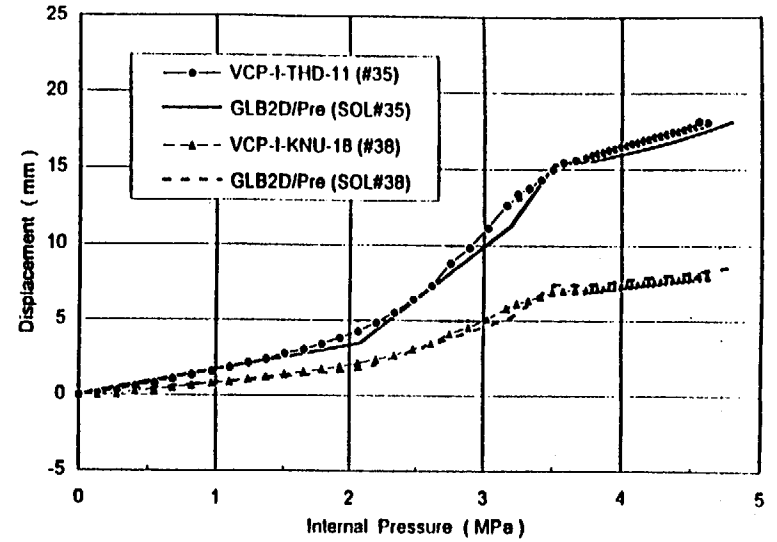


Figure 2.1-6 Comparison of Vertical Displacement at SOL#35 & #38 (THD & KNU) Results from SCV High Pressure Test and Pretest Analysis

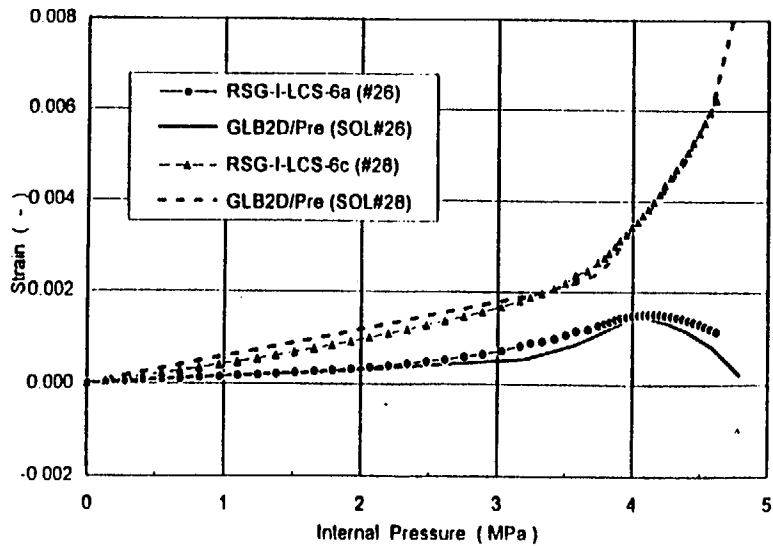


Figure 2.1-5 Comparison of Merid/Hoop Strain at SOL#26 & #28 (LCS) Results from SCV High Pressure Test and Pretest Analysis

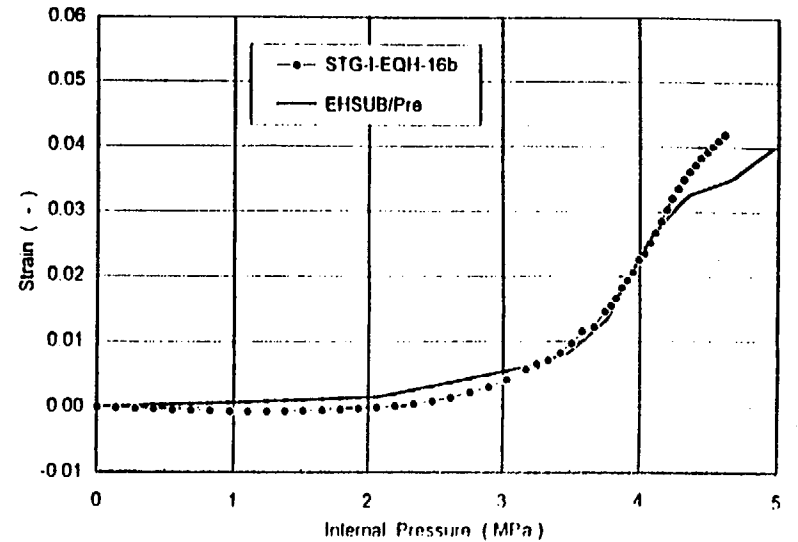


Figure 2.1-7 Comparison of Hoop Strain (near Equipment Hatch) Results from SCV High Pressure Test and Pretest Analysis

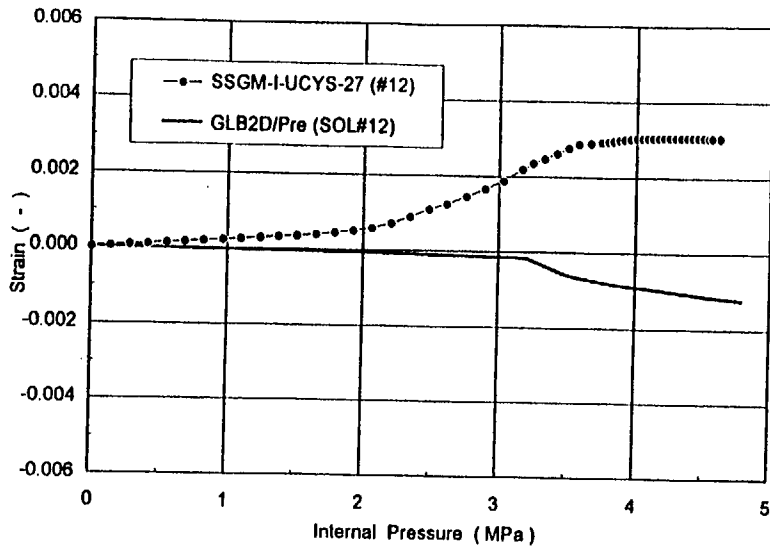


Figure 2.1-8 Comparison of Meridional Strain at SOL#12 (UCYS)
Results from SCV High Pressure Test and Pretest Analysis.

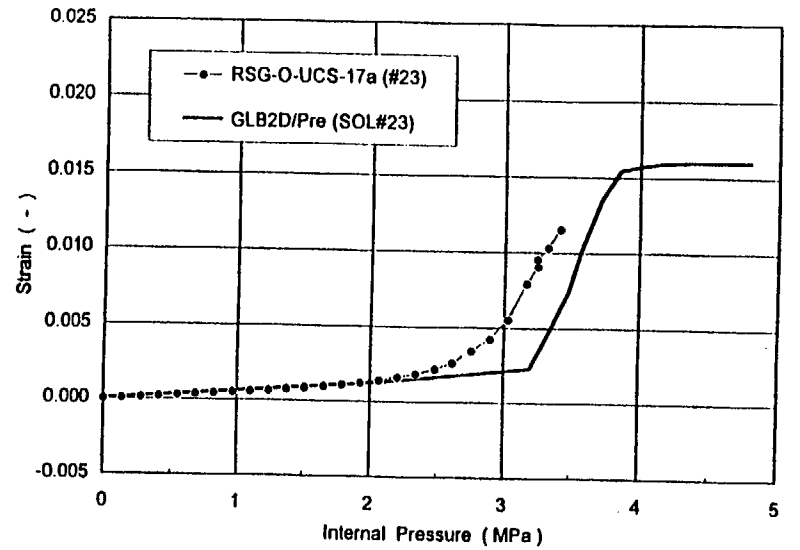


Figure 2.1-10 Comparison of Hoop Strain at SOL#23 (UCS)
Results from SCV High Pressure Test and Pretest Analysis

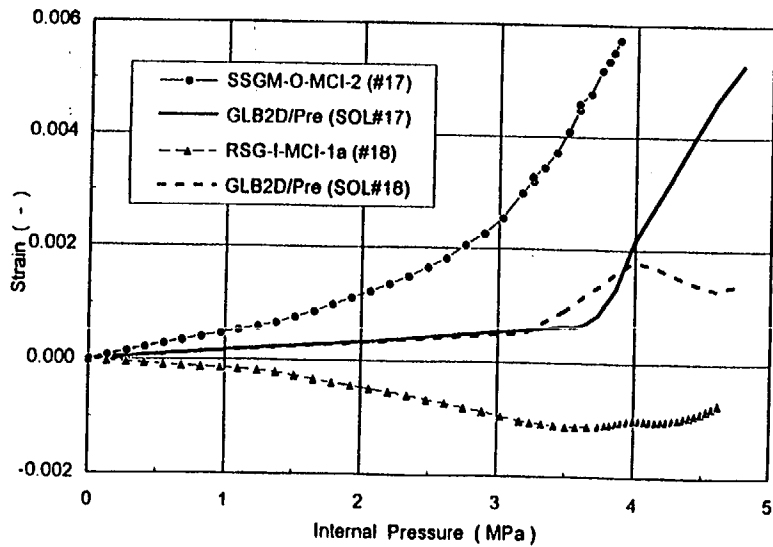


Figure 2.1-9 Comparison of Meridional Strain at SOL#17 & #18 (MCI)
Results from SCV High Pressure Test and Pretest Analysis

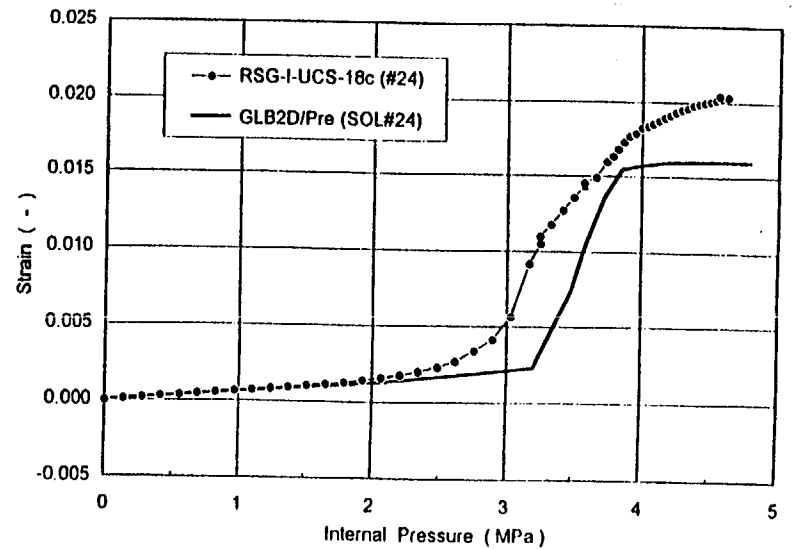


Figure 2.1-11 Comparison of Hoop Strain at SOL#24 (UCS)
Results from SCV High Pressure Test and Pretest Analysis

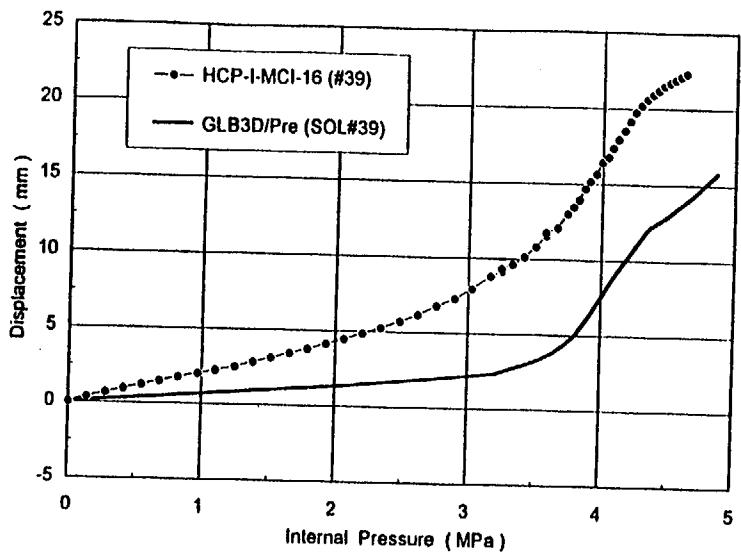


Figure 2.1-12 Comparison of Horizontal Displacement at SOL#39 (center of E/H cover) Results from SCV High Pressure Test and Pretest Analysis

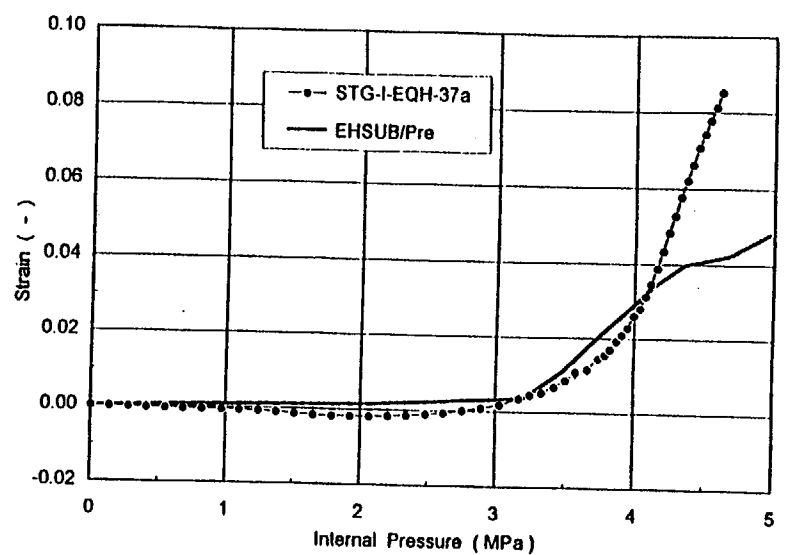


Figure 2.1-14 Comparison of Hoop Strain (near Equipment Hatch) Results from SCV High Pressure Test and Pretest Analysis

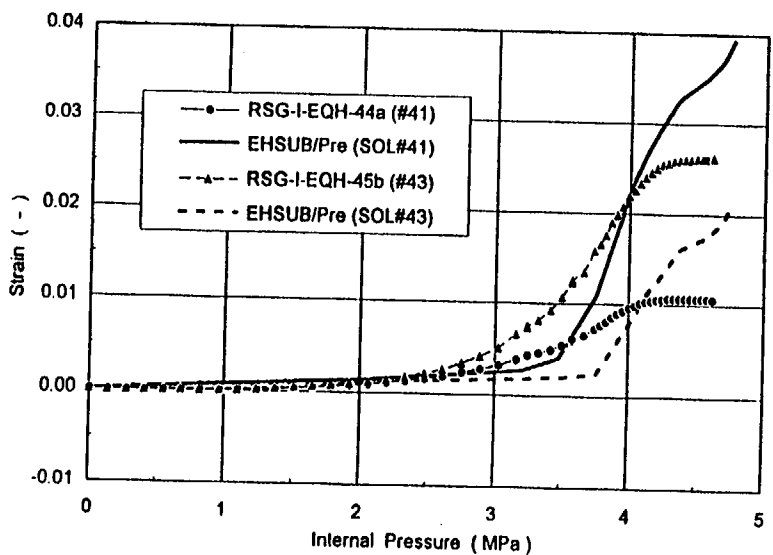


Figure 2.1-13 Comparison of Hoop Strain at SOL#41 & #43 (near Equipment Hatch) Results from SCV High Pressure Test and Pretest Analysis

B-229

7

NUREG/CR-5679

2.3 Action Plans for Posttest Analysis

Table 2.3-1 shows action plans to conduct the posttest analysis based on the above different items and the assumed reason for difference. More detailed contents are shown in section 3. And also, we performed an analysis for the second crack which was confirmed in the posttest inspection.

Table 2.3 -1 Action Plans for Posttest Analysis

Posttest Analysis	Action Plans for Posttest Analysis	Analytical Model
Analysis using Fine Mesh Model	use fine mesh to adapt analytical element location to measurement gage location	2-D axisymmetric shell global model 3-D shell global model 3-D shell E/H submodel
Analysis for Effect of Yield Condition	correct material data to simulate Tresca's yield condition	2-D axisymmetric shell global model
Analysis for Effect of Initial Imperfection	apply initial imperfection to the location around E/H based on measured dimension	3-D shell global model
Analysis for Effect of Welded Portion around Equipment Hatch	simulate the welded portion in analytical model and change the material data of welded portion	3-D shell E/H submodel
Analysis for Second Crack	simulate the weld relief hole on middle stiffener ring in analytical model	3-D Middle Conical Shell submodel

3. Posttest Analyses

3.1 Posttest Analytical Model and Analysis Cases

3.1.1 Analytical Model

The analyses using the following analytical model were conducted on the basis of the action plans for posttest analysis as shown in Table 2.3-1.

(1) Analysis using Fine Mesh Model

a. Analytical Model

Fine mesh analytical model is applied to 2-D axisymmetric shell global model, 3-D shell global model and 3-D E/H submodel.

b. Analytical Contents

With regard to marks of strain, the reason why strain in test results is positive value and that in analysis results is negative value, was considered to be caused by the effect of bending. Concretely, because tensile portion is close to compression portion in case of localized bending, there is a possibility that marks of strain is reversing unless the measurement gage location corresponds to the analytical element location successfully. The analysis using fine mesh model is performed in order to adapt the analytical element location to the measurement gage location.

(2) Analysis for Effects of Yield Condition

a. Analytical Model

Because the earlier yielding in test results is not limited to specific portion and this phenomena is global behavior, global model is required to be used in this analysis. Therefore, 2-D axisymmetric global shell mode is used.

b. Analytical Contents

Mises's yield condition was used in the pretest analysis. With regard to countermeasure to include the Tresca's yield condition, there is a method to use the user subroutines of ABAQUS. However, simplified method using corrected material data is adapted in this analysis. (Corrected method of material data is explained in section 3.3 in detail)

(3) Analysis for Effects of Initial Imperfection

a. Analytical Model

Test model has some initial imperfections. It is considered that the location with the largest effect of initial imperfection is cross sectional location of 90° direction, and in order to confirm the effect of initial imperfection, observation of global behavior is required. Therefore, 3-D global shell model including the E/H is used in this analysis.

b. Analytical Contents

According to the as-built measurement of the test model, it is confirmed that test model has an initial imperfection of about 10mm inward at E/H area. Therefore, forced displacement is applied to the area around E/H in the test model, and pressure load is applied to the deformed test model. (Applied method for initial imperfection is explained in section 3.4 in detail)

(4) Analysis for Effects of Welded Portion around E/H

a. Analytical Model

3-D E/H submodel has been already prepared because the area around E/H had been selected as a critical area in pretest analysis. However, welded portion was not simulated in this submodel. Therefore, 3-D E/H submodel including welded portion is prepared.

b. Analytical Contents

Elements to simulate the welded portion are added in boundary area between the lower conical shell and E/H reinforcement plate, which is the tearing portion occurred in the test. Additionally, corrected material data based on the measured hardness in the posttest metallurgical evaluation is used in this analysis. (Applied method for welded portion is explained in section 3.5 in detail)

3.1.2 Analysis Cases

Analysis cases conducted in the posttest analyses are shown in Table 3.1-1.

Table 3.1-1 Analysis Cases

Posttest Analysis	Analytical Model	Analytical Model Name
Analysis using Fine Mesh Model	2-D axisymmetric shell global model	GLB2D/STD
	3-D shell global model	GLB3D/STD
	3-D shell E/H submodel	EHSUB/STD
Analysis for Effect of Yield Condition	2-D axisymmetric shell global model	GLB2D/MAT
Analysis for Effect of Initial Imperfection	3-D shell global model	GLB3D/DEF
Analysis for Effect of Welded Portion around E/H	3-D shell E/H submodel	EHSUB/MAT
Analysis for Second Crack	3-D shell middle conical shell submodel	MCSSUB

3.2 Analysis using Fine Mesh Model

3.2.1 Purpose of Analysis

As a result of comparison between test and pretest analysis results, as shown in Table 2.2-1, marks of strain are reverse (test result is positive, analysis result is negative). For one of the reason, It is considered that element or node in analysis model do not exactly correspond to measurement gage locations of strain and displacement. Then, with regard to 2-D axisymmetric shell global model, 3-D shell global model and E/H submodel used in pretest analysis, analyses fitted element or node location to measurement location with new fine mesh analytical model were conducted to try to enhance an analytical accuracy.

3.2.2 Analytical Model and Condition

(1) 2-D axisymmetric global shell model (GLB2D/STD)

2-D axisymmetric global shell model is shown in Figure 3.2-1. This analytical model simulated the shell wall of SCV test model, top head flange, stiffener ring, support girder and CS with axisymmetric shell element (SAX1) based on each part shape and dimensions, and rib of ring support girder with plane stress element (CPS4R). This analytical model is about four times fine mesh model compared with pretest analysis model. This model has 3493 nodes and 3388 elements (SAX1: 1893, CPS4R: 1495).

For the boundary condition, the symmetrical condition has been given to the nodes of the top head apex and lower spherical shell bottom and vertical displacement of the node at the bottom surface of the ring support girder has been fixed.

(2) 3-D shell global model (GLB3D/STD)

3-D global shell model is shown in Figure 3.2-2. This analytical model simulated the all material component of SCV test model (shell wall, top head flange, stiffener ring, ring support girder, E/H reinforcement plate, sleeve, hatch cover) and CS covering the SCV test model with 3-D shell element (S4R), for one side of symmetric surface (180deg.) through the center of SCV test model, CS and E/H. This model has 9878 nodes and 9665 elements.

For the boundary condition, the symmetrical condition has been given to the symmetric surface nodes of the SCV test model and the CS and vertical displacement of the node the bottom surface of the ring support girder has been fixed.

(3) 3-D shell E/H submodel (EHSUB/STD)

3-D submodel of E/H portion is shown in Figure 3.2-3. This analytical model simulated the reinforcement plate of E/H portion and middle and lower conical shell, middle stiffening ring and a part of CS covered with these using 3-D shell element (S4R). This model has 6024 nodes and 5757 elements.

In this analysis model, displacement and rotation obtained from 3-D shell global model analysis were applied to the node of edge (cutting surface from global model) except for axisymmetric surface.

For the boundary condition, the symmetrical condition has been given to the symmetric surface nodes of the conical shell, stiffener ring, around E/H area and the CS.

(4) Analytical Condition of others

In each 2-D axisymmetric shell global model, 3-D global shell model and E/H submodel, the gap size between SCV test model and CS is 18mm, friction coefficient after contact is 0.2. Also, material properties and stress-strain curve given for analytical model are same as those used for pretest analysis.

3.2.3 Comparison Results

As a result of analysis, as shown in Figure 3.2-4 and Figure 3.2-5, it was confirmed that analysis could roughly simulate the test result in only upper cylindrical shell (SOL#12). However, behavior near the material change interface could not be improved. For this reason, it is considered that strain gage locations in SOL#17,18 are near welded seam. In other words, it is considered that there was a difference between test and analysis results in this portion because the difference in rigidity between base metal and welded portion was not considered in this analytical model. Also, as shown in Figure 3.2-5, it seems that there is bending in this portion because outside surface is positive and inside surface is negative. On the other hand, analysis result shows both sides are positive and does not indicate the effect of bending. It seems that the reason of these differences is derived from the difficulty of the simulation because these measurement points are near the material change interface of SGV480 and SPV490 with difference of deformation by pressure.

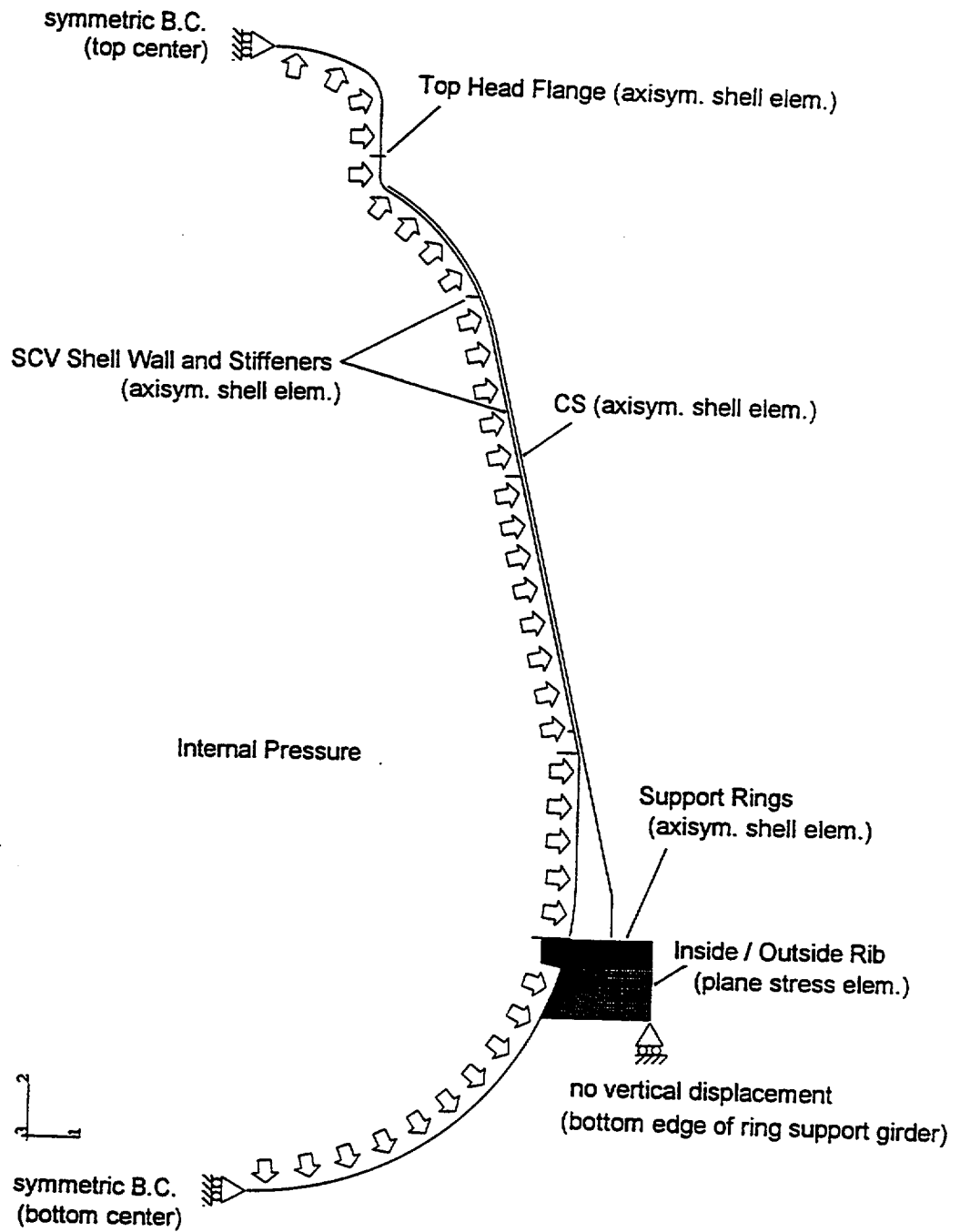
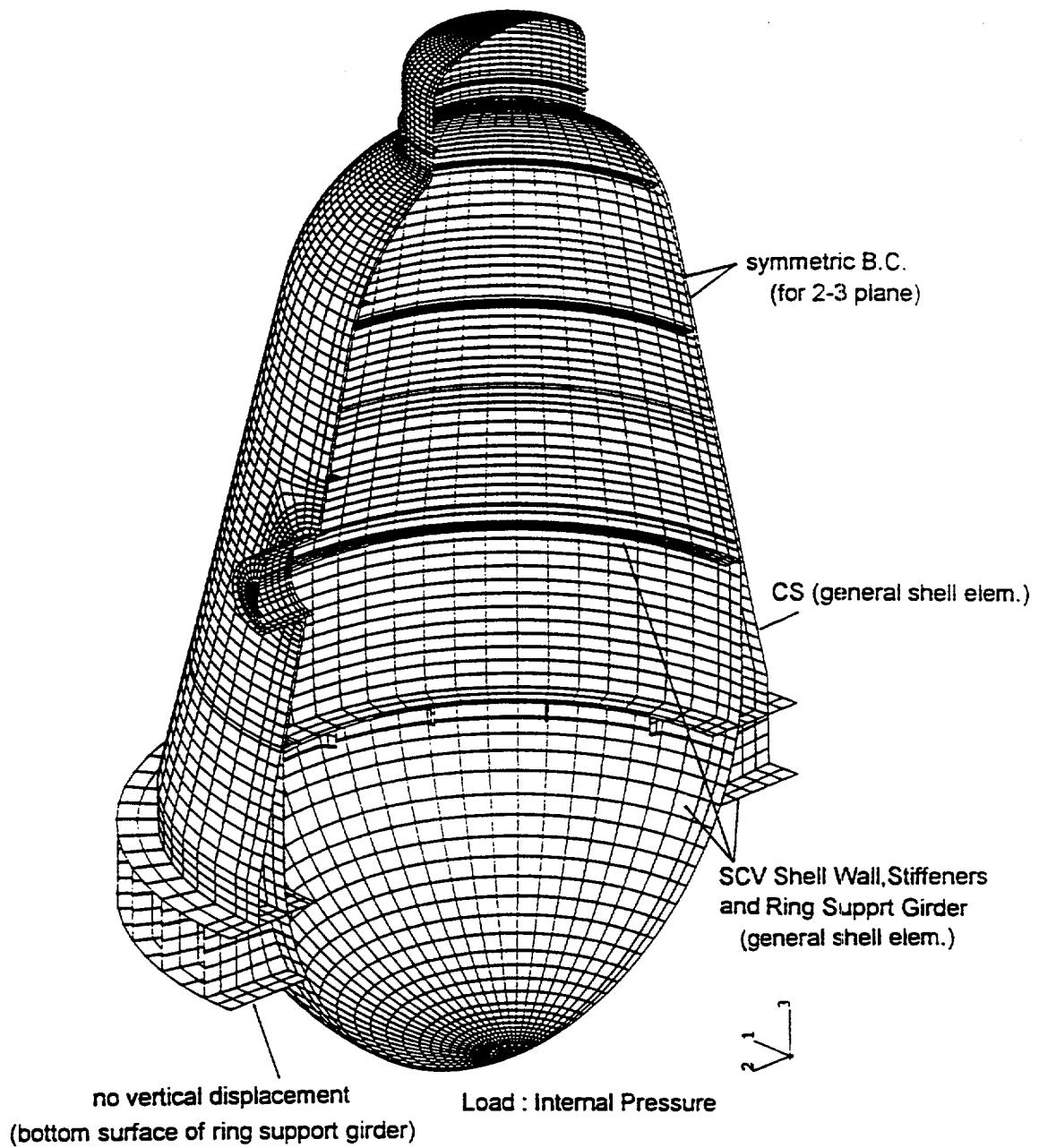
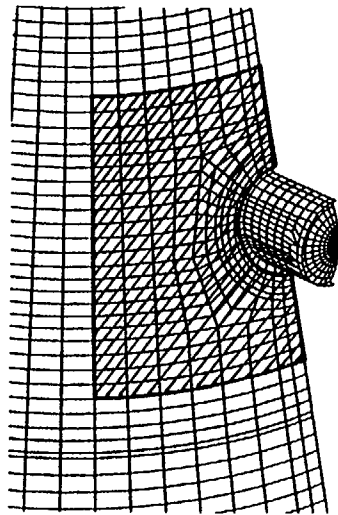


Figure 3.2-1 Global 2-D Shell Model and Analytical Conditions



[Model Inside View]

Figure 3.2-2 Global 3-D Half Shell Model with initial deformation at near the E/H area and Analytical Conditions

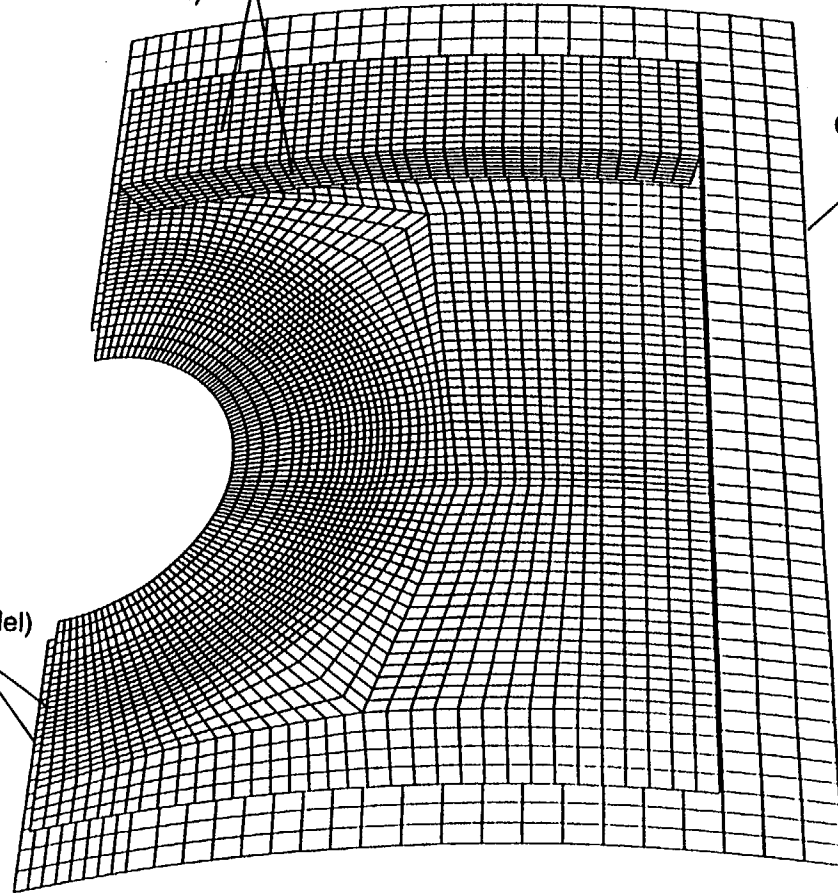


Submodel area in Global Model

SCV Shell Wall and Stiffeners
(general shell elem.)

CS (general shell elem.)

symmetric B.C.
(center edge of model)



Load : Internal Pressure (SCV shell wall)
and Disp./Rot. from Global 3D Shell Model Analysis (edge of model)

[Model Inside View]

Figure 3.2-3 Local 3-D E/H area Submodel and Analytical Conditions
[Submodel for Main Crack Position]

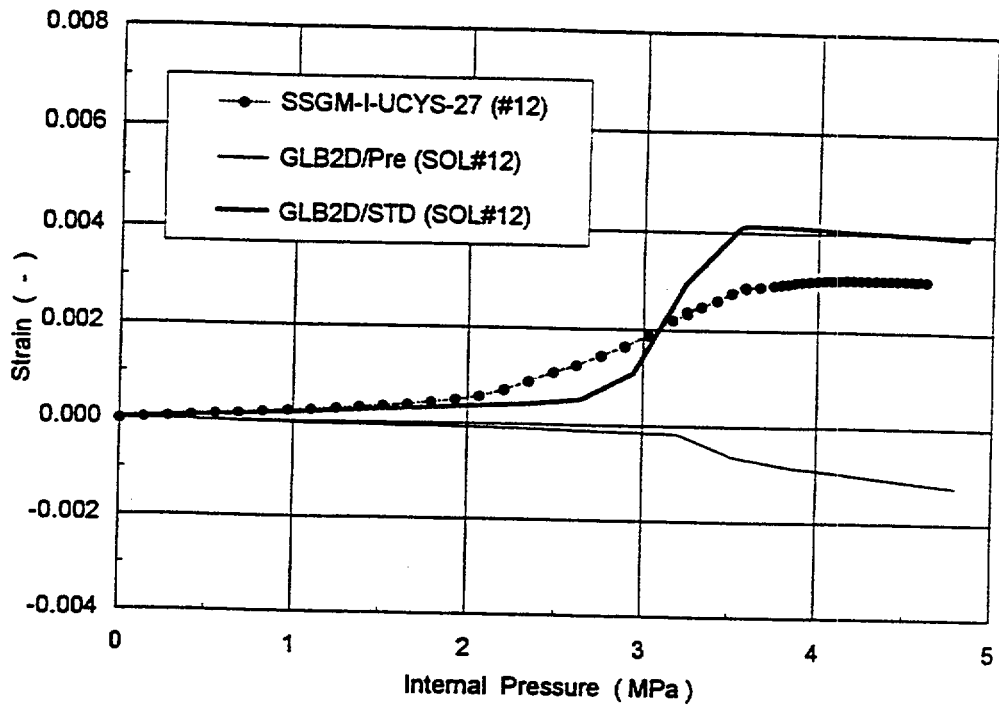


Figure 3.2-4 Comparison of Meridional Strain at SOL#12 (UCYS)
Results from SCV High Pressure Test and GLB2D Analyses

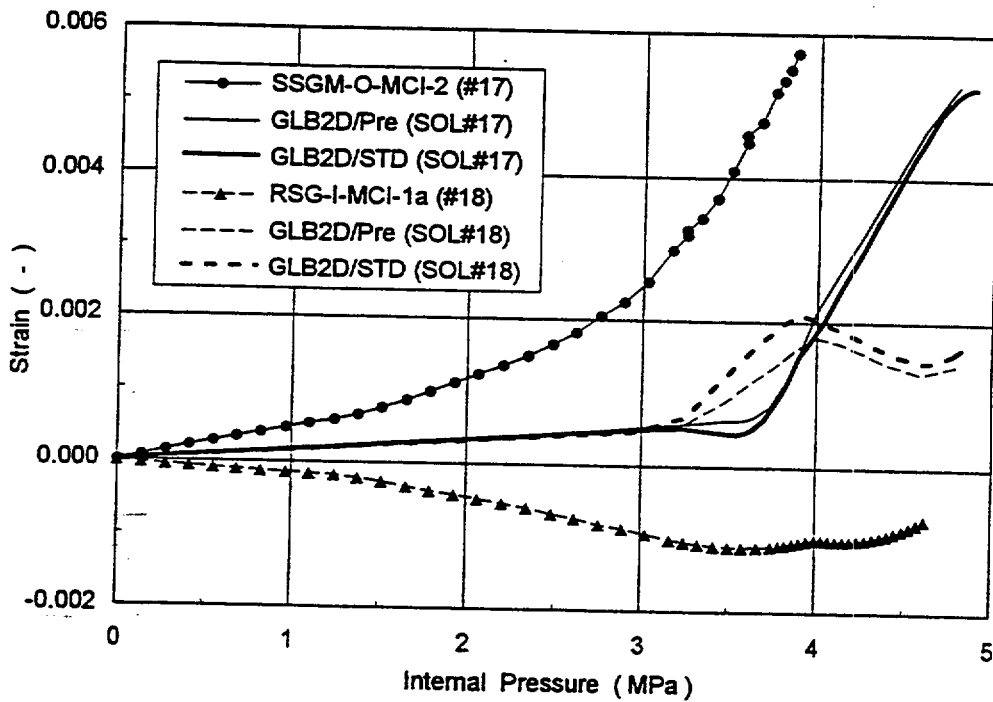


Figure 3.2-5 Comparison of Meridional Strain at SOL#17 & #18 (MCI)
Results from SCV High Pressure Test and GLB2D Analyses

3.3 Analysis for Effects of Yield Condition

3.3.1 Purpose of Analysis

As a result of comparison between measured strain data during test and pretest analysis results, it was confirmed that measured yield pressure during test was lower than predicted yield pressure in analysis. Also, it was confirmed that there was a difference in the yield point between test and analysis results in cylindrical vessel test at Japan.

According to this cylindrical vessel test results, it was confirmed that yield condition in some material was close to Tresca's yield condition. On the other hand, Mises's yield condition is used in analysis. So we performed the analysis using modified material data to confirm whether the difference of yield condition effects on the yield pressure or not.

3.3.2 Analytical Model and Condition

(1) Analytical Model (GLB2D/MAT)

In this analysis, the above mentioned 2-D axisymmetric shell global model (Figure 3.2-1) was used.

(2) Analytical Condition

Load and boundary conditions and material properties applied to this analytical model are same as those in the above mentioned 2-D axisymmetric shell global model.

Here, with regard to stress-strain curve, as shown in Figure 3.3-2 (example of SGV480) and 3.3-3 (example of SPV490), the corrected curve with approximately 13% reduction (difference between Tresca's and Mises's yield condition in case of applying pressure to cylindrical and conical structures, Figure 3.3-1) for stress-strain curve was used.

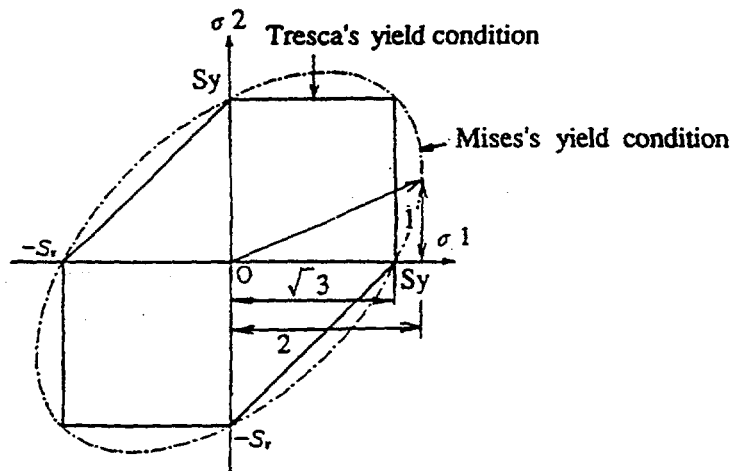


Figure 3.3-1 Tresca's and Mises's yield condition

3.3.3 Comparison Results

As a result of this analysis, in case of material data assumed Tresca's yield condition, it is confirmed that the yield point in analysis is earlier and close to that in test, however behavior over yield point in analysis does not simulate that in test as shown in Figure 3.3-4 and 3.3-5. From this results, it is confirmed that behavior in test result over about 2.8MPa show the medium between Mises's and Tresca's yield condition. And, with regard to lower conical shell (SOL#28) as shown in Figure 3.3-6, it was observed that test results was close to pretest analysis (using Mises's yield condition) and analysis using material data assumed Tresca's yield condition diverged from test results. Therefore, now it can not be judged which yield condition is reasonable. However, it is not necessarily clarified but it seems that SGV480 material follows Tresca's yield condition and SPV490 material follows Mises's yield condition. Therefore, we will study this issue including investigation of these reasons.

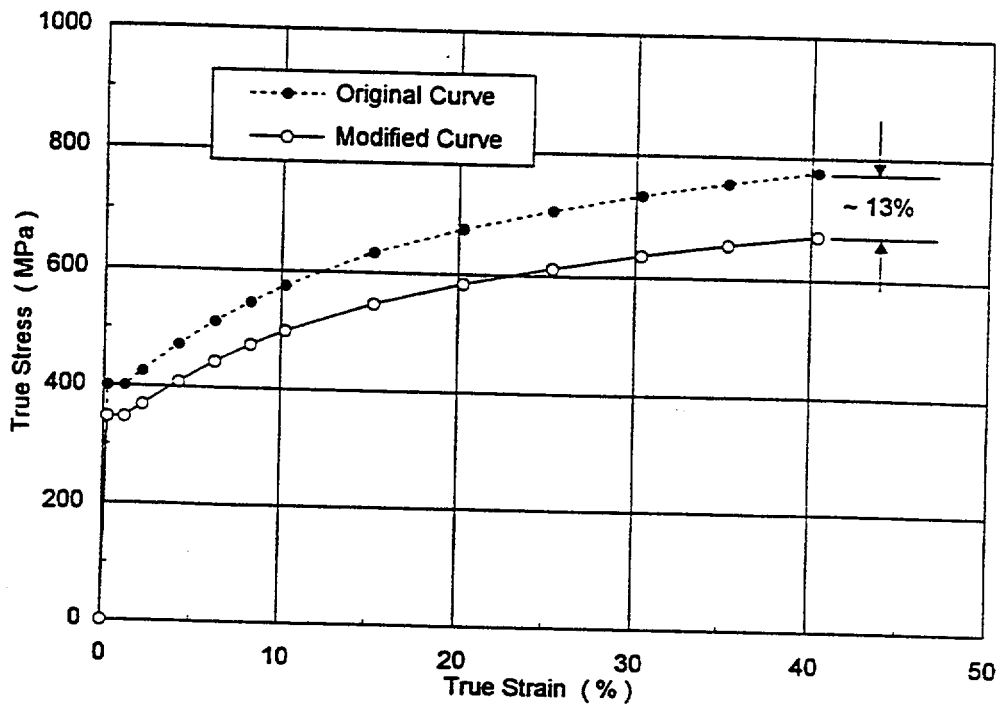


Figure 3.3-2 Assumed Stress-Strain Curve for Global 2-D Shell Model (GLB2D/MAT)
(Sample : MCS/SGV480/t8.5mm)

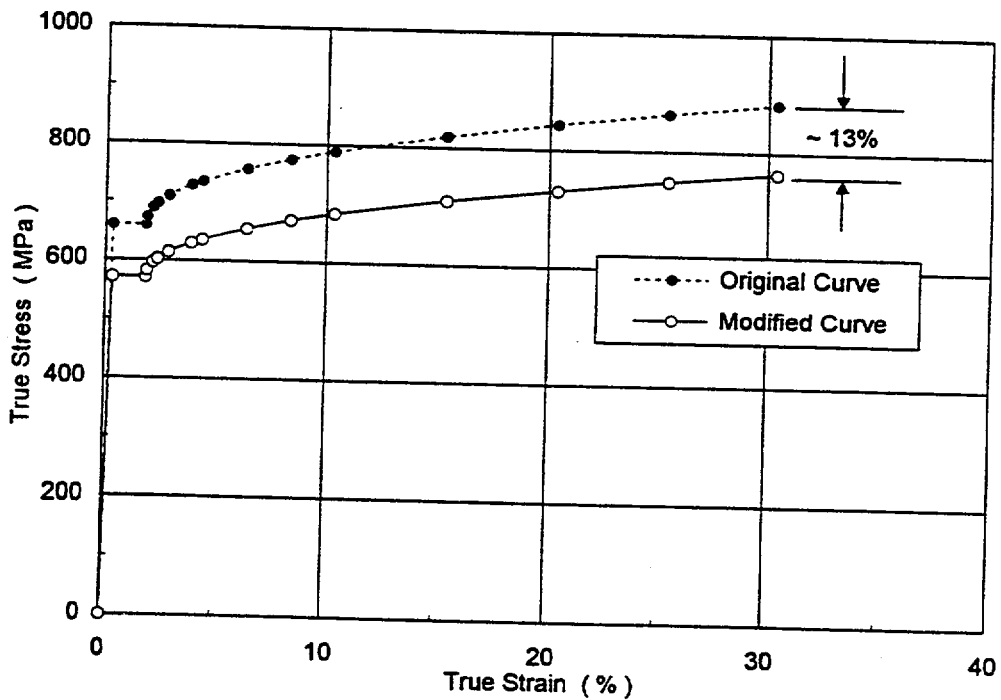


Figure 3.3-3 Assumed Stress-Strain Curve for Global 2-D Shell Model (GLB2D/MAT)
(Sample : LCS/SPV490/t9.0mm)

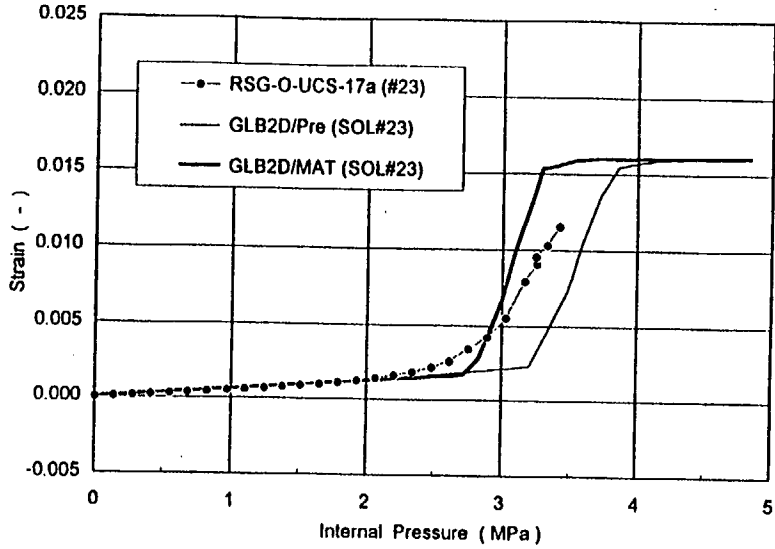


Figure 3.3-4 Comparison of Hoop Strain at SOL#23 (UCS)
Results from SCV High Pressure Test and GLB2D Analyses

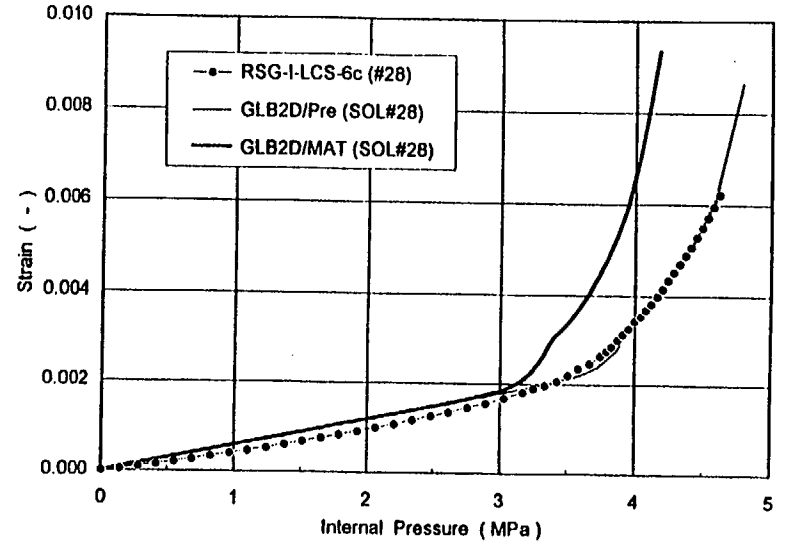


Figure 3.3-6 Comparison of Hoop Strain at SOL#28 (LCS)
Results from SCV High Pressure Test and GLB2D Analyses

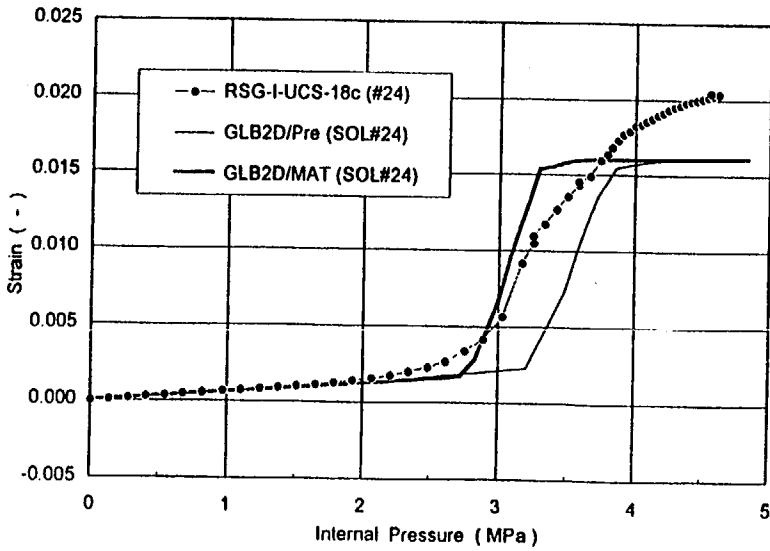


Figure 3.3-5 Comparison of Hoop Strain at SOL#24 (UCS)
Results from SCV High Pressure Test and GLB2D Analyses

3.4 Analysis for Effects of Initial Imperfection

3.4.1 Purpose of Analysis

It was observed in some portion in test results that hoop strain shows negative value in small range of pressure and variation with non-linearity from small pressure in spite of applying internal pressure. On the contrary, hoop strain in analysis results is always positive value and increase linearly up to yield point of material. And also, with regard to horizontal displacement at the center of equipment hatch cover, it was observed that there was a difference between test and analysis results in small pressure level and this difference is gradually increased. We performed an analysis using 3-D shell global model to confirm this effects because the effects due to initial imperfection, which is shown in Figure 3.4-1, is considered to be one of the reason for difference between test and analysis results.

3.4.2 Analytical Model and Condition

(1) Analytical Model (GLB3D/DFM)

In this analysis, the above mentioned 3-D shell global model (Figure 3.2-2) was used. In addition, maximum 10mm of initial imperfection is applied to this analytical model according to the following procedure.

- a. Elasto-plastic / large deformation analysis was performed to apply 10mm forced displacement to the area around E/H in above mentioned 3-D shell global model.
- b. New coordinate value was calculated from displacement in each portion derived from the above analysis of a. and was treated as initial condition. (Model on the basis of new coordinate value includes initial imperfection but not includes stress and strain.) The new coordinated 3-D shell global model at near the E/H area is shown in Figure 3.4-2, comparing with the original model.

(2) Analytical Condition

Load and boundary conditions and material properties applied to this analytical model were same as those in the above mentioned 3-D shell global model.

3.4.3 Comparison Results

Analysis considering initial imperfection was performed to confirm the cause of large difference between test and analysis results in horizontal displacement at the top of hatch cover and negative value of strain near equipment hatch in low pressure level. As a result of this analysis, it was confirmed that considering initial imperfection dissolved the large difference between test and analysis results in horizontal displacement at the top of hatch cover (SOL#39) (Figure 3.4-4). And also, with regard to negative value of strain in STG-I-EQH-16b,c and 37a, etc. in low pressure level as shown in Figure 2.1-4,7 and 14, it was confirmed that analysis considering initial imperfection could simulate test results successfully as shown in Figure 3.4-5 and 6 (Evaluation point is shown in Figure 3.4-3).

As a results, it was confirmed that it was very useful for simulating test model behavior to include initial imperfection in analytical model.

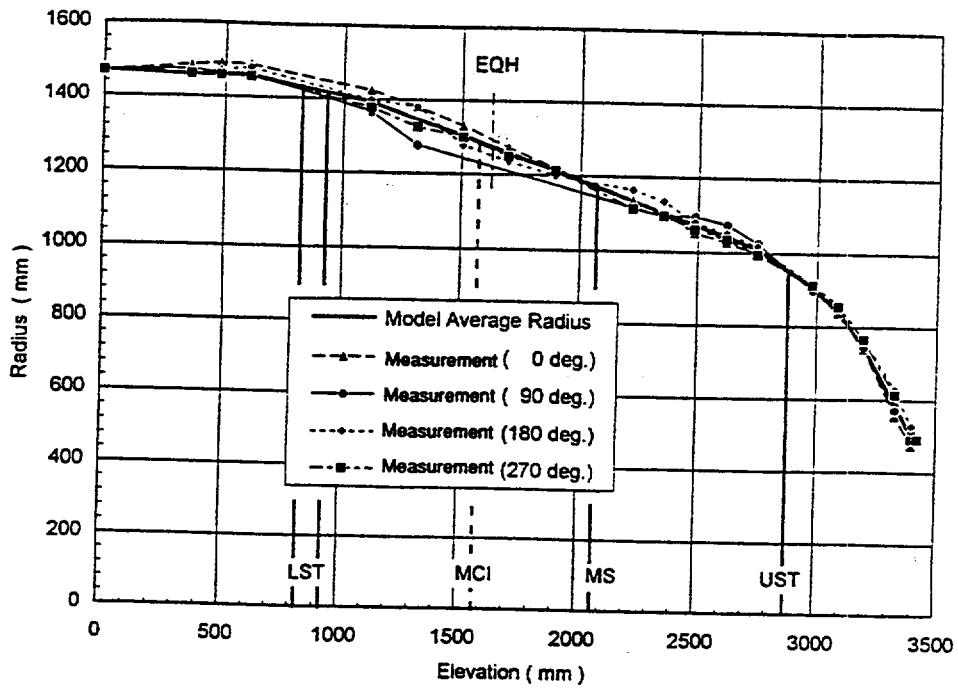
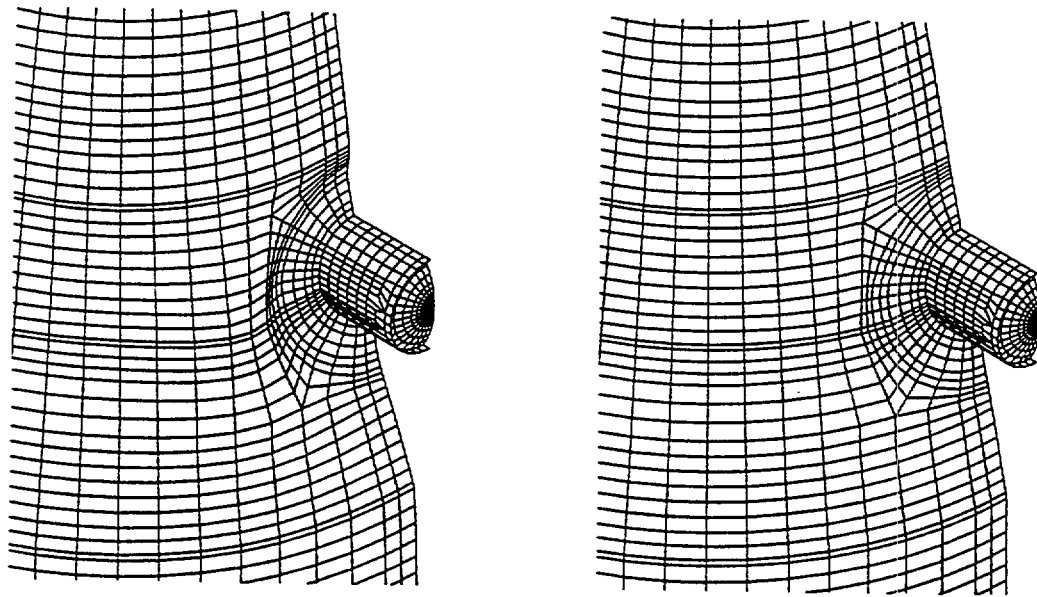


Figure 3.4-1 Measurement Results of SCV Test Model Outside Radius
 Note ; Difference of average radius and measurement radius is scaled by 10.
 Measurement radius of 90 deg. at elevation 1506mm, 1700mm and 1895mm were not exist.



deformed model [GLB3D/DFM]

undeformed (original) model [GLB3D/STD]

note ; deformed shape is scaled by 10. (D MAG=10)

Figure 3.4-2 Global 3-D Half Shell Model Shape at near the E/H area

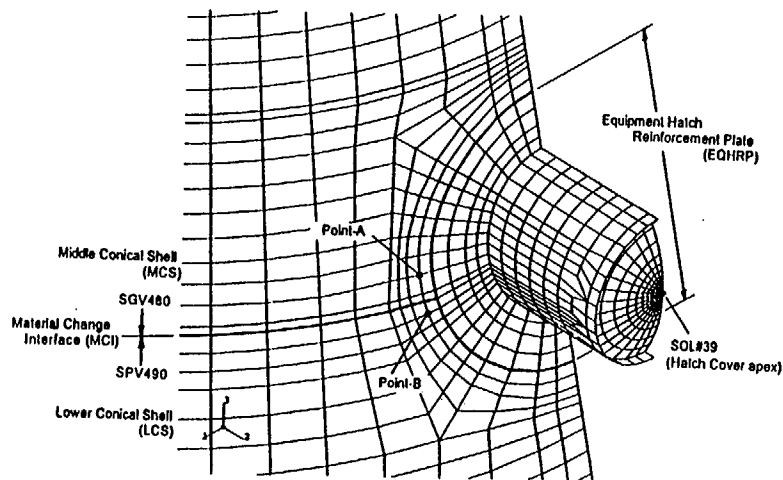


Figure 3.4-3 Horizontal Displacement and Hoop Strain Output Locations in Global 3-D Shell Model (GLB3D/STD and GLB3D/DFM)

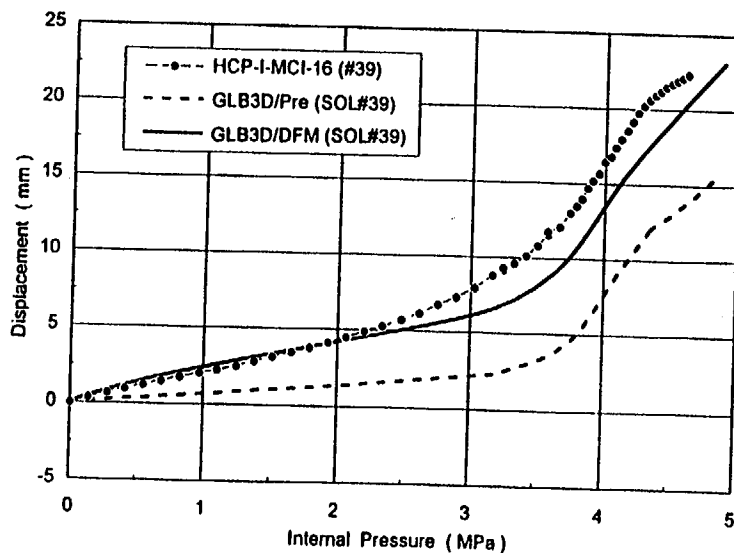


Figure 3.4-4 Comparison of Horizontal Displacement at SOL#39 (center of hatch cover) Results from SCV High Pressure Test and GLB3D Analyses

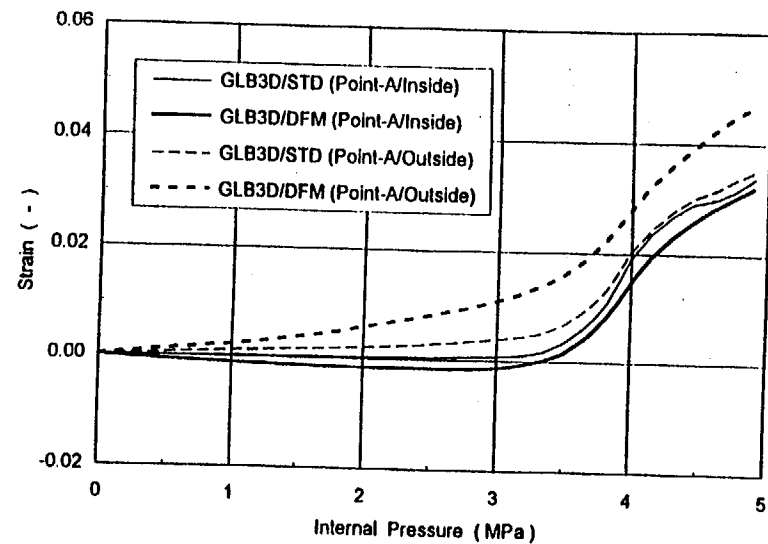


Figure 3.4-5 Comparison of Hoop Strain at near Equipment Hatch (Point-A) Results from GLB3D Analyses

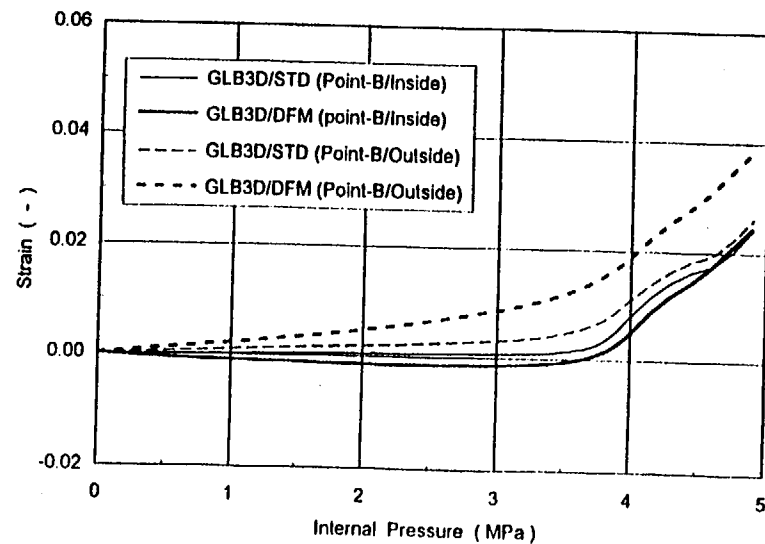


Figure 3.4-6 Comparison of Hoop Strain at near Equipment Hatch (Point-B) Results from GLB3D Analyses

3.5 Analysis for Effects of Welded Portion around Equipment Hatch

3.5.1 Purpose of Analysis

As a results of Posttest Metallurgical Evaluation for SCV High Pressure Test, it was confirmed that hardness in the heat affected zone between the equipment hatch reinforcement plate and lower conical shell was reduced. It is expected that hardness in this portion is almost same as that in SPV490 base metal because this location is the welded portion between SPV490 materials. However, it was confirmed that hardness in this portion was almost same as that in SGV480 base metal. Therefore, we performed the analysis using equipment hatch submodel considering the welded portion because it is judged that tearing is caused by the reduced hardness in the welded portion.

3.5.2 Analysis Model and Condition

(1) Analytical Model (EHSUB/MAT)

In this analysis, the above mentioned 3-D submodel of equipment hatch portion was used.

(2) Analytical Condition

Plate thickness and material in each portion used in this analysis are shown in the Figure 3.5-1. Stress-strain curves (Figure 3.5-2) same as used in pretest analysis were applied to the base metal portion (Middle conical shell, Lower conical shell, middle stiffener ring, Equipment hatch reinforcement plate and CS).

On the other hand, corrected curves (Figure 3.5-3) with approximately 7% reduction (difference in hardness between base metal and heat affected zone) for stress-strain curve used in pretest analysis were applied to the welded portion and heat affected zone between lower conical shell and equipment hatch reinforcement plate on the basis of the hardness measurement results.

Load and boundary conditions and material properties applied to this analytical model were same as those in the above mentioned 3-D submodel.

3.5.3 Comparison Results

As a result of this analysis, it was confirmed that higher strain (Figure 3.5-4) was occurred because of modeling welded portion though there was a difference of yield point in some portion. However, analysis results did not always simulate test results successfully because there were some cases that strain data in analysis results were larger than those in test results (Figure 3.5-5,6,7) or on the contrary those in test were larger than those in analysis (Figure 3.5-8). Here, with regard to SOL#41 and #43 showing a difference between test and analysis results. Both measurement points are near the welded portion between equipment hatch reinforcement plate and lower conical shell at the side of 90 and 270 degrees. And RSG-I-EQH-44a corresponding to SOL#41 at the side of 90 degree is nearest point to tearing location, while RSG-I-EQH-45b corresponding to SOL#43 and STG-I-EQH-37a at the side of 270 degree are necking locations that were confirmed in posttest inspection. From these results, it is judged that there is a difference between test and analysis results because analysis using shell element can simulate reduced plate thickness in whole the test model, but can not simulate localized necking phenomena.

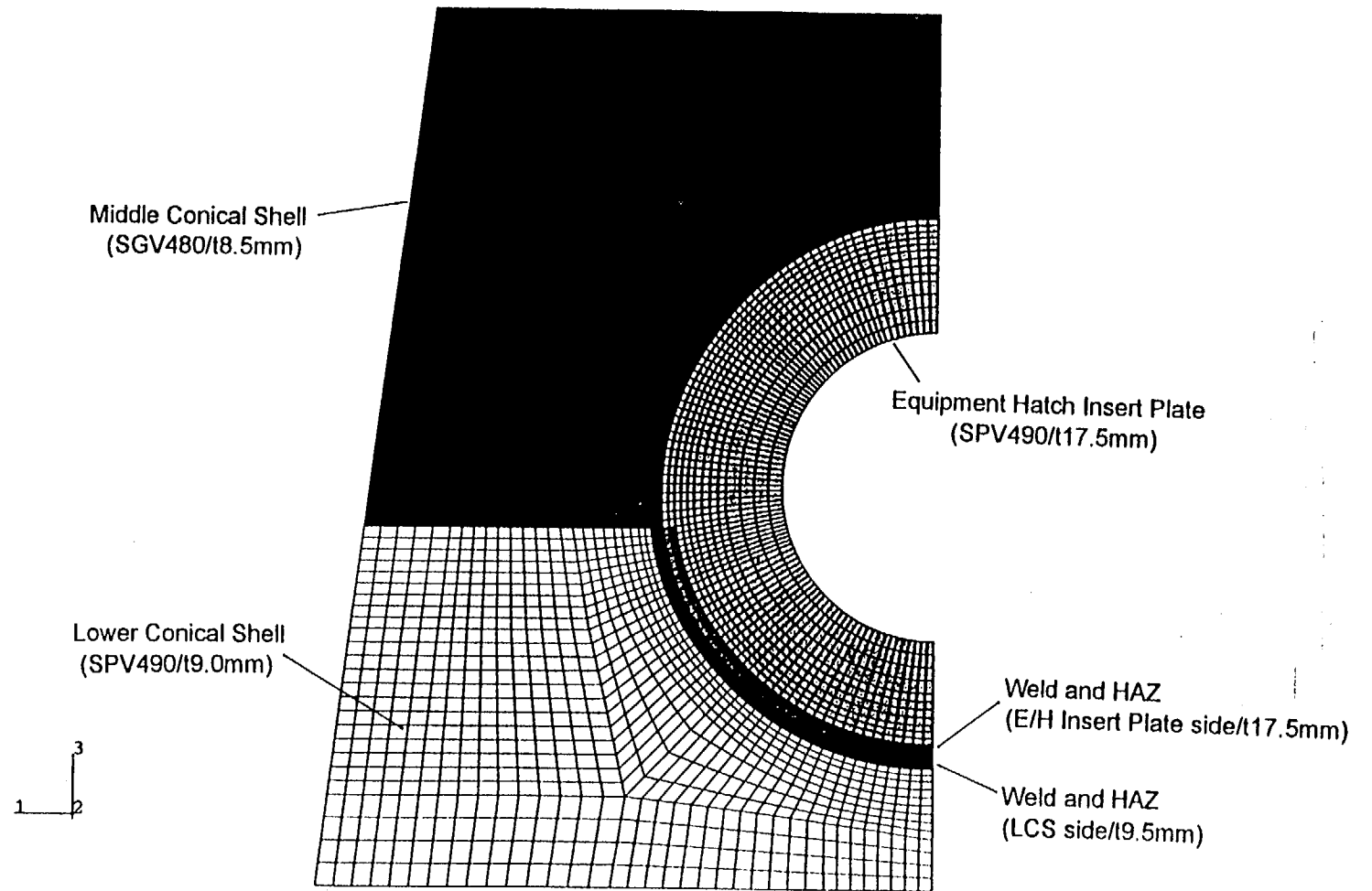


Figure 3.5-1 Thickness and Material for Local 3-D E/H area Submodel (EHSUB/MAT)

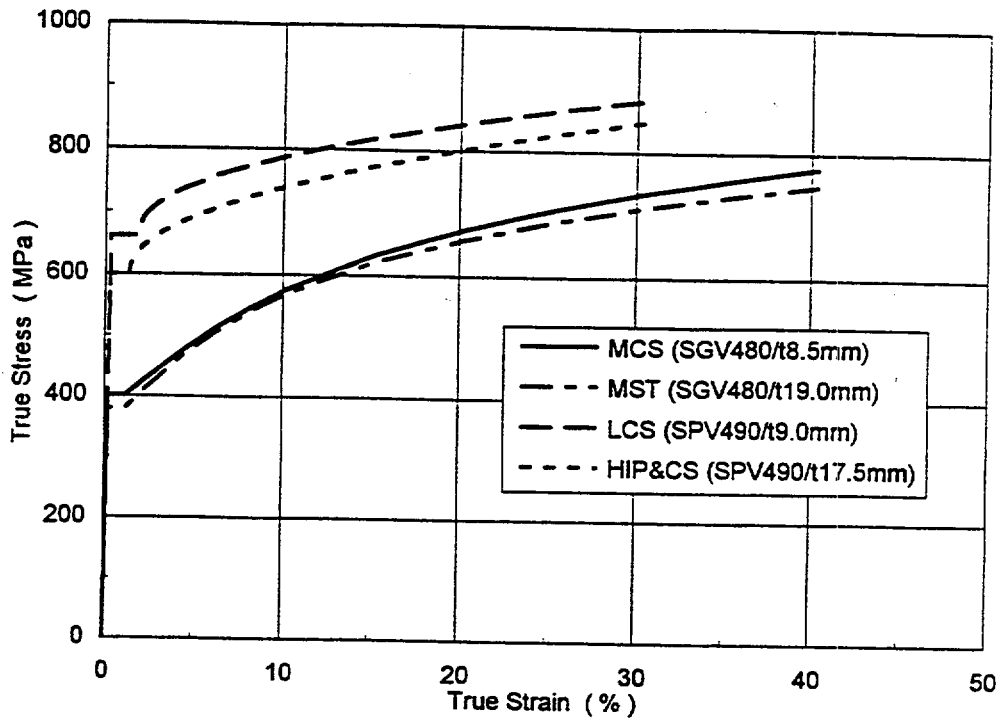


Figure 3.5-2 Stress-Strain Curve for Local 3-D E/H area Submodel (EHSUB/MAT)
(Base Material of MCS,MST,LCS,HIP&CS)

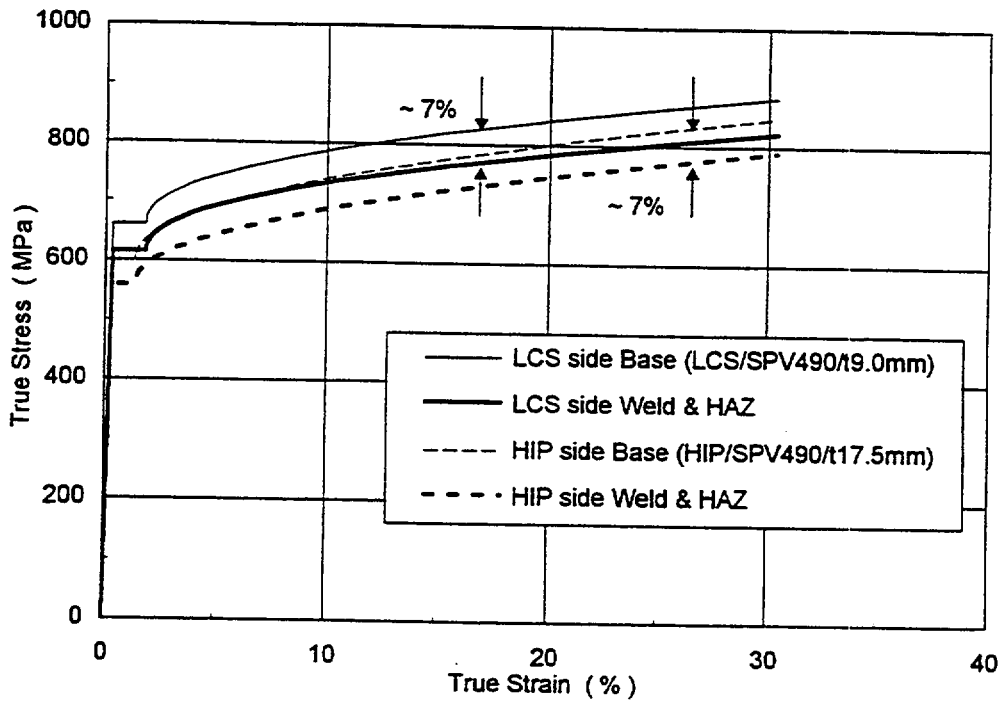
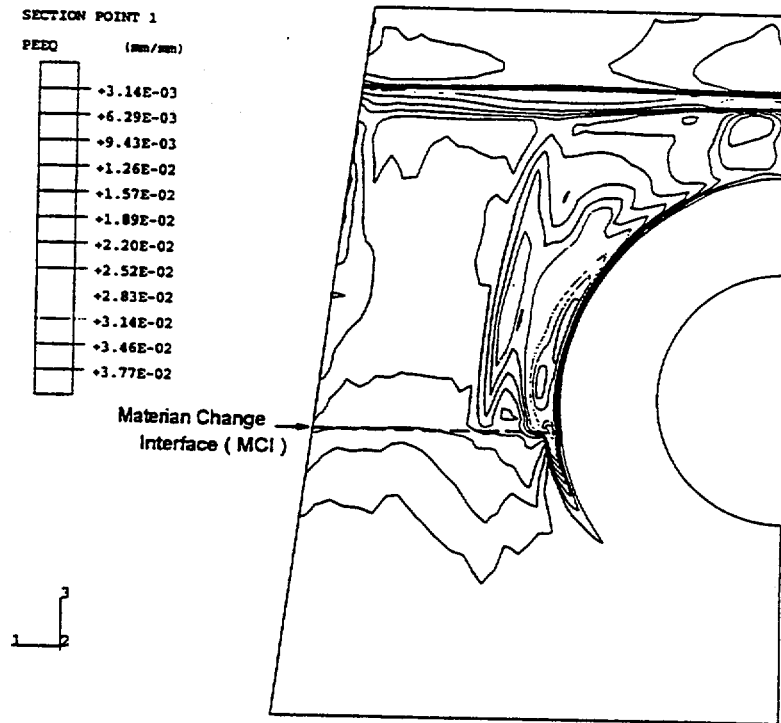
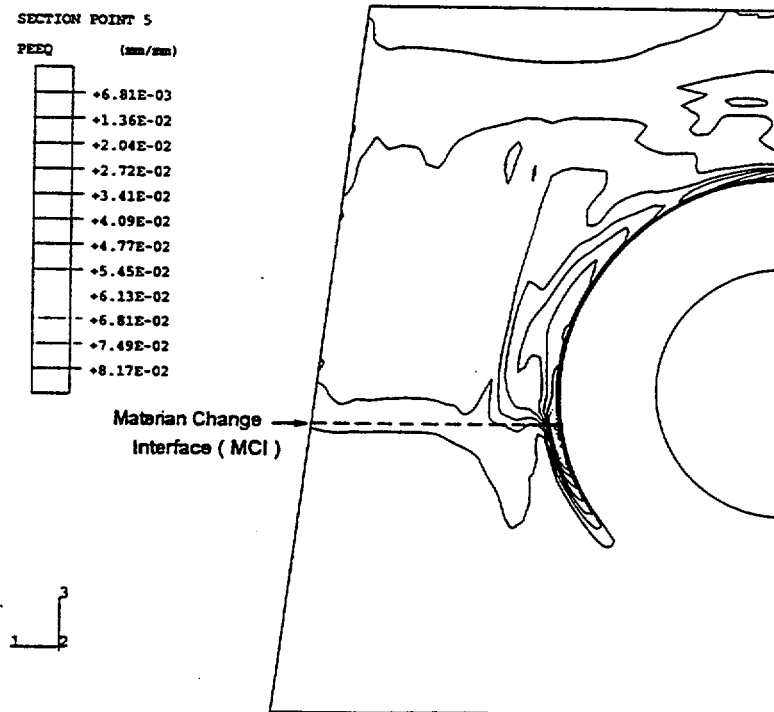


Figure 3.5-3 Assumed Stress-Strain Curve for Local 3-D E/H area Submodel (EHSUB/MAT)
(LCS to HIP Weld and HAZ)



(1) Inside Surface



(2) Outside Surface

Figure 3.5-4 Contour Plot of Equivalent Plastic Strain (Pressure : 4.42MPa)

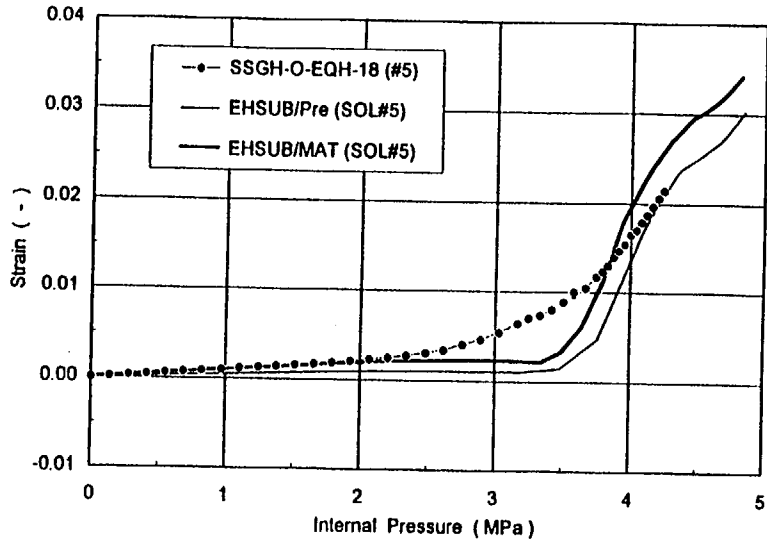


Figure 3.5-5 Comparison of Hoop Strain at SOL#5 (near Equipment Hatch)
Results from SCV High Pressure Test and EHSUB Analyses

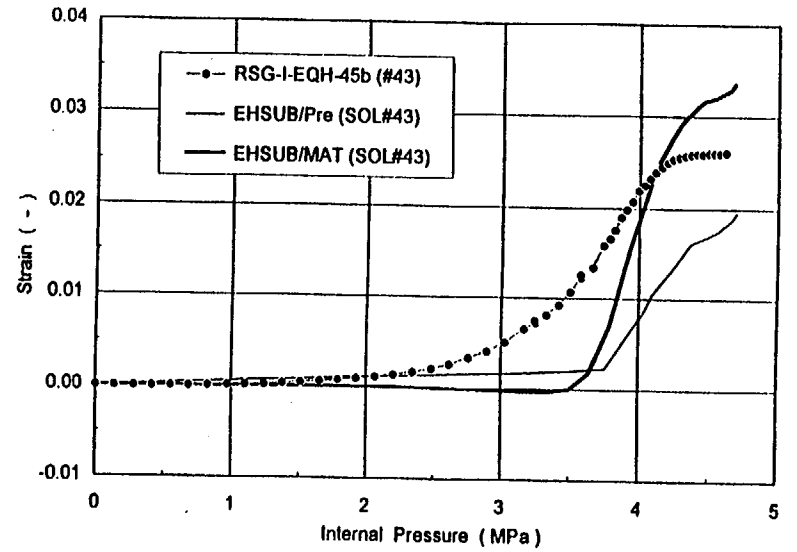


Figure 3.5-7 Comparison of Hoop Strain at SOL#43 (near Equipment Hatch)
Results from SCV High Pressure Test and EHSUB Analyses

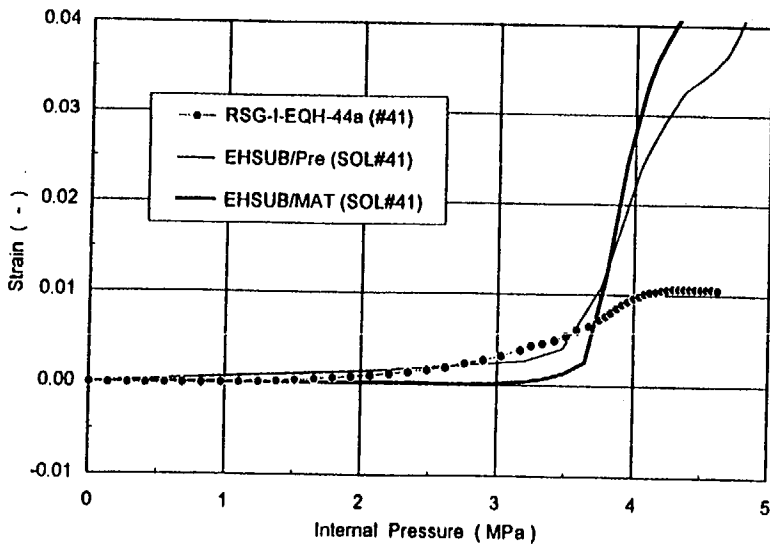


Figure 3.5-6 Comparison of Hoop Strain at SOL#41 (near Equipment Hatch)
Results from SCV High Pressure Test and EHSUB Analyses

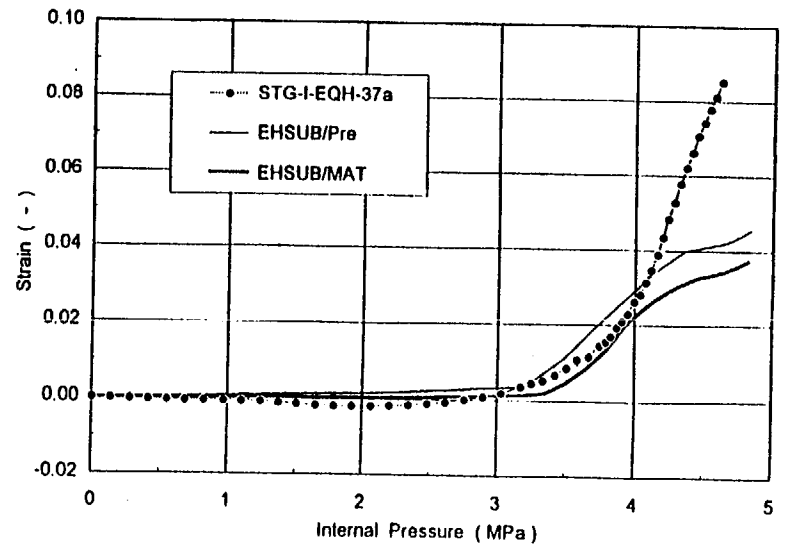


Figure 3.5-8 Comparison of Hoop Strain / STG-I-EQG-37a (near Equipment Hatch)
Results from SCV High Pressure Test and EHSUB Analyses

3.6 Analysis for Second Crack

3.6.1 Purpose of Analysis

As a result of posttest inspection, it was confirmed that tearing occurred at the location of weld relief hole on middle stiffener ring in middle conical shell. On the other hand, because pretest analytical model included middle stiffener ring but not weld relief hole, there is a possibility that higher strain in this portion can not be confirmed. Therefore, we performed the posttest analysis including weld relief hole in analytical model to confirm this effect.

3.6.2 Analytical Model and Condition

(1) Analytical Model

3-D submodel of middle conical shell (MCSSUB) is shown in Figure 3.6-1.

This analytical model simulates middle conical shell, middle stiffener ring and CS covered with these plates at 200 degree direction that tearing is confirmed in SCV test model, using 3-D shell element (S4R), and weld relief hole with 15mm of radius is included in stiffener ring. The number of node and element in this model are 6745 and 6529 respectively.

(2) Analytical Condition

Displacement and rotation obtained from the analysis results using 3-D shell global model were applied to node point on symmetrical section in conical shell, stiffener ring and CS.

In addition, the gap between SCV test model and CS is 18.0mm and friction coefficient after contact is 0.2 in this analytical model. And material property and stress-strain curve in analytical model are same as those in pretest analysis.

3.6.3 Comparison Results

Contour plots of hoop strain are shown in Figure 3.6-2 and 3.6-3. And comparison result of strain value between locations near second crack and equipment hatch is shown in Figure 3.6-4, as a reference to confirm how much strain occurs at the location near second crack in comparison with the other portion.

Peak strain location at the side of middle conical shell in analysis result was near both sides of weld relief hole and slightly close to the center of weld relief hole, and this location was almost corresponding to the second crack location found in posttest inspection. Therefore, it was confirmed that the analysis using middle conical shell submodel can simulate test results successfully. And it was supposed that the second crack was caused by localized deformation of shell at the location of weld relief hole without constraint due to middle stiffener ring and by strain concentration at middle conical shell portion.

In addition, it was confirmed that strain value in second crack location was almost same as high as that in the location near equipment hatch as shown in Figure 3.6-4.

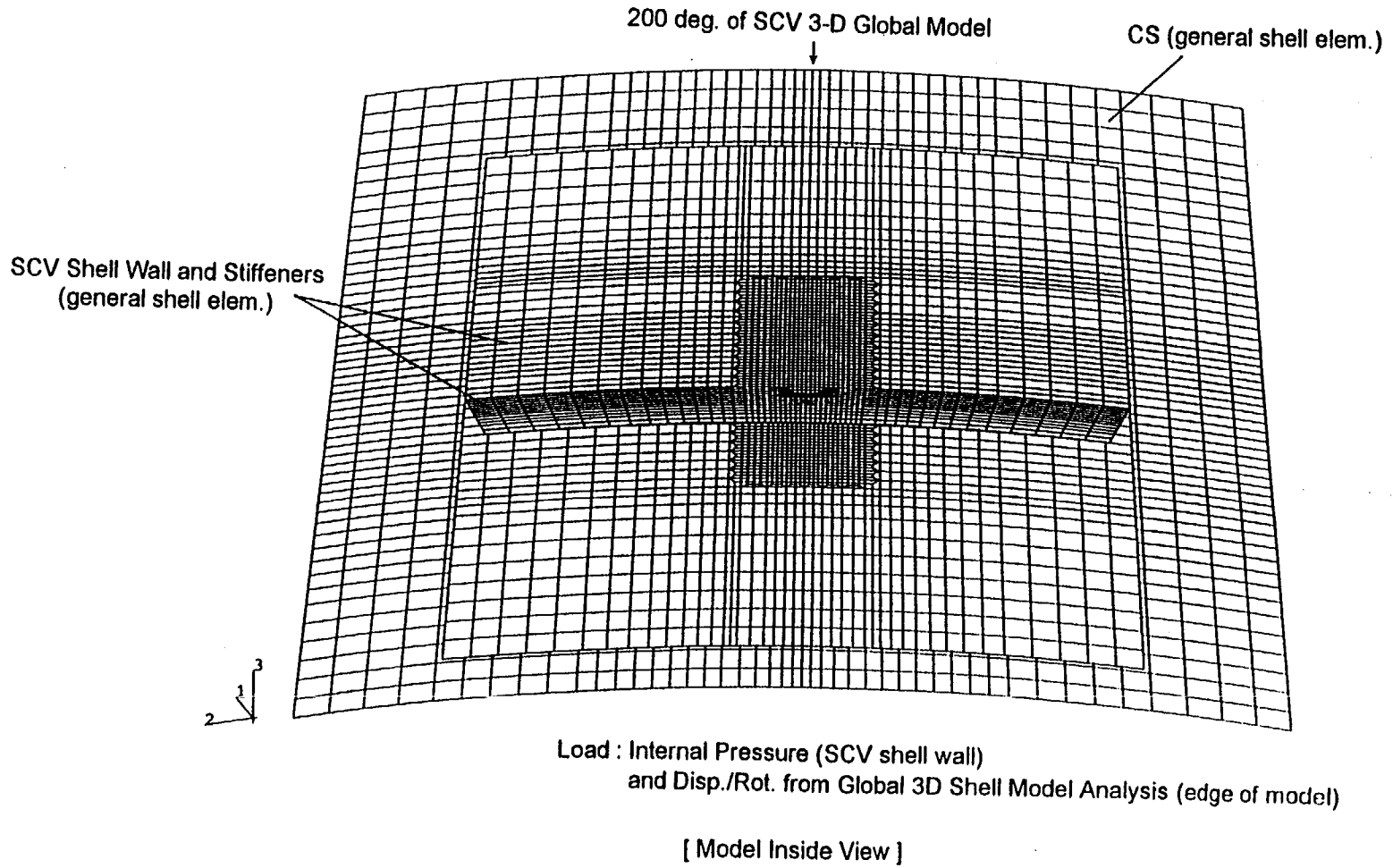


Figure 3.6-1 Local 3-D Middle Stiffener 200 deg. area Submodel and Analytical Conditions [Submodel for 2nd Crack Position]

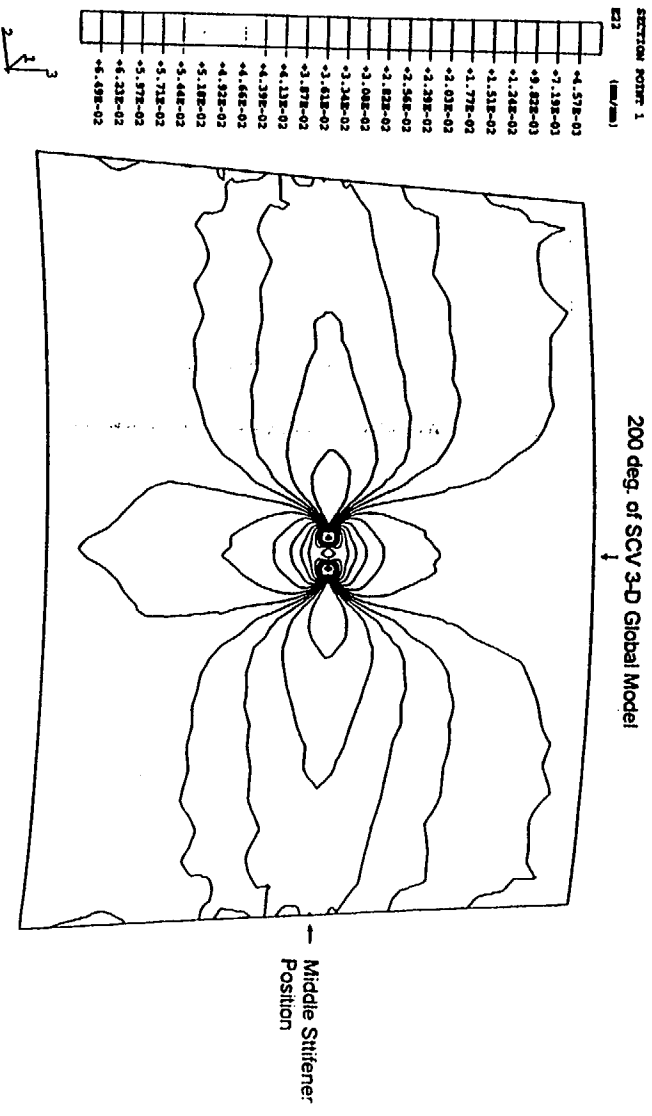


Figure 3-6-2 Contour Plot of Hoop Strain - model overview (2ND-SUB Analysis) (without MST/ Inside Surface / 4.44 MPa)

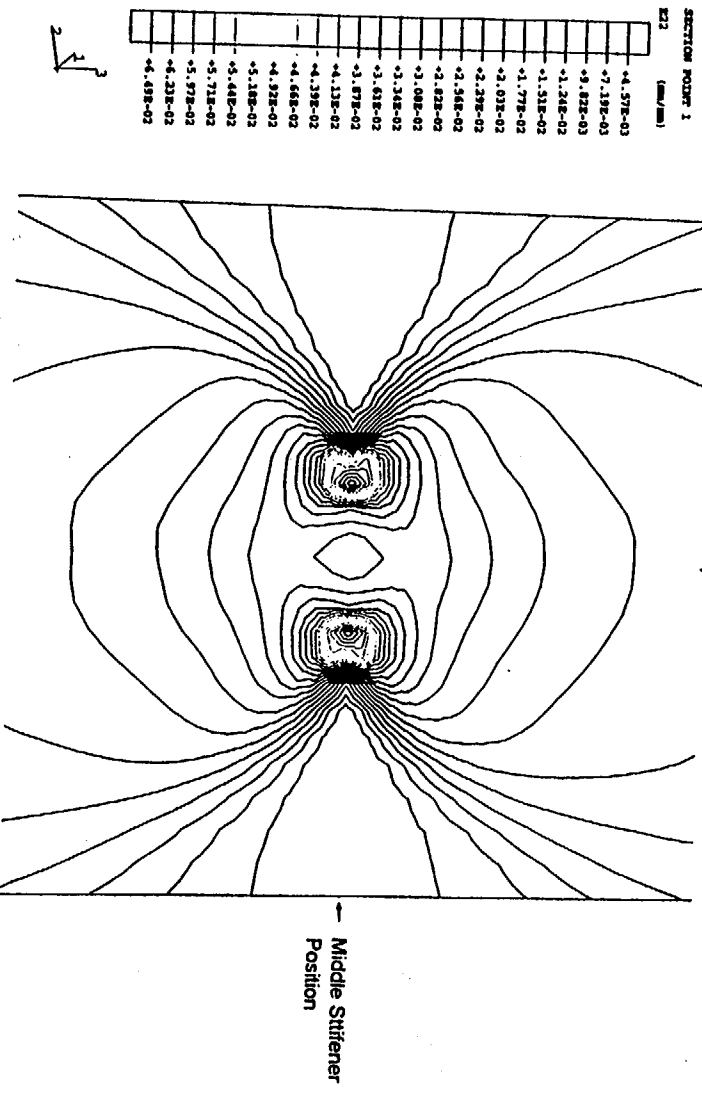
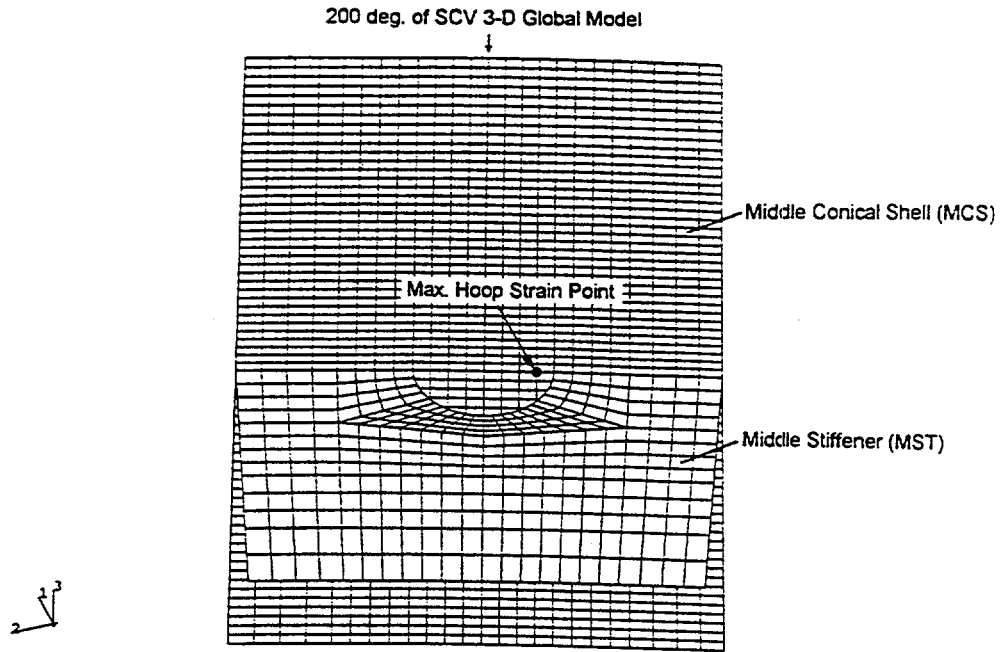


Figure 3-6-3 Contour Plot of Hoop Strain - near seal hole (2ND-SUB Analysis) (without MST/ Inside Surface / 4.44 MPa)



[2nd Crack Submodel Inside View]

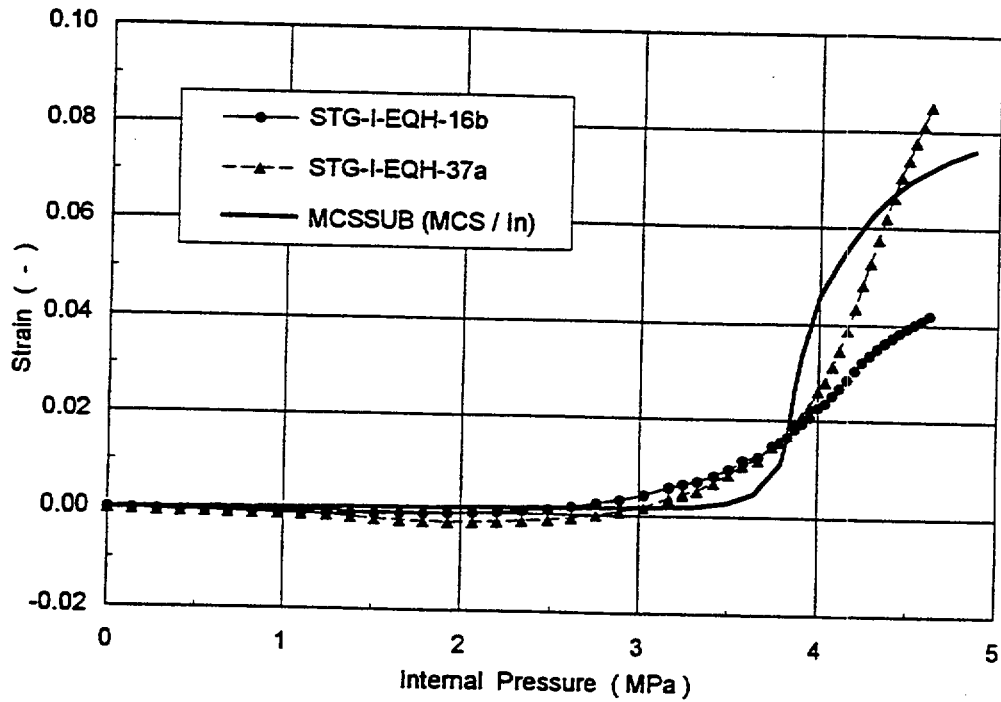


Figure 3.6-4 Comparison of Hoop Strain (near EQH and 200deg. MCS)
Results from SCV High Pressure Test and MCSSUB Analysis

4. Study for the Cause of Failure

4.1 Study for the Crack near Equipment Hatch

As a result of posttest metallurgical evaluation, it was confirmed that hardness in heat affected zone (HAZ) between equipment hatch reinforcement plate and lower conical shell was reduced. The hardness measurement results are shown in Table 4.1-1.

Table 4.1-1 Result of Posttest Hardness Measurement

	Sample	Material	Base Metal	HAZ	Fusion Zone
Crack Location near Equipment Hatch	SCV-74-1	SPV490	98.1	91.5	95.1
	SCV-74-2	SPV490	94.2	90.9	92.1*
	SCV-74-3	SGV480	89.2	92.2	—

* Fusion zone between SGV480 and SPV490; not included in averages.

As shown in the above table, with regard to SPV490 material, hardness in HAZ is lower than that in base metal and fusion zone. On the other hand, with regard to SGV480 material, hardness in HAZ is higher than that in base metal. With regard to this reason, it is reported in reference [6.5] that the increased hardness in HAZ of SGV480 material is caused by making microstructure fine due to welding process and reduced hardness in HAZ of SPV490 material is caused by making microstructure coarse due to welding process.

Based on the pretest analysis, the location near equipment hatch was one of the critical area. And the predicted failure portion was at the side of SGV480, which is lower in strength than SPV490. However, it is supposed that the crack near equipment hatch was caused by reduced hardness in HAZ between equipment hatch reinforcement plate and lower conical shell at side of SPV490. This phenomena was confirmed by the posttest analysis for effects of welded portion around equipment hatch.

4.2 Study for the Second Crack

Second crack occurred in shell plate at the level of weld relief hole on middle stiffener ring. SCV test model has 2 weld relief holes on middle stiffener ring at second crack location (200 degree direction) and its symmetrical location (20 degree direction). As a result of posttest metallurgical evaluation, it was confirmed that necking had occurred at the symmetrical location of second crack. However, there was no evidence of high strain at the location without weld relief hole. In structural comparison between stiffener ring with/without weld relief hole, difference in welded between shell and stiffener ring and difference in stiffness of ring to horizontal direction, were extracted. From this comparison, it is predicted that the deformation of stiffener ring without weld relief hole follows that of shell, however stiffener ring with weld relief hole expands outward in both sides round the center of the hole. Therefore, it is supposed that whole stiffener ring deforms in configuration of almost whole circle up to some pressure, after that, deformation in both sides of stiffener ring at the location of weld relief hole with smaller sectional area results in strain concentration on shell side and leads to crack. This phenomena was confirmed by the posttest analysis for second crack.

5. Conclusions

In order to confirm the behavior of whole test model and to clarify the cause of crack for SCV high pressure test, 2-D and 3-D global analysis were performed. In addition, in order to perform detail study for the location near crack portion, analyses using equipment hatch submodel as a scope of crack portion near equipment hatch and using middle conical shell submodel as a scope of second crack were performed.

As a result, with regard to whole behavior of SCV test model, it was confirmed that if analyses using fine mesh model and considering initial imperfection would be performed, large difference between test and analysis results were dissolved and overall the test results could be almost simulated by such analyses. On the other hand, with regard to behavior around equipment hatch, the analysis using equipment hatch submodel with shell element could not simulate correctly necking phenomena. However, it was confirmed that analysis considering welded portion could simulate higher strain corresponding to crack occurrence. From this results, it is supposed that the crack near equipment hatch was caused by reduced hardness in HAZ between equipment hatch reinforcement plate and lower conical shell. And with regard to the second crack, it was confirmed that crack occurrence location found in posttest inspection was almost corresponding to higher strain location based on this posttest analysis result, and this analysis could simulate test result. Therefore, it is supposed that the second crack is caused by deformation of weld relief hole with increasing pressure and localized strain concentration on shell plate.

As shown in the above description, it was confirmed that whole behavior could be almost simulated by analysis. However, we will continue to study remaining issues for the difference between test and analysis results in some portions.

6. References

- [6.1] "ABAQUS/Standard User's Manual Volume I", HIBBITT, KARLSON & SORENSEN, Inc.
- [6.2] "ABAQUS/Standard User's Manual Volume II", HIBBITT, KARLSON & SORENSEN, Inc.
- [6.3] SCV DESIGN PACKAGE (Branstetter, L.j., Attachment to Round Robin Letter, July 10,1995)
- [6.4] SCV High Pressure Test Data for Round Robin Analysis. (R-SN-S-007 Rev.B)
- [6.5] Posttest Metallurgical Evaluation Results for SCV High Pressure Test (R-SN-S-009 Rev.B)
- [6.6] Round Robin Pretest Analyses of a Steel Containment Vessel Model and Contact Structure Assembly Subject to Static Internal Pressurization. Rev.B

NUPEC Appendix A

Standard Output

Table A-1 Standard Output Model Identification

Category	SOL No.	Gage No.	Output Quantity	Model Name	Remarks
Equip. Hatch Area	SOL#1 (H)	RSG-I-EQH-12a	int. hoop strain	EHSUB/STD	near EQH Reinforcement Plate / 67.5 deg.
Equip. Hatch Area	SOL#1 (M)	RSG-I-EQH-12C	int. merid. strain	EHSUB/STD	near EQH Reinforcement Plate / 67.5 deg.
Equip. Hatch Area	SOL#2 (H)	RSG-I-EQH-8a	int. hoop strain	EHSUB/STD	near EQH Reinforcement Plate / 45 deg.
Equip. Hatch Area	SOL#2 (M)	RSG-I-EQH-8c	int. merid. strain	EHSUB/STD	near EQH Reinforcement Plate / 45 deg.
Equip. Hatch Area	SOL#3	STG-O-EQH-4c	ext. merid. strain	EHSUB/STD	near EQH Reinforcement Plate / 0 deg.
Equip. Hatch Area	SOL#4	STG-I-EQH-2c	int. merid. strain	EHSUB/STD	near EQH Reinforcement Plate / 0 deg.
Equip. Hatch Area	SOL#5	SSGH-O-EQH-18	ext. hoop strain	EHSUB/STD	near EQH Reinforcement Plate / 90 deg.
Equip. Hatch Area	SOL#6	STG-I-EQH-16c	int. hoop strain	EHSUB/STD	near EQH Reinforcement Plate / 90 deg.
Top Head	SOL#7 (H)	RSG-O-THD-1a	ext. hoop strain	GLB2D/STD	apex of Top Head
Top Head	SOL#7 (M)	RSG-O-THD-1c	ext. merid. strain	GLB2D/STD	apex of Top Head
Top Head	SOL#8	RSG-O-THD-9a	ext. hoop strain	GLB2D/STD	near Top Head shell min. radius / 270 deg.
Top Head	SOL#9	RSG-O-THD-9c	ext. merid. strain	GLB2D/STD	near Top Head shell min. radius / 270 deg.
Top Head	SOL#10	RSG-I-THD-10a	int. merid. strain	GLB2D/STD	near Top Head shell min. radius / 270 deg.
Transition Regions	SOL#11	STG-O-UCYS-25c	ext. merid. strain	GLB2D/STD	just below Top Flange / 0 deg.
Transition Regions	SOL#12	SSGM-I-UCYS-27	int. merid. strain	GLB2D/STD	just below Top Flange / 0 deg.
Transition Regions	SOL#13	STG-O-KNU-1c	ext. merid. strain	GLB2D/STD	just below Knuckle / 0 deg.
Transition Regions	SOL#14	STG-I-KNU-9c	int. merid. strain	GLB2D/STD	just below Knuckle / 0 deg.
Transition Regions	SOL#15	SSGM-O-MST-1	ext. merid. strain	GLB2D/STD	just above Middle Stiffener / 0 deg.
Transition Regions	SOL#16	SSGM-I-MST-7	int. merid. strain	GLB2D/STD	just above Middle Stiffener / 0 deg.
Transition Regions	SOL#17	SSGM-O-MCI-2	ext. merid. strain	GLB2D/STD	just above Material Change Interface / 0 deg.
Transition Regions	SOL#18	RSG-I-MCI-1a	int. merid. strain	GLB2D/STD	just above Material Change Interface / 0 deg.
Transition Regions	SOL#19	SSGM-O-LST-17	ext. merid. strain	GLB2D/STD	just below Lower Stiffener / 0 deg.
Transition Regions	SOL#20	SSGM-I-LST-25	int. merid. strain	GLB2D/STD	just below Lower Stiffener / 0 deg.
Free Field	SOL#21	RSG-O-UCS-17c	ext. merid. strain	GLB2D/STD	midheight of Upper Conical Shell / 45 deg.
Free Field	SOL#22	RSG-I-UCS-18a	int. merid. strain	GLB2D/STD	midheight of Upper Conical Shell / 45 deg.
Free Field	SOL#23	RSG-O-UCS-17a	ext. hoop strain	GLB2D/STD	midheight of Upper Conical Shell / 45 deg.
Free Field	SOL#24	RSG-I-UCS-18c	int. hoop strain	GLB2D/STD	midheight of Upper Conical Shell / 45 deg.
Free Field	SOL#25	RSG-O-LCS-5c	ext. merid. strain	GLB2D/STD	above Lower Conical Shell / 45 deg.
Free Field	SOL#26	RSG-I-LCS-6a	int. merid. strain	GLB2D/STD	above Lower Conical Shell / 45 deg.
Free Field	SOL#27	RSG-O-LCS-5a	ext. hoop strain	GLB2D/STD	above Lower Conical Shell / 45 deg.
Free Field	SOL#28	RSG-I-LCS-6c	int. hoop strain	GLB2D/STD	above Lower Conical Shell / 45 deg.
Free Field	SOL#29	RSG-I-SPH-2a	int. merid. strain	GLB2D/STD	midheight of Upper Spherical Shell / 45 deg.
Free Field	SOL#30	RSG-I-SPH-2c	int. hoop strain	GLB2D/STD	midheight of Upper Spherical Shell / 45 deg.
Free Field	SOL#31	RSG-I-UCS-16a	int. merid. strain	GLB2D/STD	midheight of Upper Conical Shell / 270 deg.
Free Field	SOL#32	RSG-I-UCS-16c	int. hoop strain	GLB2D/STD	midheight of Upper Conical Shell / 270 deg.
Free Field	SOL#33	RSG-I-LCS-11a	int. merid. strain	GLB2D/STD	midheight of Lower Conical Shell / 270 deg.
Free Field	SOL#34	RSG-I-LCS-11c	int. hoop strain	GLB2D/STD	midheight of Lower Conical Shell / 270 deg.
Displacements	SOL#35	VCP-I-THD-11	vertical disp.	GLB2D/STD	apex of Top Head
Displacements	SOL#36 (+)	HCP-O-UCYS-43	horizontal disp.	GLB2D/STD	just above Top Flange / 45 deg.
Displacements	SOL#36 (-)	HCP-I-UCYS-39	horizontal disp.	GLB2D/STD	just above Top Flange / 45 deg.
Displacements	SOL#37	HCP-I-KNU-17	horizontal disp.	GLB2D/STD	just below Knuckle / 0 deg.
Displacements	SOL#38	VCP-I-KNU-18	vertical disp.	GLB2D/STD	just below Knuckle / 0 deg.
Displacements	SOL#39	HCP-I-MCI-16	horizontal disp.	GLB3D/DFM	center of Hatch Cover
Equip. Hatch Area	SOL#40	RSG-I-EQH-44c	int. merid. strain	EHSUB/STD	near EQH Reinforcement Plate (LCS side)
Equip. Hatch Area	SOL#41	RSG-I-EQH-44a	int. hoop strain	EHSUB/STD	near EQH Reinforcement Plate (LCS side)
Equip. Hatch Area	SOL#42	RSG-I-EQH-45c	int. merid. strain	EHSUB/STD	near EQH Reinforcement Plate (LCS side)
Equip. Hatch Area	SOL#43	RSG-I-EQH-45b	int. hoop strain	EHSUB/STD	near EQH Reinforcement Plate (LCS side)
Equip. Hatch Area	-	STG-I-EQH-16b	int. hoop strain	EHSUB/STD	near EQH Reinforcement Plate / 91.5 deg.
Equip. Hatch Area	-	STG-I-EQH-37a	int. hoop strain	EHSUB/STD	near EQH Reinforcement Plate / 268 deg.
Free Field	-	RSG-I-UCS-10c	int. hoop strain	GLB2D/STD	midheight of Upper Conical Shell / 0 deg.
Free Field	-	RSG-I-UCS-12c	int. hoop strain	GLB2D/STD	midheight of Upper Conical Shell / 90 deg.
Free Field	-	RSG-I-UCS-14c	int. hoop strain	GLB2D/STD	midheight of Upper Conical Shell / 180 deg.
Free Field	-	RSG-O-UCS-9a	ext. hoop strain	GLB2D/STD	midheight of Upper Conical Shell / 0 deg.
Free Field	-	RSG-O-UCS-11a	ext. hoop strain	GLB2D/STD	midheight of Upper Conical Shell / 90 deg.
Free Field	-	RSG-O-UCS-13a	ext. hoop strain	GLB2D/STD	midheight of Upper Conical Shell / 180 deg.
Free Field	-	RSG-O-UCS-15a	ext. hoop strain	GLB2D/STD	midheight of Upper Conical Shell / 270 deg.

[Note] GLB2D/STD : Global 2-D Axisymmetric Shell Model (standard case / material no change)
 GLB3D/DFM : Global 3-D Shell Model (EQH area deformed model)
 EHSUB/STD : Local 3-D EQH area Submodel (standard case / material no change)

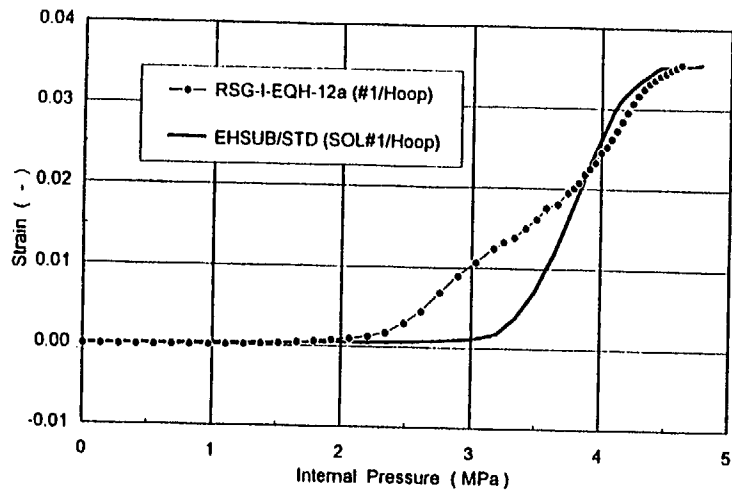


Fig. A-1 Comparison of Strain History (SOL#1 / Hoop Strain)
 [Position : near EQH / 67.5 deg. / Inside surface]

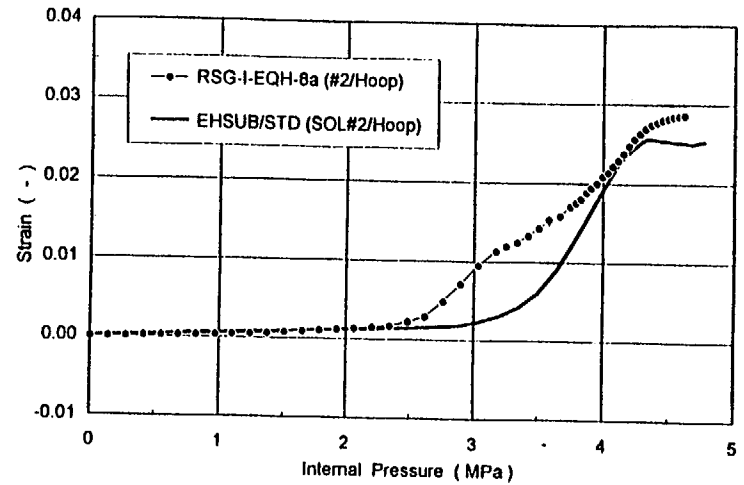


Fig. A-3 Comparison of Strain History (SOL#2 / Hoop Strain)
 [Position : near EQH / 45 deg. / Inside surface]

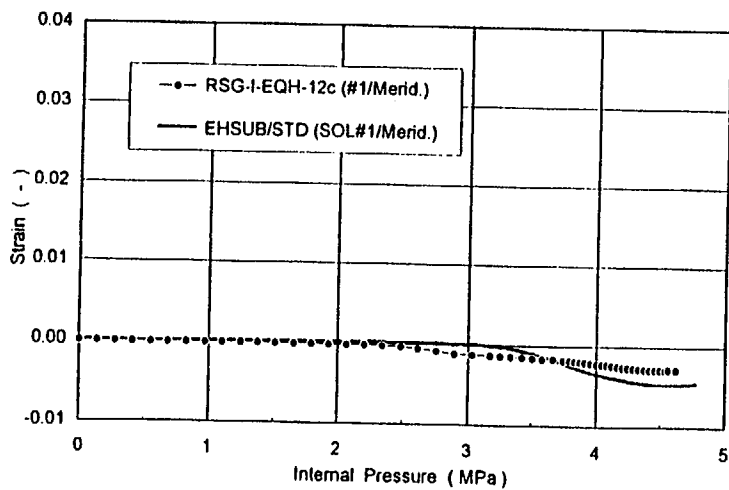


Fig. A-2 Comparison of Strain History (SOL#1 / Meridional Strain)
 [Position : near EQH / 67.5 deg. / Inside surface]

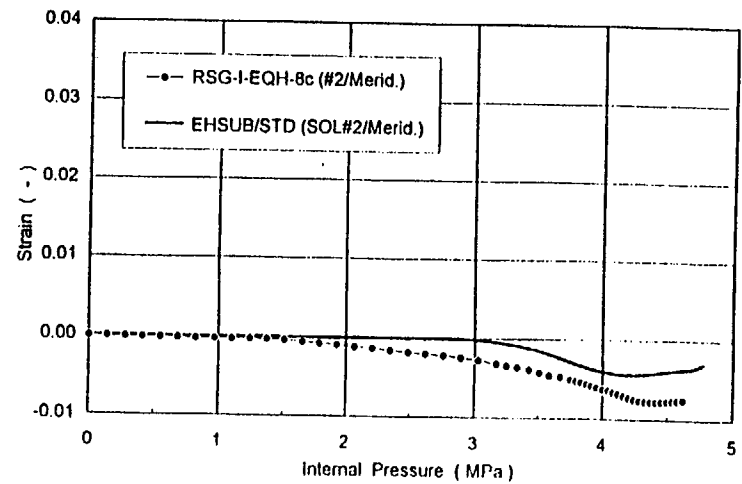


Fig. A-4 Comparison of Strain History (SOL#2 / Meridional Strain)
 [Position : near EQH / 45 deg. / Inside surface]

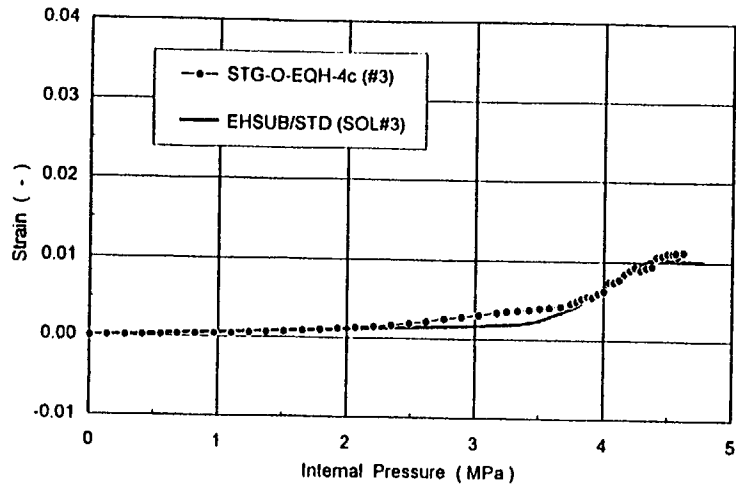


Fig. A-5 Comparison of Strain History (SOL#3 / Meridional Strain)
[Position : near EQH / 0 deg. / Outside surface]

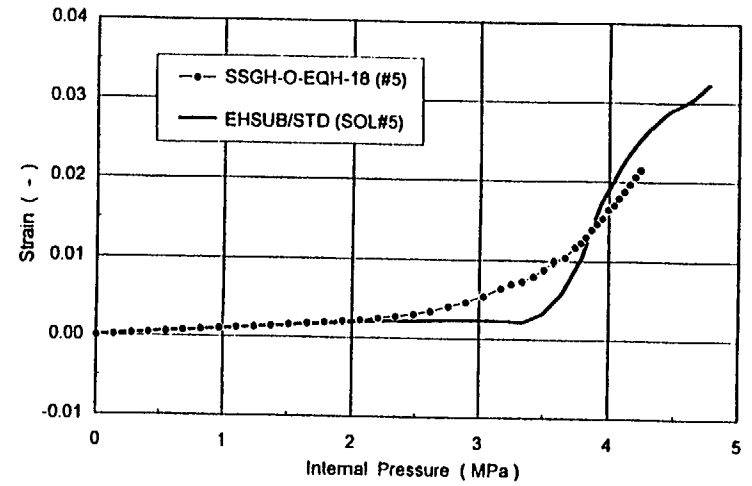


Fig. A-7 Comparison of Strain History (SOL#5 / Hoop Strain)
[Position : EQH / 90 deg. / Outside surface]

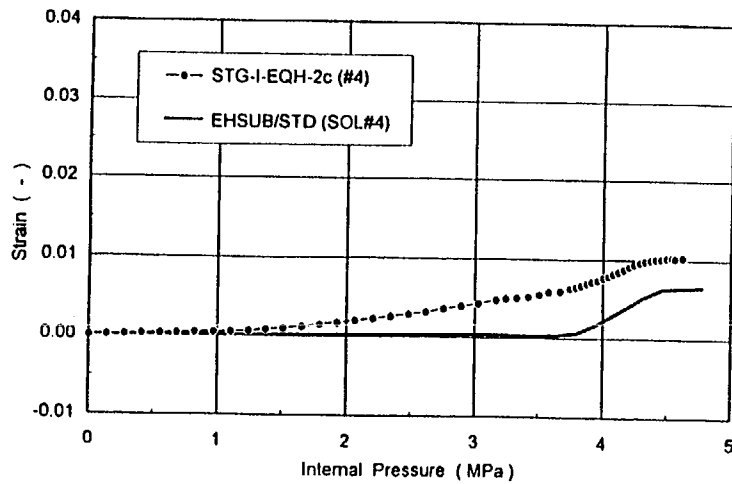


Fig. A-6 Comparison of Strain History (SOL#4 / Meridional Strain)
[Position : near EQH / 0 deg. / Inside surface]

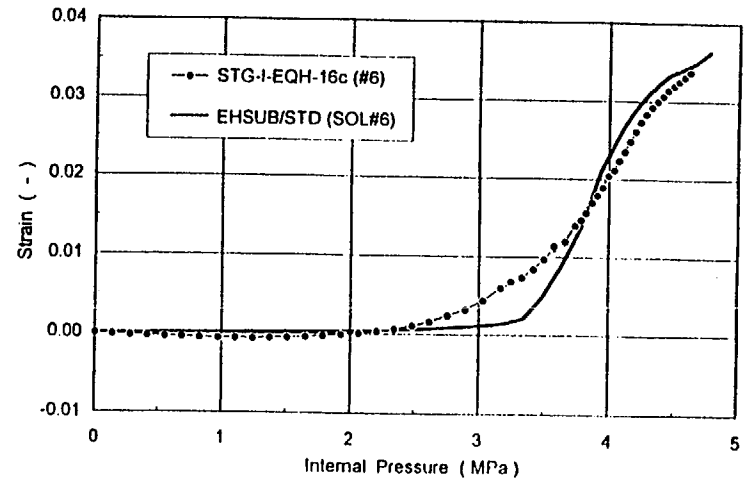


Fig. A-8 Comparison of Strain History (SOL#6 / Hoop Strain)
[Position : EQH / 90 deg. / Inside surface]

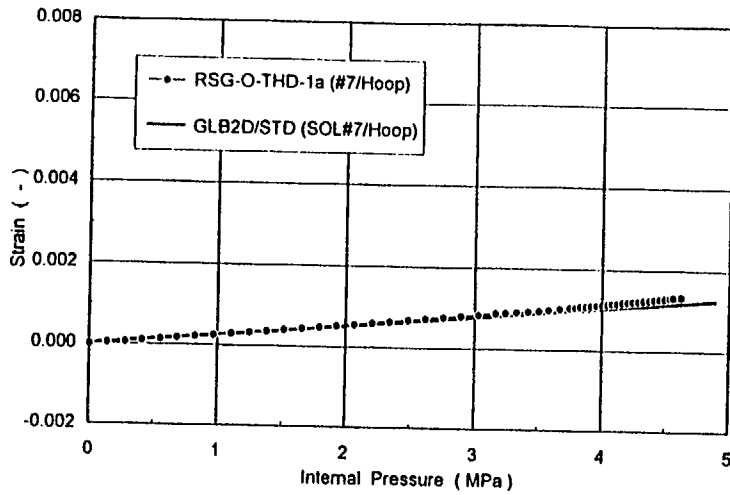


Fig. A-9 Comparison of Strain History (SOL#7 / Hoop Strain)
[Position : apex of THD / Outside surface]

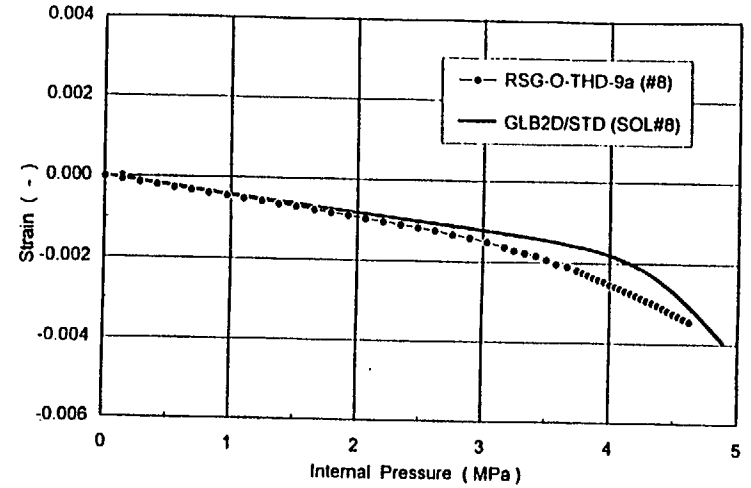


Fig. A-11 Comparison of Strain History (SOL#8 / Hoop Strain)
[Position : near THD min. radius / Outside surface]

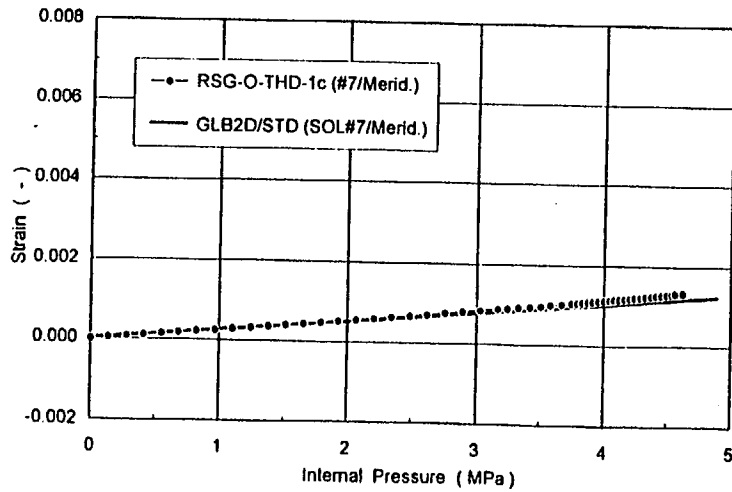


Fig. A-10 Comparison of Strain History (SOL#7 / Meridional Strain)
[Position : apex of THD / Outside surface]

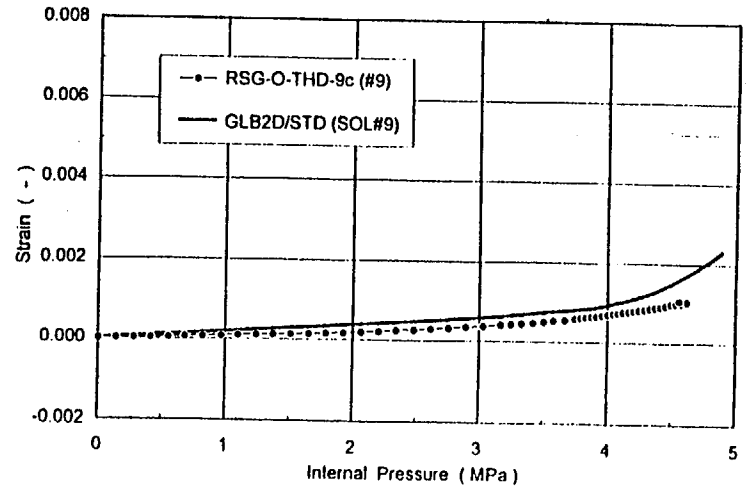


Fig. A-12 Comparison of Strain History (SOL#8 / Meridional Strain)
[Position : near THD min. radius / Outside surface]

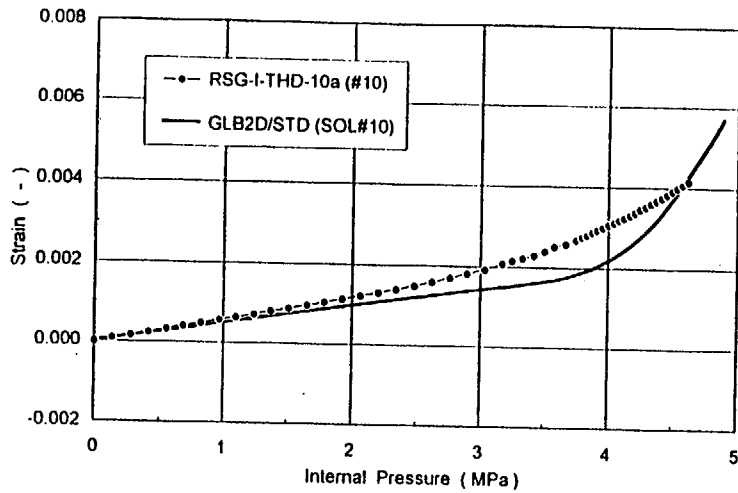


Fig. A-13 Comparison of Strain History (SOL#10 / Meridional Strain)
[Position : near THD mln. radius / Inside surface]

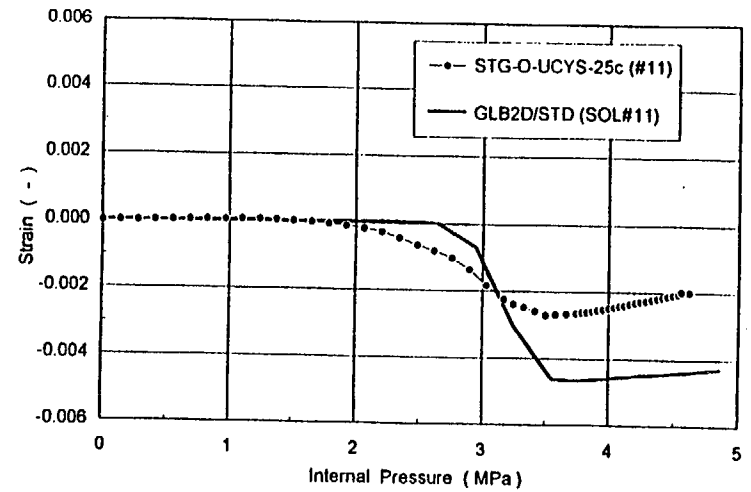


Fig. A-14 Comparison of Strain History (SOL#11 / Meridional Strain)
[Position : just below Top Flange / 0 deg. / Outside surface]

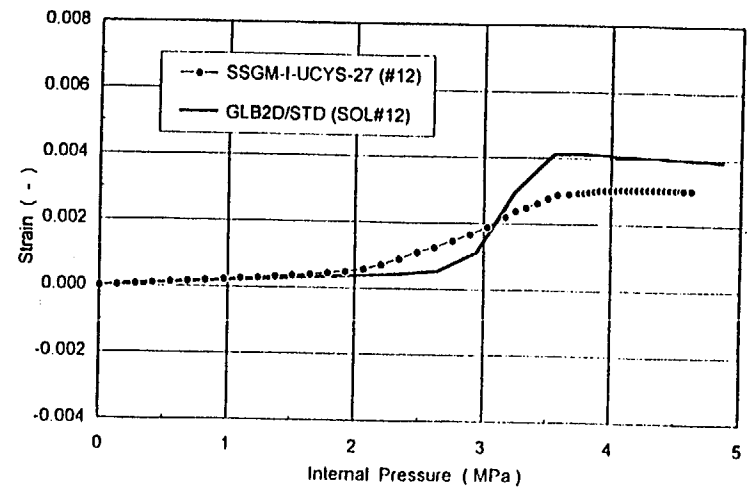


Fig. A-15 Comparison of Strain History (SOL#12 / Meridional Strain)
[Position : just below Top Flange / 0 deg / Inside surface]

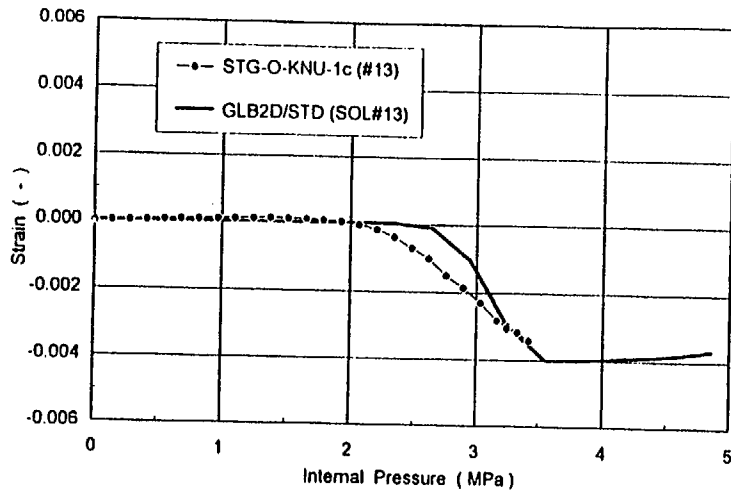


Fig. A-16 Comparison of Strain History (SOL#13 / Meridional Strain)
 [Position : just below KNU / 0 deg. / Outside surface]

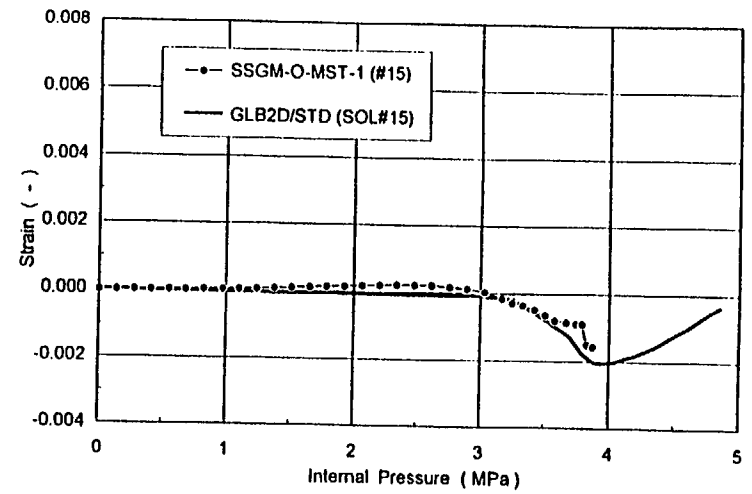


Fig. A-18 Comparison of Strain History (SOL#15 / Meridional Strain)
 [Position : just above MST / 0 deg. / Outside surface]

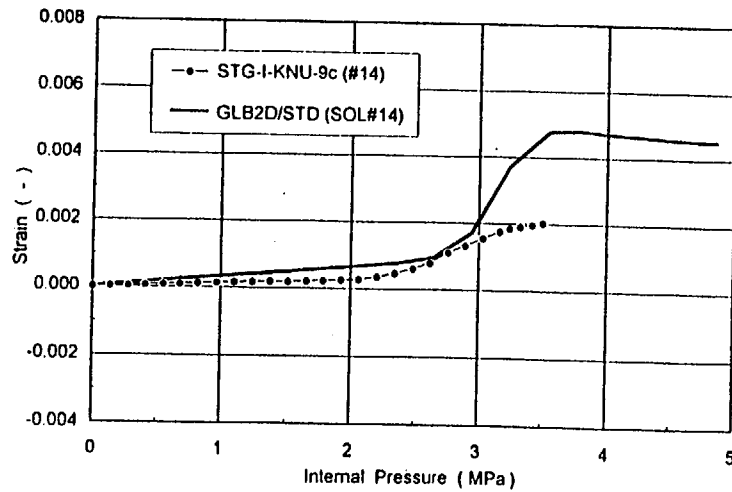


Fig. A-17 Comparison of Strain History (SOL#14 / Meridional Strain)
 [Position : just below KNU / 0 deg. / Inside surface]

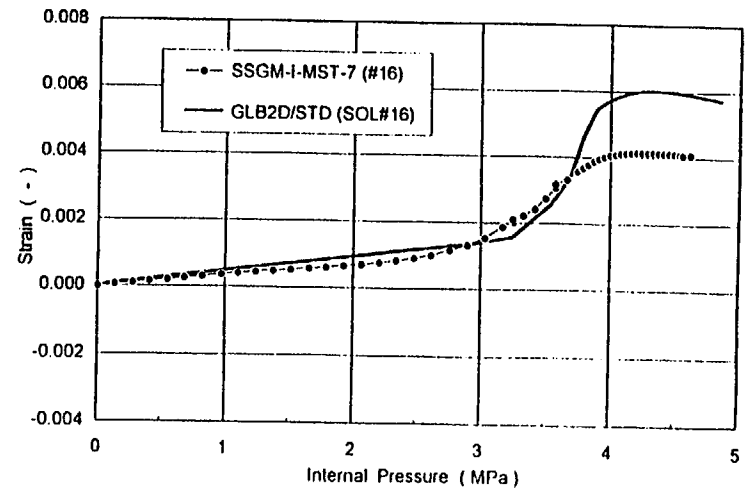


Fig. A-19 Comparison of Strain History (SOL#16 / Meridional Strain)
 [Position : just above MST / 0 deg. / Inside surface]

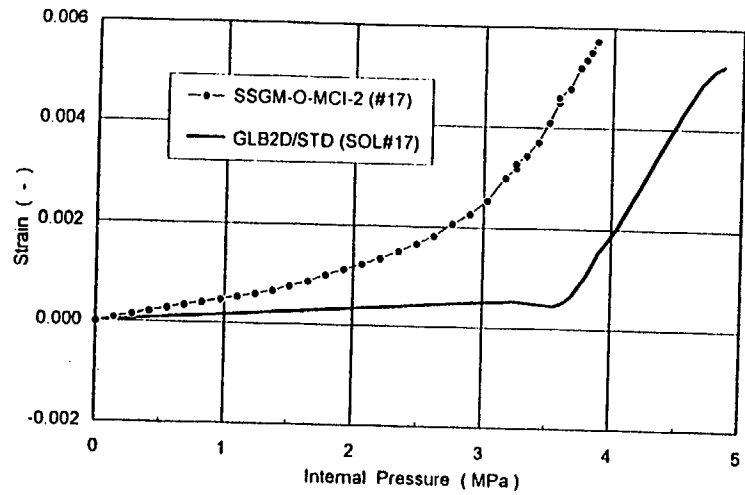


Fig. A-20 Comparison of Strain History (SOL#17 / Meridional Strain)
 [Position : just above MCI / 0 deg. / Outside surface]

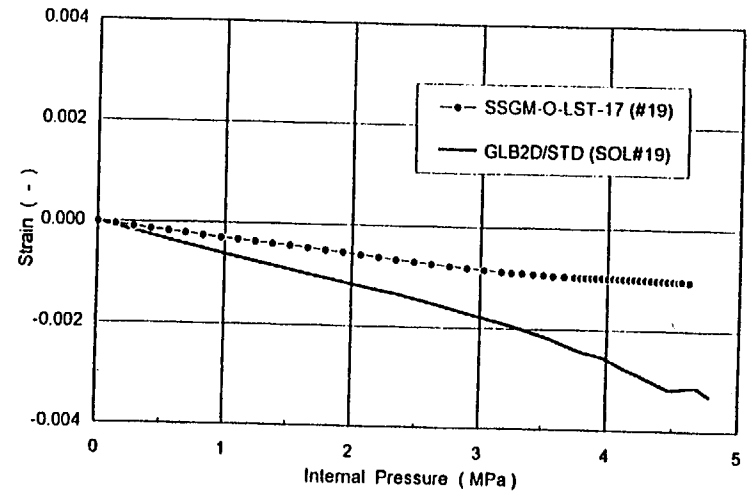


Fig. A-22 Comparison of Strain History (SOL#19 / Meridional Strain)
 [Position : just below LST / 0 deg. / Outside surface]

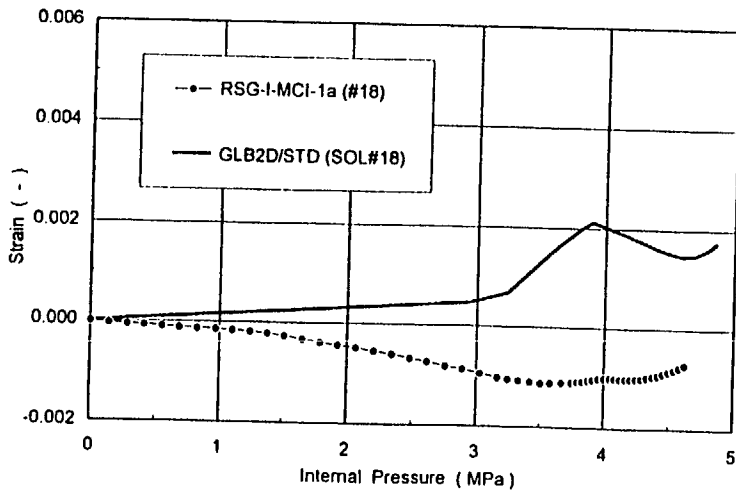


Fig. A-21 Comparison of Strain History (SOL#18 / Meridional Strain)
 [Position : just above MCI / 0 deg. / Inside surface]

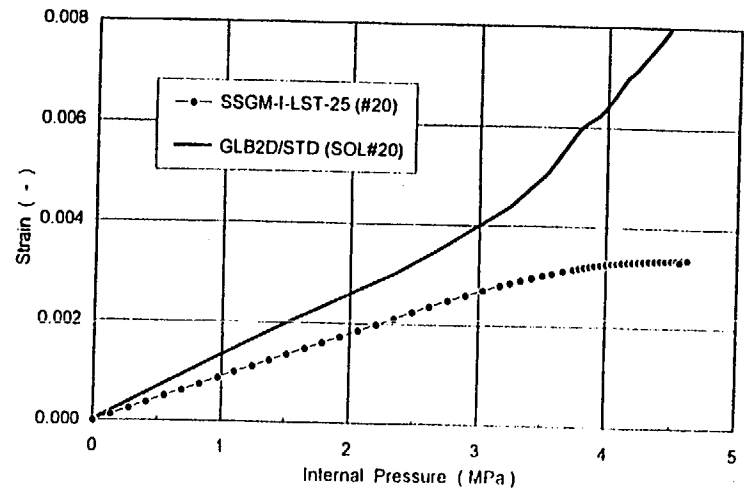


Fig. A-23 Comparison of Strain History (SOL#20 / Meridional Strain)
 [Position : just below LST / 0 deg. / Inside surface]

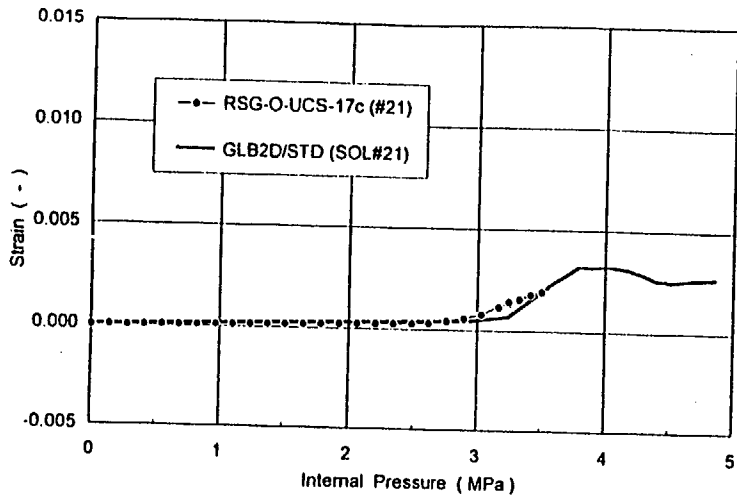


Fig. A-24 Comparison of Strain History (SOL#21 / Meridional Strain)
 [Position : midheight of UCS / 45 deg. / Outside surface]

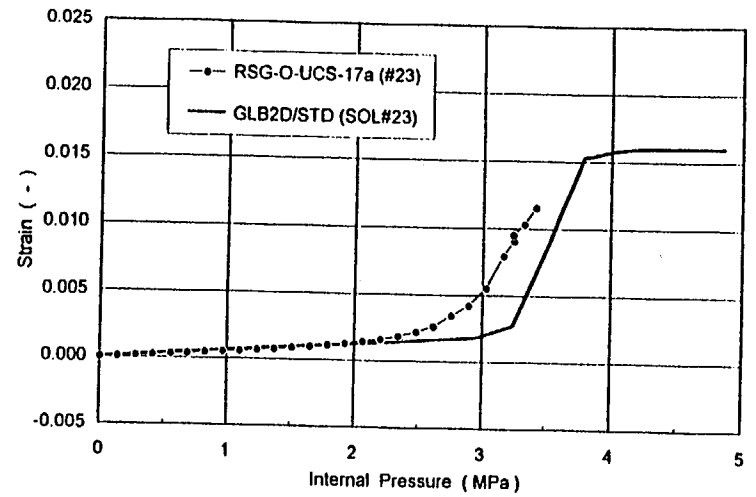


Fig. A-26 Comparison of Strain History (SOL#23 / Hoop Strain)
 [Position : midheight of UCS / 45 deg. / Outside surface]

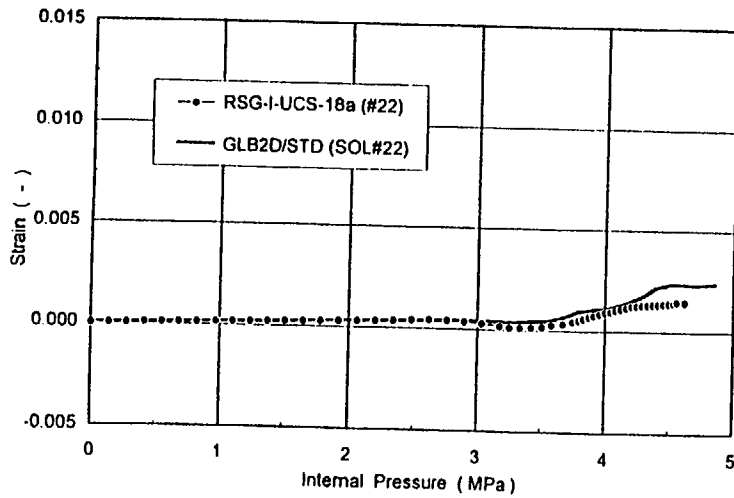


Fig. A-25 Comparison of Strain History (SOL#22 / Meridional Strain)
 [Position : midheight of UCS / 45 deg. / Inside surface]

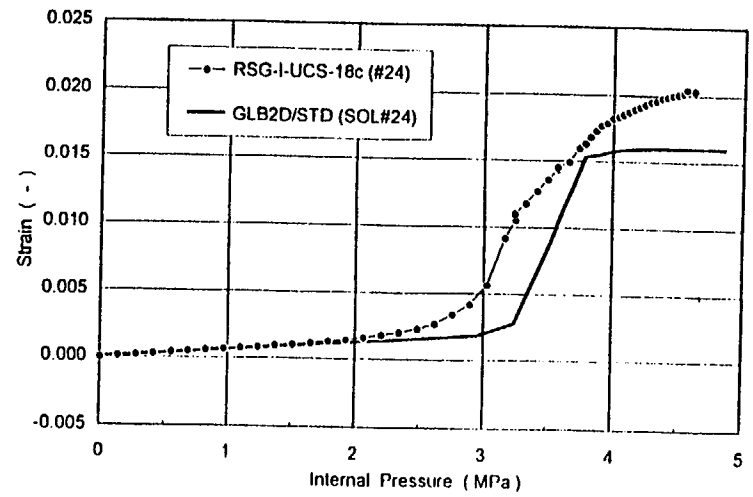


Fig. A-27 Comparison of Strain History (SOL#24 / Hoop Strain)
 [Position : midheight of UCS / 45 deg. / Inside surface]

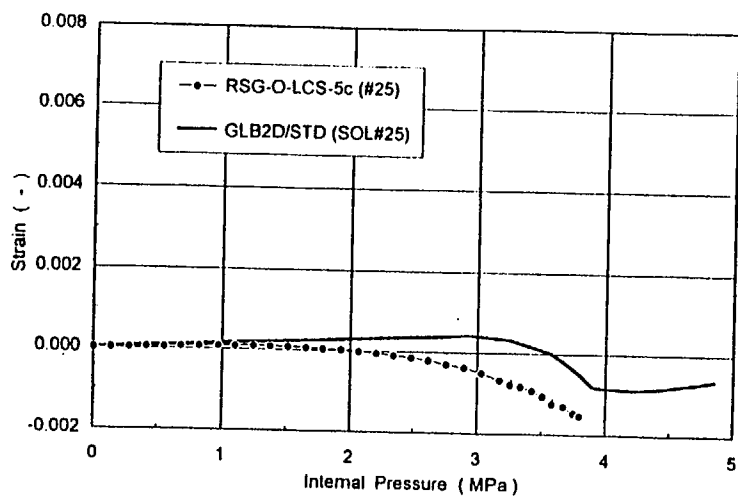


Fig. A-28 Comparison of Strain History (SOL#25 / Meridional Strain)
[Position : above LCS / 45 deg. / Outside surface]

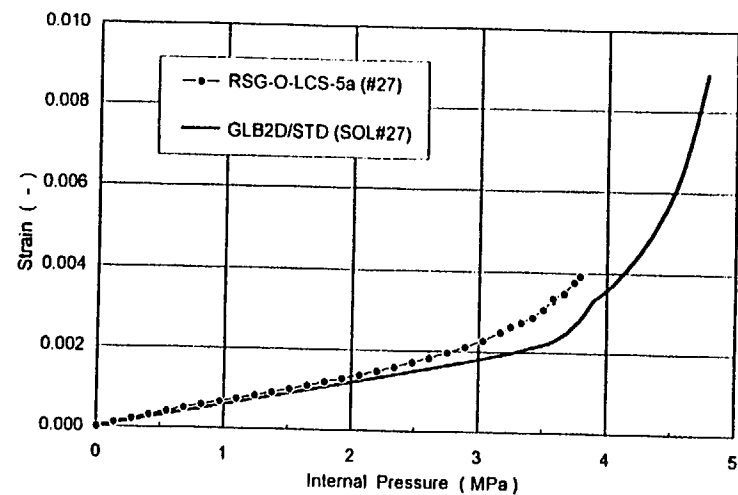


Fig. A-30 Comparison of Strain History (SOL#27 / Hoop Strain)
[Position : above LCS / 45 deg. / Outside surface]

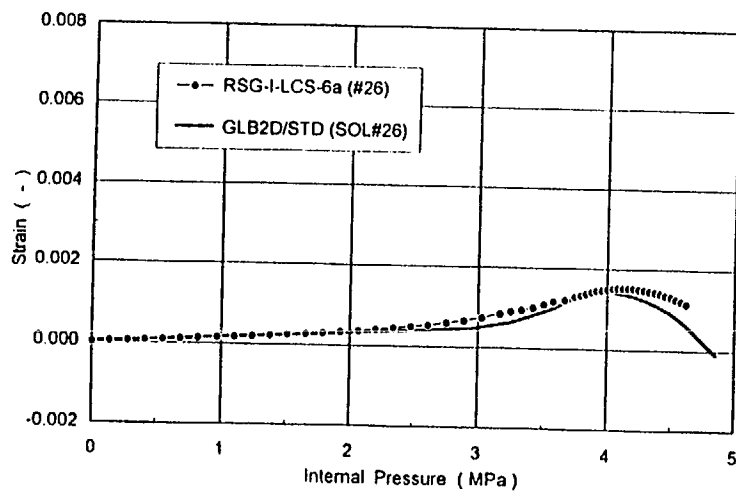


Fig. A-29 Comparison of Strain History (SOL#26 / Meridional Strain)
[Position : above LCS / 45 deg. / Inside surface]

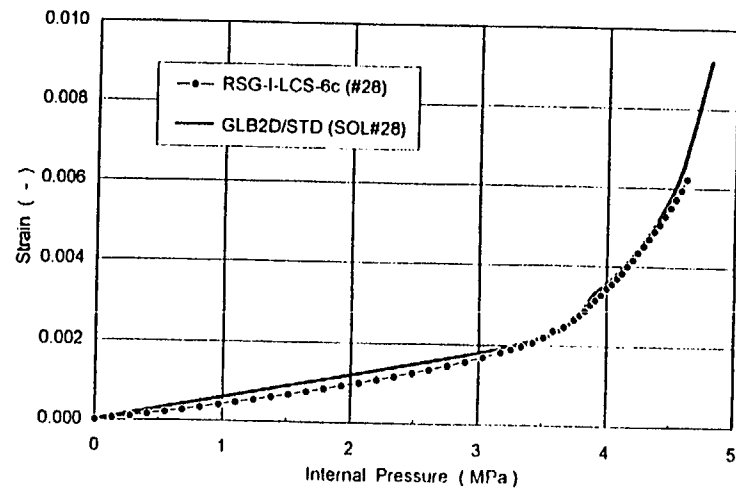


Fig. A-31 Comparison of Strain History (SOL#28 / Hoop Strain)
[Position : above LCS / 45 deg. / Inside surface]

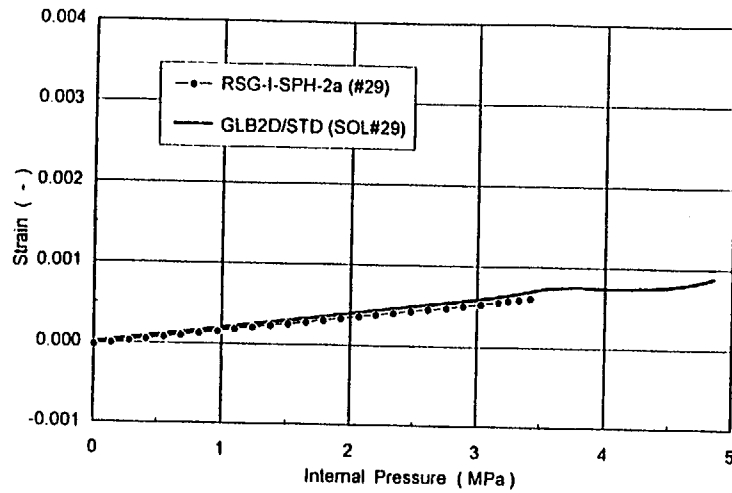


Fig. A-32 Comparison of Strain History (SOL#29 / Meridional Strain)
 [Position : midheight of SPH / 45 deg. / Inside surface]

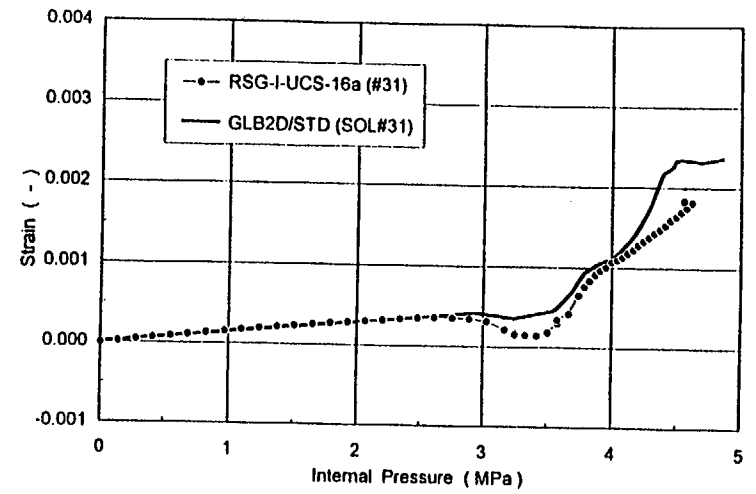


Fig. A-34 Comparison of Strain History (SOL#31 / Meridional Strain)
 [Position : midheight of UCS / 270 deg. / Inside surface]

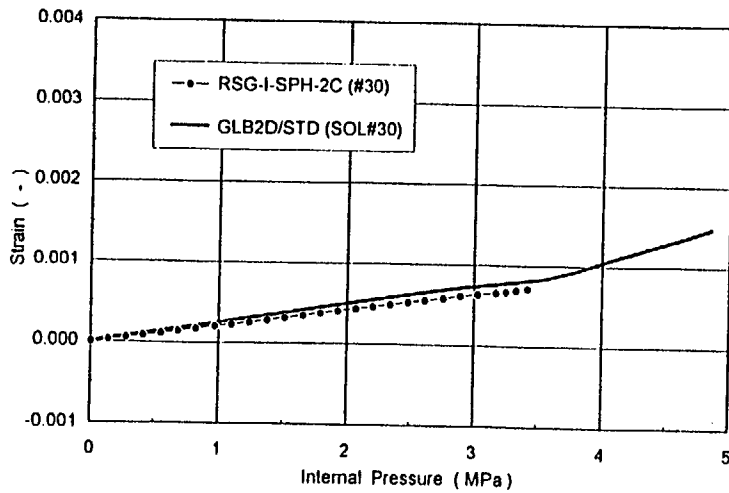


Fig. A-33 Comparison of Strain History (SOL#30 / Hoop Strain)
 [Position : midheight of SPH / 45 deg. / Inside surface]

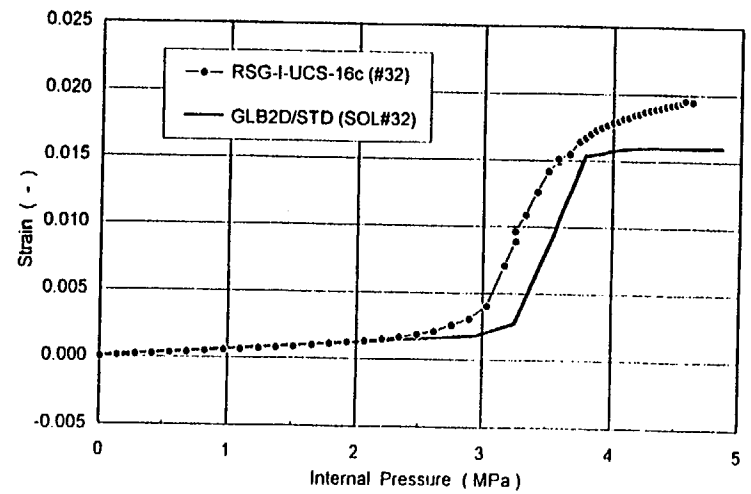


Fig. A-35 Comparison of Strain History (SOL#32 / Hoop Strain)
 [Position : midheight of UCS / 270 deg. / Inside surface]

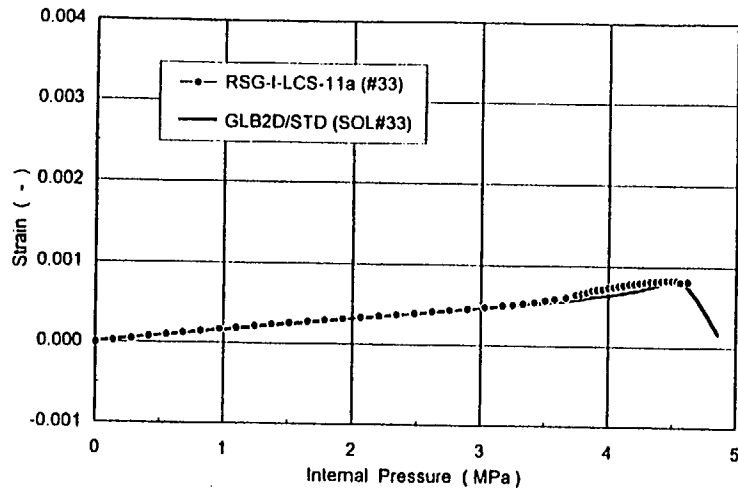


Fig. A-36 Comparison of Strain History (SOL#33 / Meridional Strain)
[Position : midheight of LCS / 270 deg. / Inside surface]

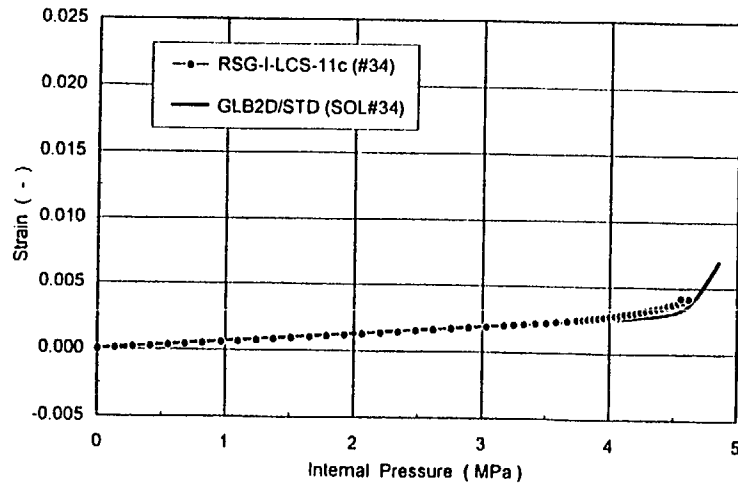


Fig. A-37 Comparison of Strain History (SOL#34 / Hoop Strain)
[Position : midheight of LCS / 270 deg. / Inside surface]

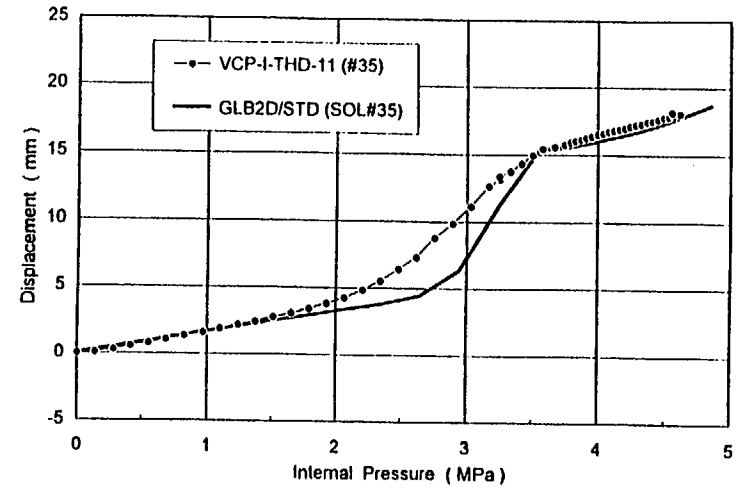


Fig. A-38 Comparison of Displacement History (SOL#35 / Vertical Displacement)
[Position : apex of THD / Inside surface]

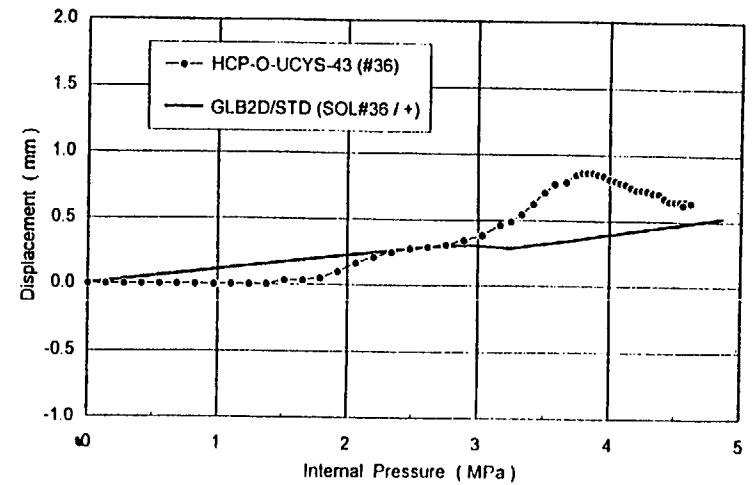


Fig. A-39 Comparison of Displacement History (SOL#36 / Horizontal Displacement)
[Position : just above Top Flange / Outside surface]

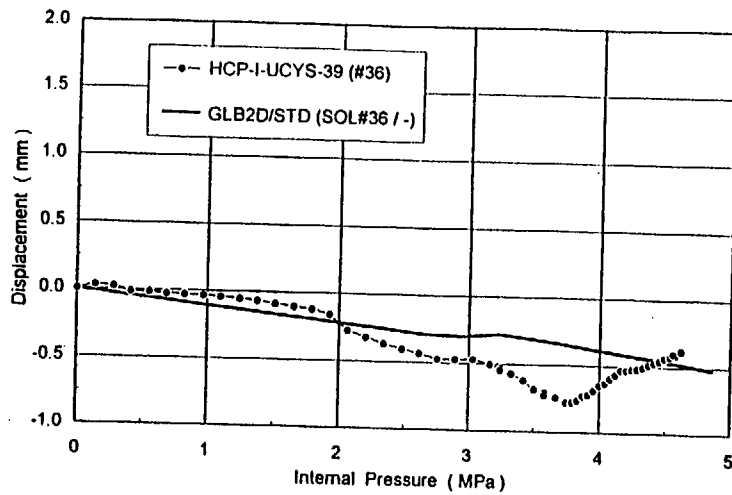


Fig. A-40 Comparison of Displacement History (SOL#36 / Horizontal Displacement)
 [Position : just above Top Flange / Inside surface]

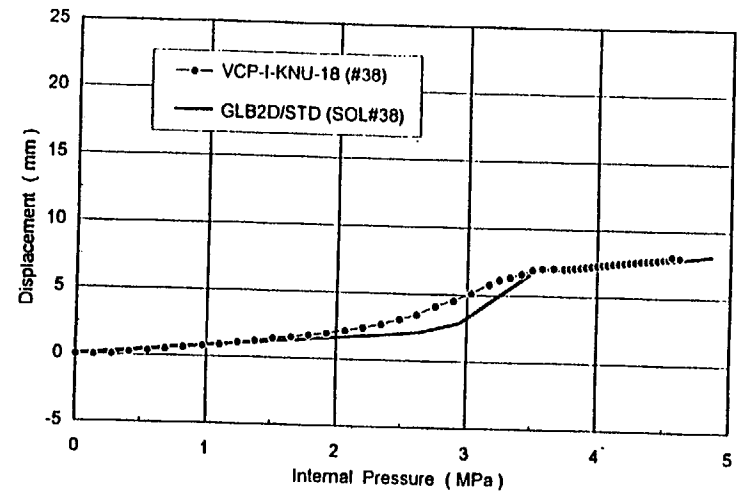


Fig. A-42 Comparison of Displacement History (SOL#38 / Vertical Displacement)
 [Position : just below KNU / Inside surface]

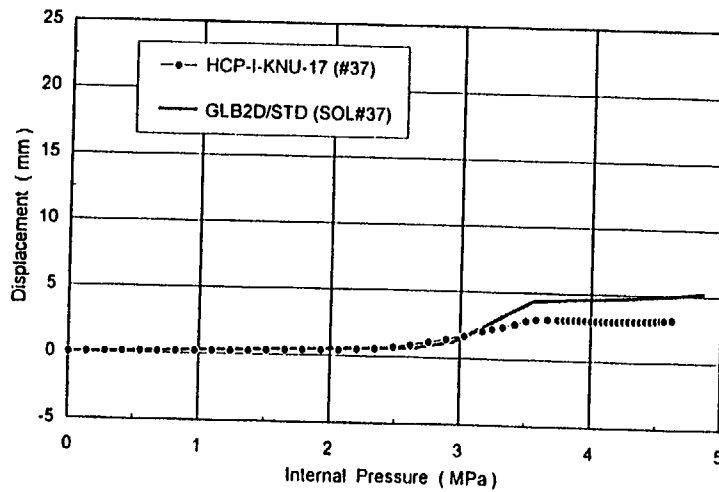


Fig. A-41 Comparison of Displacement History (SOL#37 / Horizontal Displacement)
 [Position : just below KNU / Inside surface]

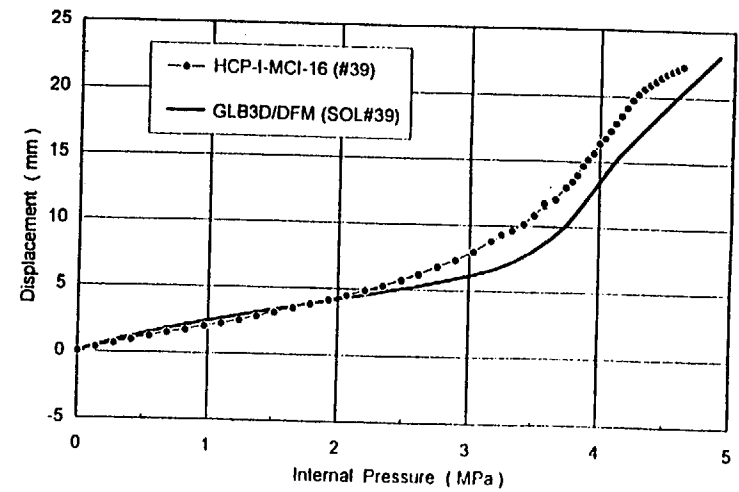


Fig. A-43 Comparison of Displacement History (SOL#39 / Horizontal Displacement)
 [Position : center of Equipment Hatch Cover / Inside surface]

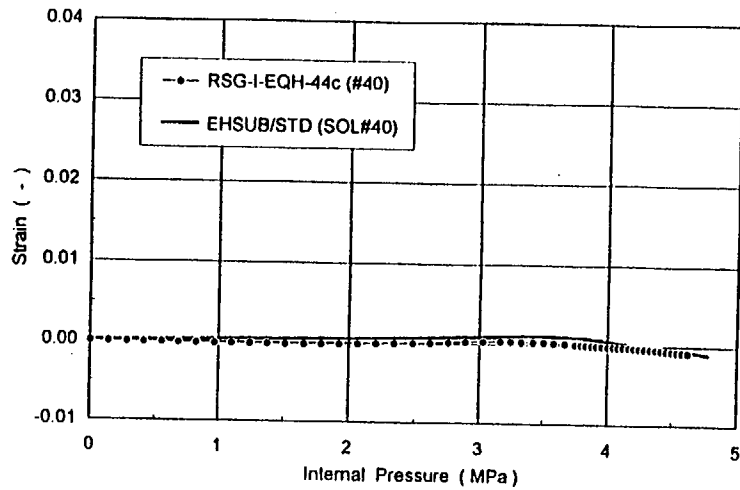


Fig. A-44 Comparison of Strain History (SOL#40 / Meridional Strain)
[Position : near EQH / Inside surface]

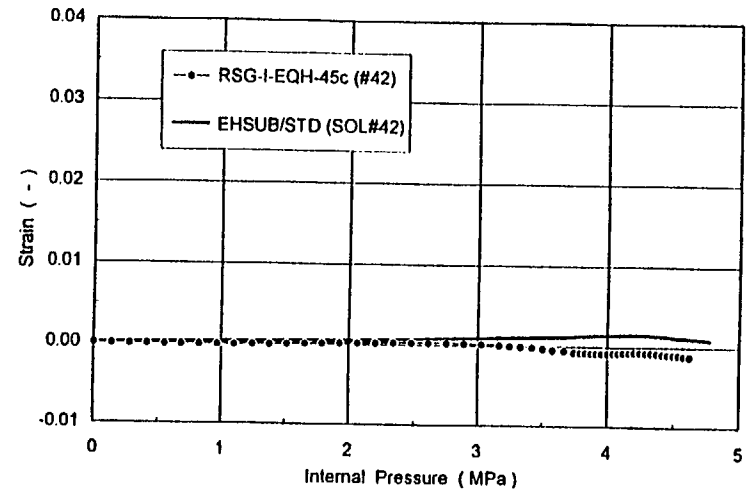


Fig. A-46 Comparison of Strain History (SOL#42 / Meridional Strain)
[Position : near EQH / Inside surface]

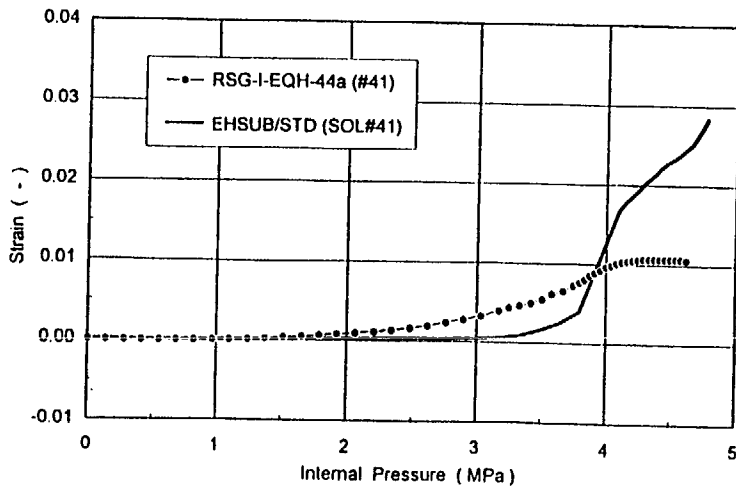


Fig. A-45 Comparison of Strain History (SOL#41 / Hoop Strain)
[Position : near EQH / Inside surface]

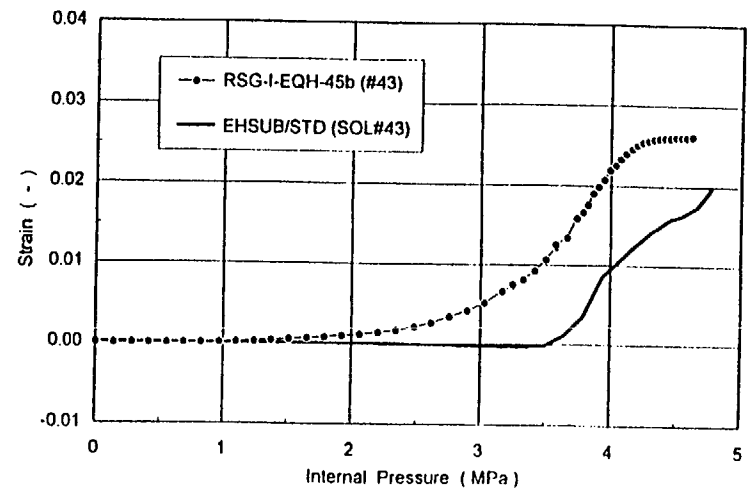


Fig. A-47 Comparison of Strain History (SOL#43 / Hoop Strain)
[Position : near EQH / Inside surface]

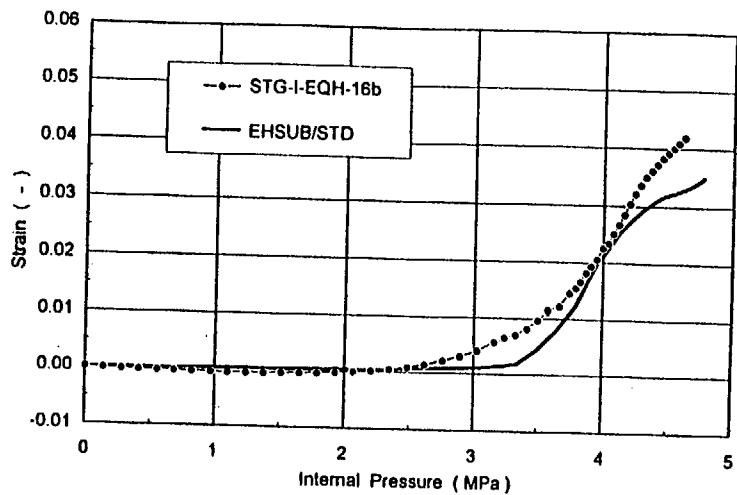


Fig. A-48 Comparison of Strain History (STG-I-EQH-16b / Hoop Strain)
 [Position : near EQH / 91.5 deg. / Inside surface]

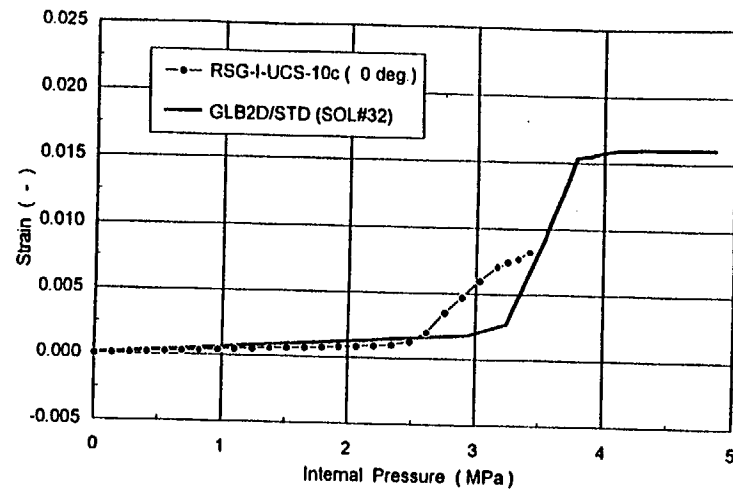


Fig. A-50 Comparison of Strain History (RSG-I-UCS-10c / Hoop Strain)
 [Position : midheight of UCS / 0 deg. / Inside surface]

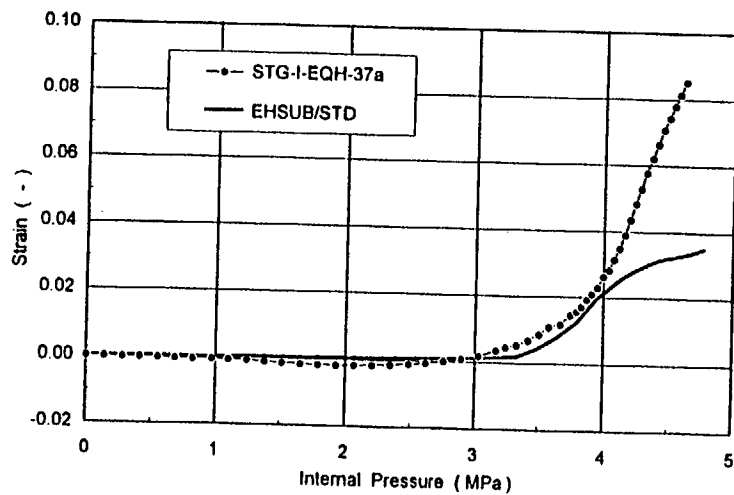


Fig. A-49 Comparison of Strain History (STG-I-EQH-37a / Hoop Strain)
 [Position : near EQH / 268 deg. / Inside surface]

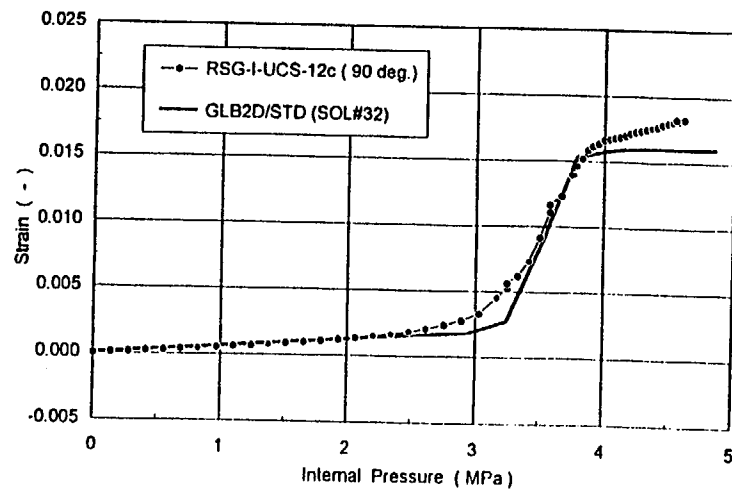


Fig. A-51 Comparison of Strain History (RSG-I-UCS-12c / Hoop Strain)
 [Position : midheight of UCS / 90 deg. / Inside surface]

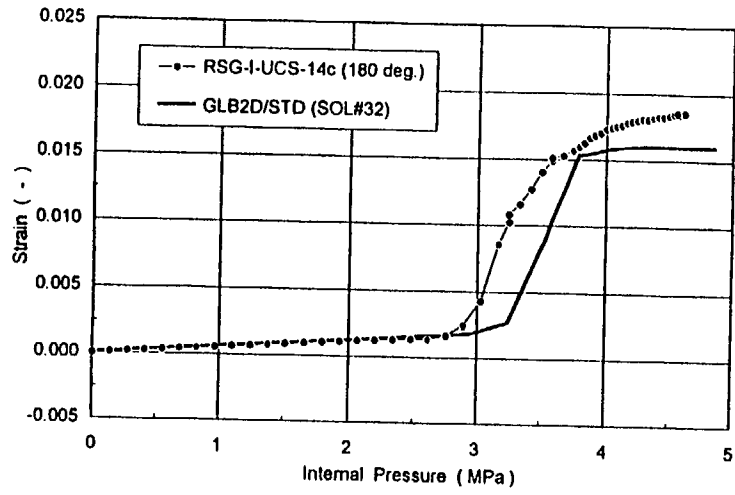


Fig. A-52 Comparison of Strain History (RSG-I-UCS-14c / Hoop Strain)
[Position : midheight of UCS / 180 deg. / Inside surface]

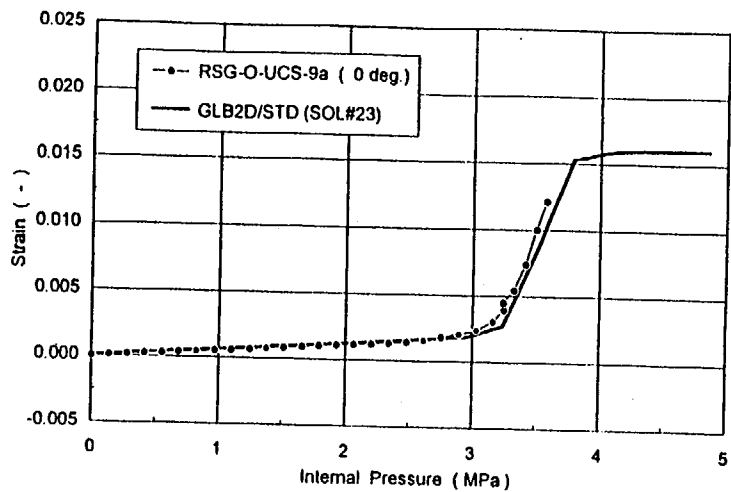


Fig. A-53 Comparison of Strain History (RSG-O-UCS-9a / Hoop Strain)
 [Position : midheight of UCS / 0 deg. / Outside surface]

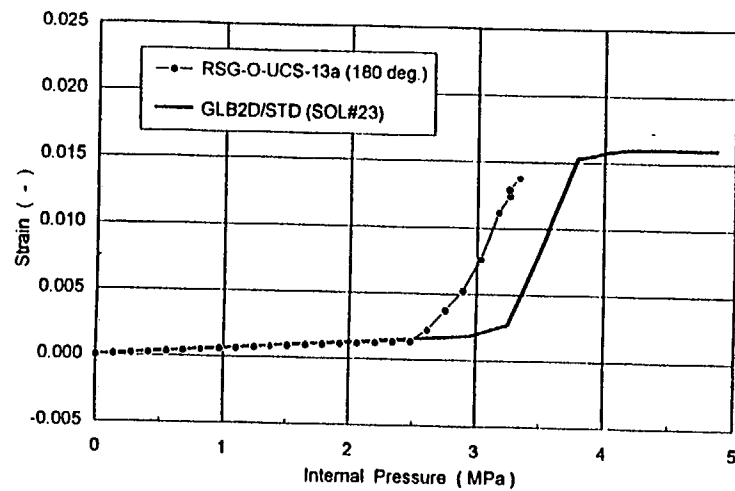


Fig. A-55 Comparison of Strain History (RSG-O-UCS-13a / Hoop Strain)
 [Position : midheight of UCS / 180 deg. / Outside surface]

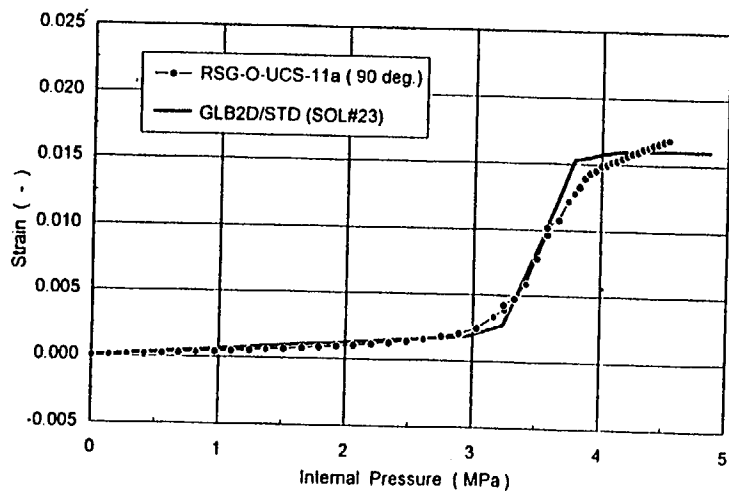


Fig. A-54 Comparison of Strain History (RSG-O-UCS-11a / Hoop Strain)
 [Position : midheight of UCS / 90 deg. / Outside surface]

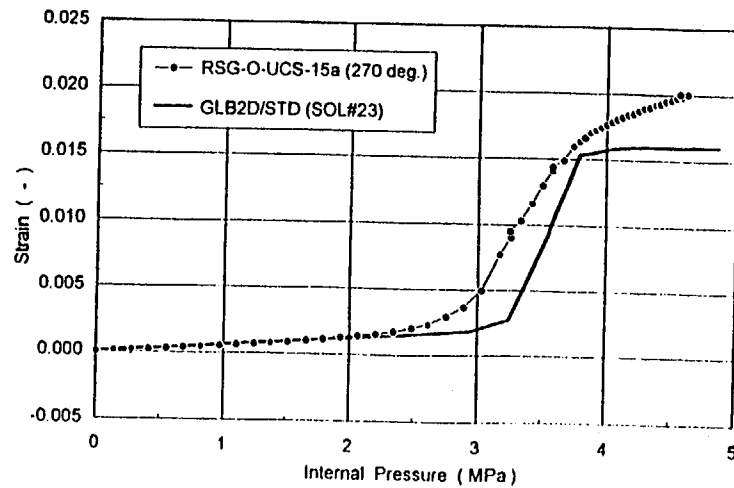


Fig. A-56 Comparison of Strain History (RSG-O-UCS-15a / Hoop Strain)
 [Position : midheight of UCS / 270 deg. / Outside surface]

Appendix B-7

Sandia National Laboratories (SNL)

U.S.

Sandia National Laboratories

**Round Robin Posttest Analysis
of the Steel Containment Vessel Model**

by:

J. S. Ludwigsen and V. K. Luk

International Nuclear Safety Department 6304, MS 0744

Contents

1. Introduction.....	B-279
2. Comparison of Pretest Analysis Results with SCV High-Pressure Test Data	B-279
2.1 Global Model Response	B-279
2.2 Strain Concentration Near the Equipment Hatch Reinforcement Plate.....	B-279
3. Material Modeling.....	B-280
3.1 Modeling of the Material Properties.....	B-280
3.2 Strength Reduction for SPV490 Heat-Affected Zone (HAZ) Material.....	B-281
4. Finite Element Analysis Models.....	B-284
5. Comparison of Pretest and Posttest Analysis Results with SCV High-Pressure Test Data	B-288
5.1 Global Results	B-288
5.2 Local Equipment Hatch Behavior	B-290
5.3 Discussions of the Results at the Standard Output Locations.....	B-291
5.4 Failure Considerations	B-292
6. Summary.....	B-292
7. References.....	B-293
Appendix A: Comparison Plots of Pretest and Posttest Analysis Results with SCV High-Pressure Test Data	B-294

1. INTRODUCTION

This report describes the posttest structural analyses of a scale model of a steel containment vessel (SCV) that was tested at Sandia National Laboratories (SNL) on December 11–12, 1996. Prior to the SCV high-pressure test, a pretest analysis of the SCV model was performed to predict model response to loads beyond the design basis conditions [1]. A portion of the pretest analysis results was included in the SCV Round Robin Pretest Analysis Report [2] at the 43 standard output locations.

The posttest analysis effort started with a detailed comparison of the pretest analysis results with the high-pressure test data. Initially the focus was on the free-field response of the SCV model and at model locations of high-strain concentrations including the two tears. This comparison identified the areas where the pretest analysis did not match well with the measured data. Based on these findings, a guide for changes to the posttest analysis effort was determined. This report summarizes the changes between the pretest and the posttest analyses and discusses their effect on the predicted behavior.

2. COMPARISON OF PRETEST ANALYSIS RESULTS WITH SCV HIGH-PRESSURE TEST DATA

The Round Robin portion of the pretest analysis results was included in Appendix E-7 of the SCV Round Robin Pretest Analysis Report [2]. As a first step, the pretest analysis results at the 43 standard output locations were compared with the test data to provide a guide for the posttest effort. In this section, the comparisons focus on two areas of SCV model responses: the global behavior of the entire model and the local behavior near the equipment hatch.

2.1 Global Model Response

In general, the global behavior of the SCV model behaves in an axisymmetric manner in the free-field areas away from the equipment hatch. Such free-field behavior is represented by the hoop strain response shown at Standard Output Location #24, where a rosette strain gage, RSG-I-UCS-18, was installed on the inside surface of the SCV model. As indicated SNL in Figure A.24 in Appendix A, a significant discrepancy between the pretest analysis results and the test data develops at pressure levels above 2 MPa. Test data indicate that local yielding started at 2.35 MPa, but the pretest prediction was for yielding to occur at 3.2 MPa. Above 3.2 MPa the strain versus pressure for the test data and the pretest prediction stay parallel and do not come together. This suggests that factors other than residual stresses were involved in the mismatch between the prediction and the measured data. These factors will be addressed in Sections 3 and 4 of this report.

2.2 Strain Concentration Near the Equipment Hatch Reinforcement Plate

The most complex detail of the SCV model was the equipment hatch and its thickened reinforcement plate. It is near this detail that the highest strains were recorded and where the failure occurred. Standard Output Location #45 near the equipment hatch measured strains as high as 9%. The pretest analyses predicted high strains near the equipment hatch area, but they failed to predict the mechanism that led to the actual failure. The failure occurred in the heat-affected zone (HAZ) near the weld between the reinforcement plate

and the 9mm steel below the material change interface. Both of the steels that were welded together were SPV490 steel, which is a high-strength steel that has had specific heat treatment during its manufacturing. The welding process resulted in a HAZ that had lower ultimate strength properties than the parent material [3]. This weakened zone ultimately lead to a significant strain concentration where the tear that caused failure occurred.

The posttest analysis took the weakened material properties of the SPV490 HAZ into account. Changes to the behavior of the model around the equipment hatch between the pretest analysis and the posttest analysis were significant.

3. MATERIAL MODELING

3.1 Modeling of the Material Properties

The pretest analysis used material models based on coupon tensile test data provided by Hitachi [2]. The measured data from the high-pressure test of the SCV model showed that the majority of the structure experienced low plastic strains, generally less than 2%. The pretest analyses concentrated more on the stress strain relationships in the high-strain (over 20%) regions so that the high strains associated with a failure could accurately be tied to the pressure load on the structure. The higher-strain mechanical properties were emphasized because one of the major goals of the pretest analysis was to try to predict the failure pressure.

To accurately predict high stress versus strain material properties in the pretest analyses, the true stress versus true strain data were used to fit a theoretical hardening curve such as a power law or inverse hyperbolic sine law. This method provided good accuracy at the higher strain values, and more importantly for the pretest analyses, it provided some confidence in the stress-strain relationship at strains past the ultimate load in the coupon test data. Unfortunately, the analytical material models had some error at the lower strains. The analytical-curve-fit models tended to overestimate the strength of the materials at low strains.

In hindsight, this emphasis on high-strain material behavior was not as important as was first thought for two reasons. The first reason, mentioned previously, is because the majority of the structure experienced strains below 2%. Only a few areas on the model experienced strains above this level. The second reason is that a finite element mesh of a large structure will not include many of the structural features that can lead to high-strain conditions. The areas that do exhibit strains beyond maximum stress levels are usually associated with a detail of the structure such as a weld or a subtle change in geometry that is smaller than the average element size. This means that the increased strains associated with these features will not be predicted or averaged over the element with the analytical model. It would require a very large analysis effort to achieve the level of detail needed to model such small features in a large, complex structure such as the SCV.

For the posttest analysis, a much simpler approach was used to model the material behavior. The material model for the plastic behavior of the materials used in the posttest analysis was simply the lower envelope of the plotted curves. The elastic portion of the stress-strain curves assumed a standard value for the Young's modulus. Figure 3.1 shows the coupon results and the stress strain curve used in the analysis for the 8.5 mm SGV480

SGV480 8.5mm

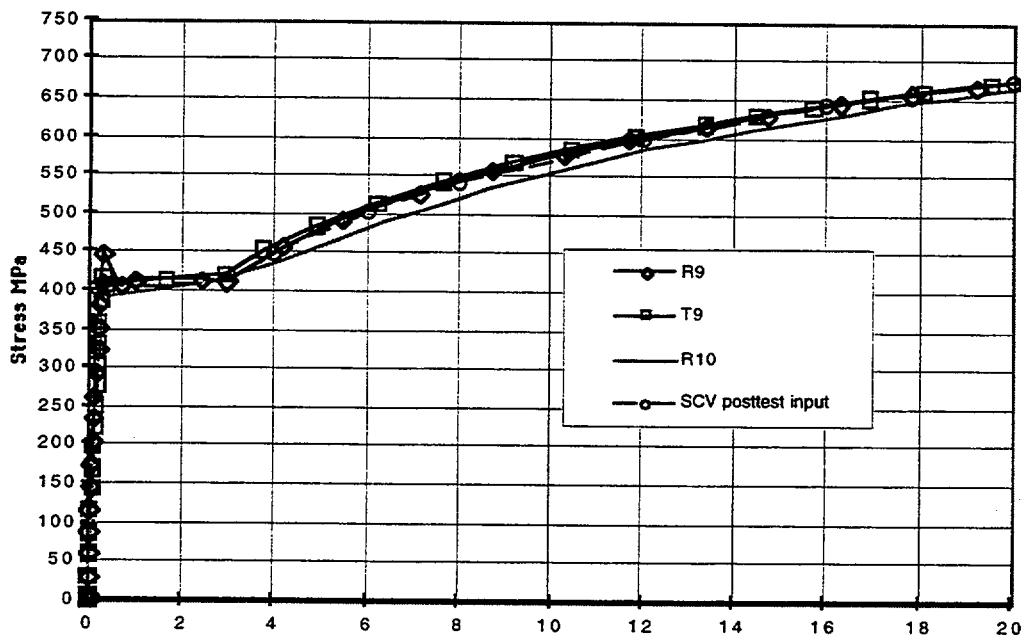


Figure 3.1. Coupon test results and the stress-strain curve used in the analysis for the 8.5mm SGV480 material.

material. The curve used in the analysis is difficult to see because it overlaps the other curves. The data from coupon test R10 was ignored because it varied significantly from the other three coupon tests.

Figure 3.2 shows the coupon test results for the 9 mm SPV490 material and the assumed stress-strain curve used in the analysis. Note the difference in the rolled direction properties and the transverse direction properties. It is not known in what orientation the plates in the SCV model were placed during the manufacturing process.

The other materials used in the SCV model were all similar to the above examples. The choice of using the lower envelope of the curves was made to be conservative with regard to material strength. Even with the use of the lower envelope, factors such as residual stresses in the as-built model and variations in material properties throughout the plate are not reflected in the material model curves.

3.2 Strength Reduction for SPV490 Heat-Affected Zone (HAZ) Material

The material properties of both the SGV480 and SPV490 material experience changes when they are welded. The SGV480 material, which is a mild steel, is not significantly affected with respect to mechanical properties during the welding process. Posttest analysis of the material in the SGV480 heat-affected zone (HAZ) showed that the ultimate strength of the material essentially remained unchanged due to the welding process [3]. The HAZ is the parent material right next to the weld that is exposed to high temperatures

SGV490 9mm

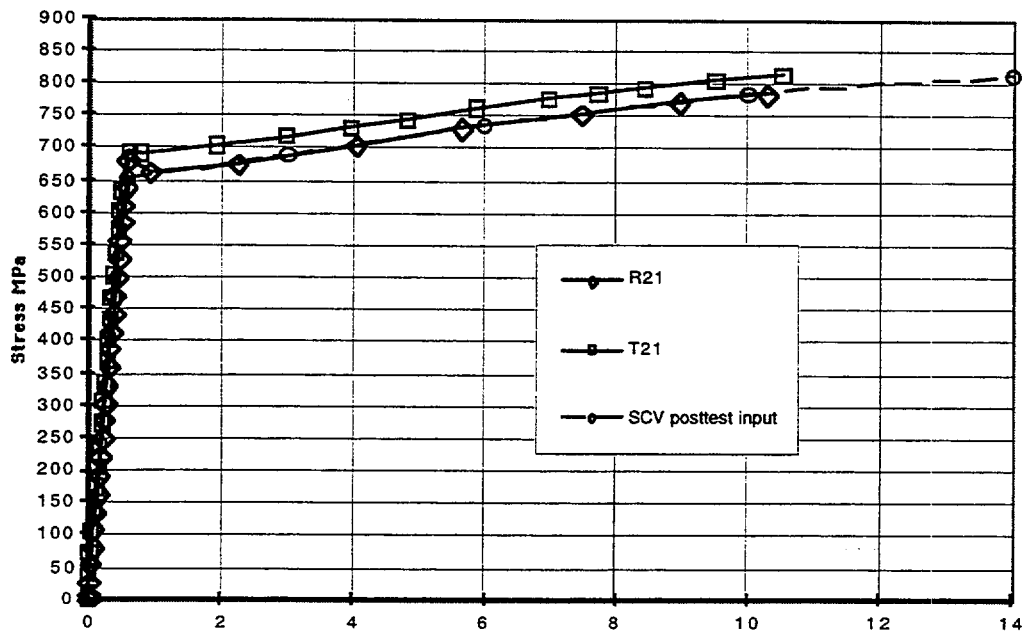


Figure 3.2. Coupon test results and the stress-strain curve used in the analysis for the 9mm SPV490 material.

during the welding process. The new material added in the weld is usually a high-yield-strength material and is not part of the HAZ material. The SGV480 material did not have any specialized heat treatment during its manufacture, so the heating and cooling from the welding process will have little effect on the mechanical properties of the material. The SPV490 material, a higher strength material, did receive specialized heat treatment during its manufacture. The HAZ for this material had mechanical properties significantly less than those of the parent material [3].

To determine the virgin material stress-strain relationship, three tensile coupons were machined from the SPV490 virgin plate that was sent with the SCV model by Hitachi in March 1995. Uniaxial tensile tests were performed on these coupons according to the ASTM specifications. All three tests resulted in virtually identical stress versus strain curves. The calculated true stress versus true strain curve for one of the tests is plotted in Figure 3.3. The Rockwell B hardness numbers were also measured on the specimens machined from the virgin plate to compare with the hardness numbers for the material from the deformed SCV model. These numbers were reported in the SCV Posttest Metallurgical Evaluation Results [3].

The intent of the material testing of SPV490 virgin plate is to obtain a set of uniaxial tensile test data and the Rockwell B hardness numbers from the same specimens. The hardness number for the virgin plate together with the posttest hardness numbers for the HAZ and

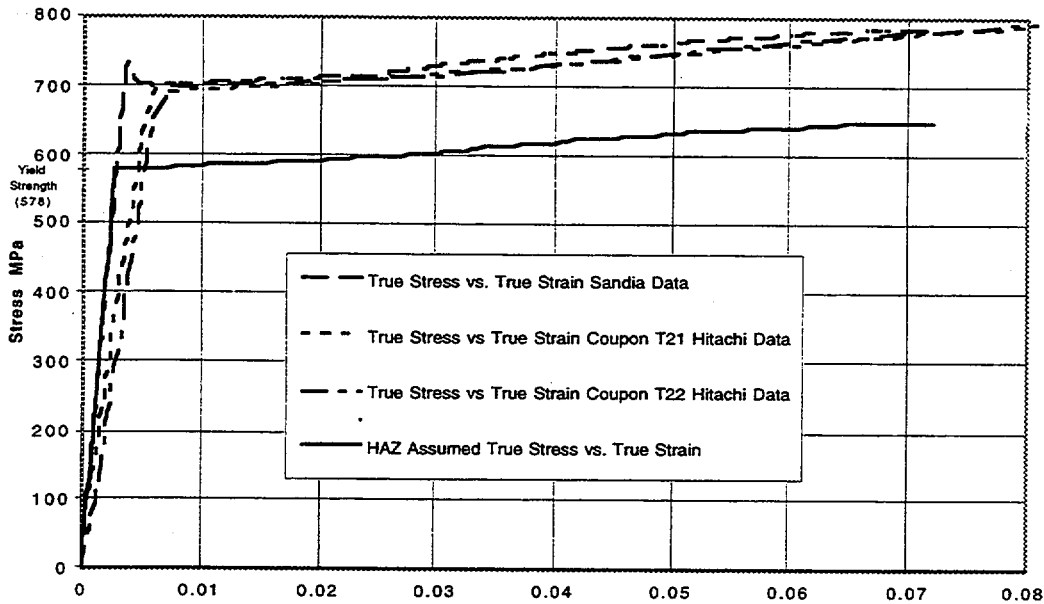


Figure 3.3. Hitachi stress versus strain data for the 9 mm SPV490 material and the reduced strength curve assumed for the HAZ material.

the local base metal of SPV490 steel are used to calculate the approximate hardness number for the HAZ prior to the High-pressure test by using the following equation :

$$H4 = H1 \times (H3/H2)$$

Where:

H1= hardness of the HAZ after the High-pressure test = 91.21

H2= hardness of local base metal after the High-pressure test = 97.4

H3= hardness of the virgin plate material = 98.8

H4= predicted hardness of the HAZ before the High-pressure test

Therefore, the approximate hardness number for SPV490 HAZ prior to the High-pressure test is:

$$H4 = 91.21 \times (98.8/97.4) = 92.52$$

The ultimate tensile strength of steels is correlated with the Rockwell B hardness number in accordance with the *Metals Handbook* (8th edition, Vol. 1, Properties and Selection of Metals, American Society for Metals, 1961). The functional relationship between these two properties is shown in Figure 3.4. Accordingly, the ultimate tensile strength of SPV490 HAZ before the High-pressure test (with hardness number of 92.52) is calculated to be 651 MPa (94.4 ksi), and that of the virgin plate (with hardness number of 98.8) is computed to be 784 MPa (113.7 ksi). Therefore, the ratio of strength reduction of SPV490 due to the presence of heat-affected zone is $651/784 = 0.83$.

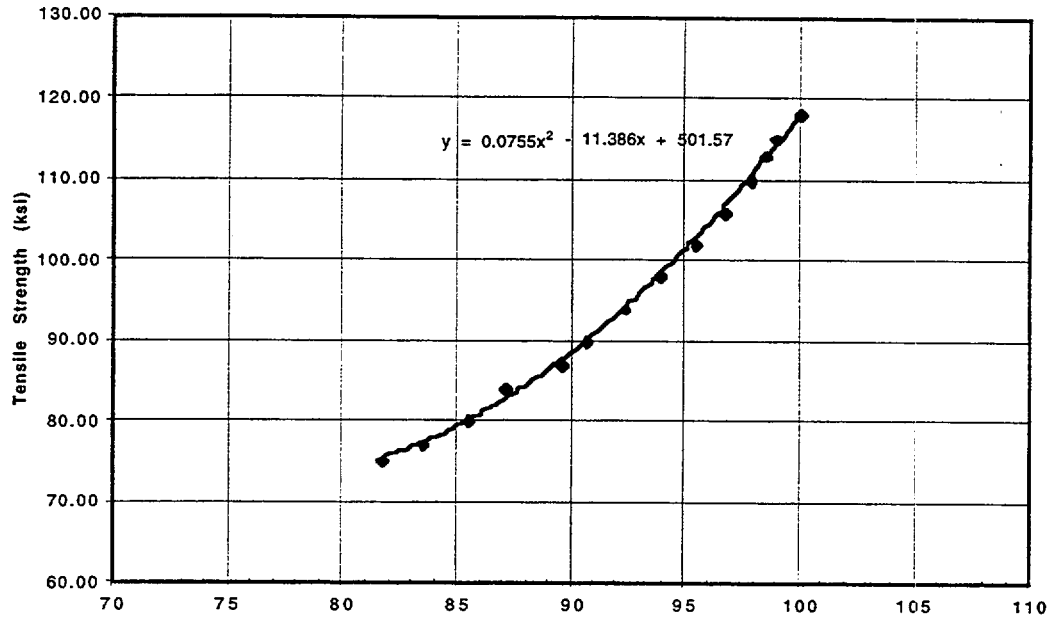


Figure 3.4. Correlation of Rockwell hardness number to the ultimate tensile strength of SPV490 steel.

Since there is no known relationship between the yield strength of steels and their hardness numbers, the same ratio of strength reduction is applied to approximate the entire portion of the post-yield, stress-strain curve of SPV490 HAZ prior to the high-pressure test. The approximate yield strength obtained with this assumption is probably higher than the actual relationship because there is a smaller amount of strain hardening at the yield limit than at the ultimate strength level, but it is impossible to quantify this uncertainty for lack of material data. This material model, also plotted in Figure 3.4, has been used to represent the SPV490 HAZ on the edge of the equipment hatch reinforcement plate in the posttest analysis.

4. FINITE ELEMENT ANALYSIS MODELS

The finite element model of the SCV and contact structure for the global 3D model appears in Figure 4.1. The ABAQUS finite element code version 5.6 was used for all structural analyses [4] for the SCV model posttest effort. The half-symmetry model used approximately 4800 four-node reduced integration shell elements with finite membrane strain capability (ABAQUS S4R elements). The only non-axisymmetric detail included in this model is the equipment hatch. Symmetric boundary conditions were imposed on all nodes lying in the vertical (xy) plane passing through the centerline of the equipment hatch, and vertical displacements were constrained at the support locations on the underside of the ring support girder. The loading consisted of internal pressure, and the analysis ran until a preset limit of 5 MPa internal pressure was reached. This was greater than the test failure pressure of around 4.7 MPa. The nominal gap between the SCV and the contact structure was increased from the nominal 18 mm specified in the design and used in the pretest

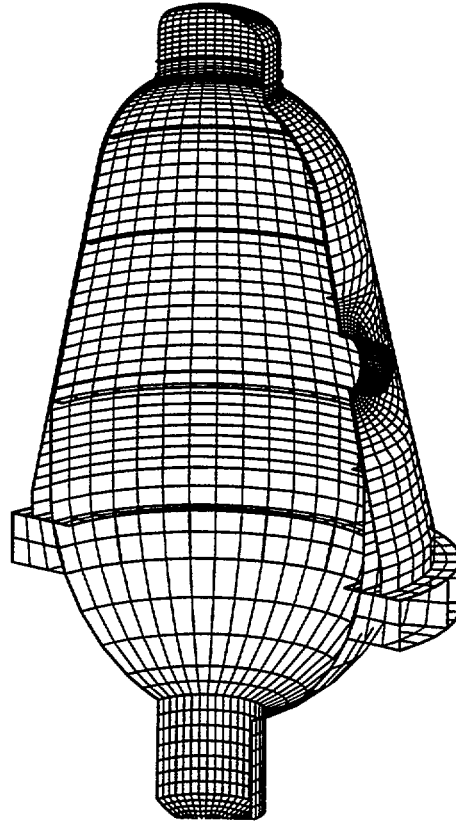


Figure 4.1. 3D global finite element model.

analysis to 22 mm to better reflect the as-built geometry. Computations for this model were performed with the ABAQUS/Standard, Version 5.6.

Many of the features used in the pretest global analyses were retained for the posttest analyses. The specifics of the modeling of the contact between the SCV and the contact structure were not changed. For both the pretest and the posttest models, a small sliding formulation was used because the relative sliding of the SCV and contact structure was assumed to be small. The friction coefficient $\mu=0.2$ was used for both as well.

The thickened equipment hatch insert plate was constructed such that it is flush with the inside surface of the SCV. The thickness eccentricity poses a problem when using shell elements in ABAQUS since there are no means for explicitly modeling a shell with uneven material distribution about a reference line. A simple elastic test case performed in the pretest analysis showed that using the *SHELL SECTION COMPOSITE option in ABAQUS is an accurate way of implicitly modeling the eccentricity at the equipment hatch insert plate [4]. The equipment hatch insert plate was modeled as a composite shell with three layers. The eccentricity was introduced by making the middle layer the same thickness as the adjacent material and then placing two shells with the same thickness on either side. The middle and outside layers were given the modulus of elasticity for the equipment hatch insert plate measured from the Hitachi tensile tests, while the inner

composite layer was given a very low dummy modulus. This formulation makes the stiffness of the inner layer of the composite shell negligible with respect to the outer layer, causing an effective eccentricity in the connection of the two materials.

Because of the eccentricity at the insert plate, the measured gap between the insert plate and the contact structure is reduced considerably to approximately 13 mm. The eccentricity formulation described above does not account for the smaller gap since the contact algorithm uses the centerline of both the composite shells in the SCV insert plate and the regular shells in the contact structure as the reference. So, the gap between the insert plate and the SCV in the finite element model is 22 mm.

The gap between the SCV model and the containment structure near the knuckle region was also increased horizontally in the radial direction by 4 mm. Because of the geometry of the model, this resulted in a gap that was too large in this area of the model. The vertical difference between the SCV model and the contact structure near the knuckle region was larger than in the actual model. The knuckle area of the 3D model showing the gap is shown in Figure 4.2. This change on the gap dimension will affect some of the vertical displacement predictions near the top head portions of the model.

The final change from the pretest model is the material change for the elements near the equipment hatch in the HAZ. The elements shown in black in Figure 4.3 were given the reduced yield strength material properties of the HAZ as previously described.

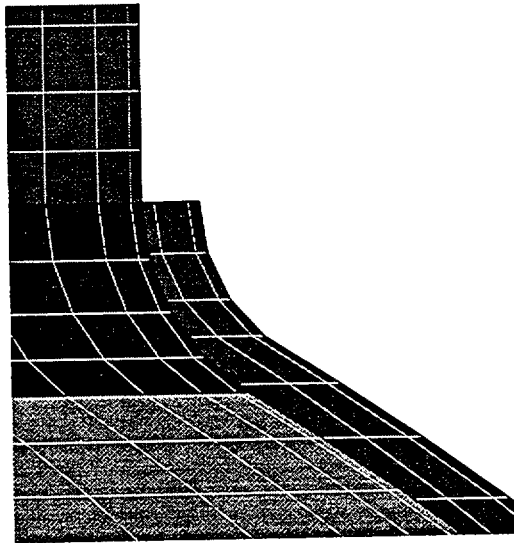


Figure 4.2. Knuckle region of the 3D global finite element model.

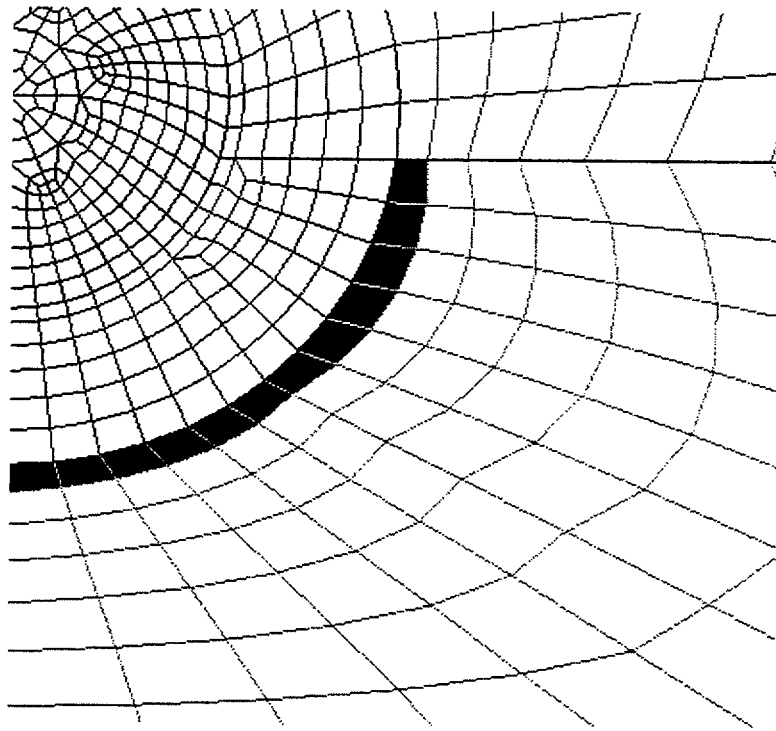


Figure 4.3. HAZ elements shown in black in the 3D global finite element model.

5. COMPARISON OF PRETEST AND POSTTEST ANALYSIS RESULTS WITH SCV HIGH-PRESSURE TEST DATA

5.1 Global Results

The SCV model with the exception of the equipment hatch detail is essentially an axisymmetric pressure vessel. For this reason, the first measure of how well the pretest analysis performed was to compare the global responses. Figure 5.1 is a plot of the deflected shape in the radial direction along the 270° meridian, or at the side opposite the equipment hatch. The pretest and posttest analysis results and the measured high-pressure test results are shown on the SCV initial shape with a magnification factor of 10 applied to the displacements. Some of the data points in the high-pressure test data are interpolated between two measured points. Thus, the difference between the measured and analysis results at elevations of 1500 mm and 2200 mm are not as severe as the figure indicates.

The pretest predictions tended to underestimate the radial displacements at the pressure of 4.5 MPa. This is consistent with the free-field hoop strain gage data, where the pretest analysis consistently overestimated the SCV stiffness. Also, because the gap was increased in the posttest analysis, the deflections at some of the points were higher simply because there was more room for the SCV wall to deflect outward. The changes to the material models in the posttest analysis in the lower-strain regions brought the deflected shape much closer to the measured deflected shape.

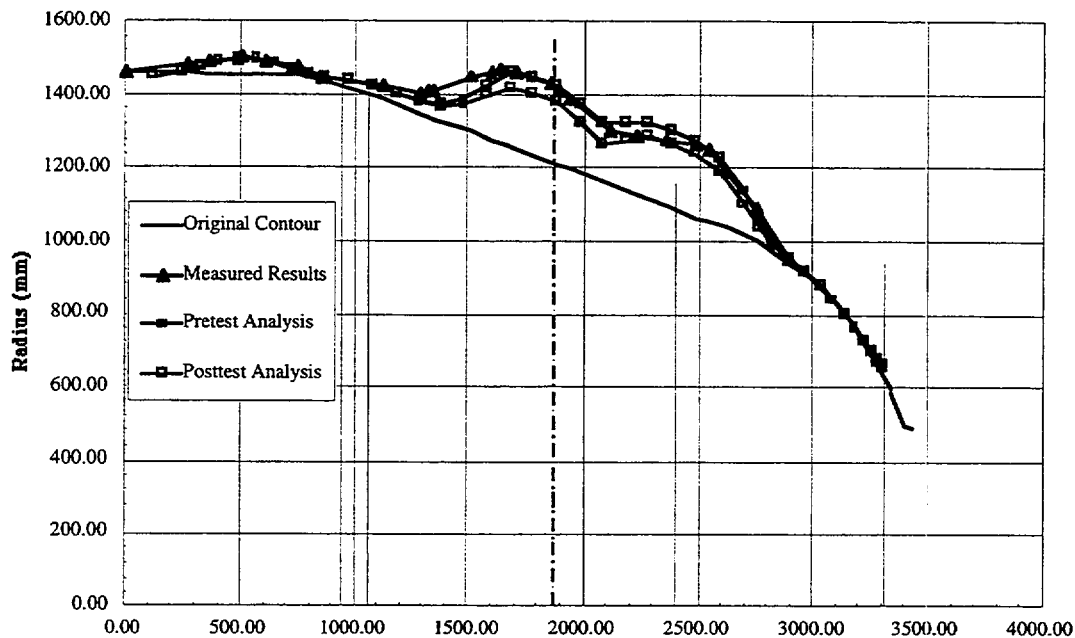


Figure 5.1. Radial deflections magnified by a factor of 10 versus model elevation.

Figure A.24 in the appendix shows the hoop strains for the Standard Output Location #24, which is in the free-field area away from the equipment hatch. The plot shows the effect of the changes to the material models and the increase in the gap between the contact structure and the SCV wall. The predicted posttest analysis strains and the measured strains eventually merged to the same value at a strain of about 2%. This difference between the two plots is very consistent with the effect that residual stresses have on material behavior at strains just past yield. Residual stresses tend to round off the Luder's strain plateau in a material stress-strain relationship. The material properties based on the coupon test results would have this plateau, while the SCV walls would not because of the residual stresses induced during the manufacturing process.

The effect of the change in the gap is very evident in Figure A.24 in this appendix. The pretest analysis shows the contact occurring at a much lower strain than the measured results. The increase in the gap to 22 mm in the posttest analysis matched the measured data well.

The hoop strains at the 270° meridian at 4.5 MPa plotted against the elevation of the model are shown in Figure 5.2. The posttest predictions and the measured strains show a very good correlation. There is some difference in the two curves at elevations between 1100 and 1600 mm. The material at this elevation is the 9 mm thick SPV490 material. This is a higher-strength steel which seems to have a slightly lower yield strength in the model than in the coupon tensile tests. This could be attributed to many factors such as residual stresses, rolling direction differences, etc.

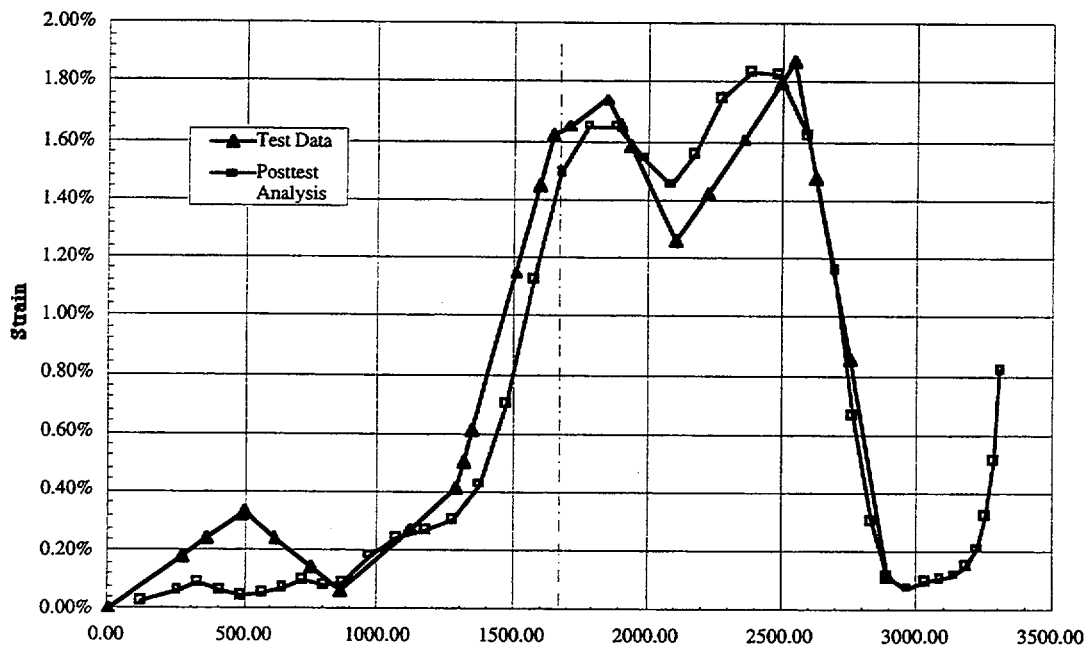


Figure 5.2. Hoop stresses at 270° meridian versus model elevation.

The major difference between the results of the pretest and posttest analyses with regard to global behavior is the more accurate modeling of the material properties and the more realistic gap used in the model. The free field hoop strains did not exceed 2%, which is only a small fraction of the ultimate strain for the materials. Attention to the low-strain behavior of each material is critical if the global behavior of a complex structure such as the SCV is to be modeled accurately.

5.2 Local Equipment Hatch Behavior

Most of the complexity of the SCV model occurs in the equipment hatch area. Adding to the complexity is the thickened insert plate around the penetration and a material change just below the centerline of the hatch. Manufacturing details such as eccentricities between the plates and a thinned area from grinding of a weld make this a critical part of the SCV model.

The failure of the model occurred to the lower left (looking from the inside of the model) of the equipment hatch in the HAZ of the weld between the insert plate and the 9 mm SPV490 material. Figure 5.3 shows the strain contours near the equipment hatch from the pretest analysis. The highest strains occur in the lower-strength material just above the material transition.

When the HAZ material properties are included in the posttest analysis, the area of highest strains moves to the higher-strength material. The reduced strength of the HAZ material changes the distribution of strains around the equipment hatch. The highest strains are now

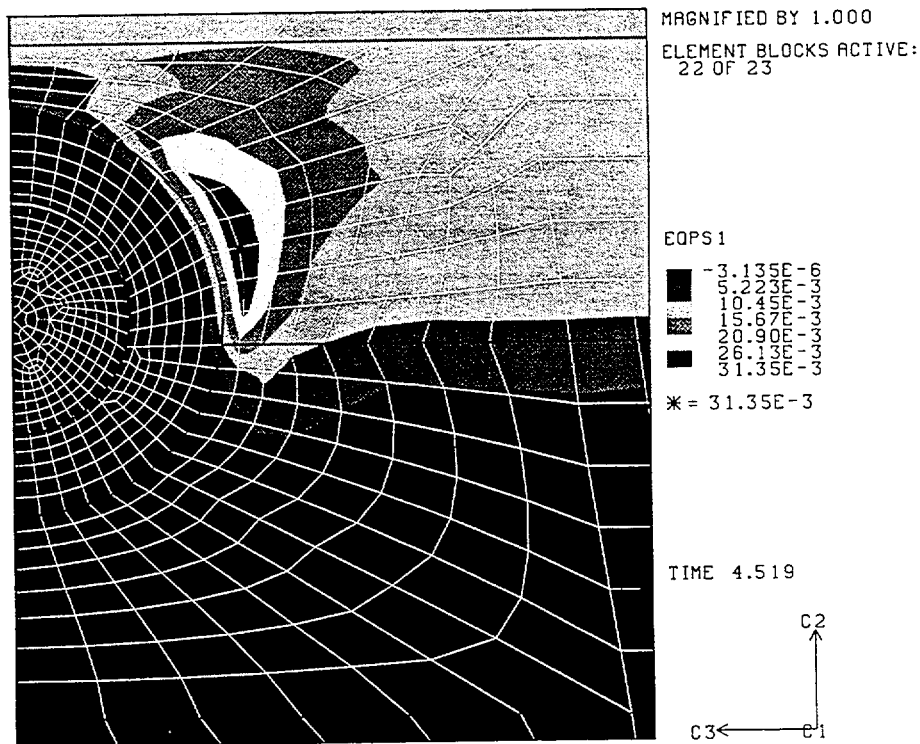


Figure 5.3. Strain contours around the equipment hatch from the pretest analysis.

located in the SPV490 material below the material change interface. The posttest prediction for the strain contours is shown in Figure 5.4. When other factors such as the reduced thickness due to grinding and possible flaws in the weld, which could initiate a tear are considered, the failure in this location is not surprising.

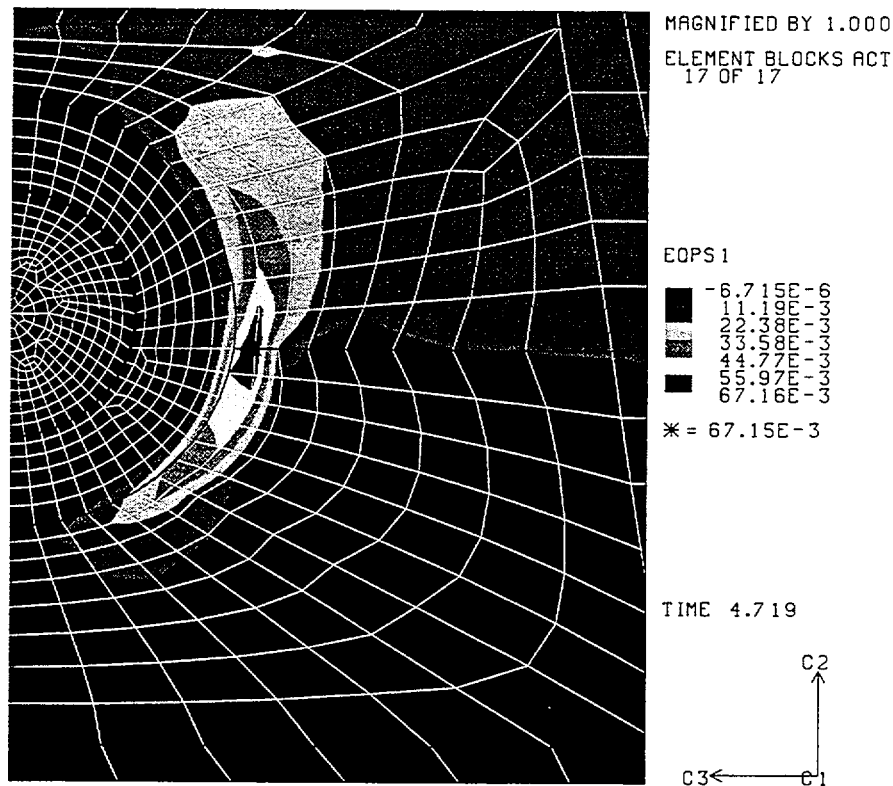


Figure 5.4 Strain contours around the equipment hatch from the posttest analysis.

5.3 Discussions of the Results at the Standard Output Locations

The posttest predictions for the standard output locations generally matched well with the measured data. One trend in many of the free-field locations away from the model details is that the posttest prediction for material yielding tended to occur at pressures slightly higher than when yielding actually occurred. What is important is that the posttest predictions and the measured data tended to come together at higher strains. This indicates that the effect of residual strains does not contribute to the global behavior once the strains are large enough to overcome their effect. The effect of the contact between the SCV model and the contact structure was predicted well with the choice of a 22 mm average gap size. In general, the predictions for the free-field locations were very good.

In standard output locations #36 through #39, the displacement predictions for areas in the knuckle region did not match well with the measured data. This is a result of not modeling the gap accurately in this location. If these details of the as-built structure were accurately

modeled in the analysis, the results would have matched better. Other locations where the correlation could have been better, such as location 12 also in the knuckle region, were generally associated with a complex detail of the SCV model. The finite element mesh was not detailed enough in these areas to accurately predict the behavior. A more detailed analysis would have improved these predictions.

5.4 Failure Considerations

To predict the failure of a complex steel structure such as the SCV model when subjected to loads causing stresses well beyond yield, two factors need to be considered carefully in any prediction of failure. First the majority of the structure will experience strains well below the failure strains for typical steels. To accurately capture the global behavior, attention must be given toward accurately modeling the stress-strain relationship in the material models for the steels. Accurately predicting global behavior is important because the loads applied to the more complex areas of a structure are a direct result of the model's global behavior.

The second factor is the accurate modeling of the details of the structure. Structures almost always fail in the details of their design where the strain concentrations take place. In the pretest analyses, the criteria used to predict failure was assumed to be an equivalent plastic strain of 8%. The highest strain recorded in the model was 9% strain in an area near the equipment hatch. The posttest analysis showed a strain of 7% in the location where the tear initiated. This is very consistent with the pretest failure criteria. For a ductile failure like the tear in the SCV, an equivalent plastic strain failure criterion based on the refinement of the analysis and the material properties seems appropriate.

6. SUMMARY

The comparison between the pretest analysis and the measured results from the high-pressure test data showed where two aspects of the analysis needed to be changed. The first aspect relating to the global or overall response of the SCV concerned the accurate modeling of the material stress versus strain relationships. The pretest analysis used material models that were too stiff at low strains. Consequently the global response tended to yield earlier than predicted and tended to have larger deformations than predicted up to failure. The posttest analysis used stress versus strain relationships that were the lower envelope of the data obtained from coupon testing. Even with the new material models used in the posttest analysis, the effect of residual stresses still resulted in predicting yield pressures higher than those measured. The posttest predictions did, in many cases, move back towards the measured strains as the strains increased.

The second aspect of the pretest analysis that needed changing was the material modeling of the HAZ around the equipment hatch in the SPV490 material. When welded this material will have a HAZ that has reduced strength when compared to the parent material. This change in material properties shifted the highest strains to the SPV490 material where failure occurred. Since complex structures such as the SCV model generally fail in their details, close attention to correctly modeling these details is critical when trying to predict both failure locations and pressures.

7. REFERENCES

1. L. Porter, P. A. Carter, and S. W. Key, "Pretest Analysis of the Steel Containment Vessel Model," NUREG/CR-6516, SAND96-2877, Sandia National Laboratories, Albuquerque, NM, November 1996.
2. V. K. Luk and E. W. Klamerus, "Round Robin Pretest Analysis of a Steel Containment Vessel Model and Contact Structure Assembly Subject to Static Internal Pressurization," NUREG/CR-6517, SAND96-2899, Sandia National Laboratories, Albuquerque, NM, November 1996.
3. J. A. Van Den Avyle and K. H. Eckelmeyer, "Posttest Metallurgical Evaluation Results for SCV High Pressure Test," SAND98-XXXX, Sandia National Laboratories, Albuquerque, NM, 1998
4. ABAQUS/Standard User's Manual, Version 5.6, Hibbitt, Karlsson, and Sorensen, Inc., Pawtucket, RI, 1995.

SNL Appendix A

Comparison Plots of Pretest and Posttest Analysis Results with SCV High-Pressure Test Data

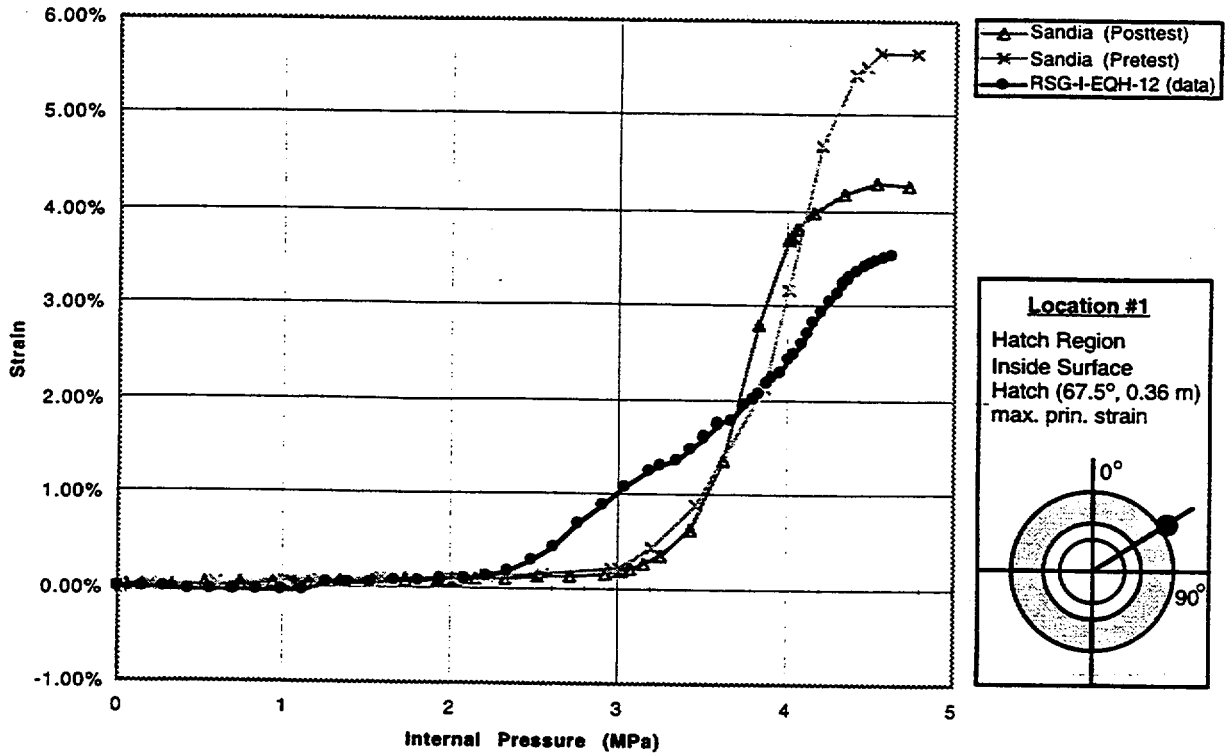


Fig.A.1 Standard Output Location #1

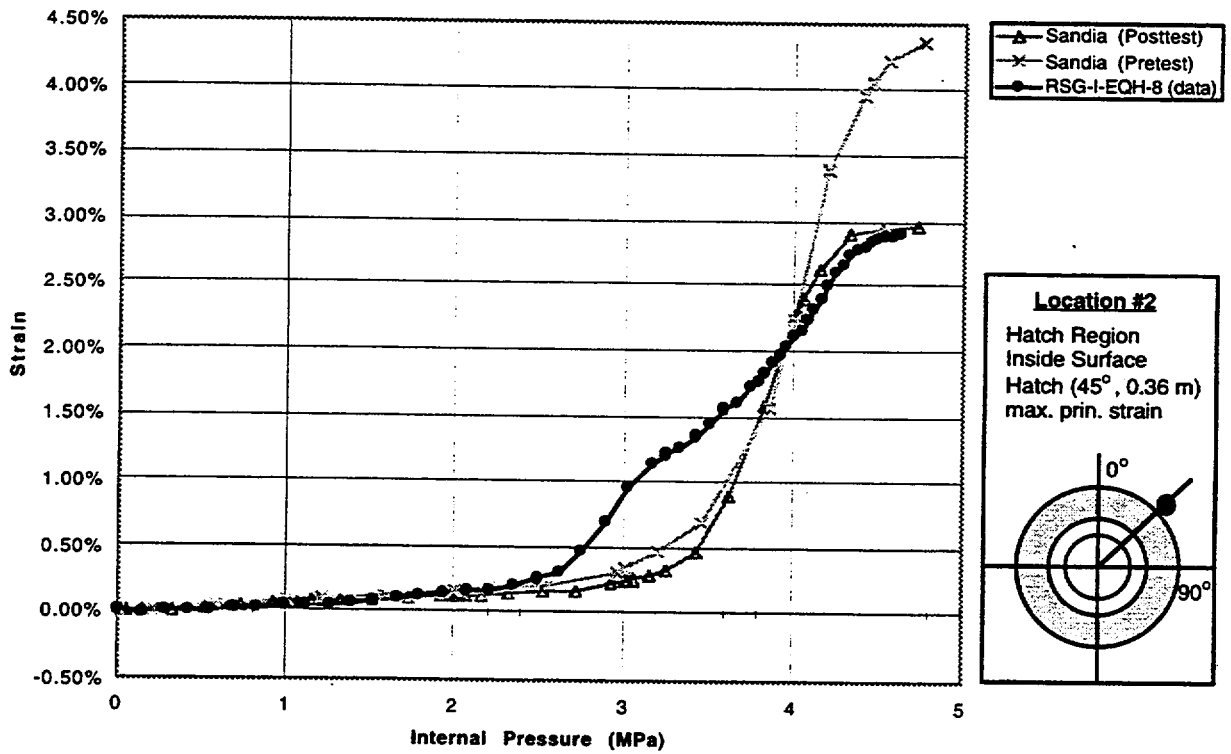


Fig.A.2 Standard Output Location #2

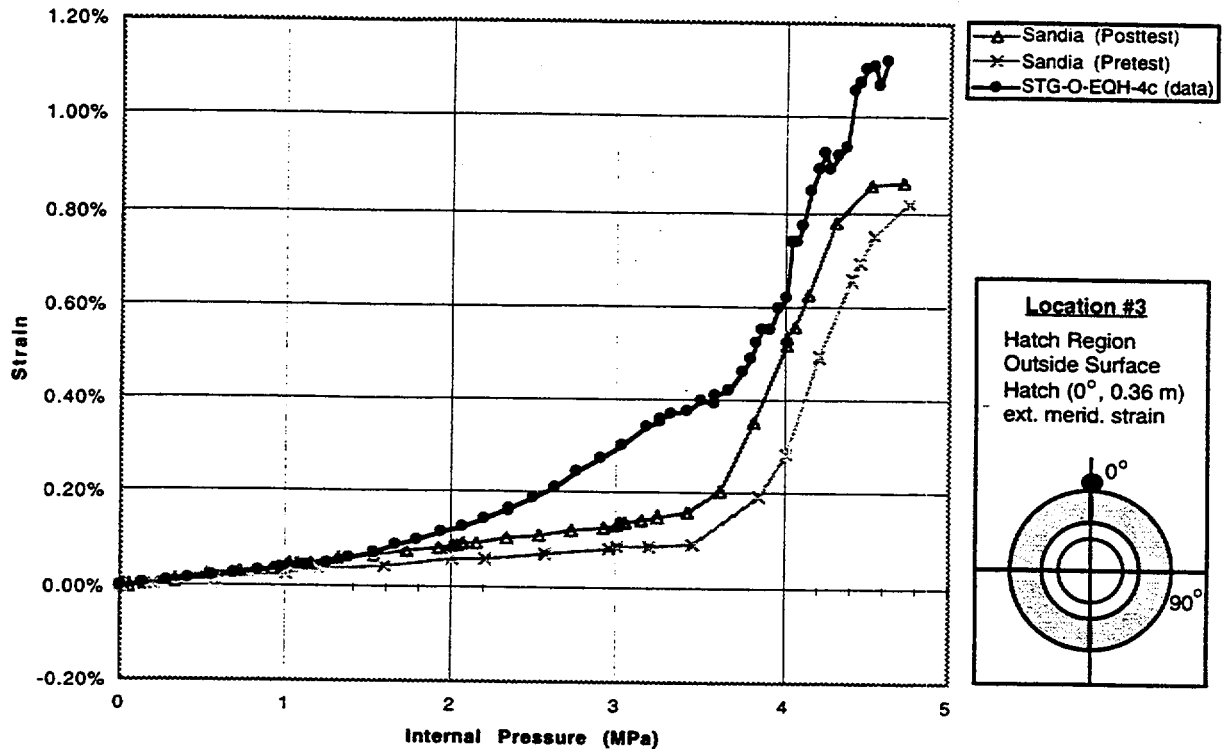


Fig.A.3 Standard Output Location #3

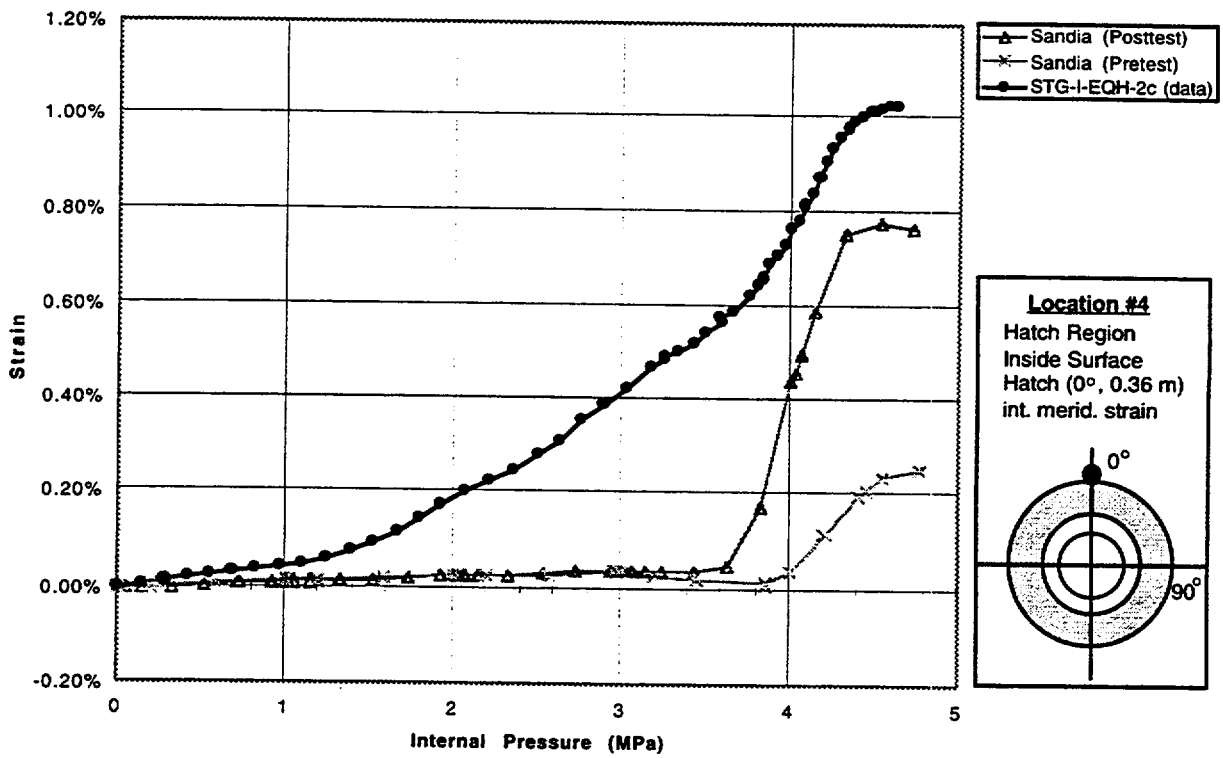


Fig.A.4 Standard Output Location #4

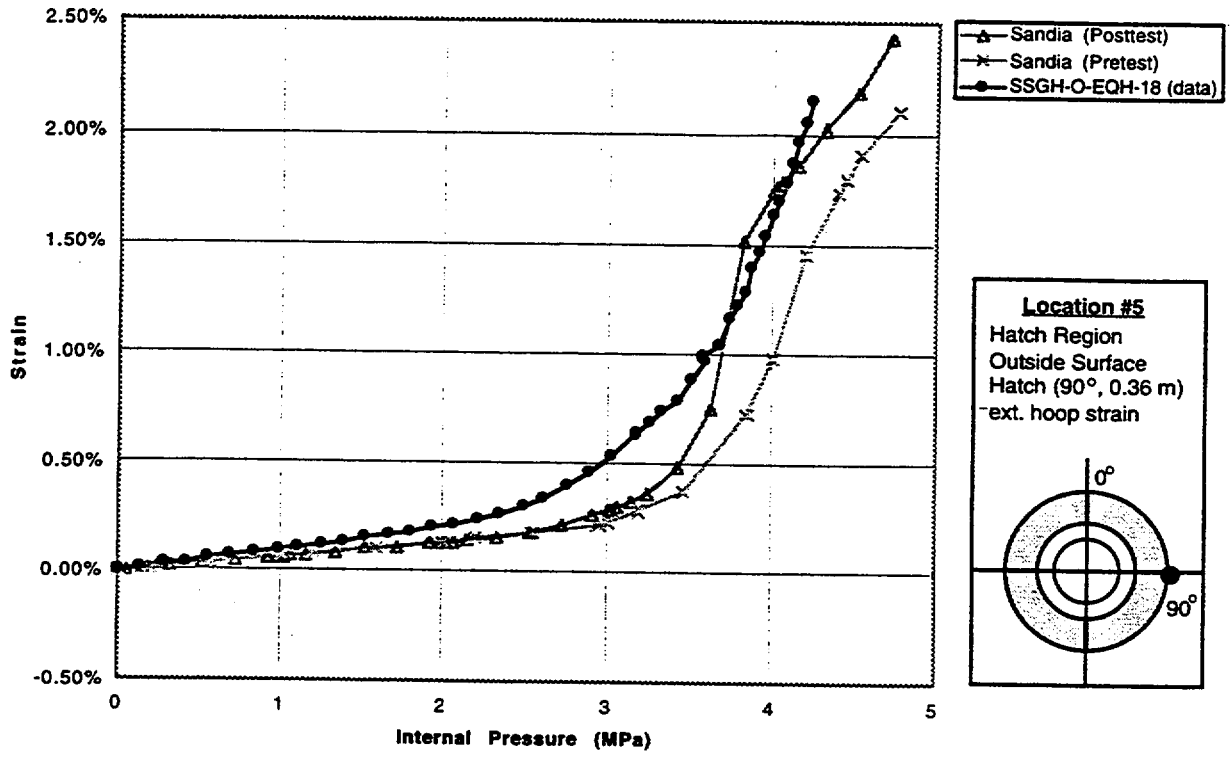


Fig.A.5 Standard Output Location #5

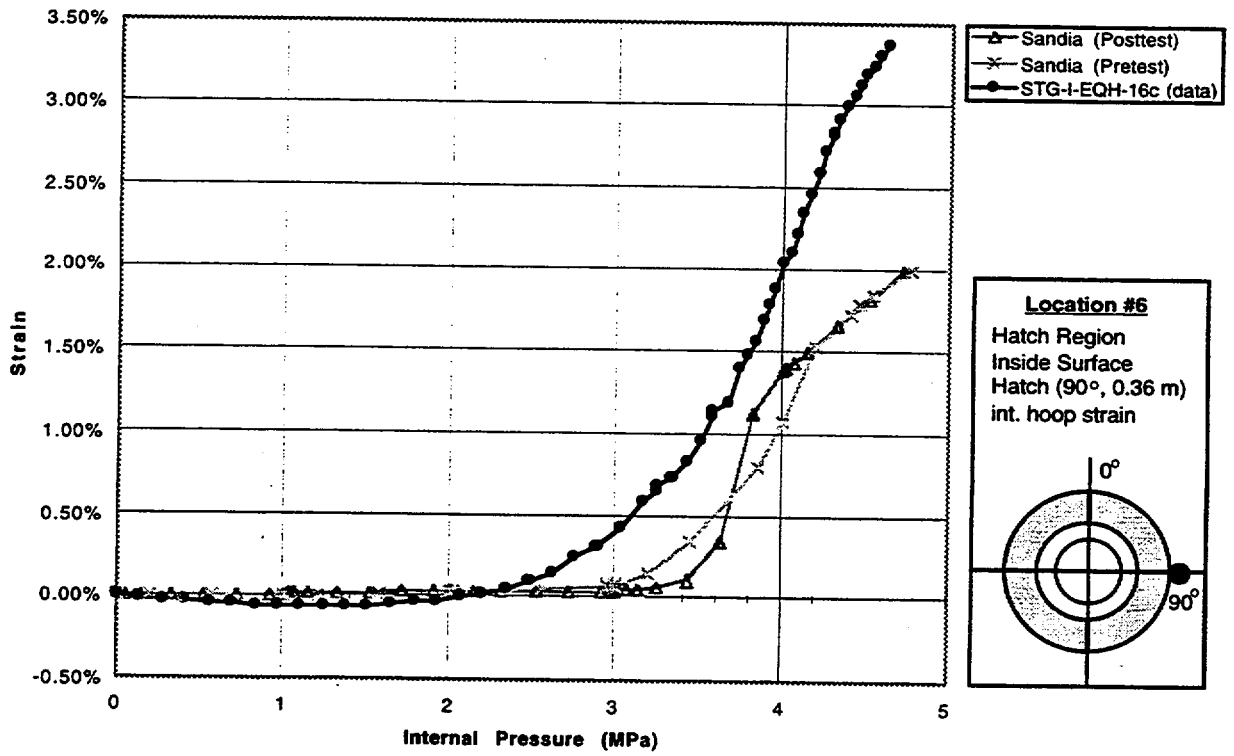


Fig.A.6 Standard Output Location #6

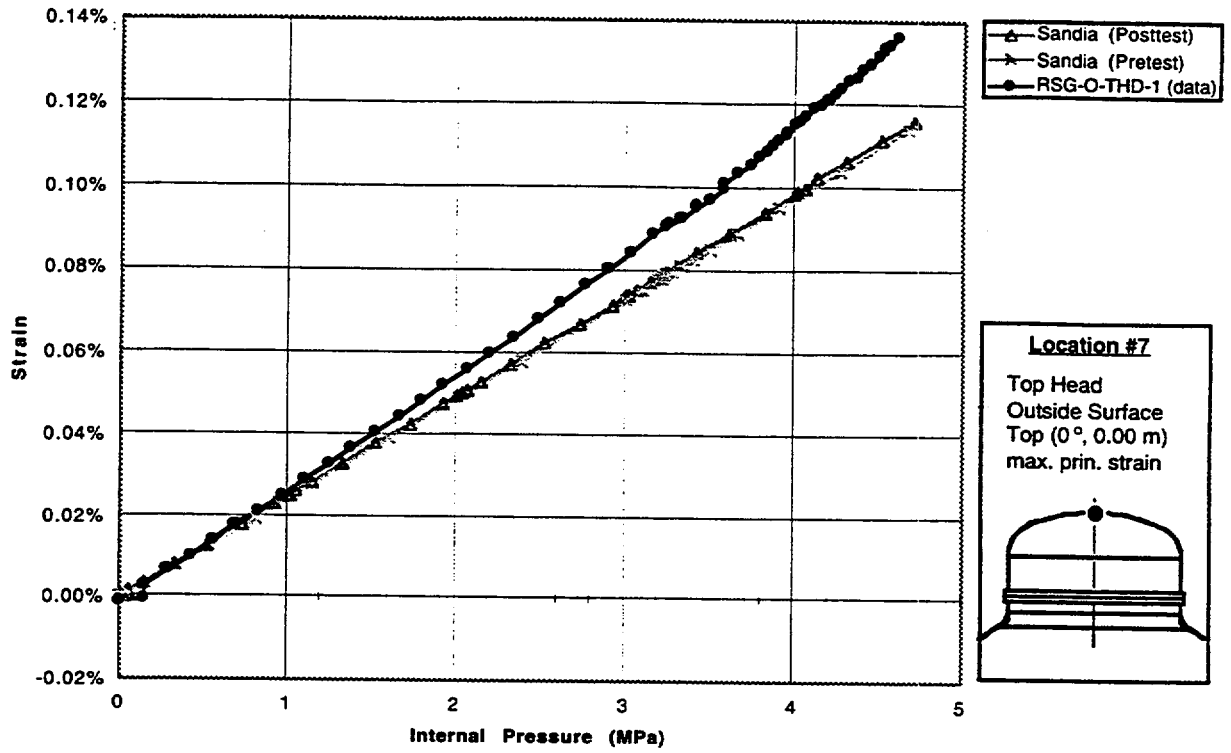


Fig.A.7 Standard Output Location #7

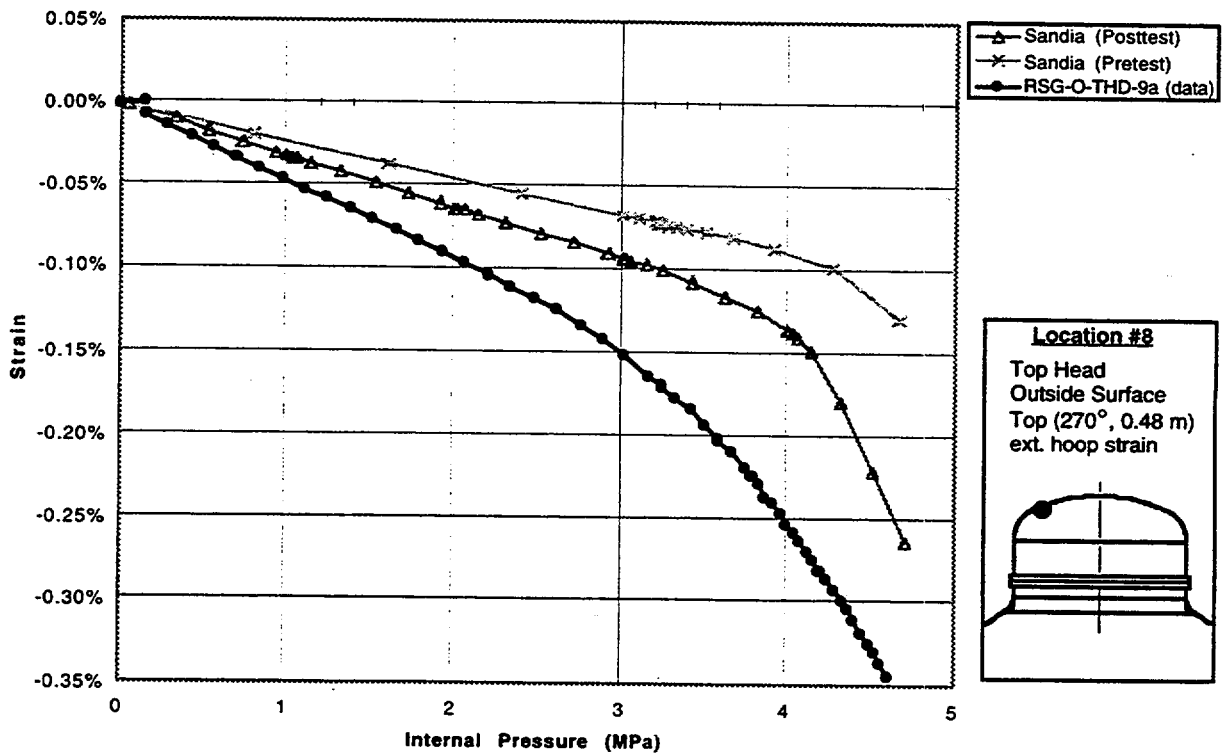


Fig.A.8 Standard Output Location #8

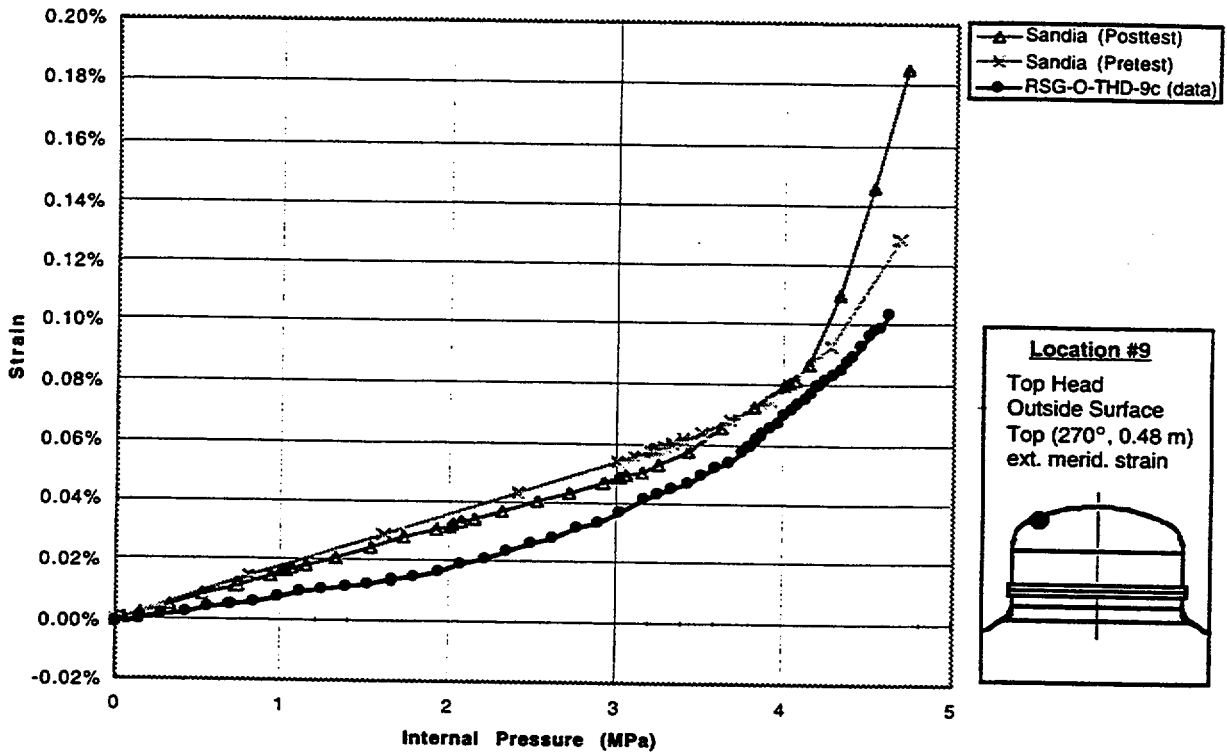


Fig.A.9 Standard Output Location #9

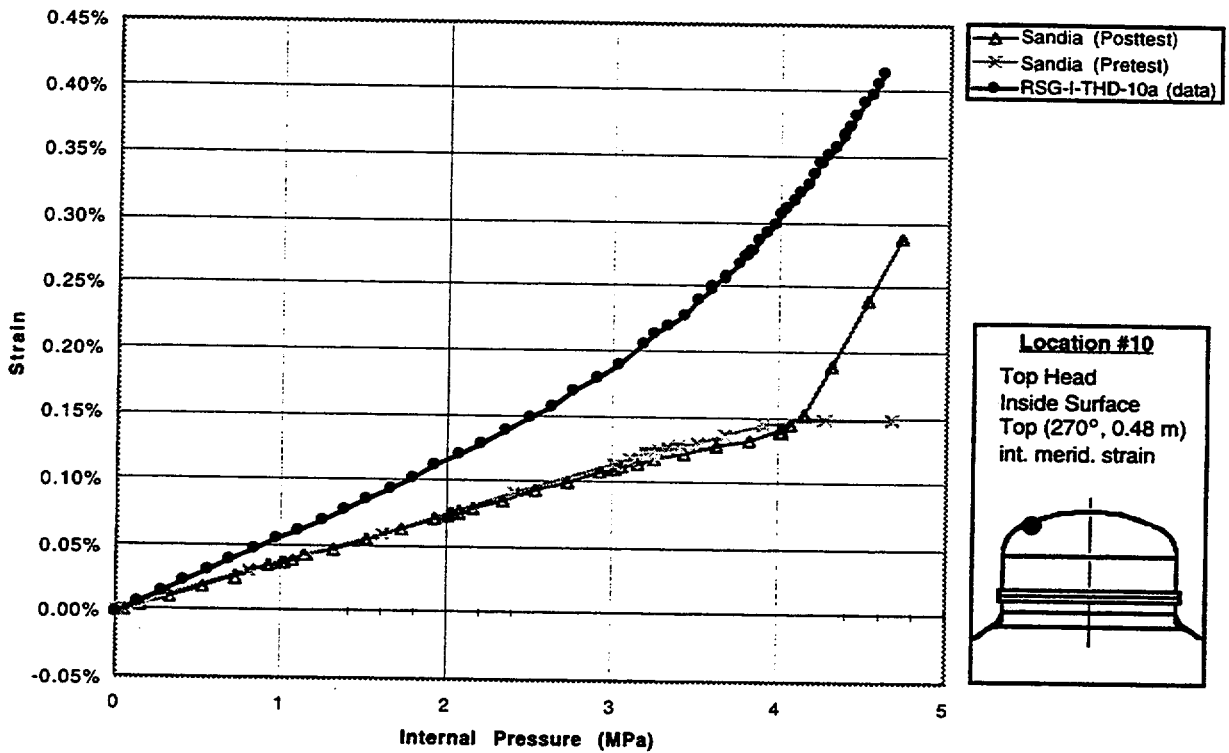


Fig.A.10 Standard Output Location #10

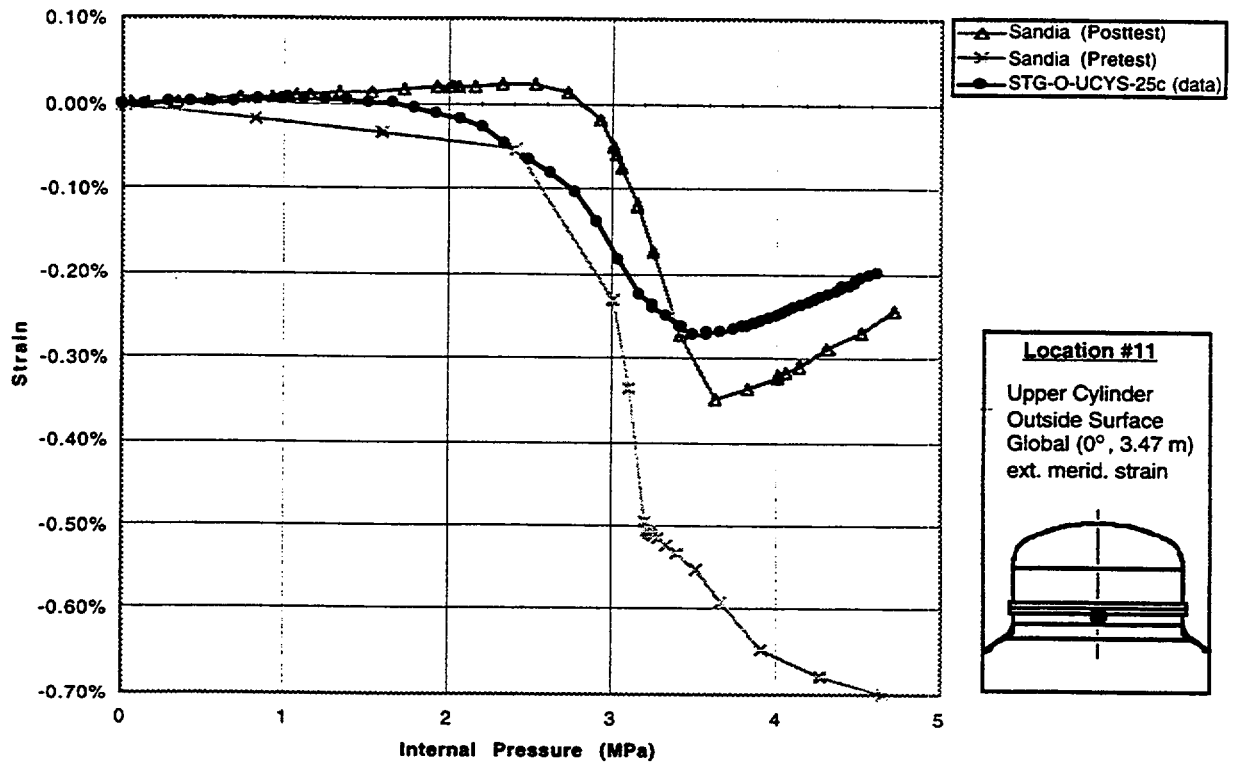


Fig.A.11 Standard Output Location #11

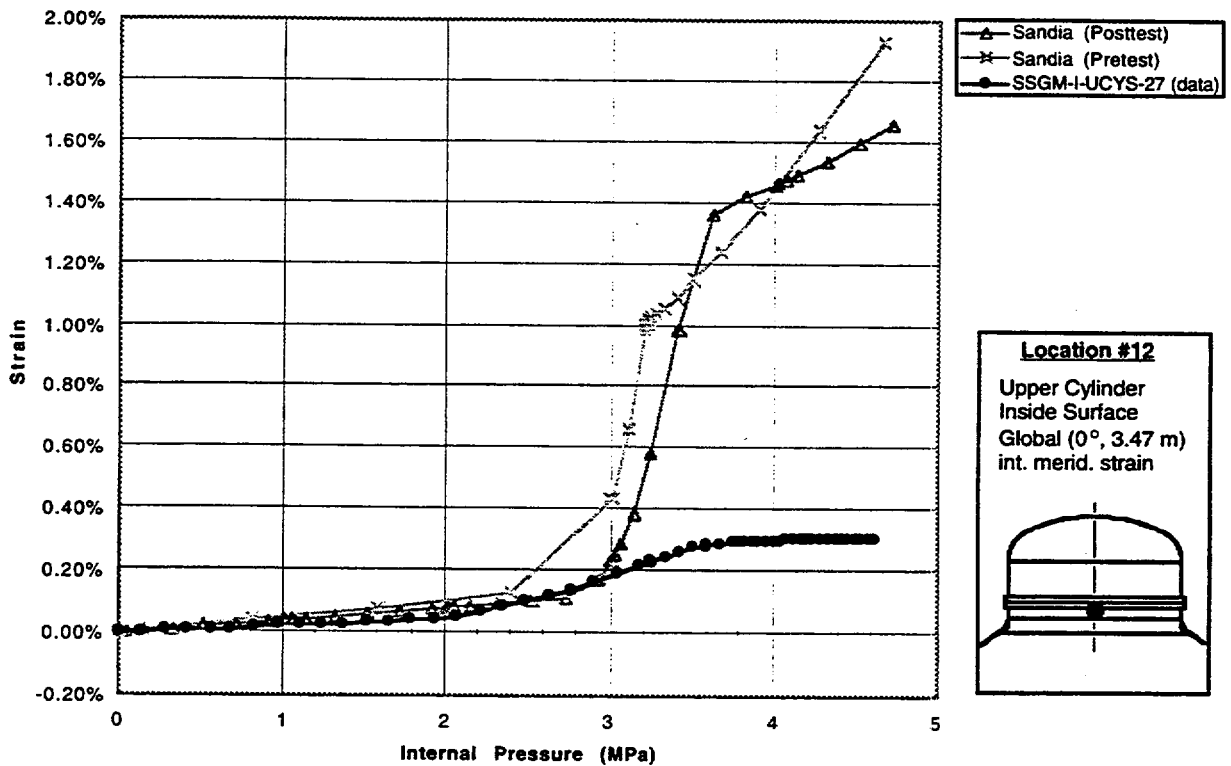


Fig.A.12 Standard Output Location #12

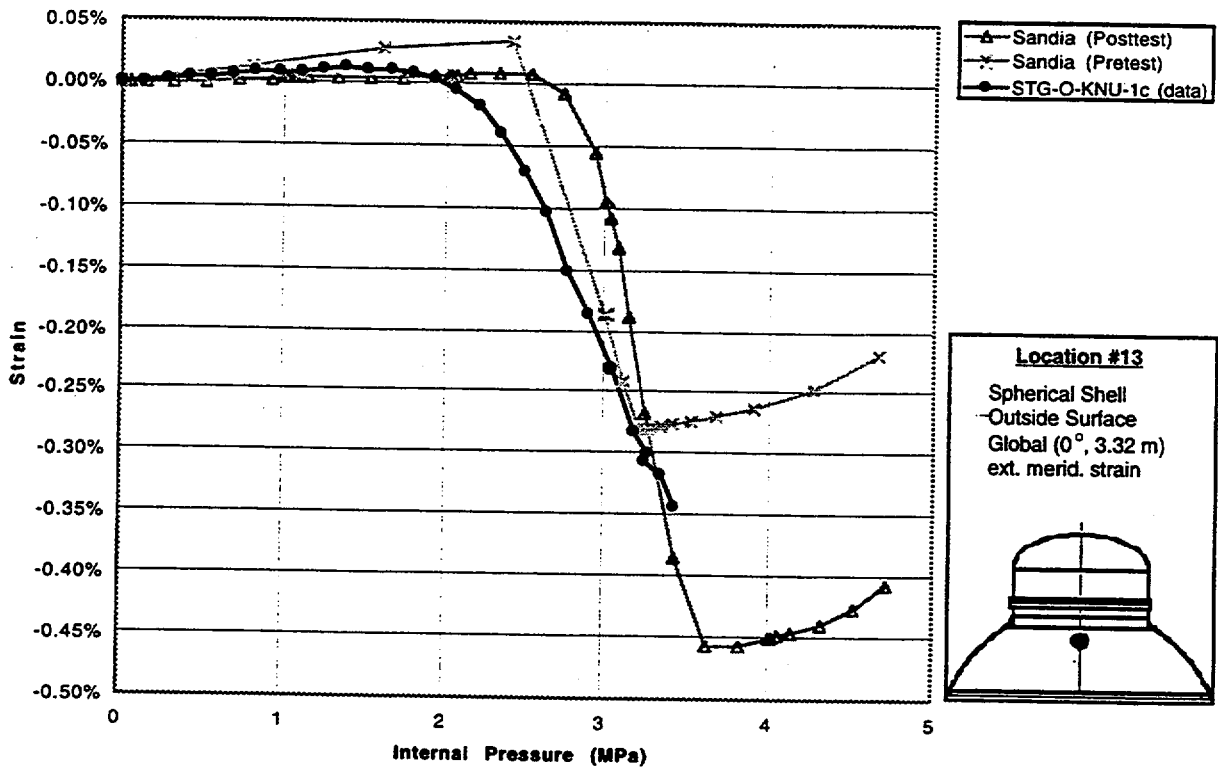


Fig.A.13 Standard Output Location #13

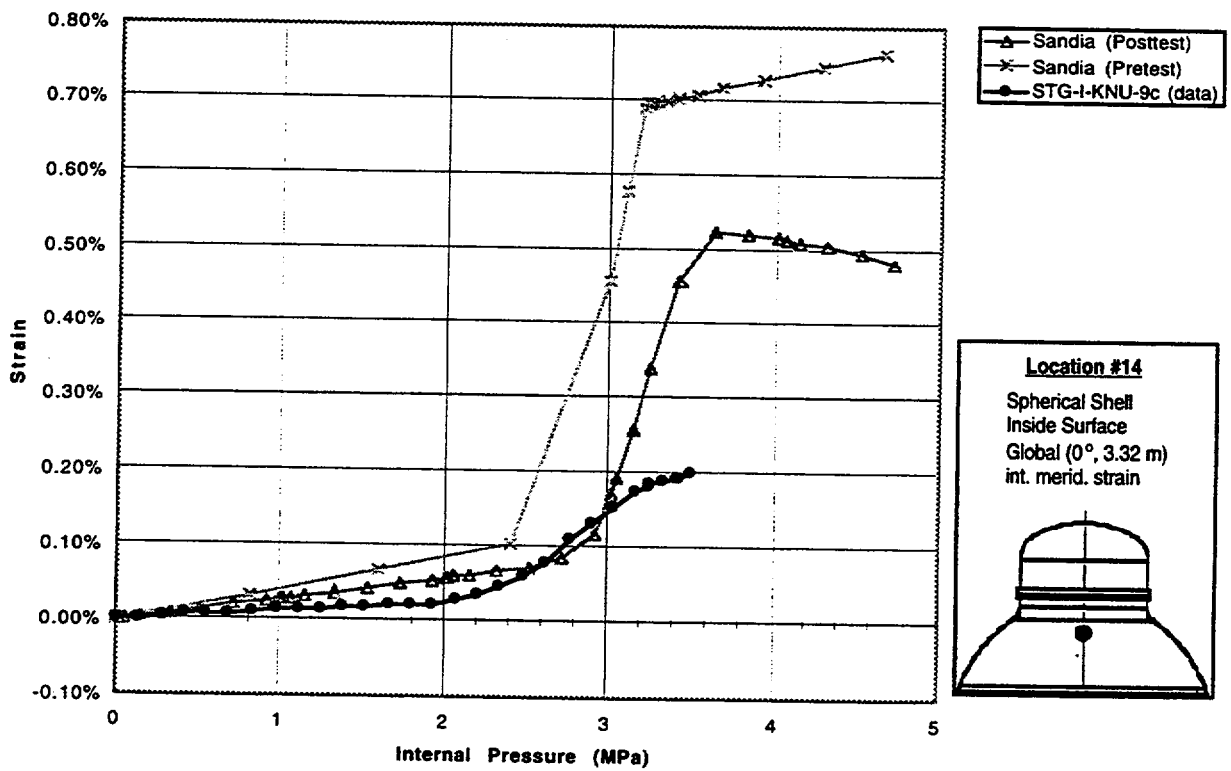


Fig.A.14 Standard Output Location #14 (nonzero friction case)

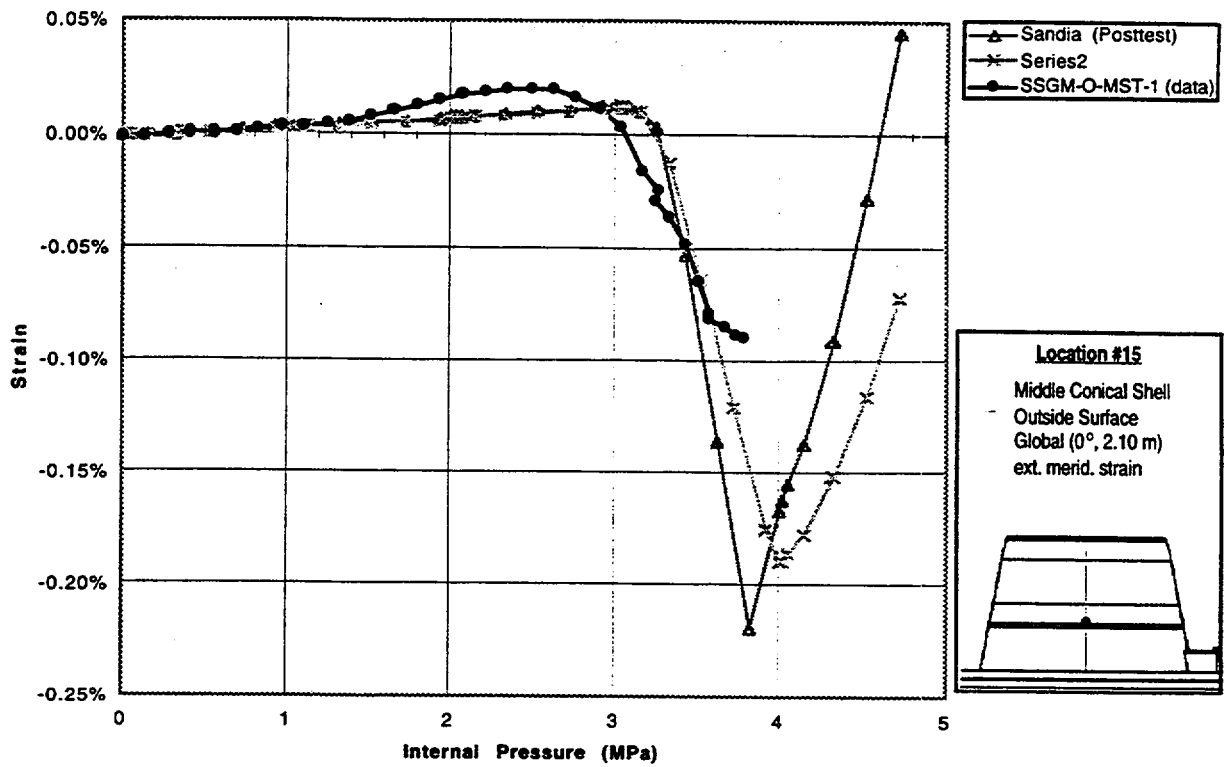


Fig.A.15 Standard Output Location #15

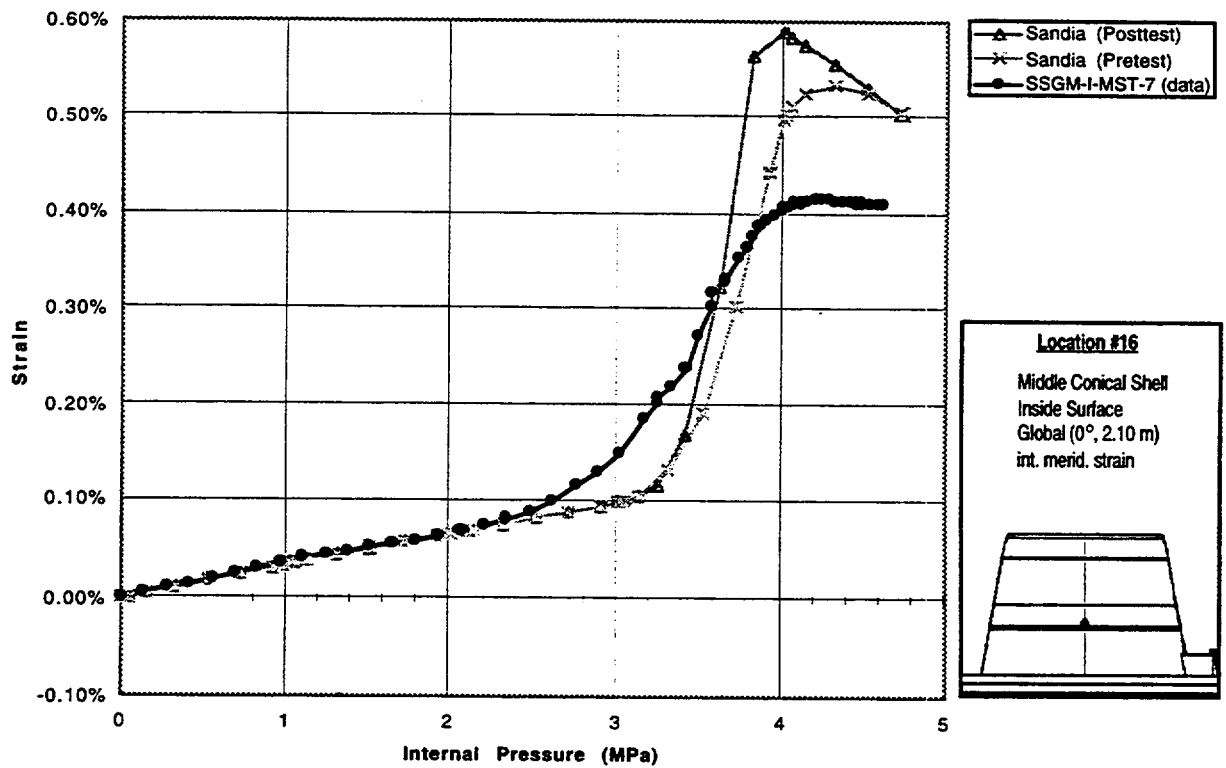


Fig.A.16 Standard Output Location #16

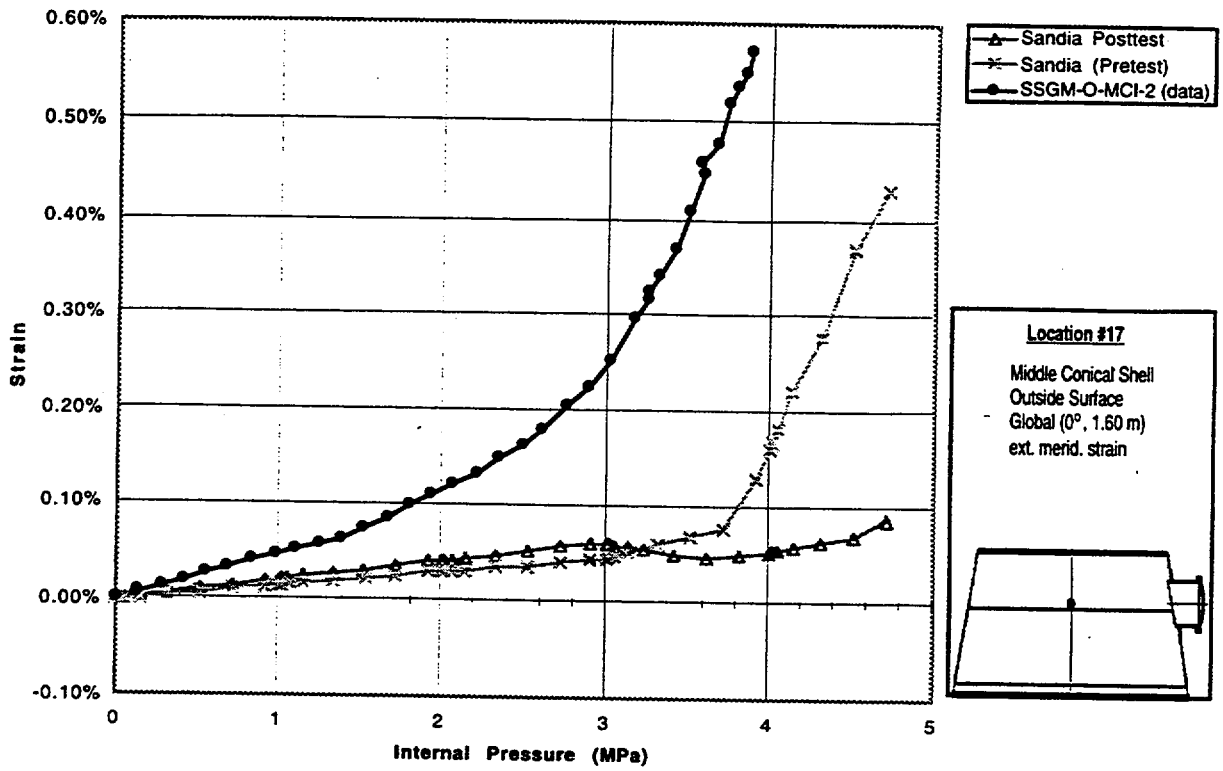


Fig.A.17 Standard Output Location #17

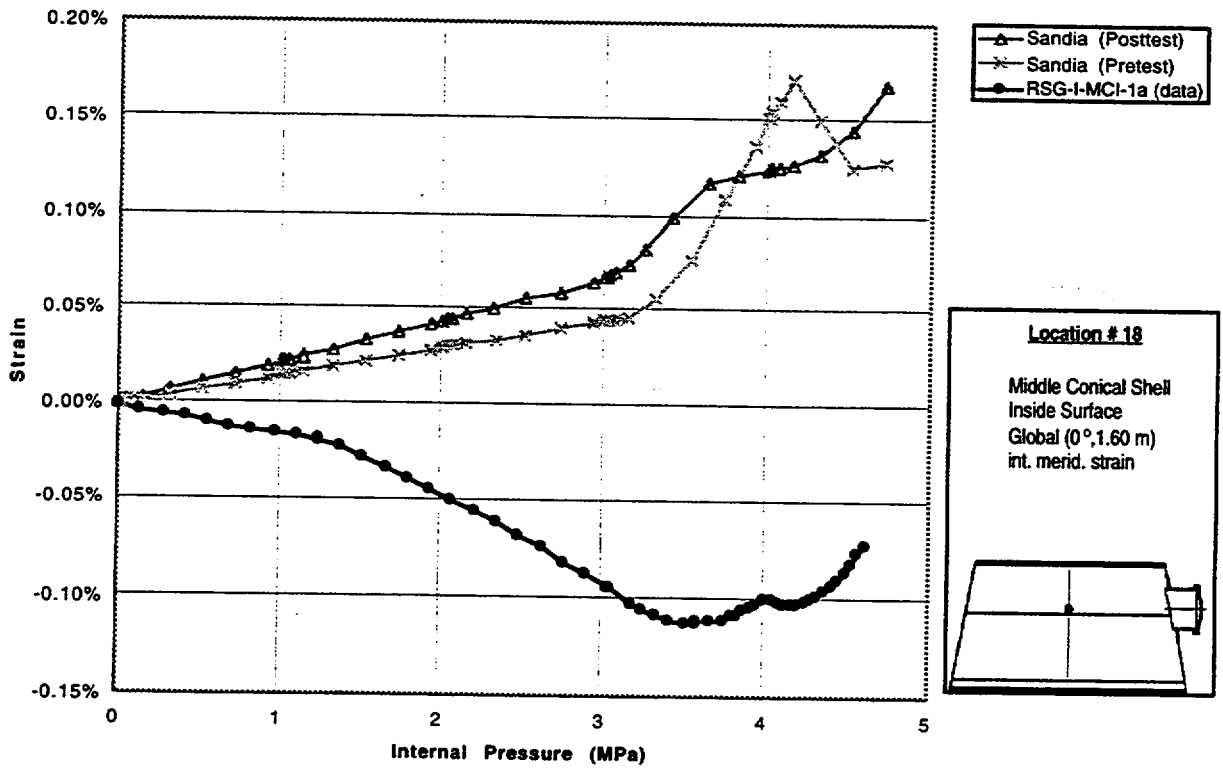


Fig.A.18 Standard Output Location #18

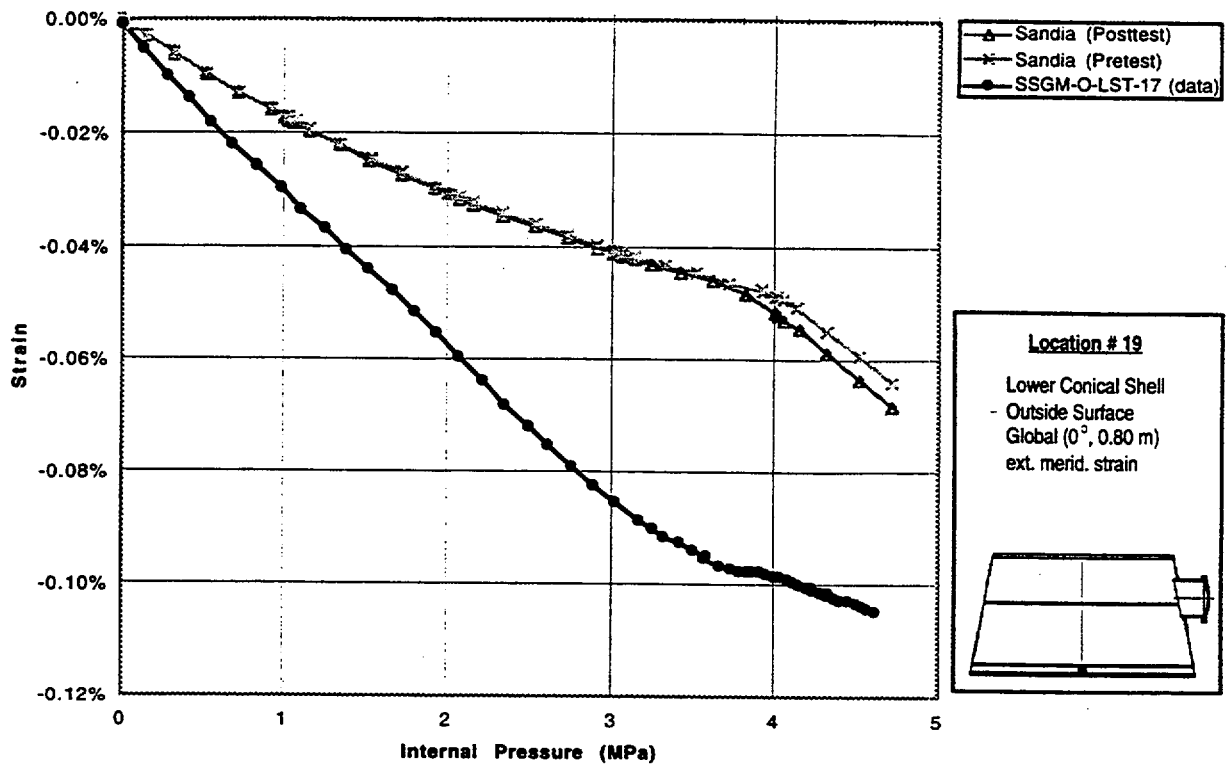


Fig.A.19 Standard Output Location #19

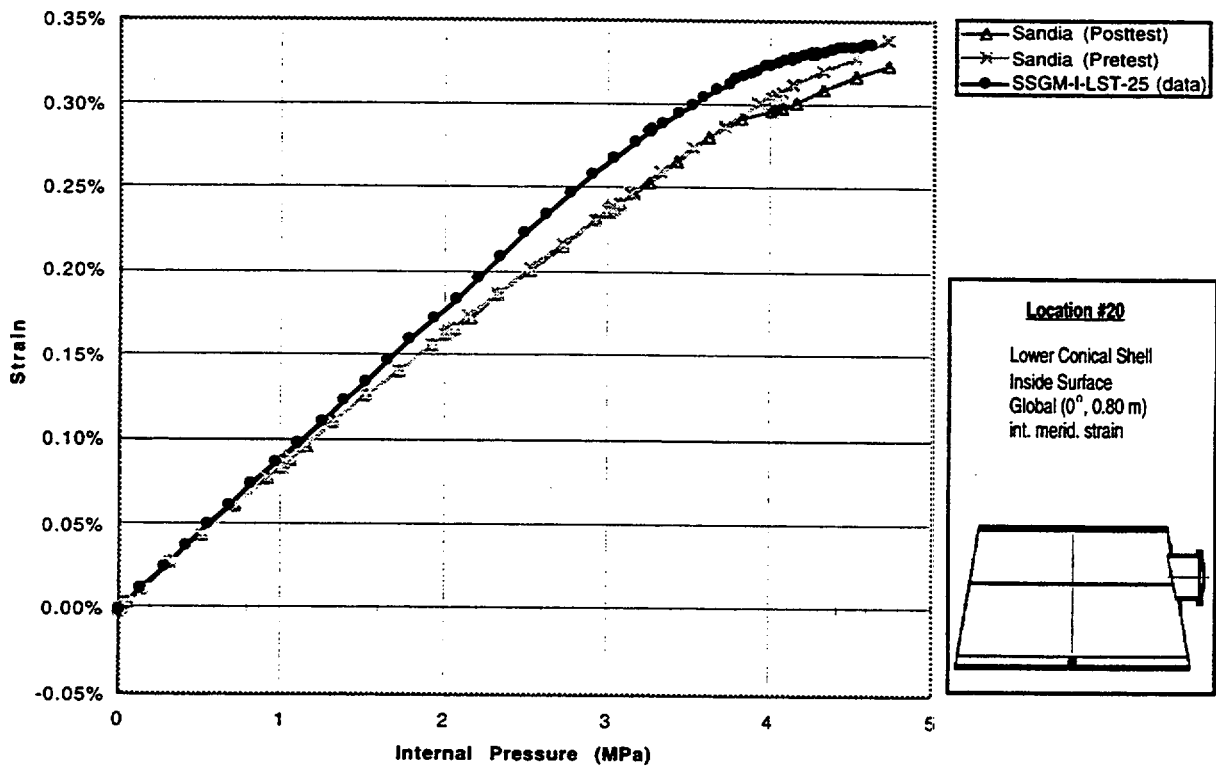


Fig.A.20 Standard Output Location #20

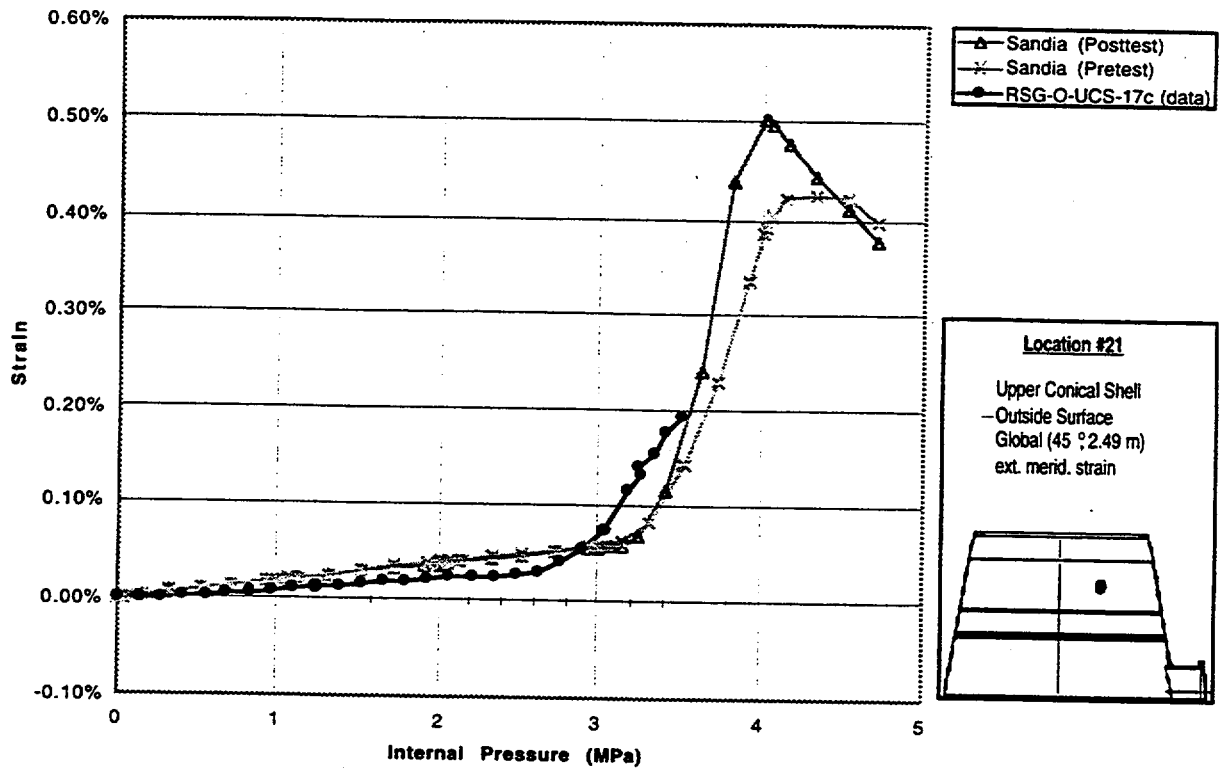


Fig.A.21 Standard Output Location #21

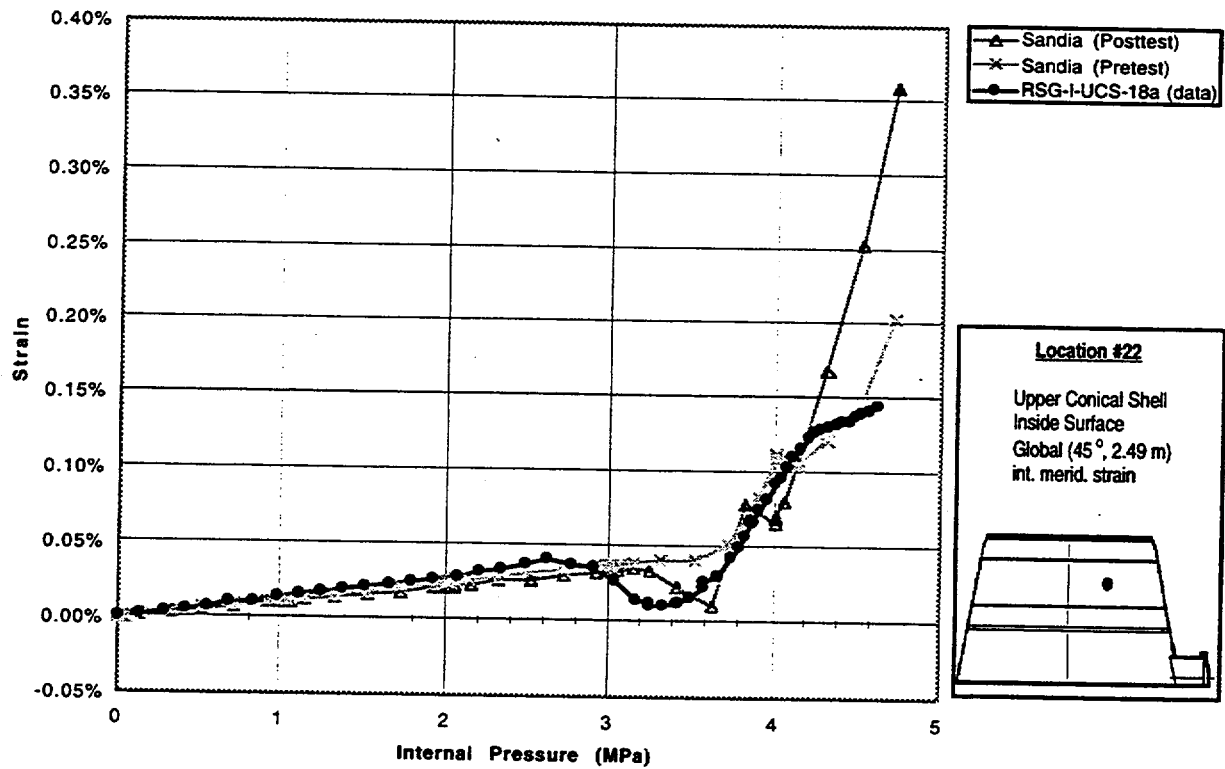


Fig.A.22 Standard Output Location #22

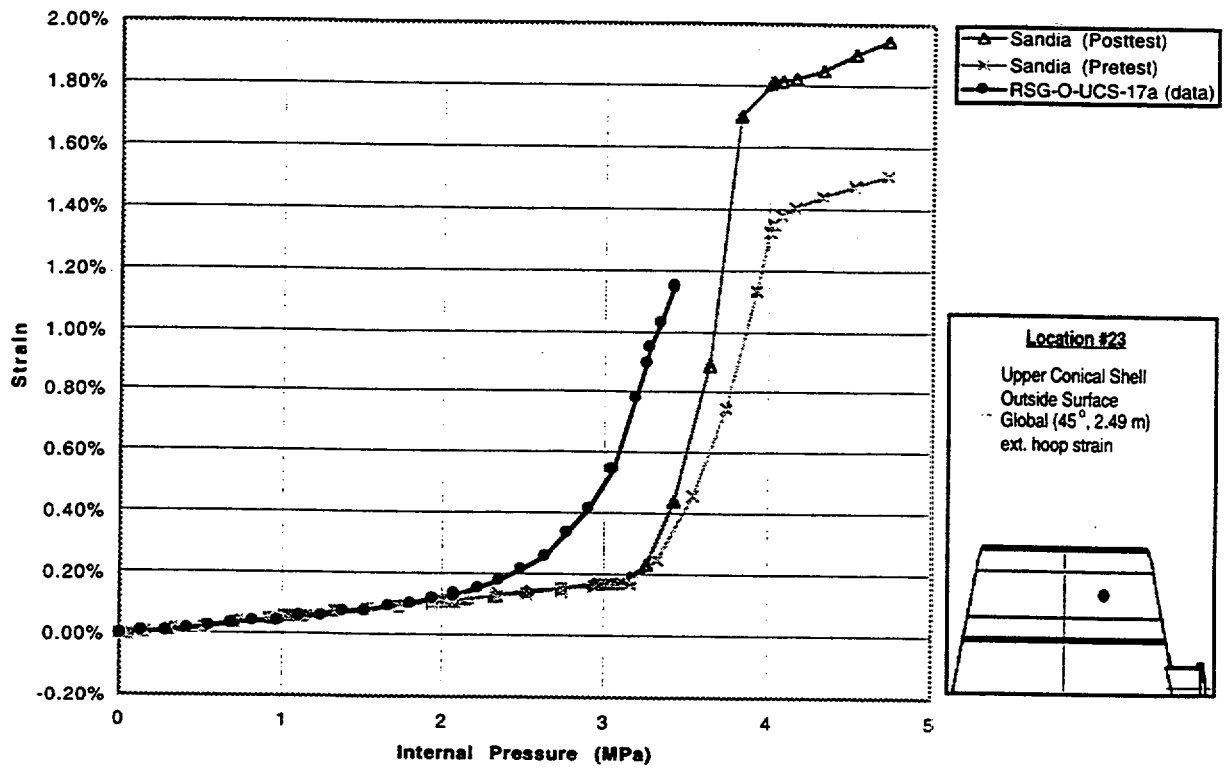


Fig.A.23 Standard Output Location #23

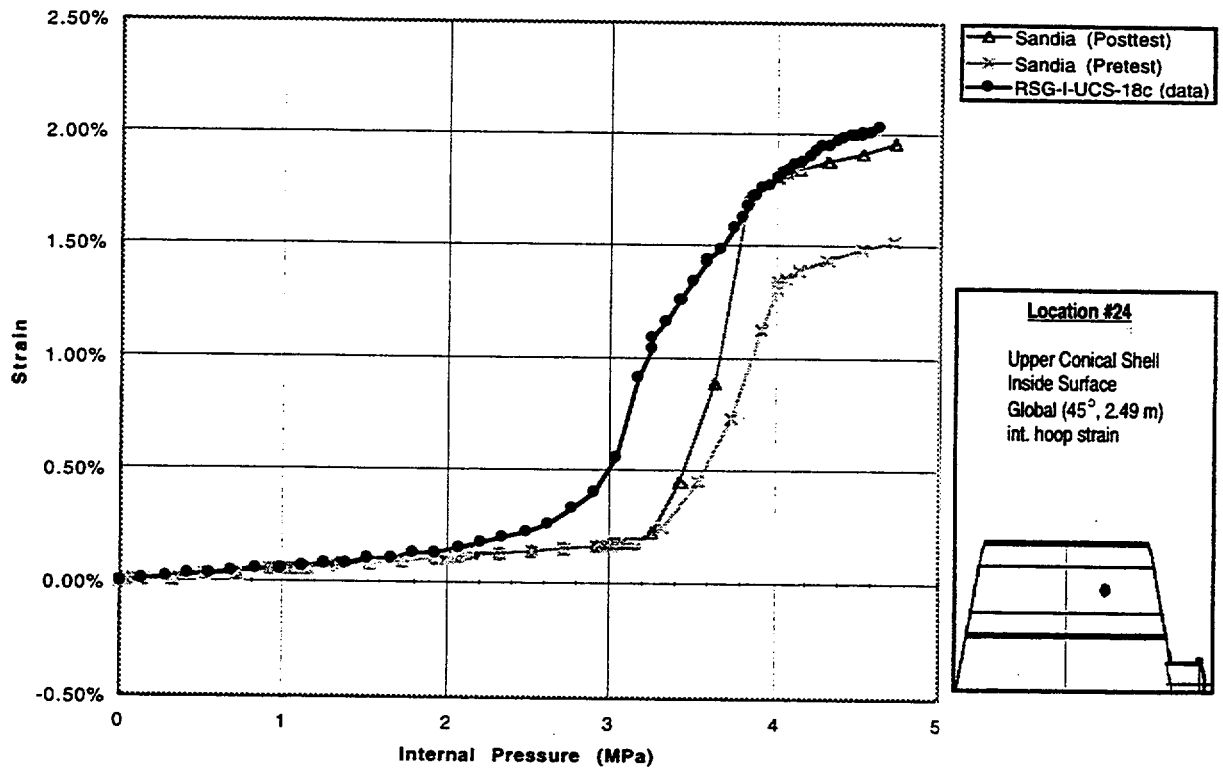


Fig.A.24 Standard Output Location #24

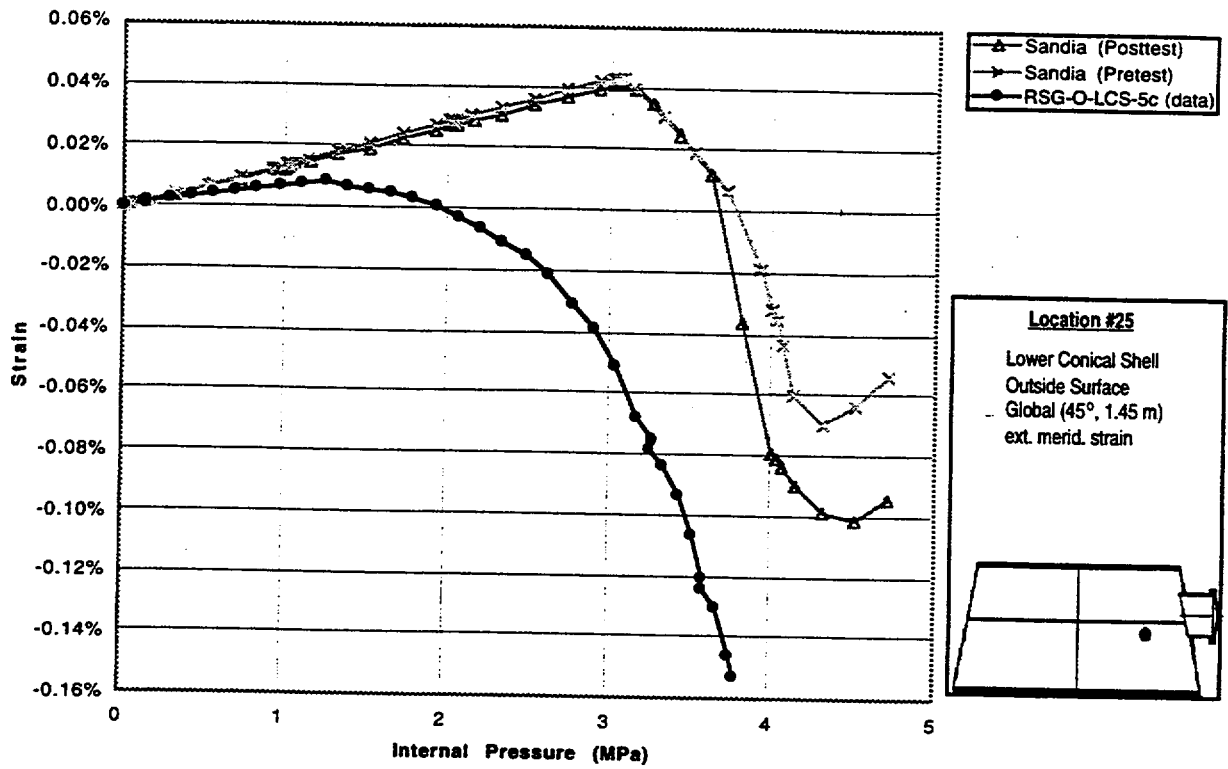


Fig.A.25 Standard Output Location #25

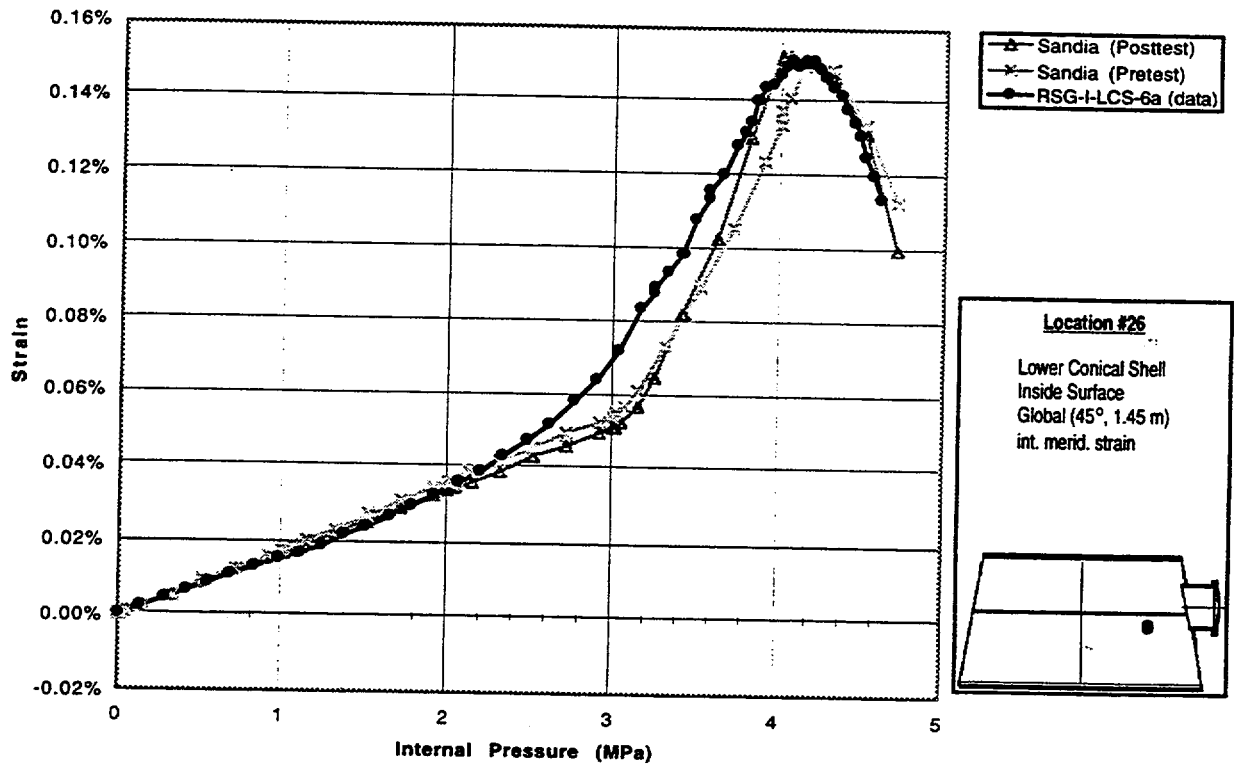


Fig.A.26 Standard Output Location #26

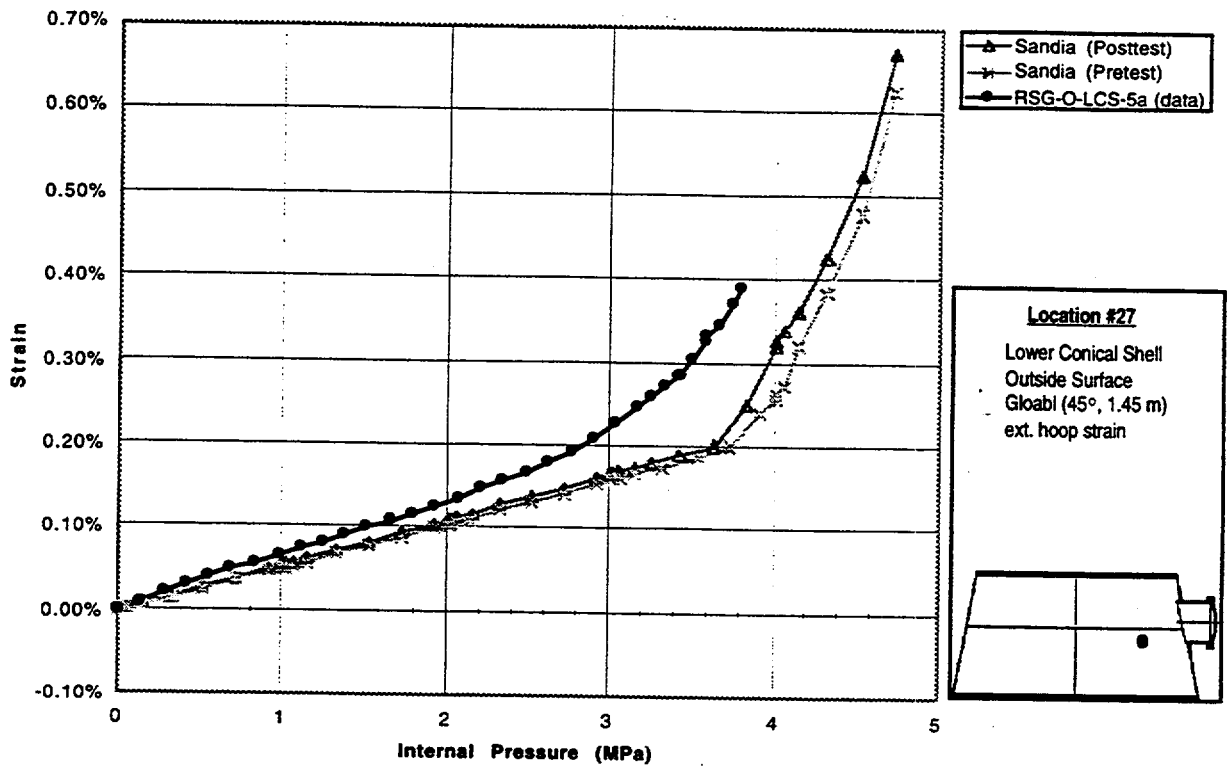


Fig.A.28 Standard Output Location #27

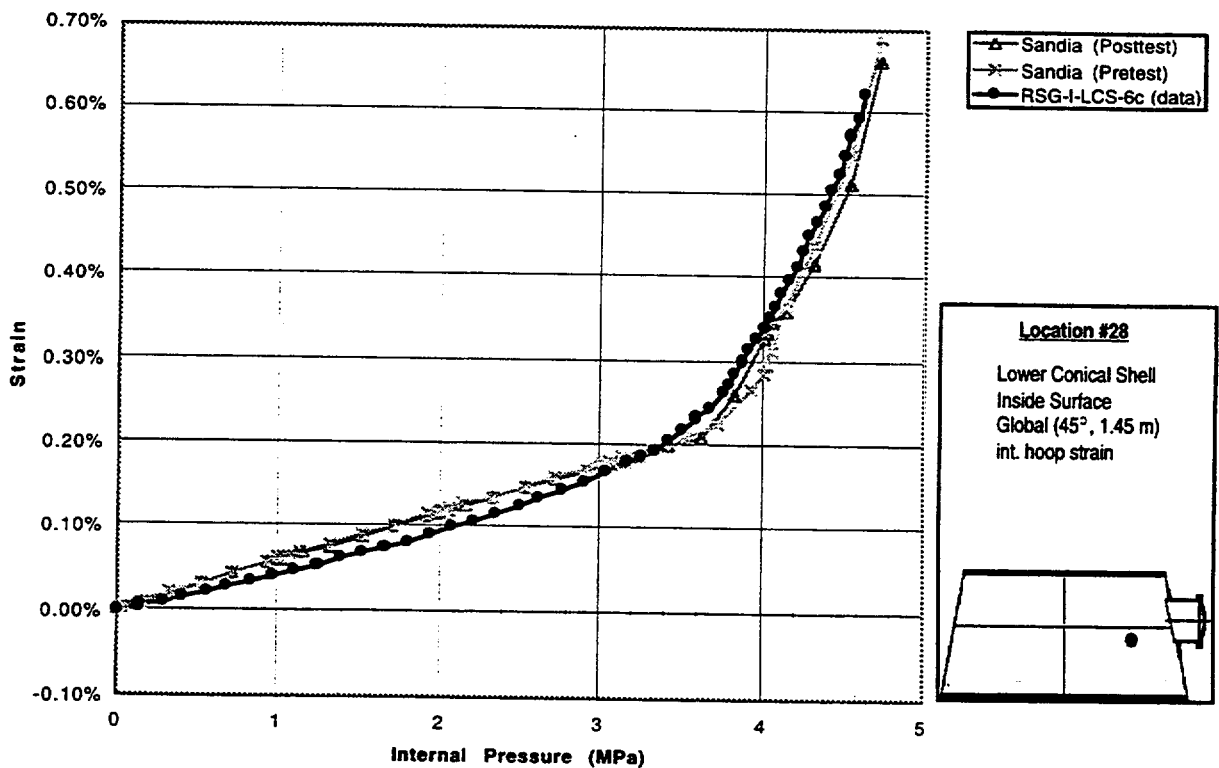


Fig.A.28 Standard Output Location #28

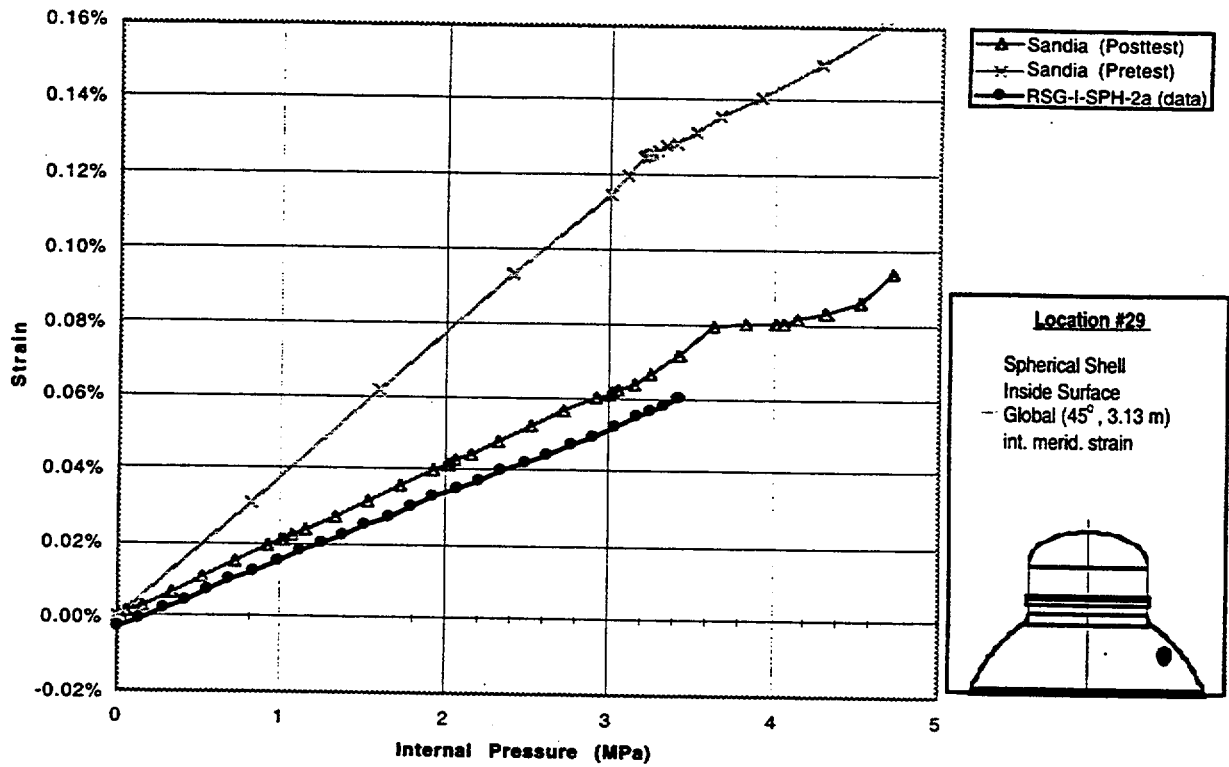


Fig.A.29 Standard Output Location #29

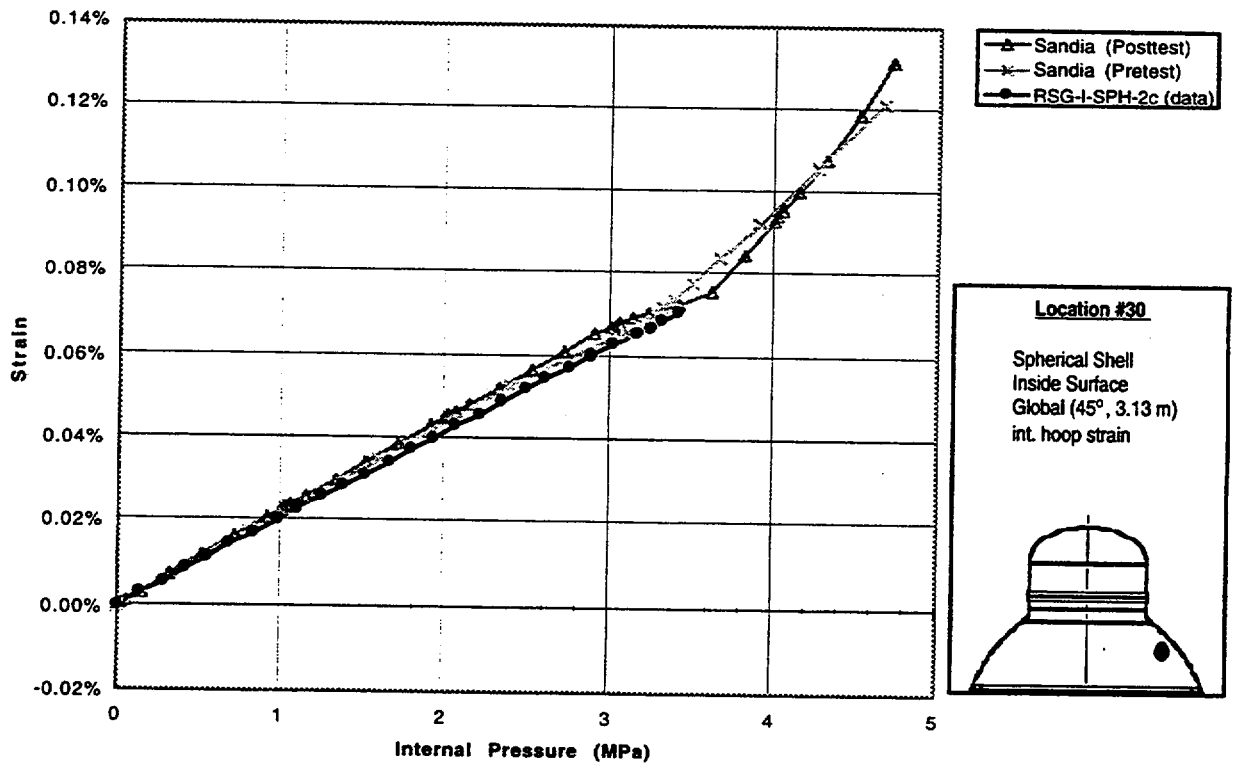


Fig.A.30 Standard Output Location #30

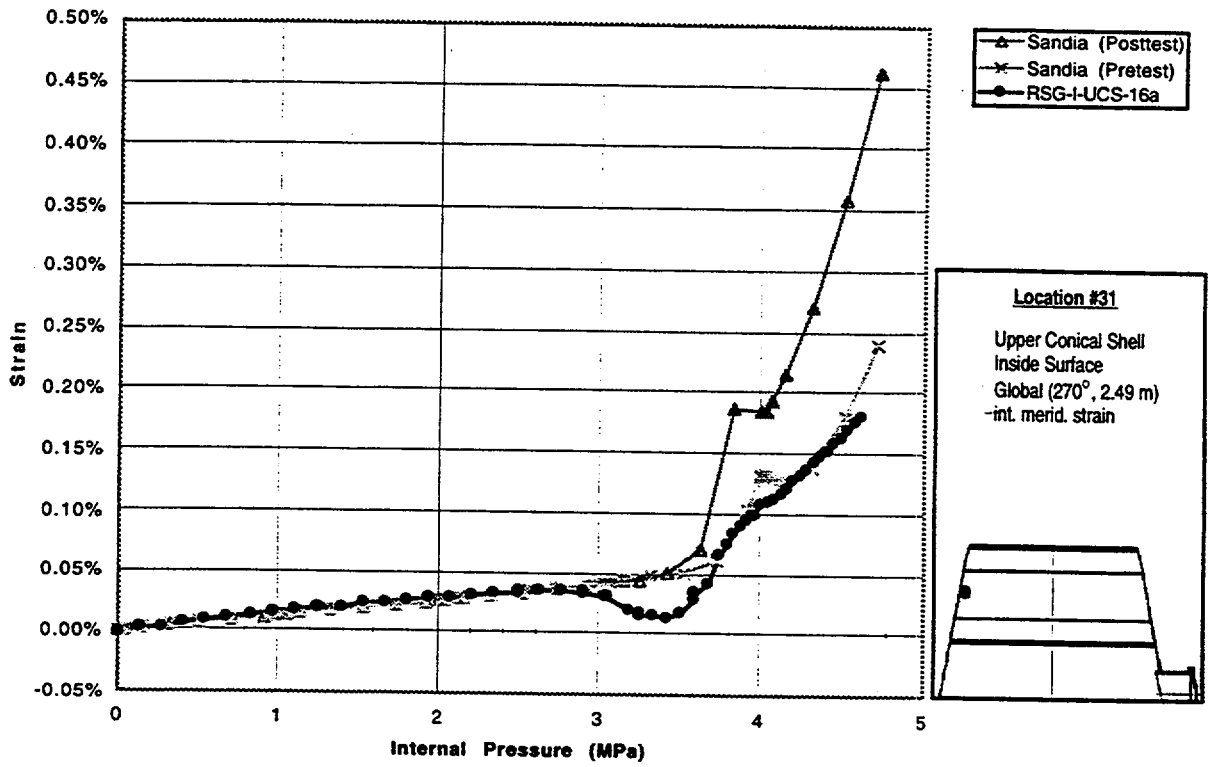


Fig.A.31 Standard Output Location #31

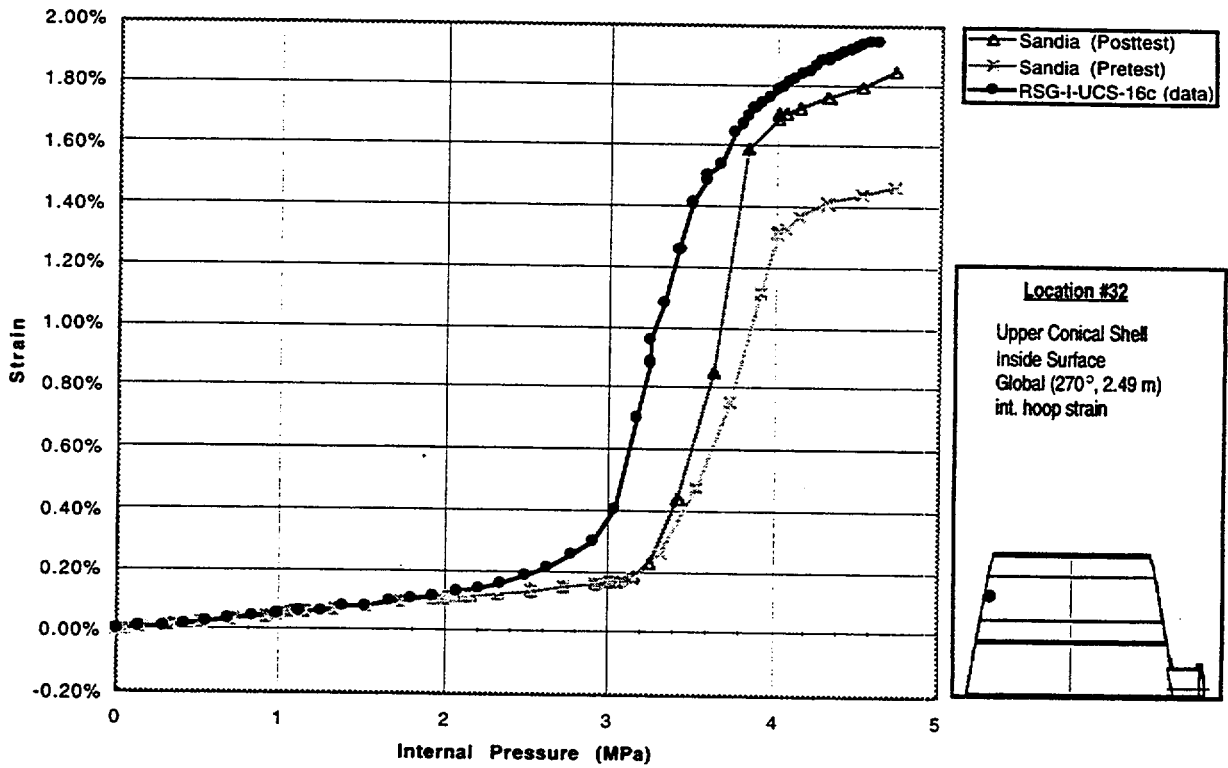


Fig.A.32 Standard Output Location #32

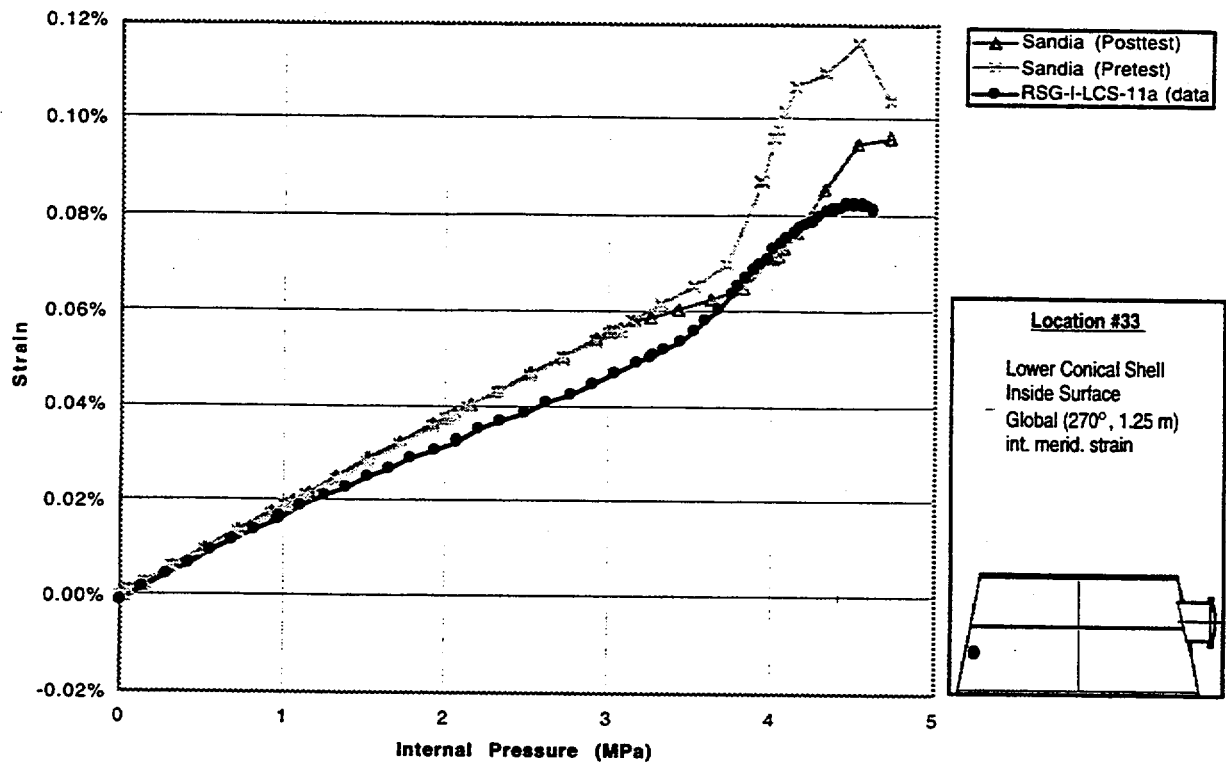


Fig.A.33 Standard Output Location #33

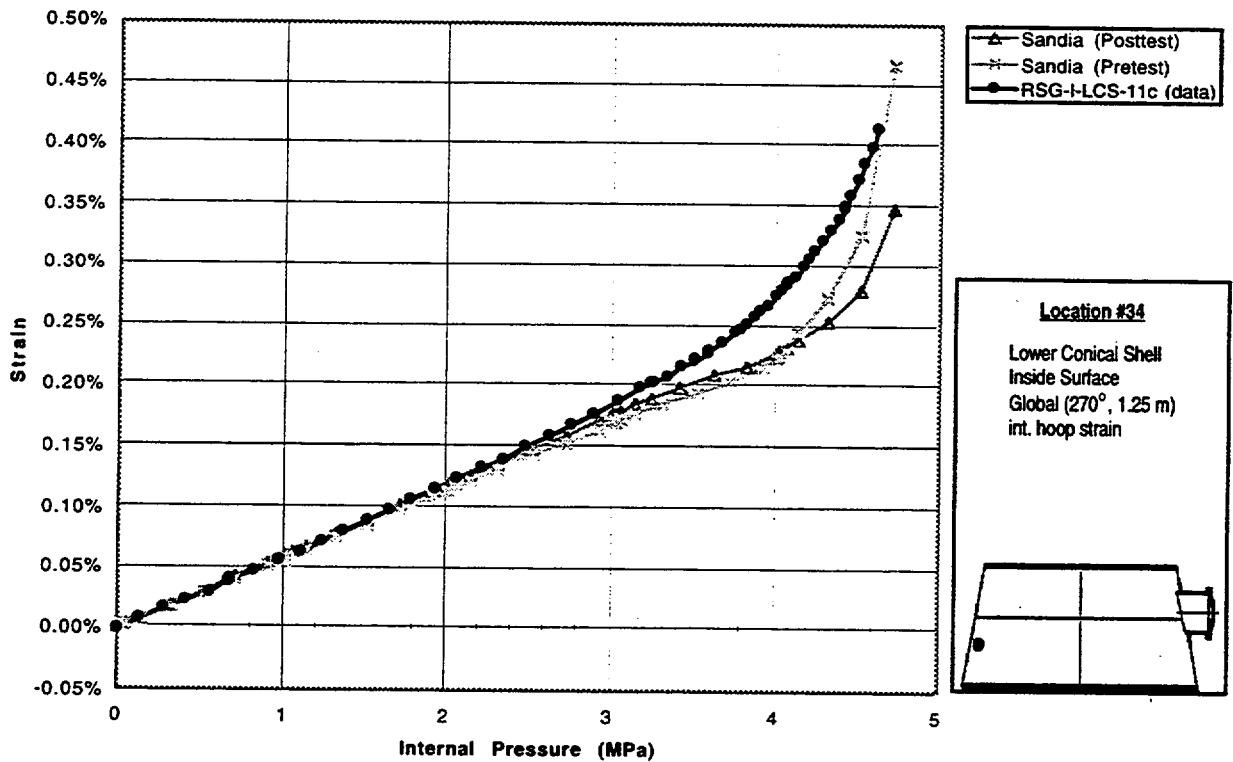


Fig.A.34 Standard Output Location #34

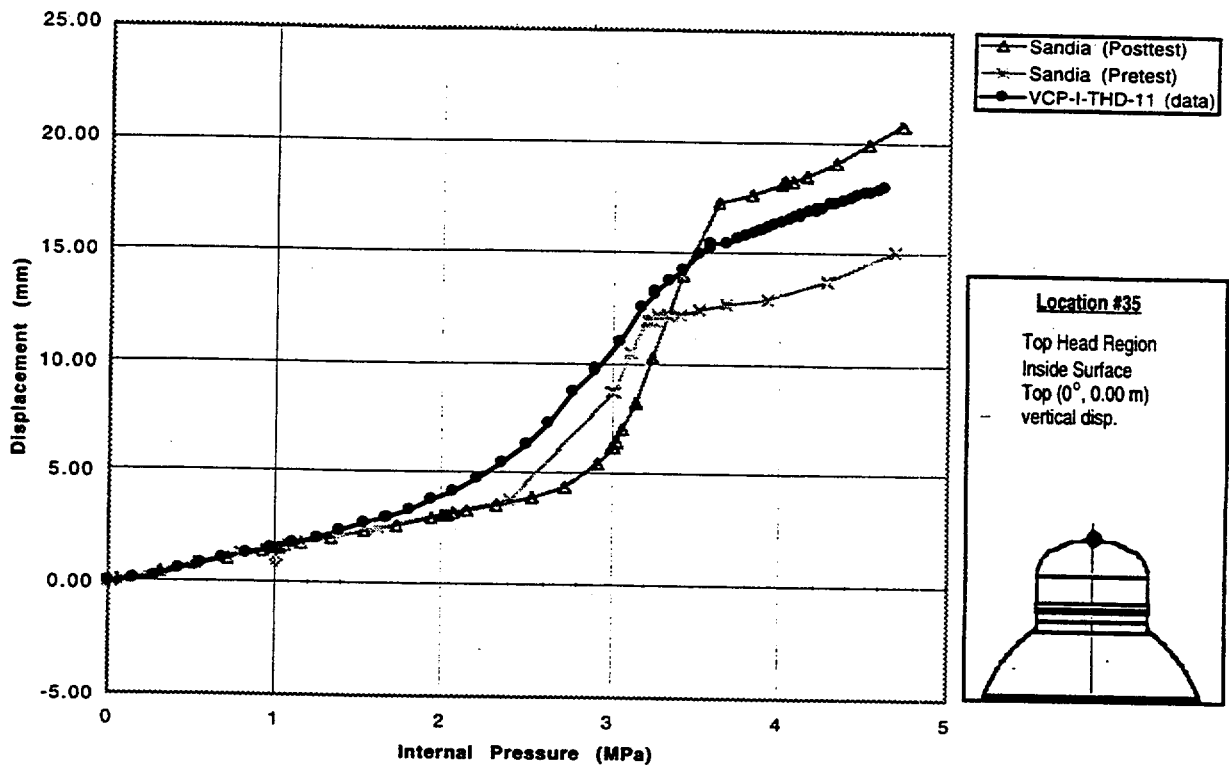


Fig.A.35 Standard Output Location #35

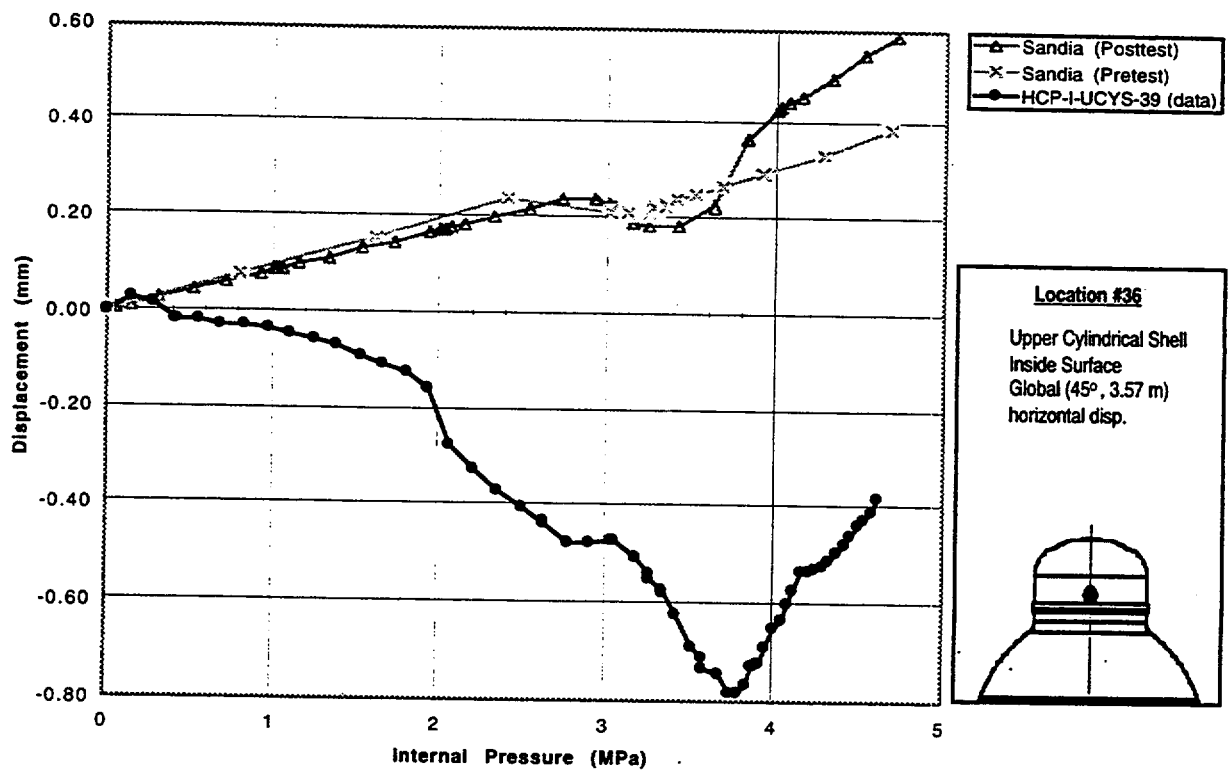


Fig.A.36a Standard Output Location #36 (interior displacement transducer)

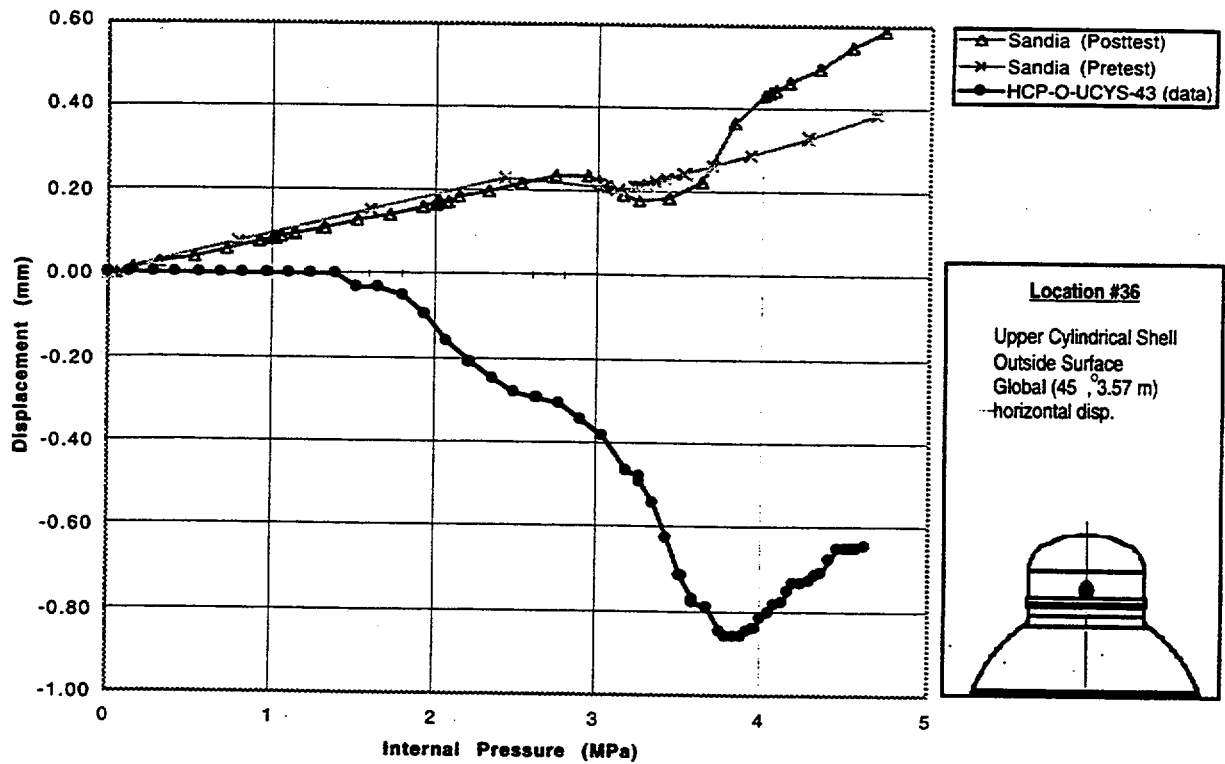


Fig.A.36b Standard Output Location #36 (exterior displacement transducer)

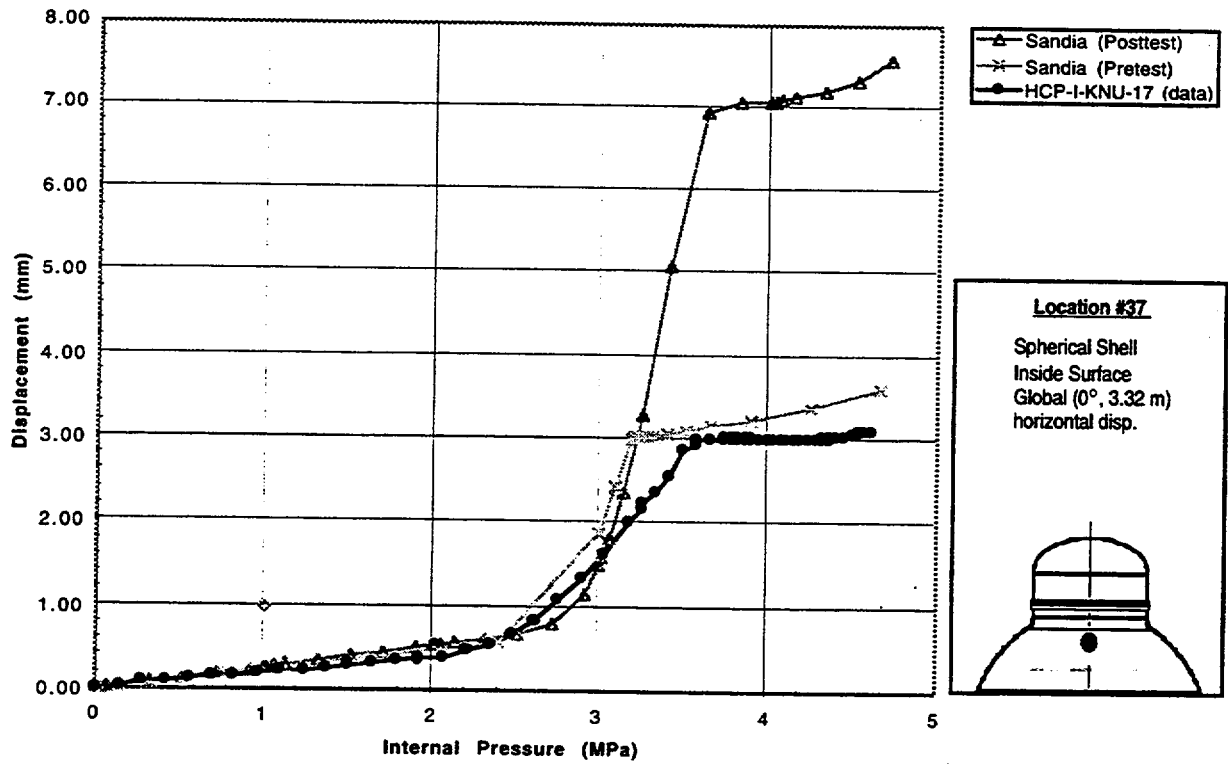


Fig.A.37 Standard Output Location #37

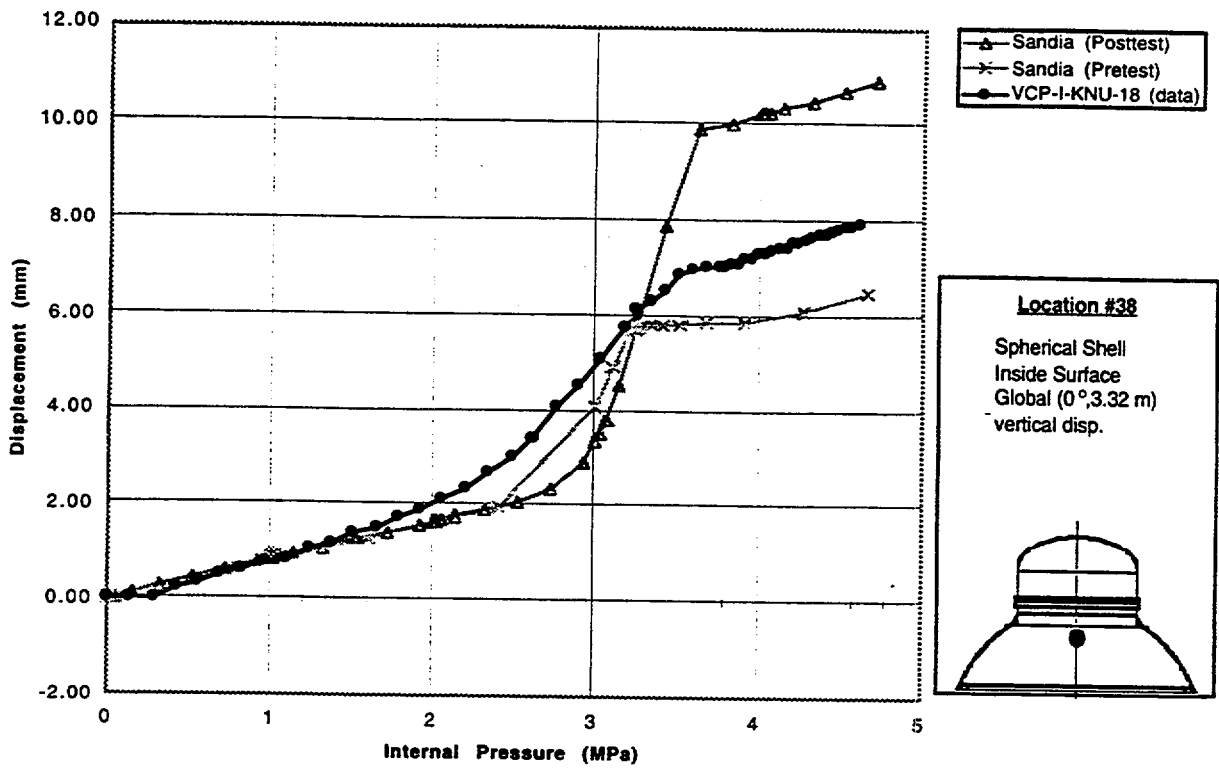


Fig.A.38 Standard Output Location #38

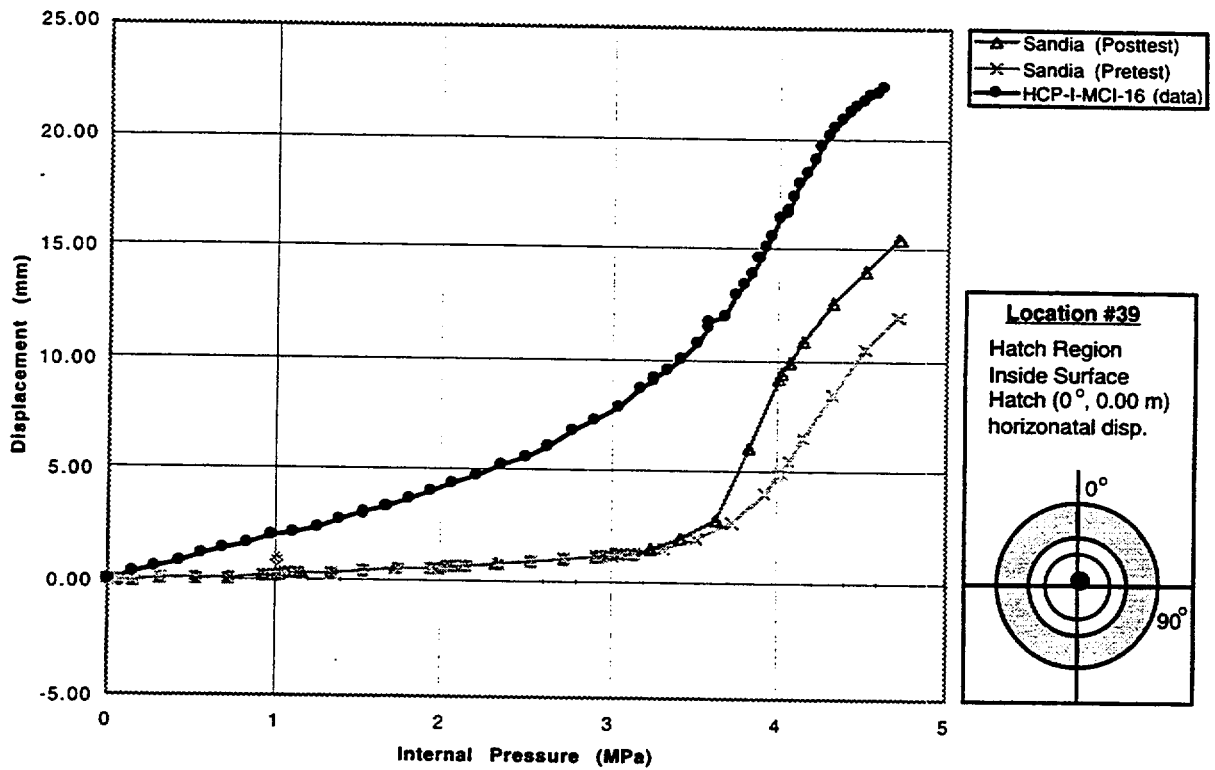


Fig.A.39 Standard Output Location #39

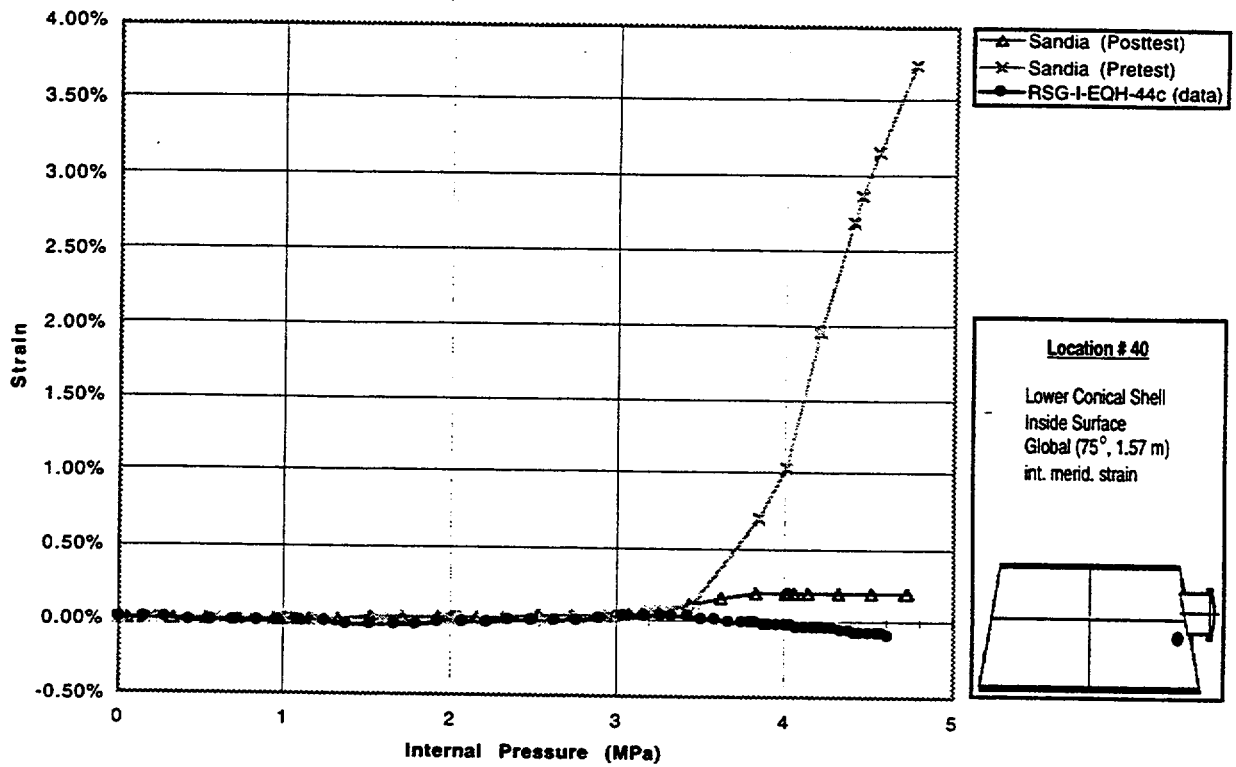


Fig.A.40 Standard Output Location #40

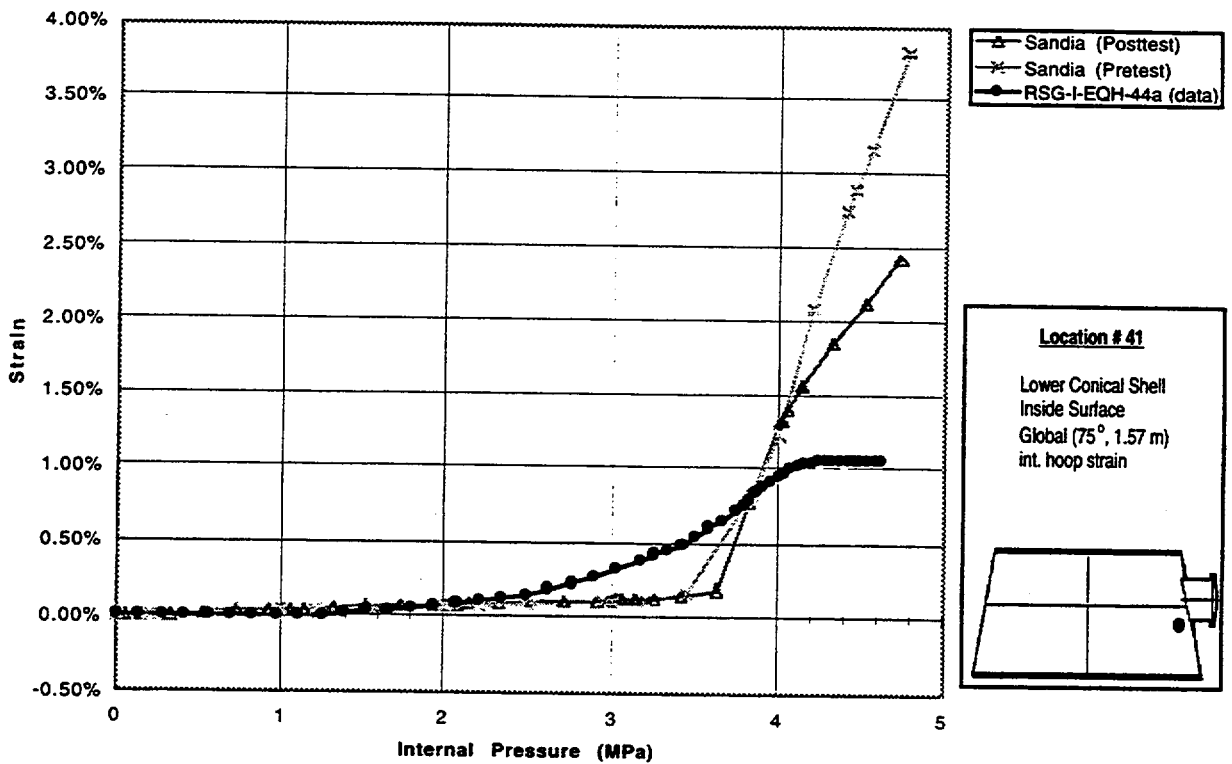


Fig.A.41 Standard Output Location #41

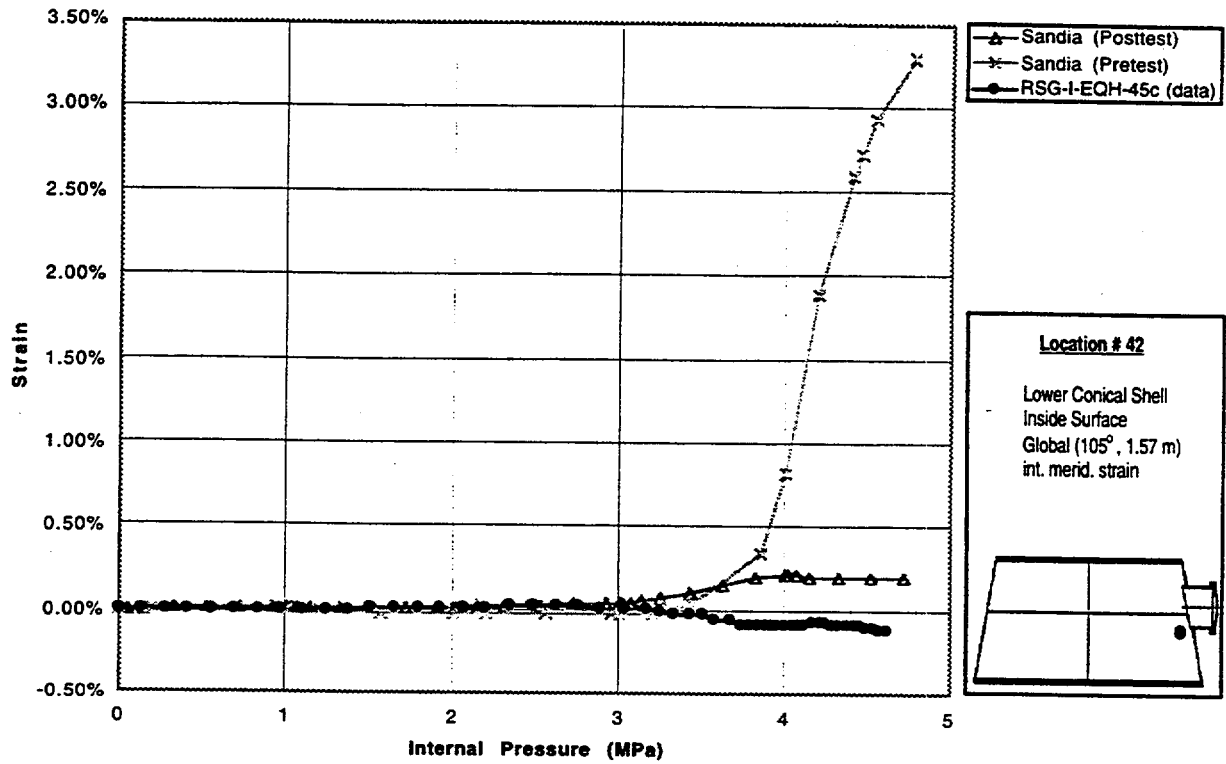


Fig.A.42 Standard Output Location #42

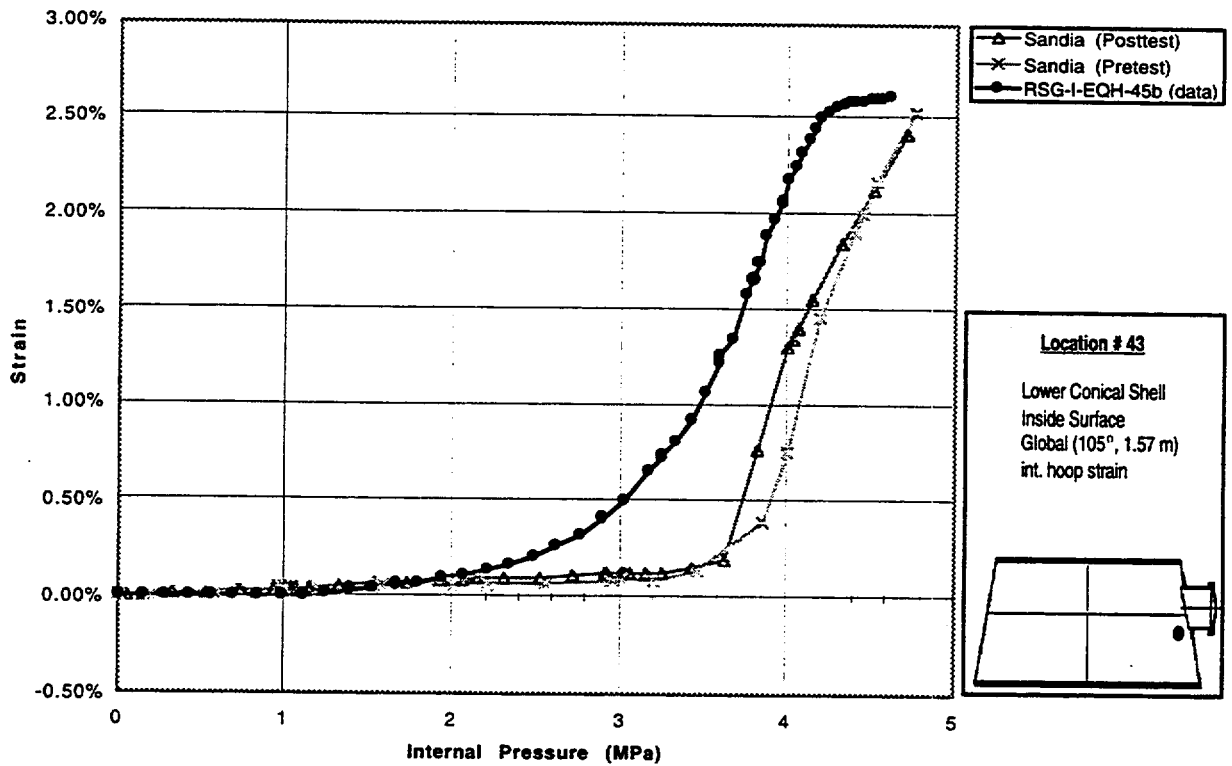


Fig.A.43 Standard Output Location #43

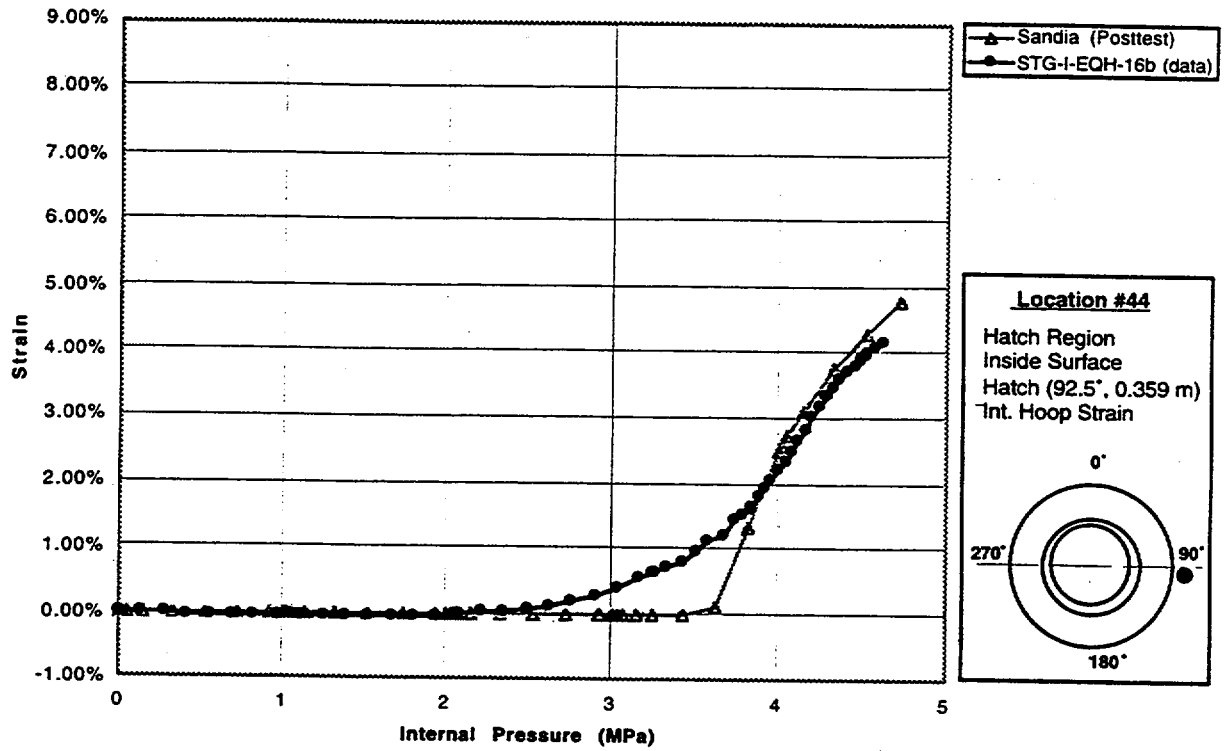


Fig.A.44 Standard Output Location #44

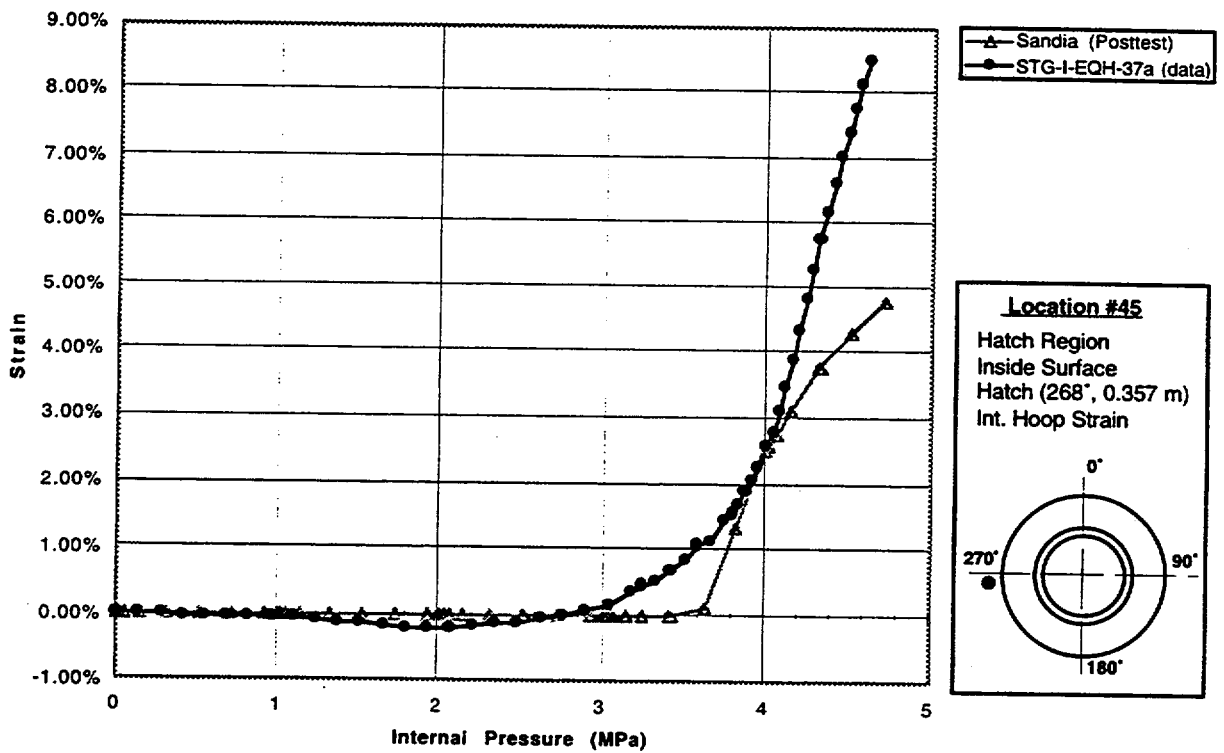


Fig.A.45 Standard Output Location #45

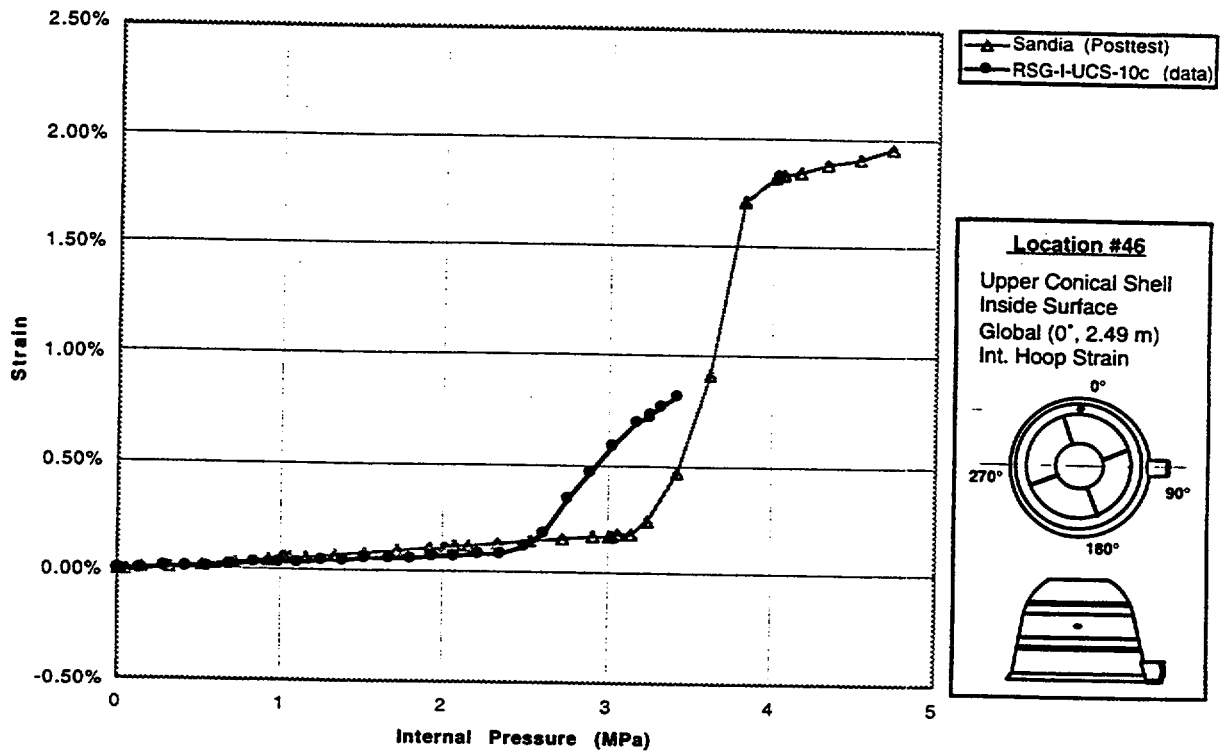


Fig.A.46 Standard Output Location #46

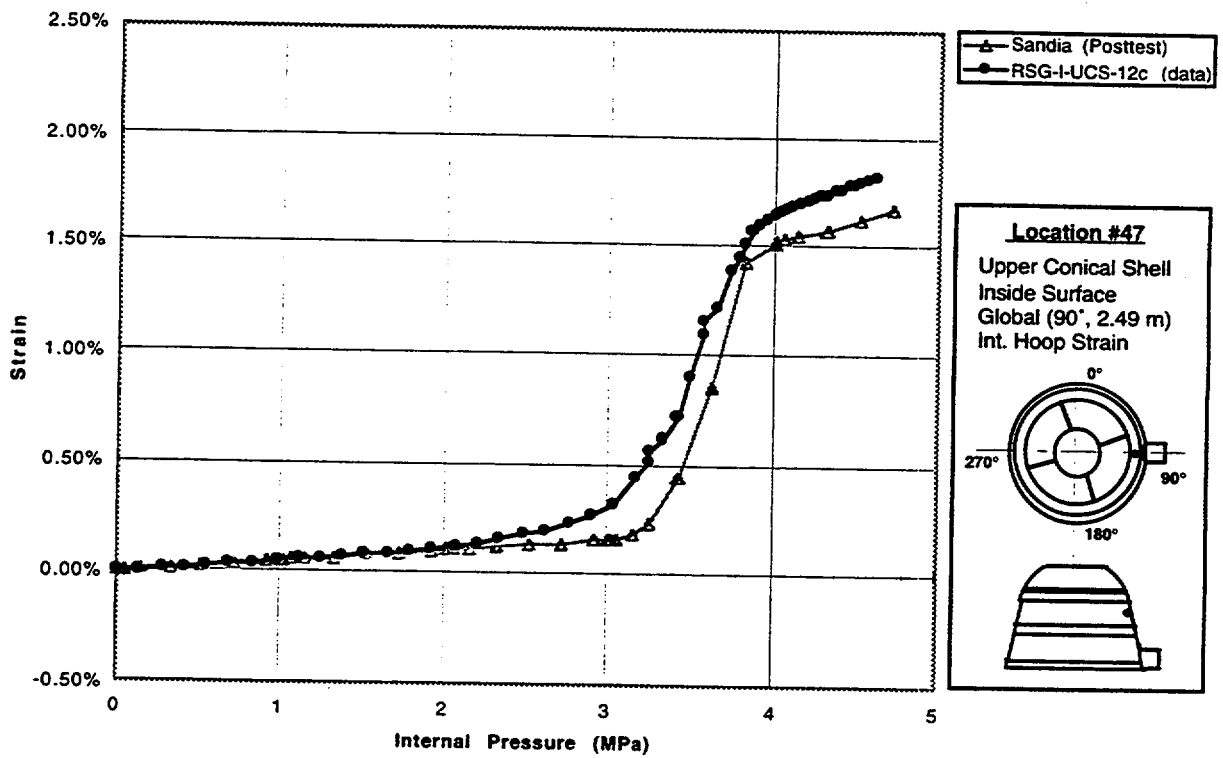


Fig.A.47 Standard Output Location #47

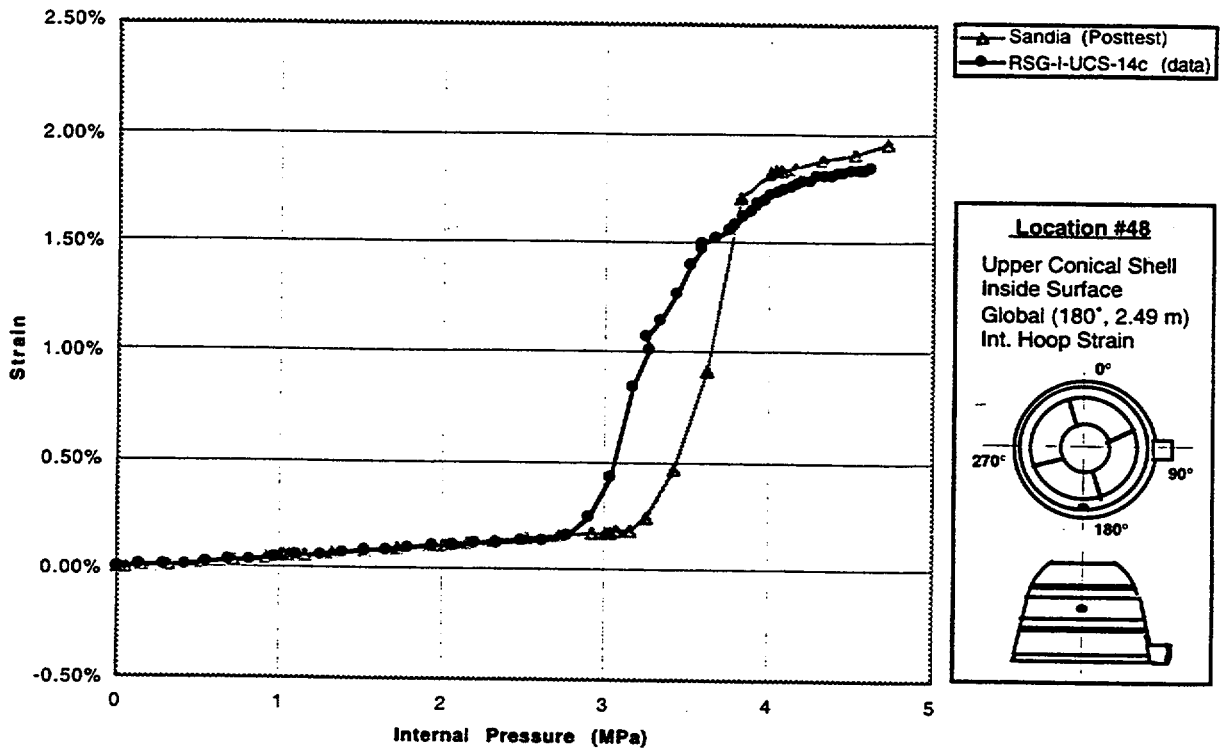


Fig.A.48 Standard Output Location #48

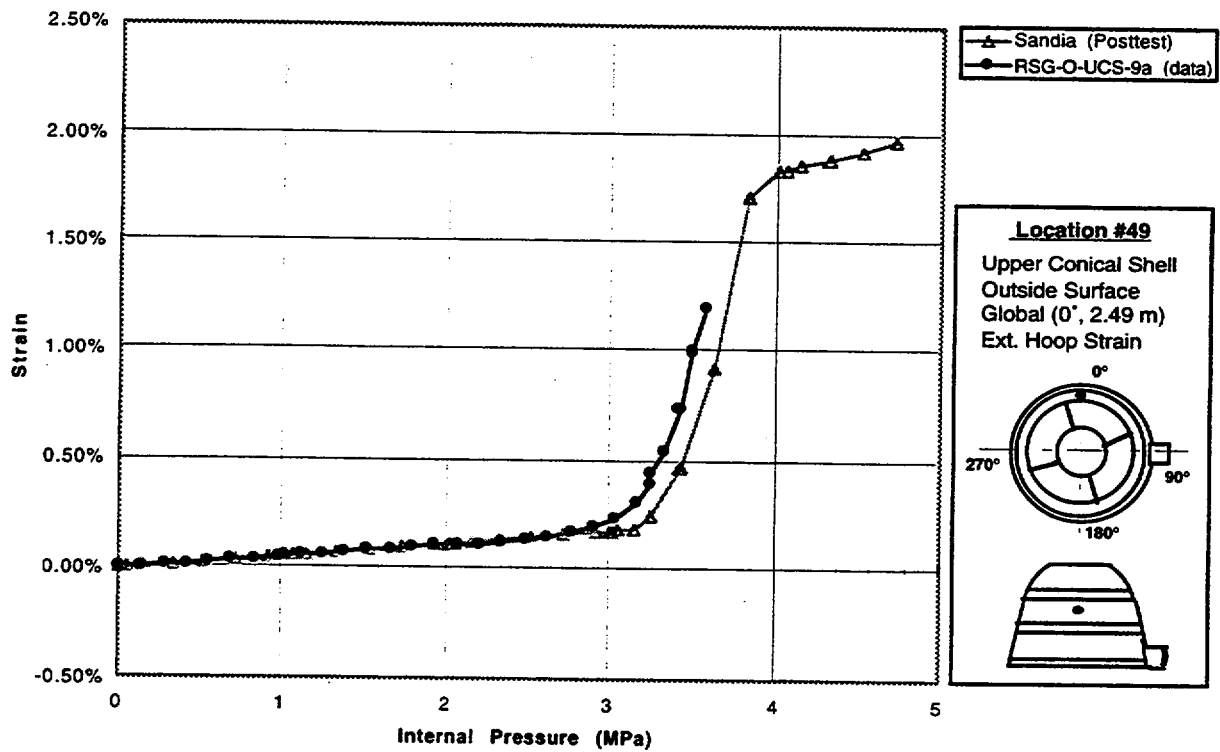


Fig.A.49 Standard Output Location #49

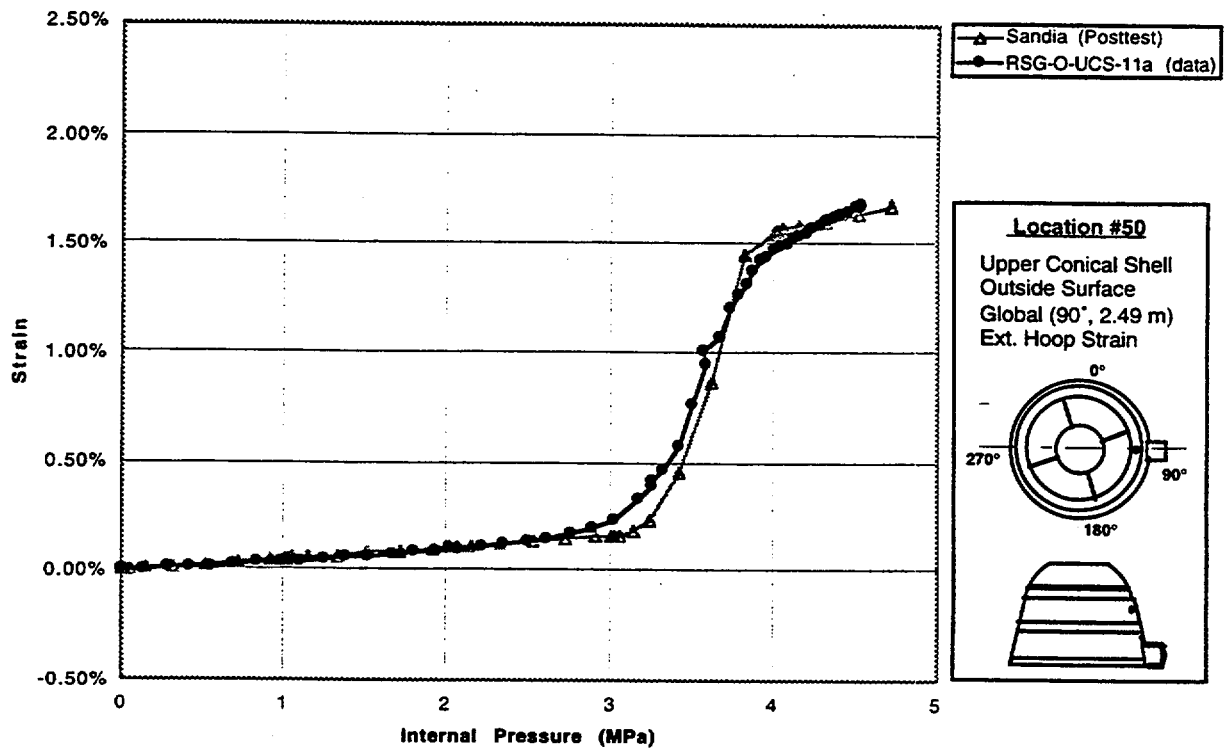


Fig.A.50 Standard Output Location #50

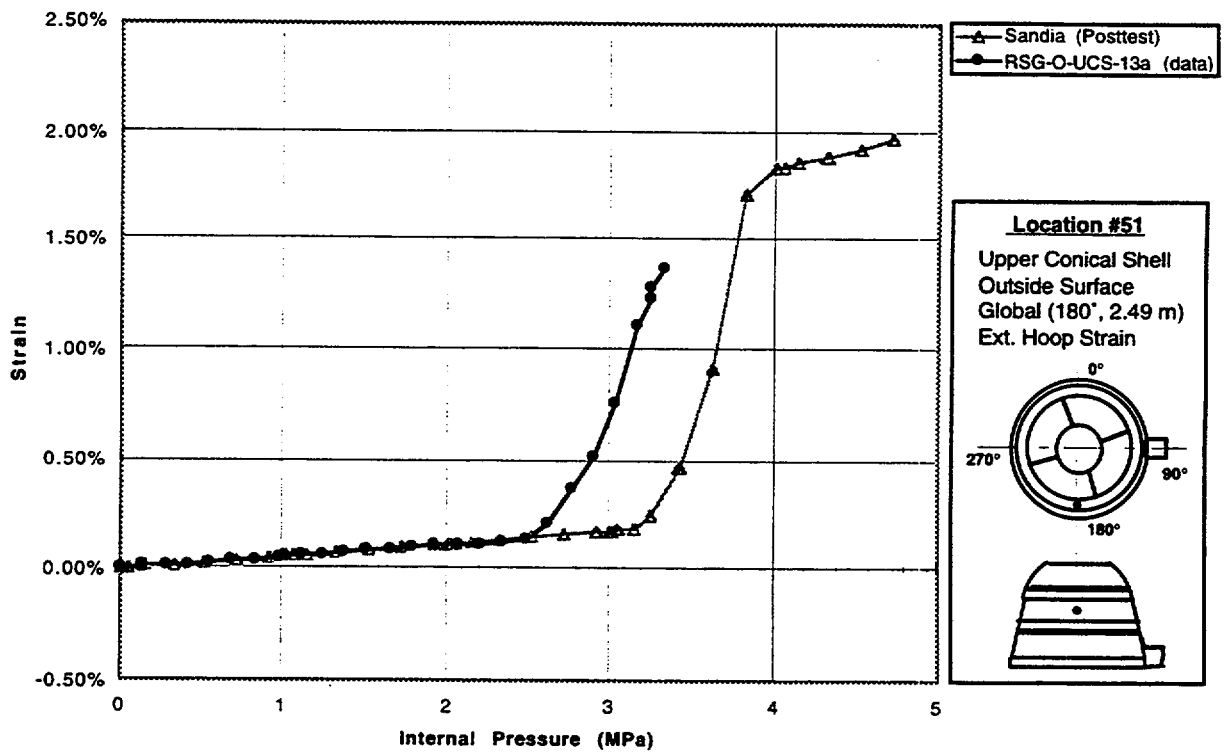


Fig.A.51 Standard Output Location #51

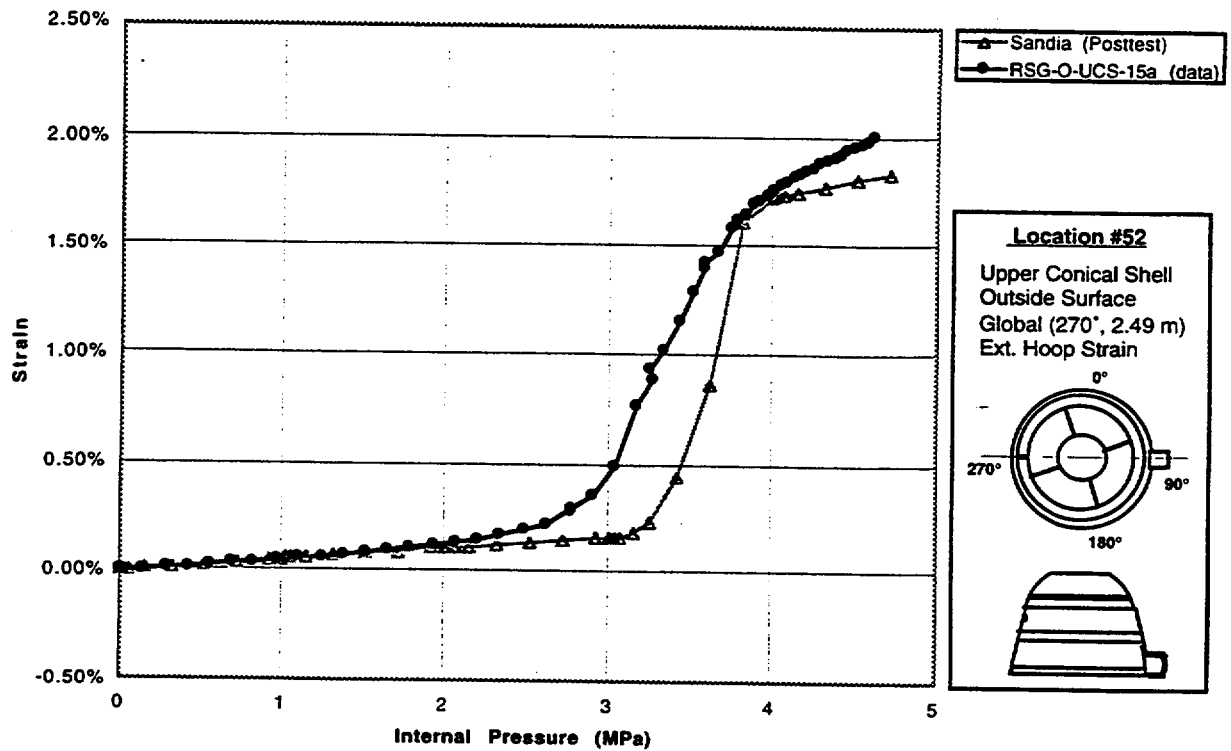
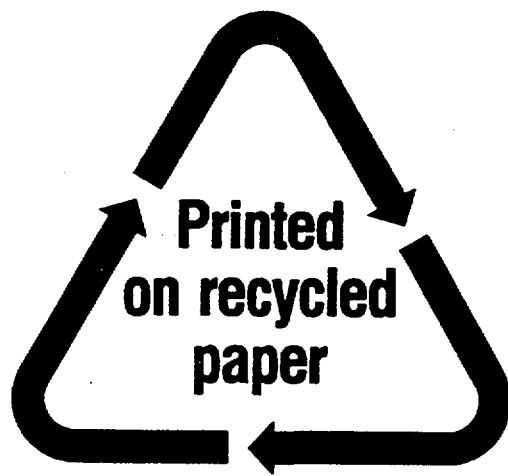


Fig.A.52 Standard Output Location #52

NRC FORM 335 (2-89) NRCM 1102, 3201, 3202	U.S. NUCLEAR REGULATORY COMMISSION	1. REPORT NUMBER (Assigned by NRC, Add Vol., Supp., Rev., and Addendum Numbers, if any.)				
BIBLIOGRAPHIC DATA SHEET (See instructions on the reverse)		NUREG/CR-5678 SAND98-2700				
2. TITLE AND SUBTITLE		3. DATE REPORT PUBLISHED				
Round Robin Posttest Analysis of a Steel Containment Vessel Model		<table border="1" style="width: 100%;"> <tr> <td style="width: 50%; text-align: center;">MONTH</td> <td style="width: 50%; text-align: center;">YEAR</td> </tr> <tr> <td style="text-align: center;">January</td> <td style="text-align: center;">2000</td> </tr> </table>	MONTH	YEAR	January	2000
MONTH	YEAR					
January	2000					
5. AUTHOR(S)		4. FIN OR GRANT NUMBER				
V.K. Luk, E.W. Klamerus		A1401				
5. AUTHOR(S)		6. TYPE OF REPORT				
V.K. Luk, E.W. Klamerus		Technical				
8. PERFORMING ORGANIZATION - NAME AND ADDRESS (If NRC, provide Division, Office or Region, U.S. Nuclear Regulatory Commission, and mailing address; if contractor, provide name and mailing address.)		7. PERIOD COVERED (Inclusive Dates)				
Sandia National Laboratories Albuquerque, NM 87185-0744		1/97 to 10/98				
9. SPONSORING ORGANIZATION - NAME AND ADDRESS (If NRC, type "Same as above"; if contractor, provide NRC Division, Office or Region, U.S. Nuclear Regulatory Commission, and mailing address.)						
Systems Safety Department Nuclear Power Engineering Corporation 17-1, 3-Chome, Toranomon, Minato-Ku Tokyo 105, Japan	Division of Engineering Technology Office of Nuclear Regulatory Research U.S. Nuclear Regulatory Commission Washington, DC 20555-0001					
10. SUPPLEMENTARY NOTES						
T. Hashimoto, NUPEC Project Manager	J.F. Costello, NRC Project Manager					
11. ABSTRACT (200 words or less)						
<p>The Nuclear Power Engineering Corporation (NUPEC) of Japan and the U.S. Nuclear Regulatory Commission (NRC) are co-sponsoring and jointly funding a containment integrity research project at Sandia National Laboratories (SNL) to conduct a failure test of a steel containment vessel (SCV) model and contact structure assembly. The SCV model, representative of an improved Mark-II Boiling Water Reactor (BWR) containment vessel, is scaled 1:10 in geometry and 1:4 in shell thickness. The contact structure, a thick bell-shaped steel shell, provides a simplified representation of a concrete reactor shield building in the actual plant. The failure test of the SCV model was conducted at SNL on December 11-12, 1996 to provide data on the structural response of the SCV model up to its failure in order to validate analytical modeling, to find its pressure capacity, and to observe the failure mode and mechanisms.</p> <p>Eight international groups participated in a Round Robin pretest analysis effort to predict the structural response of the SCV model under pressurization. Their analysis approaches and results were documented in NUREG/CR-6517. Seven of the eight participants also performed the posttest analyses to simulate the structural response of the SCV model at 52 specified locations, the failure pressure, and the failure location and mechanisms. A posttest meeting of all participants was held on May 20-21, 1998 to discuss modeling approaches and lessons learned. This report described the posttest analysis models and results submitted by the seven groups.</p>						
12. KEY WORDS/DESCRIPTORS (List words or phrases that will assist researchers in locating the report.)		13. AVAILABILITY STATEMENT				
Steel Containment Vessel, Failure Test, Model Analysis, International Participants, Failure Pressure and Mechanisms		unlimited				
12. KEY WORDS/DESCRIPTORS (List words or phrases that will assist researchers in locating the report.)		14. SECURITY CLASSIFICATION				
12. KEY WORDS/DESCRIPTORS (List words or phrases that will assist researchers in locating the report.)		(This Page)				
12. KEY WORDS/DESCRIPTORS (List words or phrases that will assist researchers in locating the report.)		unclassified				
12. KEY WORDS/DESCRIPTORS (List words or phrases that will assist researchers in locating the report.)		(This Report)				
12. KEY WORDS/DESCRIPTORS (List words or phrases that will assist researchers in locating the report.)		unclassified				
12. KEY WORDS/DESCRIPTORS (List words or phrases that will assist researchers in locating the report.)		15. NUMBER OF PAGES				
12. KEY WORDS/DESCRIPTORS (List words or phrases that will assist researchers in locating the report.)		16. PRICE				



Federal Recycling Program

**UNITED STATES
NUCLEAR REGULATORY COMMISSION**
WASHINGTON, D.C. 20555-0001



SPECIAL STANDARD MAIL
POSTAGE AND FEES PAID
USNRC
PERMIT NO. G-67